Nam-Gyu Park
Michael Grätzel
Tsutomu Miyasaka
Editors

Organic-Inorganic Halide Perovskite Photovoltaics

From Fundamentals to Device Architectures

Springer

Organic-Inorganic Halide Perovskite Photovoltaics

Nam-Gyu Park · Michael Grätzel
Tsutomu Miyasaka
Editors

Organic-Inorganic Halide Perovskite Photovoltaics

From Fundamentals to Device Architectures

Springer

Editors
Nam-Gyu Park
Sungkyunkwan University
Suwon
Korea, Republic of (South Korea)

Michael Grätzel
École Polytechnique Fédérale de Lausanne
Lausanne
Switzerland

Tsutomu Miyasaka
Graduate School of Engineering
Toin University of Yokohama
Yokohama
Japan

ISBN 978-3-319-35112-4 ISBN 978-3-319-35114-8 (eBook)
DOI 10.1007/978-3-319-35114-8

Library of Congress Control Number: 2016942016

Printed on acid-free paper

This Springer imprint is published by Springer Nature
The registered company is Springer International Publishing AG Switzerland

Preface

Photovoltaics, converting light to electricity, are one of most promising alternatives to fossil fuels. Since the discovery of photovoltaic effect from selenium by 19-year-old Edmund Becquerel in 1839, several kinds of photovoltaic materials have been discovered and their photovoltaic performances have been studied. Silicon started with power conversion efficiency (PCE) of 4.5 % in 1954, developed by Bell Labs researchers Pearson, Chapin, and Fuller, which has now surpassed 25 %. To date, the best PCE was found from GaAs, approaching 29 % with single junction structure. Chalcogenide materials such as CIGS and CdTe exhibited promising PCEs of about 22 %. In developing solar cells, materials and processing costs are as important as PCE. This means that new photovoltaic materials being able to produce low-cost electricity are of crucial importance to both academy and industry.

Organic–inorganic halide perovskite is very promising candidate for future photovoltaic society because its PCE now reached over 22 % that can be available from inexpensive and high-throughput solution process. Halide perovskite photovoltaics were introduced in 2009 by Tsutomu Miyasaka and the currently studied solid-state perovskite solar cells are based on the invention of solid-state perovskite-sensitized solar cell in 2012 by Nam-Gyu Park and Michael Grätzel. However, the origin of superb photovoltaic performance is still questionable. Structural diversity is advantage in perovskite photovoltaics, but it is still arguable which device structure is suitable for less I–V hysteresis and long-term stability. Understanding fundamentals and device architectures may lead to answers to these questions, which motivated us to write this book. In Chaps. 1 and 2, fundamentals of halide perovskites are described based on theoretical point of view. Maximum efficiency can be expected from Chap. 3. Device physics and ion migration behavior in halide perovskite are understood in Chaps. 4 through 6. More understanding on charge transport and inhibition will be expected from Chaps. 7 and 8. In Chap. 9, device and materials engineering are described to achieve high-efficiency perovskite solar cells. I–V hysteresis and stability issues will be treated in Chap. 10. Perovskite solar cell is promising resource for hydrogen evolution due to

high-voltage characteristics, which is described in Chap. 11. Perovskite is excellent light absorber even in organic bulk heterojunction-type solar cell, which is presented in Chap. 12. Intrinsic flexibility is one of strong points in halide perovskite, which is suitable for flexible solar cell as can be found in Chap. 13. Selective contact materials are issued in terms of hysteresis and stability. Inorganic hole transporting layers may provide insight into device engineering, which is described in Chap. 14. Since this book covers from fundamentals to device engineering, we hope that this book contributes to both academy and industry.

Suwon, Korea, Republic of (South Korea) Nam-Gyu Park
Lausanne, Switzerland Michael Grätzel
Yokohama, Japan Tsutomu Miyasaka

Contents

Molecular Motion and Dynamic Crystal Structures of Hybrid Halide Perovskites

Jarvist M. Frost and Aron Walsh

1 Introduction

While inorganic lead halides have been studied since the nineteenth century [1] and organic–inorganic halides have been of interest since the early twentieth century, [2] the first report of perovskite-structured hybrid halide compounds was studied by Weber in 1978 [3, 4]. He reported both $CH_3NH_3PbX_3$ (X = Cl, Br, I) and the $CH_3NH_3SnBr_{1-x}I_x$ alloy. In the subsequent decades, these materials were studied in the context of their unusual chemistry and physics, [5–7] with the first solar cell appearing in 2009 [8].

The notable achievements in the photovoltaic applications of hybrid perovskites have been the subject of many reviews. In this chapter we introduce the basics of the perovskite crystal structure and present the unique dynamic behaviour of the hybrid organic–inorganic materials, which underpins their performance in photovoltaic devices that will be discussed in the later chapters. The text is drawn from several of our earlier publications and perspectives [9–18].

2 Perovskite

The word 'perovskite' refers to the mineral form of $CaTiO_3$. It adopts a crystal structure consisting of corner-sharing TiO_6 octahedra in three dimensions, with Ca occupying the cuboctahedral cavity in each unit cell. The same crystal structure is also found for a wide range of materials with ABX_3 stoichiometry, with two notable cases being $SrTiO_3$ and $BaTiO_3$. Examples of insulating, semiconducting and

J.M. Frost · A. Walsh (✉)
Department of Chemistry, Centre for Sustainable Chemical Technologies,
University of Bath, Claverton Down, Bath BA2 7AY, UK
e-mail: a.walsh@bath.ac.uk

N.-G. Park et al. (eds.), *Organic-Inorganic Halide Perovskite Photovoltaics*,
DOI 10.1007/978-3-319-35114-8_1

superconducting perovskite structured materials are known. These materials are the archetypal systems for phases transitions with accessible cubic, tetragonal, orthorhombic, trigonal and monoclinic polymorphs depending on the tilting and rotation of the BX_3 polyhedra in the lattice [19]. Reversible phase changes can be induced by a range of external stimuli including temperature, pressure and magnetic or electric fields.

Within the formal stoichiometry of ABX_3, charge balancing ($q^A + q^B + 3q^X = 0$) can be achieved in a variety of ways. For metal oxide perovskites (ABO_3), the formal oxidation states of the two metals must sum to six ($q^A + q^B = -3q^O = 6$). I-V-O_3, II-IV-O_3 and III-III-O_3 perovskites are known with common examples being $KTaO_3$, $SrTiO_3$ and $GdFeO_3$. The range of accessible materials can be extended by partial substitution on the anion sublattice, e.g. in the formation of oxynitride and oxyhalide perovskites. With substitution on the metal sublattice, double, triple and quadruple perovskites can be formed.

For halide perovskites, the oxidation states of the two cations must sum to three ($q^A + q^B = -3q^X = 3$), so the only viable ternary combination is I-II-X_3, e.g. $CsSnI_3$. In hybrid halide perovskites such as $CH_3NH_3PbI_3$, a divalent inorganic cation is present and the monovalent metal is replaced by an organic cation of equal charge as illustrated in Fig. 1. In principle, any molecular cation could be used, once there is sufficient space to fit it within the cavity. If the cation size is too large, then the three-dimensional (3D) perovskite network is broken, as demonstrated in the series of hybrid structures with lower dimensionality in the inorganic networks [20]. For layered structures, the crystal properties become highly anisotropic with larger carrier masses and stronger exciton binding energies.

The stability of heteropolar crystals such as perovskites is influenced by the Madelung electrostatic potential. The lattice energy and site electrostatic potentials are explored for each stoichiometry in Table 1. These are calculated with a lattice summation of the formal ion charges [10]. For group VI anions (oxides and chalcogenides), the lattice energy decreases as the charge imbalance between the *A* and *B* sites is removed: a lower charge on the *A* site is favoured. However, for group VII anions (i.e. halides) the electrostatic stabilisation is reduced, with a lattice energy of just –29.71 eV/cell and an electrostatic potential on the anion site ca. 50 % of the group VI anions. Due to this weaker potential, lower solid-state ionisation potentials (electron removal energies) are expected for halide perovskites compared to, for example, metal oxides.

3 Average Crystal Structure

We now consider the detailed crystal structure of the hybrid compounds of primary interest for application in solar cells. For brevity, we refer to the methylammonium compound $CH_3NH_3PbI_3$ as MAPI and the formamidinium compound $[CH(NH_2)_2]PbI_3$ as FAPI.

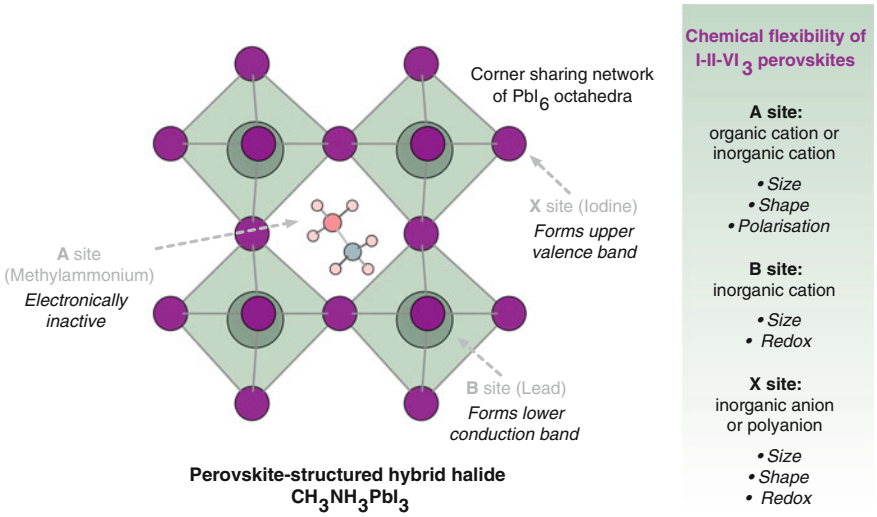

Fig. 1 Schematic of the perovskite crystal structure with respect to the *A*, *B* and *X* lattice sites reproduced from Ref. [13] under a Creative Commons license. The redox chemistry of the component ions can be used to influence the valence and conduction band energies and orbital composition, and hence the stability of electrons and holes in the material. Note that for larger molecular *A* sites, layered perovskites are formed. Beyond three-dimensional halide perovskites, a wider range of stoichiometries and superstructures are known, e.g. the Ruddlesden-Popper, Aurivillius and Dion-Jacobson phases

Table 1 Electrostatic lattice energy and site Madelung potentials for a range of ABX_3 perovskite structures (cubic lattice, a = 6.00 Å) assuming the formal oxidation state of each species

Stoichiometry	$E_{lattice}$ (eV/cell)	V_A (V)	V_B (V)	V_X (V)
I–V–VI_3	–140.48	–8.04	–34.59	16.66
II–IV–VI_3	–118.82	–12.93	–29.71	15.49
III–III–VI_3	–106.92	–17.81	–24.82	14.33
I–II–VII_3	–29.71	–6.46	–14.85	7.75

The hybrid halide perovskites are of type I–II–VII_3. Calculations are performed using the code GULP. The table is reproduced from Ref. [10]

Weber first reported MAPI in the cubic perovskite crystal structure (O_h point group), [3] which is inconsistent with the anisotropy of the static molecular building block ($CH_3NH_3^+$ is of C_{3v} point group). However, the molecular cations are orientationally disordered in the crystal, giving rise to an effective higher lattice symmetry on average [7]. Early work on the characterisation of the crystal structure identified three phases of MAPI: orthorhombic, tetragonal and cubic Bravais lattices in order of increasing temperature [21]. While the position of Bragg peaks in X-ray diffraction can distinguish between the three phases, the peak intensities arising from $CH_3NH_3^+$ relative to PbI_2 are too weak to assign accurate molecular

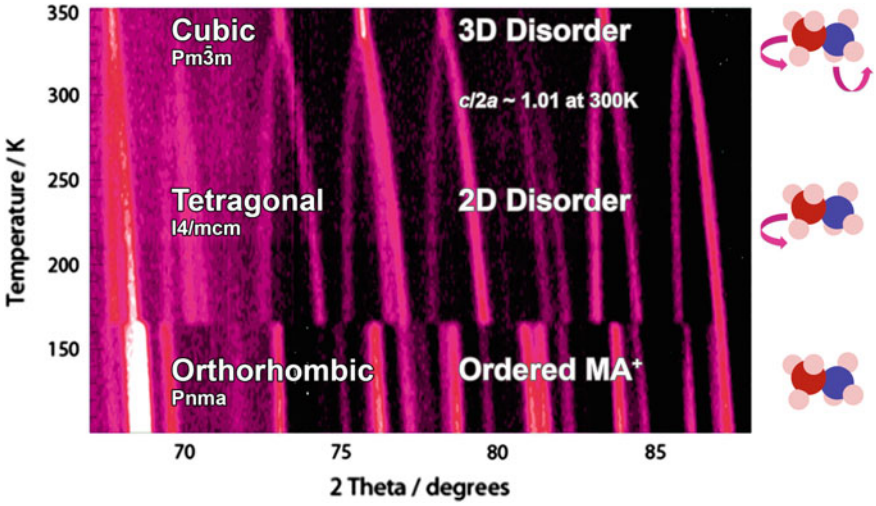

Fig. 2 Temperature-dependent (100–352 K) powder neutron diffraction pattern of $CH_3NH_3PbI_3$ from Ref. [22]—adapted by permission of the Royal Society of Chemistry. The space groups of the average crystals structures are shown, along with a schematic of the extent of disorder in the $CH_3NH_3^+$ sublattice

orientations. The recent application of high-resolution powder neutron diffraction has provided a quantitative description of the temperature-dependent average structures as summarised in Fig. 2 [22].

3.1 Orthorhombic Phase ($T < 165$ K)

The orthorhombic perovskite structure is the low temperature ground state of MAPI and maintains its stability up to ca. 165 K [5, 22]. A comparison of the enthalpy from density functional theory (DFT) calculations confirms this ordering in stability. The difference in enthalpy is 2 meV per MAPI unit compared to the most stable tetragonal phase, yet 90 meV compared to the high-temperature cubic phase [16].

Initial analysis of diffraction data assigned the $Pna2_1$ space group [5, 6]. Recent analysis of higher quality powder neutron diffraction data reassigns it to *Pnma* (a D_{2h} point group) [22]. The structure is a $\sqrt{2}a \times \sqrt{2}a \times 2a$ supercell expansion of the simple cubic perovskite lattice. In the $Pna2_1$ phase, the PbI_6 octahedra are distorted and tilt as $a^+b^-b^-$ in Glazer notation [19] with respect to the orientation of the conventional cubic cell. In this low-temperature phase, the four molecular cations in the unit cell are static on the diagonals of the *ab* planes pointing towards the undistorted facets of the cuboctahedral cavity. Correspondingly, molecules belonging to different planes are anti-aligned with a head-tail motif. Such an

antiferroelectric alignment is expected from consideration of the molecular dipole–dipole interaction [10].

In the low-temperature orthorhombic phase, the $CH_3NH_3^+$ sublattice is fully ordered (a low entropy state). The ordering may be sensitive to the material preparation and/or cooling rate into this phase, i.e. the degree of quasi-thermal equilibrium. It is possible that different ordering might be frozen into the low-temperature phase by mechanical strain or electric fields.

3.2 Tetragonal Phase (165–327 K)

At 165 K, MAPI goes through a first-order phase transition from the orthorhombic to the tetragonal space group $I4/mcm$ (D_{4h} point group), which continuously undergoes a second-order phase transition to the cubic phase by ca. 327 K [5, 22]. As with the orthorhombic phase, this can be considered a $\sqrt{2}a \times \sqrt{2}a \times 2a$ expansion of the cubic perovskite unit cell.

The molecular cations are no longer in a fixed position as in the orthorhombic phase. $CH_3NH_3^+$ is disordered between two non-equivalent positions in each cage. [7, 23] The tetragonal distortion parameter in the cubic basis is greater than unity ($\frac{c}{2a} = 1.01$ at 300 K), corresponding to an elongation of the PbI_6 octahedra along the c axis. The associated octahedral tilting pattern is $a^0a^0c^-$ in Glazer notation.

3.3 Cubic Phase (T > 327 K)

With increasing temperature the tetragonal lattice parameters become more isotropic with $\frac{c}{2a}$ moving closer to 1. The molecular disorder also increases to the point where a transition to a cubic phase occurs around 327 K. The transition can be seen clearly from changes in the heat capacity, [6] as well as in temperature-dependent neutron diffraction [22].

The cubic space group has been assigned the space group $Pm\bar{3}m$ (O_h symmetry); however, the local structure will necessarily have a lower symmetry. Indeed, for the bromide and chloride analogues of MAPI, pair-distribution function analysis of X-ray scattering data indicates a local structure with significant distortion of the lead halide framework at room temperature [24].

3.4 From Methylammonium to Formamidinium

The effective radius of the formamidinium cation (2.53 Å) is larger than methylammonium cation (2.17 Å). This produces a structure tolerance factor (an

indication of the viability of the perovskite structure for a given combination of components) of close to the ideal value of 1 [25].

For FAPI, analysis of powder neutron diffraction has assigned a room temperature space group of $Pm\bar{3}m$, which is isostructural to the high-temperature MAPI structure [17]. Faulted or twinned phases at the nanoscale can appear as hexagonal to single-crystal diffraction methods, which explains the earlier assignment of a hexagonal space group [26]. A distinction of FAPI is that the corner-sharing perovskite structure (black colour) is in competition with a face-sharing δ phase (yellow colour); [26] this is also the case for $CsSnI_3$ [27, 28].

They are as of yet no detailed studies into the low-temperature phase behaviour of FAPI, but ordering is expected in analogy to MAPI. There is also an absence of data on the structure of the $(MA_{1-x}FA_x)PbI_3$ alloy, which will likely be the subject of many experimental and computational investigations in the near future given their application in the high-efficiency solar cells [29].

4 Molecular Motion

Disordered crystalline materials display large atomic displacement parameters, which is the case for both MAPI and FAPI at room temperature [17, 22]. The constituent ions are continuously distorting through their average positions as a function of time—the thermal vibrations are large relative to the inter-atomic spacings.

In our recent research, we have addressed molecular motion in these materials using three scales of materials modelling: 1. density functional theory (DFT), 2. molecular dynamics (MD) and 3. Monte Carlo (MC) approaches, which we will now address in turn.

1. *DFT:* the standard approach in density functional theory calculations of solids is to first minimise all forces on the system by structural relaxation. In the absence of temperature, the size and shape of the crystallographic unit cell is relaxed, including all internal degrees of freedom. It is for this 'equilibrium' crystal structure that the physical properties are extracted. As a starting point, we assessed the total energy difference of different molecular orientations within a single 'quasi-cubic' unit cell of MAPI [9]. We note that any calculation on such unit cells is implicitly assuming that the methylammonium molecules are arranged into an infinite ferroelectric domain; although, it should be noted that there is no long-range electric field created with periodic 'tinfoil' boundary conditions [30]. We found that the energy difference between the low index $<100>$ (cube face), $<110>$ (cube edge) and $<111>$ (cube diagonal) orientations of the $CH_3NH_3^+$ ions are similar (within 15 meV) with small barriers between them (<40 meV), but with the facial $<100>$ orientation being preferred. Even from this static description, orientational disorder driven by thermal energy (k_BT = 26 meV at 300 K) is expected.

2. *MD:* The most simple method to incorporate temperature into first-principles simulations is through molecular dynamics (MD) based on Newton's laws of motion, where the forces are calculated as quantum-mechanically, but the ion velocities are classical and integrated numerically to positions, and rescaled by a thermostat.

Renderings of our MD simulations [10] on supercells of MAPI and FAPI are available on-line. [31, 32] It is evident that the molecules are rotationally mobile at room temperature, with a timescale of motion on the order of picoseconds. A more detailed statistical analysis gives time constants of 3 ps (MA) [18] and 2 ps (FA) [17] for molecular rotations at 300 K.

There are a range of complex motions involving relative twisting of the head and tail groups, libration of a molecular in a single orientation, and the rotation of molecules between orientations. The results expand upon the insights gained from static lattice techniques with an indication for the preference of facial $<100>$ orientations that are also evident in neutron diffraction measurements [17, 22].

Beyond the molecules themselves, the MD simulations show that the PbI_6 octahedra are far from ideal even for a cubic lattice. While the 'average' structure may appear cubic, the local structure is distorted significantly. Pb-I-Pb bond angles of 180° would be expected for an ideal network, while values of 165–172° are found in the relaxed cubic structure [33]. Pb(II) is a prototype 'lone pair' cation with a ground-state electronic configuration of $5d^{10}6s^{2}6p^{0}$. In a centrosymmetric coordination environment, on-site *sp* hybridisation is forbidden by group theory; however, local distortions allow for hybridisation that can result in electronic stabilisation. In effect, these systems display a dynamic second-order Jahn-Teller instability, [34, 35] in addition to displacive instabilities associated with rigid titling of the octahedra. These displacive motions are important as the electronic bands at the gap relevant for device operation are hybridised Pb and I atomic orbitals, and will be directly affected by such distortion. These predictions are supported by measurements of the local structure of $CH_3NH_3SnBr_3$ by X-ray scattering that indicated lone pair distortions [24].

3. *MC:* In order to simulate disordered materials on a scale relevant to photovoltaic devices, we constructed a model Hamiltonian that describes the intermolecular dipole interactions with the ability to solve the temperature-dependent equilibrium structure using on-lattice Monte Carlo (MC) [10]. A representative thin-film structure is shown in Fig. 3. Since our original publication, the STARRYNIGHT codes have been generalised to 3D boundary conditions [18] and to include defect structures [36]. The model considers rotating molecular dipoles, but these are analogous to an effective dipole of the unit cell including local lattice distortions, which is also applicable to model fully inorganic perovskites.

The strength of the methylammonium dipole moment is comparable to the electric polarisation calculated for simple models of the room temperature tetragonal phase [37]. A molecular dipole of 2.2 Debye $\approx 3\mu Ccm^{-2}$ is predicted from quantum chemistry; by calculating the torque generated around the centre of mass

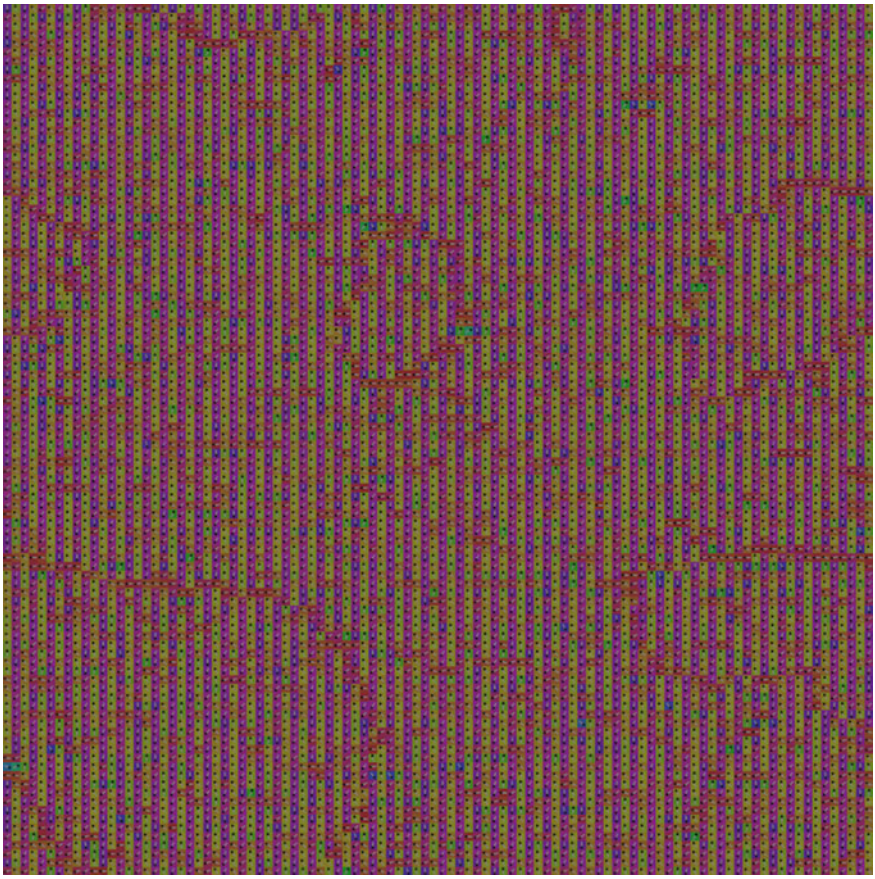

Fig. 3 Results from Monte Carlo simulations of molecular orientational disorder in $CH_3NH_3PbI_3$ at 300 K under an applied electric field. Each box represent a unit cell of the perovskite and the arrows represents the instantaneous molecular orientation. The phase texture and behaviour is discussed in more detail in Ref. [10]

due to an applied electric field, the magnitude of the dipole is rotation and position invariant even for a charged molecule. For formamidinium, the value is reduced to 0.2 Debye; however, the smaller molecular dipole can be compensated by larger structural distortions in the solid-state owing to the steric effect of the additional amine group.

The general behaviour obtained from the MC simulations is easy to follow: ordering of molecular dipoles at low T minimises the total energy of the system by maximising the dipole–dipole interactions, while disorder at high T is driven by configurational entropy. The electrostatic potential resulting from dipole alignment suggests that electrons and holes may be segregated by this structure, which was

subsequently confirmed by direct electronic structure calculations [38] and device modelling [39].

The molecular motion discussed above has been supported by recent quasi-elastic neutron scattering (QENS) investigations, [18, 40] a technique which is particularly sensitive to the motion of hydrogen atoms due to their high incoherent neutron-scattering cross-section. Analysis in one of these studies [41] suggests that only ca. 20 % of the molecules were fully rotationally active in the timescale of the measurement (200 ps), which could be explained by the presence of ordered domains. The application of ultrafast pump-probe vibrational spectroscopy to realistic films has validated the timescale of the motions in MAPI: a fast libration ('wobbling in a cone') motion at 300 fs, and a slower rotation (reorientation) with a 3 ps signature [14]. Here the decay of the polarisation anisotropy within the 10 ps measurement window indicates that 80 % of the molecules were rotationally active during this time, and that any ordered domains must therefore be continuously interconverting [14]. The time constant for reorientation in FAPI is calculated as 2 ps at 300 K, [17] with no direct measurements available at this time. The associated frequency range for molecular rotations of 0.3–0.5 THz overlaps with the low end of the vibrational spectrum [16].

The various rotations and librations of molecular cations in hybrid perovskite introduce a complexity that goes beyond standard photovoltaic materials. However, in addition the ions exhibit translational mobility.

5 Ion Transport

Mass transport in inorganic halide perovskites is well established, with large anion vacancy diffusion coefficients. The activation energy in $CsPbCl_3$ was measured to be 0.29 eV (0.69 eV including the vacancy formation energy) with a diffusion coefficient of $2.66 \times 10^{-3} cm^2 S^{-1}$ [42].

In methylammonium lead iodide, we have predicted that the Schottky defect formation energy (the energy required to form a stoichiometric amount of isolated charged vacancies) is low (0.14 eV per defect); in Kröger-Vink notation:

$$nil \rightarrow V'_{MA} + V''_{Pb} + 3V^{\bullet}_{I} + MAPbI_3 \quad (1)$$

Even for a stoichiometric material, there is a thermodynamic driving force for the formation of a high concentration of vacant lattice sites independent of the growth conditions [43]. The enthalpic cost of defect formation (0.14 eV per defect) is offset by the gain in configurational entropy of the system to an extent beyond the dilute defect limit. Fortunately, these defects do not result in deep electronic states in the band gap, and thus Shockley-Read-Hall type non-radiative recombination is avoided [44, 45].

The low formation energy of charged point defects also explains the low carrier concentrations and the difficulty in extrinsica doping: carriers are heavily compensated by ionic defects, which is common in wide band gap semiconductors such as ZnO [46].

A reservoir of available charged point defects in the lattice could support a significant ionic current, the signatures of which have been observed in impedance spectroscopy of MAPI [47]. However, the mobility of each species depends on the activation energy for solid-state diffusion (ΔH^{diff}), with a hopping rate given by:

$$\Gamma = v^* exp\left(-\frac{\Delta H^{diff}}{k_B T}\right) \tag{2}$$

where v^* represents an effective frequency of the diffusing species in the direction of the saddle point [48].

Considering a material placed under an applied bias with ion blocking electrodes. After the current is turned on ions and electrons will flow, but the ions will gradually cease to be available for transport. The initial equilibration of the ionic distribution relies on the solid-state diffusion pathways discussed above, which are activated processes that are slow and can give rise to a temporal change in the current-voltage behaviour before equilibrium is reached. Electromigration of ions due to momentum transfer from the photovoltaic current in an operating solar cell can also occur, while ion leakage into the electron and hole contacts is also a possibility. Ion transport is considered the origin of the slow component of the reported hybrid perovskite current-voltage 'hysteresis' [49] and the reversible photocurrents [50].

The microscopic origin of ion transport is currently in debate with proposals of majority: (a) proton diffusion; [51] (b) methylammonium diffusion [52]; and (c) iodide diffusion [15, 53]. While a combination of several processes are likely to occur in real systems, the three key factors that determine the contribution of individual ions are the concentration, activation energy and attempt frequency (Eq. (2)). Given the structural disorder of these materials discussed previously, the hybrid perovskites are expected to exhibit non-ideal diffusion kinetics due to the range of local coordination environments and migration pathways. Unlike electron transport with electrons and hole wavefunctions delocalised over many unit cells, ion transport is more sensitive to the local structure.

Concerning proton diffusion, free H^+ ions are unlikely to present in abundance since methylammonium is a weak acid. The reaction $CH_3NH_3^+ \rightleftharpoons CH_3NH_2 + H^+$ has an equilibrium constant K_a of $\sim 4 \times 10^{-11}$ at 300 K. Taking into account the density of MAPI, this would correspond to a nominal H^+ concentration of 10^{11}cm^{-3}, which may be affected by the preparatory conditions (e.g. humidity) and reactions with iodine, but nonetheless is minor compared to the other defects present.

There should be a supply of charged Pb^{2+}, I^- and $CH_3NH_3^+$ vacancies with predicted concentrations of $10^{17} - 10^{20}$ cm^{-3} within the assumptions of equilibrium

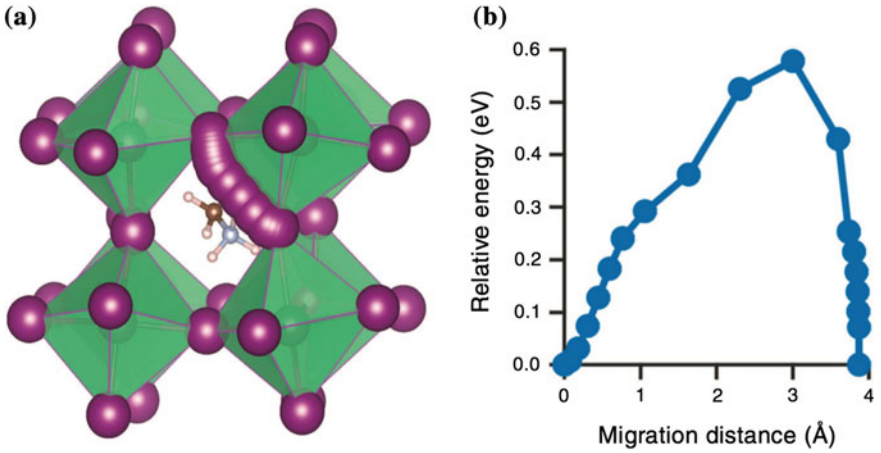

Fig. 4 Iodide ion vacancy migration in $CH_3NH_3PbI_3$ from density functional theory calculations reproduced from Ref. [15] under a Creative Commons license. (*left*) Calculated migration path indicating a slightly curved path and local relaxation/tilting of the octahedra. **b** Corresponding energy profile from nudged-elastic-band calculations

and non-interacting defects [43]. Due to the orientational disorder of the molecular cations, long-range diffusion of $CH_3NH_3^+$ will be slower with transport between successive cages being a relatively complex process, thus lowering the attempt frequency. The frequency should be largest for iodide, as diffusion consists of short jumps over small distances, which is aided by the high polarisability and large thermal displacements for anions in a perovskite crystal. There is evidence of fast vacancy-mediated anion diffusion in inorganic halide perovskites with a low activation energy (see Fig. 4), and thus we consider this to be the dominant process in MAPI and FAPI. Further evidence is provided by the rapid anion exchange process between the chloride, bromide and iodide perovskites, which itself is an exceptional phenomenon [54, 55]. A cation exchange process has also recently been observed between MAPI and FAPI, [56] which is slower than anion exchange and hence consistent with anion diffusion being more rapid.

6 Dielectric Response

A typical solid-state dielectric will exhibit a combination of fast electronic (ε_∞) and slow ionic (ε_{ionic}) polarisation, which both contribute to the macroscopic static dielectric response ($\varepsilon_0 = \varepsilon_\infty + \varepsilon_{ionic}$). An additional molecular response ($\varepsilon_{molecular}$) can occur for materials containing molecules with a permanent dipole, which will occur more slowly (due to the moment of inertia of the molecules, and kinetically limited reordering of domains). This orientational effect is a signature of polar liquids and is particularly sensitive to temperature and the frequency of the applied

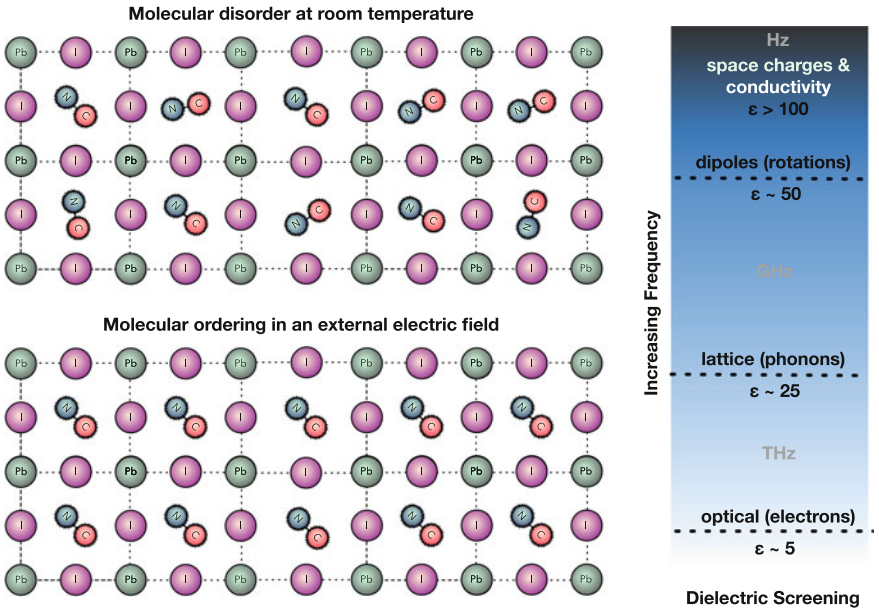

Fig. 5 Schematic of the ordering of molecular dipoles in the presence of an external electric field, as well as the four regimes in the dielectric response from lowest frequency (electronic excitations) to highest frequency (space charges and electronic or ionic conductivity). Each process will have a characteristic relaxation time and can combine to give a complex temporal response to a perturbation. Reproduced from Ref. [13] under a Creative Commons license

field. Finally, the microstructure and conductivity including space charges (ε_{other}) will contribute to the measurable response of a thin film. The magnitude and effective frequency of these contributions are summarised in Fig. 5, with estimates for the bulk response at 300 K being $\varepsilon_0\,(33) = \varepsilon_\infty\,(5) + \varepsilon_{ionic}\,(19) + \varepsilon_{molecular}\,(9)$.

The measured frequency-dependent permittivity of a hybrid perovskite thin-film is compared with the outer yellow skin of a banana in Fig. 6. Both samples show a rapidly increasing dielectric response with decreasing frequency of the applied electric field. The banana is lossy dielectric composite due to its ionic conductivity, which is an apparent hysteresis in current-voltage measurements at low-frequencies in the regime where charging and discharging processes at the electrode interfaces are dominant [57]. The similarity with the response of $CH_3NH_3PbI_3$ is notable, with the added complication of contributions from electronic carriers whose concentration are influenced by the light intensity [58].

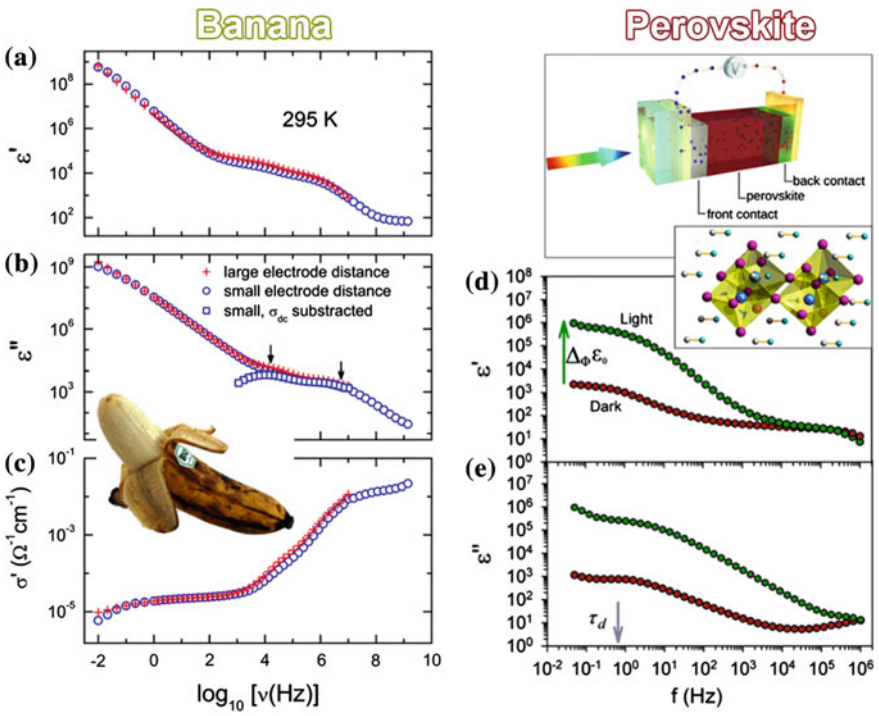

Fig. 6 Comparison of the frequency-dependent dielectric response of a banana (adapted from Ref. [57] with permission by the Institute of Physics, Copyright 2008) and $CH_3NH_3PbI_3$ (adapted from Ref. [58] with permission by the American Chemical Society, Copyright 2014). Broadband spectra of **a** real and **b** imaginary dielectric permittivity and **c** conductivity of a banana skin at room temperature. The **d** real and **e** imaginary permittivity of a $CH_3NH_3PbI_3$ thin-film under dark and 1 sun illumination conditions. The free carrier concentration is increased with above band gap illumination

7 Summary

In this chapter, we have presented a number of fundamentals relating to the crystal structures of halide perovskites. The dynamic behaviour discussed is intimately connected to their application in photovoltaic devices as utilised in rapid ion-exchange processes and as evident in current-voltage hysteresis. The timescales of the various processes are summarized in Table 2. The dielectric screening and spatial electrostatic potential fluctuations are also likely to be connected to the long electron and hole diffusion lengths and slow recombination rates that are measured;

Table 2 Summary of dynamic processes and estimates of their associated time constants in $CH_3NH_3PbI_3$

Process	Microscopic origin	Timescale	Frequency	Diffusion coefficient
Lattice vibrations	Vibrational entropy	10 fs–1 ps	1–100 THz	
Molecular libration	Vibrational entropy	0.5 ps	2 THz	
Molecular rotation	Rotational entropy	3 ps	0.3 THz	
Electron transport	Drift and diffusion	~1 fs	~1000 THz	10^{-6} cm^2s^{-1}
Hole transport	Drift and diffusion	~1 fs	~1000 THz	10^{-6} cm^2s^{-1}
Ion transport	Drift and diffusion	~1 ps	~1 THz	10^{-12} cm^2s^{-1}

however, this can only be verified as more quantitative models are developed and more comprehensive experiments performed. This chapter may have concluded, but the field is fertile for further investigations.

Acknowledgements The research discussed in this chapter has benefited from extensive collaboration, including A. Leguy, P. F. Barnes, B. O'Regan, L. M. Peter, P. Cameron, A. A. Bakulin, A. Petrozza, M. T. Weller, D. O. Scanlon, J. M. Skelton, F. Brivio, K. T. Butler, C. H. Hendon, A. B. Walker, M. van Schilfgaarde, M. S. Islam and C. Eames.

References

1. Wells, H.L.: Uber die Caesium- und Kalium-Bleihalogenide. Zeitschrift fur Anorg. Chemie **3**(1), 195–210 (1893)
2. Wyckoff, R.W.G.: The crystal structures of monomethyl ammonium chlorostannate and chloroplatinate. Am. J. Sci. **s5-16**, 349–359 (1928)
3. Weber, D.: $CH_3NH_3SnBr_xI_{3-x}$ (x = 0–3), a Sn(II)-System with the Cubic Perovskite Structure. Zeitschrift für Naturforsch. **33b**, 862–865 (1978)
4. Weber, D.: $CH_3NH_3PbX_3$, a Pb(II)-System with Cubic Perovskite Structure. Zeitschrift für Naturforsch. B, **33b**, 1443–1445 (1978)
5. Poglitsch, A., Weber, D.: Dynamic disorder in methylammoniumtrihalogenoplumbates (II) observed by millimeter-wave spectroscopy. J. Chem. Phys. **87**, 6373 (1987)
6. Onoda-Yamamuro, N., Matsuo, T., Suga, H.: Calorimetric and IR spectroscopic studies of phase transitions in methylammonium trihalogenoplumbates (II). J. Phys. Chem. Solids **51**, 1383–1395 (1990)
7. Wasylishen, R., Knop, O., Macdonald, J.: Cation rotation in methylammonium lead halides. Solid State Commun. **56**(7), 581–582 (1985)
8. Kojima, A., Teshima, K., Shirai, Y., Miyasaka, T.: Organometal halide perovskites as visible-light sensitizers for photovoltaic cells. J. Am. Chem. Soc. **131**, 6050–6051 (2009)
9. Brivio, F., Walker, A.B., Walsh, A.: Structural and electronic properties of hybrid perovskites for high-efficiency thin-film photovoltaics from first-principles. APL Mater. **1**(4), 042111 (2013)
10. Frost, J.M., Butler, K.T., Walsh, A.: Molecular ferroelectric contributions to anomalous hysteresis in hybrid perovskite solar cells. APL Mater. **2**, 081506 (2014)
11. Brivio, F., Butler, K.T., Walsh, A., van Schilfgaarde, M.: Relativistic quasiparticle self-consistent electronic structure of hybrid halide perovskite photovoltaic absorbers. Phys. Rev. B **89**, 155204 (2014)

12. Butler, K.T., Frost, J.M., Walsh, A.: Band alignment of the hybrid halide perovskites $CH_3NH_3PbCl_3$, $CH_3NH_3PbBr_3$ and $CH_3NH_3PbI_3$. Mater. Horiz. **2**, 228–231 (2015)
13. Walsh, A.: Principles of chemical bonding and band gap engineering in hybrid organic-inorganic halide perovskites. J. Phys. Chem. C **119**, 5755–5760 (2015)
14. Bakulin, A.A., Selig, O., Bakker, H.J., Rezus, Y.L.A., Müller, C., Glaser, T., Lovrincic, R., Sun, Z., Chen, Z., Walsh, A., Frost, J.M., Jansen, T.L.C.: Real-time observation of organic cation reorientation in methylammonium lead iodide perovskites. J. Phys. Chem. Lett. **6**, 3663–3669 (2015)
15. Eames, C., Frost, J.M., Barnes, P.R.F., ORegan, B.C., Walsh, A., Islam, M.S.: Ionic transport in hybrid lead iodide perovskite solar cells. Nat. Commun. **6**, 7497 (2015)
16. Brivio, F., Frost, J.M., Skelton, J.M., Jackson, A.J., Weber, O.J., Weller, M.T., Goni, A.R., Leguy, A.M.A., Barnes, P.R.F., Walsh, A.: Lattice dynamics and vibrational spectra of the orthorhombic, tetragonal, and cubic phases of methylammonium lead iodide. Phys. Rev. B **92**, 144308 (2015)
17. Weller, M.T., Weber, O.J., Frost, J.M., Walsh, A.: The cubic perovskite structure of black formamidinium lead iodide, α-$[HC(NH_2)_2]PbI_3$, at 298 K. J. Phys. Chem. Lett. **6**, 3209–3212 (2015)
18. Leguy, A.M.A., Frost, J.M., McMahon, A.P., Sakai, V.G., Kochelmann, W., Law, C., Li, X., Foglia, F., Walsh, A., ORegan, B.C., Nelson, J., Cabral, J.T., Barnes, P.R.F.: The dynamics of methylammonium ions in hybrid organic-inorganic perovskite solar cells. Nat. Commun. **6**, 7124 (2015)
19. Glazer, A.M.: The classification of tilted octahedra in perovskites. Acta Crystallogr. Sect. B **28**, 3384–3392 (1972)
20. Mitzi, D.B.: Templating and structural engineering in organic-inorganic perovskites. J. Chem. Soc. Dalt. Trans. **2001**(1), 1–12 (2001)
21. Onoda-Yamamuro, N., Yamamuro, O., Matsuo, T., Suga, H.: p-T phase relations of $CH_3NH_3PbX_3$ (X = Cl, Br, I) crystals. J. Phys. Chem. Solids **53**(2), 277–281 (1992)
22. Weller, M.T., Weber, O.J., Henry, P.F., Di Pumpo, A.M., Hansen, T.C.: Complete structure and cation orientation in the perovskite photovoltaic methylammonium lead iodide between 100 and 352 K. Chem. Commun. **51**, 4180–4183 (2015)
23. Baikie, T., Fang, Y., Kadro, J.M., Schreyer, M., Wei, F., Mhaisalkar, S.G., Gratzel, M., White, T.J.: Synthesis and crystal chemistry of the hybrid perovskite $(CH_3NH_3)PbI_3$ for solid-state sensitised solar cell applications. J. Mater. Chem. A **1**(18), 5628 (2013)
24. Worhatch, R.J., Kim, H.J., Swainson, I.P., Yonkeu, A.L., Billinge, S.J.L.: Study of local structure in selected cubic organic-inorganic perovskites. Chem. Mater. **20**, 1272–1277 (2008)
25. Kieslich, G., Sun, S., Cheetham, T.: Solid-state principles applied to organic-inorganic perovskites: new tricks for an old dog. Chem. Sci. **5**, 4712–4715 (2014)
26. Stoumpos, C.C., Malliakas, C.D., Kanatzidis, M.G.: Semiconducting tin and lead iodide perovskites with organic cations: Phase transitions, high mobilities, and near-infrared photoluminescent properties. Inorg. Chem. **52**, 9019–9038 (2013)
27. Chung, I., Song, J.H., Im, J., Androulakis, J., Malliakas, C.D., Li, H., Freeman, A.J., Kenney, J.T., Kanatzidis, M.G.: $CsSnI_3$: Semiconductor or metal? High electrical conductivity and strong near-infrared photoluminescence from a single material. High hole mobility and phase-transitions. J. Am. Chem. Soc. **134**, 8579–8587 (2012)
28. Silva, E.L., Skelton, J.M., Parker, S.C., Walsh, A.: Phase stability and transformations in the halide perovskite $CsSnI_3$. Phys. Rev. B **91**, 144107 (2015)
29. Jeon, N.J., Noh, J.H., Yang, W.S., Kim, Y.C., Ryu, S., Seo, J., Seok, S.I.: Compositional engineering of perovskite materials for high-performance solar cells. Nature **517**, 476–480 (2015)

30. de Leeuw, S.W., Perram, J.W., Smith, E.R.: Simulation of electrostatic systems in periodic boundary conditions. I. Lattice sums and dielectric constants. Proc. R. Soc. A **373**(1752), 27–56 (1980)
31. https://www.youtube.com/watch?v=PPwSIYLnONY (2015). Accessed 25 Dec 2015
32. https://www.youtube.com/watch?v=jwEgBq9BIkk (2015). Accessed 25 Dec 2015
33. https://github.com/WMD-group/hybrid-perovskites (2015). Accessed 25 Dec 2015
34. Walsh, A., Payne, D.J., Egdell, R.G., Watson, G.W.: Stereochemistry of post-transition metal oxides: revision of the classical lone pair model. Chem. Soc. Rev. **40**(9), 4455–4463 (2011)
35. Young, J., Stroppa, A., Picozzi, S., Rondinelli, J.M.: Anharmonic lattice interactions in improper ferroelectrics for multiferroic design. J. Phys.: Condens. Matter **27**(28), 283202 (2015)
36. Grancini, G., Srimath Kandada, A.R., Frost, J.M., Barker, A.J., De Bastiani, M., Gandini, M., Marras, S., Lanzani, G., Walsh, A., Petrozza, A.: Role of microstructure in the electronhole interaction of hybrid lead halide perovskites. Nat. Photonics, **7**, 695–702 (2015)
37. Stroppa, A., Quarti, C., De Angelis, F., Picozzi, S.: Ferroelectric polarization of $CH_3NH_3PbI_3$: a detailed study based on density functional theory and symmetry mode analysis. J. Phys. Chem. Lett. **6**, 2223–2231 (2015)
38. Ma, J., Wang, L.-W.: Nanoscale charge localization induced by random orientations of organic molecules in hybrid perovskite $CH_3NH_3PbI_3$. Nano Lett. **15**, 248–253 (2014)
39. Sherkar, T., Koster, J.A.: Can ferroelectric polarization explain the high performance of hybrid halide perovskite solar cells? Phys. Chem. Chem. Phys. **18**, 331–338 (2016)
40. Chen, T., Foley, B.J., Ipek, B., Tyagi, M., Copley, J.R.D., Brown, C.M., Choi, J.J., Lee, S.-H.: Rotational dynamics of organic cations in $CH_3NH_3PbI_3$ perovskite. Phys. Chem. Chem. Phys. **17**, 31278–31286 (2015)
41. Chen, T., Foley, B.J., Ipek, B., Tyagi, M., Copley, J.R.D., Brown, C.M., Choi, J.J., Lee, S.-H.: Rotational dynamics of organic cations in $CH_3NH_3PbI_3$ perovskite. arXiv:1506.02205 [cond-mat]
42. Mizusaki, J., Arai, K., Fueki, K.: Ionic conduction of the perovskite-type halides. Solid State Ionics **11**, 203–211 (1983)
43. Walsh, A., Scanlon, D.O., Chen, S., Gong, X.G., Wei, S.-H.: Self-regulation mechanism for charged point defects in hybrid halide perovskites. Angew. Chemie Int. Ed. **54**, 1791–1794 (2015)
44. Kim, J., Lee, S.H., Lee, J.H., Hong, K.H.: The role of intrinsic defects in methylammonium lead iodide perovskite. J. Phys. Chem. Lett. **5**(8), 1312–1317 (2014)
45. Yin, W.-J., Shi, T., Yan, Y.: Superior photovoltaic properties of lead halide perovskites: insights from first-principles theory. J. Phys. Chem. C **119**, 5253–5264 (2015)
46. Catlow, C.R.A., Sokol, A.A., Walsh, A.: Microscopic origins of electron and hole stability in ZnO. Chem. Commun. **47**(12), 3386–3388 (2011)
47. Yang, T.-Y., Gregori, G., Pellet, N., Grätzel, M., Maier, J.: The significance of ion conduction in a hybrid organic-inorganic lead-iodide-based perovskite photosensitizer. Angew. Chemie Int. Ed. **54**, 7905–7910 (2015)
48. Harding, J.H.: Calculation of the free energy of defects in calcium fluoride. Phys. Rev. B **32**, 6861 (1985)
49. Snaith, H.J., Abate, A., Ball, J.M., Eperon, G.E., Leijtens, T., Noel, N.K., Stranks, S.D., Wang, J.T.W., Wojciechowski, K., Zhang, W.: Anomalous hysteresis in perovskite solar cells. J. Phys. Chem. Lett. **5**, 1511–1515 (2014)
50. Xiao, Z., Yuan, Y., Shao, Y., Wang, Q., Dong, Q., Bi, C., Sharma, P., Gruverman, A., Huang, J.: Giant switchable photovoltaic effect in organometal trihalide perovskite devices. Nat. Mater. **14**, 193–198 (2015)

51. Egger, D.A., Kronik, L., Rappe, A.M.: Theory of hydrogen migration in organic-inorganic halide perovskites. Angew. Chemie Int. Ed. **54**, 12437–12441 (2015)
52. Azpiroz, J.M., Mosconi, E., Bisquert, J., De Angelis, F.: Defects migration in methylammonium lead iodide and their role in perovskite solar cells operation. Energy Environ. Sci. **8**, 2118–2127 (2015)
53. Haruyama, J., Sodeyama, K., Han, L., Tateyama, Y.: First-principles study of ion diffusion in perovskite solar cell sensitizers. J. Am. Chem. Soc. **137**, 10048–10051 (2015)
54. Pellet, N., Teuscher, J., Maier, J., Grätzel, M.: Transforming hybrid organic inorganic perovskites by rapid halide exchange. Chem. Mater. **27**, 2181–2188 (2015)
55. Nedelcu, G., Protesescu, L., Yakunin, S., Bodnarchuk, M.I., Grotevent, M., Kovalenko, M.V.: Fast anion-exchange in highly luminescent nanocrystals of cesium lead halide perovskites ($CsPbX_3$, X = Cl, Br, I). Nano Lett. **15**, 5635–5640 (2015)
56. Eperon, G.E., Beck, C.E., Snaith, H.: Cation exchange for thin film lead iodide perovskite interconversion. Mater. Horiz. **3**, 63–71 (2016)
57. Loidl, A., Krohns, S., Hemberger, J., Lunkenheimer, P.: Bananas go paraelectric. J. Phys. Condens. Matter **20**(19), 191001 (2008)
58. Juarez-Perez, E.J., Sanchez, R.S., Badia, L., Garcia-Belmonte, G., Kang, Y.S., Mora-Sero, I., Bisquert, J.: Photoinduced giant dielectric constant in lead halide perovskite solar cells. J. Phys. Chem. Lett. **5**, 2390–2394 (2014)

First-Principles Modeling of Organohalide Thin Films and Interfaces

Edoardo Mosconi, Thibaud Etienne and Filippo De Angelis

Abstract Organohalide perovskites have emerged as a class of materials with a unique combination of optoelectronic properties, suitable for a plethora of applications ranging from solar cells to photoelectrochemical tandem cells, to lasing and lighting. Theoretical and computational modeling can deliver an hitherto inaccessible atomistic view of the crucial material properties and heterointerfaces ruling the operational mechanisms in all these devices. Here we present a unified view of recent activity in the computational modeling of interfaces relevant to perovskites solar cells. The performance of the proposed simulation toolbox along with the fundamental modeling strategies are illustrated using selected examples of relevant materials and representative interfaces. In particular, we discuss interfaces between the prototype methylammonium lead iodide perovskite with TiO_2 and ZnO semiconductors (acting as electron selective contacts in solar cells), exploring different surface terminations and doping by chloride ions. Also the effect of defects at the interface with TiO_2 is analyzed and their impact on solar cell performance is discussed. Finally, the heterogeneous interface between methylammonium lead iodide and water is analyzed, revealing dynamical hints on the perovskite degradation by water.

1 Introduction

Organohalide perovskites recently revolutionized the field of photovoltaics [1], and has been discovered that these materials are able to exhibit remarkable performances in terms of photocurrent generation. After lead–halide compounds were first suggested for photovoltaic applications in the 1980s [2, 3], one had to wait

E. Mosconi · T. Etienne · F. De Angelis (✉)
Computational Laboratory for Hybrid/Organic Photovoltaics (CLHYO), CNR-ISTM,
via Elce di Sotto, 06123 Perugia, Italy
e-mail: filippo@thch.unipg.it

E. Mosconi · F. De Angelis
CompuNet, Istituto Italiano di Tecnologia, Via Morego 30, 16163 Genoa, Italy

N.-G. Park et al. (eds.), *Organic-Inorganic Halide Perovskite Photovoltaics*,
DOI 10.1007/978-3-319-35114-8_2

2009 for Kojima et al. to report first actual use of perovskites for photovoltaics [4]. This first report has considerably gained interest and hence paved the way to a large number of contributions in the field, strongly motivated by the increasing performance of the light-conversion devices built from perovskites.

TiO_2 surface pretreatment prior to perovskites adsorption has further lead to a power conversion efficiency improvement from the firstly reported [4] 3.8 to 6.5 % [5], before the exploitation of spiro-MeOTAD hole transporting material (HTM) could lead to an increased performance (9.7 and 10.2 % PCE) and stability of the device [6, 7].

Design and material morphology monitoring advances then allowed for a significant improvement relatively to the PCE, with remarkable results coming up to 12, 15 and 15.4 % of PCE, respectively, performed by Seok and coworkers [8], Grätzel and coworkers [9], and Snaith and coworkers [10], which succeeded to obtain a planar heterojunction topography which, from a technological point of view, aroused considerable interest in particular in terms of reproducibility and stability of the built devices.

Up to now [11], the highest certified PCE and NREL efficiencies are now of 19.3 and 20.1 %, which places the perovskite solar cells technology as highly competitive in the field of photovoltaics when compared to known thin-film technologies [12].

Further technical improvement also allowed to investigate the more basic features of perovskite materials, such as optical and transport properties of methylammonium (MA) lead–halide perovskites [7]. Crystalline order markers could even be identified according to vibrational spectroscopy experiments [13, 14], and the importance of MA cation configuration space evolution in $MAPbI_3$ perovskites has also been highlighted by these means [15].

The diffusion length of photogenerated entities in $MAPbI_3$ at a micrometer scale has been revealed by photoluminescence and time-resolved UV-Vis absorption spectroscopy. These studies have actually evidenced low photogenerated species recombination rates in such materials, [16] which constitutes a highly desired feature for charge-separation-based photovoltaics. Similar systems, doped with chlorine [17] ($MAPbI_{3-x}Cl_x$) were also investigated with similar protocols. For these particular doped systems, it was showed that the charged entities generated by light-absorption are mostly free electrons and holes [18]. Hole (electron) transporting interfaces were also evidenced to show a singular ambipolar behavior of the photoactive perovskite material in solar devices [19, 20].

2 Tin and Lead Perovskites for Establishing a Reliable Computational Protocol

Structural properties of lead–halide perovskites are known to be reliably predicted by computational protocols involving the Generalized Gradient Approximation (GGA) of Density Functional Theory (DFT) [21–23, 36]. While the relevance of these DFT protocols is established for simulating geometrical structures, it is also

known that such level of theory is unable to provide transferable appropriate bandgap data, the latter quantity being most often underestimated by GGA-DFT. In particular, the previous statement holds for semiconductors and for ABO_3 perovskites. Some examples evidenced this underestimation, for instance ZnO, which bandgap is underestimated by about 2.5 eV when using GGA-DFT. A comparison has also been addressed between GLLB-SC and PBE functional for computing the bandgap of ABO_3 perovskites. In that case, PBE (a standard GGA exchange-correlation functional in DFT) has been shown to deviate from experimental data by ca. 0.5 eV.

Improvements in bandgap calculations by computational methods have been brought to the field, as for instance the use of hybrid xc-functionals (like B3LYP or HSE06 for example). Post-DFT methods were also used to increase the accuracy of theoretical bandgap predictions. Among these methods, we find the self-energy corrected GW approximation [24–28]. Note that hybrid functionals and GW methods have already been combined into a more elaborated computational protocol, which use for a perovskites bandgap benchmark lead to deviations remaining within a 0.2 eV [28].

On the other hand, lead perovskites bandgaps computed with GGA-DFT were shown to be in a good agreement with experiments, with for instance $CH_3NH_3PbI_3$ and $PbTiO_3$ bandgaps of [29, 30] ca. 1.30–1.60 and 1.68 eV computed theoretically, to be compared with the experimental values of [4, 7] 1.55 eV and [21] 1.70 eV, respectively. Unfortunately, the GGA-DFT protocol performance has been showed not to be transferable to tin-halide perovskites, for which the computed bandgaps were underestimating the experimental values [22, 31]. This is also true for $BaSnO_3$ and $SrSnO_3$ and, more generally, for structures of the type $ASnX_3$. However, in both cases, the relative bandgap difference is in agreement with experiments.

The low deviation between experimental and theoreticallead-based perovskites bandgaps has further [29, 32] been attributed to the lack of a proper treatment of electron correlation and relativistic phenomena (particularly important inPb atoms) in the calculations by GGA-DFT. These relativistic effects can be included in the calculation through the use of scalar-relativistic schemes or by evaluating the spin-orbit coupling (SOC). Therefore, it was suggested that the agreement observed between theory and experiments for this class of perovskites could be attributed to a fortuitous cancelation of errors taking place between electron correlation and SOC effects [32]. This was further confirmed by calculations involving large SOC magnitude [33].

At different temperatures, methylammonium lead and tin iodide perovskites have a tetragonal structure [34] with typical bandgaps at, respectively, 1.2 and 1.6 eV [34, 35], but while some tin iodide perovskites were shown experimentally to be able to perform hole transport [34, 36], methylammonium lead iodide and its chlorine-doped relative were shown to efficiently transport both holes and electrons [7, 37]. From these results, it appears that one of the key theoretical targets for the understanding of perovskites electronic structure is the elaboration of a reliable theoretical protocol able to retrieve optical and electronic properties of these

remarkable materials. Currently, SOC-GW calculations [38, 39] have been made affordable and are now able to correctly predict the optical, electronic and transport properties of methylammonium lead and tin iodide perovskites. These achievements actually pave the way to a reliable design of new perovskite structures for highly performant materials with outstanding conversion efficiencies [39].

3 Importance of the Interfacial Chlorine in TiO_2/Organohalide Perovskites Junction

Methylammonium lead iodide perovskites doped with chlorine, with a meso-superstructured and planar heterojunctions were shown to exhibit variable optical properties [18] and superior performances with respect to $MAPbI_3$ materials [10, 17, 40]. In a first stage, this performance improvement was attributed to carrier mobility, while it has been later attributed to lower reduced carrier recombination in chlorine-doped methylammonium lead iodide with respect to $MAPbI_3$ itself. Overall, the influence of chlorine in this performance enhancement remained uncertain. The structure of the material itself also remained unclear, though theoretical and experimental (X-ray diffraction) results pointed the possibility of a reduced chlorine inclusion into $MAPbI_3$ (one to four percents only) and low cell volume concentration (0.7 %) in $MAPbI_{3-x}Cl_x$ [41], which confirms the thermodynamically predicted low probability of solid $MAPbI_3$/$MAPbCl_3$ solutions formation [32, 42]. Mechanistic hypotheses were also introduced relatively to the perovskite growth assisted by chlorine in the doped MA lead iodide perovskite, while EDX (for Energy Dispersive X-ray analysis) measurments were unable to detect chlorine in the $MAPbI_3$ structure [43]. It was also reported that doping $MAPbBr_3$ with chlorine also enhances the photovoltaic performances without chlorine being detected by EDX, while still being present in the material according to XPS (X-ray photoelectron spectroscopy) analyses; it was therefore concluded that the chlorine species should be present at the vicinity or onto the perovskite/titanium oxide interface [44].

Though the chlorine-containing $MAPbI_{3-x}Cl_x$ perovskites were shown to have an oriented growth along the [110] direction (see Fig. 1), [8–10, 30, 40, 41, 43, 45–48] the $MAPbI_3$ perovskite on the other hand was globally exhibiting nonoriented structures, independently of the number of synthesis steps (one or two) [8, 9, 30, 43, 46–49]. Tentative explanations were involving the variable solvent (GBL or DMF/DMSO). The presence of a lead–chlorine precursor was also suspected as a possible reason for this growth variability. As multiple contributions [26, 50] have already highlighted the importance of perovskite morphology when relating it to charge-separation efficiency, cell stability [51, 52] and photovoltaic performances, one is now talking in terms of a so-called “chlorine effect”.

Theoretical electronic structure calculations were performed in order to assess the impact of the presence of chlorine on a prototypical TiO_2/perovskite junction. Those calculations have been performed on interfaces representative of mesoporous

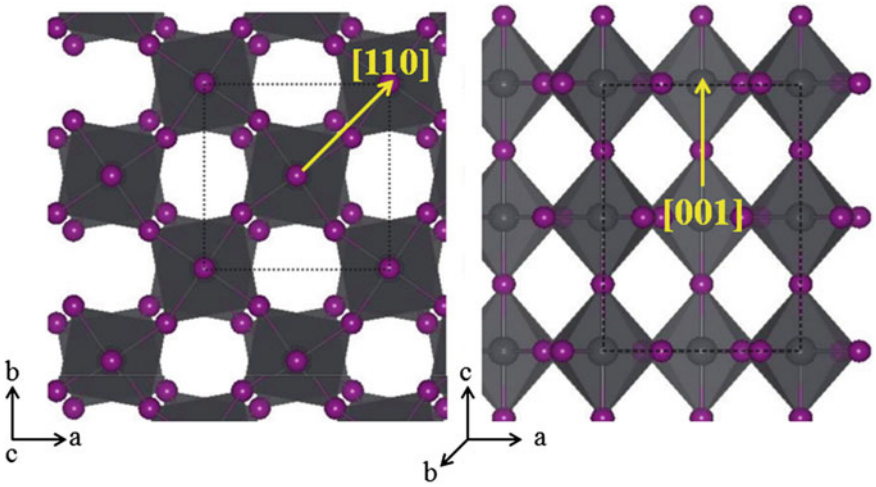

Fig. 1 Schematic representation of the methylammonium lead iodide perovskite X-ray structure projected along the *c* axis (*left*) and the *ab* plane (*right*)

and flat titanium oxide structure. The models were extracted from an optimized MA lead iodide structure, [32] obtained according to experimental X-ray data [29]. No symmetry constraint was used during these simulations, but the absence of inversion symmetry along the *c* axis was reproduced according to the I4 cm space group proposed previously for describing this system [30]. The lattice parameters of the tetragonal phase [53] were used for deriving the pseudo-cubic (001) and the tetragonal (110) surfaces. This means that since the tetragonal phase is representative of the actual structure of $MAPbI_3$ at room temperature, the simulations are aiming at reproducing reallistically this structure for the (110) surface. On the other hand (001) surface was also chosen for better reproducing the titanium oxide lattice. It should be noted that, however, these two surfaces share similar topology. Indeed, the (001) tetragonal phase surface matches with one out of the three (equivalent) cubic phase surfaces. As it has been established that SOC can be crucial to a proper theoretical treatment of Pb-perovskites electronic structure [33, 39, 54], and though scalar-relativistic (SR) schemes are correctly reproducing those properties [32, 39], spin-orbit coupling has been included into the simulation protocol protocol, while the GW approximation was not applied due to the system size, reducing the impact that GW could have on the calculations accurary.

According to a previous report related to the titanium oxide/perovskite heterointerface, the perovskite slabs have a 60:45:150 MA:Pb:I stoichiometry for a 3x5x3 scaffold as a starting model [55, 56]. This starting model has further been modified in order to include chlorine doping agent: fifteen I atoms were replaced by Cl ones at the interface, according to previous statements related to the hypothetical location of those chlorine atoms at the TiO_2/perovskite surface [41, 44]. The titanium oxide supercell for its part was simulated with the experimental cell parameters

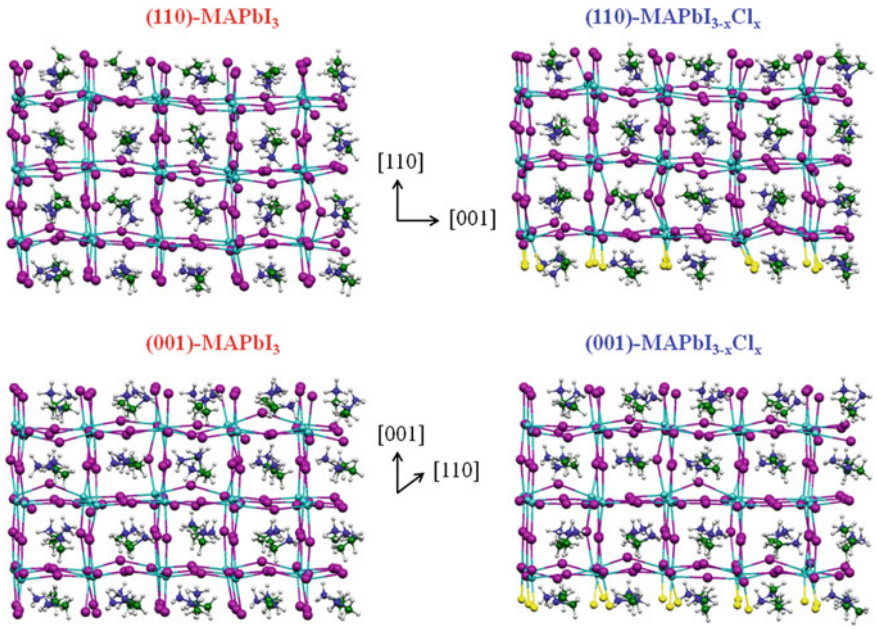

Fig. 2 Optimized structures of doped ($MAPbI_{3-x}Cl_x$—*right*) and undoped ($MAPbI_3$—*left*) (001) —*bottom*—and (110)—*top*—surface slabs

(a = 18.92 Å and b = 30.72 Å). An empty 10 Å space was also inserted along the nonperiodic direction, normal to the surface. The structure of the (110) and (001) slabs surfaces of doped and undoped perovskites are displayed in Fig. 2.

The outcome of these investigations can be summarized as follows: The bandgap for the optimized (110) methylammonium lead iodide slab calculated with (SOC-DFT) and without (SR-DFT) including spin-orbit coupling are, respectively, of 1.32 and 1.96 eV, and from a structural point of view only +0.36 (*a*) and +1.92 % (*b*) deviations along the titanium oxide directions for the (110) surfaces were obtained, while for the pseudo-cubic surfaces (001) those values are of +0.75 and −1.85 %. It was also deduced that a −6.40 and −13.52 % structural deviation is obtained from calculations for the tetragonal (001) surface with the same titanium oxide slab. The use of experimental $MAPbI_3$ (110) surface's cell parameters on another hand induced a 0.4 eV total energy decrease (corresponding to a 1.87 eV bandgap). This has lead to the conclusion that a minimal structural strain in the simulation is responsible for the variations between the two simulated structures. Moving from extended to finite system has also expectedly [31] introduced an upper bandgap shift for the bulk tetragonal $MAPbI_3$ phase. It was further showed that when the size extension of the perovskite slab is doubled along the nonperiodic [110] direction, a 1.55 eV bandgap value is found with SR-DFT for the (110) surface, which can be compared to the one obtained for the bulk with identical protocol. Scalar-relativistic and SOC-DFT delivered larger bandgap values

(2.37 and 1.50 eV, respectively) for the methylammonium lead iodide (001) surface. As a consequence to the fact that chlorine doping agents only introduce occupied levels below the VB (Valence Band) edge, [32] substituting iodine with chlorine did not actually have an impact on the bandgap.

Both undoped and chlorine-doped $MAPbI_3$ have a higher stability with (110) surfaces. Actually, titanium oxide increases the stability of such surface according to a favorable relative configuration between undercoordinated Ti atoms and the halide atoms on perovskite surfaces. The observed time stability enhancement of doped cells was then partly assigned to the increased binding energy between perovskite and titanium oxide, due to the presence of these interfacial atoms. Moreover, it was showed that titanium oxide-doped perovskite interfacial interactions have an impact on the electronic structure of titanium oxide. In particular, increased coupling between Pb *p* and Ti *d* conduction band states were evidenced theoretically. The titanium oxide conduction band was also showed to be slightly upshifted. More importantly, it has been reported that interfacial chlorine produces a conduction band edge asymmetry in chlorine-doped $MAPbI_3$ with respect to its undoped relative. This actually leads to an enhanced charge-transfer between the $MAPbI_{3-x}Cl_x$ structure and titanium oxide, which can explain the importance of the light-absorption generated electrons flow in direction of the titanium oxide surface.

4 PbI_2-Modified TiO_2/$MAPbI_3$ Heterointerface Electronic Coupling

As underlined in various contributions, a proper understanding of structural and electronic features of the perovskite/titanium oxide junction properties is of seminal importance for optimizing functional devices [55, 57, 58]. Unfortunately the characterization of this mesoporous interface by experimental techniques still remains quite challenging, even if levels alignement were already studied by means of XPS/UPS and EBIC [20, 59–61]. Unfortunately, though the current energetic features of these materials at the interface are quite favorable for photocurrent generation, the charge-separation at the heterojunction is still not optimal [62, 63] which results in some undesired charge accumulation phenomenon.

Some investigations are reporting how titanium oxide-containing $MAPbI_3$ perovskite cell stability, efficiency and hysteresis could be improved by using non-stoichiometric ratio for the MAI:PbI_2 precursor. Ten to twenty percentage of PbI_2 excess were reported [6, 64] to bring a desired effect for photovoltaic applications with respect to the one-to-one ratio. A recent combined experimental/theoretical study [65] has reported on the effect of PbI_2 on the heterojunction electronic properties, assuming that the PbI_2 excess remains in the vicinity of the interface, and showing that the presence of this excess favorably modifies the energy levels alignment and the interfacial electronic coupling, which can ease the interfacial electron transfer and might help to prevent a fast quenching, unlike for the 1:1 precursor. Micro-Raman measurements have suggested that the PbI_2 in

excess can also impact the crystallization dynamics. These data together with SEM imagery have confirmed that the excess of PbI_2 is homogeneously distributed possibly at the titanium oxide/perovskite interface.

Tetragonal (110) $MAPbI_3$ surface was then simulated by means of SOC-DFT electronic structure method, based on a scalar-relativistically optimized structure, under two forms: MAI- and PbI_2-terminated $MAPbI_3$, the latter representing the PbI_2-rich growth conditions. These structures were further placed in contact with a 120 titanium oxide anatase 5 × 3 × 2 slab, with a mostly exposed (101) surface (see Fig. 3). The supercells structures were built by using TiO_2 cell parameters, for a lattice deviation not exceeding two percents. Again, it was showed that the methylammonium–iodine termination of perovskites is responsible for interfacial interactions, implying iodine into a binding mode with undercoordinated surficial titanium atoms. For the lead–iodine-terminated perovskite on the other hand, the junction interactions were shown to occur through the formation of lead–oxygen and iodine–titanium interactions, as reported in Fig. 3.

Each scaffold was shown to be possibly existing, as only a slight (less than 0.1 eV) binding energy difference was deduced from the calculations. As far as the electronic properties of the two interfaces are concerned, though one is aware that the theoretical protocol cannot retrieve the adequate level alignment, still a proper relative effect arising from the various surface terminations is expected to be reliably treated during the simulations. The MAI-terminated $MAPbI_3$ conduction band

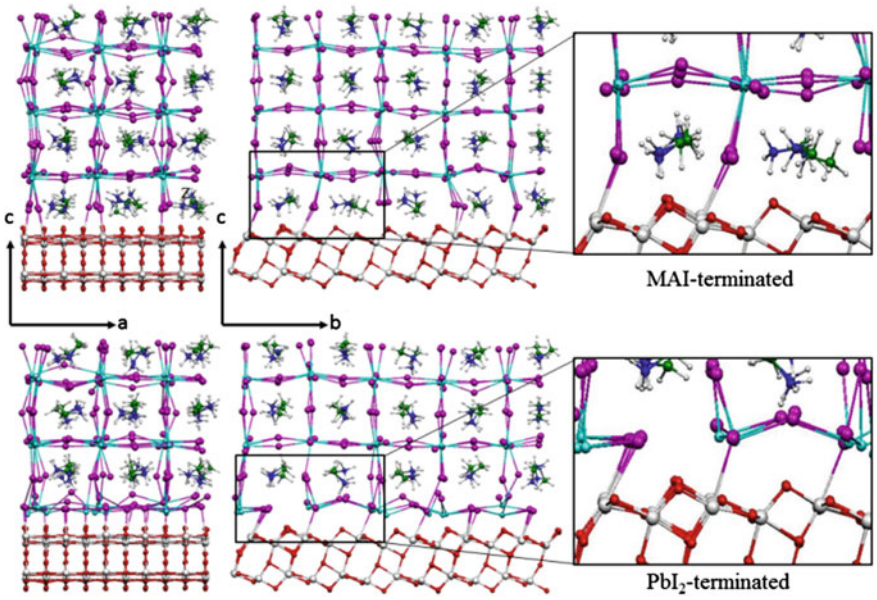

Fig. 3 (110) Titanium oxide/perovskite interface (optimized structures) for methylammonium-iodine-terminated (*top*) and PbI_2-terminated (*bottom*) agencements. *Light* and *dark blue colors* are pointing the lead and nitrogen, while *purple*, *green* and *white* are, respectively, pointing iodine, carbon and hydrogen

edge was calculated to be at around 0.8 eV, with a deviation of 0.4 eV with respect to the experimental value [59]. One could notice from the theoretical results that while the VB and CB are slightly down-shifted when going from the methylammonium-iodine to the lead–iodine-terminated interface. Unlike the former, for which a sharp CB edge has been obtained, the latter actually exhibits a tail of perovskite states remaining at approximately one electronvolt below the main CB window. From these results one can conclude that there exists an improved electronic coupling between perovskite and titanium oxide in the case of lead–iodine-terminated structure. This has been attributed to the reduced distance (2.8 Å, to be compared with 3.3 Å) between lead *6p* and titanium *3d* states in the case of lead–iodine-terminated structure. These two states were considered for comparison, as they are the main constituents of the perovskite and titanium oxide conduction bands. Since the electronic coupling is known to decay exponentially with the distance, such a slight distance variation can induce a substantial coupling shift. Density of states (DOS) calculations (see Fig. 4) have been reported to highlight the fact that unlike for methylammonium–iodine termination, the conduction band bending obtained for the lead–iodine one is more substantial. This is representative

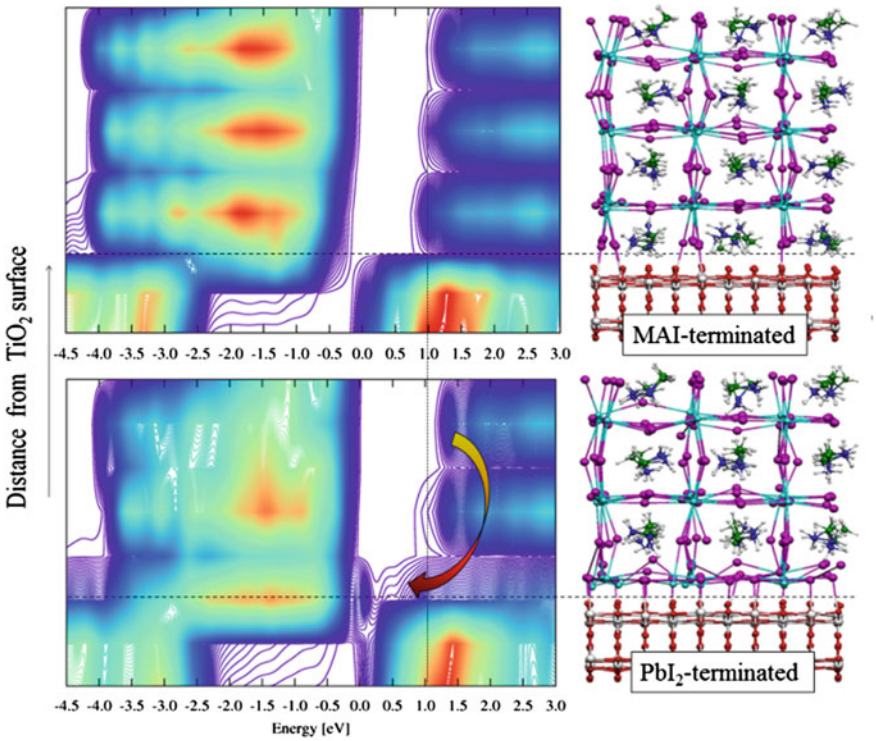

Fig. 4 Isodensity plot of integrated density of states, reported with respect to the distance from anatase surface. Increased DOS values are represented by a *blue-to-red* color variation. In the case of lead–iodine termination panel (*bottom left*) the arrow points the band bending

of a stronger coupling, which is in good agreement with the previous conclusions (see above), and with a predicted enhanced interfacial charge injection, as experimentally reported.

5 $MAPbI_3$ Thin Films Deposited on Zinc Oxide—a Thermal Instability Survey

Though perovskite solar cells are known to constitute a highly promising alternative for renewable energy technologies, the devices built from such materials are still suffering from film instability and hence reduced device lifetimes. As for third-generation solar cells, various possibilities exist for depositing perovskite material onto a surface when mounting a photovoltaic device. Among these options one finds for instance titanium oxide (TiO_2), indium tin oxide (ITO) or zinc oxide (ZnO).

A recent joint experimental/theoretical investigation [66] reported on the thermally annealed zinc oxide/$MAPbI_3$ films by means of in situ absorbance spectroscopy and grazing incidence X-ray diffraction (GIXRD) and density functional theory calculations. This survey allowed to elucidate the decomposition mechanism of the deposited perovskite, which has been shown to be caused by acid/base reaction at the heterojunction: with time, the MA cation deprotonation occurs and leads to the formation of CH_3NH_2. This was partially assigned to the basicity of zinc oxide surface, which has been shown to be reduceable by a preliminary annealing treatment of the zinc oxide film, taking place before depositing $MAPbI_3$. Such a problem is less likely to be encountered in titanium oxide or ITO-containing devices, as these surfaces appear to be more acidic than zinc oxide.

These experimental deductions were further confirmed by a computational analysis performed on the zinc oxide/$MAPbI_3$ interface [55, 57], with a comparison given with respect to interfaces substituting zinc oxide by titanium oxide. To this end, a $3 \times 5 \times 3$ tetragonal slab of $CH_3NH_3PbI_3$ was deposited onto a $6 \times 6 \times 3$ wurtzite ZnO slab. The former slab exposes its (110) surface while the zinc oxide slab exposes its apolar (1010) surfaces. The structural deviations (lattice mismatch) were showed to be very low (1.7 % for *a* and 2.3 % for *b* cell dimension). In both cases the perovskite material displays an orientation exposing the MAI terminations to the surfaces, which highly favors iodine–metal (undercoordinated zinc or titanium) bond formation, as well as MA-O hydrogen bonds formation. Scalar-relativistic geometry optimization of the zinc oxide/$MAPbI_3$ junction leads to a 19.5 eV interaction energy with evaluating the joint and isolated systems energy difference. This value can be compared to the 24.2 eV one for titanium oxide/$MAPbI_3$ [57]. These data actually correspond to a 1.3 eV (ZnO) and 1.6 eV (TiO_2) energy value per undercoordinated metal atom. One can therefore deduce from these theoretical results that the perovskite deposition on ZnO is less effective than the one on titanium oxide.

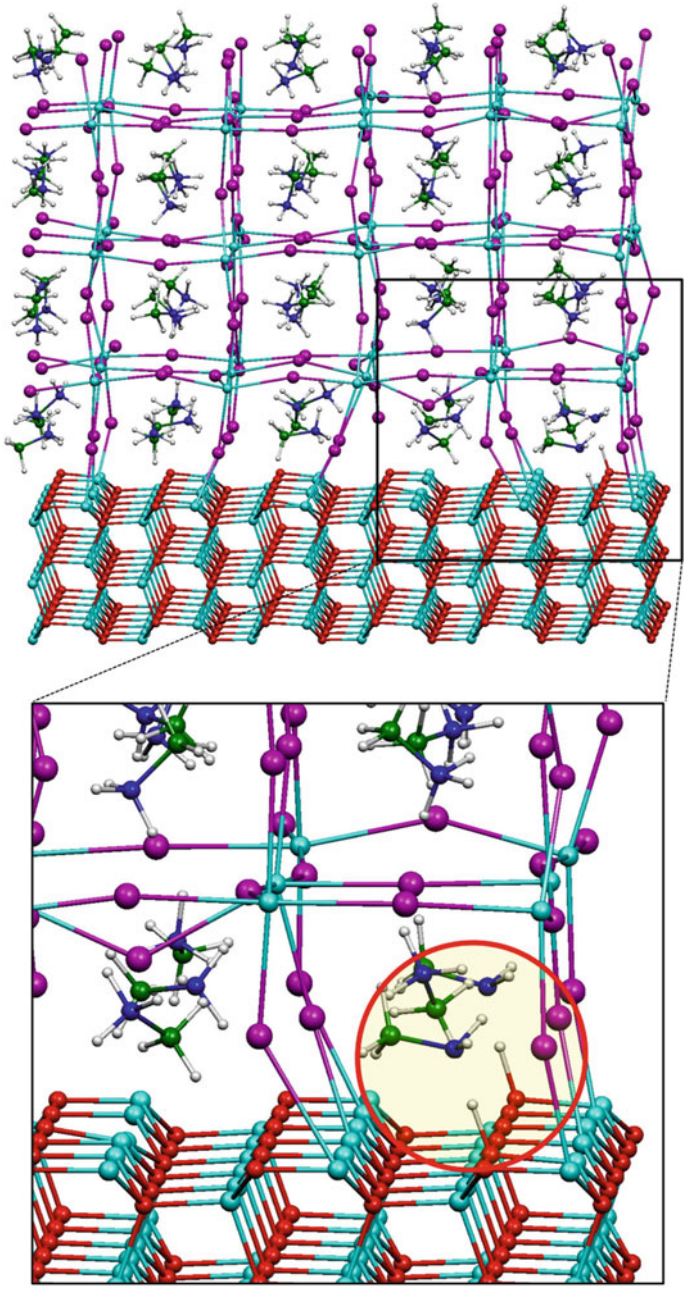

Fig. 5 Zinc oxide/$MAPbI_3$ heterojunction structure, optimized by scalar-relativistic DFT. *Bottom pannel* is a zoom of this structure, intending to evidence the MA deprotonation by an oxygen atom from zinc oxide

Moreover, it was noticed that for the zinc oxide/perovskite interface, two (out of fifteen) MA species have been deprotonated during the relaxation, leading to methylamine. The two protons extracted during the deprotonation process are present, adsorbed on zinc oxide by oxygen atoms. Four MA entities out of 15 have been shown to be deprotonated when the $MAPbI_3$ (001) surface is exposed to the zinc oxide slab. On the other hand, deposition of $CH_3NH_3PbI_3$ onto a titanium oxide slab did not exhibit such feature [15], confirming the difference in acidity properties between the two slabs. Figure 5 displays an optimized $CH_3NH_3PbI_3$ structure, with a zoom graphically evidencing the deprotonation of a methylammonium cation by vicinal zinc oxide oxygen atom.

Note that besides these results consolidating the mechanistic hypothesis responsible for the deposited film thermal instability, further experimental characterizations have been carried out in the same contribution in order to assess the influence of interfacial hydroxyl groups or the presence of residual organic ligands.

6 Defect Migration in $MAPbI_3$ and Its Effect on the $MAPbI_3/TiO_2$ Interface

Among the various limitations encountered when developing new perovskite cell devices, one often cites the J-V curves hysteresis phenomenon or the slow photoconductivity response. A possible feature at the origin of these undesired phenomena could be the ion/defect migration, which is an often referred hypothesis. In order to unravel the impact of defect migration on the properties of the perovskite solar cells, a theoretical study was conducted [67] on the titanium oxide/methylammonium lead iodide perovskite interface. Tetragonal supercells were used to evaluate some previously reported most probable $MAPbI_3$ defects [68–72] migration energetics. A very low (ca. 0.1 eV) activation energy was found for iodide vacancies and interstitial defects, while a 0.5 eV and 1.0 eV value has been attributed to the migration of the methylammonium and lead, respectively. It has been concluded from the simulations that the fast iodide defect migration are unlikely to be responsible for the slow $MAPbI_3$ response, while on the other hand the migration of methylammonium vacancies could be an explanation. A quantitative model was elaborated in order to explain the defects migration by locating the preferential defects at the vicinity of the interface with titanium oxide.

A simulation cell [13] was created with thirty-two $CH_3NH_3PbI_3$ units (for a total of 384 atoms). For the sake of comparison, similar calculations have been performed on $MAPbBr_3$ by using pseudo-cubic cell parameters. A migration path was modeled in order to determine the hypothetical defect migration through the perovskite crystal for the four types of defects studied (see Fig. 6). Saddle points were also located. In the following, vacancies will be pointed by a "V" while interstitials will be assigned by an "i" subscript, substitutions by MA_{Pb} or Pb_{MA} and anti-site substitution by MA_I, Pb_I, I_{MA} and I_{Pb}.

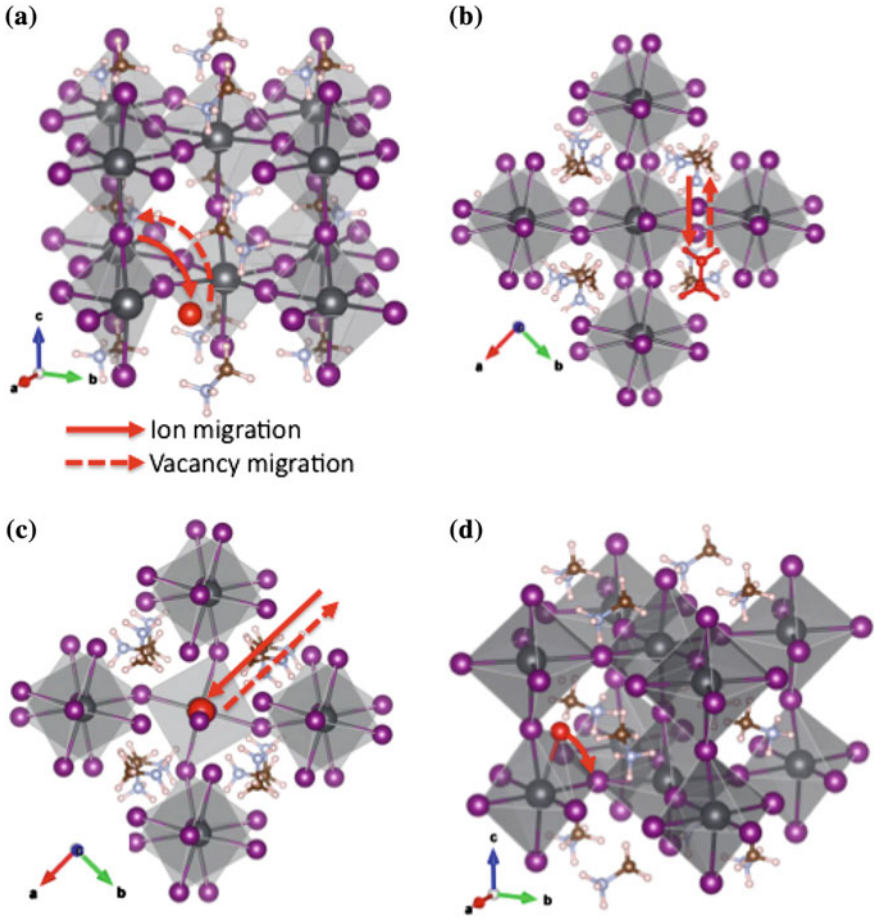

Fig. 6 **a** V_I, **b** V_{MA}, **c** V_{Pb} and **d** I_i defects diffusion paths. Ions (vacancy) migration pathways are represented by *solid* (*dashed*) *lines*. The *white color* is used for pointing hydrogens, *brown color* for carbons, *blue* for nitrogen, *purple* for iodine, *black* for lead atoms

The iodide vacancies (V_I) were simulated by generating a vacancy in an equatorial position. This vacancy was then allowed to migrate in the direction of an axial site (Fig. 6a) Unlike V_I which exhibits iso-energetic axial/equatorial sites migration, the axial and equatorial sites are not iso-energetic for the vacancies of bromine (V_{Br}), with a difference of 0.07 eV in favor of the axial site. As far as the methylammonium vacancies (V_{MA}) are concerned, the inter-site vacancy hopping is occuring between two adjacent cavities, located in the *ab* plane (Fig. 6b). Similarly, lead vacancies (V_{Pb}) are migrating along the four-lead-iodide atoms square (Fig. 6c). As far as iodide interstitials (I_i) are concerned, it has been shown that, similarly to V_I, those are following a path along the *c* axis (see Fig. 6d). It is important to note that for these analyses, a similar migration energy has been

Table 1 Activation energies (E_a, expressed in eV) and rate constants (k, in s^{-1}) related to defects migration in $CH_3NH_3PbX_3$ (X = I, Br)

	$MAPbI_3$		$MAPbBr_3$	
Defect	E_a (eV)	k (s^{-1})	E_a (eV)	k (s^{-1})
$V_{I/Br}$	0.08 (0.16)	1.7×10^{12} (7.7×10^{10})	0.09	1.2×10^{12}
V_{MA}	0.46	6.5×10^{5}	0.56	1.3×10^{4}
V_{Pb}	1.06	4.6×10^{-5}	–	–
I_i	0.08 (0.16)	1.7×10^{12} (7.7×10^{10})	–	–

The values reported in parentheses for the methylammonium lead iodide material are referring to the activation energies and rate constants of two consecutive hopping events

attributed to various defects corresponding to identical chemical entities. For instance, pathways implying the methylammonium migration (MA_{Pb} or MA_i) are characterized by an activation energy similar to the one obtained for V_{MA}. As a matter of fact, the V_I and I_i activation energies were deduced to be equal. Obviously, a similar reasoning also takes place for methylammonium lead bromide perovskite material.

We see in Fig. 6 that path length of V_{MA} and V_{Pb} is twice the one of V_I and I_i. In other terms, the two first will travel along one unit cell while V_I and I_i hop along half a cell. As a consequence, and in order to have a proper comparison of the four processes, the iodide-related activation energies were doubled, which actually corresponds to two hopping actions taking place consecutively. The activation energies (E_a) were calculated for the various defects migration and are displayed in Table 1, and can be placed into the Arrhenius equation in order to evaluate the migration rate:

$$k = \frac{k_B T}{\hbar} e^{-\frac{E_a}{RT}} \tag{1}$$

The main conclusions that can be drawn from reading Table 1 can be expressed as follows: the migration of lead vacancies (V_{Pb}) in $MAPbI_3$ can be regarded as a slow process, while the methylammonium vacancies diffusion is reported to have a 0.46 eV energy barrier, which is in good agreement with the 0.45 eV value deduced experimentally [73]. On the other hand iodide vacancies and interstitials are predicted to have a very flat energy pathway.

If one is now interested in comparing the methylammonium lead bromide and iodide structures, it can be seen that higher hopping activation energy is found for iodide vacancies than for bromide vacancies. We also see that MA migration between two unit cells is more difficult for iodide-containing material.

Without any field, the defects bearing a charge would travel along a random migration path through the perovskite layer. If one observes the symmetric energy landscape (see Fig. 7a), we see that backward and forward defect motions cannot be differentiated in any given crystallographic direction. In working conditions there exists a photogenerated field, which favors the migration of charged defects in the direction of the side of the perovskite film in contact with the so-called hole/electron

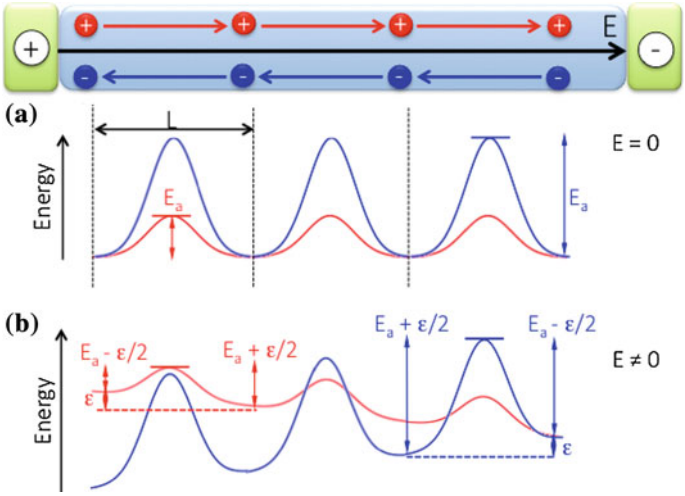

Fig. 7 Energy landscape of iodide (*red*) and methylammonium vacancies (*blue*) migration, at zero (**a**) and non-zero (**b**) electric field

transporting layer (HTL/ETL). The defects get stabilized through their path toward the selective contacts, which is explained by a higher interaction of electrostatic nature with the electrode. This stabilization, written ε/2 independent on the activation energy for defects sharing the same charge, and estimated to ca. 2 meV in cell working conditions, can be seen as a migration driving force. From this assumption, one could state that for $MAPbI_3$ this driving force is reducing (increasing) the activation energy of direct (reverse) migration by a ε/2 factor at the transition state (see Fig. 7b). One can deduce from these results that the predicted forward hopping event kinetics are twice faster than those of the backward one.

Note that the time for iodide vacancies or interstitials defects in the middle of a perovskite layer of 300 nm to reach the selective contact has been estimated to be of the order of tens of nanoseconds, which is actually faster than usual photovoltaic measurements scanning rates. On the other hand, methylammonium vacancies would reach the ETL in tens of milliseconds, which can be seen as possibly affecting the J-V measurements, and can constitute an hypothetic cause for the slow response and hysteresis in perovskite solar cells. Finally, lead vacancies were shown not to be mobile enough for affecting the cell operation.

As it is now established that in bulk $CH_3NH_3PbI_3$ the most mobile defects are iodide vacancies and interstitials, as well as methylammonium vacancies, this assumption allows to draw further conclusions related to the influence of their motion on the overall cell functioning (see Fig. 8) with a focus on the migration of iodide and methylammonium in particular, due to its reported low energy cost of 0.08 eV [71].

In working conditions, the cell will exhibit an electric field induced by light-absorption, pointing from ETL to HTL (e.g., from titanium oxide to Spiro-MeO-TAD-coated Au—see Fig. 8a). This field will induce the motion of

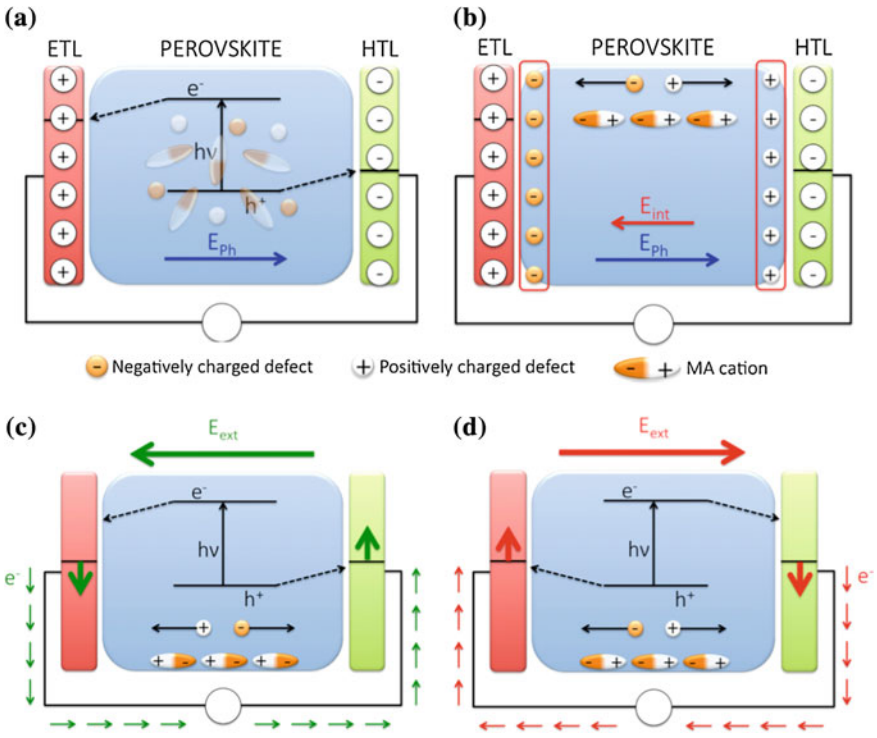

Fig. 8 Defect migration sketch: **a** photogenerated potential-induced charge carriers separation and even point defects distribution, random MA cations orientation; **b** MA cations point defects migration and reorientation, in response to absorption generated field (E_{Ph}) and the induced internal potential (E_{int}); (**c**, **d**) poling: switchable current as a function of the applied field

iodide (MA) vacancies toward HTL (ETL), as shown in Fig. 8b. Therefore, an accumulation of these migrated defects will induce the generation of an electrostatic potential across the $MAPbX_3$ film, in the opposite direction to the one generated by photon absorption and driving the charge-separation in the cell, which impacts the transport properties, hence the performance of the functioning cell.

Additionally, it might be noticed from Fig. 8b that the methylammonium cations can undergo a reorientation in response to the photoinduced field, causing an additional contribution to the defects-generated internal potential.

Note that it was hypothesized [74] that positive (negative) charge defects develop states close to (above) the perovskite CB (VB), inducing an n(p)-doping of the perovskite in contact with the anode (cathode). Positive poling (Fig. 8c) makes the cell to behave like an n-i-p junction. The current will therefore follow the perovskite doping-created gradient. On the other hand, negative poling makes the cell to behave like a p-i-n configuration (Fig. 8d).

The electronic structure of (110) perovskite slab in contact with a (101) titanium oxide slab (anatase) was calculated (see Fig. 9a). The V_I (V_{MA}) diffusion toward

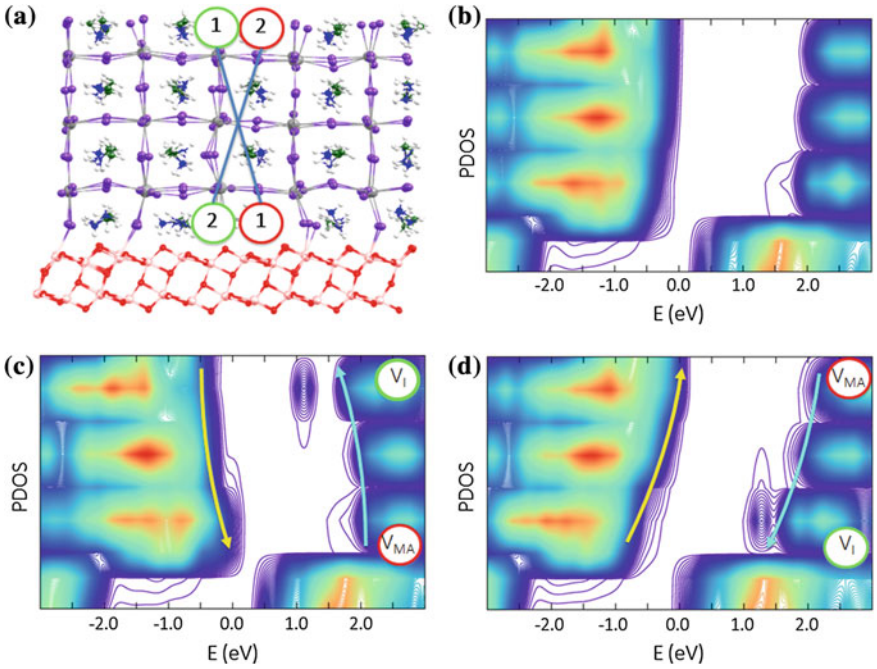

Fig. 9 **a** Perovskite/TiO_2 interface model, where we see V_I (*green circles*) and V_{MA} (*red circles*); Local Density of States (DOS), projected along the direction normal to the perovskite/TiO_2 junction: non-defective model (**b**), and defective models **1** (**c**) and **2** (**d**). *Light-blue* (*yellow*) *arrows* point the evolution of light-absorption generated electrons (holes)

HTL (ETL) is hereafter named **1**. An iodide (MA) vacancy was created at the $MAPbI_3$ surface exposed to vacuum (the $MAPbI_3$ oxide-contacting side—see Fig. 9b). Positive charge migration toward the $CH_3NH_3PbI_3$/titanium oxide contact is further named **2** and is highlighted at Fig. 9c. No geometry relaxation was performed after defects creation in both cases for a direct assessment of the introduction of defects on the electronic structure.

Figure 9 depicts the electronic structure of the two defective models (**1** and **2**). The one of the pristine interface is also present. The partial density of states of titanium oxide and methylammonium lead iodide is displayed together with its local projection along the normal direction to the titanium oxide surface. One can see in the part (b) of the figure that there is an intrusion of perovskite valence band into the titanium oxide bandgap, while the unoccupied states are overlapping with the oxide conduction band. Despite the finite size of the system and the level of theory used for the simulation, [75] we see that the calculations reproduce correctly the energy levels alignment at the titanium oxide/perovskite interface.

Interfacial interactions can be observed by noticing the bending of the perovskite band structure in the vicinity of the titanium oxide surface [55]. If one looks at the influence of defects presence on the electronic structure of a perovskite slab as well as on the interface, we see that the iodide vacancy generates an unoccupied state

below the perovskite conduction band edge (approximately 0.5 eV below, to be relativized due to the overestimation of the perovskite slab bandgap with respect to bulk $CH_3NH_3PbI_3$ material). It therefore appears that there is an overlap between the pervoskite conduction band edge and the state introduced by the iodide vacancy, which is in a good agreement with previous theoretical results [69, 72]. Note that since SOC has been shown to play an important role in the relative positioning of $MAPbI_3$ defective levels, [76] and since spin-orbit coupling is not included in the present calculations, the positioning mentioned above should only be considered on a qualitative basis.

Independently from the level of theory, we see that the presence of positive and negative defects disposed at the opposite sides of the film strongly modifies the perovskite valence/conduction band landscape. For model **2,** one notices the strong directional gradient of unoccupied states close to the titanium oxide substrate due to the presence of iodide vacancy. This actually leads to an increment (a depletion) of unoccupied states at the interface (in the perovskite bulk), which can be seen as a phenomenon boosting interfacial charge injection, also supported by the methylammonium vacancy in **2** which bends the perovskite valence band by introducing an electronic state above the valence band edge (when compared to the pristine valence band edge [69, 72]). Holes migration from the titanium oxide substrate should be facilitated by the slope of the occupied states.

On the other hand, model **1** (Fig. 9c) places iodide vacancies away from the TiO_2 slab and prohibits the electron injection (hole diffusion) into (toward) ETL (HTL), which highly compromises the photovoltaic efficiency of the cell.

Models **1** and **2** have then been modified by considering solely iodide and methylammonium vacancy in the perovskite sides pointing at vacuum and titanium oxide in order to evaluate whether the band edges are overestimated as a consequence of the strong electrostatic interaction existing between positively/negatively charged vacancies. Though the band bending has been reduced by model modification, the valence/conduction band landscape remains quite similar to the unmodified models. Therefore, and beyond the switchable photovoltaic effect, one can consider that the reported results are in good agreement with previous contributions relatively to holes accumulation [77, 78]. Besides, it was suggested that negatively charged defects as iodide interstitials or methylammonium vacancies might be located preferentially in the vicinity of the titanium oxide interface in the absence of an electric field, due to the electron acceptor behavior of undercoordinated titanium atoms. Cationic defects might be more likely to be distributed across the $MAPbI_3$ film. This hypothesis has been reinforced by theoretical results showing a ca. 0.4 eV stabilization energy for model **1** when compared to model **2** using non-relaxed structures. This confirms the role of the substrate in the determination of defects initial concentration close to the selective contacts [79] which is found to be in agreement with recent XPS results pointing the presence of V_{MA} in the surroundings of the titanium oxide/perovskite interface [80].

When computing the stabilization energy of lowest **1** and **2** triplet states, i.e., after the passage of an electron from the perovskite valence band edge to the titanium oxide conduction band (see Fig. 10), one sees that the stability trend is

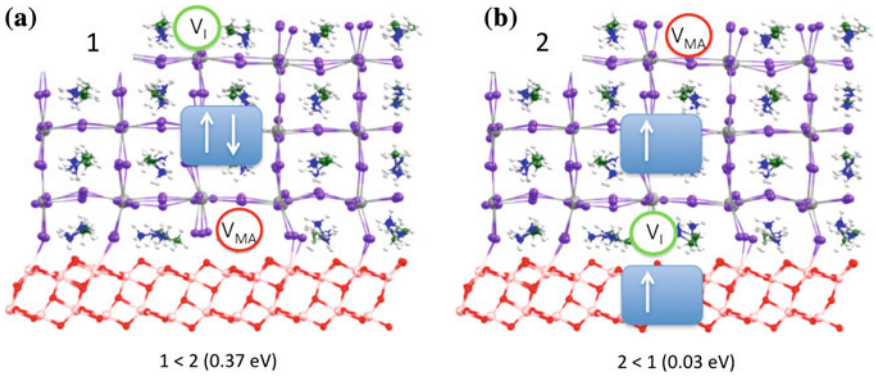

Fig. 10 Iodide and methylammonium vacancies location before (a) and after (b) charge-separation

actually reversed, and that there is no preferential zone for the location of iodide and methymmonium vacancies, which corresponds to an open-circuit cell with a low defect migration driving force. However, the perovskite electronic states landscape was also shown in these results to be quite unchanged by light-induced excitation.

7 The $MAPbI_3$/Water Heterogeneous Interface: Hints on Perovskite Degradation by Water

Among the crucial points characterizing the organohalide perovskite performances we find the perovskite stability. When degradation processes are concerned, one often mentions the presence of moisture, and recent investigations have been devoted to protecting the perovskite layer from the presence of water [81, 82]. Indeed, it has been reported that in the presence of water vapor, hydrated species such as $MAPbI_3{\cdot}H_2O$ or $MA_4PbI_3{\cdot}2H_2O$ can be observed and induce an increase of the cell hysteresis [83]. It has also been shown that PbI_2 can be produced from the irreversible decomposition of $MAPbI_3$ in contact with liquid water, and that at simulated environmental conditions with eighty percent of humidity, a cell aging shows a characteristic perovskite degradation [84]. It was hypothesized that this degradation lead to HI generation [85], which is able to react with the contact electrode silver layer [84]. The water-induced perovskite degradation has also been reported to be a thermodynamically favored process in air [81], and from a mechanistic point of view it was pointed that the first degradation step involves the generation of an intermediate phase containing PbI_6^{4-} as isolated species [82] The degradation process, admittedly accompanied by the generation of this hydrated intermediate phase [86], has also been hypothesized to be assisted by a weakening of the hydrogen bonds connecting the organic to the inorganic parts of MAPbI

through photoexcitation [88]. Such bond weakening favors the perovskite-water interaction, hence perovskite degradation by water.

Considering the impact of humidity on perovskite degradation and cell stability, protection strategies have been suggested, like for example the adjunction of aluminium oxide insulator layer to the device as a way to prevent moisture-caused degradation and TiO_2-spiro-MeOTAD electron recombination [88].

Regarding these issues, attention has been also focused on the role of the hole transporting material [82, 89] (HTM) since the film side on which it is deposited is exposed to the counter electrode. In order to improve the cell resistance to water effects, the replacement of organic HTM by single-wall carbon nanotubes functionalized by a polymer and embedded into an insulator (a polymer matrix) has been suggested [89]. Carbon layers have alternatively been proposed for devices without HTM [90]. Note also that water permeation has been partly suppressed by the implication of vacuum production [92]. On the other hand, it has been reported that ambient air environment (i.e. humid conditions) for the thermal annealing growth of a perovskite precursor film positively impacted the film quality, carrier mobility, grain size and lifetime [93]. It therefore appears that among the various investigations regarding the impact of the presence of water in the vicinity of the perovskite layer, all the conclusions are not strictly convergent and would benefit from a further theoretical insight.

To this end, ab initio molecular dynamics simulations have been performed in order to analyze the nature of the $MAPbI_3/H_2O$ heterointerface, and to characterize the solvation processes responsible for the perovskite degradation and the resulting solvated species [93]. Pending iodine ions nucleophilic substitution has been shown to be a mechanistically possible way for the solvation of MAI-terminated surfaces, supported by methylammonium cation solvation. For its part, the surface terminated by PbI_2 was shown to be less sensitive to the presence of water. This surface, characterized by shorter lead-iodine bonds with respect to the bulk, has therefore been suggested as acting as a protective layer, since no degradation of this surface has been observed within the ten picoseconds timescale of the simulations. Instead, a water molecule insertion into perovskite inorganic framework is observed. $(PbI_2)_n$ vacancy defects generated in PbI_2-poor conditions [94] were shown to lead to a cooperative degradation of the PbI_2-terminated surface, accompanied by the production of solvated species such as $[PbI(H_2O)_5]^+$ or $[PbI_2(H_2O)_6]$. When the perovskite electronic structure is concerned, the impact of hydration is shown to consist in a band gap increase.

Three 2 × 2 slabs have been cut from the bulk $MAPbI_3$ tetragonal crystal structure for simulating the perovskite (001) surfaces (MAI-, PbI_2-terminated and defective surfaces). Those are displayed at Fig. 11. They have been obtained from an optimized bulk structure, for which the methylammonium cations are placed in an isotropic way. Six out of eight PbI units have been removed from the PbI -terminated surface in order to generate a stable defective surface [94]. The a and b cell parameters were taken to be twice the experimental one, i.e. $a = b = 17.71$ Å while $c = 49.67$ Å has been used for the molecular dynamics simulations in water. The water molecules were used to fill the volumes above and below the perovskite

slab, using the experimental liquid water density. Larger water/$MAPbI_3$ ratio has been used for MAI-terminated and PbI_2-defective cases than for PbI_2-terminated simulation, with respectively 284, 235 and 226 water molecules. Similar calculations were performed without water using the same *a* and *b* parameter values and leaving a 10 Å vacuum in the direction perpendicular to the $MAPbI_3$ surface for the sake of comparison. The Car-Parrinello molecular dynamics [95] (CPMD) calculations have been performed using the Quantum Espresso program [96] with the PBE functional [97]. Electron-ion interactions were treated by using a scalar relativistic ultrasoft pseudopotential with electrons from O, N and C 2s, 2p; H 1s; I 5s, 5p; Pb 6s, 6p, 5d shells explicitly included into the calculations. The plane-wave basis set cutoffs were of 25 and 200 Ry respectively for the smooth part of the wavefunctions and for the augmented density. Integration time step of 10 au has been used for the CPMD calculation, for a total simulation time of approximately ten picoseconds. Fictious masses of 1000 au were used for treating the electronic degrees of freedom, while a 5 amu value has been used invariably for all the atomic masses in order to enhance the dynamical sampling. Prior to the use of any thermostat, a thermalization process has been used to reach a 350–400 K temperature by using an initial ions position randomization, and the PWscf code was used, including dispersion contributions [98], for the $4MAPbI_3{\cdot}H_2O$ variable cell geometry optimization, with 50 and 400 Ry cutoffs for the plane wave basis set characterizing the smooth part of the wavefunctions and the augmented density, respectively. The $\Delta G_{form} = E(4MAPbI_3{\cdot}H_2O) - E(4MAPbI_3) - E(H_2O)$ expression has been used for evaluating the formation energy of the hydrated $4MAPbI_3{\cdot}H_2O$ species. Geometry optimization and density of states (DOS) analyses of the hydrated species have been performed using the PWscf code with plane-wave basis sets using cutoff values of 25 and 200 Ry respectively for the smooth part of the wavefunctions and for the augmented density.

The structure of MAI- and PbI_2-terminated slabs were characterized by calculating their radial distribution functions (RDFs). Those were averaged over the dynamics trajectories. Bulk perovskite [13] and bare slabs structures were also compared. It has been shown that the finite size of the models used in the calculations does not significantly alter the crystal structure since bulk RDF properties were seen to be transferred to the bare MAI- and PbI_2- terminated slabs. Note also that the MAI-terminated slabs equatorial Pb-I bond lengths were shown to coincide with those of the bulk, with a 3.21 Å average value, while the average value is 3.19 Å for the PbI_2-terminated surfaces, indicating slightly stronger bonds than in the bulk. This result suggests that such surface may protect the perovskite.

Figure 12 shows the RDFs computed for studying the perovskite/water interfaces for each of the exposed surfaces. Analyzing those RDFs shows us that water molecules have the possibility to bind either to the surface iodine anions (I–H bonds) or to the methylammonium cations (H_{MA}-O bonds) for the MAI-terminated slabs (Fig. 12a), with the typical hydrogen bond length (the average distances are of 2.57 and 1.75 Å respectively). Few short Pb-O bonds were also formed with a 2.75 Å average distance value, which means that water can reach lead by going through the iodine and methylammonium ions network. As far as the PbI -terminated facet

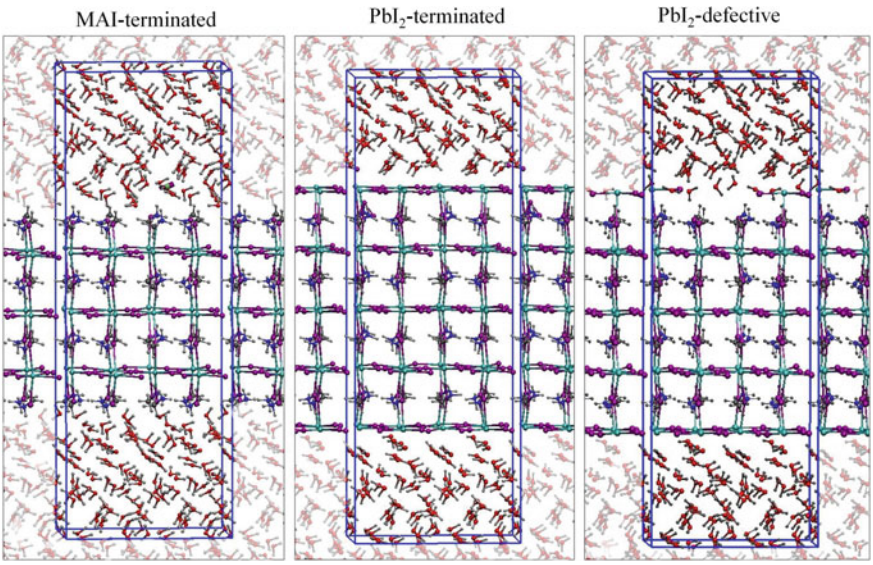

Fig. 11 Structure of the three heterointerfaces (MAI- and PbI_2-terminated, PbI_2-defective slabs) with the simulation cell pointed in blue

is concerned, we see on Fig. 12b that short Pb-O bonds (ca 2.5 Å) can be formed which can be justified from the fact that lead cation is regarded as a borderline hardness acid, which means that it has the possibility to bind soft ligands or hard bases such as the iodine anion from the perovskite or a water molecule respectively. Broad distribution of such pairs has been observed, which suggests a less directional interaction, hence weaker binding between solvent molecules and equatorial iodine atoms in the PbI_2-terminated slab.

One can be interested in describing the dynamical features of the methylammonium lead iodide perovskite, more particularly the methylammonium cation dynamics that can be followed by considering for instance the angle between the ab plane of the perovskite and the MA carbon-nitrogen axis. This angle, written here φ, takes two preferential values ($\pm 30^o$) isotropically distributed in the optimized bulk [13]. When the non-hydrated MAI-terminated surface is concerned, it was shown that for the outermost surface methylammonium cation layers are structured so that the NH groups are pointing toward the surface while the methyl groups are pointing outward, due to stabilizing hydrogen bonds between ammonium and surface iodine atoms. The case of the innermost layer is different: the two peaks at $\varphi = \pm 30^o$ are recovered, indicating that the original MA orientation prevails. If we now focus on the hydrated MAI-terminated surface, we see that the possibility to form interfacial hydrogen bonds with water molecules induces a loss of the preferential orientation described above. Things are less evident for the PbI_2-terminated slab, for which there is a preferential orientation for the ammonium groups that are able to form hydrogen bonds with the surface iodide ions and therefore point toward the surface.

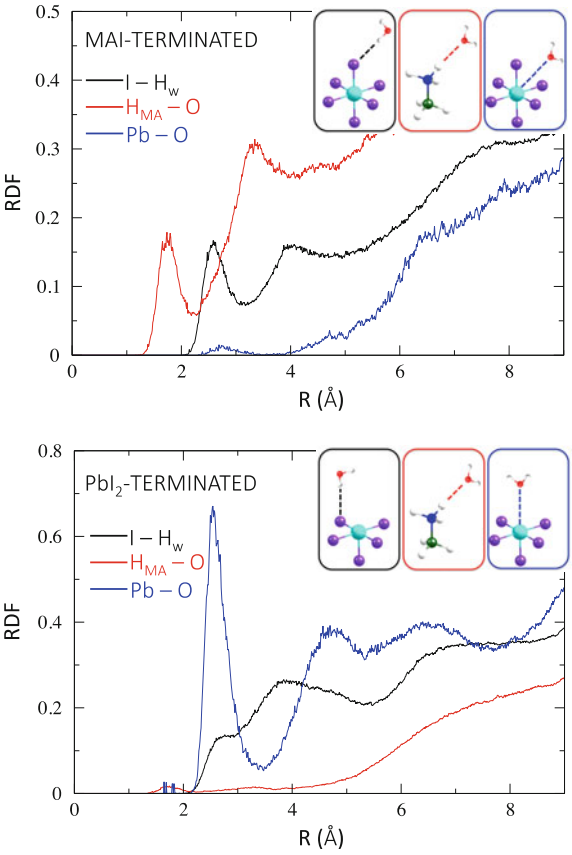

Fig. 12 I–H_w (*black*), H_{MA}–O (*red*), and Pb–O Radial Distribution Functions (RDFs) at the interface between the MAI- (*top panel*) and PbI_2-terminated perovskite slabs (*bottom panel*) and the water layer

This arrangement also impacts the inner layers for which a broad φ angle distribution is observed.

Figure 13 a, b reports the time-evolution of MAI-terminated surface geometrical features. Through the CPMD simulations, observing the Pb-I, Pb-O and Pb-N distances (Fig. 13b) lead to the conclusion that the attack of a water molecule to the surface iodine atoms (Fig. 13a) induces the generation of a seven-coordinated surface lead center, prior to a substitution of iodine by water in the lead coordination sphere, and the release of solvated iodide. The substitution process is characterized by a concerted Pb-I bond weakening (bond length increase) as long as the lead-water bond is formed (decrease of the Pb-water bond length). Moreover, it was shown that due to the iodide release, a vicinal methylammonium cation was detached from the perovskite surface, which prevents the destabilization of the crystal by positive charge accumulation. Through the dynamics, it has been shown that one MAI unit is solvated in 8.5 ps. Though this time scale does not lie within the experimental time scales representative of reaction kinetics, the outcome of these simulations are suggesting that the iodine substitution by water is a fast and

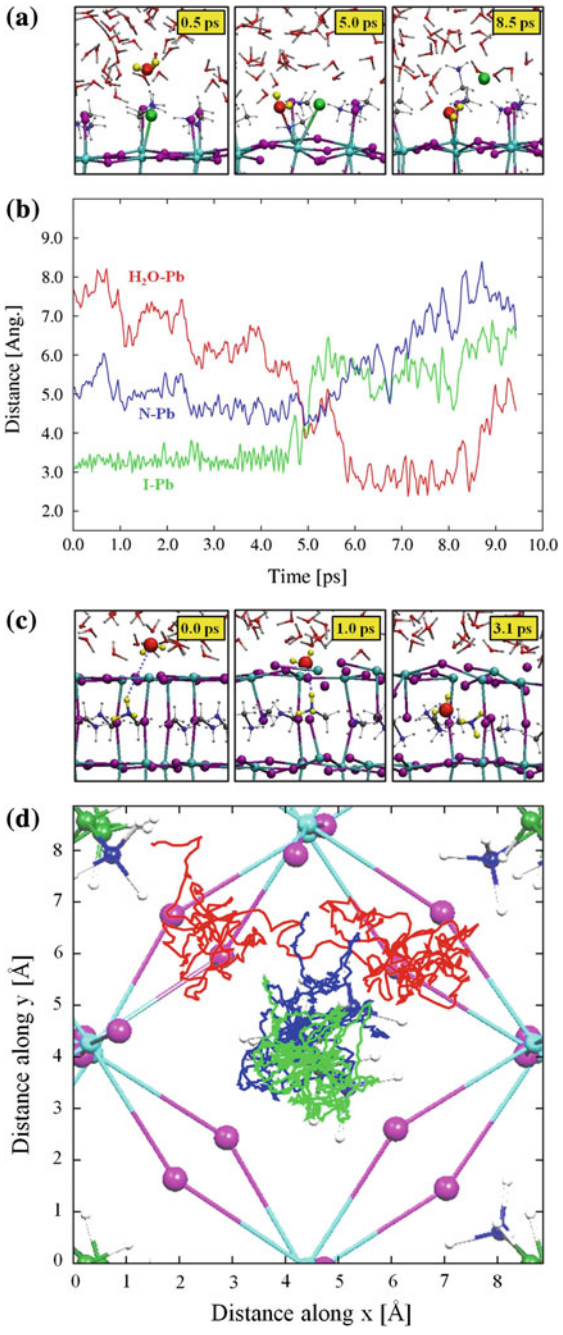

Fig. 13 **a** Nucleophilic substitution of a surface iodide atom by a water molecule in the MAI-terminated $MAPbI_3$ slab, showing the snapshots of the key steps (*top*), and **b** the evolution of the distances (*bottom*) between the water oxygen atom and the lead atom (O–Pb, *red line*), the exiting iodide atom and the lead atom (I–Pb, *green line*), and the MA nitrogen atom and the lead atom (N–Pb, *blue line*). **c** Incorporation of a water molecule to the PbI_2-terminated slab, showing the snapshots of the key steps. **d** Dynamics of the water oxygen atom inside the PbI_2-terminated slab (*red*), along with the trajectories of the MA nitrogen (*blue*) and carbon (*green*) atoms

energetically favorable process, which is in good agreement with previous experimental investigations reporting the MAI solvation as a first step in the perovskite degradation mechanism [99].

Unlike the previous MAI-terminated perovskite slab, the PbI_2-terminated one does not undergo such degradation process despite the existence of strong interactions between water molecules and surface lead atoms. It therefore appears that such PbI_2-terminated surface is more stable with respect to water-induced perovskite decomposition than the MAI-terminated one.

Moreover, one can observe the incorporation of one solvent unit into the methylammonium lead iodide perovskite cavity (Fig. 13c). Indeed, after approximately one picosecond of simulation the water molecule penetrates the cavity by crossing the first PbI layer. A hydrogen bond is further created with a methylammonium cation which, after rotation, traps the water molecule inside of the cavity. This rotation actually follows he path of the water molecule (the ammonium group points toward the water molecule) which was shown to only slightly affect the inorganic scaffold geometry during the simulation. Figure 13d also shows that during the simulation time, the water molecule is sampling two sides of the cavity.

The PbI_2-defective model was further investigated theoretically in order to assess the influence of surface defects and relate them to the relative stability of the water/perovskite heterointerface. To this end, and following previous work [94] indicating that under PbI_2-poor conditions $(PbI_2)_n$ vacancies were stable, six PbI units were removed from the PbI_2-terminated slab, which left two undercoordinated lead atoms on the exposed surface. As reported in Fig. 14, such defective surface can undergo a fast degradation process. Indeed, we see that the two undercoordinated lead atoms can rapidly desorb from the surface and migrate as solvated species. In Fig. 14a we see that one of the lead atoms was initially bonded one water molecule and to the MAPbI surface through four iodine atoms while the second lead atom was shown to bind three iodine atoms and two interfacial water molecules (Fig. 14b). Both have in common that after departing from the surface, they form solvated complexes, respectively $[PbI_2(H_2O)_4]$ and $[PbI(H_2O)_5]$ as displayed in Fig. 14c in which the coordination number of these two undercoordinated lead atoms is reproduced through the dynamics trajectory. In summary, these results show that imperfections at the perovskite surface may play a crucial role in the degradation process of MAPbI perovskite. The importance of the preparation of crystals and thin films without defect is therefore pointed as a relevant element for further considering the elaboration of stable devices based on perovskite material.

The interaction between MAI- and PbI-terminated slabs and a monolayer of eight H_2O molecules has been investigated in order to assess the influence of surface hydration on the slabs electronic structure. The local DOS is displayed in Fig. 15 for the considered perovskite slabs. Note that the MA cations arrangement induces the absence of any dipole across the slabs, which is desired for examinating the surface termination and hydration effects solely. Note also that the number of water molecules has been chosen so as to correspond to a saturation of the undercoordinated sites of all the surface. A strong driving force has been reported

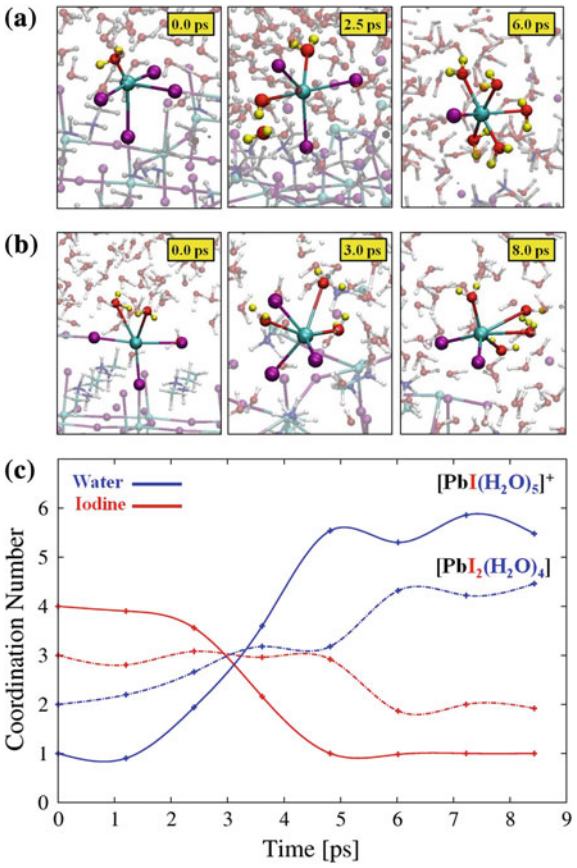

Fig. 14 Representative geometrical structures of the formation of **a** $[PbI_2(H_2O)_4]$ and **b** $[PbI(H_2O)_5]^+$ complexes. **c** Evolution of the Pb–I (*red*) and Pb–H_2O (*blue*) coordination numbers for the formation of $[PbI_2(H_2O)_4]$ (*dot-dashed lines*) and $[PbI(H_2O)_5]^+$ (*solid lines*) species

for this surface hydration, with formation energies being respectively of −0.49 and −0.44 eV for the MAI- and PbI_2-terminated hydrated slabs.

Interestingly, it was also noticed that using a scalar relativistic DFT protocol allows one to accurately reproduce the band-gap of MAPbI [32,33], but in a fortuitous way. Indeed, there exists a possible error cancellation [39] between spin-orbit coupling and post-DFT correlation which respectively reduces and augments the gap. Local perovskite structure, and more particularly the PbI octahedra tilting [54], was shown to be responsible for the influence of spin-orbit coupling, though this contribution is quasi constant across the slabs. It is therefore expected that the computational protocol employed is able to qualitatively reproduce the electronic structure variations characterizing the bare and hydrated surfaces.

It was observed that the bare MAI-terminated surface band-gap gets sharper when moving inward through the perovskite layers, which can be explained by the stabilization of the external valence band edge when compared to the inner one (see Fig. 15a) and the interaction between methylammonium cations and the external

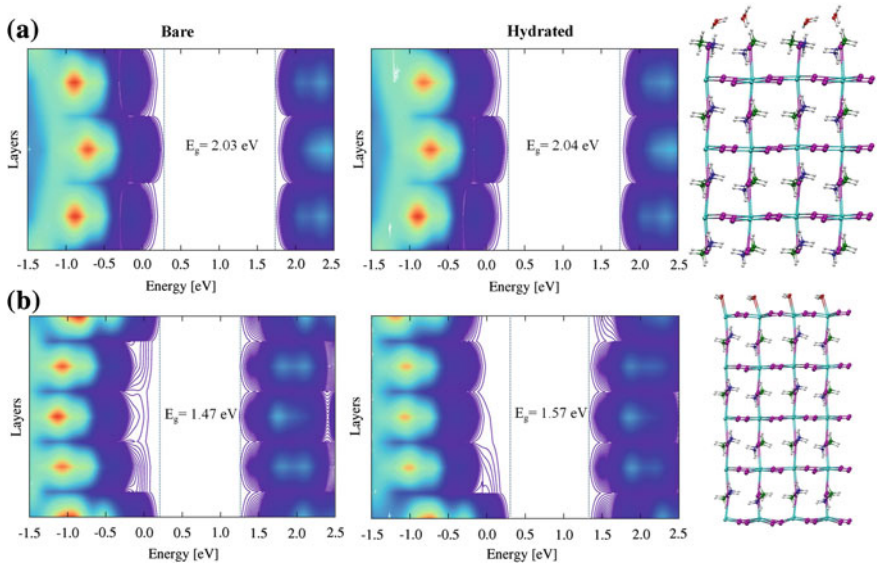

Fig. 15 Isodensityplot of the local density of states across the various perovskite layers found in the [001] direction, i.e., along the crystal *c* axis, in the bandgap region for **a** the bare and hydrated MAI-terminated; and **b** the PbI_2-terminated perovskite slabs. Also reported are the global bandgap values. The vertical dashed lines represent the valence and conduction bands for an isodensity value of 1 state/eV

iodine atoms, which lowers their energy levels. Conversely, for the PbI_2-terminated surface, the band-gap broadens when moving inward through the perovskite layers because of the undercoordinated lead atoms present at the surface. It has also been noticed that while for the PbI -terminated slab the valence band edge is located at the perovskite surface, which may ultimately lead to a trapping of the photogenerated holes, only a limited effect of MAPbI has been suggested to occur for the MAI-terminated slab, due to the fact that no surface states intrudes into the perovskite gap. Hydration effect has been shown to produce quasi no effect on the MAI-terminated model, as hydrogen bonds are mostly responsible for the water/perovskite interfacial interactions. As far as the PbI_2-terminated model is concerned, it was shown that the valence band edge is stabilized in the hydrated interfacial region with respect to the bare surface, with a water-induced valence band down-shift, which was explained by the restoration of the surface lead atoms coordination sphere. This shift is however not compensated by a conduction band shift, which leads to a local band-gap increase of ca. 0.3 eV.

In the continuity of the results related to the incorporation of one H_2O molecule into the PbI_2-terminated slab, the effect on the electronic structure of the inclusion of one water molecule into the bulk perovskite was also investigated, using a bare and a mono-hydrated 48-atom tetragonal unit cell. Geometry relaxation was performed on these two systems and showed that water insertion into the perovskite

cavity is thermodynamically favored by ca. 0.45 eV which indicates the possible spontaneous formation of the hydrated phase, as resulting from the CPDM simulation. Hydration also impacts the band-gap energy value, increasing from 1.45 eV for the bare system to 1.50 eV for the hydrated one. Note also that only a slight cell volume increase was reported (1.3 %) due to the hydration, and that the overall tetragonal shape was preserved, with a c/a ratio moving from 1.48 for the bare MAPbI to 1.47 for the hydrated system. These results indicate the possible existence of a new intermediate hydrated phase characterized by a 4:1 $MAPbI_3$:H_2O ratio (different from the 1:1 and the 1:2 ratio previously reported in the literature [83]) preserving the overall structure and electronic features apart for the slight band-gap modifications. Indeed, it has then been demonstrated that the methylammonium lead iodide perovskite electronic properties might be modulated by exposing the perovskite to water, while the structural parameters are left unaltered by such treatment.

It can therefore be concluded that such results are of importance for understanding the effect of the environment on the stability of these $MAPbI_3$ perovskites as the water-induced degradation of these systems are considered as the main perovskite alteration channel.

This computational investigation aimed at understanding these water/perovskite interactions at the atomic scale, by considering MAI- and PbI_2-terminated surfaces characterizing the most probable systems grown under MAI-rich and poor conditions. The interaction between water and lead sites in the MAI-terminated surfaces drives the rapid solvation of these facets and the release of solvated iodine atoms following a nucleophilic substitution of iodine by water and the desorption of methylammonium cations, resulting in the net solvation of a methylammonium iodide ion pair, which was in good agreement with the previously reported experimental conclusions. PbI_2-terminated slabs did not exhibit such behavior when in contact with water molecules, indicating the possible action of such surface as a protective layer for the perovskite against water-caused degradation. However, water percolation has been observed for this type of slab, suggesting the existence of a novel form of hydrated bulk phase preserving geometrical parameters unaltered. On the other hand, PbI -defective systems were showed to be more susceptible to undergo water-induced degradation.

The MAI- and PbI_2-terminated systems hydration was computationally shown to be exergonic, and hydration was shown to have a non-significant impact on the electronic strucutre of the MAI-terminated system, given that the adsorption is mostly driven by hydrogen bond formation between water and the methylammonium cations. Conversely, it has been shown that the valence band edge of the PbI_2-terminated slabs is stabilized in the interfacial zone in the presence of a water monolayer. A band-gap increase of approximately 0.3 eV was also observed in such case. The impact on the perovskite electronic structure of water incorporation into bulk MAPbI has also been studied using a 4:1 perovskite:water ratio. It was shown that such process causes the increase of the perovskite band-gap from 1.45 to 1.50 eV, while the structural parameters remained unaltered, with only a one-percent volume increase, which indicates that the incorporation of one water molecule

could possibly occur without being detected by usual structural characterization techniques. Based on these novel knowledge, it is now possible to imagine new interfacial alterations and to generate more stable perovskite architectures, which in turn could play a role in new performant solar cells devices.

References

1. Bisquert, J.: The swift surge of perovskite photovoltaics. J. Phys. Chem. Lett. **4**, 2597–2598 (2013)
2. Salau, A.M.: Fundamental absorption edge in PbI2:KI alloys. Solar Energy Mater. **2**, 327–332 (1980)
3. Gao, P., Gratzel, M., Nazeeruddin, M.K.: Organohalide lead perovskites for photovoltaic applications. Energy Environ. Sci. **7**, 2448–2463 (2014)
4. Kojima, A., Teshima, K., Shirai, Y., Miyasaka, T.: Organometal halide perovskites as visible-light sensitizers for photovoltaic cells. J. Am. Chem. Soc. **131**, 6050–6051 (2009)
5. Im, J.-H., Lee, C.-R., Lee, J.-W., Park, S.-W., Park, N.-G.: 6.5 % efficient perovskite quantum-dot-sensitized solar cell. Nanoscale **3**, 4088–4093
6. Kim, H.-S., Lee, C.-R., Im, J.-H., Lee, K.-B., Moehl, T., Marchioro, A., Moon, S.-J., Humphry-Baker, R., Yum, J.-H., Moser, J.E., Grätzel, M., Park, N.-G.: Lead Iodide perovskite sensitized all-solid-state submicron thin film mesoscopic solar cell with efficiency exceeding 9 %. Sci. Rep. **2**, 591 (2012)
7. Lee, M.M., Teuscher, J.l., Miyasaka, T., Murakami, T.N., Snaith, H.J.: Efficient hybrid solar cells based on meso-superstructured organometal halide perovskites. Science **338**, 643–647
8. Heo, J.H., Im, S.H., Noh, J.H., Mandal, T.N., Lim, C.-S., Chang, J.A., Lee, Y.H., Kim, H.-J., Sarkar, A., NazeeruddinMd, K., Gratzel, M., Seok, S.I.: Efficient inorganic-organic hybrid heterojunction solar cells containing perovskite compound and polymeric hole conductors. Nat. Photon. **7**, 486–491 (2013)
9. Burschka, J., Pellet, N., Moon, S.-J., Humphry-Baker, R., Gao, P., Nazeeruddin, M.K., Gratzel, M.: Sequential deposition as a route to high-performance perovskite-sensitized solar cells. Nature **499**, 316–319 (2013)
10. Liu, M., Johnston, M.B., Snaith, H.J.: Efficient planar heterojunction perovskite solar cells by vapour deposition. Nature **501**, 395–398 (2013)
11. Zhou, H., Chen, Q., Li, G., Luo, S., Song, T.-B., Duan, H.-S., Hong, Z., You, J., Liu, Y., Yang, Y.: Interface engineering of highly efficient perovskite solar cells. Science **345**, 542–546 (2014)
12. Green, M.A., Ho-Baillie, A., Snaith, H.J.: The emergence of perovskite solar cells. Nat. Photon. **8**, 506–514 (2014)
13. Quarti, C., Mosconi, E., De Angelis, F.: Interplay of orientational order and electronic structure in methylammonium lead Iodide: implications for solar cell operation. Chem. Mater. **26**, 6557–6569 (2014)
14. Quarti, C., Grancini, G., Mosconi, E., Bruno, P., Ball, J.M., Lee, M.M., Snaith, H.J., Petrozza, A., Angelis, F.D.: The Raman spectrum of the $CH_3NH_3PbI_3$ hybrid perovskite: interplay of theory and experiment. J. Phys. Chem. Lett. **5**, 279–284 (2013)
15. Mosconi, E., Quarti, C., Ivanovska, T., Ruani, G., De Angelis, F.: Structural and electronic properties of organo-halide lead perovskites: a combined IR-spectroscopy and ab initio molecular dynamics investigation. Phys. Chem. Chem. Phys. **16**, 16137–16144 (2014)
16. Wehrenfennig, C., Eperon, G.E., Johnston, M.B., Snaith, H.J., Herz, L.M.: High charge carrier mobilities and lifetimes in organo lead trihalide perovskites. Adv. Mater. **26**, 1584–1589 (2014)

17. Stranks, S.D., Eperon, G.E., Grancini, G., Menelaou, C., Alcocer, M.J.P., Leijtens, T., Herz, L.M., Petrozza, A., Snaith, H.J.: Electron-hole diffusion lengths exceeding 1 micrometer in an organometal trihalide perovskite absorber. Science **342**, 341–344 (2013)
18. D'Innocenzo, V., Grancini, G., Alcocer, M.J.P., Kandada, A.R.S., Stranks, S.D., Lee, M.M., Lanzani, G., Snaith, H.J., Petrozza, A.: Excitons versus free charges in organo-lead tri-halide perovskites. Nat. Commun. **5**, 3586 (2014)
19. Edri, E., Kirmayer, S., Henning, A., Mukhopadhyay, S., Gartsman, K., Rosenwaks, Y., Hodes, G., Cahen, D.: Why lead methylammonium tri-iodide perovskite-based solar cells require a mesoporous electron transporting scaffold (but not necessarily a hole conductor). Nano Lett. **14**, 1000–1004 (2014)
20. Edri, E., Kirmayer, S., Mukhopadhyay, S., Gartsman, K., Hodes, G., Cahen, D.: Elucidating the charge carrier separation and working mechanism of CH3NH3PbI3–xClx perovskite solar cells. Nat. Commun. **5**, 3461 (2014)
21. Lv, H., Gao, H., Yang, Y., Liu, L.: Density functional theory (DFT) investigation on the structure and electronic properties of the cubic perovskite $PbTiO_3$. App. Catal. A **404**, 54–58 (2011)
22. Borriello, I., Cantele, G., Ninno, D.: Ab initio investigation of hybrid organic-inorganic perovskites based on tin halides. Phys. Rev. B **77**, 235214 (2008)
23. Castelli, I.E., Olsen, T., Datta, S., Landis, D.D., Dahl, S., Thygesen, K.S., Jacobsen, K.W.: Computational screening of perovskite metal oxides for optimal solar light capture. Energy Environ. Sci. **5**, 5814–5819 (2012)
24. Hedin, L.: New method for calculating the one-particle green's function with application to the electron-gas problem. Phys. Rev. **139**, A796–A823 (1965)
25. Hybertsen, M.S., Louie, S.G.: Electron correlation in semiconductors and insulators: band gaps and quasiparticle energies. Phys. Rev. B **34**, 5390–5413 (1986)
26. Umari, P., Qian, X., Marzari, N., Stenuit, G., Giacomazzi, L., Baroni, S.: Accelerating GW calculations with optimal polarizability basis. Phys. Status Solidi B **248**, 527–536 (2011)
27. Di Valentin, C., Pacchioni, G., Selloni, A.: Electronic structure of defect states in hydroxylated and reduced rutile TiO_2 (110) surfaces. Phys. Rev. Lett. **97**, 166803 (2006)
28. Berger, R.F., Neaton, J.B.: Computational design of low-band-gap double perovskites. Phys. Rev. B **86**, 165211 (2012)
29. Umebayashi, T., Asai, K., Kondo, T., Nakao, A.: Electronic structures of lead iodide based low-dimensional crystals. Phys. Rev. B **67**, 155405 (2003)
30. Baikie, T., Fang, Y., Kadro, J.M., Schreyer, M., Wei, F., Mhaisalkar, S.G., Grätzel, M., White, T.J.: Synthesis and crystal chemistry of the hybrid perovskite $(CH_3NH_3)PbI_3$ for solid-state sensitised solar cell applications. J. Mater. Chem. A **1**, 5628–5641 (2013)
31. Takahashi, Y., Obara, R., Lin, Z.-Z., Takahashi, Y., Naito, T., Inabe, T., Ishibashi, S., Terakura, K.: Charge-transport in tin-iodide perovskite $CH_3NH_3SnI_3$: origin of high conductivity. Dalton Trans. **40**, 5563–5568 (2011)
32. Mosconi, E., Amat, A., Nazeeruddin, M.K., Grätzel, M., De Angelis, F.: First-principles modeling of mixed halide organometal perovskites for photovoltaic applications. J. Phys. Chem. C **117**, 13902–13913 (2013)
33. Even, J., Pedesseau, L., Jancu, J.-M., Katan, C.: Importance of spin-orbit coupling in hybrid organic/inorganic perovskites for photovoltaic applications. J. Phys. Chem. Lett. **4**, 2999–3005 (2013)
34. Stoumpos, C.C., Malliakas, C.D., Kanatzidis, M.G.: Semiconducting Tin and Lead Iodide perovskites with organic cations: phase transitions, high mobilities, and near-infrared photoluminescent properties. Inorg. Chem. **52**, 9019–9038 (2013)
35. Papavassiliou, G.C., Koutselas, I.B.: Structural, optical and related properties of some natural three- and lower-dimensional semiconductor systems. Synthetic Met. **71**, 1713–1714 (1995)
36. Chung, I., Lee, B., He, J., Chang, R.P.H., Kanatzidis, M.G.: All-solid-state dye-sensitized solar cells with high efficiency. Nature **485**, 486–489 (2012)

37. Etgar, L., Gao, P., Xue, Z., Peng, Q., Chandiran, A.K., Liu, B., Nazeeruddin, M.K., Grätzel, M.: Mesoscopic $CH_3NH_3PbI_3/TiO_2$ heterojunction solar cells. J. Am. Chem. Soc. **134**, 17396–17399 (2012)
38. Sakuma, R., Friedrich, C., Miyake, T., Blügel, S., Aryasetiawan, F.: GW calculations including spin-orbit coupling: application to Hg chalcogenides. Phys. Rev. B **84**, 085144 (2011)
39. Umari, P., Mosconi, E., De Angelis, F.: Relativistic GW calculations on $CH_3NH_3PbI_3$ and $CH_3NH_3SnI_3$ perovskites for solar cell applications. Sci. Rep. **4**, 4467 (2014)
40. Lee, M.M., Teuscher, J., Miyasaka, T., Murakami, T.N., Snaith, H.J.: Efficient hybrid solar cells based on meso-superstructured organometal halide perovskites. Science **338**, 643–647 (2012)
41. Colella, S., Mosconi, E., Fedeli, P., Listorti, A., Gazza, F., Orlandi, F., Ferro, P., Besagni, T., Rizzo, A., Calestani, G., Gigli, G., De Angelis, F., Mosca, R.: $MAPbI_{3-x}Cl_x$ mixed halide perovskite for hybrid solar cells: the role of chloride as dopant on the transport and structural properties. Chem. Mater. **25**, 4613–4618 (2013)
42. Yamada, K., Nakada, K., Takeuchi, Y., Nawa, K., Yamane, Y.: Tunable perovskite semiconductor $CH_3NH_3SnX_3$ (X: Cl, Br, or I) characterized by X-ray and DTA. Bull. Chem. Soc. Jpn. **84**, 926–932 (2011)
43. Zhao, Y., Zhu, K.: CH3NH3Cl-assisted one-step solution growth of CH3NH3PbI3: structure, charge-carrier dynamics, and photovoltaic properties of perovskite solar cells. J. Phys. Chem. C **118**, 9412–9418 (2014)
44. Edri, E., Kirmayer, S., Kulbak, M., Hodes, G., Cahen, D.: Chloride inclusion and hole transport material doping to improve methyl ammonium lead bromide perovskite-based high open-circuit voltage solar cells. J. Phys. Chem. Lett. **5**, 429–433 (2014)
45. Conings, B., Baeten, L., De Dobbelaere, C., D'Haen, J., Manca, J., Boyen, H.-G.: Perovskite-based hybrid solar cells exceeding 10 % efficiency with high reproducibility using a thin film sandwich approach. Adv. Mater. **26**, 2041–2046 (2013)
46. Kim, H.-B., Choi, H., Jeong, J., Kim, S., Walker, B., Song, S., Kim, J.Y.: Mixed solvents for the optimization of morphology in solution-processed, inverted-type perovskite/fullerene hybrid solar cells. Nanoscale
47. Chen, Q., Zhou, H., Hong, Z., Luo, S., Duan, H.-S., Wang, H.-H., Liu, Y., Li, G., Yang, Y.: Planar heterojunction perovskite solar cells via vapor-assisted solution process. J. Am. Chem. Soc. **136**, 622–625 (2013)
48. Qiu, J., Qiu, Y., Yan, K., Zhong, M., Mu, C., Yan, H., Yang, S.: All-solid-state hybrid solar cells based on a new organometal halide perovskite sensitizer and one-dimensional TiO_2 nanowire arrays. Nanoscale **5**, 3245–3248 (2013)
49. Liang, P.-W., Liao, C.-Y., Chueh, C.-C., Zuo, F., Williams, S.T., Xin, X.-K., Lin, J., Jen, A.K. Y.: Additive enhanced crystallization of solution-processed perovskite for highly efficient planar-heterojunction solar cells. Adv. Mater. **26**, 3748–3754 (2014)
50. Eperon, G.E., Burlakov, V.M., Docampo, P., Goriely, A., Snaith, H.J.: Morphological control for high performance, solution-processed planar heterojunction perovskite solar cells. Adv. Funct. Mater. **24**, 151–157 (2014)
51. Noh, J.H., Im, S.H., Heo, J.H., Mandal, T.N., Seok, S.I.: Chemical management for colorful, efficient, and stable inorganic-organic hybrid nanostructured solar cells. Nano Lett. **13**, 1764–1769 (2013)
52. Kim, H.-S., Mora-Sero, I., Gonzalez-Pedro, V., Fabregat-Santiago, F., Juarez-Perez, E.J., Park, N.-G., Bisquert, J.: Mechanism of carrier accumulation in perovskite thin-absorber solar cells. Nat. Commun. **4** (2013)
53. Poglitsch, A., Weber, D.: Dynamic disorder in methylammoniumtrihalogenoplumbates (II) observed by millimeter-wave spectroscopy. J. Chem. Phys. **87**, 6373–6378 (1987)
54. Amat, A., Mosconi, E., Ronca, E., Quarti, C., Umari, P., Nazeeruddin, M.K., Grätzel, M., De Angelis, F.: Cation-induced band-gap tuning in organohalide perovskites: interplay of spin-orbit coupling and octahedra tilting. Nano Lett. **14**, 3608–3616 (2014)

55. Roiati, V., Mosconi, E., Listorti, A., Colella, S., Gigli, G., De Angelis, F.: Stark effect in perovskite/TiO2 solar cells: evidence of local interfacial order. Nano Lett. **14**, 2168–2174 (2014)
56. Mitzi, D.B.: Solution-processed inorganic semiconductors. J. Mater. Chem. **14**, 2355–2365 (2004)
57. Mosconi, E., Ronca, E., De Angelis, F.: First-principles investigation of the TiO2/organohalide perovskites interface: the role of interfacial chlorine. J. Phys. Chem. Lett. **5**, 2619–2625 (2014)
58. Feng, H.-J., Paudel, T.R., Tsymbal, E.Y., Zeng, X.C.: Tunable optical properties and charge separation in CH3NH3SnxPb1–xI3/TiO2-based planar perovskites cells. J. Am. Chem. Soc. **137**, 8227–8236 (2015)
59. Lindblad, R., Bi, D., Park, B.-W., Oscarsson, J., Gorgoi, M., Siegbahn, H., Odelius, M., Johansson, E.M.J., Rensmo, H.: Electronic structure of TiO2/CH3NH3PbI3 perovskite solar cell interfaces. J. Phys. Chem. Lett. **5**, 648–653 (2014)
60. Miller, E.M., Zhao, Y., Mercado, C.C., Saha, S.K., Luther, J.M., Zhu, K., Stevanovic, V., Perkins, C.L., van de Lagemaat, J.: Substrate-controlled band positions in CH3NH3PbI3 perovskite films. Phys. Chem. Chem. Phys. **16**, 22122–22130 (2014)
61. Schulz, P., Edri, E., Kirmayer, S., Hodes, G., Cahen, D., Kahn, A.: Interface energetics in organo-metal halide perovskite-based photovoltaic cells. Energy Environ. Sci. **7**, 1377–1381 (2014)
62. Baena, J.P.C., Steier, L., Tress, W., Saliba, M., Neutzner, S., Matsui, T., Giordano, F., Jacobsson, T.J., Kandada, A.R.S., Zakeeruddin, S. M., Petrozza, A., Abate, A., Nazeeruddin, M.K., Gratzel, M., Hagfeldt, A.: Highly efficient planar perovskite solar cells through band alignment engineering. Energy Environ. Sci. **8**, 2928–2934 (2015)
63. Tress, W., Marinova, N., Moehl, T., Zakeeruddin, S.M., Nazeeruddin, M.K., Grätzel, M.: Understanding the rate-dependent J–V hysteresis, slow time component, and aging in CH3NH3PbI3 perovskite solar cells: the role of a compensated electric field. Energy Environ. Sci. **8**, 995–1004 (2015)
64. Roldan-Carmona, C., Gratia, P., Zimmermann, I., Grancini, G., Gao, P., Graetzel, M., Nazeeruddin, M.K.: High efficiency methylammonium lead triiodide perovskite solar cells: the relevance of non-stoichiometric precursors. Energy Environ. Sci. **8**, 3550–3556 (2015)
65. Mosconi, E., Grancini, G., Roldan-Carmona, C., Gratia, P., Zimmermann, I., Nazeeruddin, M. K., De Angelis, F.: Enhanced TiO2/MAPbI3 electronic coupling by interface modification with PbI2. Chem. Mater. (submitted to, 2016)
66. Yang, J., Siempelkamp, B.D., Mosconi, E., De Angelis, F., Kelly, T.L.: Origin of the thermal instability in CH3NH3PbI3 thin films deposited on ZnO. Chem, Mater (2015)
67. Azpiroz, J.M., Mosconi, E., Bisquert, J., De Angelis, F.: Defect migration in methylammonium lead iodide and its role in perovskite solar cell operation. Energy Environ. Sci. **8**, 2118–2127 (2015)
68. Agiorgousis, M.L., Sun, Y.-Y., Zeng, H., Zhang, S.: Strong covalency-induced recombination centers in perovskite solar cell material CH3NH3PbI3. J. Am. Chem. Soc. **136**, 14570–14575 (2014)
69. Buin, A., Pietsch, P., Xu, J., Voznyy, O., Ip, A.H., Comin, R., Sargent, E.H.: Materials processing routes to trap-free halide perovskites. Nano Lett. **14**, 6281–6286 (2014)
70. Du, M.H.: Efficient carrier transport in halide perovskites: theoretical perspectives. J. Mater. Chem. A **2**, 9091–9098 (2014)
71. Walsh, A., Scanlon, D.O., Chen, S., Gong, X.G., Wei, S.-H.: Self-regulation mechanism for charged point defects in hybrid halide perovskites. Angew. Chem. Int. Ed. **53**, 1–5 (2014)
72. Yin, W.-J., Shi, T., Yan, Y.: Unusual defect physics in CH3NH3PbI3 perovskite solar cell absorber. Appl. Phys. Lett. **104**, 063903 (2014)
73. Almora, O., Zarazua, I., Mas-Marza, E., Mora-Sero, I., Bisquert, J., Garcia-Belmonte, G.: Capacitive dark currents, hysteresis, and electrode polarization in lead halide perovskite solar cells. J. Phys. Chem. Lett. **6**, 1645–1652 (2015)

74. Xiao, Z., Yuan, Y., Shao, Y., Wang, Q., Dong, Q., Bi, C., Sharma, P., Gruverman, A., Huang, J.: Giant switchable photovoltaic effect in organometal trihalide perovskite devices. Nat. Mater. **14**, 193–198 (2014)
75. Mosconi, E., Amat, A., Nazeeruddin, K., Grätzel, M., De Angelis, F.: First-principles modeling of mixed halide organometal perovskites for photovoltaic applications. J. Phys. Chem. C **117** (2013)
76. Du, M.-H.: Density functional calculations of native defects in CH3NH3PbI3: effects of spin-orbit coupling and self-interaction error. J. Phys. Chem. Lett. **6**, 1461–1466 (2015)
77. Bergmann, V.W., Weber, S.A.L., Ramos, F.J., Nazeeruddin, M.K., Grätzel, M., Li, D., Domanski, A.L., Lieberwirth, I., Ahmad, S.: Real-space observation of unbalanced charge distribution inside a perovskite-sensitized solar cell. Nat. Commun. 1–9 (2014)
78. Edri, E., Kirmayer, S., Mukhopadhyay, S., Gartsman, K., Hodes, G., Cahen, D.: Elucidating the charge carrier separation and working mechanism of CH3NH3PbI3–xClx perovskite solar cells. Nat. Commun. 1–8 (2014)
79. Snaith, H.J., Abate, A., Ball, J.M., Eperon, G.E., Leijtens, T., Noel, N.K., Stranks, S.D., Wang, J.T.-W., Wojciechowski, K., Zhang, W.: Anomalous hysteresis in perovskite solar cells. J. Phys. Chem. Lett. **5**, 1511–1515 (2014)
80. Xing, G., Wu, B., Chen, S., Chua, J., Yantara, N., Mhaisalkar, S., Mathews, N., Sum, T.C.: Interfacial electron transfer barrier at compact TiO2/CH3NH3PbI3 heterojunction. Small **11**, 3606–3613 (2015)
81. Niu, G., Li, W., Meng, F., Wang, L., Dong, H., Qiu, Y.: Study on the stability of CH3NH3PbI3 films and the effect of post-modification by aluminum oxide in all-solid-state hybrid solar cells. J. Mater. Chem. A **2**, 705–710 (2014)
82. Yang, J., Siempelkamp, B.D., Liu, D., Kelly, T.L.: Investigation of CH3NH3PbI3 degradation rates and mechanisms in controlled humidity environments using in situ techniques. ACS Nano **9**, 1955–1963 (2015)
83. Leguy, A., Hu, Y., Campoy-Quiles, M., Alonso, M.I., Weber, O.J., Azarhoosh, P., van Schilfgaarde, M., Weller, M.T., Bein, T., Nelson, J., Docampo, P., Barnes, P.R.F.: The reversible hydration of CH3 NH3PbI3 in films, single crystals and solar cells. Chem. Mater. **27**, 3397–3407 (2015)
84. Han, Y., Meyer, S., Dkhissi, Y., Weber, K., Pringle, J.M., Bach, U., Spiccia, L., Cheng, Y.-B.: Degradation observations of encapsulated planar CH3NH3PbI3 perovskite solar cells at high temperatures and humidity. J. Mater. Chem. A **3**, 8139–8147 (2015)
85. Frost, J.M., Butler, K.T., Brivio, F., Hendon, C.H., van Schilfgaarde, M., Walsh, A.: Atomistic origins of high-performance in hybrid halide perovskite solar cells. Nano Lett. **14**, 2584–2590 (2014)
86. Christians, J.A., Miranda Herrera, P.A., Kamat, P.V.: Transformation of the excited state and photovoltaic efficiency of CH3NH3PbI3 perovskite upon controlled exposure to humidified air. J. Am. Chem. Soc. **137**, 1530–1538 (2015)
87. Gottesman, R., Haltzi, E., Gouda, L., Tirosh, S., Bouhadana, Y., Zaban, A., Mosconi, E., De Angelis, F.: Extremely slow photoconductivity response of CH3NH3PbI3 perovskites suggesting structural changes under working conditions. J. Phys. Chem. Lett. **5**, 2662–2669 (2014)
88. Dong, X., Fang, X., Lv, M., Ling, B., Zhang, S., Ding, J., Yuan, N.: Improvement of the humidity stability of organic-inorganic perovskite solar cells using ultrathin Al2O3 layers prepared by atomic layer deposition. J. Mater. Chem. A **3**, 5360–5367 (2015)
89. Habisreutinger, S.N., Leijtens, T., Eperon, G.E., Stranks, S.D., Nicholas, R.J., Snaith, H.J.: Carbon nanotube/polymer composites as a highly stable hole collection layer in perovskite solar cells. Nano Lett. **14**, 5561–5568 (2014)
90. Mei, A., Li, X., Liu, L., Ku, Z., Liu, T., Rong, Y., Xu, M., Hu, M., Chen, J., Yang, Y., Grätzel, M., Han, H.: A hole-conductor–free, fully printable mesoscopic perovskite solar cell with high stability. Science **345**, 295–298 (2014)

91. Xie, F.X., Zhang, D., Su, H., Ren, X., Wong, K.S., Grätzel, M., Choy, W.C.H.: Vacuum-assisted thermal annealing of CH3NH3PbI3 for highly stable and efficient perovskite solar cells. ACS Nano **9**, 639–646 (2015)
92. You, J., Yang, Y., Hong, Z., Song, T.-B., Meng, L., Liu, Y., Jiang, C., Zhou, H., Chang, W.-H., Li, G.: Moisture assisted perovskite film growth for high performance solar cells. Appl. Phys. Lett. **105**, 183902 (2014)
93. Mosconi, E., Azpiroz, J.M., De Angelis, F.: Ab Initio molecular dynamics simulations of methylammonium lead iodide perovskite degradation by water. Chem. Mater. **27**, 4885–4892 (2015)
94. Haruyama, J., Sodeyama, K., Han, L., Tateyama, Y.: Termination dependence of tetragonal CH3NH3PbI3 surfaces for perovskite solar cells. J. Phys. Chem. Lett. **5**, 2903–2909 (2014)
95. Car, R., Parrinello, M.: Unified Approach for molecular dynamics and density-functional theory. Phys. Rev. Lett. **55**, 2471–2474 (1985)
96. Giannozzi, P., Baroni, S., Bonini, N., Calandra, M., Car, R., Cavazzoni, C., Ceresoli, D., Guido, L.C., Cococcioni, M., Dabo, I., Corso, A.D., Gironcoli, S.D., Fabris, S., Fratesi, G., Gebauer, R., Gerstmann, U., Gougoussis, C., Kokalj, A., Lazzeri, M., Martin-Samos, L., Marzari, N., Mauri, F., Mazzarello, R., Paolini, S., Pasquarello, A., Paulatto, L., Sbraccia, C., Scandolo, S., Sclauzero, G., Seitsonen, A.P., Smogunov, A., Umari, P., Wentzcovitch, R.M.: QUANTUM ESPRESSO: a modular and open-source software project for quantum simulations of materials. J. Phys.: Condens. Matter **21**, 395502 (2009)
97. Perdew, J.P., Burke, K., Ernzerhof, M.: Generalized gradient approximation made simple. Phys. Rev. Lett. **77**, 3865–3868 (1996)
98. Grimme, S.: Semiempirical GGA-type density functional constructed with a long-range dispersion correction. J. Comp. Chem. **27**, 1787–1799 (2006)
99. Hailegnaw, B., Kirmayer, S., Edri, E., Hodes, G., Cahen, D.: Rain on methylammonium lead iodide based perovskites: possible environmental effects of perovskite solar cells. J. Phys. Chem. Lett. **6**, 1543–1547 (2015)

Maximum Efficiency and Open-Circuit Voltage of Perovskite Solar Cells

Wolfgang Tress

Abstract This chapter serves as an introduction to the general working principles of solar cells. It starts from the thermodynamics of terrestrial solar cells and fundamentals of semiconductor-based photovoltaics, where the theoretical limits of efficiency and open-circuit voltage as a function of the bandgap are discussed. The chapter describes the prediction of the open-circuit voltage when the photovoltaic action spectra and the electroluminescence quantum efficiency are known. The role of subgap states and several sources of nonradiative recombination, including interfaces to the charge-transport layers, are investigated at open-circuit voltage and fill factor of state-of-the-art perovskite solar cells. Based on these factors, organic–inorganic perovskite solar cells with different architectures and compositions are compared with other solar cell technologies. Low disorder and weak nonradiative recombination are shown to be responsible for the superior performance of mixed cation mixed halide perovskite solar cells, allowing for open-circuit voltages of 1.2 V to be achieved at a bandgap of 1.6 eV.

1 Maximum Power-Conversion Efficiency of a Terrestrial Solar Cell

1.1 Thermodynamics and Black Body Radiation

A solar cell converts energy of light emitted from the sun into electrical energy. The energy flux from the sun is primarily thermal radiation and can be approximated by a black body spectrum at a temperature T_S of ≈5800 K outside the earth atmosphere. Prior to reaching the earth's surface, narrow spectral bands have been filtered out by gases in the atmosphere, such as ozone, oxygen, and water vapor (Fig. 1). The spectrum is then called AM X, where X denotes the distance that the

W. Tress (✉)
Laboratory of Photonics and Interfaces (LPI), École polytechnique fédérale de Lausanne (EPFL), 1015, Lausanne, Switzerland
e-mail: wolfgang.tress@epfl.ch

N.-G. Park et al. (eds.), *Organic-Inorganic Halide Perovskite Photovoltaics*,
DOI 10.1007/978-3-319-35114-8_3

light has traveled through the atmosphere in multiples of its thickness. The standard spectrum for solar cell characterization is AM 1.5 global corresponding to an angle of incidence of $48^{\circ} = \cos^{-1}(1.5^{-1})$.

Upon absorption of sun light, the absorber's temperature increases to T_A meaning that the energy transferred from the sun heats the absorber "medium". Thus, the solar cell can be treated as a heat engine transforming thermal energy into work in the form of electrical energy. The maximum conversion efficiency of a heat engine is the Carnot efficiency, which considers the conservation of entropy contained in thermal radiation. This entropy ΔS has to be released with a heat flux $\Delta Q = T_0 \Delta S$, with T_0 being the temperature of the surroundings, because electrical energy is entropy-free [1]. Thus, the Carnot efficiency is

$$\eta_C = \frac{T_A - T_0}{T_A} = 1 - \frac{T_0}{T_A}. \tag{1}$$

In order to obtain the maximum Carnot efficiency, the temperature difference between the medium and the surroundings should be maximized to avoid a large heat flux associated with the conservation of entropy. As the temperature of the surroundings is fixed, the medium should be as hot as possible.

Coming back to the energy source, we notice that the heat is transferred from the sun to the medium by radiation. In the optimum case, the medium itself is capable of absorbing all the incident radiation. Thus, it is a black body as well, which according to Kirchhoff's law reemits part of the absorbed photon flux. Spectrum

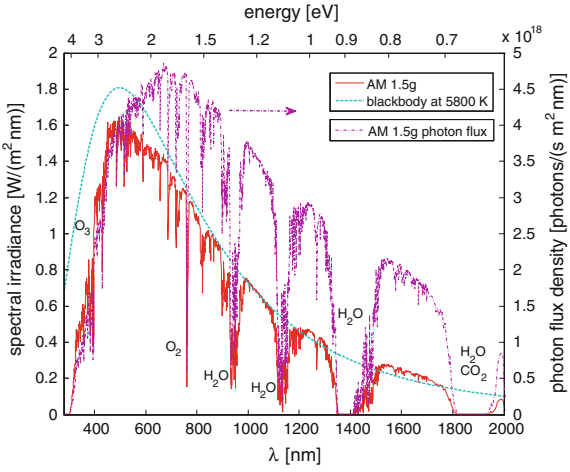

Fig. 1 The standard solar spectrum, AM1.5 g, used for solar cell characterization. The irradiance integrated over wavelength results in 100 mW cm^{-2}. The spectral shape can be approximated with a black body radiator at 5800 K. The gaps are due to absorption of compounds in the atmosphere (O_3, O_2, H_2O, …). *Dash-dotted* is the corresponding photon flux, obtained when dividing the irradiance spectrum (*red*) by the photon energy at each wavelength

$B(\lambda, T)$ and emitted power per surface area (I) are described by Planck's and the Stefan–Boltzmann law, respectively:

$$B(\lambda, T) = \frac{2hc^2}{\lambda^5} \frac{1}{\exp \frac{hc}{\lambda k_B T} - 1}, \tag{2a}$$

$$I = \sigma T^4, \tag{2b}$$

with wavelength λ, Planck's constant h, speed of light c, Boltzmann constant k_B, and Stefan–Boltzmann constant σ. Thus, the higher T_A, the more intense the emission. If work is not extracted from the absorber medium, it reaches equilibrium with the sun and the surroundings. For a maximum concentration of the sun light, i.e., a situation where all the emitted flux from the absorber medium is redirected toward the sun, the medium would reach the temperature of the sun (surface) T_S and emit the solar spectrum back to the sun. However, in this situation work cannot be extracted. This requires a lower temperature of the absorber medium, and the fraction of extractable energy can be written as the difference between absorbed and emitted energy flux according to the Stefan–Boltzmann law:

$$\eta_{rad} = \frac{\sigma\left(T_S^4 - T_A^4\right)}{\sigma T_S^4} = 1 - \frac{T_A^4}{T_S^4}. \tag{3}$$

This equation demands for a low T_A, which is in contrast to the requirements for obtaining a high Carnot efficiency. Consequently, the highest solar to work conversion efficiency is reached at a T_A such that $T_0 < T_A < T_S$. The optimum T_A is 2478 K with a corresponding $\eta_{max} = \eta_{rad}\eta_C$ of 85 %. For a conversion of, e.g., mechanical work of the heat engine into electricity, we can imagine a generator with almost 100 % power-conversion efficiency. Consequently, the highest power-conversion efficiency of a terrestrial solar cell might approach but cannot exceed 85 %.

In case of a nonconcentrated system, the thermodynamic limit is reduced as the medium will emit into a larger solid angle and thus increase the entropy. The solid angle of the sun seen from the earth is 6.8×10^{-5} (resulting from the long distance between the earth and the sun and the sun's diameter), which is a factor 46,200 smaller than the solid angle of emission into a hemisphere [1, 2]. This factor should be considered in the emitted intensity in Eq. 3 and reduces η_{max} to only a few percent. Thus, efficient solar–thermal energy conversion using a heat engine requires concentration of sun light. This is not necessarily the case for photovoltaic systems using bandedge absorbers as we will see in the following sections. They can operate efficiently at low concentrations of the sun light and at ambient temperatures. Nevertheless, every solar-based energy converter, independent of its implementation, is tied to the 85 % limit.

1.2 Semiconductor-Based Photovoltaics

A semiconductor is characterized by a bandgap E_g making its optical properties differ from those of a black body. In an ideal semiconductor, only photons with energy higher than E_g are absorbed by promoting an electron from the valence to the conduction band and leaving a hole in the valence band (Fig. 2). Thus, the onset of the absorption spectrum is at the energy of the bandgap. Incident photons with lower energies are transmitted. The peak energy of the emitted photon spectrum is located close to the bandgap energy as well and almost independent of temperature in contrast to the black body radiation. Mainly the spectral width increases with temperature due to an increased thermal energy of electrons and holes in their respective bands. To be distinguished from thermal (i.e., black body) radiation, this kind of narrow radiation is called luminescence.

To harvest as many solar photons as possible, the bandgap of the semiconductor should be minimized (Fig. 1), which allows for the highest electron-hole generation rate, and we can write the below equation for the photocurrent:

$$J_{\mathrm{ph,ideal}} = e \int_{E_g}^{\infty} \Phi_{\mathrm{AM1,5g}}(E) dE \tag{4}$$

with $\Phi_{\mathrm{AM1,5g}}$ describing the spectral photon flux, i.e., the number of photons per area, time, and energy (or wavelength) interval. To generate a net electrical current in an external circuit, electrons and holes have to be extracted at two different contacts. For the moment, we only introduce the concept of so-called charge-selective contacts: an electron-selective contact would only allow electrons to pass and reject holes, and vice versa for a hole-selective contact. We will come to implementations of such selective contacts later.

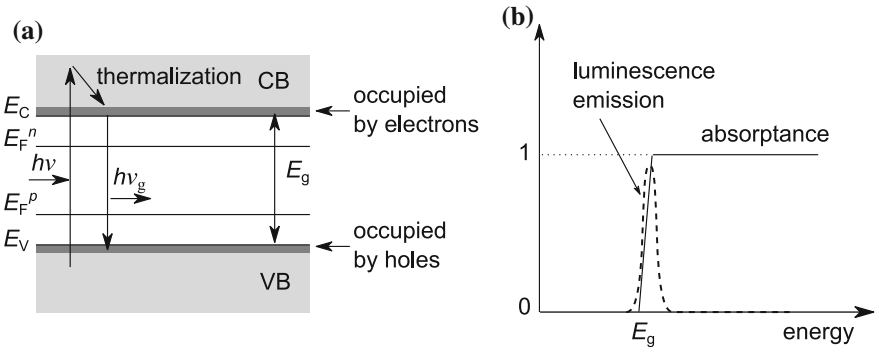

Fig. 2 Optoelectronic basics of semiconductors **a** Sketch of band diagram with bandgap E_g, conduction and valence band edge E_C and E_V, respectively, and quasi-Fermi levels for electrons E_F^n and holes E_F^p, which are split due to illumination. **b** Schematics of ideal absorptance and emission

However, a large photocurrent is not sufficient: the relevant parameter is the electrical power of the extracted charge flux. This power is the product of flux and the (average) free energy of one extracted electron-hole pair, which is proportional to the voltage measurable externally. Thus, we need an expression for this energy, which is mainly electrochemical in nature and depends on the electrical potential energy as well as the concentration of charges (chemical energy). We expect the potential energy of the electron-hole pair to scale with the bandgap, consistent with the fact that the peak of luminescence radiation is located at the bandgap energy. This holds even for absorbed photons with much higher energy, which create an electron (hole) that is located much higher (deeper) in the conduction (valence) band compared to the band edges. However, this electron relaxes quickly (ps) to the band edge due to energy transfer to phonons (Fig. 2a), analogously to Kasha's rule in the photochemistry of electronically excited molecules. The excess energy is lost as heat and the average energy of the electron remains at $E_C + \frac{3}{2} k_B T$. This fast process assisted by phonons is called thermalization. Consequently, the higher the bandgap, the lower are the overall thermalization losses, when absorbing a broad spectrum such as AM1.5 g. Therefore, when tuning the bandgap to reach high efficiency, there is a tradeoff between harvesting as many photons as possible and maximizing the energy of extracted charges.

To determine the optimum bandgap, we need to find an expression for the electrical energy of an extracted electron-hole pair. Coming back to the previous section on thermodynamics, we know that electrical energy is an entropy-free part of the energy. Thus, we need to know the entropy of an electron (hole) in the electron (hole) gas in the conduction (valence) band. After longer derivation [1] it is found that the entropy-free part of the energy, i.e., the electrochemical potential η_e of an electron in the conduction band, is:

$$\eta_e = E_C - k_B T \ln \frac{N_C}{n}, \tag{5}$$

where n is the electron density (number of electrons per unit volume) and N_C is the effective density of states, i.e., a parameter that represents the amount of available states close to the band edge. The second term increases linearly with temperature as expected for an energy flux related to entropy ($\Delta Q = T\Delta S$). ΔQ becomes 0 either at $T \to 0$ K or when the density of states is completely filled ($n = N_C$), i.e., there is only one microscopic state possible without any permutations (although in this case, this equation does not hold any more as it contains approximations valid for low n only) [2]. Analogously, we obtain for (positively charged) holes p:

$$-\eta_h = E_V + k_B T \ln \frac{N_V}{p}. \tag{6}$$

In steady state, one electron is extracted together with one hole to conserve charge and obey a continuity equation for electrons. The total energy is then the sum of the electrochemical potentials

$$eV = \eta_e + \eta_h = E_C - E_V - k_B T \ln \frac{N_C N_V}{np} = E_g - k_B T \ln \frac{N_C N_V}{np}. \quad (7)$$

Here, we introduce the externally measurable voltage V, which is expressed as the energy of one extractable electron-hole pair in the electron gas divided by the elementary charge e. This equation shows that the idea of a large bandgap required to maximize the energy of an extracted electron-hole pair is correct.

From Eqs. 5 and 6, we recognize that the electrochemical potentials are the quasi-Fermi energies:

$$n = N_C \exp\left(-\frac{E_C - E_F^n}{k_B T}\right) \rightarrow E_F^n = \eta_e \quad (8a)$$

$$p = N_V \exp\left(-\frac{E_F^p - E_V}{k_B T}\right) \rightarrow E_F^p = -\eta_h \quad (8b)$$

As electrons are fermions, their concentration is determined by Fermi Dirac statistics. The Fermi level E_F is defined as the energy at which the probability of finding the fermion is ½. In a metal E_F describes the highest energy for electrons in the bands at $T \rightarrow 0\,\mathrm{K}$.

To obtain the electron density in general, the statistics is multiplied by the energetic distribution of available states (so-called density of states, DOS). For electrons in the conduction band (CB) we get

$$\begin{aligned} n &= \int_{CB} f(E) \times \mathrm{DOS}_{CB}(E) dE = \int_{CB} \frac{1}{1 + \exp\frac{E - E_F}{k_B T}} \times \mathrm{DOS}_{CB}(E) dE \\ &\approx \int_{CB} \exp\left(-\frac{E - E_F}{k_B T}\right) \times \mathrm{DOS}_{CB}(E) dE \end{aligned} \quad (9)$$

This approach results in the previous equations considering a certain DOS and the Boltzmann approximation. Under equilibrium, i.e., no voltage applied or generated by light, we obtain

$$E_F^n = E_F^p \quad (10)$$

and

$$np = n_i^2 = N_C N_V \exp\left(-\frac{E_g}{k_B T}\right), \quad (11)$$

with the intrinsic (i.e., thermally generated) charge carrier density n_i. The definition of quasi-Fermi levels under illumination or applied voltage (nonequilibrium) is possible as thermalization within a band is commonly much faster than a spontaneous transition of an electron from conduction to valence band (i.e., electron-hole

recombination). Thus, electrons and holes are in equilibrium within their respective band but not amongst each other. This situation can be called quasiequilibrium, described by two separate Fermi distributions for electrons and holes.

In Eq. 7 the electrochemical energy of the extracted electron-hole pair is not solely determined by the bandgap, but also contains a term that depends on electron and hole concentrations (chemical energy). In a solar cell under illumination, the concentration of charges is built-up by the absorption of light (the so-called charge carrier generation G), but it cannot reach infinitely large numbers as the competing process of recombination sets in. The rate of band-to-band recombination of an electron with a hole can be expressed as

$$R = \beta np. \tag{12}$$

Intuitively we can say that the recombination rate R scales with the probability of an electron finding a hole. In steady state at open circuit under a given light intensity $\propto G$, all charges recombine, i.e., $R = G$ and therefore the open-circuit voltage is (Eq. 12 in Eq. 7):

$$eV_{\mathrm{oc}} = E_{\mathrm{g}} - k_{\mathrm{B}}T \ln \frac{N_{\mathrm{C}}N_{\mathrm{V}}\beta}{G}. \tag{13}$$

This equation describes V_{oc} as a function of temperature, light intensity (which is $\propto G$), and bandgap. An expression for the radiative recombination constant β will be derived subsequently.

1.3 Radiative Limit of the Open-Circuit Voltage

We want to start from the equilibrium situation and extend it to the operation points of the solar cell. Here, equilibrium means that the semiconductor is in the dark without any applied bias. In this case, "dark" describes a surrounding at a temperature $T_0 = 300\,\mathrm{K}$. This temperature gives rise to a background radiation with a black body spectrum at T_0 according to Planck's law

$$\Phi_{\mathrm{BB}}(E) = \frac{1}{4\pi^2\hbar^3c^2} \frac{E^2}{\exp\left(\frac{E}{k_{\mathrm{B}}T_0}\right) - 1}. \tag{14}$$

This equation is identical to Eq. 2a, but expressed in terms of a photon flux as a function of energy (instead of intensity as a function of wavelength). The semiconductor absorbs part of this spectrum and has to emit the same part because it is in equilibrium with the surrounding

$$\Phi_{\mathrm{abs},0} = \int a(E)\Phi_{\mathrm{BB}}(E)dE = \Phi_{\mathrm{em},0}. \tag{15}$$

Here, $a(E)$ is the absorptance (0…1), where we could use a Heaviside step function switching from 0 to 1 at E_g for an ideal semiconductor as we did in Eq. 4.

This equality is true not only for the absolute flux, but also for each energy (or wavelength) according to the principle of "detailed balance":

$$\Phi_{\mathrm{em},0}(E) = a(E)\Phi_{\mathrm{BB}}(E). \tag{16}$$

It means that the emission spectrum $\Phi_{\mathrm{em}}(E)$ can be predicted when absorption coefficient and temperature are known [3].

To experimentally determine the emission spectrum, we consider the nonequilibrium case: Additional electrons and holes need to be generated in the semiconductor, either by light or by applying a voltage and injecting charges. The former option results in photoluminescence, and the latter in electroluminescence. We verify the applicability of the detailed balance theory for a $CH_3NH_3PbI_3$ perovskite solar cell. Rather than using the absorption spectrum, we use the photocurrent action spectrum (external quantum efficiency EQE_{PV}), which ideally is proportional to the absorption spectrum and easier to obtain experimentally. Based on an extended version of the reciprocity between absorption, emission, and electronic charge transport, $a(E)$ can be interchanged with $EQE_{PV}(E)$ [4]. A measured EQE_{PV} onset is shown in Fig. 3a. By multiplying the $EQE_{PV}(E)$ with $\Phi_{\mathrm{BB}}(E)$, shown as dashed line for $T_0 = 320\,\mathrm{K}$, we calculate an emission spectrum (Fig. 3b), which fits the measured electroluminescence spectrum very well. This indicates that the assumption of an unmodified spectrum even under illumination or applied voltage is justified. Coming back to Eq. 12, we can write in equilibrium:

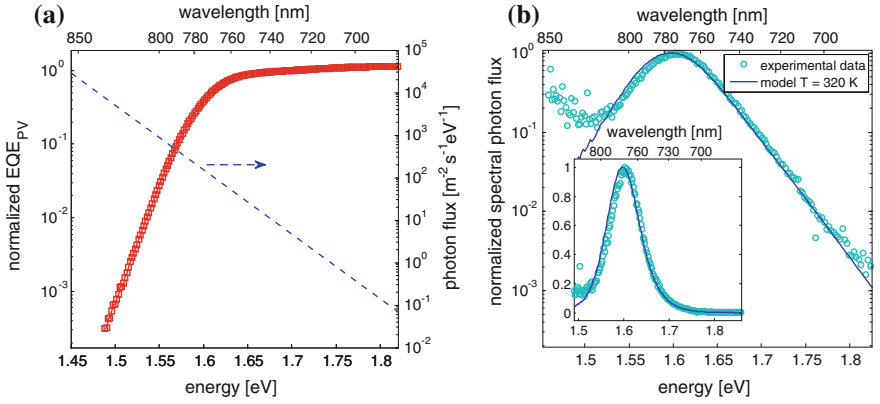

Fig. 3 Bandedge of $CH_3NH_3PbI_3$ **a** Spectral photocurrent onset in terms of the external quantum efficiency of a solar cell (*solid line*) and black body photon flux at 320 K (*dashed*). **b** Measured and calculated electroluminescence emission. Data originally published in Ref. [6]

$$G_0 = \int \alpha(E)\Phi_{BB}(E)dE = \beta n_0 p_0 = \beta n_i^2. \tag{17}$$

Thus, the radiative recombination constant β can be calculated knowing the intrinsic charge carrier density n_i (Eq. 11) and the absorption coefficient $\alpha(E)$. Assuming parabolic band minima (DOS) with an effective electron (hole) mass $m^* = 0.228\,(0.293)m_0$ (m_0 is the electron rest mass) [5], we can derive $N_{C,V}$ using Eq. 9 ($\rightarrow N_{C,V} = 2\left(\frac{2\pi m^* k_B T}{h^2}\right)^{\frac{3}{2}}$, derivation not shown), and in turn n_i (Eq. 11). With Eq. 17 we obtain the value of $\beta \approx 10^{-11}\mathrm{cm}^3\mathrm{s}^{-1}$.

Under bias (or illumination), n and p become larger than n_i and the common Fermi level (Eq. 10) splits into separate (quasi) Fermi levels for electrons and holes according to Eq. 8a, 8b, leading to $np = n_i^2 \exp\frac{E_F^n - E_F^p}{k_B T}$.

Thus, recognizing that eV is the difference between the quasi-Fermi levels at the contacts, the enhanced recombination gives rise to an emitted photon flux Φ_{em} exponentially increasing with the applied voltage:

$$\Phi_{em} = \Phi_{em,0} \exp\frac{eV}{kT}. \tag{18}$$

If we think of the device operated as a light-emitting diode, Φ_{em} is achieved at a particular electric current injected into the device:

$$J_{rad} = e\left(\Phi_{em,0} \exp\frac{eV}{k_B T} - \Phi_{em,0}\right) = e\Phi_{em,0}\left(\exp\frac{eV}{k_B T} - 1\right). \tag{19}$$

We recognize that this equation is identical to the Shockley diode equation when the saturation current is set as $J_0 = e\Phi_{em,0}$.

If the device is operated as a solar cell under illumination, the photocurrent J_{ph} should be added to Eq. 19:

$$J_{ideal} = e\Phi_{em,0}\left(\exp\frac{eV}{k_B T} - 1\right) - J_{ph}. \tag{20}$$

Now, we can write an equation for the open-circuit voltage, setting J_{ideal} to 0:

$$V_{oc,rad} = \frac{k_B T}{e} \ln\left(\frac{J_{ph}}{e\Phi_{em,0}} + 1\right). \tag{21}$$

This is the ideal V_{oc} of a solar cell if only radiative recombination is present. For $CH_3NH_3PbI_3$ perovskite solar cells, we calculate a value of 1.33 V [6, 7]. Variations in bandgap as a function of film morphology can slightly (by $\approx \pm 0.02$V) alter this value. As we will discuss later, (partially) substituting atoms/ions on the perovskite lattice is a strategy to modify the bandgap.

1.4 Shockley–Queisser Limit

Since current is not extracted at V_{oc}, and the power is the product of current and voltage, the power at open circuit is 0. Instead, it is largest at the so-called maximum power point (MPP), which is found by searching for the maximum of $J \times V$. For $CH_3NH_3PbI_3$ perovskite with a bandgap of ≈1.55–1.6 eV, the maximum efficiency would be 31–30 %. The ideal current-voltage curve according to Eq. 20 is visualized in Fig. 4a, including the extractable power. The fill factor is defined as $FF = \frac{J_{MMP}V_{MPP}}{J_{sc}V_{oc}} = \frac{\eta I_{light}}{J_{sc}V_{oc}}$ with the short-circuit current density $J_{sc} = J_{ph}$ and the incident light intensity I_{light}. Figure 4b shows the maximum J_{SC} as a function of the bandgap calculated using Eq. 4 with varied E_g. For an $E_g$of 1.6 eV, we expect a theoretical photocurrent of 25 mA cm^{-2}, which does not include any optical or electrical losses that reduce this value by 1–3 mA cm^{-2} for the best perovskite solar cells [8, 9]. The resulting power-conversion efficiency (Shockley–Queisser, SQ limit [10]) as a function of the bandgap is shown in Fig. 4c, where an E_g between 1.1 and 1.4 eV allows an efficiency of ≈33 %. The decrease of η for larger E_g is due to transmission losses and thus low photon harvesting (low J_{SC}, cf. Fig. 4b). For reduced E_g, the voltage is low and most of the energy is lost due to thermalization.

The losses discussed so far are unavoidable. However, in implementations of solar cells, additional losses occur, which will be discussed in the following sections of this chapter. The circles in Fig. 4c show how closely solar cells based on different semiconductor material with different E_g approach their theoretical radiative limit. Solar cells based on the direct semiconductor GaAs reach an efficiency >28 % coming very close to their theoretical limit. Photovoltaic devices based on silicon, the most common commercial material, show additional losses, but have an efficiency still exceeding 25 %. Perovskite and CIGS solar cells exhibit similar performance, where today's best perovskite solar cell is already closer to the Shockley–Queisser limit than the best CIGS cell.

2 The Bandgap

2.1 Absorption Onset and Subgap Urbach Tail

The SQ limit was calculated for a step function in absorption. However, as shown in Fig. 3a, the absorption is not a Heaviside function but contains a contribution below E_g. This is detrimental, because these subgap states hardly contribute to photocurrent. However, they do participate in recombination entering Eq. 15 enhanced by a multiplication with $\Phi_{BB}(E)$. Thus, a steep absorption onset is preferred. It should follow at least $\exp\left(\frac{E}{k_B T_0}\right)$ to compensate for the exponential increase of $\Phi_{BB}(E)$ with decreasing energy. Figure 5 shows the absorption onset of $CH_3NH_3PbI_3$ perovskite in comparison with other solar cell materials [12]. Due to

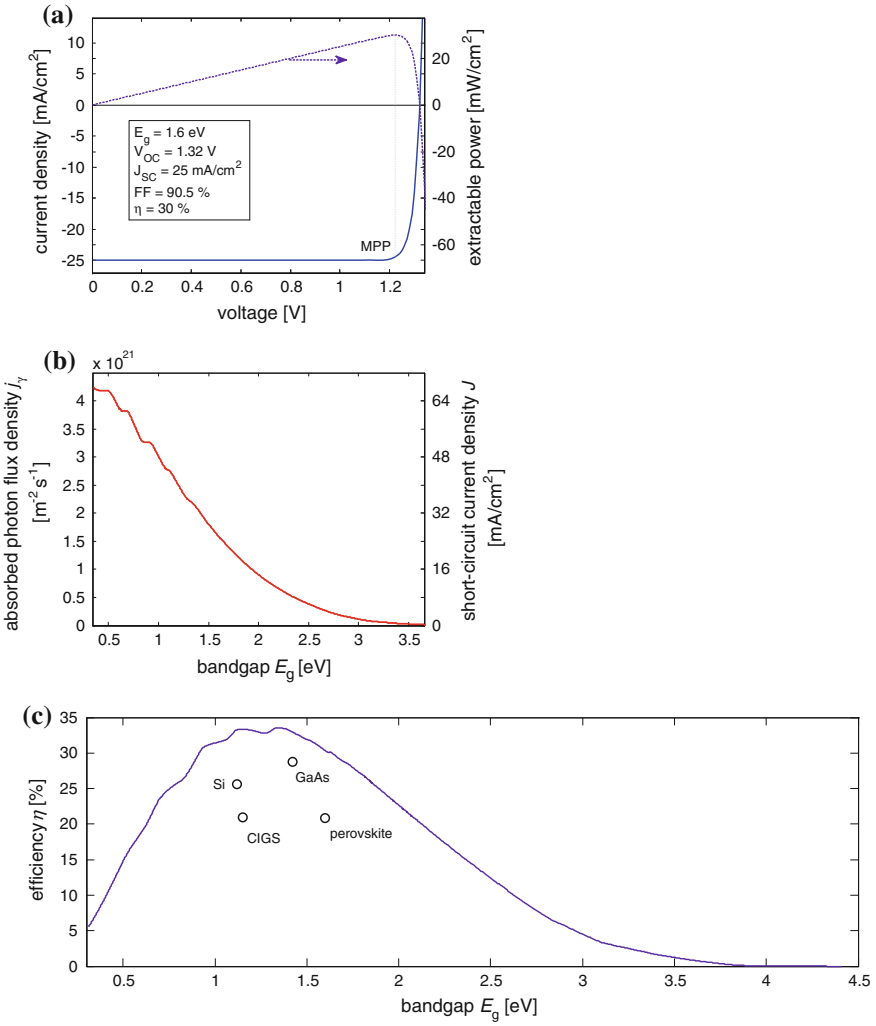

Fig. 4 Shockley–Queisser limit **a** Theoretical *J-V* curve and power output for an ideal semiconductor with a bandgap of 1.6 eV. **b** Harvested photon flux and short-circuit current density as a function of the bandgap. **c** Maximum power-conversion efficiency as a function of bandgap and record values [9, 11] experimentally achieved so far

its direct bandgap the absorption coefficient above bandgap is similar to the one of GaAs and much steeper than in crystalline or amorphous Si. Additionally, the distribution of subgap states is narrow.

The absorption coefficient below the bandgap shows a so-called Urbach tail. Its origin is from various sources of disorder that generate exponentially decaying densities of states below the conduction and above the valence band. Those could be impurities, ionic positional disorder, vibrational fluctuations of atoms, etc. Their

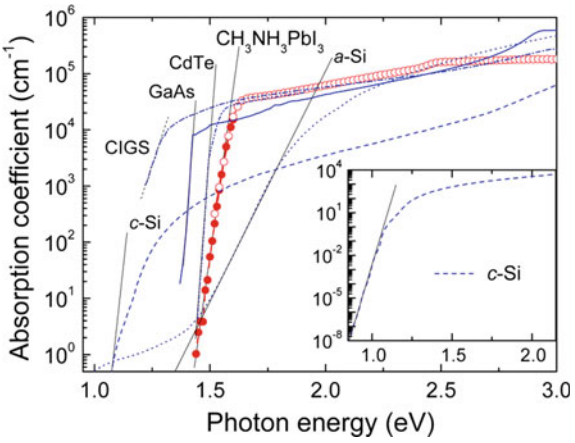

Fig. 5 Absorption coefficient of different solar cell materials. The *black lines* denote an exponential fit to the Urbach tail. Reprinted with permission from [12]. Copyright 2014 American Chemical Society

common feature is that they locally perturb the periodic crystal potential giving rise to fluctuations of the potential that electrons close to the band edges see. The steep rise and resulting low Urbach energy indicates that the disorder in the $CH_3NH_3PbI_3$ perovskite is low due to its high (nano-) crystallinity. In general, the absorption onset of nano-crystalline perovskite depends on the morphology of the film, mainly on the crystallite size. It shifts toward larger energies with smaller crystallites, possibly due to strain in the material [13].

2.2 *Tuning of the Bandgap and Tandem Devices*

Until now we have discussed the $CH_3NH_3PbI_3$ perovskite with a bandgap of 1.55 to 1.6 eV. Similar to other compound semiconductors, a partial replacement of components with others of the same ionic charge and fitting into the lattice (Goldschmidt tolerance factor) facilitates tuning of the bandgap of the perovskite. Here, the organic cation has only minor influence, as it is not directly contributing to the valence and conduction band but changing lattice parameters. Replacing methylammonium (CH_3NH_3) by the bigger formamidinium ($HC(NH_2)_2$) results in a decrease of E_g (by ≈50 meV), slightly shifting the maximum η toward its optimum [14–17]. Using the smaller Cs instead increases the bandgap by ≈100 meV [14, 17]. This trend follows the tight-binding model of more closely spaced atoms having more interaction, and thus stronger splitting of their states into broader bands which in turn results in a more narrow bandgap. In case of the perovskite, size effects controlling the metal–halide–metal bond angles [18] are accompanied with further effects such as modified hydrogen bonding and spin orbit coupling when interchanging the monovalent (organic) cation [19]. Note that due to the antibonding nature of the valence states, the bandgap shows an anomalous decrease with temperature [20].

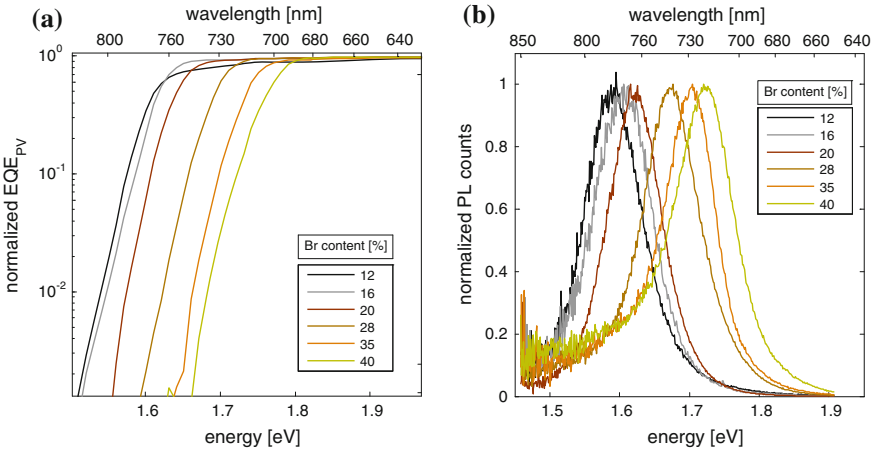

Fig. 6 Mixed MA-FA perovskites with mixed halides **a** The photocurrent onset as a function of the molar Br content, not showing any considerable changes in the Urbach energy. **b** Photoluminescence spectra confirming a shift of the bandgap. The signal at 1.5–1.6 eV might be due to some iodine rich phases in the samples with larger bromine content

More influential are replacements of the halide itself using, e.g., Br [17, 21]. Figure 6 shows photocurrent response (EQE_{PV}) and PL spectra for perovskites with different I:Br molar ratios in the precursor solutions. (These compounds contain a mixture for the organic cation as well because formamidinium–iodide is added to the precursor solution). The data shows that E_g increases monotonically upon increasing substitution of I with Br (similar to highly efficient Cs $HC(NH_2)_2$ mixed systems [22]). At the same time, the Urbach tail is maintained at low energies of approx. 15 meV. Calculating the maximum V_{oc} using Eq. 21, we get an increase of $V_{oc,rad}$ from 1.33 to 1.47 V, when the Br content reaches 40 %. However, the maximum η would decrease from 30 to 27 %. Thus, for a single junction solar cell, there is no reason for increasing E_g except that a higher voltage is preferred to a higher current due to practical reasons such as reduction of resistive losses.

However, tuning the bandgap becomes important when making multijunction solar cells, where several solar cells are stacked on top of each other with the solar cell with the largest E_g employed as the front cell. This approach is a strategy to overcome the Shockley–Queisser limit, as thermalization losses are reduced by collecting the high energy photons at higher voltage. The ideal combination for a two-junction (tandem) solar cell would yield a maximum η of > 42 % with E_{g1} = 1.0 eV and E_{g2} = 1.9 eV [23]. Technologically interesting is a combination of perovskite with silicon [24–26]. For a monolithic integration the photocurrent should be matched, meaning that Si, which delivers a maximum current of almost 42 mA cm^{-2}, should be combined with a perovskite solar cell providing 21 mA cm^{-2}. Ideally, this current could be achieved using a mixed halide perovskite with a bandgap of 1.75 eV. Then, half of the incident photon flux is converted into charges that are collected at a larger voltage compared to the voltage

obtainable with silicon. This boosts the theoretical efficiency from 33 to >40 %. Using realistic values including optical and electrical losses for Si and perovskite solar cell, efficiencies of around 30 % are expected to be feasible in a tandem configuration [27, 28].

3 Nonradiative Recombination

3.1 Quantum Efficiency of Electroluminescence

So far, the solar cell was treated as ideal, which means that only theoretically unavoidable loss processes have been considered. Regarding recombination, this is radiative recombination only. In that case, the solar cell operates at its radiative limit. However, in reality nonradiative losses are present in addition, reducing charge carrier densities in Eq. 7 and consequently the V_{oc}.

Coming back to the derivation of V_{oc} based on detailed balance (Eq. 19), we consider a quantum efficiency of emission for the injection current:

$$J_{rad}(V) = \mathrm{EQE}_{EL} J_{inj}(V). \tag{22}$$

EQE_{EL} is the external quantum efficiency of electroluminescence. We can expand the equation for V_{oc} (Eq. 21) to

$$V_{oc} = \frac{k_B T}{e} \ln\left(\mathrm{EQE}_{EL} \frac{J_{ph}}{e\Phi_{em,0}} + 1\right) \approx V_{oc,rad} - \frac{k_B T}{e} \ln \mathrm{EQE}_{EL}. \tag{23}$$

Thus, a reduction of the EQE_{EL} by a factor of 10 is equivalent to a decrease of V_{oc} by $\frac{k_B T}{e} \ln 10 = 60$ mV at room temperature. The EQE_{EL} should be determined at V_{oc}. Practically, it is measured in the dark by driving the solar cell as an LED, detecting the emitted photon flux and dividing it by the injected electron flux.

Knowing EQE_{EL} and EQE_{PV}, which is required to calculate J_{ph} and $e\Phi_{em,0}$ (Eqs. 4 and 15):

$$J_{ph} = e \int \mathrm{EQE}_{PV}(E) \Phi_{AM1,5g}(E) dE; e\Phi_{em,0} = e \int \mathrm{EQE}_{PV}(E) \Phi_{BB}(E) dE, \tag{24}$$

we can predict the real V_{oc} of a given solar cell [4, 29]. Differences in V_{oc} for different experimental implementations of a solar cell with the same semiconductor are mainly caused by variations of the nonradiative loss that decrease EQE_{EL}. These changes explain the differences observed in V_{oc} for perovskite solar cells, which are reported between 0.7 and 1.2 V, whereas $V_{oc,rad} \approx 1.33$ V is a material property. Table 1 shows examples for perovskite fabricated by different methods and employed in different device architectures [6, 9]. Avoiding a hole transport layer decreases EQE_{EL}

Table 1 Measured J_{sc} and V_{oc} compared to calculated values based on measured EQE_{PV} and EQE_{EL}

		J_{sc} [mA cm^{-2}]	$V_{oc,\ measured}$ [V]	$e\Phi_{em,0}$ [mA cm^{-2}]	$V_{oc,\ rad}$ [V]	EQE_{EL} at $J_{inj} = J_{sc}$	nonrad. loss [V]	$V_{oc,\ calc}$ [V]
Two-step 2014	TiO_2	20	**1.01**	9×10^{-22}	**1.33**	4×10^{-6}	0.32	**1.01**
	Al_2O_3	19	**1.02**	10^{-21}	**1.32**	3×10^{-5}	0.27	**1.05**
	No HTL	11	**0.77**	3×10^{-22}	**1.34**	2×10^{-9}	0.52	**0.82**
One-step 2016		20	**1.18**[a]	$\approx 10^{-21}$	**1.33**	3×10^{-3a}	0.15	**1.18**

[a]nonstabilized

The perovskite in the two-step method is $CH_3NH_3PbI_3$, [6, 30] whereas it is a mixed cation mixed halide perovskite in the one-step device [9]

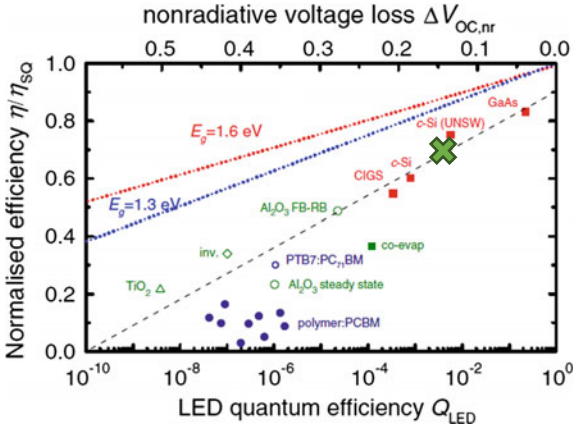

Fig. 7 Power-conversion efficiency for different solar cell technologies normalized to the Shockley-Queisser limits as a function of EQE_{EL} (here denoted as Q_{LED}), equivalent to the nonradiative V_{oc} loss of $\Delta V_{oc,nr} = -26\,mV \times \ln EQE_{EL}$ (*top axis*). The *dotted lines* define the theoretical limits of various EQE_{EL} at the denoted bandgaps. Different $CH_3NH_3PbI_3$ perovskite fabrication technologies are shown in *green*. The *green cross* marks the most efficient perovskite solar cell. Different organic solar cells are shown in *blue*. The *dashed line* is a guide to the eye representing the approximate experimental trend. Reprinted and modified with permission from [31]. Copyright 2015 by the American Physical Society

due to surface recombination. On the other hand, employing hole transport layer and tuning the morphology increases EQE_{EL} and thus the measured V_{oc}.

Figure 7 compares the record value of EQE_{EL} for perovskite solar cells [9] (marked with a green cross) with other technologies [31]. The direct semiconductor GaAs yields the highest values due to a high internal luminescence yield. In silicon, EQE_{EL} is limited by Auger and surface recombination [32, 33]. The trend line (dashed) visualizes that in experiment the factor determining the efficiency is EQE_{EL} defining how closely V_{oc} approaches $V_{oc,rad}$.

3.2 Identifying Recombination Mechanisms

The exact source of nonradiative recombination in perovskites has not yet been identified. In addition to recombination at the contacts, defect recombination in the material itself plays a role. Defects might originate from impurities, grain boundaries, or additional crystalline/amorphous phases, e.g., resulting from unreacted precursors. Furthermore, intrinsic defects due to dislocations, interstitials, vacancies, or antisites might give rise to electronically active states. Theoretical studies on whether these defects are active as recombination centers yielded rather contradictory results [34–37] .

Shockley-Read-Hall (SRH) theory [38] describes recombination through defects states:

$$R = \frac{np - n_i^2}{\tau_p(n + n_1) + \tau_n(p + p_1)} \tag{25}$$

with $n_1 = N_C \exp\left(-\frac{E_C - E_T}{k_B T}\right)$, $p_1 = N_V \exp\left(-\frac{E_T - E_V}{k_B T}\right)$, and lifetimes for electrons and holes $\tau_{n,p}$. E_T is the energy of the trap. For multiple traps or for a distribution in energy, the right-hand side of Eq. 25 is a sum over all E_T. Investigating Eq. 25, we find that midgap traps ($E_C - E_T \approx E_T - E_V$) are most active as recombination centers. This is in line with the intuitive explanation that midgap traps allow for equally efficient electron and hole capture. Assuming that most of the present charge carriers are photogenerated, thus $n \gg n_1$ and $n \gg n_i$, and considering one dominating SRH lifetime τ, we can approximate R:

$$R \propto \frac{n}{\tau}. \tag{26}$$

Following the same procedure as for direct recombination in Eqs. 11 and 12, we express V_{oc} as a function of light intensity in case of SRH recombination

$$eV_{oc} = E_g - 2k_B T \ln \frac{\sqrt{N_C N_V}\tau}{G}. \tag{27}$$

In general, we can write for the slope of V_{oc} versus $\log_{10} G/(1\mathrm{m}^{-3}\mathrm{s}^{-1})$: $n_{ID} k_B T \ln 10$, where $n_{ID} = 1$ for radiative recombination and $n_{ID} = 2$ for SRH recombination. The parameter n_{ID} is called the ideality factor and lies between 1 and 2, if both recombination processes are present. It is introduced for the dark J-V curve (cf. Eq. 9) as well:

$$J_{inj} = J_0 \left(\exp \frac{eV}{n_{ID} k_B T} - 1 \right). \tag{28}$$

Figure 8a shows the *J-V* curve of a perovskite solar cell in the dark (blue). It is governed by shunt and series resistances for voltages <0.8 and >1.2 V, respectively. The exponential increase of J between the resistance limited regions is described by Eq. 28, where $n_{\mathrm{ID}} = 2$. Consequently, the dominant recombination mechanism is of SRH type. The red curve shows the emitted photon flux with an exponential rise in the same voltage range as the dark curve, but with $n_{\mathrm{ID,rad}} = 1$ proving that radiative recombination results from the recombination of an electron in the conduction band with a hole in the valence band. The greater increase of emission current with voltage, compared to overall current, gives rise to an $\mathrm{EQE_{EL}}$(green) that increases with voltage. When plotted as a function of the injection current (Fig. 8b), the $\mathrm{EQE_{EL}}$ increases linearly as expected when comparing Eq. 27 with 23 for SRH recombination being dominant.

Having both recombination processes (Eq. 12 and 26) running in parallel, we can write a rate equation assuming that spatial variations in recombination rates and charge carrier densities are negligible, and the majority of the charge carriers are photogenerated:

$$\frac{dn}{dt} = -\beta n^2(t) - \frac{1}{\tau} n(t). \tag{29}$$

This equation can be solved analytically for n as a function of time t, which can be monitored by the emission as a function of t doing a photoluminescence (PL) decay measurement. A varied light intensity of the laser pulse can be used to tune the initial charge carrier density $n(0)$, which allows a more reliable determination of τ and β. Figure 9a shows PL transients including a fit according to the solution of Eq. 29 ($n(t) = \frac{1}{\tau\beta} \frac{1}{e^{\frac{t}{\tau}} \left(\frac{1}{\tau\beta n(0)} + 1 \right) - 1}$), with $\beta \approx 10^{-11}\mathrm{cm^3 s^{-1}}$ and $\tau = 350$ ns. The value for β coincides with what is expected from the radiative limit, confirming that direct electron-hole recombination is radiative. More sophisticated models including the dynamics of trapping and exciton formation can be applied to fit the

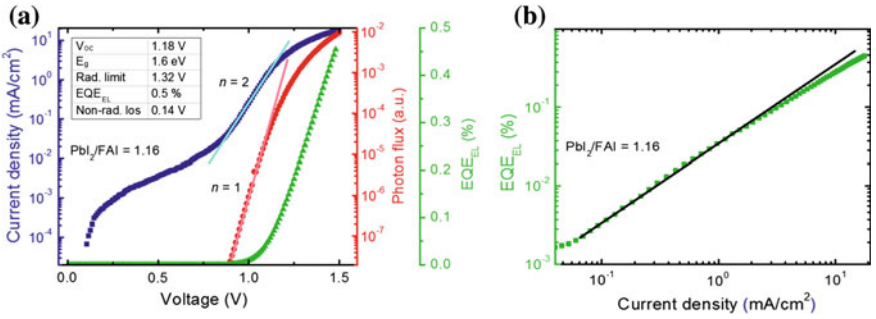

Fig. 8 Highly luminescent perovskite solar cells: **a** Injection current (*blue*), emitted photon flux (*red*) and $\mathrm{EQE_{EL}}$ as a function of the applied voltage. **b** $\mathrm{EQE_{EL}}$ as a function of the injection current. The *black line* describes a linear relation between $\mathrm{EQE_{EL}}$ and the injection current. From [9]. Reprinted with permission from AAAS

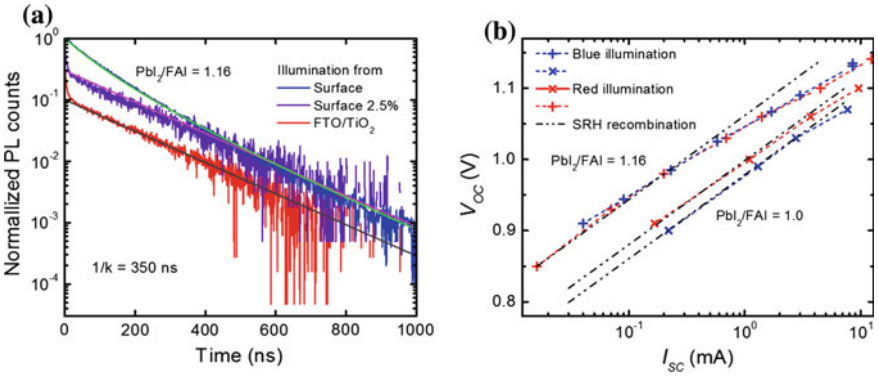

Fig. 9 Optoelectronic characterization of mixed perovskite devices **a** PL decay for illumination from the surface or through the substrate and with high and with 40 times lower light intensity. **b** V_{oc} as a function of illumination intensity under *red* and *blue* light for two different mixed perovskite devices. From [9]. Reprinted with permission from AAAS

PL decay, or other techniques such as transient THz spectroscopy, yielding $\beta \approx 10^{-11}-10^{-10}\mathrm{cm}^3\mathrm{s}^{-1}$ [39–41].

The SRH lifetime $\tau \propto \frac{1}{N_T \sigma_T}$ depends on the density (N_T) and capture cross section (σ_T) of electronically active recombination centers. For a charged defect, the latter is inversely proportional to the dielectric constant, which characterizes the ability of the material to screen charge [42]. Thus, the high dielectric constant of $CH_3NH_3PbI_3$ perovskite reported to up to 70 [43] combined with a low N_T for states close to midgap allows for a τ of several 100 s of ns. Here, the role of crystal size, grain boundaries, and passivation agents is not well understood yet [9].

To understand the effect of τ on the solar cell's performance, we calculate V_{oc} as a function of light intensity for varied τ (Fig. 10). In the radiative limit, V_{oc} increases with light intensity showing a slope of 60 mV/decade (dashed), whereas it shows 120 mV/decade in the case of SRH recombination, which dominates at low light intensity. Investigating V_{oc} at 1 sun (Fig. 10b), we find that a nonradiative lifetime τ of 10 µs would be sufficient to practically reach the radiative limit. The experimental data (symbols) for two perovskite solar cells based on mesoporous TiO_2 are consistent with a τ reaching more than 100 ns.

So far, we have assumed that charge carrier densities and recombination rates in the perovskite film do not depend on the position within the film. However, the direction of incident illumination and vertical inhomogeneities in the morphology of the perovskite layer and different properties at the contacts give rise to lateral inhomogeneities in recombination parameters and charge carrier densities. A treatment of inhomogeneities requires numerical simulations. However, first conclusions can be drawn from qualitative investigations exploiting different inhomogeneities introduced in $G(x)$ by monochromatic illumination. Blue light penetrates the film less than red light, giving rise to a steeper $G(x)$. A modified V_{oc} indicates different charge carrier lifetimes close to the surface and in the bulk.

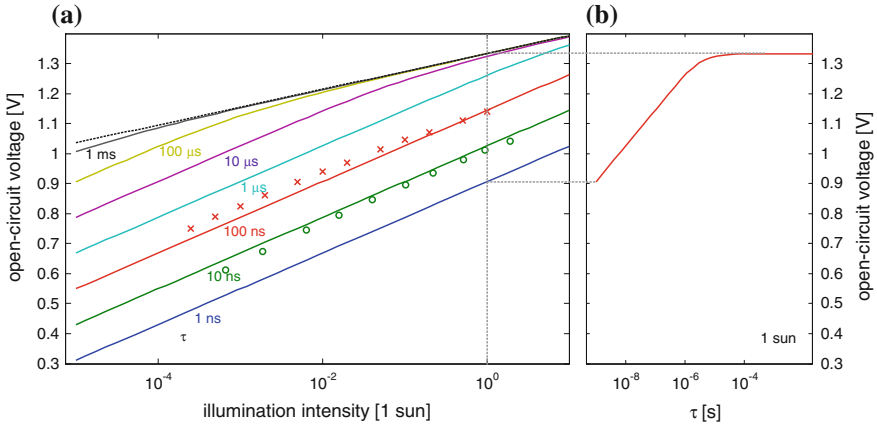

Fig. 10 Calculated influence of the SRH lifetime τ on V_{oc} for a 300 nm thick $CH_3NH_3PbI_3$ perovskite with a bandgap of 1.6 eV and a radiative recombination constant of 10^{-11} cm^3s^{-1}. **a** V_{oc} as a function of illumination intensity and **b** V_{oc} as a function of τ at 1 sun. When SRH recombination is dominant, V_{oc} decreases with 120 mV/decade with illumination intensity and with $1/\tau$. Symbols in (**a**) show experimental data for two-step $CH_3NH_3PbI_3$ solar cells from Ref. [44] (*circles*) and for one-step mixed perovskite [45] obtained by a measurement with pulsed light (*crosses*). Most of the changes in V_{oc} are due to an increased lifetime, as the bandgap changes only by a value <50 meV. A $\tau > 100$ ns is consistent with the PL decay in Fig. 9

The experimental data in Fig. 9b indicates that recombination is stronger at the TiO_2 contact for the device with the lower V_{oc} [9].

Nonradiative recombination influences the fill factor (FF) as well. This can be seen in Eq. 20, where the ideality factor needs to be introduced in front of k_BT. In case of negligible series or shunt resistance losses, the FF only depends on recombination. It can be expressed as a function of recombination rate, and thus of V_{oc}. In the radiative limit at 1 sun, it exceeds 90 % (cf. Fig. 4a) and decreases toward 83 % at 1.2 V and 80 % at 1.0 V (Fig. 11). Thus, a perovskite solar cell with a bandgap of 1.6 eV with optimized contacts and a J_{sc} of 24 mA cm^{-2}, but operating at only 1.0 V cannot deliver a FF greater than 80 %. However, a (slightly) larger FF is possible if recombination does not result from the perovskite itself but from surfaces. This seems to be the case for C_{60}-based electron transport layers [46] in inverted perovskite solar cells, where a FF as high as 85 % is reported for a V_{oc} of 1.03 V [47]. This value requires an $n_{ID} < 2$, when derived from V_{oc} as a function of light intensity. This would be an additional indication for surface recombination limiting V_{oc} [48]. Note that an excessively high FF might result from transient phenomena during measurement, giving rise to hysteresis in the *J-V* curve [49, 50]. On the other hand, surface recombination can decrease the FF as well. In real solar cells, a low FF is caused by resistive effects due to inhibited charge transport in the absorber or parasitic shunt and series resistances.

The proximity of the FF to the recombination limit (in case of negligible shunting) can be experimentally verified applying the Suns-V_{oc} method [44, 51, 52].

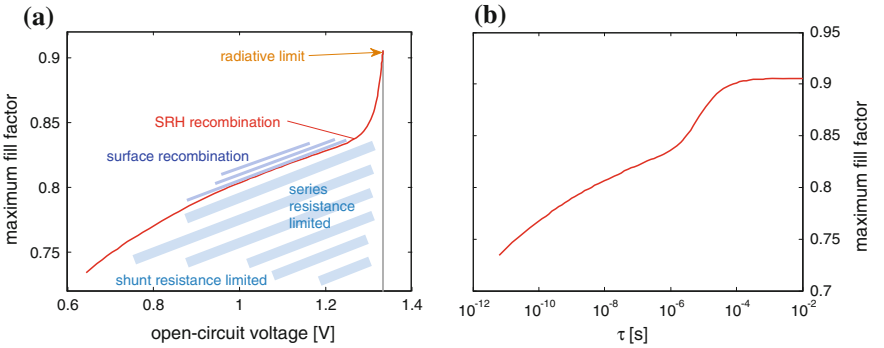

Fig. 11 Calculated fill factor for $CH_3NH_3PbI_3$ perovskite with a bandgap of 1.6 eV and a radiative recombination constant of 10^{-11} cm^3s^{-1}. **a** The fill factor decreases with lower V_{oc} due to its definition (cf. Fig. 4a). Additionally, a change from the radiation limit to SRH recombination gives rise for the rapid decrease. **b** Fill factor as a function of SRH lifetime τ

Employing this method, a pseudo-*J*-*V* curve is constructed from light intensity-dependent V_{oc} data. Series resistance effects are excluded because when measuring V_{oc}, current does not flow. Assuming that the light intensity is proportional to current, the pseudo-*J*-*V* curve for a particular intensity I_0 reads:

$$J(V_{oc}(I)) = J_{sc}(I_0)\left(1 - \frac{I}{I_0}\right). \tag{30}$$

Figure 12 shows such curves (dashed) for a $CH_3NH_3PbI_3$ perovskite solar cell at different illumination intensities I_0 compared to the measured *J*-*V* curves (solid lines) [44]. Both curves coincide at 0.25 suns indicating that charge transport losses in the perovskite are negligible. At higher light intensities and the consequently higher photocurrents, the series resistance limits the FF, mainly due to the resistance of the transparent conductive oxide.

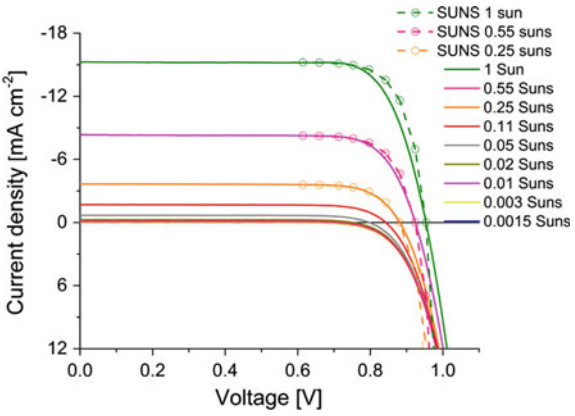

Fig. 12 Current-voltage curves (*solid lines*) at different illumination intensities. Pseudo-*J*-*V* curves (*dashed*) obtained using the Suns-V_{oc} method. Reprinted with permission from [44]. Copyright 2015 American Chemical Society

3.3 Role of the Charge Transport Layers

In the theoretical discussions, we assumed that contacts were perfect. Through experiments, we have already seen that they can change EQE_{EL} and thus be a source of nonradiative recombination, e.g., if a hole transport layer (HTL) is not used (cf. Table 1).

Thus, an essential role of the charge transport layers is to provide a selective contact. The electron transport layer (ETL) should only allow electrons to pass and block holes, and the HTL vice versa. This property can be put into practice by a large energy barrier for electron (hole) transfer due to offsets in conduction (valence) band. Additionally, recombination at the interface between the absorber and the charge transport layer should be avoided. This type of recombination, where charge recombines at the surface of the absorber, is called surface recombination and it is characterized by a surface recombination velocity. For metals, the surface recombination velocity is usually very high for both electrons and holes. Hence, metals are not a good choice for selective contacts.

In general, interfaces between two materials (heterojunctions) might fulfill the role of separation of charge or excited states, as in the case of organic donor–acceptor heterojunctions [2]. However, from the previous discussions, there are no indications that interfaces are essential for the photovoltaic working principle of perovskite solar cells. Thus, charges are generated and dissociated in the perovskite itself, creating a splitting of the quasi-Fermi levels, which gives rise to the photovoltage. The charge transport layers just serve as contacts. However, this raises the question on the operational principle of perovskite solar cells, where no intentional pn junction is introduced, in contrast to conventional solar cells. From the discussions above, we know that a pn junction itself is not a requirement for a solar cell. Instead, selective contacts are sufficient. The solar cell architecture comprises of a metal–insulator (semiconductor)-metal structure. Charges can be driven toward their respective interface simply by diffusion. Usually, a difference in work function of the two metals (or transparent conductive oxides) is beneficial, though not required, as it introduces a built-in potential similar to the different types of doping in a pn junction. To date it is not clear whether the assumption of a constant electric field in the perovskite is justified. Space charge regions could result from unintentional doping, the existence of mobile ionic species, grain boundaries, or other inhomogeneities in the film.

A lot of research focuses on interchanging ETL or HTL to increase performance and in particular V_{oc}. Regarding the ETL, high $V_{oc} > 1$V has been obtained with several materials such as TiO_2 with TiO_2 or Al_2O_3 scaffold [6], PCBM [53], ZnO [54], or Ti(Nb)O_x [55]. Record values of 1.2 V have been achieved with TiO_2 [9] and SnO_2 [56], where the high V_{oc} is mainly attributed to an improved morphology of the perovskite. One approach commonly taken up is the tuning of the HOMO level of the organic HTL. It is anticipated that a lower lying HOMO increases V_{oc}. The experimental effort on testing HTLs to increase V_{oc} has only been partly successful [57–59] but clear trends are mostly missing [60–64]. Instead,

improvements of V_{oc} were obtained by modifying the perovskite [9]. This is expected from the discussion in this chapter. Modifying the HTL or ETL to increase V_{oc} is only important if recombination at the HTL(Au)/perovskite interface reduces V_{oc} (possibly independent of HOMO position), as it is the case for, e.g., too thin HTL [44] or PEDOT:PSS as HTL [65]. A deeper lying HOMO accompanied by a higher work function of a doped HTL could increase the built-in potential and thus reduce surface recombination as less charges are reaching the wrong electrode. However, if the surface is well passivated, i.e., recombination at the electrode is not an issue, changes in the HOMO of the HTL will not affect V_{oc}. In addition, the formation of interface dipoles can change band alignment compared to the case predicted by assuming a constant vacuum level at the interface.

Theoretically, V_{oc} can exceed the difference between the work functions of the contacts or the difference between the conduction and the valence band of electron and hole transport layer, respectively. This is thought to be counter intuitive, but with restrictions this is as normal as the fact that it is possible to apply a voltage larger than those offsets. The results for Br-based perovskite on TiO_2 and HTL spiro-OMeTAD with V_{oc} approaching 1.5 V indicate that this is possible in experiment as well [66]. Thus, it is more important to tune the HTL and ETL to reduce recombination centers on their surfaces, which might result from additives, and use the charge transport layers to passivate the perovskite surface instead of solely focusing on the energetics.

Acknowledgments I thank Amita Ummadisingu for carefully reading the text and suggesting improvements regarding language. Marko Stojanovic, Juan Pablo Correa Baena, T. Jesper Jacobsson, Yiming Cao, and Somayyeh Gholipour are acknowledged for commenting on the manuscript. I thank Dongqin Bi for providing I:Br samples, and Clémentine Renevier and Björn Niessen for the collaboration regarding the characterization of those samples. Financial support from SNF-NanoTera (SYNERGY) is kindly acknowledged.

References

1. Wurfel, P.: Physics of Solar Cells: From Basic Principles to Advanced Concepts. (Wiley)
2. Tress, W.: Organic Solar Cells—Theory, Experiment, and Device Simulation
3. Trupke, T., Daub, E., Würfel, P.: Absorptivity of silicon solar cells obtained from luminescence. Sol. Energy Mater. Sol. Cells **53**, 103–114 (1998)
4. Rau, U.: Reciprocity relation between photovoltaic quantum efficiency and electroluminescent emission of solar cells. Phys. Rev. B **76**, 085303 (2007)
5. Giorgi, G., Fujisawa, J.-I., Segawa, H., Yamashita, K.: Small photocarrier effective masses featuring ambipolar transport in methylammonium lead iodide perovskite: a density functional analysis. J. Phys. Chem. Lett. **4**, 4213–4216 (2013)
6. Tress, W., et al.: Predicting the open-circuit voltage of CH3NH3PbI3 perovskite solar cells using electroluminescence and photovoltaic quantum efficiency spectra: the role of radiative and non-radiative recombination. Adv. Energy Mater. **5**, 140812 (2015)
7. Tvingstedt, K., et al.: Radiative efficiency of lead iodide based perovskite solar cells. Sci. Rep. **4**, 6071 (2014)

8. Ball, J.M., et al.: Optical properties and limiting photocurrent of thin-film perovskite solar cells. Energy Environ. Sci. **8**, 602–609 (2015)
9. Bi, D., et al.: Efficient luminescent solar cells based on tailored mixed-cation perovskites. Sci. Adv. **2**, e1501170 (2016)
10. Shockley, W., Queisser, H.J.: Detailed balance limit of efficiency of p-n junction solar cells. J. Appl. Phys. **32**, 510–519 (2004)
11. Green, M.A., Emery, K., Hishikawa, Y., Warta, W., Dunlop, E.D.: Solar cell efficiency tables (version 46). Prog. Photovolt. Res. Appl. **23**, 805–812 (2015)
12. De Wolf, S., et al.: Organometallic halide perovskites: sharp optical absorption edge and its relation to photovoltaic performance. J. Phys. Chem. Lett. **5**, 1035–1039 (2014)
13. D'Innocenzo, V., Srimath Kandada, A.R., De Bastiani, M., Gandini, M., Petrozza, A.: Tuning the light emission properties by band gap engineering in hybrid lead halide perovskite. J. Am. Chem. Soc. **136,** 17730–17733 (2014)
14. Stoumpos, C.C., Malliakas, C.D., Kanatzidis, M.G.: Semiconducting tin and lead iodide perovskites with organic cations: phase transitions, high mobilities, and near-infrared photoluminescent properties. Inorg. Chem. **52**, 9019–9038 (2013)
15. Pang, S., et al.: NH2CH═NH2PbI3: an alternative organolead iodide perovskite sensitizer for mesoscopic solar cells. Chem. Mater. **26**, 1485–1491 (2014)
16. Pellet, N., et al.: Mixed-organic-cation perovskite photovoltaics for enhanced solar-light harvesting. Angew. Chem. Int. Ed. **53**, 3151–3157 (2014)
17. Eperon, G.E., et al.: Formamidinium lead trihalide: a broadly tunable perovskite for efficient planar heterojunction solar cells. Energy Environ. Sci. **7**, 982–988 (2014)
18. Filip, M.R., Eperon, G.E., Snaith, H.J. Giustino, F.: Steric engineering of metal-halide perovskites with tunable optical band gaps. Nat. Commun. **5**, (2014)
19. Amat, A., et al.: Cation-induced band-gap tuning in organohalide perovskites: interplay of spin-orbit coupling and octahedra tilting. Nano Lett. **14**, 3608–3616 (2014)
20. Umebayashi, T., Asai, K., Kondo, T., Nakao, A.: Electronic structures of lead iodide based low-dimensional crystals. Phys. Rev. B **67**, 155405 (2003)
21. Noh, J.H., Im, S.H., Heo, J.H., Mandal, T.N., Seok, S.I.: Chemical management for colorful, efficient, and stable inorganic-organic hybrid nanostructured solar cells. Nano Lett. **13**, 1764–1769 (2013)
22. McMeekin, D.P., et al.: A mixed-cation lead mixed-halide perovskite absorber for tandem solar cells. Science **351**, 151–155 (2016)
23. Henry, C.H.: Limiting efficiencies of ideal single and multiple energy gap terrestrial solar cells. J. Appl. Phys. **51**, 4494–4500 (1980)
24. Albrecht, S., et al.: Monolithic perovskite/silicon-heterojunction tandem solar cells processed at low temperature. Energy Environ. Sci. (2015). doi:10.1039/C5EE02965A
25. Werner, J., et al.: Efficient monolithic perovskite/silicon tandem solar cell with cell area >1 cm2. J. Phys. Chem. Lett. **7**, 161–166 (2016)
26. Mailoa, J.P., et al.: A 2-terminal perovskite/silicon multijunction solar cell enabled by a silicon tunnel junction. Appl. Phys. Lett. **106**, 121105 (2015)
27. Löper, P., et al.: Organic–inorganic halide perovskite/crystalline silicon four-terminal tandem solar cells. Phys. Chem. Chem. Phys. **17**, 1619–1629 (2014)
28. Filipič, M., et al.: CH_3NH_3PbI_3 perovskite/silicon tandem solar cells: characterization based optical simulations. Opt. Express **23**, A263 (2015)
29. Smestad, G., Ries, H.: Luminescence and current-voltage characteristics of solar cells and optoelectronic devices. Sol. Energy Mater. Sol. Cells **25**, 51–71 (1992)
30. Burschka, J., et al.: Sequential deposition as a route to high-performance perovskite-sensitized solar cells. Nature **499**, 316–319 (2013)
31. Yao, J., et al.: Quantifying losses in open-circuit voltage in solution-processable solar cells. Phys. Rev. Appl. **4**, 014020 (2015)
32. Tiedje, T., Yablonovitch, E., Cody, G.D., Brooks, B.G.: Limiting efficiency of silicon solar cells. IEEE Trans. Electron Devices **31**, 711–716 (1984)

33. Kerr, M.J., Cuevas, A., Campbell, P.: Limiting efficiency of crystalline silicon solar cells due to Coulomb-enhanced Auger recombination. Prog. Photovolt. Res. Appl. **11**, 97–104 (2003)
34. Kim, J., Lee, S.-H., Lee, J.H., Hong, K.-H.: The Role of Intrinsic Defects in Methylammonium Lead Iodide Perovskite. J. Phys. Chem. Lett. 1312–1317 (2014). doi:10.1021/jz500370k
35. Yin, W.-J., Shi, T., Yan, Y.: Unusual defect physics in CH3NH3PbI3 perovskite solar cell absorber. Appl. Phys. Lett. **104**, 063903 (2014)
36. Buin, A., et al.: Materials processing routes to trap-free halide perovskites. Nano Lett. **14**, 6281–6286 (2014)
37. Agiorgousis, M.L., Sun, Y.-Y., Zeng, H., Zhang, S.: Strong Covalency-Induced Recombination Centers in Perovskite Solar Cell Material CH3NH3PbI3. J. Am. Chem. Soc. **136**, 14570–14575 (2014)
38. Shockley, W., Read, W.T.: Statistics of the recombinations of holes and electrons. Phys. Rev. **87**, 835–842 (1952)
39. Wehrenfennig, C., Eperon, G.E., Johnston, M.B., Snaith, H.J., Herz, L.M.: High charge carrier mobilities and lifetimes in organolead trihalide perovskites. Adv. Mater. **26**, 1584–1589 (2014)
40. Stranks, S.D., et al.: Recombination kinetics in organic-inorganic perovskites: excitons, free charge, and subgap states. Phys. Rev. Appl. **2**, 034007 (2014)
41. Yamada, Y., Nakamura, T., Endo, M., Wakamiya, A., Kanemitsu, Y.: Photocarrier Recombination Dynamics in Perovskite CH3NH3PbI3 for Solar Cell Applications. J. Am. Chem. Soc. **136**, 11610–11613 (2014)
42. Brandt, R.E., Stevanović, V., Ginley, D.S., Buonassisi, T.: Identifying defect-tolerant semiconductors with high minority-carrier lifetimes: beyond hybrid lead halide perovskites. MRS Commun. **5**, 265–275 (2015)
43. Lin, Q., Armin, A., Nagiri, R.C.R., Burn, P.L., Meredith, P.: Electro-optics of perovskite solar cells. Nat. Photonics (advance online publication), (2014)
44. Marinova, N., et al.: Light harvesting and charge recombination in CH3NH3PbI3 perovskite solar cells studied by hole transport layer thickness variation. ACS Nano (2015). doi:10.1021/acsnano.5b00447
45. Giordano, F., et al.: Enhanced electronic properties in mesoporous TiO2 via lithium doping for high-efficiency perovskite solar cells. Nat. Commun. **7**, 10379 (2016)
46. Ponseca, C.S., et al.: Mechanism of charge transfer and recombination dynamics in organo metal halide perovskites and organic electrodes, PCBM, and spiro-OMeTAD: role of dark carriers. J. Am. Chem. Soc. **137**, 16043–16048 (2015)
47. Wu, C.-G., et al.: High efficiency stable inverted perovskite solar cells without current hysteresis. Energy Environ. Sci. **8**, 2725–2733 (2015)
48. Tress, W., Leo, K., Riede, M.: Dominating recombination mechanisms in organic solar cells based on ZnPc and C60. Appl. Phys. Lett. **102**, 163901 (2013)
49. Snaith, H.J., et al.: Anomalous hysteresis in perovskite solar cells. J. Phys. Chem. Lett. **5**, 1511–1515 (2014)
50. Tress, W., et al.: Understanding the rate-dependent J-V hysteresis, slow time component, and aging in CH3NH3PbI3 perovskite solar cells: the role of a compensated electric field. Energy Environ. Sci. **8**, 995–1004 (2015)
51. Pysch, D., Mette, A., Glunz, S.W.: A review and comparison of different methods to determine the series resistance of solar cells. Sol. Energy Mater. Sol. Cells **91**, 1698–1706 (2007)
52. Schiefer, S., Zimmermann, B., Glunz, S.W., Wurfel, U.: Applicability of the suns-V method on organic solar cells. IEEE J. Photovolt. **4**, 271–277 (2014)
53. Malinkiewicz, O., et al.: Perovskite solar cells employing organic charge-transport layers. Nat. Photonics **8**, 128–132 (2014)
54. Liu, D., Kelly, T.L.: Perovskite solar cells with a planar heterojunction structure prepared using room-temperature solution processing techniques. Nat. Photonics **8**, 133–138 (2014)
55. Chen, W., et al.: Efficient and stable large-area perovskite solar cells with inorganic charge extraction layers. Science **350**, 944–948 (2015)

56. Baena, J.P.C., et al.: Highly efficient planar perovskite solar cells through band alignment engineering. Energy Environ. Sci. (2015). doi:10.1039/C5EE02608C
57. Heo, J.H., Song, D.H., Im, S.H.: Planar CH3NH3PbBr3 hybrid solar cells with 10.4 % power conversion efficiency, fabricated by controlled crystallization in the spin-coating process. Adv. Mater. n/a–n/a (2014). doi:10.1002/adma.201403140
58. Yan, W., et al.: High-performance hybrid perovskite solar cells with open circuit voltage dependence on hole-transporting materials. Nano Energy. doi:10.1016/j.nanoen.2015.07.024
59. Ryu, S., et al.: Voltage output of efficient perovskite solar cells with high open-circuit voltage and fill factor. Energy Environ. Sci. (2014). doi:10.1039/C4EE00762J
60. Liu, J., et al.: A dopant-free hole-transporting material for efficient and stable perovskite solar cells. Energy Environ. Sci. **7**, 2963–2967 (2014)
61. Polander, L.E., et al.: Hole-transport material variation in fully vacuum deposited perovskite solar cells. APL Mater. **2**, 081503 (2014)
62. Di Giacomo, F., et al.: High efficiency CH3NH3PbI(3−x)Clx perovskite solar cells with poly (3-hexylthiophene) hole transport layer. J. Power Sources **251**, 152–156 (2014)
63. Bi, D., Yang, L., Boschloo, G., Hagfeldt, A., Johansson, E.M.J.: Effect of different hole transport materials on recombination in CH3NH3PbI3 perovskite-sensitized mesoscopic solar cells. J. Phys. Chem. Lett. **4**, 1532–1536 (2013)
64. Jeon, N.J., et al.: Efficient inorganic-organic hybrid perovskite solar cells based on pyrene arylamine derivatives as hole-transporting materials. J. Am. Chem. Soc. **135**, 19087–19090 (2013)
65. Zhao, D., et al.: High-efficiency solution-processed planar perovskite solar cells with a polymer hole transport layer. Adv. Energy Mater. **5,** n/a–n/a (2015)
66. Arora, N., Dar, M.I., Hezam, M., Tress, W., Jacopin, G., Moehl, T., Gao, P., Aldwayyan, A.S., Benoit, D., Grätzel, M., Nazeeruddin, M.K.: Photovoltaic and amplified spontaneous emission studies of high-quality formamidinium lead bromide perovskite films. Adv. Func. Mat.

Defect Physics of $CH_3NH_3PbX_3$ (X = I, Br, Cl) Perovskites

Yanfa Yan, Wan-Jian Yin, Tingting Shi, Weiwei Meng and Chunbao Feng

Abstract The properties of defects, including point defects, grain boundaries, and surfaces in photovoltaic absorbers play critical roles in determining the nonradiative recombination behavior, and, consequently, the performance of solar cells made of these absorbers. Here, we review our theoretical understanding of the defect properties of organic–inorganic methylammounium lead halide perovskites, $CH_3NH_3PbX_3$ (X = I, Br, Cl), using density-functional theory calculations. We show that $CH_3NH_3PbI_3$ perovskites exhibit unique defect properties—point defects with low formation energy values only create shallow levels, whereas point defects with deep levels have high formation energies. Surfaces and grain boundaries do not produce deep levels. These unique defect properties are attributed to the anti-bonding coupling between Pb lone-pair *s* and I *p* orbitals, the high ionicity, and the large lattice constants. We further show that $CH_3NH_3PbI_3$ exhibits an intrinsic ambipolar self-doping behavior with electrical conductivity tunable from *p*-type to *n*-type via controlling the growth conditions. However, $CH_3NH_3PbBr_3$ exhibits unipolar self-doping behavior. It demonstrates a preference for *p*-type conductivity if synthesized under thermal equilibrium growth conditions. $CH_3NH_3PbCl_3$ may exhibit a compensated self-doping behavior due to its large bandgap. Doping $CH_3NH_3PbI_3$ using external dopants may improve the *p*-type conductivity, but not the *n*-type conductivity due to compensation from intrinsic defects.

Keywords Halide perovskite · Point defect · Grain boundaries · Doping

Y. Yan (✉) · W.-J. Yin · T. Shi · W. Meng · C. Feng
Department of Physics and Astronomy, and Wright Center for Photovoltaic Innovation and Commercialization, The University of Toledo, Toledo, OH 43606, USA
e-mail: yanfa.yan@utoledo.edu

N.-G. Park et al. (eds.), *Organic-Inorganic Halide Perovskite Photovoltaics*,
DOI 10.1007/978-3-319-35114-8_4

1 Introduction

The organic–inorganic lead halide perovskites such as $CH_3NH_3PbX_3$ (X = I, Br, Cl) have shown enormous potential for producing low-cost and high efficiency thin-film solar cells. Since the first application of $CH_3NH_3PbI_3$ in dye-sensitized solar cells, the efficiency of lead halide perovskite-based thin-film solar cells has increased rapidly with the record power conversion efficiency reaching 22.1 % [1–25]. Studies have shown that lead halide perovskite absorbers exhibit superior photovoltaic properties, such as, extremely high optical absorption coefficient [8, 26] and long carrier diffusion lengths [10, 11]. The conversion efficiency of a solar cell is determined by three parameters: open-circuit voltage (V_{OC}), short-circuit current (J_{SC}), and fill factor (FF). Among these, the V_{OC} is the most difficult parameter to improve for polycrystalline thin-film solar cells. This is because polycrystalline thin films typically contain more defects, including point defects and grain boundaries (GBs) than their single-crystal counterparts. The defects may cause nonradiative recombination, which is very detrimental to the V_{OC}. The most useful method to check whether a solar cell is attaining a high V_{OC} is to calculate the V_{OC} deficit, defined by $E_g/q - V_{OC}$ (where E_g is the absorber bandgap and q is the elementary charge). Very recently, $CH_3NH_3PbI_3$-based solar cells have achieved a maximum V_{OC} of 1.19 eV, giving a V_{OC} deficit of about 0.36 V (assuming a bandgap of 1.55 eV), which is even smaller than that of the best single-crystal Si (0.38 V) and is approaching that of the best epitaxial single-crystal GaAs thin-film solar cells (0.30 V) [17, 27]. Considering that these solar cells were made of polycrystalline perovskite thin-films fabricated by solution processes at low temperatures, the V_{OC} deficit of 0.36 V is truly remarkable. To achieve such high V_{OC} performance, the defects including point defects, surfaces, and grain boundaries in $CH_3NH_3PbI_3$ must be electrically benign, which has not been seen in conventional inorganic photovoltaic absorbers such as Si, GaAs, $CuInSe_2$, CdTe, etc.

In this chapter, we review our theoretical understanding of the defect properties of $CH_3NH_3PbX_3$ through density-functional theory (DFT) calculations [28–34]. We show that $CH_3NH_3PbI_3$ perovskites exhibit unique defect properties—point defects with low formation energy values only create shallow levels, whereas point defects with deep levels have high formation energies. Intrinsic surface and GBs do not produce deep level states. We explain that these unique defect properties are attributed to the antibonding coupling between Pb lone-pair s and I p orbitals, the high ionicity, and the large lattice constant of $CH_3NH_3PbI_3$. We further show that $CH_3NH_3PbI_3$ exhibits an intrinsic ambipolar self-doping behavior with electrical conductivity tunable from p-type to n-type via controlling the growth conditions. However, $CH_3NH_3PbBr_3$ exhibits a unipolar self-doping behavior, it demonstrates preferential p-type conductivity if synthesized under thermal equilibrium growth conditions. $CH_3NH_3PbCl_3$ may exhibit a compensated self-doping behavior due to its large bandgap. We show that the p-type conductivity of $CH_3NH_3PbI_3$ can be further increased by incorporating some group IA, IB, or VIA elements at I-rich/Pb-poor growth conditions. However, due to the compensation from intrinsic

point defects, the *n*-type conductivity of $CH_3NH_3PbI_3$ cannot be improved under thermal equilibrium growth conditions through extrinsic doping due to the compensation from intrinsic point defects.

2 Computational Details

DFT has been used to calculate the structural, electronic, optical, and defect properties of $CH_3NH_3PbX_3$ perovskites. Before the first report of lead halide perovskite-based solar cells, the electronic properties of lead halide perovskites have been studied using DFT caluclations [35, 36]. The calculations reported here were carried out using the VASP code with the standard frozen-core projector augmented-wave (PAW) method [37, 38]. The cut-off energy for basis functions was 400 eV. The general gradient approximation (GGA) was used for exchange-correlation [39]. Atomic positions were relaxed until all forces on the atoms are below 0.05 eV/Å. The GGA calculation reproduces reliable structures but leads to considerable errors in the self-interaction calculation, underestimating bandgaps for most system. To accurately predict the bandgap values, Heyd–Scuseria–Ernzerhof (HSE06) [40, 41] functionals and many body perturbation theory, within the GW [42, 43] approach have been adopted to describe electronic properties of a system. It has been reported that it is important to include the effect of spin-orbital coupling (SOC) in DFT calculations of the electronic and optical properties of $CH_3NH_3PbX_3$ due to the strong relativistic effect of Pb [44–47]. However, SOC-GGA significantly underestimates the bandgap of halide perovskites. To predict the bandgap correctly, hybrid functional HSE06 plus SOC has been used [46]. Meanwhile, SOC-GW is the most advanced approach that successfully predicts bandgaps and has been used for calculating the electronic and optical properties of perovskites [48]. However, so far, both SOC-HSE and SOC-GW calculations are very time consuming and can only be feasible for calculations with small unit cells. In our study of defect properties, most calculations used large super cells (768 atoms). For these calculations, it was not possible to use SOC-HSE or SOC-GW. On the other hand, the reliability of defect calculation by HSE is questionable. Although the inclusion of partial exact-exchange in HSE can correct the bandgap calculation, it is not proven to correctly predict the position of defect states. For GW methods, the limitation on atomic relaxation becomes a main bottleneck for its use on defect calculations. Fortunately, it is known that the errors of using GGA and non-SOC cancel with each other when used concurrently [49]. We have compared the calculated optical absorption coefficient of $CH_3NH_3PbI_3$ using non-SOC-GGA with that measured experimentally by spectroscopic ellipsometry (Fig. 1). It is seen that the calculated non-SOC-GGA coefficient spectrum matches well with experimental results. This is largely due to the fact that the main characteristics of the conduction and valence bands of $CH_3NH_3PbI_3$ produced by SOC-GW and by non-SOC DFT calculations do not exhibit significant differences. Because the defect levels, especially the shallow acceptor/donor levels, are mostly

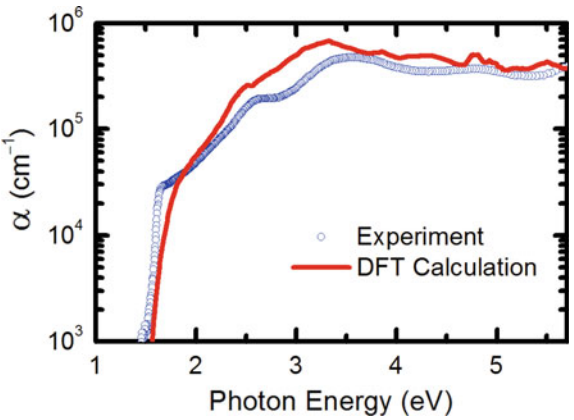

Fig. 1 Comparison of optical absorption coefficients of $CH_3NH_3PbI_3$ from a non-SOC-GGA-DFT calculation and a spectroscopic ellipsometry measurement

derived from either the upper valence or the lower conduction bands, it is reasonable to expect that the calculated shallow energy levels using non-SOC should not exhibit significant errors. Since the accurate energy positions of deep levels are not very important in the current study, it does not matter that the errors for deep levels can be large. GBs are modeled using supercells containing two identical GBs with opposite arrangements. The atomic structures of GBs in halide perovskites are adopted from the atomic structures of the same GBs in perovskite oxides, which have been determined by atomic-resolution transmission electron microscopy [50].

At finite temperatures, $CH_3NH_3PbI_3$ may exhibit three phases: the cubic (α), tetragonal (β), and orthorhombic (γ) phases, as shown in Fig. 2a, b, c, respectively. Transitions between those structures at finite temperatures often happen in most perovskites [51, 52]. It was reported that the α to β and β to γ phase transitions happen at 330 K and 160 K, respectively [53]. The large solid boxes and the small dashed boxes in Fig. 2b, c indicate the relationship between the unit cells of α, β and γ phases and the unit cells of the α phase. $CH_3NH_3PbBr_3$ and $CH_3NH_3PbCl_3$ only exhibit the α phase. Due to their structural similarity, the α, β, and γ phases exhibit

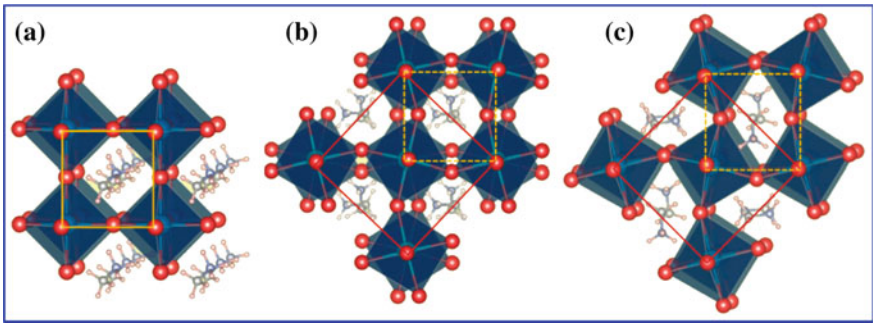

Fig. 2 Atomic structures for **a** α phase, **b** β phase, and **c** γ phase $CH_3NH_3PbI_3$. Adapted with permission from Ref. [32]. Copyright 2014 American Chemical Society

very similar electronic structures. Therefore, for better comparison, we calculated the defect properties based on the α phase, which has a $Pm\bar{3}m$ space group.

The calculation of the transition energies and formation energies of defects include the following [54–57]: We first calculate the total energy $E(\alpha, q)$ for a supercell containing defect α in charge state q, then calculate the total energy E (host) of the same supercell without the defect, and, finally, calculate the total energy of the involved elemental solids or gases at their stable phases. The defect formation energy also depends on the atomic chemical potentials μ_i and the electron Fermi energy E_F. From these quantities, the defect formation energy, $\Delta H_f(\alpha, q)$, can be obtained by:

$$\Delta H_f(\alpha, q) = \Delta E(\alpha, q) + \Sigma n_i \mu_i + qE_F \tag{1}$$

where $\Delta E(\alpha, q) = E(\alpha, q) - E(\text{host}) + \Sigma n_i E(i) + q\varepsilon_{\text{VBM}}(\text{host})$, E_F is referenced to the valence band maximum (VBM) of the host, μ_i is the chemical potential of constituent i referenced to elemental solid/gas with energy $E(i)$, n_i is the number of elements, and q is the number of electrons transferred from the supercell to the reservoirs in forming the defect cell. The transition energy for the defect α from charge state q to charge state q', $\varepsilon_\alpha(q/q')$, can be obtained by

$$\varepsilon_\alpha(q/q') = [\Delta E(\alpha, q) - \Delta E(\alpha, q')]/(q' - q). \tag{2}$$

The formation energy of a charged state is then given by

$$\Delta H_f(\alpha, q) = \Delta H_f(\alpha, 0) - q\varepsilon(0/q) + qE_F, \tag{3}$$

where $\Delta H_f(\alpha, 0)$ is the formation energy of the charge-neutral defect and E_F is the Fermi level with respect to the VBM.

3 Results and Discussions

Nonradiative recombination and carrier scattering are often caused by defects that generate deep gap states. These defects include both point defects and structural defects such as surfaces and GBs. We found that $CH_3NH_3PbI_3$ perovskites exhibit unique defect properties that have not been observed in other semiconductors, i.e., surfaces, GBs, and dominant point defects do not create deep levels and are, therefore, electrically benign. Some point defects generate deep gap states, but these defects have high formation energies, and their concentrations are expected to be low in synthesized lead halide perovskite thin films. We further found that these unique defect properties are attributed to the strong Pb lone-pair *s*–halogen *p* anti-bonding coupling, the ionic characteristics, and the large lattice constants.

3.1 General Trend of Defect Levels in $CH_3NH_3PbX_3$ Perovskites

We first provide a qualitative understanding on the general trend of defect levels in $CH_3NH_3PbI_3$ based on atomic orbital theory, which has been successfully used to predict the oxygen energy levels in oxides [58]. Our discussion is relying on two facts: (i) The energy bands are formed by atomic orbital mixing (either through ionic or covalent interactions or in-between) between bonded atoms and (ii) The defect levels of both point and structural defects are formed due to the breaking or addition of bonds, namely, dangling bonds and wrong bonds. In this way, we can understand the atomic origins of defect levels starting from the basic electronic structure of the host material. The formation of the conduction band and valence bands of $CH_3NH_3PbI_3$ is depicted in Fig. 3a. The conduction bands of $CH_3NH_3PbI_3$ are mainly derived from the empty Pb *p* orbitals. Due to the ionic characteristic of $CH_3NH_3PbI_3$, the covalent antibonding coupling between Pb *p* and I *p* is not strong. Therefore, the conduction band minimum (CBM) should not be much higher than the atomic Pb *p* states, as shown in Fig. 3a. The valence bands of $CH_3NH_3PbI_3$ is mainly derived from I *p* states with small components of Pb *s* states. Because of the strong Pb *s*–I *p* antibonding coupling, the VBM is above the I *p* atomic orbital level, as shown in Fig. 3a. For an I vacancy, the defect state is formed by the Pb dangling bonds surrounding the I vacancy. The defect state will therefore be located between the Pb *p* atomic orbital level and the CBM of $CH_3NH_3PbI_3$, as shown in Fig. 3b. Because the difference between the Pb *p* atomic orbital level and the CBM of $CH_3NH_3PbI_3$ is small as discussed above, the I vacancy level should be close to the CBM, forming a shallow donor state (D_d). For a Pb vacancy, the defect state is formed by I dangling bonds surrounding the Pb vacancy, and therefore it should be between the VBM and the I *p* atomic orbital level. Due to the strong Pb *s*–I *p* antibonding coupling, the VBM is higher in energy

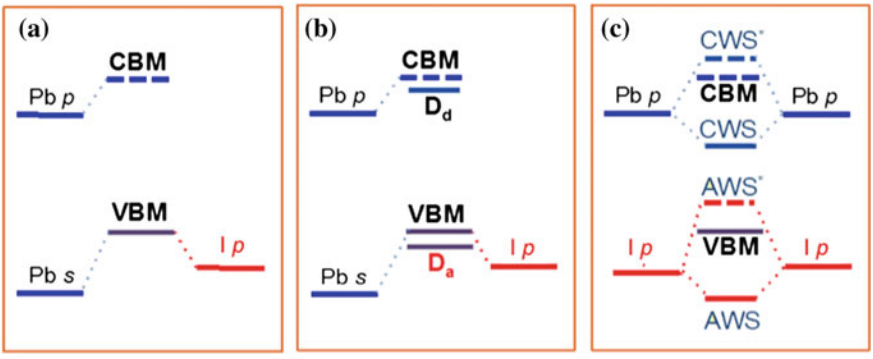

Fig. 3 Schematics depicting the formation of **a** VBM and CBM, **b** donor-like and acceptor-like defects from cation and anion vacancies; and **c** defects from cation–cation and anion–anion wrong bonds. Adapted with permission from Ref. [32]. Copyright 2014 American Chemical Society

than the I *p* atomic orbital level, as shown in Fig. 3a. Therefore, the Pb vacancy level should be below the VBM, forming a shallow acceptor level (D_a). The formation of defect states of anti-site defects are from either cation–cation or anion–anion wrong bonds. The formation of defect states of interstitial defects can also be derived from either dangling bonds or wrong bonds, depending on the defect configuration. Wrong bonds could create deep gap states. For example, Pb *p*–Pb *p* and I *p*–I *p* wrong bonds in $CH_3NH_3PbI_3$ may create deep levels, as shown in Fig. 3c. The CWS and AWS* states could be deep in the bandgap. CWS denotes cation–cation wrong bond state and AWS denotes anion–anion wrong bond state. The asterisk denotes the corresponding antibonding state.

3.2 *Calculated Transition Energies of Intrinsic Point Defects*

We have calculated the transition levels for all possible intrinsic point defects in $CH_3NH_3PbI_3$: CH_3NH_3, Pb, and I vacancies (V_{MA}, V_{Pb}, V_I), CH_3NH_3, Pb, and I interstitials (MA_i, Pb_i, I_i), CH_3NH_3 on Pb and Pb on CH_3NH_3 cation substitutions (MA_{Pb}, Pb_{MA}) and four anti-site substitutions: CH_3NH_3 on I (MA_I), Pb on I (Pb_I), I on CH_3NH_3 (I_{MA}), and I on Pb (I_{Pb}). The calculated transition energies for these point defects are shown in Fig. 4. It is seen that all the vacancy defects and most interstitial defects exhibit rather shallow transition energy levels. The defects that generate deep levels are I_{MA}, I_{Pb}, Pb_i, MA_I, and Pb_I. These defects are mostly cation

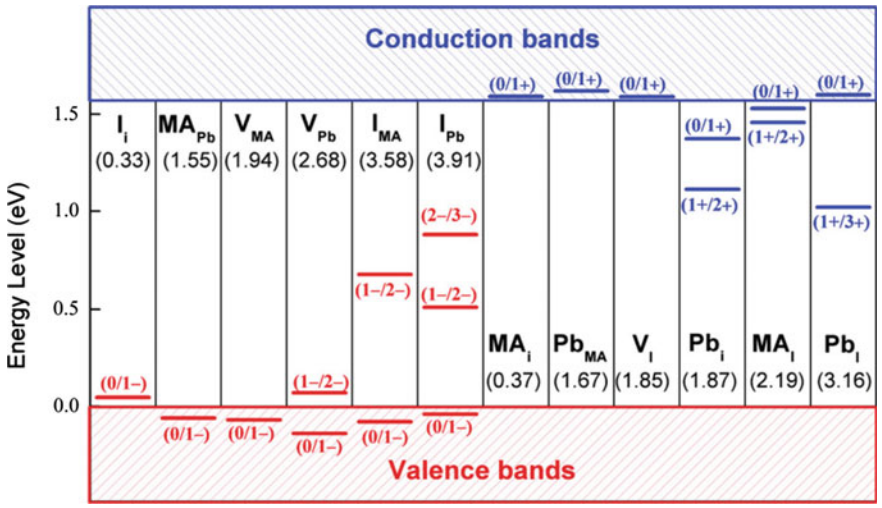

Fig. 4 Calculated transition energy levels of donor-like and acceptor-like point defects in $CH_3NH_3PbI_3$. Adapted with permission from Ref. [29]. Copyright 2014 Wiley-VCH Verlag GmbH & Co. KGaA

or anion anti-site defects, except for Pb_i. The results are consistent with the picture shown in Fig. 3. We found that the reason why Pb_i creates deep gap states is due to the crystal field splitting of the Pb *p* orbital at the interstitial site, which pulls the Pb p_z orbital below the p_x/p_y orbital. As discussed above, the reason why V_{Pb} and MA_{Pb} are shallow acceptors is attributed to the strong *s-p* antibonding states at the VBM of $CH_3NH_3PbI_3$. Without Pb *s* lone-pair orbitals, the VBM should be derived only from I *p* orbitals. The *s-p* antibonding coupling between Pb lone-pair *s* and I *p* orbitals pushes the VBM up to a higher level, such that the acceptors are generally shallower than in the case without strong *s-p* antibonding coupling. The shallow defect levels of MA_i and V_I are due to the high ionicity of $CH_3NH_3PbI_3$. A MA_i has no covalent bonding with the Pb–I framework and therefore does not create additional gap states. It is noted that various atomic structures have been proposed for Pb_i and I_i in $CH_3NH_3PbI_3$ by others [59, 60]. We have tested all the structures and have considered the configurations with the lowest energies.

The wave functions of shallow level defects are usually delocalized, whereas they are localized for deep level defects. For example, the V_{Pb} is a shallow acceptor. The acceptor level is below the VBM. As seen from Fig. 5a, the charge density of the V_{Pb} level, which is one level below the VBM, is quite delocalized. However, the calculated charge density is rather localized for Pb_i level, which creates a defect level above the VBM.

The calculated transition energy levels of intrinsic defects in $CH_3NH_3PbBr_3$ are shown in Fig. 6. The donor-like defects are shown at the left and the acceptor-like defects are at the right side. It is seen that there are only four defects, i.e., Pb_i, Pb_{Br}, Br_{MA}, and Br_{Pb} that produce deep levels in the bandgap of $CH_3NH_3PbBr_3$. All other defects create only shallow levels. MA_i, Pb_{MA}, V_{Br}, and MA_{Br} are shallow donors, whereas Br_i, MA_{Pb}, V_{MA}, and V_{Pb} are shallow acceptors. The trend is very similar to that of the intrinsic defects observed in $CH_3NH_3PbI_3$.

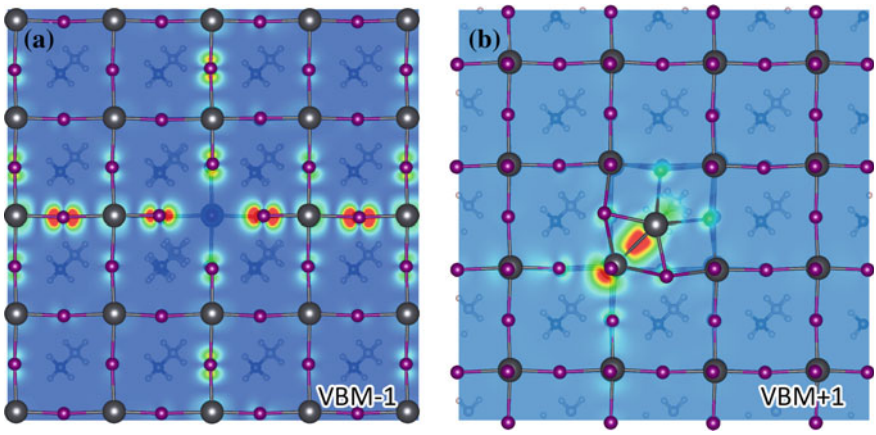

Fig. 5 Calculated charged density maps of **a** the state below the VBM of a V_{Pb} and **b** the states above the VBM of Pb_i

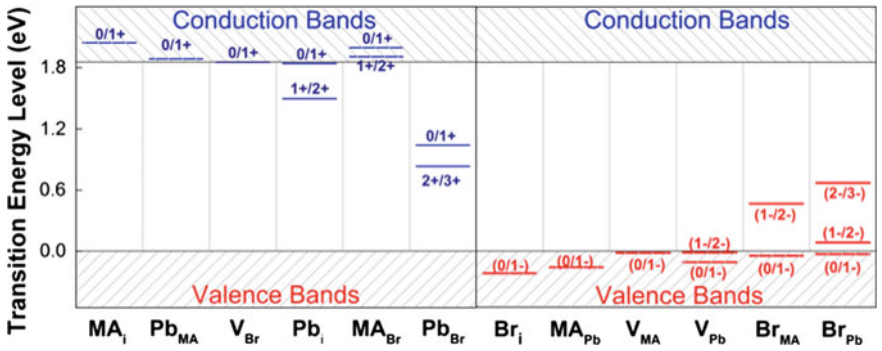

Fig. 6 Calculated transition energy levels of intrinsic point defects in $CH_3NH_3PbBr_3$. Adapted with permission from Ref. [33]. Copyright 2014 AIP Publishing LLC

3.3 Calculated Formation Energy of Intrinsic Point Defects

The electrical properties of a semiconductor are determined by the dominant point defects formed in the semiconductor. Therefore, to determine which of the above point defects may dominate the electronic properties of $CH_3NH_3PbI_3$, we have calculated the formation energy of the defects considered above. As shown in Sect. 2, the formation energy of a point defect depends on the chemical potentials of constituent elements. Taking $CH_3NH_3PbI_3$ as an example, in thermodynamic equilibrium growth conditions, the chemical potentials are constrained to ranges that promote the growth of $CH_3NH_3PbI_3$ and exclude the formation of secondary phases such as PbI_2 and CH_3NH_3I. Therefore, the chemical potentials should satisfy [56, 57]

$$\mu_{MA} + \mu_{Pb} + 3\mu_I = \Delta H(MAPbI_3) = -5.26 \text{ eV} \tag{4}$$

where μ_i is the chemical potential of the constituent element in reference to its most stable phase and $\Delta H(CH_3NH_3PbI_3)$ is the formation enthalpy of $CH_3NH_3PbI_3$. For μ_{MA}, we used the body-centered-cubic phase of CH_3NH_3 following Cs. To exclude the possible secondary phases of PbI_2 and CH_3NH_3I (rock-salt phase), the following constrains must also be satisfied.

$$\mu_{MA} + \mu_I = \Delta H(MAI) = -2.87 \text{ eV} \tag{5}$$

$$\mu_{Pb} + 2\mu_I = \Delta H(PbI_2) = -2.11 \text{ eV} \tag{6}$$

The chemical potentials of Pb and I satisfying Eqs. (4)–(6) are shown in the middle red region in Fig. 7. This narrow and long chemical range indicates the growth conditions for synthesizing the $CH_3NH_3PbI_3$ phase in equilibrium conditions. The narrow but long chemical potential range indicates that the growth conditions should be carefully controlled to form the desirable $CH_3NH_3PbI_3$ perovskite phase. The small chemical range is consistent with the calculated small

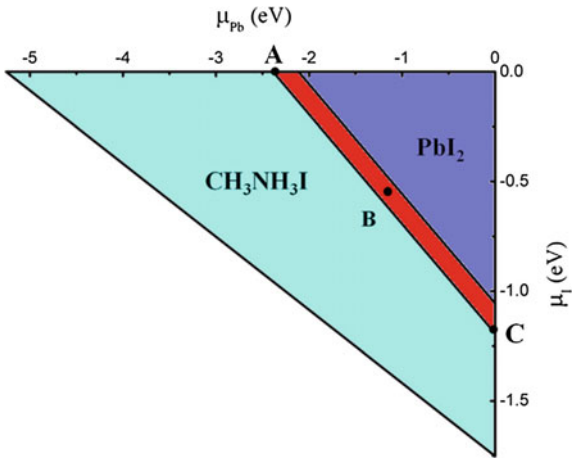

Fig. 7 Calculated chemical ranges for forming $CH_3NH_3PbI_3$ (*middle red region*), PbI_2 (*upper right blue region*), and CH_3NH_3I (*left green region*). Three representative points *A* ($\mu_{MA} = -2.87$ eV, $\mu_{Pb} = -2.39$ eV, $\mu_I = 0$ eV), *B* ($\mu_{MA} = -2.41$ eV, $\mu_{Pb} = -1.06$ eV, $\mu_I = -0.60$ eV), and *C* ($\mu_{MA} = -1.68$ eV, $\mu_{Pb} = 0$ eV, $\mu_I = -1.19$ eV) were used for calculating the formation energy of point defects. Adapted with permission from Ref. [28]. Copyright 2014 AIP Publishing LLC

dissociation energy of $CH_3NH_3PbI_3$, only 0.27 eV, as defined by $E(CH_3NH_3I) + E(PbI_2) - E(CH_3NH_3PbI_3)$.

To evaluate the dependence of the formation energy of point defects on the chemical potentials of the constituent elements, we have chosen three representative points, A (I-rich/Pb-poor), B (moderate), C (I-poor/Pb-rich), shown in Fig. 7. The formation energy of the considered point defects as a function of Fermi level position at chemical potential A, B, and C are shown in Fig. 8a–c, respectively. For clarity, only the defects with low formation energy are shown in solid colored lines. The defects with high formation energy are shown in light gray lines. At chemical point A, i.e., I-rich/Pb-poor, $CH_3NH_3PbI_3$ should be intrinsically *p*-type, because the Fermi level is close to the VBM. At chemical point B, i.e., moderate, $CH_3NH_3PbI_3$ should be intrinsic (low conductivity). At chemical point C, i.e., I-poor/Pb-rich, $CH_3NH_3PbI_3$ should be intrinsically good *n*-type, since the Fermi level is close to the CBM. In $CH_3NH_3PbI_3$, the dominant defects are donor MA_i and acceptor V_{Pb}, which have comparable formation energy. The low formation energy of V_{Pb} in $CH_3NH_3PbI_3$ is due to the energetically unfavorable *s*-*p* antibonding coupling, which resembles the *p*-*d* antibonding coupling in CIS [61]. The fully occupied antibonding states between Pb *s* and I *p* coupling do not gain electronic energy and, thus, tend to break the bond and form a vacancy. The lower formation energy of MA_i could be explained by its weak interaction with the Pb–I framework. The Fermi level is pinned by the formation of these two shallow defects. A recent report has demonstrated that the conductivity of $CH_3NH_3PbI_3$ can be tuned from *p*-type to *n*-type by modifying the growth conditions [62].

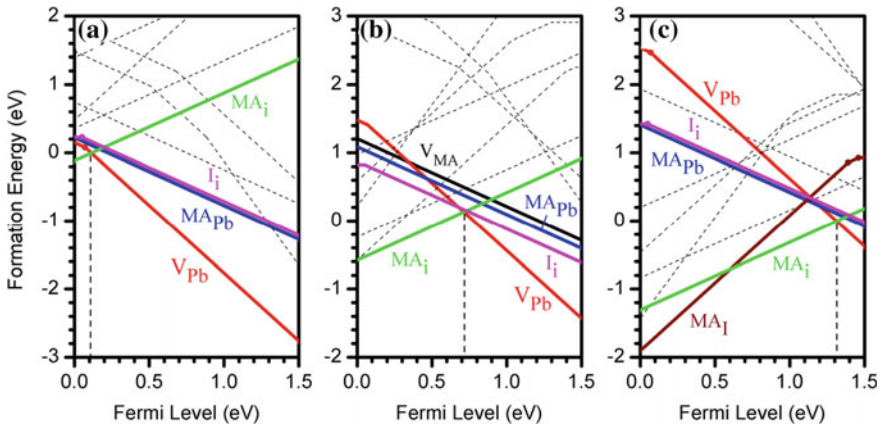

Fig. 8 Calculated formation energy of point defects as a function of the Fermi level at three chemical potential points, **a** A, **b** B, and **c** C, shown in Fig. 7. Adapted with permission from Ref. [28]. Copyright 2014 AIP Publishing LLC

It is seen that the defects that have low formation energy, such as MA_i, V_{Pb}, MA_{Pb}, I_i, V_I, and V_{MA}, have transition energy levels less than 0.05 eV above (below) the VBM (CBM) of $CH_3NH_3PbI_3$. On the other hand, all the defects that create deep levels, such as I_{Pb}, I_{MA}, Pb_i, Pb_I, have a high formation energy. Because only the defects with deep levels are responsible for nonradiative recombination, these formation energies strongly indicate that $CH_3NH_3PbI_3$ should intrinsically have a low nonradiative recombination rate.

We have also calculated the formation energy of the point defects as a function of the Fermi level position at chemical potential points Br-rich/Pb-poor, moderate, and Br-poor/Pb-rich. The results are shown in Fig. 9a–c, respectively. It is seen that the conductivity of $CH_3NH_3PbBr_3$ depends on the growth conditions. At chemical potential point Br-rich/Pb-poor, the Fermi level is determined by the formation of V_{Pb} and is inside the VB. This indicates that $CH_3NH_3PbBr_3$ grown under this condition should be degenerately doped and should exhibit excellent *p*-type conductivity. The conductivity is expected to be better than the intrinsic *p*-type conductivity of $CH_3NH_3PbI_3$. At the moderate growth condition, the Fermi level is pinned at 0.25 eV above the VBM by V_{Br} and V_{Pb}. In this case, the $CH_3NH_3PbBr_3$ should still exhibit a moderate *p*-type conductivity. At chemical potential point Br-poor/Pb-rich, $CH_3NH_3PbBr_3$ should be either intrinsic or slightly *n*-type, as the Fermi level is pinned at 1.07 eV above the VBM by V_{Br} and V_{MA}. Therefore, unlike $CH_3NH_3PbI_3$, $CH_3NH_3PbBr_3$ exhibits a unipolar self-doping behavior, i.e., it can only have good *p*-type conductivity under thermal equilibrium growth conditions. Good *n*-type conductivity is not achievable for $CH_3NH_3PbBr_3$. Thus, $CH_3NH_3PbBr_3$ may be used as a low-cost hole transport material for lead halide perovskite solar cells. It has been shown [18] that the *n*-type conductivity of $CH_3NH_3PbI_3$ is due to the low formation energy of MA_i. However, the formation

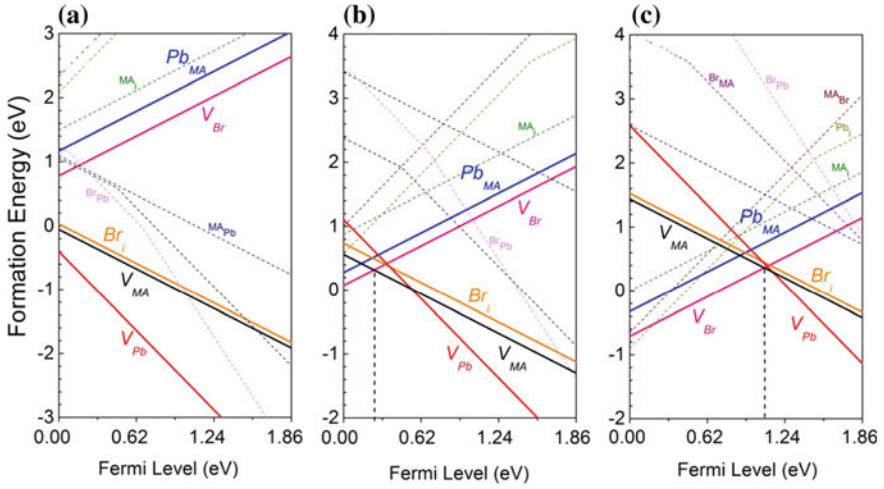

Fig. 9 Calculated formation energy of considered intrinsic point defects in $CH_3NH_3PbBr_3$ as a function of the Fermi level at three chemical potential points: **a** Br-rich/Pb-poor, **b** moderate, and **c** Br-poor/Pb-rich. Defects with high formation energy are shown in *dashed lines*. Adapted with permission from Ref. [33]. Copyright 2014 AIP Publishing LLC

energy of MA_i is too high to make $CH_3NH_3PbBr_3$ *n*-type. The higher formation energy of MA_i in $CH_3NH_3PbBr_3$ is due to the smaller lattice constant compared to $CH_3NH_3PbI_3$. The low formation energy of V_{Pb} in both $CH_3NH_3PbI_3$ and $CH_3NH_3PbBr_3$ is due to the energetically unfavorable *s-p* antibonding coupling. The fully occupied antibonding between Pb *s* and I *p*/Br *p* coupling does not gain electronic energy and, thus, tends to break the bond and form Pb and Br vacancies. Because the Pb *s* and Br *p* antibonding coupling is stronger than the Pb *s* and I *p* antibonding coupling, V_{Pb} has smaller formation energy in $CH_3NH_3PbBr_3$ than in $CH_3NH_3PbI_3$. These are the fundamental reasons why $CH_3NH_3PbI_3$ exhibits an ambipolar self-doping behavior, but $CH_3NH_3PbBr_3$ exhibits a unipolar self-doping behavior. It is noted that the four point defects that produce deep levels, Pb_i, Pb_{Br}, Br_{MA}, and Br_{Pb}, have rather high formation energies. Therefore, they are not the dominant defects in $CH_3NH_3PbBr_3$, partially explaining why high V_{OC}'s can be achieved for $CH_3NH_3PbBr_3$-based solar cells.

3.4 Calculated Surface States

Based on the mechanism of defect formation shown in Fig. 3b, the surfaces of $CH_3NH_3X_3$ perovskites should not produce deep gap states. The surface properties of $CH_3NH_3PbI_3$ have been studied by DFT calculations [63]. Here we show our DFT results on the (110) surface of $CH_3NH_3PbI_3$. The (110) surface is the most important surface as most perovskite films in solar cell devices show the (110) preferential

orientation. The (110) surface could have two terminations, the flat PbI_2 and MAI, as shown in Fig. 10a, b, respectively. The surfaces are modeled using slab supercells. In our calculations, the atoms in bulk regions (three PbI_6 octahedral layers) were fixed and only atoms in the surface regions were allowed to relax.

We calculated the total density of states (TDOSs) of these two slabs with surfaces and compared them with the TDOS of $CH_3NH_3PbI_3$ bulk unit cell. The TDOS of the flat PbI_2-terminated and MAI-terminated (110) surfaces are shown in Fig. 11a, b, respectively. The TDOS of the slab that contains only bulk $CH_3NH_3PbI_3$ is shown in Fig. 11c. The TDOS of the slabs with PbI_2-terminated (110) surface shows almost no bandgap, while the TDOS of the supercell containing the MAI-terminated surface shows a much reduced bandgap compared to the bulk. The results suggest that the surfaces create deep levels. This is not consistent with the defect trend shown in Fig. 3.

To understand whether the valence and conduction band edges are localized surface states, we plotted the charge density maps associated with the valence and conduction band edges. As shown in Fig. 12a, b, the charges are located on the

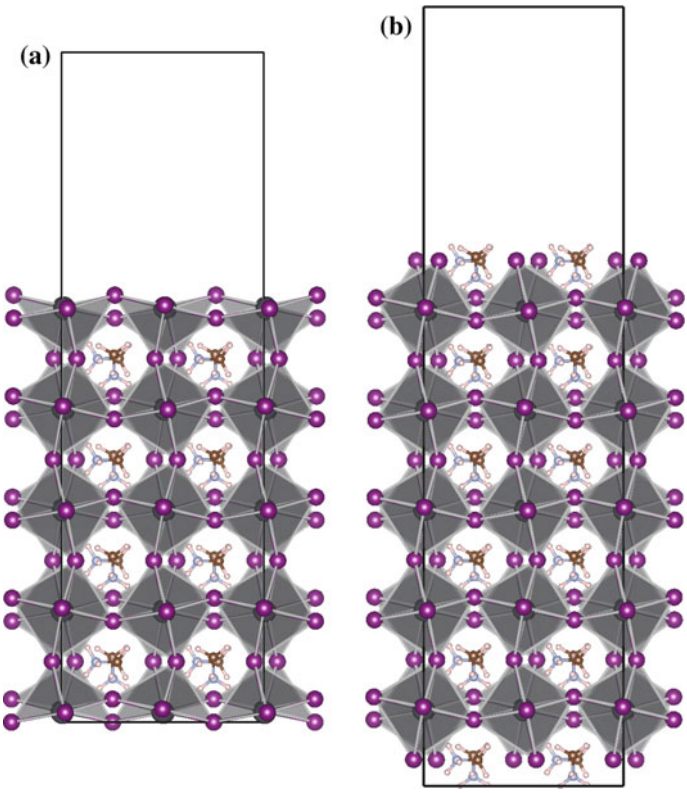

Fig. 10 *Side view* of the (110) surface of $CH_3NH_3PbI_3$ with the **a** flat PbI_2 and **b** MAI terminations

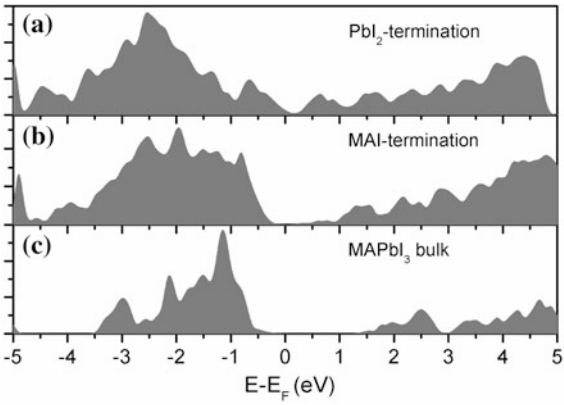

Fig. 11 Calculated TDOS of slabs with **a** (110) PbI_2-terminated flat surface, **b** MAI-terminated surface, and **c** bulk

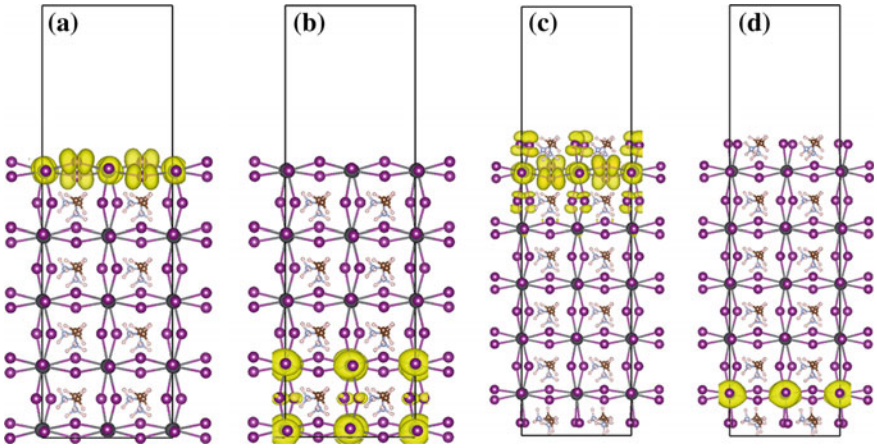

Fig. 12 Charge density maps of **a** VBM and **b** CBM of a supercell with the flat PbI_2 surfaces and **c** VBM and **d** CBM of a supercell with the MA surface

surface layers, indicating that the surfaces introduce localized states. This suggests that the surfaces produce deep levels. This is not consistent with the general trend shown in Fig. 3.

However, when we calculated the partial density of states (PDOSs) of each PbI_6 layer, a different scenario was obtained. As shown in Fig. 13, the PDOSs exhibit very similar characteristics, including bandgap, for all layers from the upper surface to the bottom surface for both the (110) PbI_2 flat surface (Fig. 13a) and the MAI surface (Fig. 13b). The only observable difference is the systematic shift of the PDOS to lower energy for the layers below the upper surfaces. Except for the

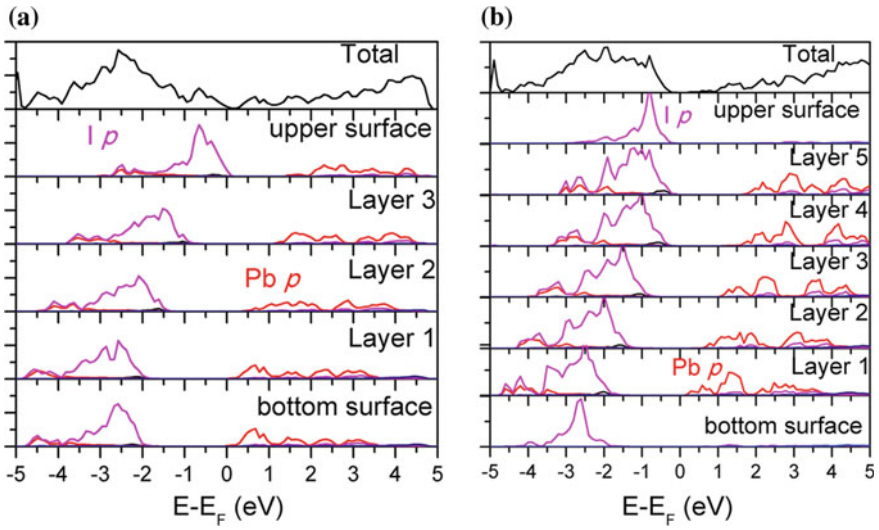

Fig. 13 Calculated PDOS of each layer of the slabs with **a** (110) PbI_2 flat surface and **b** MAI surface

energy shift, the PDOS of the surface layers are very similar to the PDOS of the layers in the bulk regions. Therefore, the surfaces actually do not produce any deep levels. The narrowed bandgaps, or, the so-called surface states, in Fig. 13 are due to the shift of the PDOS of different layers. We found that the energy shift of the PDOS is likely caused by the surface dipoles induced mainly by the Pb–I bonds on the surfaces. The CH_3NH_3 molecules on the MAI surfaces introduce additional dipoles, but much weaker than that induced by Pb–I bonds.

3.5 Calculated Grain Boundary States

In conventional inorganic solar cell absorbers such as GaAs, CIGS, CZTS, and CdTe, intrinsic GBs create deep levels within the bandgap and are considered detrimental to solar cell performance. Recent theoretical studies have shown that cation–cation and anion–anion wrong bonds are mainly responsible for the deep gap states [64–67], which is akin to the scenario shown in Fig. 3c. We have therefore calculated the electronic properties of GBs in $CH_3NH_3PbI_3$ perovskite. Because there is no experimental data available for the atomic structure of GBs in $CH_3NH_3PbI_3$, we have adopted the atomic structures of GBs seen in perovskite oxides by atomic-resolution transmission electron microscopy [50]. To maintain the periodicity, each supercell contains two identical GBs, which are oriented in the opposite directions. Figure 14 shows the atomic structure of a supercell containing two identical Σ5(310) GBs. The atomic structure is adopted from the same GB in

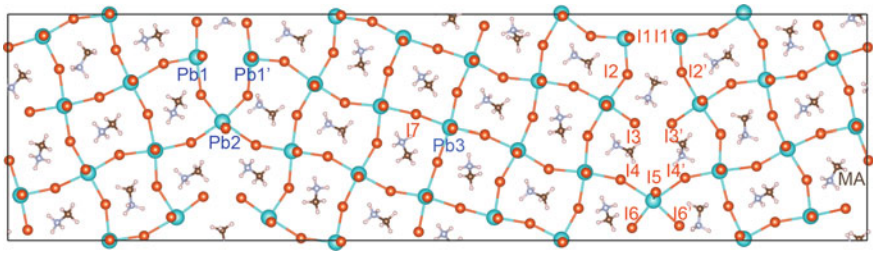

Fig. 14 The structural model of Σ5(310) GBs in $CH_3NH_3PbI_3$. Two identical GBs are included the supercell to allow the periodicity. Adapted with permission from Ref. [29]. Copyright 2014 Wiley-VCH Verlag GmbH & Co. KGaA

perovskite $SrTiO_3$. To investigate the effect of interaction between the two GBs in the supercell, supercells with various widths between the two GBs were constructed. When the distance between the GBs reaches 38.32 Å, the interaction between the two GBs becomes negligible. The fully relaxed GB structure is shown in Fig. 14. Some of the Pb and I atoms in the boundary regions that have dangling bonds or wrong bonds are labeled. The Pb1–Pb1', I1–I1', I2–I2', I3–I3' distances are 4.870, 4.636, 4.856, and 3.776 Å, respectively. This is mainly due to the large lattice constant of $CH_3NH_3PbI_3$. Such large distances indicate that there is no strong Pb–Pb and I–I wrong bonding. The GBs contain mainly Pb and I dangling bonds, Pb–I–Pb wrong bond angles, and extra bonds (Pb2). As discussed above, Pb and I dangling bonds should generate shallow levels. Therefore, the GBs are expected to be electrically benign.

Our density of states (DOS) analysis, indeed, shows that the GBs in $CH_3NH_3PbI_3$ are intrinsically, electrically benign. Figure 15a shows the

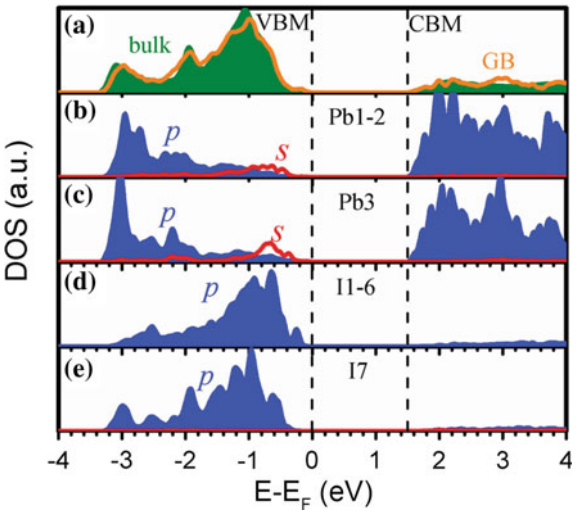

Fig. 15 **a** Calculated total TDOS of a supercell with $CH_3NH_3PbI_3$ bulk and a supercell containing two Σ5 (310) GBs. **b–e** PDOS of selected atoms near GB planes. The PDOS are enlarged for clarity. Adapted with permission from Ref. [29]. Copyright 2014 Wiley-VCH Verlag GmbH & Co. KGaA

comparison of the calculated TDOS of a supercell containing $CH_3NH_3PbI_3$ bulk and a supercell containing two Σ5(310) GBs with opposite arrangements. The two TDOS are almost identical in the bandgap regions, indicating that the GBs do not generate any states within the bandgap of $CH_3NH_3PbI_3$. The benign GB properties could be explained by the shallow nature of point defects formed by dangling bonds. We have also plotted the PDOS of Pb and I atoms such as Pb1, Pb2, I1, I2, I3, I4, I5, and I6 in the Σ5(310) GB regions and Pb3 and I7 atoms in the bulk region (Fig. 14b–e). It is seen that no gap states are observed. We have also considered the Σ3(111) GB, another common GB in perovskites. The benign GB properties in $CH_3NH_3PbI_3$ are consistent with its shallow defect trend shown in Fig. 3c.

To test the impact of the bond length or lattice constant, we compress the GB regions to see how the level of the I–I antibonding state changes. Figure 16 shows the calculated I–I $pp\sigma^*$ level relative to the VBM as a function of the compression ratio. It is seen that the I–I $pp\sigma^*$ level is below the VBM when no compression is considered, as discussed above. The compressive strain clearly increases I–I coupling strength and pushes the I–I $pp\sigma^*$ level further into the bandgap. At about 3 % compressive strain, the I–I $pp\sigma^*$ level moves just above the VBM. At about 10 % strain, the I–I $pp\sigma^*$ level is at about 0.20 eV above the VBM, which becomes a deep defect state. It is noted that a previous report [68] has shown that increasing the lattice parameter with tensile strain at the GBs of $CuInSe_2$ can effectively push the anion–anion $pp\sigma^*$ level out of the bandgap and the GB becomes electrically benign.

Although there are no deep gap states in the Σ5(310) GB, the defect states are close to the VBM and thus reduce the hole mobility. Cl and O passivation in GBs could reduce the defect states and improve hole mobility. Both theoretical and experimental observations have suggested that Cl is unlikely in the $MAPbI_3$ bulk. We examined the possibility of Cl at the GBs because defect segregation at the GBs is a common phenomenon [64–66, 69, 70] in thin-film solar cells such as CdTe,

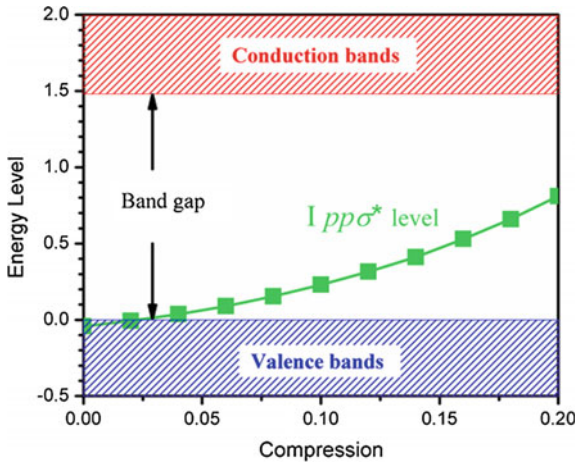

Fig. 16 The variations of $pp\sigma^*$ defect state as a function of the ratio of compressive strain at the Σ5(310) GB core region

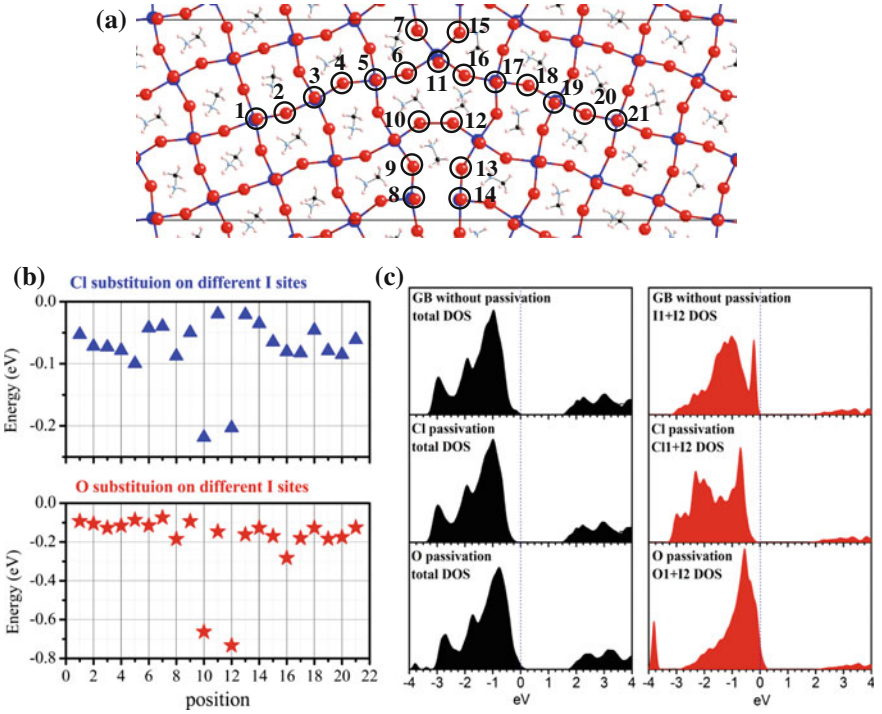

Fig. 17 **a** Different I positions considered as Cl/O substitution sites in the $CH_3NH_3PbI_3$ Σ5(310) GB. The model structure is fully relaxed from a snapshot in MD simulation. **b** The relative total energy when Cl/O substitutes on different I sites in (**a**). The unsymmetrical behavior is attributed to the random orientations of the CH_3NH_3 molecule. **c** TDOS and PDOS at wrong bonds of unpassivated, Cl-passivated and O-passivated $CH_3NH_3PbI_3$ Σ5(310) GBs. Adapted with permission from Ref. [34]. Copyright 2015 Wiley-VCH Verlag GmbH & Co. KGaA

$CuInSe_2$, and $Cu_2ZnSnSe_4$. We found that in the Σ5(310) GB (Fig. 17a), the total energy of Cl_I at I–I wrong bond sites is about 0.2 eV lower than that in bulk, as shown in Fig. 17b, indicating that Cl can spontaneously segregate into the GB region. The fact that Cl favors the I–I wrong bond site at GBs is due to its smaller size: replacing I by Cl can cause a large strain in the system, thus costing energy, but it costs less energy at the GB than that in the grain interior region. The Cl–I bond length at the GB increases from 3.72 Å (I–I bond) to 3.80 Å—i.e., the bond is weakened. The weakening of the Cl–I bond and the high electronegativity of Cl at the GBs will pull down and thus deactivate the hole trap state. Because many experimental results did not show Cl in $MAPbI_3$, we can perform a straightforward estimate of the amount of Cl necessary to passivate the GBs. Considering a grain size of 200 nm (ranging from 50 to 2000 nm in experiments), we estimate that a 0.3 % atomic ratio of Cl is enough to passivate all the I–I wrong bonds at GBs. This assumption is based on all the GBs having wrong bond-derived trap states. Actually, some GBs, such as Σ3(111), do not have trap states. As a result, the actual

amount of Cl, which is dependent on the grain size and energetic processes, should be even less. This result may explain why a small amount of Cl (perhaps within experimental detectability) can enhance the carrier transportation.

The possible existence of Cl at GBs was indirectly evidenced by both Kelvin probe force microscopy (KPFM) and EBIC measurements. Edri et al.'s experiments detected a small electrostatic barrier ($\sim$40 meV [71]) across the $MAPbI_3$ GB; however, no barrier is found for $MAPbI_{3-x}Cl_x$ GBs [71]. A similar effect with O is also found in our calculation, as shown in Fig. 17b. However, the difference between O and Cl is that Cl is isovalent with I, whereas O at the I site is an acceptor and makes the materials *p*-type, as shown in Fig. 17c, where the calculated Fermi level for O passivation is below the bulk VBM. A recent experimental report by Ren et al. [72] demonstrated that the thermal-assisted oxygen annealing led to a substantial increase in power conversion efficiency. Apart from chemical passivation by Cl or O, PCBM/fullerene films are also found to have a passivation effect at the GBs and eliminates current–voltage (I–V) hysteresis. The passivation mechanism is still puzzling [73]. Based on our theory large-size fullerenes diffusing into $MAPbI_3$ GBs would stretch the I–I bond length, weaken the wrong bond strength, and thus pull the trap state below the VBM.

Though the ideal GBs in perovskites are electrically benign, GBs in real perovskite films could contain additional intrinsic point defects, such as I and Pb interstitials. It has been reported that I atoms migrate through the GBs in perovskite films. The migration of I atoms are suspected to be partially responsible for the hysteretic phenomenon observed in the current–voltage measurements of solar cell devices. We found that an interstitial I at the Σ5(210) GB (Fig. 18a) has an energy level about 0.26 eV lower than the one in the bulk regions, suggesting that some I interstitials will likely segregate into GBs and alter the GB properties. Figure 18b shows the calculated TDOS of the Σ5(210) GB with an I interstitial. It can be seen

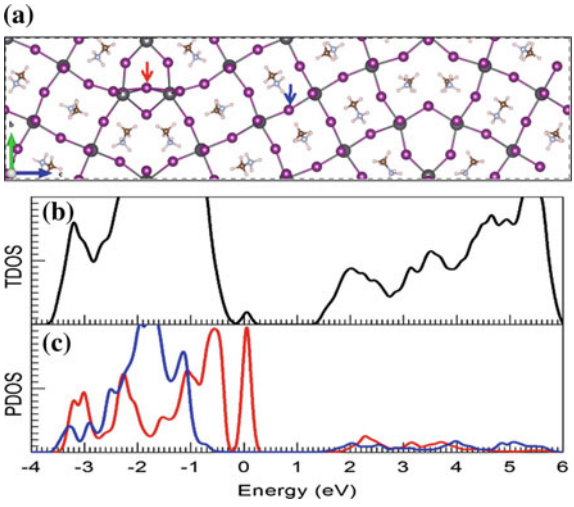

Fig. 18 **a** The structural model of Σ5(210) GBs in $CH_3NH_3PbI_3$ with an interstitial I atom at the left GB. **b** Calculated TDOS of the supercell with an interstitial I atom at the left GB and **c** PDOS of the interstitial I atom and an I atom in the bulk region

that a small sharp peak appears above the valence band, indicating that the interstitial I at the GB produces a deep level. To reveal this level more clearly, the PDOS' associated with the interstitial I at the GB (marked by the red arrow) and an I atom in the bulk region (marked by the blue arrow) are plotted in Fig. 18c. Consistent with the general trend seen in Fig. 3c, the sharp gap state as seen in Fig. 18c is derived from I *p*–I p antibonding state. The bond length between the interstitial I and the nearest neighboring I atom is 3.47 Å, which is shorter than the shortest I–I bond length in the Σ5(210) GB without interstitial I atoms.

3.6 Doping Properties of $CH_3NH_3PbI_3$

We have calculated the effect of external doping of group IA IB, IIA, IIB, IIA, VA, and VIA elements. For group IA and IB elements, we considered K, Na, Rb, and Cu on interstitial sites (Na_i, K_i, Rb_i, and Cu_i) as donors and on Pb sites (Na_{Pb}, K_{Pb}, Rb_{Pb}, and Cu_{Pb}) as acceptors. For group-IIA and IIB elements, we considered Sr, Ba, Zn, and Cd on MA site (Sr_{MA}, Ba_{MA}, Zn_{MA}, and Cd_{MA}) as donors and on Pb site (Sr_{Pb}, Ba_{Pb}, Zn_{Pb}, and Cd_{Pb}) as neutral defects. For group IIIA and VA elements, we considered Al, Ga, In, Sb and Bi, on Pb sites (Al_{Pb}, Ga_{Pb}, In_{Pb}, Sb_{Pb}, and Bi_{Pb}) as potential donors. For group VIA elements, we considered O, S, Se, and Te on I sites (O_I, S_I, Se_I, and Te_I) as potential acceptors.

The calculated transition energy levels of shallow donors and acceptors are shown in Fig. 19. For donors, the transition energy levels are referenced to the CBM of $CH_3NH_3PbI_3$, whereas the levels are referenced to the VBM for acceptors. It is seen that interstitial group IA and -IB elements, Na_i, K_i, Rb_i, and Cu_i, are shallow donors. Group-IIA elements such as Sr and Ba occupying MA sites are also shallow donors. They are neutral defects when they occupy Pb sites. Our calculations revealed that Zn_{MA}, Cd_{MA}, Al_{Pb}, Ga_{Pb}, and In_{Pb} are deep donors. Therefore, these dopants are not considered. Bi_{Pb} and Sb_{Pb} are shallow donors with transition

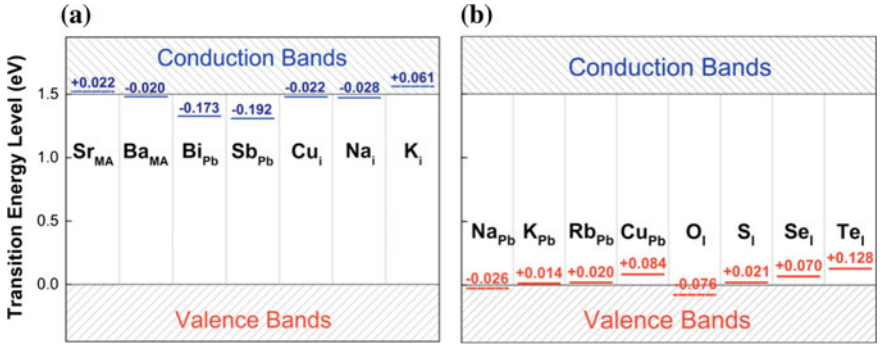

Fig. 19 Calculated transition energy levels of considered extrinsic dopants. Adapted with permission from Ref. [30]. Copyright 2014 American Chemical Society

energy levels of −0.17 eV and −0.19 eV, respectively. The calculated transition energy levels of Na_{Pb}, K_{Pb}, Rb_{Pb}, and Cu_{Pb} are −0.026 eV, 0.014 eV, 0.020 eV, and 0.084 eV, respectively. The calculated transition energy levels for O_I, S_I, Se_I, and Te_I are −0.076 eV, 0.021 eV, 0.070 eV, and 0.128 eV, respectively. The negative transition energies for Na_{Pb} and O_I mean that their levels are below the VBM, indicating spontaneous ionizations.

To evaluate the extrinsic doping properties of $CH_3NH_3PbI_3$, we have calculated the formation energy of the above dopants as a function of the Fermi level under two representative growth conditions: I-rich/Pb-poor and I-poor/Pb-rich. To calculate the formation energy of the dopants, the chemical potentials of considered dopant elements must satisfy additional constraints to exclude the formation of dopant-related secondary phases. For example, when doping using group IA elements such as Na, K, and Rb, we exclude the possible secondary phases of NaI, KI, and RbI. Therefore, the following constraints must also be satisfied: $\mu_{Na} + \mu_I < \Delta H(NaI) = -2.59$ eV, $\mu_K + \mu_I < \Delta H(KI) = -3.01$ eV, and $\mu_{Rb} + \mu_I < \Delta H(RbI) = -3.03$ eV. Similar constraints are necessary to exclude the formation of other possible dopant-related secondary phases: for examples, CuI, SrI_2, BaI_2, SbI_3, BiI_3, PbO, PbS, PbSe, and PbTe.

Figure 20a, b show the calculated formation energy as a function of the Fermi level for group IA and IB dopants at I-rich/Pb-poor and I-poor/Pb-rich growth conditions, respectively. The dashed line shows the intrinsic defects with the lowest formation energy. At the I-rich/Pb-poor condition, acceptors Na_{Pb}, K_{Pb}, Rb_{Pb}, and Cu_{Pb} have a much lower formation energy than the donors, Na_i, K_i, Rb_i, and Cu_i. Therefore, the majority of these dopants should occupy Pb sites and dope

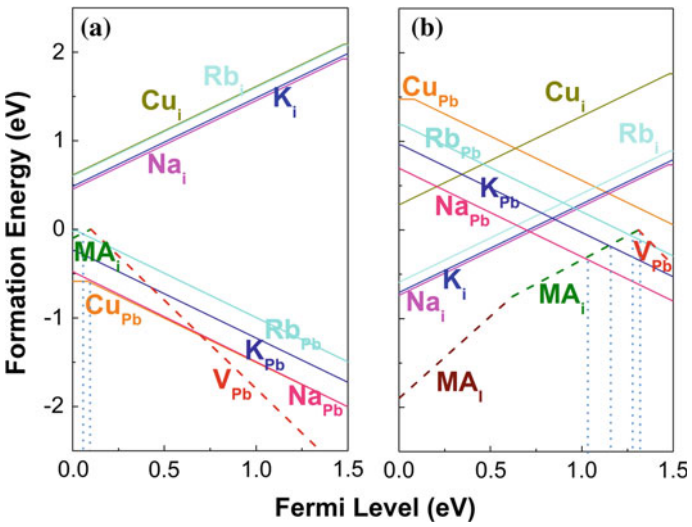

Fig. 20 Calculated formations energy as a function of the Fermi level for group IA and IB dopants at **a** I-rich/Pb-poor and **b** I-poor/Pb-rich conditions. Adapted with permission from Ref. [30]. Copyright 2014 American Chemical Society

$CH_3NH_3PbI_3$ *p*-type. The compensation from intrinsic donor defect, MA_i, is very weak. For Na and K doping, the Fermi level is pinned below the VBM, indicating degenerate *p*-type doping. For Cu doping, the Fermi level is pinned by the Cu_{Pb} (0/−1) transition, which is about 0.09 eV above the VBM. For Rb doping, the Fermi level is pinned at about 0.06 eV above the VBM by Rb_{Pb} and MA_i. Therefore, under the I-rich/Pb-poor growth condition, group 1A and 1B doping should lead to improved *p*-type conductivity compared to undoped $CH_3NH_3PbI_3$. At the I-poor/Pb-rich growth condition, the compensation from intrinsic donor defects and extrinsic acceptor defects becomes strong. For Na, K, and Rb doping, the Fermi level is pinned at 1.02 eV, 1.26 eV, and 1.31 eV by Na_{Pb}, K_{Pb}, Rb_{Pb} and MA_i, respectively. For Cu doping, the Fermi level is pinned by the intrinsic defects, MA_i and V_{Pb}. Therefore, at the I-poor/Pb-rich growth condition, group IA and IB doping would lead to more insulating $CH_3NH_3PbI_3$ as compared to the undoped case.

Figure 21a, b show the calculated formation energy as functions of the Fermi level for group-IIA dopants at the I-rich/Pb-poor and I-poor/Pb-rich conditions, respectively. It is seen that the formation energy of Sr_{MA} and Ba_{MA} are, in general, higher than that of Sr_{Pb} and Ba_{Pb}, and intrinsic defects V_{Pb} (Pb vacancy) and MA_i. This may be due to a couple of reasons. It is known that the fully occupied *s* orbital of Pb^{2+} has strong antibonding coupling with the I *p* orbital. The *s*-*p* antibonding coupling is energetically unfavorable [47, 74, 75]. When a Pb is substituted by a Sr^{2+} or Ba^{2+} that does not have a fully occupied *s* orbital, the energetically unfavorable

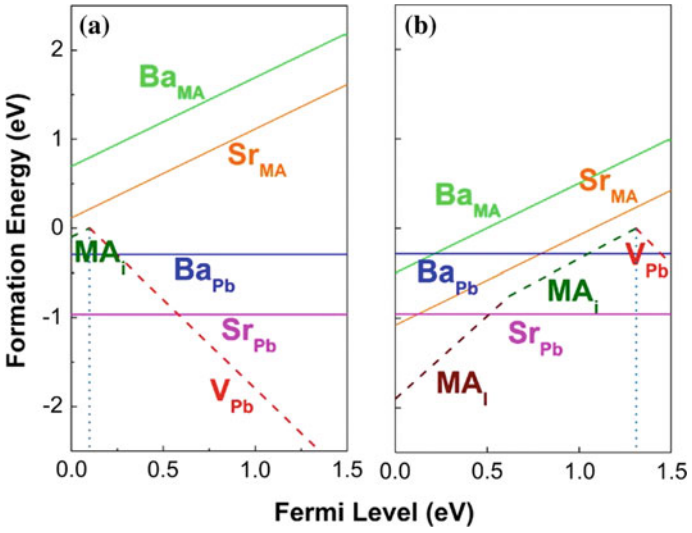

Fig. 21 The calculated formation energy as a function of Fermi level for group-IIA at I-rich/Pb-poor (**a**) and I-poor/Pb-rich (**b**), showing that the formation energy of Sr_{MA} and Ba_{MA} are generally higher than that of Sr_{Pb} and Ba_{Pb}, and intrinsic defects V_{Pb} (Pb vacancy) and MA_i. Adapted with permission from Ref. [30]. Copyright 2014 American Chemical Society

s-p antibonding coupling is eliminated, leading to energetically favorable substitutions. Another possible reason is that Sr and Ba are isovalent with Pb. While Sr_{MA} and Ba_{MA} introduce electrons to the conduction band, Sr_{Pb} and Ba_{Pb} do not. Furthermore, Sr_{Pb} and Ba_{Pb} may introduce less lattice strain than Sr_{MA} and Ba_{MA} due to a decreased size mismatch. Therefore, group-IIA elements are not expected to produce better *n*-type $MAPbI_3$ than intrinsic defects, though, these dopants can produce very shallow donor levels.

Doping using Sb and Bi at the I-rich/Pb-poor condition is strongly compensated by the formation of V_{Pb} as shown in Fig. 22a. The Fermi level is pinned at 0.16 eV and 0.19 eV above the VBM, respectively. Therefore, Sb and Bi doping at the I-rich/Pb-poor condition cannot lead to *n*-type $MAPbI_3$. At the I-poor/Pb-rich condition, the Fermi level is pinned by the intrinsic defect, MA_i and V_{Pb}, as shown in Fig. 22b. Therefore, Sb and Bi doping is not expected to produce better *n*-type $MAPbI_3$ than the intrinsic *n*-type under thermal equilibrium growth conditions.

For doping with group VIA elements, we found that only O may improve the *p*-type conductivity of $CH_3NH_3PbI_3$ under the I-rich/Pb-poor growth condition. Other group VIA elements such as S, Se, and I do not improve the *p*-type conductivity of $CH_3NH_3PbI_3$. Figure 23a, b reveal the calculated formation energy as a function of Fermi level for group VIA elements on I sites at the I-rich/Pb-poor and I-poor/Pb-rich conditions, respectively. The chemical potentials for O, S, Se, and Te are constrained to avoid the formation of secondary phases of PbO, PbS, PbSe, and PbTe. The calculated formation enthalpies are −2.96 eV, −1.16 eV, −1.25 eV and −0.96 eV for PbO, PbS, PbSe, and PbTe, respectively. The dashed lines show the

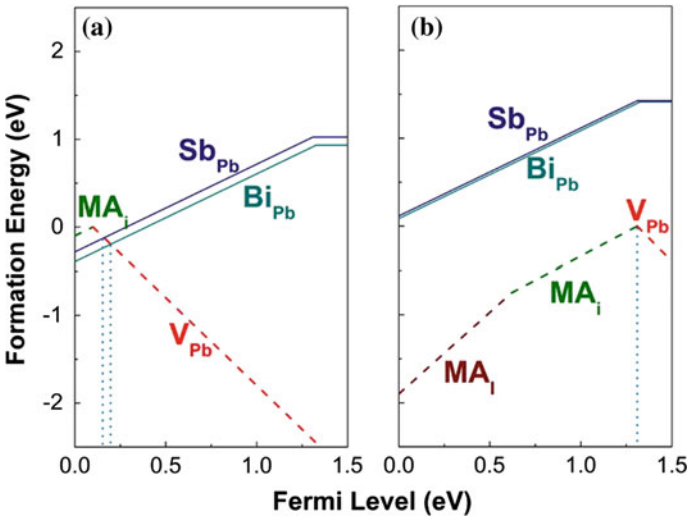

Fig. 22 The calculated formation energy as function of Fermi level for Sb and Bi at **a** I-rich/Pb-poor and **b** I-poor/Pb-rich conditions. Adapted with permission from Ref. [30]. Copyright 2014 American Chemical Society

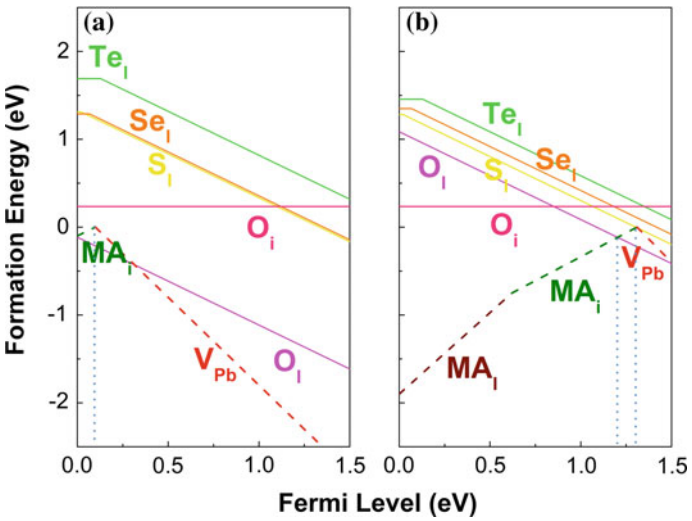

Fig. 23 The calculated formation energy as a function of the Fermi level for group VIA dopants at **a** I-rich/Pb-poor and **b** I-poor/Pb-rich. Adapted with permission from Ref. [30]. Copyright 2014 American Chemical Society

intrinsic defects with the lowest formation energy. It is seen that at the I-rich/Pb-poor growth condition (Fig. 23a), the Fermi level for doping with O is pinned at the top of the VBM by MA_i and O_I. Therefore, the *p*-type conductivity is expected to be better than intrinsic $CH_3NH_3PbI_3$ grown at the same growth condition (the Fermi level is pinned by MA_i and V_{Pb} at $\sim$0.1 eV above the VBM). An interstitial O atom at the site that binds to two H atoms of a MA molecule has the lowest energy. This configuration resembles an interstial O in a Si crystal. Similarly, the O interstitial in $MAPbI_3$ does not produce any gap states and, therefore, is a neutral defect. At the I-poor/Pb-rich condition, doping is strongly compensated by the formation of intrinsic point defects. Therefore, when doping using group VIA elements, only O leads to improved *p*-type conductivity at the I-rich/Pb-poor condition compared to intrinsic $CH_3NH_3PbI_3$ grown at the same condition.

4 Conclusion

We have reviewed the unique defect properties of $CH_3NH_3PbI_3$ perovskite—point defects with low formation energies only create shallow levels, whereas point defects with deep levels have high formation energies; intrinsic surfaces and GBs do not produce deep levels. These unique defect properties are attributed to the antibonding coupling between Pb lone-pair *s* and X *p* orbitals, the high ionicity, and

the large lattice constants of $CH_3NH_3PbI_3$. $CH_3NH_3PbI_3$ exhibits an intrinsic ambipolar self-doping behavior with conductivities tunable from *p*-type to *n*-type via controlling the growth conditions. However, $CH_3NH_3PbBr_3$ exhibits a unipolar self-doping behavior—it exhibits a preference for *p*-type conductivity if synthesized under thermal equilibrium growth conditions. $CH_3NH_3PbCl_3$ is expected to exhibit compensated self-doping behavior due to its large bandgap. The *p*-type conductivity of $CH_3NH_3PbI_3$ can be further improved by incorporating some group IA, IB, or VIA elements at the I-rich/Pb-poor growth conditions. However, the *n*-type conductivity of $CH_3NH_3PbI_3$ cannot be improved under thermal equilibrium growth conditions through extrinsic doping due to the compensation from intrinsic point defects.

Acknowledgments We thank Nikolas Podraza for providing the absorption coefficient of $CH_3NH_3PbI_3$ measured by spectroscopic ellipsometry. This work was supported by the U.S. Department of Energy (DOE) SunShot Initiative under the Next Generation Photovoltaics 3 program (DE-FOA-0000990) and Ohio Research Scholar Program. This research used the resources of the Ohio Supercomputer Center and the National Energy Research Scientific Computing Center, which is supported by the Office of Science of the U.S. Department of Energy under Contract No. DE-AC02-05CH11231.

References

1. Kojima, A., Teshima, K., Shirai, Y., Miyasaka, T.: J. Am. Chem. Soc. **131**, 6050–6051 (2009)
2. Im, J.H., Lee, C.R., Lee, J.W., Park, S.W., Park, N.G.: Nanoscale **3**, 4088–4093 (2011)
3. Kim, H.S., Lee, C.R., Im, J.H., Lee, K.B., Moehl, T., Marchioro, A., Moon, S.J., Humphry-Baker, R., Yum, J.H., Moser, J.E., Gratzel, M., Park, N.G.: Sci. Rep. **2**, 591 (2012)
4. Chung, I., Lee, B., He, J., Chang, R.P., Kanatzidis, M.G.: Nature **485**, 486–489 (2012)
5. Lee, M.M., Teuscher, J., Miyasaka, T., Murakami, T.N., Snaith, H.J.: Science **338**, 643–647 (2012)
6. Burschka, J., Pellet, N., Moon, S.J., Humphry-Baker, R., Gao, P., Nazeeruddin, M.K., Gratzel, M.: Nature **499**, 316–319 (2013)
7. Liu, M., Johnston, M.B., Snaith, H.J.: Nature **501**, 395–398 (2013)
8. Noh, J.H., Im, S.H., Heo, J.H., Mandal, T.N., Seok, S.I.: Nano Lett. **13**, 1764–1769 (2013)
9. Park, N.-G.: J. Phy. Chem. Lett. **4**, 2423–2429 (2013)
10. Xing, G., Mathews, N., Sun, S., Lim, S.S., Lam, Y.M., Gratzel, M., Mhaisalkar, S., Sum, T.C.: Science **342**, 344–347 (2013)
11. Stranks, S.D., Eperon, G.E., Grancini, G., Menelaou, C., Alcocer, M.J., Leijtens, T., Herz, L. M., Petrozza, A., Snaith, H.J.: Science **342**, 341–344 (2013)
12. Chen, Q., Zhou, H., Hong, Z., Luo, S., Duan, H.S., Wang, H.H., Liu, Y., Li, G., Yang, Y.: J. Am. Chem. Soc. **136**, 622–625 (2014)
13. Jeon, N.J., Noh, J.H., Kim, Y.C., Yang, W.S., Ryu, S., Seok, S.I.: Nat. Mater. **13**, 897–903 (2014)
14. Mei, A., Li, X., Liu, L., Ku, Z., Liu, T., Rong, Y., Xu, M., Hu, M., Chen, J., Yang, Y., Gratzel, M., Han, H.: Science **345**, 295–298 (2014)
15. Zhou, H., Chen, Q., Li, G., Luo, S., Song, T.B., Duan, H.S., Hong, Z., You, J., Liu, Y., Yang, Y.: Science **345**, 542–546 (2014)

16. Tao, C., Neutzner, S., Colella, L., Marras, S., Srimath Kandada, A.R., Gandini, M., Bastiani, M.D., Pace, G., Manna, L., Caironi, M., Bertarelli, C., Petrozza, A.: Energy Environ. Sci. **8**, 2365–2370 (2015)
17. Baena, J.P.C., Steier, L., Tress, W., Saliba, M., Neutzner, S., Matsui, T., Giordano, F., Jacobsson, T.J., Kandada, A.R.S., Zakeeruddin, S.M., Petrozza, A., Abate, A., Nazeeruddin, M.K., Gratzel, M., Hagfeldt, A.: Energy Environ. Sci. **8**, 2928–2934 (2015)
18. Ahn, N., Son, D.Y., Jang, I.H., Kang, S.M., Choi, M., Park, N.G.: J. Am. Chem. Soc. **137**, 8696–8699 (2015)
19. Jeon, N.J., Noh, J.H., Yang, W.S., Kim, Y.C., Ryu, S., Seo, J., Seok, S.I.: Nature **517**, 476–480 (2015)
20. Roldán-Carmona, C., Gratia, P., Zimmermann, I., Grancini, G., Gao, P., Graetzel, M., Nazeeruddin, M.K.: Energy Environ. Sci. **8**, 3550–3556 (2015)
21. Chen, W., Wu, Y., Yue, Y., Liu, J., Zhang, W., Yang, X., Chen, H., Bi, E., Ashraful, I., Gratzel, M., Han, L.: Science **350**, 944–948 (2015)
22. Yang, D., Yang, R., Zhang, J., Yang, Z., Liu, S., Li, C.: Energy Environ. Sci. **8**, 3208–3214 (2015)
23. Yang, W.S., Noh, J.H., Jeon, N.J., Kim, Y.C., Ryu, S., Seo, J., Seok, S.I.: Science **348**, 1234–1237 (2015)
24. NREL Best Research-Cell Efficiencies. . Accessed Mar 2016
25. Zhao, Y., Zhu, K.: Chem. Soc. Rev. (2016). doi:10.1039/C4CS00458B
26. Sun, S., Salim, T., Mathews, N., Duchamp, M., Boothroyd, C., Xing, G., Sum, T.C., Lam, Y. M.: Energy Environ. Sci. **7**, 399–407 (2014)
27. De Wolf, S., Holovsky, J., Moon, S.J., Loper, P., Niesen, B., Ledinsky, M., Haug, F.J., Yum, J.H., Ballif, C.: J. Phys. Chem. Lett. **5**, 1035–1039 (2014)
28. Yin, W.-J., Shi, T., Yan, Y.: Appl. Phys. Lett. **104**, 063903 (2014)
29. Yin, W.J., Shi, T., Yan, Y.: Adv. Mater. **26**, 4653–4658 (2014)
30. Shi, T., Yin, W.-J., Yan, Y.: J. Phy. Chem. C **118**, 25350–25354 (2014)
31. Yin, W.-J., Yang, J.-H., Kang, J., Yan, Y., Wei, S.-H.: J. Mater. Chem. A **3**, 8926–8942 (2015)
32. Yin, W.-J., Shi, T., Yan, Y.: J. Phy. Chem. C **119**, 5253–5264 (2015)
33. Shi, T., Yin, W.-J., Hong, F., Zhu, K., Yan, Y.: Appl. Phys. Lett. **106**, 103902 (2015)
34. Yin, W.-J., Chen, H., Shi, T., Wei, S.-H., Yan, Y.: Adv. Electron. Mater. **1**, 1500044 (2015)
35. Chang, Y.H., Park, C.H., Matsuishi, K.: J. Korean Phys. Soc. **44**, 889–893 (2004)
36. Borriello, I., Cantele, G., Ninno, D.: Phys. Rev. B **77**, 235214 (2008)
37. Kresse, G., Furthmüller, J.: Phys. Rev. B **54**, 11169–11186 (1996)
38. Kresse, G., Joubert, D.: Phys. Rev. B **59**, 1758–1775 (1999)
39. Perdew, J.P., Burke, K., Ernzerhof, M.: Phys. Rev. Lett. **77**, 3865–3868 (1996)
40. Heyd, J., Scuseria, G.E., Ernzerhof, M.: J. Chem. Phys. **118**, 8207 (2003)
41. Krukau, A.V., Vydrov, O.A., Izmaylov, A.F., Scuseria, G.E.: J. Chem. Phys. **125**, 224106 (2006)
42. Hedin, L.: Phys. Rev. **139**, A796–A823 (1965)
43. Hybertsen, M.S., Louie, S.G.: Phys. Rev. B **34**, 5390–5413 (1986)
44. Even, J., Pedesseau, L., Jancu, J.-M., Katan, C.: J. Phy. Chem. Lett. **4**, 2999–3005 (2013)
45. Giorgi, G., Fujisawa, J., Segawa, H., Yamashita, K.: J. Phy. Chem. Lett. **4**, 4213–4216 (2013)
46. Menéndez-Proupin, E., Palacios, P., Wahnón, P., Conesa, J.C.: Phys. Rev. B **90**, 045207 (2014)
47. Brivio, F., Butler, K.T., Walsh, A., van Schilfgaarde, M.: Phys. Rev. B **89**, 155204 (2014)
48. Umari, P., Mosconi, E., De Angelis, F.: Sci. Rep. **4**, 4467 (2014)
49. Mosconi, E., Amat, A., Nazeeruddin, M.K., Grätzel, M., De Angelis, F.: J. Phy. Chem. C **117**, 13902–13913 (2013)
50. Imaeda, M., Mizoguchi, T., Sato, Y., Lee, H.S., Findlay, S.D., Shibata, N., Yamamoto, T., Ikuhara, Y.: Phys. Rev. B **78**, 245320 (2008)
51. Stoumpos, C.C., Malliakas, C.D., Kanatzidis, M.G.: Inorg. Chem. **52**, 9019–9038 (2013)

52. Baikie, T., Fang, Y., Kadro, J.M., Schreyer, M., Wei, F., Mhaisalkar, S.G., Graetzel, M., White, T.J.: J. Mater. Chem. A **1**, 5628 (2013)
53. Ball, J.M., Lee, M.M., Hey, A., Snaith, H.J.: Energy Environ. Sci. **6**, 1739 (2013)
54. Zhang, S.B., Northrup, J.E.: Phys. Rev. Lett. **67**, 2339–2342 (1991)
55. Van de Walle, C.G., Laks, D.B., Neumark, G.F., Pantelides, S.T.: Phys. Rev. B **47**, 9425–9434 (1993)
56. Yan, Y., Wei, S.-H.: Phys. Status Solidi B **245**, 641–652 (2008)
57. Wei, S.-H.: Comp. Mater. Sci. **30**, 337–348 (2004)
58. Yin, W.-J., Wei, S.-H., Al-Jassim, M.M., Yan, Y.: Appl. Phys. Lett. **99**, 142109 (2011)
59. Du, M.H.: J. Mater. Chem. A **2**, 9091 (2014)
60. Agiorgousis, M.L., Sun, Y.Y., Zeng, H., Zhang, S.: J. Am. Chem. Soc. **136**, 14570–14575 (2014)
61. Chen, S., Walsh, A., Gong, X.G., Wei, S.H.: Adv. Mater. **25**, 1522–1539 (2013)
62. Wang, Q., Shao, Y., Xie, H., Lyu, L., Liu, X., Gao, Y., Huang, J.: Appl. Phys. Lett. **105**, 163508 (2014)
63. Haruyama, J., Sodeyama, K., Han, L., Tateyama, Y.: J. Phys. Chem. Lett. **5**, 2903–2909 (2014)
64. Li, C., Wu, Y., Poplawsky, J., Pennycook, T.J., Paudel, N., Yin, W., Haigh, S.J., Oxley, M.P., Lupini, A.R., Al-Jassim, M., Pennycook, S.J., Yan, Y.: Phys. Rev. Lett. **112**, 156103 (2014)
65. Yin, W.-J., Wu, Y., Noufi, R., Al-Jassim, M., Yan, Y.: Appl. Phys. Lett. **102**, 193905 (2013)
66. Yin, W.-J., Wu, Y., Wei, S.-H., Noufi, R., Al-Jassim, M.M., Yan, Y.: Adv. Energy Mater. **4**, 1300712 (2014)
67. Feng, C., Yin, W.-J., Nie, J., Zu, X., Huda, M.N., Wei, S.-H., Al-Jassim, M.M., Yan, Y.: Solid State Commun. **152**, 1744–1747 (2012)
68. Yan, Y., Jiang, C.S., Noufi, R., Wei, S.H., Moutinho, H.R., Al-Jassim, M.M.: Phys. Rev. Lett. **99**, 235504 (2007)
69. Abou-Ras, D., Schmidt, S.S., Caballero, R., Unold, T., Schock, H.-W., Koch, C.T., Schaffer, B., Schaffer, M., Choi, P.-P., Cojocaru-Mirédin, O.: Adv. Energy Mater. **2**, 992–998 (2012)
70. Abou-Ras, D., Schaffer, B., Schaffer, M., Schmidt, S.S., Caballero, R., Unold, T.: Phys. Rev. Lett. **108**, 075502 (2012)
71. Edri, E., Kirmayer, S., Henning, A., Mukhopadhyay, S., Gartsman, K., Rosenwaks, Y., Hodes, G., Cahen, D.: Nano Lett. **14**, 1000–1004 (2014)
72. Ren, Z., Ng, A., Shen, Q., Gokkaya, H.C., Wang, J., Yang, L., Yiu, W.K., Bai, G., Djurisic, A. B., Leung, W.W., Hao, J., Chan, W.K., Surya, C.: Sci. Rep. **4**, 6752 (2014)
73. Shao, Y., Xiao, Z., Bi, C., Yuan, Y., Huang, J.: Nat. Commun. **5**, 5784 (2014)
74. Filippetti, A., Mattoni, A.: Phys. Rev. B **89**, 125203 (2014)
75. Amat, A., Mosconi, E., Ronca, E., Quarti, C., Umari, P., Nazeeruddin, M.K., Gratzel, M., De Angelis, F.: Nano Lett. **14**, 3608–3616 (2014)

Ionic Conductivity of Organic–Inorganic Perovskites: Relevance for Long-Time and Low Frequency Behavior

Giuliano Gregori, Tae-Youl Yang, Alessandro Senocrate, Michael Grätzel and Joachim Maier

Abstract This chapter is focused on the relevance of the ionic transport in hybrid organic–inorganic perovskites. The occurrence of significant ionic conductivity along with electronic conductivity leads to stoichiometric polarization on current flow. Such a polarization yields a large apparent dielectric constant at low frequencies and a pronounced hysteresis behavior in *i-V* sweep experiments. We describe electrochemical background, precise measurements, and the impact of these phenomena for the photo-perovskites.

1 Introduction

Since the first demonstration of methylammonium lead halides as light-harvesting active material [1], hybrid organic–inorganic halometallate perovskites have been used to develop a new solid-state solar cell device, named perovskite solar cell (PSC), that appeared in 2012 with a power conversion efficiency of 9.7 % [2]. Since then, PSC have made great progress in efficiency, reaching a certified value of 20.1 % in 2015, thanks to improved device fabrication [3–6], materials [7, 8], and cell structures. To account for the key features responsible for such performances,

G. Gregori · T.-Y. Yang · A. Senocrate · J. Maier (✉)
Max Planck Institute for Solid State Research, Stuttgart, Germany
e-mail: s.weiglein@fkf.mpg.de

G. Gregori
e-mail: g.gregori@fkf.mpg.de

T.-Y. Yang
e-mail: t.yang@fkf.mpg.de

A. Senocrate
e-mail: a.senocrate@fkf.mpg.de

A. Senocrate · M. Grätzel
École Polytechnique Fédérale de Lausanne, Lausanne, Switzerland
e-mail: michael.graetzel@epfl.ch

N.-G. Park et al. (eds.), *Organic-Inorganic Halide Perovskite Photovoltaics*,
DOI 10.1007/978-3-319-35114-8_5

optical, dielectric, and charge transport properties as well as mobile defect properties of these compounds have been investigated.

The present chapter focuses on the charge carrier transport properties of hybrid perovskites with emphasis on the significant ionic transport. As presented in the following sections, the ionic disorder can explain in a straightforward way the origin of the anomalous capacitive behavior at long time scale (low frequencies) as well as the hysteresis in current–voltage (*i-V*) sweep experiments [9].

1.1 Capacitive Anomalies in Perovskite Solar Cells

A number of studies on the electrical properties of hybrid halometallate perovskites have revealed high electrical susceptibilities reflected by a high apparent dielectric constant ε_r' at low frequencies [10, 11] and in a hysteric behavior during *i-V* sweeps [12–15].

It is noteworthy that while at high frequencies,ε_r' is typically associated with atomic and electronic polarizabilities, mobile charge carriers being blocked at grain boundaries or electrodes cause stoichiometric polarizations in the low frequency range. In the case of mixed conductors, this blockade leads to a built-up of concentration profiles in the bulk, to which the very low frequency range refer to [16].

In PSC, ε_r' exhibits strikingly high values at low frequencies. Thus, Juarez-Perez et al. [10] measured $\varepsilon_r' \approx 10^3$ (for $\nu < 1$ Hz) on a cell consisting of FTO|TiO_2|$MAPbI_{3-x}Cl_x$|spiro-OMeTAD|Au under dark conditions. This value rose further with increasing light intensity up to $\varepsilon_r' \approx 10^6$ under one-sun illumination.

The origin of these anomalous capacitive phenomena has been long debated and various explanations have been suggested, the most supported hypotheses being ferroelectricity, charge-trapping, or the presence of mobile ionic species. The claim of ferroelectricity is based on the possible alignment of the organic dipole or on lattice polarization [10, 11, 17]. This assertion is supported by current-voltage (*i-V*) sweep curves collected on $CH_3NH_3PbI_3$ single crystals showing a non-Ohmic, hysteretic behavior [18], which seems to resemble a ferroelectric loop. However, such a hysteresis is normally observed at frequencies much lower than those expected for ferroelectricity. Moreover, the claim is also incompatible with the enhanced polarizability under illumination. Additionally, NMR studies show a fully disordered distribution of organic dipoles even at room temperature for Cl-, Br-, and I- based hybrid halide perovskites [19–21]. In addition, the below discussed impedance studies show a rather small bulk dielectric constant of 33 at room temperature. While various contributions referred to a possible ion migration, the detailed measurements of the ionic conductivities, and the quantitative discussion as to the impact of mixed conductivity on low frequency phenomena has only be given in Ref. [9], on which this contribution is largely based.

1.1.1 Hysteresis in *i*-V Sweep Curves

Typically, the efficiency of solar cell devices is evaluated by measuring the current (i) while sweeping an applied voltage (V) across the electrodes (terminals) under a standardized illumination condition (AM 1.5 G, 100 mW cm^2 irradiation). The voltage is scanned at a given rate from the short-circuit condition toward forward bias up to open-circuit voltage and back again. This test is commonly used to provide the steady-state power output of a solar cell. However, in PSC the shape of current–voltage (i-V) curves changes with specific measurement conditions, such as voltage sweep rate, sweep direction, or illumination history.

Nonetheless, in PSC such a hysteretic behavior has been detected even at very low scan rates. Interestingly, the extent of the hysteresis depends also on device architecture, electrode material, composition of hybrid halometallate perovskites, film thickness, and morphology. Generally, perovskite solar cells with mesoporous structure exhibit less hysteresis compared to devices with a thin-film planar structure, and the width of hysteresis depends on the thickness of TiO_2 mesoporous layer [5, 13]. Mitigation of the hysteresis has been achieved for an inverted device structure, in which an n-type fullerene layer was infiltrated in between the perovskite grains [22–24]. A significantly reduced hysteresis was also observed in a composite material of $MAPbI_3$ and phenyl-C_{61}-butyric acid methyl ester (PCBM), where PCBM was homogeneously distributed through grain boundaries of the light-absorbing layer [25]. Finally, perovskite solar cells containing millimeter-sized grains show hysteresis-free i-V curves, despite the planar structure [26].

1.2 Evidences of Ionic Transport

For PSCs, the detailed analysis of the electronic and ionic conductivity together with the quantitative discussion on their relevance for the above-mentioned anomalies has been presented in Ref. [9]. This chapter largely relies on those findings, nonetheless qualitatively ion transport has been referred to in the literature before, which is addressed in the following.

The presence of a perceptible ionic contribution to the overall electrical transport properties of halide perovskites with IV-group B-cations has been reported in a number of studies. Yamada et al. observed halide conductivities in Ge- and Sn-based compounds, such as $CH_3NH_3GeCl_3$, $CsSnI_3$, $CH_3NH_3SnI_3$ [27–30]. Fully inorganic perovskites ($CsPbCl_3$ and $CsPbBr_3$) also exhibited vacancy-mediated halide conductivity at high temperatures ($T > 573$ K) [31]. The conductivity of these compounds was 3×10^{-3} S cm^{-1} at $T \approx 673$ K, with a fraction of ionic conductivity (i.e. ionic transference numbers) exceeding 0.90 and activation energies in the range of 0.25–0.3 eV. It is noteworthy that these values are similar to those obtained for the corresponding binary lead halides ($PbBr_2$, $PbCl_2$) [32, 33].

Dualeh et al. [34] performed impedance spectroscopy analysis on $CH_3NH_3PbI_3$ and showed the presence of a low frequency contribution, which was assigned to the migration of slow charged species. More recently, Xiao et al. [35] reported a significant switching of the photocurrent of PSC depending on the bias, which was ascribed to ionic drifting under the applied electric field. Interestingly, such effect appeared in devices using $MAPbI_3$ as well as $FAPbI_3$, $MAPbBr_3$, and $MAPbI_{3-x}Cl_x$. By using Kelvin probe force microscopy, the formation of a reversible p-i-n junction was observed immediately after poling a device. In particular, the anode became transparent and rich of pinholes due to a loss of perovskite material attributed to the transport of $V_{Pb}^{\bullet\bullet}$ and/or $V_{MA}^{\bullet}$ from the cathode side. Temperature and applied bias, along with film stoichiometry and morphology appeared to greatly affect the poling process. Similar conclusions were drawn from other independent studies, in which the interface charges of a ITO|PEDOT:PSS|$MAPbI_xCl_{3-x}$|PCBM|Al and a ITO|PEDOT:PSS|$MAPbI_3$|MoO_3|Al cell respectively were investigated [15, 36]. Upon a brief application of a bias voltage (few seconds), a reverse current (I_{SC}) was detected under short-circuit conditions, whose magnitude decayed with time. The authors observed that the interface charge (obtained by integrating the reverse current over time) was proportional to the intensity of the applied bias. A similar behavior was recorded also in measurements performed under light. Such findings were interpreted in terms of ionic accumulation at the interfaces. This is in agreement with Chen et al. [37], in which the transient I_{SC} as a function of applied bias in a cp-TiO_2|$MAPbI_3$|Spiro-OMeTAD was studied.

Further evidences of ionic migration were provided by Yuan et al. [38], by employing a number of different techniques such as in situ photothermal-induced resonance (PTIR, IR spectra and AFM maps used simultaneously) as well as Kelvin probe force microscopy (KPFM). Unbiased $MAPbI_3$ showed a uniform distribution of both IR signal (tuned on the deformation of the methyl group) and surface potential in the area between the electrodes. After poling the device, accumulation of MA^+ at the negative electrode was detected, resulting in asymmetric PTIR/KPFM maps. An ion mobility of 1.5×10^{-9} cm^2 V s^{-1} was estimated. By measuring V_{OC} of the cell as a function of poling bias (also at different temperatures) two differently fast contributions could be identified: An initial (low bias) "fast ion" attributed to MA^+ motion (E_A = 0.36 eV) and a subsequent high bias "slow ion." Leijtens et al. [39] also reported a direct observation of polarization (diode-like) behavior in poled $MAPbI_3$ films with gold electrodes, which was assigned to MA^+ transport. Field-dependent formation of AgI on an Ag film separated from the perovskite by an isopropanol drop showed the existence of a polar-solvent-induced iodide motion.

Recently, Bag et al. [40] observed a second semicircle in the low frequency range of the impedance spectra (only present under illumination), which was assigned to semi-infinite ionic diffusion (Warburg-like response). Nonetheless, direct evidences of the moving species were not provided.

1.2.1 Computational Studies on Defects and Transport

It is clear that the presence of such ionic conductivity points toward a significant ionic disorder in these materials. Based on structural observations and by considering both the rapidity of degradation and the volatility of the precursors shown by most hybrid organic–inorganic perovskites, one expects these materials to exhibit large intrinsic defect concentrations. Several computational studies reported low formation energies of point defects, albeit there is scarce agreement on the nature of the dominant ionic defect. Yin et al. [41] performed ab initio DFT calculations (VASP code) on $CH_3NH_3PbI_3$, and obtained defect formation energies for several possible point defects as a function of the chemical potential of the constituents (I and Pb). Specifically, the resulting dominant defects are predicted to be lead vacancies (in I-rich/Pb,-poor conditions) and methylammonium interstitials (in I-poor/Pb-rich conditions) with formation energies of 0.29 eV and 0.20 eV, respectively. Both these defects present energy levels less than 0.05 eV above (below) the valence band top (conduction band bottom), making them extremely shallow trap states. In general, defects with low formation energies are reported to have energy levels close to the valence or conduction band, while higher formation energy defects seem to exhibit energy levels lying deeper within the bandgap. This is in agreement with Buin et al. [42], that concluded that the most common point defects in $CH_3NH_3PbI_3$ ($V_I^{\bullet}, V_{MA}', V_{Pb}'', I_i', MA_i^{\bullet}, Pb_i^{\bullet\bullet}$) present shallow transition states. Similar results were obtained by Agiorgousis et al. [43], with the exception of V_I' and Pb_i'' that were reported to have deep in-gap transition states. Walsh et al. [44] also applied DFT (VASP code) and found remarkably low formation enthalpies for Schottky defects in $CH_3NH_3PbI_3$, with a more favorable partial Schottky reaction leading rather to MAI loss instead of PbI_2 loss (Table 1). Opposite conclusions were, however, drawn by Kim et al. [45], who estimated a more probable formation of PbI_2 vacancies with respect to methylammonium iodide vacancies (Table 1).

It is noteworthy that for such low values of ΔHs (0.08 eV), the concentration of V_{MA}' and $V_I^{\bullet}$ should be extremely high already at room temperature (4 % of the available lattice sites).

Theoretical studies have also allowed for a prediction of the activation energy related to the ionic transport. Table 2 summarizes the values obtained in several contributions. For example, using ab initio DFT (VASP code), Eames et al. [46] concluded that the migration of iodine vacancies is the energetically most favorable one. The claim is supported by photocurrent relaxation time measurements as a

Table 1 Formation enthalpies of Schottky defects in $CH_3NH_3PbI_3$

Defect reaction	ΔH_S (eV)	Reference
$nil \rightleftharpoons V_{MA}' + 3V_I^{\bullet} + V_{Pb}'' + MAPbI_3$	0.14	Walsh et al. [44]
$nil \rightleftharpoons V_{MA}' + V_I^{\bullet} + MAI$	0.08	Walsh et al. [44]
	1.803	Kim et al. [45]
$nil \rightleftharpoons V_{Pb}'' + 2V_I^{\bullet} + PbI_2$	0.22	Walsh et al. [44]
	0.027−0.073	Kim et al. [45]

Table 2 Activation energy for the migration of several point defects in $CH_3NH_3PbI_3$

Defect	E_A (eV)	Reference
$V_I^{\bullet}$	0.58	Eames et al. [46]
	0.08	Azpiroz et al. [48]
	0.32−0.45	Haruyama et al. [47]
I_i'	0.08	Azpiroz et al. [48]
V_{MA}'	0.84	Eames et al. [46]
	0.46	Azpiroz et al. [48]
	0.55−0.89	Haruyama et al. [47]
V_{Pb}''	2.31	Eames et al. [46]
	0.80	Azpiroz et al. [48]

function of temperature (after biasing a device), from which an activation energy of 0.60−0.68 eV was extracted. Haruyama et al. [47] also estimated a more favorable activation energy for $V_I^{\bullet}$ motion, while Azpiroz et al. [48] reported an equally favorable activation energy for $V_I^{\bullet}$ and I_i', albeit much lower than the two previous contributions (Table 1).

1.3 Experimental Elucidation of the Ionic and Electronic Transport Properties

A clear measurement of ionic and electronic conductivities was described in Ref. [9]. High apparent dielectric constants at low frequencies and hysteresis in sweep experiments were shown to be a direct consequence of the mixed conductivity (stoichiometry polarization). The following sections of the chapter are devoted to describing the background of these experiments and their conclusions.

2 Methods: D.C. Polarization and A.C. Impedance Spectroscopy

Before addressing these issues, let us start with general remarks on mixed conductors (ionic and electronic) and their behavior under current. Figure 1a shows the voltage response of a mixed conductor (MC) as a function of time on switching on a constant current (galvanostatic measurement) when the material is contacted by electrodes that are reversible for electrons but not for ions. Note that the behavior on switching off the current after having reached the steady state is symmetrical. Figure 1b displays the corresponding Nyquist plot of the complex impedance. For a more detailed treatment, the reader is referred to the following Refs. [16, 49–52].

At high frequencies or very short polarization times (typically 1 ns or GHz) all carriers (electronic and ionic) contribute. According to the equivalent circuit the

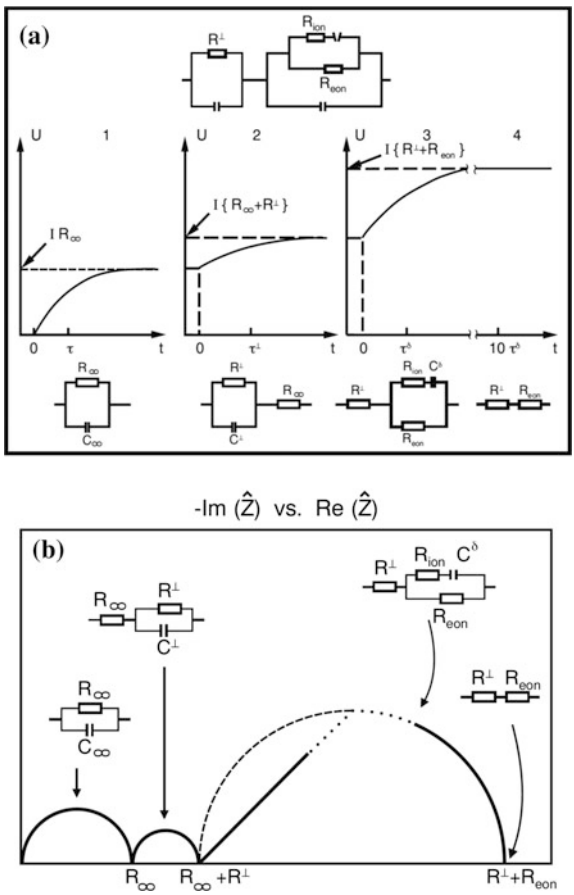

Fig. 1 **a** Voltage response during a galvanostatic experiment in which the mixed conductor is contacted by electrodes that are reversible for electrons but not for ions. **b** Corresponding Nyquist plot of the complex impedance. Reproduced with permission of Springer from [51]

time/frequency behavior is determined by the dielectric constant. At less short times/high frequencies (μs, MHz) interfacial polarization effects are seen corresponding to a charge transfer resistance in parallel with an interface capacitance (e.g. depletion layer). Such interfaces can be electrode contacts or perpendicular grain boundaries. For polycrystalline materials, the individual resistances and inverse capacitances sum, resulting in time/frequency regimes on the order of ms/kHz. At very long times/low frequencies a typical effect of the neighboring phases (electrodes) on the bulk of the sample occurs.

According to Kirchhoff's laws, for the situation under consideration the voltage response to a constant current i is [51]

$$V(t) = iR_{\infty}(1 - e^{-t/\tau_{\infty}}) + iR_{\perp}(1 - e^{-t/\tau_{\perp}}) + iR_{\text{eon}}t_{\text{ion}}(1 - e^{-t/\tau^{\delta}}), \qquad (1)$$

with $t_{\text{ion}} = \frac{R_{\text{eon}}}{R_{\text{eon}} + R_{\text{ion}}}$ being the ionic transference number, while the corresponding complex impedance can be written as

$$\hat{Z} = \frac{R_\infty}{1+\omega^2\tau_\infty^2} + \frac{R_\perp}{1+\omega^2\tau_\perp^2} + \frac{R_{\text{eon}}t_{\text{ion}}}{1+\omega^2(\tau^\delta)^2} - j\omega\left(\frac{\tau_\infty}{1+\omega^2\tau_\infty^2} + \frac{\tau_\perp}{1+\omega^2\tau_\perp^2} + \frac{R_{\text{eon}}t_{\text{ion}}\tau^\delta}{1+\omega^2(\tau^\delta)^2}\right). \quad (2)$$

Equation (1) (and the corresponding part in (2)) neglects modifications in the third term for $\tau_\infty, \tau_\perp \ll t < \tau^\delta$ or $\tau_\infty, \tau_\perp \ll \omega^{-1} < \tau^\delta$. Here, instead of the exponential, a square root behavior, or a Warburg impedance (linear behavior in Fig. 1b corresponding to a transmission line) is realized.

A stoichiometry polarization is observed as a natural consequence of the inability of the electrodes to allow all carriers to pass. It can only be avoided by using special so-called reversible electrodes, such as Ag for silver halides or chalcogenides, being reversible for Ag^+ and e^- or O_2, Pt for oxides that exhibit oxygen ion and electron conductivities.

Usually electrodes block either electrons (Ag|AgI|…) and let through ions (Ag|AgI; O_2,Pt|YSZ|…) or, what is normally the case, block the ions and let through the electrons (such as C|… or Au|…). In such cases, a gradient of the concentration of the blocked carrier is established being compensated by a gradient of the non-blocked species in order to maintain electroneutrality (see Fig. 2).

The polarization experiment is characterized by an exponential behavior at long times and a square root behavior at short times. This corresponds to a Warburg impedance at low frequencies and a semicircular behavior at very low frequencies. (Usually τ^δ is very different from the time constants τ_∞ and $\tau_\perp$ and depends, unlike those, on sample thickness).

Note that for a full description also the space charge polarization has to be considered. In the space charge zone close to the electrode a non-zero charge

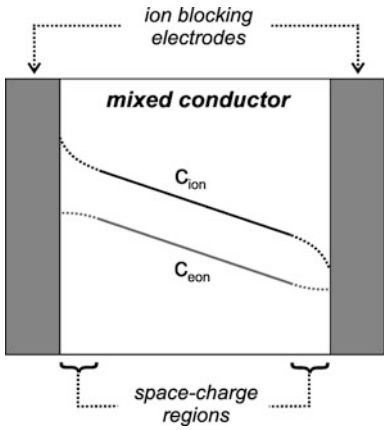

Fig. 2 Schematic representation of the concentration profiles of the mobile charge carriers once the steady-state situation has been reached during a d.c. polarization experiment. Within the space-charge zones, the profiles are affected by the equilibrium potentials. The indices ion and eon refer to the mobile dominant ionic and electronic charge carriers

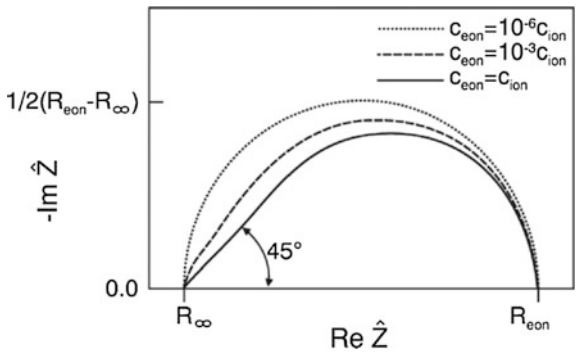

Fig. 3 A.c. impedance spectrum of mixed conductors sandwiched between two ionically blocking electrodes having different concentrations of electronic and ionic charge carriers. The electronic mobility is a factor 10 larger than the ionic one, the ratio between sample length and Debye length L/λ is equal to 10^4 and $z_{ion} = -z_{eon} = 1$. Reproduce from Ref. [53]

density occurs. Such a phenomenon also occurs in the case of pure ionic conductors. The time constant of a space charge polarization is on the order of $\tau_\perp$, quite different from τ^δ [9, 46]. As shown in Fig. 3, the inclusions of space charge polarization modify the shape of the diffusional arc (cf. Figure Fig. 1b) as a function of the ratio between ionic and electronic conductivity.

The central quantity in this context is τ^δ, the time constant of the relaxation process. In terms of chemical resistance R^δ, chemical capacitance C^δ, sample thickness L and chemical diffusion coefficient D^δ, one can formulate [54]

$$\tau^\delta \propto \frac{L^2}{D^\delta} \propto R^\delta C^\delta \tag{3}$$

with

$$R^\delta = R_{ion} + R_{eon} \propto (\sigma_{ion}^{-1} + \sigma_{eon}^{-1}) \tag{4}$$

and

$$\frac{1}{C^\delta} = \frac{d\mu}{dc} \propto \left(\frac{\chi_{ion}}{c_{ion}} + \frac{\chi_{eon}}{c_{eon}}\right). \tag{5}$$

Figure 4 shows two other equivalent representations of the frequency behavior. Figure 4a gives the Gaussian plot for the complex capacitance $\hat{K} = (j\omega\hat{Z})^{-1}$, Fig. 4b shows the frequency dependence of the real K' and imaginary part K'' of $\hat{K}$. Normalization of K' to electrode distance and area gives an apparent dielectric constant, which coincides with the bulk dielectric constant only for $\tau_\infty^{-1} \sim \omega \gg \tau_\perp^{-1}, (\tau^\delta)^{-1}$.

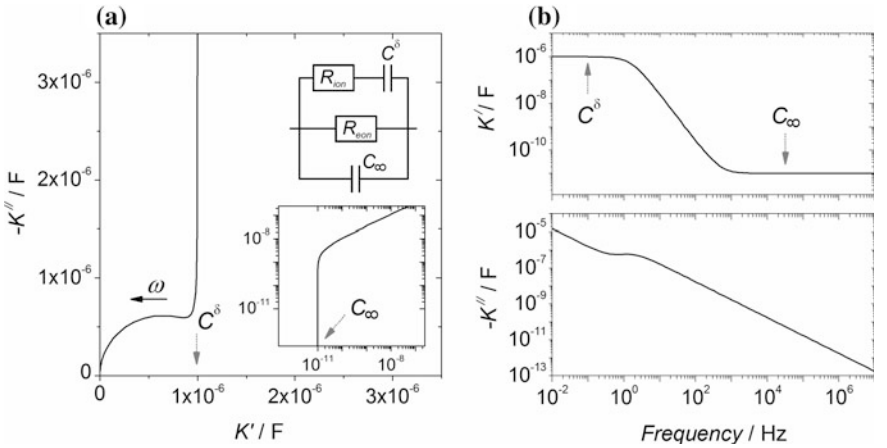

Fig. 4 **a** Gaussian plot of the complex capacitance $\hat{K}$ corresponding to the equivalent circuit with $R_{ion} = 0.1$ MΩ, $R_{eon} = 1$ MΩ, $C^{\delta} = 10^{-6}$ F and $C_{\infty} = 10^{-11}$ F. In the inset a detail (in log-log scale) of the high frequency (ω) range. **b** Bode plots of the real and imaginary parts of the complex capacitance

So far we referred to galvanostatic polarization; the depolarization behavior is analogous [52]. Note that the d.c. polarization/depolarization is the same for a series of such pulses if the time intervals are large enough to allow for equilibration. It is different if triangular sweep experiments are performed. As there is no resting period in between, obviously hysteresis is expected.

Such stoichiometry polarization phenomena are not only responsible for many degradation processes of electroceramics, they can also be applied to separate ionic and electronic contributions.

3 Electrical Transport Measurements on $CH_3NH_3PbI_3$

In the following, a series of independent experiments are discussed which provide clear evidences of the mixed conducting (ionic and electronic) nature of $CH_3NH_3PbI_3$. Note that all the experiments were carefully carried out under argon atmosphere and—if not differently specified—under dark conditions. The ionic as well as electronic transport properties were investigated by carrying out a.c. impedance and d.c. polarization measurements on cold-pressed $CH_3NH_3PbI_3$ pellets, which were prepared as described in [9]. Two graphite pellets have been used as selective electrodes, i.e., electron-conducting and ion-blocking, in the following cell configuration: graphite| $CH_3NH_3PbI_3$|graphite. In order to achieve good electrical contact at the interfaces, graphite and $CH_3NH_3PbI_3$ powders were pressed simultaneously at 400 MPa uniaxially.

3.1 Impedance Spectroscopy

Figure 5 shows typical a.c. impedance spectra acquired from 1 MHz–1 Hz and consisting of a single distorted semicircle. As shown in Fig. 5b, for $\nu > 10^4$ Hz the real part of the complex permittivity ε_r' (which in this frequency range corresponds to the bulk dielectric constant $\varepsilon_{r,\infty}$) is slightly reduced as the temperature increases. In the lower frequency range, however, ε_r' rapidly rises by more than one order of magnitude compared to the bulk situation. Interestingly, at such frequencies, these high values of ε_r' show a different temperature dependence, namely they increase with increasing temperature. Such a behavior resembles what Juarez-Perez et al. observed from $MAPbI_3$ containing solar cells [10].

From the capacitance values, the relative dielectric constant was found to span between 31 and 34. Such a value points toward the observed single semicircle of the impedance spectra (Fig. 5a) to correspond to the bulk properties of the material [55]. The resulting bulk conductivity increases with temperature with an activation energy of 0.43 eV (Fig. 6) in agreement with previous literature [56].

We note that neither the absolute values nor the temperature dependence of the dielectric constant suggest ferroelectricity. This is consistent with previous studies showing the ferroelectric behavior of $CH_3NH_3PbI_3$ to appear only upon the phase transition from a tetragonal to orthorhombic crystal symmetry which occurs below 161 K [19].

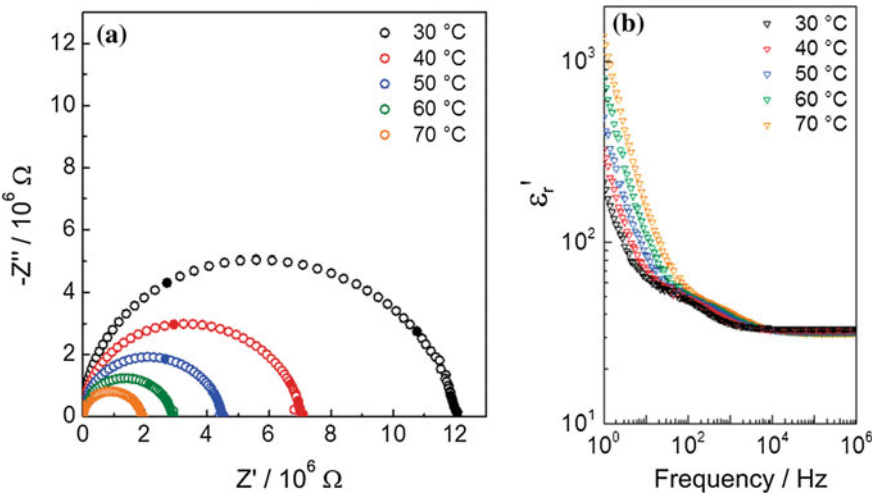

Fig. 5 **a** A.C. impedance spectra acquired from 1 MHz–1 Hz. The *solid symbols* correspond to data collected at 1 kHz and 100 Hz, respectively. **b** The real part of complex permittivity as a function of frequency. Modified from Ref. [9] by permission of John Wiley & Sons, Inc

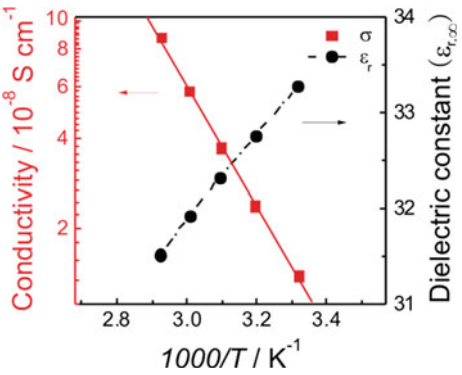

Fig. 6 Temperature dependence of the a.c. conductivity of the bulk relative dielectric constant. Modified from Ref. [9] by permission of John Wiley & Sons, Inc

3.2 *Stoichiometry Polarization*

Galvanostatic d.c. polarization measurements are an effective tool to establish which are the majority mobile charge carrier in a compound. As illustrated in Fig. 7a, the voltage variation on switching a 2 nA d.c. current reveals a clear mixed conducting behavior. In such a situation, with ion-blocking electrodes (graphite), upon switching on the current the voltage instantaneously reaches a finite value V_0 (in this case 25 mV) and then it progressively increases up to the saturation value V_S. Such a transient behavior is typical for stoichiometric polarization, which stems from the graphite electrodes blocking the mobile ions. In this way, an ionic concentration gradient builds up, which is followed by the electronic concentration gradient to satisfy electro-neutrality. The equivalent circuit that can be used to model such a behavior is shown in Fig. 7b.

The instantaneous value V_0 by turning on the current corresponds to the total electrical resistance (12.5 MΩ, which is obtained also from the a.c. impedance measurement) resulting from both the electronic and the ionic transport ($V_0 = i(R_{\text{ion}} \cdot R_{\text{eon}}/(R_{\text{ion}} + R_{\text{eon}}))$.

In the steady state, the electrochemical potential gradient of the ions disappears, and only electrons flow ($i = i_{\text{eon}}$, $i_{\text{ion}} = 0$) with $V_S = iR_{\text{eon}}$. From V_S, the electronic conductivity σ_{eon} follows as 1.90×10^{-9} S cm^{-1} and hence the ionic conductivity as 7.7×10^{-9} S cm^{-1} ($\sigma_{\text{tot}} = \sigma_{\text{eon}} + \sigma_{\text{ion}}$). Quite remarkably, under dark conditions $\sigma_{\text{eon}} < \sigma_{\text{ion}}$.

As demanded for a chemical diffusion, [50, 57] the transient curve fits a $\sqrt{t}$-law for short times (i.e. for $t < \tau^{\delta}$, with τ^{δ} being the polarization time constant), while for longer time ($t > \tau^{\delta}$) it follows an exponential behavior (Fig. 2b,c). Both functionalities are excellently verified with virtually identical τ^{δ} values of 1.6×10^4 s and 2.1×10^4 s, respectively. From τ^{δ}, the chemical diffusion coefficient of the mobile ion ($D^{\delta} = L^2/(\pi^2 \tau^{\delta})$ with L being the sample thickness, i.e., the diffusion length), is found to be as high as 2.4×10^{-8} cm^2 s^{-1}.

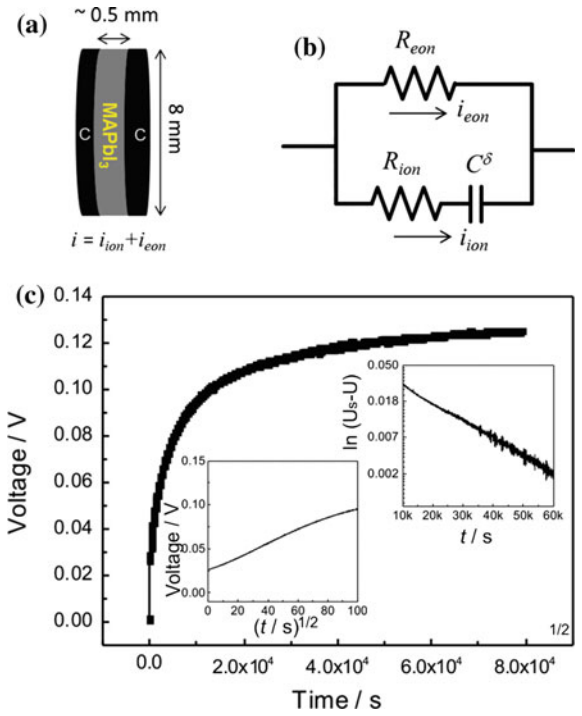

Fig. 7 **a** Galvanostatic d.c. polarization curve for a graphite|$CH_3NH_3PbI_3$|graphite cell measured at 30 °C under Ar-flow and in the dark by applying a current of 2 nA. **b** Voltage versus square root of time for $t < 10^4$ s. **c** Semi-log plot of voltage versus time for $t > 10^4$ s. **d** Equivalent circuit used to model the d.c. polarization (R_{eon}: electronic resistance, R_{ion}, ionic resistance C^{δ}: chemical capacitance) at very long times (modeling of the short range part of the stoichiometric polarization requires a transmission line). Modified from Ref. [9] by permission of John Wiley & Sons, Inc

3.3 Open-Circuit Voltage Measurements

Open-circuit voltage (V_{OC}) measurements are also a useful tool for promptly verifying the nature of the majority mobile charge carriers. For this purpose, a symmetrical cell consisting of graphite|$MAPbI_3$|graphite was first exposed to moderate electrolyzing conditions (d.c. current of 300 nA applied for about 1 h) and the voltage was measured. As depicted in Fig. 8, on switching off the d.c. current, V_{OC} immediately dropped to 788 mV and then slowly diminished with time owing to the finite electronic transport. This behavior is typical of a mixed conductor.

More detailed V_{OC} measurements were carried out by using the asymmetrical galvanic cells (Pb,PbI_2)|$MAPbI_3$|(Cu,CuI) and (Pb,PbI_2)|$MAPbI_3$|(Ag,AgI). The different metal/metal iodide mixtures result in different iodine chemical potentials and thus in the formation of chemical potential gradients in the organic–inorganic perovskite. Since for this kind of tests a rather high exchange rate is required, V_{OC} was measured at 400 K after a pretreatment at 453 K. As it can be recognized in

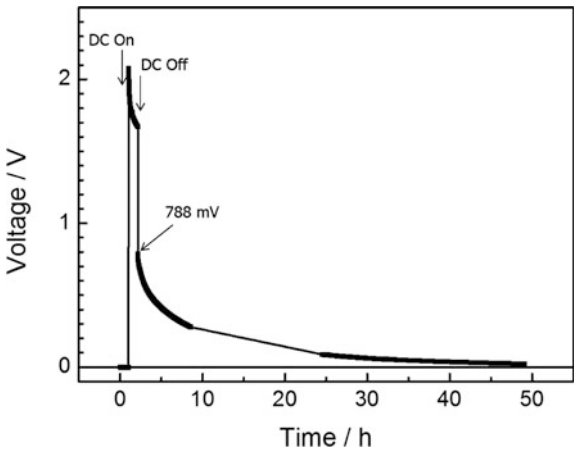

Fig. 8 V_{OC} measurement of the symmetric cell graphite|$CH_3NH_3PbI_3$|graphite. Electrolysis was achieved by applying a d.c. current of 300 nA for about 1 h. After turning off the current the V_{OC} is 788 mV. The V_{OC} then slowly decays to zero in approximately 50 h. Modified from Ref. [9] by permission of John Wiley & Sons, Inc

Fig. 9, V_{OC} values at electrochemical equilibrium were 90 and 122 mV, respectively. Note that the electromotive force of such a cell is given by

$$V_{OC} = \bar{t}_{\text{ion}} \Delta\mu_I / 2F \tag{6}$$

with $\bar{t}_{\text{ion}}$ being the average ionic transference number of the sample exposed to the iodine chemical potential

$$\Delta\mu_I = \frac{1}{2}\Delta\mu_{I_2} = \frac{1}{2} RT\Delta \ln P_{I_2}, \tag{7}$$

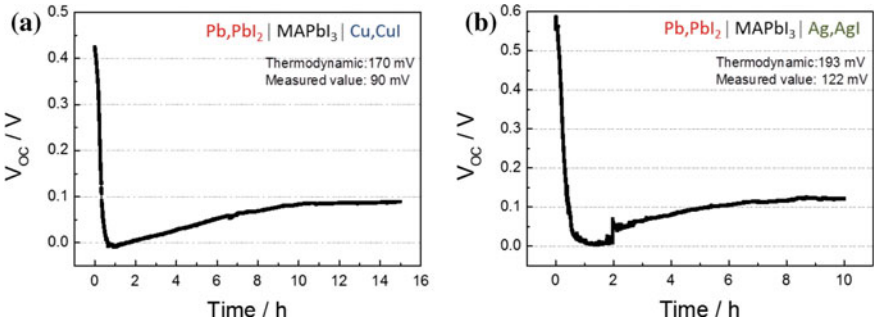

Fig. 9 Open circuit voltage (V_{OC}) measurement on two different galvanic cells: **a** (Pb,PbI_2)|$MAPbI_3$|(Ag,AgI) and **b** (Pb,PbI_2)|$MAPbI_3$|(Cu,CuI). The measurements were performed until the cells reached the equilibrium at 400 K in argon atmosphere. The initial part of the $V_{OC}(t)$ curve is influenced by sample conditioning. Modified from Ref. [9] by permission of John Wiley & Sons, Inc

Table 3 Thermodynamic data of PbI_2, CuI, and AgI used for the chemical potential gradient experiments

	$\Delta_f G$/ kJ mol^{-1}	$\Delta_f H$/ kJ mol^{-1}
PbI_2	−172.3	−191.9
CuI	−69.7	−75.5
AgI	−67.5	−69.3

where P_{I_2} is iodine partial pressure. In particular $V_{OC} = 0$ for a pure electronic conductor.

The ionic transference numbers obtained by comparing these values with the theoretical ones (170 and 193 mV, which were calculated from $\{\Delta_f G(PbI_2 - 2\Delta_f G(AgI \text{ or } CuI)\}/2F$, with $\Delta_f G$ being the molar Gibbs energy of formation and F the Faraday constant—see Table 3) amount to 0.53 and 0.63 at 400 K. These are consistent with the ionic transference number of 0.5 obtained from polarization data acquired at the same temperature. Note that the transference number is an average over the difference of the iodine potential. For a material with predominant ionic disorder, the electronic (but not the ionic) conductivity varies with P_{I_2}.

3.4 *Identification of the Species Determining the Ionic Conductivity*

In order to identify the majority mobile ionic species, a solid-state electrochemical cell (Pb|$MAPbI_3$|AgI|Ag) consisting of one electronic (Pb) and one ionic electrode (AgI|Ag) was assembled as shown in Fig. 10a. Since such a configuration leads to chemical changes on current flow, the various interfaces (labeled A, B, C, and D in Figs. 10 and 11) were investigated after having applied a d.c. current of 10 nA for a week under argon atmosphere and dark conditions (with the Pb electrode taken as positive and the Ag electrode as negative pole). It is worth noting that if lead ions were the majority mobile ions in $MAPbI_3$, then a PbI_2 layer would grow at the interface C. On the contrary, if iodine anions were the fastest moving species, then PbI_2 would be formed at the interface B. In the case of methylammonium being the predominant migrating defect, MAI and PbI_2 would be present at interface C and B, respectively.

A careful inspection of the various interfaces at the conclusion of the test revealed that only interface B exhibited a modified surface compared to the pristine situation (cf. interface A and B in Fig. 10b). SEM analysis (Fig. 10c, d and e) allowed for the detection of irregular conglomerates on the surface of B. X-ray diffraction (XRD) patterns acquired from the surface were characterized by the presence of peaks (at $2\theta = 11.4°$ and 12.4°, respectively), which belong to the PbI_2 phase. This was also confirmed by energy dispersive X-ray spectroscopy (EDX), whose spectra showed the presence of Pb and I signals (Fig. 10e) with an atomic I-to-Pb ratio equal to 2.2.

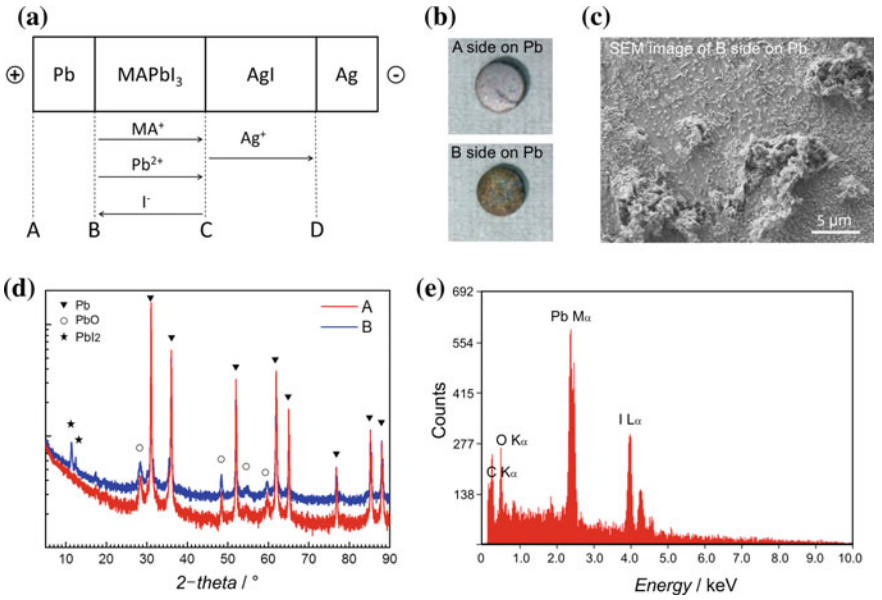

Fig. 10 **a** Schematic cartoon showing the flow directions of the mobile charged ionic species in a Pb|$MAPbI_3$|AgI|Ag cell under electrical bias. **b** Images for surface A and B and **c** scanning electron microscope (SEM) image of surface B on the Pb pellet. **d** XRD patterns of surfaces A and B of the Pb disk after applying a d.c current of 10 nA for a week. **e** EDX spectrum for surface B of Pb. Reproduced from Ref. [9] by permission of John Wiley & Sons, Inc

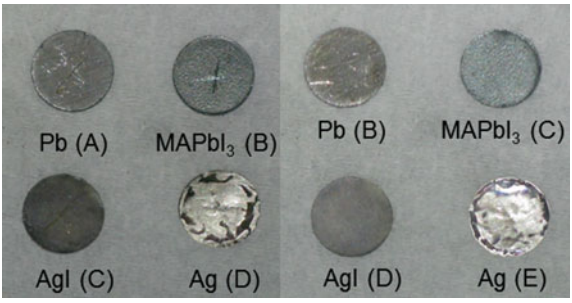

Fig. 11 Optical images of each pellets after the control experiment, during which the cell assembled as in Fig. 10a was aged at 50 °C for a week in Ar atmosphere with no current applied. All surfaces remained unaffected. Reproduced from Ref. [9] by permission of John Wiley & Sons, Inc

Such findings indicate that iodine is the conductivity-determining ion inducing the occurrence of the stoichiometric polarization during galvanostatic measurements, in which electronically conducting electrodes (graphite) are used. A control experiment was performed, in which the same cell configuration under the same ambient conditions but without applying any current was tested. As illustrated in

Fig. 11, none of all interfaces displayed any modification at the end of the test. This confirms that the formation of the PbI_2 phase at the B interface is due only to the iodine migration and not to a local chemical instability.

4 Chemical Diffusion Coefficient and Chemical Capacitance

The conductivity data presented in Sect. 3—according to which the electronic and ionic conductivities are comparable—point toward $CH_3NH_3PbI_3$ to be characterized by a predominant ionic disorder. This results straightforwardly if one considers typical mobility values of the charge carriers present in $MAPbI_3$. Since in the solid state the mobility of ionic defects at room temperature is hardly greater than 10^{-2} cm^2 V^{-1} s^{-1} and the mobility of the electrons/holes is reported to be more than 3 orders of magnitude larger [18, 58], the concentration of the mobile ionic species must exceed the concentration of electronic defects by several orders of magnitude. Not only would the total conductivity be electronic without trapping, but it would be orders of magnitude larger than observed.

The origin of such an extended ionic disorder is most likely related to the formation of Schottky defects due to a deficiency of (MA)I or PbI_2 [44, 46], while pronounced Frenkel disorder is less probable, as indicated also by theoretical studies [41, 59]. In addition to native defects (e.g. $V'_{MA}, V''_{Pb}, V_I, I'_i$), one should not exclude the possibility of having foreign defects such as oxygen replacing iodine O'_I and thus acting as an acceptor.

In the presence of a large ionic disorder and at low temperatures trapping of electronic charge carriers by the ionic defects is expected. For example, the concentration of holes would be kept small by trapping at iodine interstitials [60, 61]. In other cases, trapping by negatively charged cation vacancies or acceptors is possible. Such details are however not decisive for the following considerations, in which we refer to the most mobile iodine defect ($V_I^{\bullet}$ or I'_i) as "ion" and the most mobile electronic defect ($h^{\bullet}$) as "eon."

In the light of these considerations, it is worth considering the chemical diffusion coefficient D^{δ}, which is generally expressed as [62]

$$D^{\delta} = \frac{\sigma_{\text{eon}}}{\sigma_{\text{ion}} + \sigma_{\text{eon}}} D_{\text{ion}} \chi_{\text{ion}} + \frac{\sigma_{\text{ion}}}{\sigma_{\text{ion}} + \sigma_{\text{eon}}} D_{\text{eon}} \chi_{\text{eon}}, \tag{8}$$

where χ_{ion} and χ_{eon} denote the differential trapping factors of ion and electronic carriers, respectively, and D_{ion} and D_{eon} are the individual diffusivities being proportional to the respective mobility. As D_{eon} is usually much larger than D_{ion} and

the ionic conductivity exceed the electronic conductivity, Eq. (8) can be simplified to

$$D^{\delta} = D_{\mathrm{eon}} \mathcal{X}_{\mathrm{eon}}. \tag{9}$$

We note that without trapping, i.e., for $\chi_{\mathrm{eon}} = 1$, expression (9) would deviate from the experimental data by several orders of magnitude, as D_{eon} is expected to be on the order of 10^{-1} cm^2 V^{-1}s^{-1} [18], and D^{δ} is instead on the order of 10^{-8} cm^2 V^{-1} s^{-1}. Hence, strong trapping plays a key role in this material [63].

At this point, two different situations need to be considered.

(i). First, we assume a situation where iodine vacancies $V_I^{\bullet}$ are the majority iodine defects compensated by either intrinsic V'_{MA}, V''_{Pb}, or extrinsic O'_I, the holes are largely trapped (by $[T'] = [V''_{Pb}]$ or $[O'_I]$, etc.). As long as $[T'] \gg [T^x] \gg [h^{\bullet}]$ we arrive at

$$D^{\delta} = D_{\mathrm{eon}}[h^{\bullet}]/[\mathrm{T}^{\mathrm{x}}]. \tag{10}$$

This follows from

$$D^{\delta} = \frac{1}{F^2} \frac{\sigma_{\mathrm{eon}} \sigma_{\mathrm{ion}}}{\sigma} \frac{\mathrm{d}\mu_{\mathrm{I}}}{\mathrm{d}c_{\mathrm{I}}} \tag{11}$$

and

$$\frac{\mathrm{d}\mu_{\mathrm{I}}}{\mathrm{d}c_{\mathrm{I}}} = \left(-\frac{\mathrm{d}\mu_{\mathrm{V}_{\mathrm{I}}^{\bullet}}}{\mathrm{d}c_{\mathrm{I}}} - \frac{\mathrm{d}\mu_{\mathrm{n}}}{\mathrm{d}c_{\mathrm{I}}} \right) = \left(-\frac{\mathrm{d}\mu_{\mathrm{V}_{\mathrm{I}}^{\bullet}}}{\mathrm{d}c_{\mathrm{I}}} + \frac{\mathrm{d}\mu_{\mathrm{T}^{\mathrm{x}}} - \mathrm{d}\mu_{\mathrm{T}^{\prime}}}{\mathrm{d}c_{\mathrm{I}}} \right) \tag{12}$$

As the charge in iodine stoichiometry is realized by changes in $[V_I^{\bullet}]$ and hole concentration, the latter being given by variation in the trap budget, we have

$$\mathrm{d}c_{\mathrm{I}} = -\mathrm{d}c_{\mathrm{V}_{\mathrm{I}}^{\bullet}} = \mathrm{d}[\mathrm{T}^{x}] = -\mathrm{d}[\mathrm{T}^{\prime}], \tag{13}$$

and it follows

$$D^{\delta} = \frac{RT}{F^2} \frac{\sigma_{\mathrm{eon}} \sigma_{\mathrm{ion}}}{\sigma} \left(\frac{1}{c_{\mathrm{V}_{\mathrm{I}}^{\bullet}}} + \frac{1}{[\mathrm{T}^{\prime}]} + \frac{1}{[\mathrm{T}^{\mathrm{x}}]} \right) \tag{14}$$

and hence Eq. (10), with $[T^x]$ being the concentration of trapped holes (occupied traps). This directly explains the magnitude of D^{δ} by the small fraction of free holes.

(ii). If iodine interstitials I_i' are the majority iodine defects, then the situation is determined by trapping between I_i' and holes, if most of the holes are trapped viz. in the form of $\mathrm{I}_{\mathrm{i}}^{\mathrm{x}}$, $\mathrm{d}c_{\mathrm{I}} = \mathrm{d}c_{\mathrm{I}^{\mathrm{x}}}$. Since $\mathrm{d}\mu_{\mathrm{I}} = \mathrm{d}\mu_{\mathrm{I}^{\mathrm{x}}}$, we directly get to

$$\frac{d\mu_I}{dc_I} = \frac{d\mu_{I^x}}{dc_{I^x}} = \frac{RT}{c_{I^x}} \tag{15}$$

and hence Eq. (10), whereby now $[T^x]$ corresponds to the stoichiometry δ, as T^x corresponds to a majority carrier [63]

$$D^\delta = D_h[h^\bullet]/\delta. \tag{16}$$

where $\delta \simeq [I_i^x] = [T^x]$.

4.1 Stoichiometric Polarization and Large Apparent Dielectric Constant

Starting from these results, let us now examine the chemical capacitance associated with the stoichiometric polarization observed in Fig. 7. As the polarization time constant can be written as the product of the chemical resistance and the chemical capacitance

$$\tau^\delta = R^\delta C^\delta, \tag{17}$$

we can express C^δ in terms of the ambipolar conductivity (which is given by $\sigma^\delta = \sigma_{ion}\sigma_{eon}/\sigma_{ion} + \sigma_{eon}$), geometrical factors ($A$ is the cross-sectional area and L the thickness of the sample), and chemical diffusivity, namely Eq. (10) or (16) [64]:

$$C^\delta = \tau^\delta \sigma^\delta \frac{A}{L} = \frac{AL}{\pi^2}\frac{\sigma^\delta}{D^\delta} \propto AL[T^x]. \tag{18}$$

From this expression, it is evident that C^δ linearly depends on the concentration of trapped holes (occupied traps). If we insert in Eq. (18), the values obtained from the measurement of Fig. 7 and the geometry of the sample (diameter 8 mm and thickness 0.5 mm), we obtain $C^\delta = 2.3 \times 10^{-4}$ F yielding an apparent dielectric constant $\varepsilon_r' = 3.6 \times 10^8$. This clearly indicates that the large value of ε_r' in the low frequency range can be explained by the large chemical capacitance associated to the stoichiometric polarization even before the occurrence of a Warburg behavior.

This finding can be further validated if we now consider more closely the simplified equivalent circuit of Fig. 7b. The corresponding complex impedance resulting from Eq. (2) is

$$\hat{Z} = \left(\frac{R_{\text{eon}} t_{\text{ion}}}{1 + \omega^2 (\tau^{\delta})^2} + \frac{R}{1 + \omega^2 \tau^2} \right) + j \left(\frac{\omega R_{\text{eon}} t_{\text{ion}} \tau^{\delta}}{1 + \omega^2 (\tau^{\delta})^2} - \frac{\omega R \tau}{1 + \omega^2 \tau^2} \right) \tag{19}$$

with

$$R = \frac{R_{\text{ion}} \cdot R_{\text{eon}}}{R_{\text{ion}} + R_{\text{eon}}}. \tag{20}$$

Correspondingly, the real part of complex capacitance $\hat{K} = (j\varpi\hat{Z})^{-1}$ reads

$$\begin{aligned} K' &= \frac{-\omega Z''}{\omega^2 (Z')^2 + \omega^2 (Z'')^2} = \frac{(R_{\text{ion}} + R_{\text{eon}})^2 C^{\delta}}{(R_{\text{ion}} + R_{\text{eon}})^2 + (R_{\text{ion}})^2 \omega^2 (R_{\text{ion}} + R_{\text{eon}})^2 (C^{\delta})^2} \\ &= \frac{C^{\delta}}{1 + (R_{\text{ion}} \omega C^{\delta})^2}. \end{aligned} \tag{21}$$

From this and since

$$\varepsilon_r' = \frac{K' L}{\varepsilon_0 A}, \tag{22}$$

it is straightforward to realize that K' (and thus ε_r') is frequency-dependent with the ionic resistance R_{ion} and the chemical capacitance C^{δ} only. Quite remarkably, the electronic transport R_{eon} comes into play only in the $\sqrt{t}$-law range (Warburg regime). In the case of a Warburg situation (transmission line model)

$$Z_w' = \frac{R}{1 + \omega^2 \tau^2} + \frac{\sqrt{2} R_{\text{eon}} t_{\text{ion}}}{\pi \sqrt{\omega \tau^{\delta}}}; \; Z_w'' = -\frac{\omega R \tau}{1 + \omega^2 \tau^2} - \frac{\sqrt{2} R_{\text{eon}} t_{\text{ion}}}{\pi \sqrt{\omega \tau^{\delta}}}, \tag{23}$$

follow [51], from which

$$K_w' = \frac{\frac{\sqrt{2} R_{\text{eon}} t_{\text{ion}}}{\pi \sqrt{\omega \tau^{\delta}}} + \frac{\omega R \tau}{1 + \omega^2 \tau^2}}{\omega \cdot \left(\frac{\sqrt{2} R_{\text{eon}} t_{\text{ion}}}{\pi \sqrt{\omega \tau^{\delta}}} + \frac{\omega R \tau}{1 + \omega^2 \tau^2} \right)^2 + \omega \cdot \left(\frac{\sqrt{2} R_{\text{eon}} t_{\text{ion}}}{\pi \sqrt{\omega \tau^{\delta}}} + \frac{R}{1 + \omega^2 \tau^2} \right)^2}. \tag{24}$$

results, in which the dependence of K_w' on R_{eon} is evident.

All the considerations made above hold under dark conditions; it is now worth discussing how illumination can affect the apparent dielectric constant ε_r'. Since under light the concentration of the electronic mobile carriers is enhanced, we expect an increase of the concentration of occupied traps, which according to Eq. (18) lead to a larger C^{δ} and thus a larger K'. This is exactly what has been observed experimentally as shown in Fig. 12.

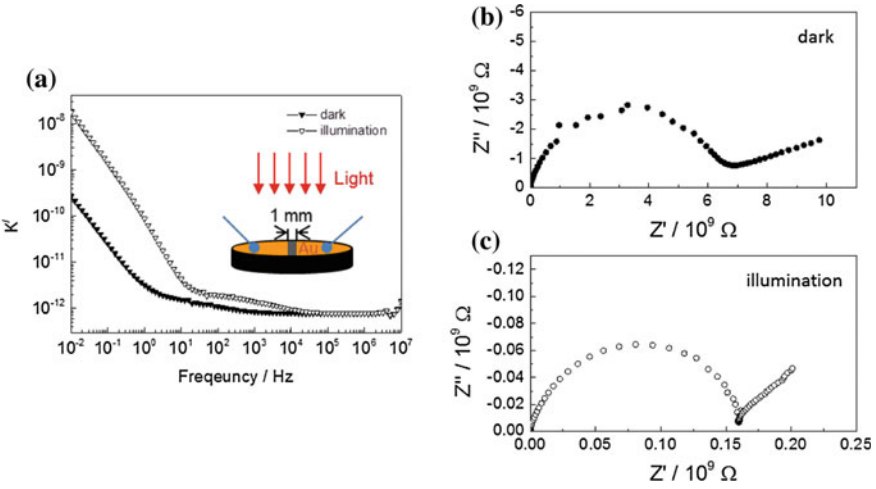

Fig. 12 A.c. impedance measurements were performed on $CH_3NH_3PbI_3$ pellets with gold electrodes on one surface under **b** the dark conditions and **c** during illumination using a halogen lamp (150 W). **a** The real part of complex capacitance as a function of frequency is improved under illumination compared to dark conditions. Modified from Ref. [9] by permission of John Wiley & Sons, Inc

4.2 *Hysteresis During i-V Sweep*

The further important consequence of the observed stoichiometric polarization has to do with the occurrence of the hysteretic behavior during *i-V* sweep experiments. As it is illustrated in Fig. 13, as prepared $MAPbI_3$ samples (which exhibit the characteristic polarization due to the presence of ionic and electronic mobile species) show a non-ohmic behavior and a clear voltage hysteresis when the d.c. current is swept between −20 and 20 nA in Fig. 13b.

The same experiment was repeated on samples exposed to an atmosphere of high iodine partial pressure. Here the concentration of the p-type carriers is enhanced (with the concentration of the ionic carriers staying relatively constant) making the sample predominantly electronic conducting (Fig. 13c). In this case, no voltage hysteresis was detected during the current sweep in Fig. 13d. Analogous results were obtained from samples exposed to oxygen, in which the incorporation of O_I' is expected to be compensated by holes. This is consistent with the disappearance of hysteresis for samples that have seen ambient conditions at elevated temperature [26].

As one can notice in Fig. 13b, the extent of the hysteresis (ΔV for $i = 0$) is affected by the sweep rate α (note that $i = \alpha t$). Clearly, the key aspect is how the time t_u, at which the current is reversed, compares to characteristic polarization time constant τ^δ of the sample (cf. also Fig. 14e). For $\tau^\delta \ll t_u$, we note that the higher the sweep rate α, the larger the hysteresis. On the other hand, if $\tau^\delta > t_u$ the

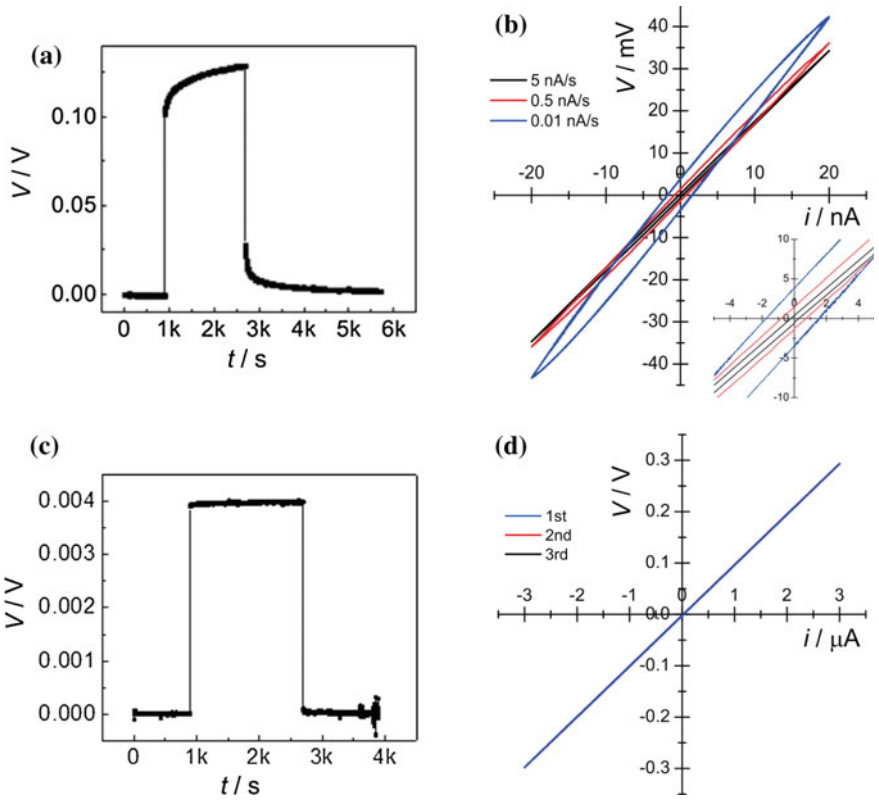

Fig. 13 **a** Galvanostatic measurement in Ar atmosphere showing mixed (ionic and electronic) conduction and **b** its current-voltage curve for $MAPbI_3$. Hysteresis loops upon the current sweep between −20 and 20 nA with varying the scan rate, which clearly illustrates the changes of the open-circuit voltage when the current sweep rate is changed. **c** Galvanostatic measurement in iodine vapor flowing with Ar carrier gas (Note that this sample exhibits only electronic conduction.) and **d** a corresponding current-voltage curve. Modified from Ref. [9] by permission of John Wiley & Sons, Inc

hysteresis narrows with increasing α. Here, only the last case was observed as $\tau^{\delta} \sim 10^4$ s and $t_u = 4$ s (2000 s) for $\alpha = 5$ nA s^{-1} (0.01 nA s^{-1}). In the literature instead, various behaviors during *i-V* sweeps were reported for PSCs [5, 13] and as shown in Sect. 4.3 we ascribe this to different values of τ^{δ}.

It is worth noting that on illumination the hysteresis becomes less pronounced if $\tau^{\delta} \ll t_u$ and disappears for $\sigma_{eon} \gg \sigma_{ion}$ (note that the width of the hysteresis is proportional to $R_{eon}C^{\delta}$ and hence to $1/c_{eon}$).

Finally, let us extend the discussion of the above phenomena to the case of thin films or perovskite infiltrated in mesoporous titania, which are the typical configurations used in real devices [5]. In such cases, both the chemical capacitance and the relaxation time τ^{δ} are reduced, since both K' as well as τ^{δ} are proportional to L^2

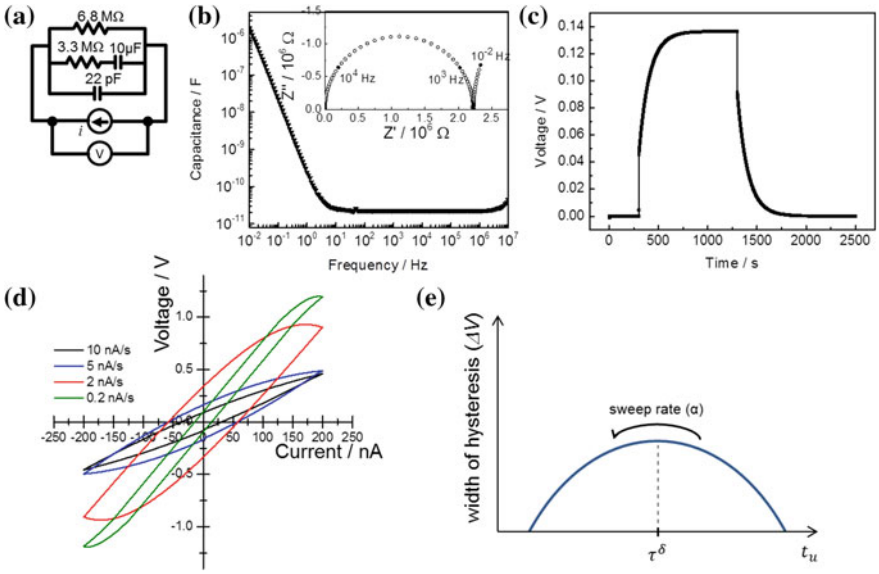

Fig. 14 **a** The electrical circuit mimicking the polarization behavior is composed of a resistor (6.8 MΩ) corresponding to R_{eon}, the series of a resistor (3.3 MΩ) and a capacitor (10 μF) corresponding to R_{ion} and C^{δ}, and a capacitor (22 pF) corresponding to C_{bulk}, respectively. **b** The real part of the complex capacitance as a function of the frequency obtained from the circuit considered here. In the inset, the Nyquist plot of the complex impedance acquired from 10 to 10 MHz. **c** D.c. polarization curve obtained from a galvanostatic measurement of the model circuit shown in (**a**) by applying a current of 2 nA. **d** *i-V* hysteresis by the current sweep between 200 and −200 nA obtained by applying various current sweep rates. **e** Schematic diagram showing the relationship between the width of hysteresis and current sweep rate. Modified from Ref. [9] by permission of John Wiley & Sons, Inc

(L being the thickness of the sample, i.e. the diffusion length). For this reason, a quicker polarization and lower apparent ε_r' are expected at low frequencies.

Interestingly, on illumination τ^{δ} decreases further (because R^{δ} decreases), while —as shown before— ε_r' increases. This explains why the hysteresis in the solar cell narrows with decreasing α (corresponding to $\tau^{\delta} \ll t_u$). As the width of the hysteresis is proportional to $R_{eon}^2 C^{\delta}$ and hence to L^3, for thinner films a decreased hysteresis is expected.

4.3 *Electrical Circuit Mimicking the Material Behavior*

In order to further validate the considerations made above, the electrical transport properties of $MAPbI_3$ are mimicked in the following by an electrical circuit as the

one depicted in Fig. 14a [52]. The resistors and capacitors utilized here were chosen so as to allow for a reasonable polarization time constant τ^{δ} on the order of 100 s.

We note that the behavior of the real part of the complex capacitance as a function of the frequency (Fig. 14b)

$$K' = \frac{C^{\delta}}{1 + \left(R_{\text{ion}} \varpi C^{\delta}\right)^2}$$

together with the characteristic polarization (Fig. 14c) compares well with the behavior of the experimental data as shown in Fig. 12.

By varying the sweep rate, both extremely fast as well as extremely slow current scan rate leads to a linear voltage response. Conversely, intermediate scan rates yield a hysteretic voltage loop, whose width (ΔV at $t = 0$) depends on how the specific rate compares with the circuit time constant τ^{δ} (cf. Fig. 14d). As shown below, we note that if $\tau^{\delta} > t_u$ then slower scan rates result in wider hysteresis, while if $\tau^{\delta} < t_u$ the extent of the hysteresis decreases with decreasing scan rate (cf. Fig. 14e).

These observations can be formalized by considering the voltage response $V(t)$ of the circuit on a current ramp $i = \alpha t$, with α and t being current rate and time, respectively. For simplicity, we assume here $\tau^{\delta} \ll t_u$, with t_u being the reversal time (at which the maximum current is reached).

$$\begin{aligned} V(t) &= R_{\text{eon}} i_{\text{eon}} = R_{\text{eon}}(i - i_{\text{ion}}) = R_{\text{eon}}(\alpha t - i_{\text{ion}}) \\ &= R_{\text{ion}} i_{\text{ion}} + \frac{Q}{C^{\delta}}, \end{aligned} \tag{25}$$

with Q being the charge. By differentiating with respect to time, one obtains

$$(R_{\text{eon}} + R_{\text{ion}}) \frac{di_{\text{ion}}}{dt} + \frac{i_{\text{ion}}}{C^{\delta}} - \alpha R_{\text{eon}} = 0 \tag{26}$$

and hence

$$i_{\text{ion}}(t) = \alpha R_{\text{eon}} C^{\delta} \left(1 - e^{-t/\tau^{\delta}}\right) \tag{27}$$

$$V(t) = R_{\text{eon}} i_{\text{eon}} = \alpha R_{\text{eon}} \left[t - \alpha R_{\text{eon}} C^{\delta} \left(1 - e^{-t/\tau^{\delta}}\right)\right]. \tag{28}$$

Once the sweep reversal time has been reached ($t = t_u$, corresponding to the maximum current), i is decreased according to $i = \alpha(t_u - t')$, where $t' = t - t_u$. Under the assumption of $t_u \gg \tau^{\delta}$, for $t' = 0$ both

$$i_{ion}(0) = \alpha R_{eon} C^{\delta} \tag{29}$$

$$V(0) = i_{\mathrm{eon}}(0) R_{\mathrm{eon}} = \alpha R_{\mathrm{eon}} t_u - \alpha R_{\mathrm{eon}}^2 C^{\delta} \tag{30}$$

result and

$$\frac{Q}{C^{\delta}} + R_{\mathrm{ion}} i_{\mathrm{ion}} = R_{\mathrm{eon}} i_{\mathrm{eon}} = R_{\mathrm{eon}}(i - i_{\mathrm{eon}}) = R_{\mathrm{eon}}[\alpha(t - t') - i_{\mathrm{ion}}] \tag{31}$$

leading to

$$i_{\mathrm{ion}} = \alpha R_{\mathrm{eon}} C^{\delta} \left(2e^{-t'/\tau^{\delta}} - 1\right) \tag{32}$$

$$V = i_{\mathrm{eon}} R_{\mathrm{eon}} = \alpha R_{\mathrm{eon}} \left[t_u - t' - R_{\mathrm{eon}} C^{\delta} \left(2e^{-t'/\tau^{\delta}} - 1\right)\right]. \tag{33}$$

It is noteworthy that for $t' = t_u$ (and thus $t = 0$)

$$V(t' = t_u) = \alpha R_{\mathrm{eon}}^2 C^{\delta}, \tag{34}$$

meaning that during the backward sweep the voltage assumes a finite value for $t = 0$ (cf. Fig. 14d), which can be treated as a measure of the width of the hysteresis. The above equations lead to a further interesting result, namely that if $R_{\mathrm{eon}} > R_{\mathrm{ion}}$ the voltage exhibits a maximum during the backward sweep.

5 Concluding Remarks

The results presented in this chapter clearly demonstrate a remarkable ionic conductivity in hybrid organic–inorganic perovskites stemming from an extensive and predominant ionic disorder. Polarization phenomena observed at low frequency are an inevitable consequence, if electrodes are used that block ion transfer. Notably, the large concentration of point defects results in a considerable trapping of the electronic charge carriers, which affects the electric transport properties of such materials. Starting from these experimental evidences, a systematic study of the defect chemistry of these compounds (dependence of charge carrier concentration on exact composition, i.e. in particular as a function of I_2 partial pressure, as well as on temperature and doping) is required, in order to identify the key parameters necessary to further adjust the electronic properties of such promising perovskites. It will be interesting in the future to investigate whether or not ionically induced phenomena affect also the efficiency of solar cells.

References

1. Kojima, A., Teshima, K., Shirai, Y., Miyasaka, T.: Organometal halide perovskites as visible-light sensitizers for photovoltaic cells. J. Am. Chem. Soc. **131**(17), 6050–6051 (2009). doi:10.1021/ja809598r
2. Kim, H.S., Lee, C.R., Im, J.H., Lee, K.B., Moehl, T., Marchioro, A., Moon, S.J., Humphry-Baker, R., Yum, J.H., Moser, J.E., Grätzel, M., Park, N.G.: Lead iodide perovskite sensitized all-solid-state submicron thin film mesoscopic solar cell with efficiency exceeding 9 %. Sci. Rep. **2**, 591 (2012). doi:10.1038/srep00591
3. Burschka, J., Pellet, N., Moon, S.-J., Humphry-Baker, R., Gao, P., Nazeeruddin, M.K., Gratzel, M.: Sequential deposition as a route to high-performance perovskite-sensitized solar cells. Nature **499**(7458), 316–319 (2013). doi:10.1038/nature12340
4. Chen, Q., Zhou, H., Hong, Z., Luo, S., Duan, H.-S., Wang, H.-H., Liu, Y., Li, G., Yang, Y.: Planar heterojunction perovskite solar cells via vapor assisted solution process. J. Am. Chem. Soc. **136**(2), 622–625 (2013). doi:10.1021/ja411509g
5. Jeon, N.J., Noh, J.H., Kim, Y.C., Yang, W.S., Ryu, S., Seok, S.I.: Solvent engineering for high-performance inorganic–organic hybrid perovskite solar cells. Nat. Mater. **13**(9), 897–903 (2014). doi:10.1038/nmat4014
6. Liu, M., Johnston, M.B., Snaith, H.J.: Efficient planar heterojunction perovskite solar cells by vapour deposition. Nature **501**(7467), 395–398 (2013). doi:10.1038/nature12509
7. Lee, M.M., Teuscher, J., Miyasaka, T.: Efficient hybrid solar cells based on meso-superstructured organometal halide perovskites. Science **643** (2012). doi:10.1126/science.1228604
8. Pellet, N., Gao, P., Gregori, G., Yang, T.-Y., Nazeeruddin, M.K., Maier, J., Grätzel, M.: Mixed-Organic-Cation perovskite photovoltaics for enhanced solar-light harvesting. Angew. Chem. Int. Ed. **53**(12), 3151–3157 (2014). doi:10.1002/anie.201309361
9. Yang, T.-Y., Gregori, G., Pellet, N., Grätzel, M., Maier, J.: The Significance of ion conduction in a hybrid organic-inorganic lead-iodide-based perovskite photosensitizer. Angew. Chem. Int. Ed. **54**(27), 7905–7910 (2015). doi:10.1002/anie.201500014
10. Juarez-Perez, E.J., Sanchez, R.S., Badia, L., Garcia-Belmonte, G., Kang, Y.S., Mora-Sero, I., Bisquert, J.: Photoinduced giant dielectric constant in lead halide perovskite solar cells. J. Phys. Chem. Lett. **5**(13), 2390–2394 (2014). doi:10.1021/jz5011169
11. Sanchez, R.S., Gonzalez-Pedro, V., Lee, J.-W., Park, N.-G., Kang, Y.S., Mora-Sero, I., Bisquert, J.: Slow dynamic processes in lead halide perovskite solar cells. characteristic times and hysteresis. J. Phys. Chem. Lett. **5**(13), 2357–2363 (2014). doi:10.1021/jz5011187
12. Reenen, S.V., Kemerink, M., Snaith, H.J.: Modeling anomalous hysteresis in perovskite solar cells. J. Phys. Chem. Lett. **6**, 3808–3814 (2015). doi:10.1021/acs.jpclett.5b01645
13. Snaith, H.J., Abate, A., Ball, J.M., Eperon, G.E., Leijtens, T., Noel, N.K., Stranks, S.D., Wang, J.T.W., Wojciechowski, K., Zhang, W.: Anomalous hysteresis in perovskite solar cells. J. Phys. Chem. Lett. **5**(9), 1511–1515 (2014). doi:10.1021/jz500113x
14. Unger, E.L., Hoke, E.T., Bailie, C.D., Nguyen, W.H., Bowring, A.R., Heumuller, T., Christoforo, M.G., McGehee, M.D.: Hysteresis and transient behavior in current-voltage measurements of hybrid-perovskite absorber solar cells. Energy Environ. Sci. **7**, 3690–3698 (2014). doi:10.1039/C4EE02465F
15. Zhang, Y., Liu, M., Eperon, G.E., Leijtens, T.C., McMeekin, D., Saliba, M., Zhang, W., de Bastiani, M., Petrozza, A., Herz, L.M., Johnston, M.B., Lin, H., Snaith, H.J.: Charge selective contacts, mobile ions and anomalous hysteresis in organic–inorganic perovskite solar cells. Mater. Horiz. **2**, 315–322 (2015). doi:10.1039/C4MH00238E
16. Hebb, M.H.: Electrical conductivity of silver sulfide. J. Chem. Phys. **20**(1), 185–190 (1952). doi:10.1063/1.1700165
17. Frost, J.M., Butler, K.T., Brivio, F., Hendon, C.H., van Schilfgaarde, M., Walsh, A.: Atomistic origins of high-performance in hybrid halide perovskite solar cells. Nano Lett. **14**(5), 2584–2590 (2014). doi:10.1021/nl500390f

18. Stoumpos, C.C., Malliakas, C.D., Kanatzidis, M.G.: Semiconducting tin and lead iodide perovskites with organic cations: phase transitions, high mobilities, and near-infrared photoluminescent properties. Inorg. Chem. **52**(15), 9019–9038 (2013). doi:10.1021/ic401215x
19. Onoda-Yamamuro, N., Matsuo, T., Suga, H.: Dielectric study of CH3NH3PbX3 (X = Cl, Br, I). J. Phys. Chem. Solids **53**(7), 935–939 (1992). doi:10.1016/0022-3697(92)90121-S
20. Poglitsch, A., Weber, D.: Dynamic disorder in methylammoniumtrihalogenoplumbates (II) observed by millimeter-wave spectroscopy. J. Chem. Phys. **87**(11), 6373–6378 (1987). doi:10.1063/1.453467
21. Wasylishen, R.E., Knop, O., Macdonald, J.B.: Cation rotation in methylammonium lead halides. Solid State Commun. **56**(7), 581–582 (1985). doi:10.1016/0038-1098(85)90959-7
22. Shao, Y., Xiao, Z., Bi, C., Yuan, Y., Huang, J.: Origin and elimination of photocurrent hysteresis by fullerene passivation in CH3NH3PbI3 planar heterojunction solar cells. Nat. Commun. **5**, 5784 (2014). doi:10.1038/ncomms6784
23. Xiao, Z., Bi, C., Shao, Y., Dong, Q., Wang, Q., Yuan, Y., Wang, C., Gao, Y., Huang, J.: Efficient, high yield perovskite photovoltaic devices grown by interdiffusion of solution-processed precursor stacking layers. Energy Environ. Sci. **7**(8), 2619–2623 (2014). doi:10.1039/C4EE01138D
24. You, J., Yang, Y., Hong, Z., Song, T.-B., Meng, L., Liu, Y., Jiang, C., Zhou, H., Chang, W.-H., Li, G., Yang, Y.: Moisture assisted perovskite film growth for high performance solar cells. Appl. Phys. Lett. **105**(18), 183902 (2014). doi:10.1063/1.4901510
25. Xu, J., Buin, A., Ip, A.H., Li, W., Voznyy, O., Comin, R., Yuan, M., Jeon, S., Ning, Z., McDowell, J.J., Kanjanaboos, P., Sun, J.-P., Lan, X., Quan, L.N., Kim, D.H., Hill, I.G., Maksymovych, P., Sargent, E.H.: Perovskite-fullerene hybrid materials suppress hysteresis in planar diodes. Nat. Communi. **6** (2015). doi:10.1038/ncomms8081
26. Nie, W., Tsai, H., Asadpour, R., Blancon, J.C., Neukirch, A.J., Gupta, G., Crochet, J.J., Chhowalla, M., Tretiak, S., Alam, M.A., Wang, H.L., Mohite, A.D.: High-efficiency solution-processed perovskite solar cells with millimeter-scale grains. Science **347**(6221), 522–525 (2015). doi:10.1126/science.aaa0472
27. Yamada, K., Isobe, K., Okuda, T., Furukawa, Y.: Successive Phase Transitions and High Ionic Conductivity of Trichlorogermanate(II) Salts as Studied by 35Cl NQR and Powder X-Ray Diffraction. Z. Naturforsch. A J. Phys. Sci. **49**(1–2), 258–266 (1994). doi:10.1515/zna-1994-1-238
28. Yamada, K., Isobe, K., Tsuyama, E., Okuda, T., Furukawa, Y.: Chloride ion conductor CH3NH3GeCl3 studied by Rietveld analysis of X-ray diffraction and 35Cl NMR. Solid State Ionics **79**, 152–157 (1995). doi:10.1016/0167-2738(95)00055-B
29. Yamada, K., Kuranaga, Y., Ueda, K., Goto, S.: Phase transition and electric conductivity of ASnCl3 (A = Cs and CH3NH3). Bull. Chem. Soc. Japan **71**, 127-127 (1998). doi:10.1246/bcsj.71.127
30. Yamada, K., Matsui, T., Tsuritani, T., Okuda, T., Ichiba, S.: 127I-NQR, 119 Sn Mössbauer effect, and electrical conductivity of MSnI3 (M = K, NH4, Rb, Cs, and CH3NH3). Z. Naturforsch. A **45**(3–4), 307–312 (1990). doi:10.1515/zna-1990-3-416
31. Mizusaki, J., Arai, K., Fueki, K.: Ionic conduction of the perovskite-type halides. Solid State Ionics **11**, 203–211 (1983). doi:10.1016/0167-2738(83)90025-5
32. Hoshino, H., Yamazaki, M., Nakamura, Y., Shimoji, M.: Ionic conductivity of lead chloride crystals. J. Phys. Soc. Jpn. **26**(6), 1422–1426 (1969). doi:10.1143/JPSJ.26.1422
33. Hoshino, H., Yokose, S., Shimoji, M.: Ionic conductivity of lead bromide crystals. J. Solid State Chem. **7**(1), 1–6 (1973). doi:10.1016/0022-4596(73)90113-8
34. Dualeh, A., Moehl, T., Tétreault, N., Teuscher, J., Gao, P., Nazeeruddin, M.K., Grätzel, M.: Impedance spectroscopic analysis of lead iodide perovskite-sensitized solid-state solar cells. ACS Nano **8**(1), 362–373 (2013). doi:10.1021/nn404323g
35. Xiao, Z., Yuan, Y., Shao, Y., Wang, Q., Dong, Q., Bi, C., Sharma, P., Gruverman, A., Huang, J.: Giant switchable photovoltaic effect in organometal trihalide perovskite devices. Nat. Mater. **14**, 193–198 (2014). doi:10.1038/nmat4150

36. Zhao, Y., Liang, C., Zhang, H.M., Li, D., Tian, D., Li, G., Jing, X., Zhang, W., Xiao, W., Liu, Q., Zhang, F., He, Z.: Anomalously large interface charge in polarity-switchable photovoltaic devices: an indication of mobile ions in organic-inorganic halide perovskites. Energy Environ. Sci. **8**, 1256–1260 (2015). doi:10.1039/C4EE04064C
37. Chen, B., Yang, M., Zheng, X., Wu, C., Li, W., Yan, Y., Bisquert, J., Garcia-Belmonte, G., Zhu, K., Priya, S.: Impact of capacitive effect and ion migration on the hysteretic behavior of perovskite solar cells. J. Phys. Chem. Lett. **6**(23), 4693–4700 (2015). doi:10.1021/acs.jpclett.5b02229
38. Yuan, Y., Chae, J., Shao, Y., Wang, Q., Xiao, Z., Centrone, A., Huang, J.: Photovoltaic switching mechanism in lateral structure hybrid perovskite solar cells. Adv. Energy Mater. (JUNE), n/a-n/a (2015). doi:10.1002/aenm.201500615
39. Leijtens, T., Hoke, E.T., Grancini, G., Slotcavage, D.J., Eperon, G.E., Ball, J.M., De Bastiani, M., Bowring, A.R., Martino, N., Wojciechowski, K., McGehee, M.D., Snaith, H.J., Petrozza, A.: Mapping electric field-induced switchable poling and structural degradation in hybrid lead halide perovskite thin films. Adv. Energy Mater. **5**, 1500962 (2015). doi:10.1002/aenm.201500962
40. Bag, M., Renna, L.a., Adhikari, R., Karak, S., Liu, F., Lahti, P.M., Russell, T.P., Tuominen, M.T., Venkataraman, D.: Kinetics of ion transport in perovskite active layers and its implications for active layer stability. J. Am. Chem. Soc. **137**(40), 13130–13137 (2015). doi:10.1021/jacs.5b08535
41. Yin, W.-J., Shi, T., Yan, Y.: Unusual defect physics in CH3NH3PbI3 perovskite solar cell absorber. Appl. Phys. Lett. **104**(6), 063903 (2014). doi:10.1063/1.4864778
42. Buin, A., Pietsch, P., Voznyy, O., Comin, R.: Materials processing routes to trap-free halide perovskites. Nano Lett. **14**(11), 6281–6286 (2014). doi:10.1021/nl502612m
43. Agiorgousis, M.L., Sun, Y.-Y., Zeng, H., Zhang, S.: Strong Covalency-induced recombination centers in perovskite solar cell material CH3NH3PbI3. J. Am. Chem. Soc. **136**(41), 14570–14575 (2014). doi:10.1021/ja5079305
44. Walsh, A., Scanlon, D.O., Chen, S., Gong, X.G., Wei, S.-H.: Self-Regulation mechanism for charged point defects in hybrid halide perovskites. Angew. Chem. Int. Ed. **54**(6), 1791–1794 (2015). doi:10.1002/anie.201409740
45. Kim, J., Lee, S.-H., Lee, J.H., Hong, K.-H.: The role of intrinsic defects in methylammonium lead iodide perovskite. J. Phys. Chem. Lett. **5**(8), 1312–1317 (2014). doi:10.1021/jz500370k
46. Eames, C., Frost, J.M., Barnes, P.R.F., Oregan, B.C., Walsh, A., Islam, M.S.: Ionic transport in hybrid lead iodide perovskite solar cells. Nat Commun. **6** (2015). doi:10.1038/ncomms8497
47. Haruyama, J., Sodeyama, K., Han, L., Tateyama, Y.: First-principles study of ion diffusion in perovskite solar cell sensitizers. J. Am. Chem. Soc. **137**, 10048–10051 (2015). doi:10.1021/jacs.5b03615
48. Azpiroz, J.M., Mosconi, E., Bisquert, J., De Angelis, F.: Defect migration in methylammonium lead iodide and its role in perovskite solar cell operation. Energy Environ. Sci. **8**(7), 2118–2127 (2015). doi:10.1039/C5EE01265A
49. Yokota, I.: On the electrical conductivity of cuprous sulfide: a diffusion theory. J. Phys. Soc. Jpn. **8**(5), 595–602 (1953). doi:10.1143/JPSJ.8.595
50. Yokota, I.: On the theory of mixed conduction with special reference to conduction in silver sulfide group semiconductors. J. Phys. Soc. Jpn. **16**(11), 2213–2223 (1961). doi:10.1143/JPSJ.16.2213
51. Maier, J.: Solid state electrochemistry ii: devices and techniques. In: Vayenas, C., White, R.E., Gambpa-Aldeco, M.E. (eds.) Modern aspects of electrochemistry, vol. 41. pp. 1−128. Springer, New York (2007)
52. Maier, J.: Evaluation of electrochemical methods in solid state research and their generalization for defects with variable charges. Z. Phys. Chem. Neue Fol. **140**, 191–215 (1984). doi:10.1524/zpch.1984.140.2.191
53. Jamnik, J., Maier, J., Pejovnik, S.: A powerful electrical network model for the impedance of mixed conductors. Electrochim. Acta **44**(24), 4139–4145 (1999). doi:10.1016/S0013-4686(99)00128-0

54. Jamnik, J., Maier, J.: Generalised equivalent circuits for mass and charge transport: chemical capacitance and its implications. Phys. Chem. Chem. Phys. **3**(9), 1668–1678 (2001). doi:10.1039/B100180I
55. Brivio, F., Walker, A.B., Walsh, A.: Structural and electronic properties of hybrid perovskites for high-efficiency thin-film photovoltaics from first-principles. APL Mater. **1**(4), 042111 (2013). doi:10.1063/1.4824147
56. Knop, O., Wasylishen, R.E., White, M.A., Cameron, T.S.: Oort, M.J.v.: Alkylammonium lead halides. Part 2. CH3NH3PbX3 (X = Cl, Br, I) perovskites: cuboctahedral halide cages with isotropic cation reorientation. Can. J. Chem. **68**(3), 412–422 (1990). doi:10.1139/v90-063
57. Maier, J.: Physical chemistry of ionic materials. WILEY, Chichester (2004)
58. Mitzi, D.B.: Templating and structural engineering in organic-inorganic perovskites. J. Chem. Soc. Dalton Trans. (1), 1−12 (2001). doi:10.1039/B007070J
59. Du, M.H.: Efficient carrier transport in halide perovskites: theoretical perspectives. J. Mater. Chem. A **2**(24), 9091–9098 (2014). doi:10.1039/C4TA01198H
60. Duan, H.S., Zhou, H., Chen, Q., Sun, P., Luo, S., Song, T.B., Bob, B., Yang, Y.: The identification and characterization of defect states in hybrid organic-inorganic perovskite photovoltaics. Phys. Chem. Chem. Phys. **17**(1), 112–116 (2015). doi:10.1039/c4cp04479g
61. Samiee, M., Konduri, S., Ganapathy, B., Kottokkaran, R., Abbas, H.A., Kitahara, A., Joshi, P., Zhang, L., Noack, M., Dalal, V.: Defect density and dielectric constant in perovskite solar cells. Appl. Phys. Lett. **105**(15), 153502 (2014). doi:10.1063/1.4897329
62. Maier, J.: Mass transport in the presence of internal defect reactions—concept of conservative ensembles: i, chemical diffusion in pure compounds. J. Am. Ceram. Soc. **76**(5), 1212–1217 (1993). doi:10.1111/j.1151-2916.1993.tb03743.x
63. Maier, J., Amin, R.: Defect chemistry of LiFePO4. J. Electrochem. Soc. **155**(4), A339–A344 (2008). doi:10.1149/1.2839626
64. Maier, J.: Electrochemical investigation methods of ionic transport properties in solids. Solid State Phenom. **39**(40), 35–60 (1994). doi:10.4028/www.scientific.net/SSP.39-40.35

Ion Migration in Hybrid Perovskite Solar Cells

Yongbo Yuan, Qi Wang and Jinsong Huang

1 Introduction

In organometal trihalide perovskite (OTP) solid films, charged ions are another type of species in addition to charge carriers that are mobile under applied electrical field. The ion migration phenomenon in halide-based perovskite materials has been known for more than 30 years [1]. Nevertheless, the corresponding ion migration in OTPs did not draw considerable attention until the broad observation of current-voltage (*I-V*) hysteresis problem in OTP solar cells. At 2013 MRS fall meeting, Hoke et al. [2] and Snaith et al. [3] first reported their observations of anomalous *I-V* hysteresis behavior (i.e., the *I-V* curves do not overlap while varying the voltage sweeping directions and speeds) in mesoporous structure OTP solar cells (Fig. 1a). The *I-V* hysteresis problem introduced a new challenge in the device efficiency characterization, and also raised concerns of long-term stability of the perovskite solar cells. Therefore, the understanding of its origins and the elimination of the *I-V* hysteresis have become an emerging problem before the practical application of OTP solar cells can be considered. In order to explain the origins of the *I-V* hysteresis, three mechanisms have been proposed by Snaith, i.e., charge trapping effect, ferroelectricity effect, and ion migration effect [2, 3]. In 2014, Xiao et al. first reported the giant switchable photovoltaic effect in OTP solar cells with a planar heterojunction structure and symmetric electrode, in which the direction of photocurrent and photovoltage were completely flipped by changing the voltage sweeping direction (Fig. 1b) [4]. In addition, the surface morphology and material

Y. Yuan · Q. Wang · J. Huang (✉)
Department of Mechanical and Materials Engineering,
University of Nebraska-Lincoln, Lincoln, NE 68588, USA
e-mail: jhuang2@unl.edu

Y. Yuan
Hunan Key Laboratory of Super-microstructure and Ultrafast Process,
School of Physics and Electronics, Central South University, 410083 Hunan, PR China

N.-G. Park et al. (eds.), *Organic-Inorganic Halide Perovskite Photovoltaics*,
DOI 10.1007/978-3-319-35114-8_6

composition in that lateral structure device changed significantly after extended electric poling. This discovery provided strong and solid evidences for the presence of electric field-induced ion migration in OTP materials. ($MAPbI_3$). The OTP materials were then known as both semiconductors and ionic conductors, i.e., the measured current in methylammonium (MA) lead triiodide ($MAPbI_3$) film is a mixture of charge carrier flow and ion flow (Fig. 1c, the dark current peak around 30 s is caused by ion migration at room temperature during the poling process). Similar to other ionic conductions, the ion migration in OTPs-based solar cells can generate a Warburg component in the low frequency part of its impedance spectroscope (Fig. 1d) [5]. The local excess ions were demonstrated to chemically dope OTP films, on the grounds of the surface work function changes in electrically poled perovskite films as indicated by Kevin probe force microscopy (KPFM) [4]. As a consequence, controlling the ion migration direction become a feasible way to form switchable *p-i-n* junctions in pristine OTP films with relative small bias (e.g., close to open-circuit voltage of the perovskite solar cells, V_{OC}, Fig. 1e). These discoveries indicate that the ion migration may play an important role in the *I-V* hysteresis. Moreover, ion migration was found to be general and intrinsic in OTP materials, because similar switchable photovoltaic effects have been observed in solar cells with different structures (e.g., vertical and lateral structures), different hybrid perovskite materials (e.g., $MAPbI_3$, methylammonium lead bromide ($MAPbBr_3$), and formamidinium lead triodides ($FAPbI_3$)), and in the devices with different electrode materials (e.g., gold (Au), platinum, nickel, gallium, and carbon). Later, Unger et al. [2] and Tress et al. [6] supported the ion migration explanation in their publication although no direct evidence was shown.

Up to now, ion migration has received broad attention due to its significant impacts on OTP solar cells [7]. In addition to the *I-V* hysteresis and switchable photovoltaic effect, ion migration might be the origin or important contributing factor of many other anomalous phenomena observed in OTP films and device, such as the diminish of transistor behavior at room temperature [8], giant dielectric constant at low frequency [9, 10], light-induced phase separation [11], light-induced self-poling effect (LISP) [12], and the reversible structural conversion between $MAPbI_3$ and lead iodide (PbI_2) under electrical field [13]. A comprehensive understanding about the ion migration in OTP materials is thus highly desired.

In this chapter, we introduce the current experimental and theoretical understanding of ion migration behaviors in hybrid perovskite solar cells and discuss its impacts on the device efficiency and stability. Section 2 gives a brief overview of the general understanding of ion migration in solid materials. In Sect. 3, we review the recent advances in the studies of ion migration in OTP solar cells from both theoretical and experimental aspects. In Sect. 4, we discuss the impacts of the ion migration on the performance of perovskite solar cells. Finally, in Sect. 5 we introduce the emerging efforts about suppressing ion migration in perovskite films.

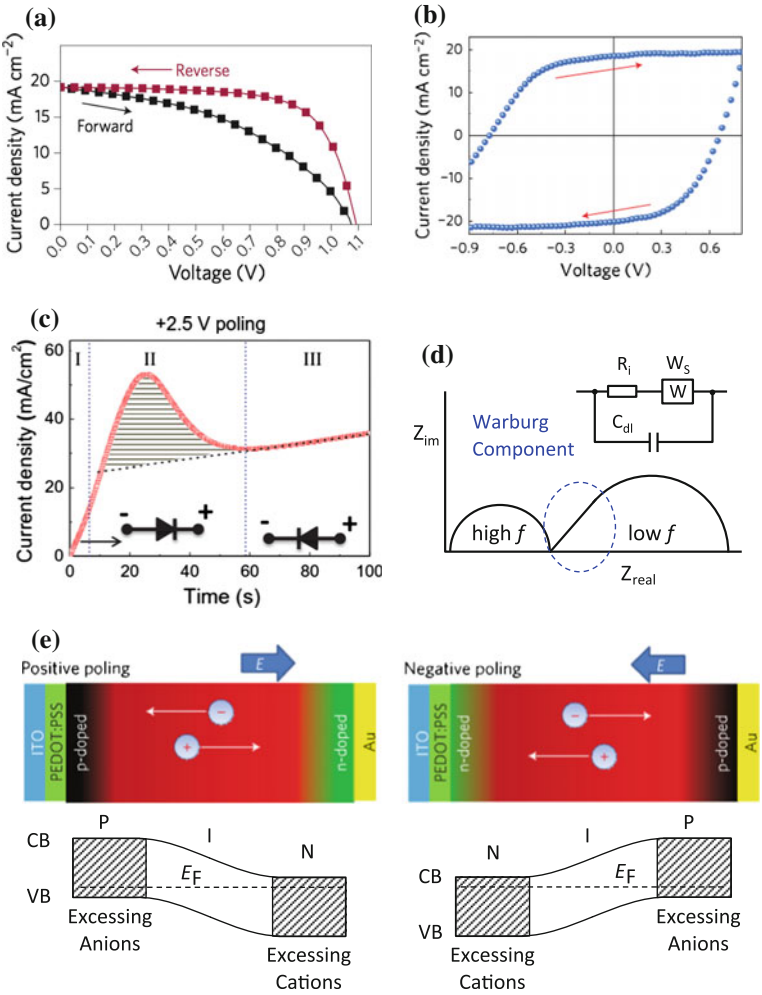

Fig. 1 Typical *I-V* curves of OTP solar cells with nonsymmetrical electrodes (**a**, reproduced from Ref. [48] with permission from Nature Publishing Group) and symmetrical electrodes (**b**); **c** Dark current of OTP solar cells with symmetrical electrodes during electrical poling, which consists of both charge carrier conduction and ion conduction. **d** Typical Nyquist plot for mixed conductor system including ion migration process featured as a linear portion in the low frequency regime (Warburg component). The equivalent circuit for the ion conduction is shown as inset, where W_s is the Warburg component, R_i is the resistance for ion migration, and C_i is the double layer capacitance formed by the accumulation of ions around electrode. **e** Schematics of ion migration directions in OTP solar cells during positive and negative poling and the formation of p-type and n-type doping region in pristine $MAPbI_3$ film due to excess ion, respectively. **b**, **e** reproduced from Ref. [4] with permission from Nature Publishing Group

2 Ion Migrations in Solid State Materials

In solid state materials, bulk ion migrations are usually mediated by defects such as Schottky defects (Fig. 2a), Frenkel defects (Fig. 2b) or impurities. The Schottky defects are sole lattice vacancies or stoichiometric vacancies' pairs which provide vacancies available for ion migration; The Frenkel defects are lattice vacancies together with their corresponding interstitial ions in the crystal lattice. The concentration of thermally excited defects (n) in a crystal with lattice sites of N and possible interstitial sites of N' can be described as $n = \sqrt{NN'}e^{-E_I/2k_BT}$, where k_BT is the thermal energy with k_B and T to be the Boltzmann constant and temperature, respectively, and E_I is the formation energy of interstitial ions.

The capability for ions to migration (i.e., migration rate, r_m) is mainly determined by their activation energies (E_A): $r_m \propto \exp(-\frac{E_A}{k_BT})$. The concentration of mobile ions (N_i) can be determined either by temperature independent defects, such as extrinsic defects of impurities or no-stoichiometric compound, or temperature-dependent defects, such as thermal-excited point defects with formation energy of E_D (intrinsic defects), i.e., $N_i \propto \exp(-\frac{E_D}{2k_BT})$. The conductivity by ion migration (σ_i) can hence described as $\sigma_i \propto \exp(-\frac{E_A}{k_BT})\exp(-\frac{E_D}{2k_BT})$ for the intrinsic case, or $\sigma_i \propto \exp(-\frac{E_A}{k_BT})$ for the extrinsic case. Usually, the value of the E_A (extrinsic defects region), or $E_A + E_D/2$ (intrinsic defects region) can be extracted from the slope of the $\ln\sigma_i$-$1/T$ curves (Fig. 2c). Sometimes, the shape of $\ln\sigma_i$-$1/T$ curve might be more complex due to crystal phase transition or/and the formation of defect clusters, among many other possible reasons.

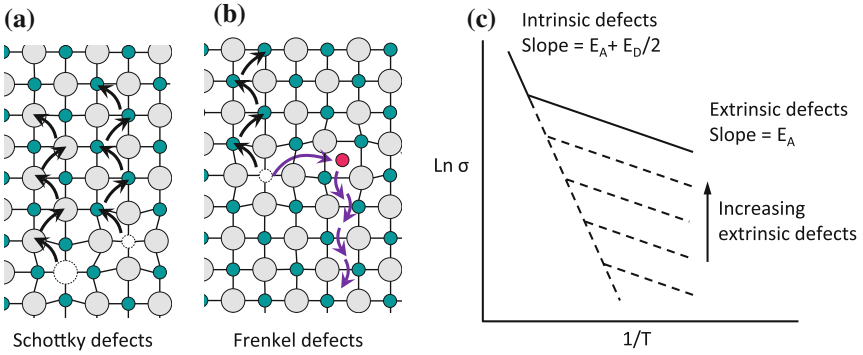

Fig. 2 Illustration of **a** Schottky defects **b** Frankel defects in crystals and the related ion migrations. **c** Typical $\ln\sigma$-$1/T$ curves for ion conduction in solid with different amount of extrinsic defects, where E_A is the activation energy for ion migration, E_D is the formation energy for thermal-excited point defects. **a, b** reproduced from Ref. [7] with permission from American Chemical Society

For materials with multiple ion species, the dominating mobile ions are those with lowest activation energy. The E_A for each kind of ion is determined by the faced energy barrier when ions jump through their minimum energy path (MEP), respectively. Generally, there are several major facts that affecting the E_A value, such as crystal structure, ion radius, and the valence state of the ions.

The structure of the crystal lattice plays an extremely important role in the formation of ionic migration channel. The sub-lattice of each component determines the possible interstices for the ion to reside at. For example, in the α-phase AgI (a typical superionic compounds), the I^- has a body-centered cubic (bcc) arrangement and the mobile ions are Ag^+. In each unit cell, there are 6 octahedral (*oct*), 12 tetrahedral (*tet*), and 24 trigonal (*trig*) interstices as the available sites (42 in all) for the Ag^+ ions to reside at [14]. The migration of Ag^+ from one unit cell to another unit cell can be via the *tet*, *oct,* and *trig* sites, respectively [14, 15]. Besides, the crystal structure determines the distance between the nearest neighbor ions, which impacts a lot on the E_A of ion migration. For example, in some inorganic ionic conductors with ABO_3 perovskite-type structure, such as $La_{1-x}Sr_xBO_{3-\delta}$ family (B can be Mg, Ga, Co, Fe, or their combinations) [16, 17]. The migration path of the O^{2-} ions in the perovskite structure is along the O-O edge of the $BO_{6-\delta}$ octahedron ($a/\sqrt{2}$), the distance of which is smaller than that between the A sites (a) and B sites (a), respectively. Moreover, the type of crystal structure impacts on the connection of ion migration paths. For example, in cubic perovskite-type structure (e.g., $La_{1-x}Sr_xBO_{3-\delta}$ family [18, 19]) and cubic fluorite-type structure (e.g., $Ce_{1-x}Y_xO_{2-\delta}$ [20] and $Y_{1-x}Ta_xO_{2-\delta}$ [21]), the migration paths are three-dimensional networks, as a contrast, in the tetragonal double perovskite-type structure, such as $La_{0.64}Ti_{0.92}Nb_{0.08}O_{2.99}$, the migration path is a two-dimensional network.

The ionic radius is another key factor influencing the activation energy. Small size ions are generally more ready to move. In most cases, cations are smaller than anions. That is why there are many kinds of mobile cations (e.g., H^+, Li^+, Cu^+, Ag^+, K^+, and etc.) but very limited mobile anions (e.g., F^- and O^{2-}).

Besides crystal structures and ion radius, the valence state of the ions is important to the activation energy of mobile ions. Ions with more charges tend to be confined in the lattice due to a stronger Columbic attraction with its neighboring ions with opposite charges. Therefore, the cations with valence over two are hard to migration despite of its small ion radius, such as the Ga^{3+} and Co^{3+} ions in cubic perovskite oxide.

Using first-principles method, the dominating mobile ions can be inferred theoretically by calculating the activation energy individually for each kind of ion with proposed migration pathways. Those calculated E_A values can be compared with the E_A value obtained experimentally for the identification, such as the E_A value from temperature-dependent ionic conduction [22] (Arrhenius plot, Fig. 2c), impedance spectroscopy, [5] relative dielectric constant, [23] or transient photocurrent [24]. On the other hand, the mobile ions can be inferred by *Tubandt's* method [1], in which the ionic conductor was contained in a solid state electrochemical cell and undergo a long-term DC bias polarization (generally in days).

After the polarization, interfacial reaction products caused by ion migration, together with the weight and composition change at different parts of the solid state electrochemical cell, can provide hints for the mobile ions identifications.

3 Ion Migration in Organolead Trihalide Perovskite Films

3.1 What Is (Are) the Moving Ion(s) in OTP Films

In this section, the discussion of ion migration will be mainly focused on $MAPbI_3$ material since it has been intensively studied. For the studies of ion migration in OTP films, one of the chief questions is which ion(s) is (are) moving in the polycrystalline perovskite films? The possible mobile ions in $MAPbI_3$ crystal include MA^+ ions, Pb^{2+} ions, I^- ions, and other impurities such as hydrogen-related impurities (H^+, H^0, and H^-). Although the radius of I^- ions (206 pm) is large, the migration of the halide ions in other ABX_3 perovskite materials, such as $CsPbI_3$ and $CsPbBr_3$, have been observed previously [1]. In $MAPbI_3$ perovskite, the I^- ions in the edge of the PbI_6 octahedron have the shortest distance with its nearest neighbors ($\sim$4.46 Å), which is less than that of MA^+ and Pb^{2+} ions ($\sim$6.28 Å) [22]. It is quite reasonable to expect that the I^- ions are the most likely mobile ions in the $MAPbI_3$. In fact, this hypothesis has been supported by several theoretical works [22, 25].

Based on first-principles method, the ion migration in the presence of neighbor vacancy (Schottky defect) has been analyzed by several groups separately [22, 25]. Briefly speaking, although there are some inconsistencies in the calculated activation energies for each kind of ion, all the theoretical works come to a conclusion that I^- ions is more ready to move in $MAPbI_3$ than other ions. For example, Eames et al. calculated the activation energies for the migration of I^-, Pb^{2+}, and MA^+ ions in $MAPbI_3$ film, respectively [22]. In their theoretical work, I^- ions migrating along the I-I edge of the PbI_6 octahedron with a slightly curved pathway (path-A in Fig. 3a, b) have the lowest activation energy of 0.58 eV; the MA^+ ions migrating through the unit cell face comprising four I^- ions (path-D in Fig. 3b) have higher activation energy of 0.84 eV; and the Pb^{2+} ions migrating along the diagonal of the cubic unit cell (<110> direction, path-B in Fig. 3b) have a much higher migration energy barrier of 2.31 eV. By fitting their temperature- and time-dependent photocurrent results, Eames et al. experimentally obtained an E_A value of 0.60 −0.68 eV, which is close to the calculated E_A for I^- ions migration. Therefore, I^- ions were suggested as the majority mobile ions and its diffusion coefficient was estimated to be 10^{-12} cm^2s^{-1} at 320 K. Later, in another theoretical work, Azpiroz et al. calculated the E_A value of the I^- ions (along path-A in Fig. 3b), Pb^{2+} ions (along path-C in Fig. 3b) and MA^+ ions (along path-D in Fig. 3b) to be 0.08 eV, 0.80 eV, and 0.46 eV, respectively [25]. The E_A value for I^- ions obtained in that work (0.08 eV) is much smaller with Eames et al.'s result (0.58 eV) despite of similar migration pathways were used. It is worth to mention that Azpiroz et al. did

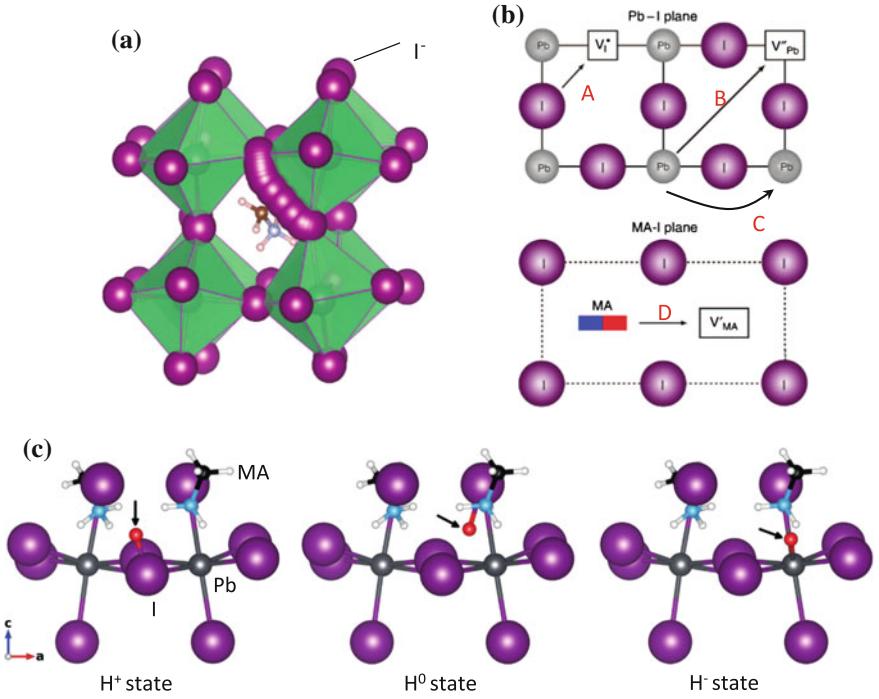

Fig. 3 **a** Schematic of the migrating path of I^- ions along the I^--I^- edge of the PbI_6^{4-} octahedron in the unit cell of $MAPbI_3$, as calculated from density functional theory (DFT) method; **b** Schematic of the proposed most likely migrating paths for I^- ions (path-A), Pb^{2+} ions (path-B or path-C) in the Pb-I plane, and MA^+ ions (path-D) in the MA-I plane that to be used for the calculation of activation energies; **3a**, **b** reproduced from Ref. [22] with permission from Nature Publishing Group. (c) Schematic of the hydrogenic impurities (H^+, H^0, and H^-) with different charge state, where H^+ (*left*), H^0 (*middle*), and H^-(*right*) are stabilized around I anion site, interstitial Pb-I site, and Pb site, respectively; Fig. 3c reproduced from Ref. [27] with permission from John Wiley and Sons

not attribute the photocurrent hysteresis to I^- ions migration due to its very small E_A value of 0.08 eV. According to Azpiroz's estimation, the I^- ions can migrate through the $MAPbI_3$ film within 1 μs under operating bias, which is too fast to be responsible for the hysteresis effect in the $MAPbI_3$ film (in a time scale of 0.01 −100 s). The majority ions responsible to the observed hysteresis are suggested to be MA^+ or Pb^{2+} ions. Similarly, Haruyama et al.'s calculation give a E_A value of ∼0.33 eV for I^- ions migration and a E_A value of ∼0.55 eV for MA^+ ions migration [26].

Hydrogenic impurities (H^+, H^0, and H^-) are also proposed to be important in $MAPbI_3$ film by Egger et al. [27]. It can be introduced during the fabrication process due to the absorbed moisture or generated by the decomposition of $MAPbI_3$ materials. Mobile hydrogenic impurities have been proved to play important roles in other inorganic thin film solar cells such as copper indium gallium di-selenide

(CIGS) [28]. In $MAPbI_3$ crystal, according to density functional theory (DFT) calculations [27], the hydrogenic impurities can capture or loss electrons, and hence to be stabilized at different location as interstitials (Fig. 3c) because of their varied charge states, which promote the hydrogen migration (i.e., ionization-enhanced migration) [29]. The activation energy for H^+ jump along iodide-iodide path is calculated to be around 0.17−0.29 eV, depending on the degree of lattice relaxation, which means hydrogenic impurities are also readily to move in $MAPbI_3$ film.

It should be noticed that, the ion migration study is still an emerging research field. So far, the existing theoretical works do not cover all the possibilities for the ion migration. For example, the existing calculations dealt with the ion migration in the bulk crystal which generally is less important than the ion migration occurs in the grain boundaries of polycrystalline films. Insights for the ion migration occurring at the grain boundaries are still desired. In addition, investigation focusing on the interstitial ions hopping in the perovskite crystal is lacked. Generally, the generation of interstitial ions (Frenkel defect) faces a larger energy barrier than the Schottky defects. However, there is a calculation indicating that the formation energies of I^- (0.23−0.83 eV) and MA^+ (0.20−0.93 eV) interstitial defects are comparable to the activation energies for I^- ions (e.g., 0.08−0.58 eV) and MA^+ ions (e.g., 0.46−0.84 eV) to hop to their neighbor vacancies [30]. For evaluating of the possible interstitial ions migration in OTP films, more related theoretical analysis are desired.

Although I^- ions or/and hydrogenic impurities have been predicted to be the majority mobile ions in the $MAPbI_3$ film, the migration of MA^+ ion at room temperature has been first proved by direct experimental evidence. In Yuan et al.'s study, by employing a photothermal induced resonance (PTIR) microscopy technique, the concentration of MA^+ ions in $MAPbI_3$ film can be detected with a lateral spatial resolution of tens of nanometers [13]. After applying a moderate electrical field of 1.6 V/μm for 100−200 s on a lateral structure $MAPbI_3$ solar cell (Fig. 4a), a depletion of MA^+ ions from anode to the center region and an accumulation of MA^+ around cathode region was observed, which proves a quick MA^+ ions migration under electric field. In that study, the activation energy for the ions migration was estimated to be 0.36 eV from the temperature-dependent conductivity of $MAPbI_3$ film (Arrhenius plot). This obtained E_A is somewhat smaller than the value predicted by first-principle method (0.46 eV [25], 0.55 eV [26], or 0.84 eV [22]). The inconsistency is not surprising because the calculated activation energy only accounts for the ion migration inside bulk crystal, while the experimentally measured activation energy is most likely dominated by the ion migration in grain boundaries. In addition, this study does not exclude the migration of I^- ions which might dominate the ion migration in this experiment. Nevertheless, Leijtens et al. studied the ion migration in $MAPbI_3$ film in ambient condition with Auger electron spectroscopic mapping method [31]. It was found that the migration of MA^+ ions is much more significant than I^- ions in the present of moisture. The migration of I^- ions, as wells as Pb^+ ions, around cathode region was only observed when the $MAPbI_3$ film degraded obviously.

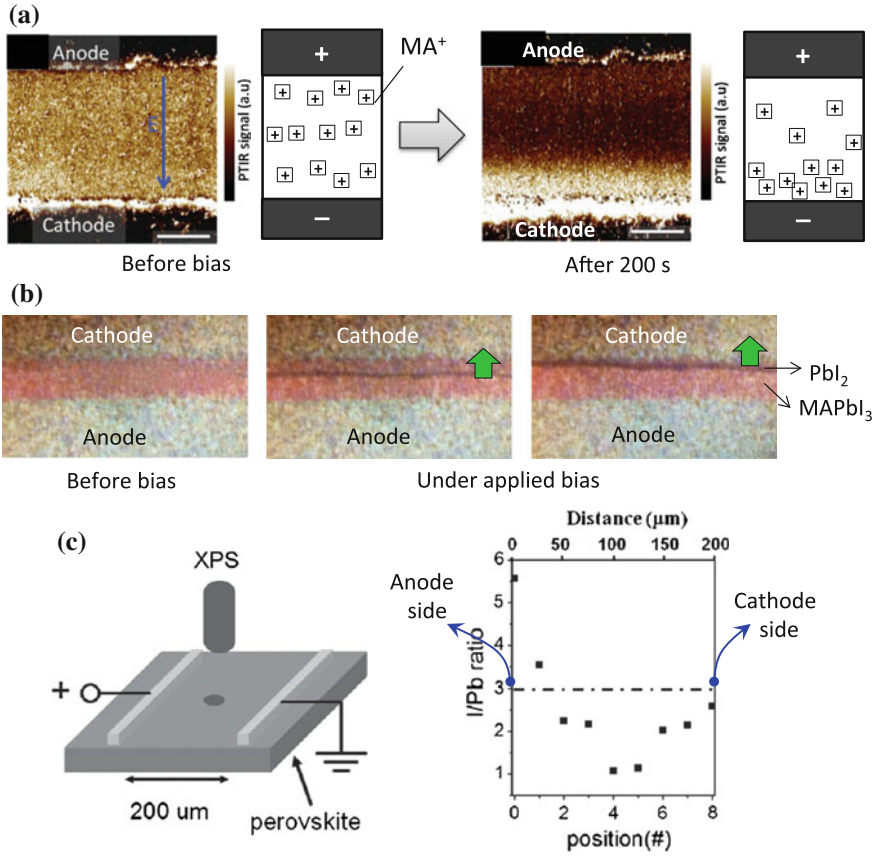

Fig. 4 **a** PTIR images and corresponding illustrations showing the distribution of MA^+ ions before and after electrical poling (1.6 V/μm) for 200 s, respectively, where the spacing between anode and cathode is 100 μm; **a** reproduced from Ref. [13] with permission from John Wiley and Sons. **b** Optical images of lateral $MAPbI_3$ perovskite solar cell with a PbI_2 thread migrating from anode to cathode due to an applied positive bias at 330 K. **b** reproduced from Ref. [33] with permission from John Wiley and Sons. **c** Schematics of the mapping of the elements distribution in lateral $MAPbI_{3-x}Cl_x$ solar cells with XPS method (*left*) and the obtained I/Pb ratio against position from anode side to cathode side (*right*). **c** reproduced from Ref. [36] with permission from John Wiley and Sons

As the migration of MA^+ ions has been firmly proved, more experimental evidences are needed to find out whether I^- ions are mobile. While the I^- ion migration under the operation or measurement condition of the perovskite devices at room temperature has not yet been revealed experimentally, Yang et al. contribute a hint pointing to the possible I^- ions migration at elevated temperature of 323 K under very long poling study [32]. In that study, the $MAPbI_3$ film was embedded in a solid state electrochemical cell with a structure of Pb-anode/$MAPbI_3$/AgI/Ag-cathode, followed by a long-term DC bias polarization (*Tubandt's method*

[1]). After applying a DC bias at 323 K for one week, formation of PbI_2 at the Pb-anode/$MAPbI_3$ interface was observed, which can be explained as the mobile I^- ions reaching the anode and reacting with the Pb atoms. However, it needs to mention that the decomposition of the $MAPbI_3$ film due to the MA^+ migration can also lead to the formation of PbI_2 at the Pb-anode/$MAPbI_3$ interface, which have been previously observed in Xiao et al.'s study [4]. Therefore, an additional inspection of the weight changes at each part of the solid state electrochemical cell was needed for the identification of I^- ions migration. In another investigation, Yuan et al. observed a massive I^- ions migration at an elevated temperature. In that study, lateral structure $MAPbI_3$ solar cells were electrically poled at an elevated temperature of 330 K. A PbI_2 thread was formed in the area between two electrodes (see Fig. 4b). The formed PbI_2 thread, visualized under optical microscopy, can migrate along the applied electrical field (3 V/μm), which was explained by a field-driven conversion between $MAPbI_3$ and PbI_2 phases in combination with a massive migration of MA^+ ions and I^- ions [33]. In recent studies, more evidences for the migration of I^- ions at room temperature have been obtained. In lateral structure $MAPbI_3$ devices with Ag as electrodes, Bastiani et al. observed that only the anode electrodes were damaged after biasing, which should be caused by the reaction between the Ag and the I^- ions in $MAPbI_3$ [34]. However, it is not clear whether the reaction was selectively enhanced by positively charged Ag surface. In another work, the I^- ions distribution has been studied using Auger electron spectroscopic mapping [31]. The depletion of I^- ions was observed after the $MAPbI_3$ film degraded at the presence of moisture. Besides, under gradually increased applied bias, Zhang et al. observed a blue shift in the electroluminescence spectrum of $MAPbI_{3-x}Br_x$-based light-emitting electrochemical cells, which is related to the reduced amount of I^- ions in the light emission zone by I^-/Br^- ions migration [35]. Later, Li et al. studied the I/Pb ratio again the position in electrically poled lateral $MAPbI_{3-x}Cl_x$ film by X-ray photoemission spectroscopy (XPS) with a spatial resolution of 50 μm [36]. An increase of I/Pb ratio from around $\sim$3.03 to $\sim$5.65 around anode side and decrease of I/Pb ratio in the middle and cathode region has been observed, which proves the migration of I^- ions under electrical bias (Fig. 4c). The accumulated I^- ion can diffuse back gradually, as witnessed by the recovering of the I/Pb ratio to $\sim$3 after restored the sample for 6 h. It should be noted that all the study using lateral structure devices rely on elongated poling to obtain the migration of a large amount of ions so that they can be observed with the relatively less sensitive mapping techniques.

So far, experimental results firmly supported that both the MA^+ ions and I^- ions are mobile in the $MAPbI_3$ films, while the Pb^{2+} ions are difficult to move. All these studies well demonstrated our discovery that the mobile ions is a very important reason for the *I-V* hysteresis [4].

3.2 Mobile Ions Formation and Their Migration Channels in Solid Perovskite Film

Understanding the origins of the mobile ions is important since it provides hints for the development of OTP materials with improved stabilities. Generally, ion migration under electric field is much related to the presence of defects in the solid films. It is known that there is large density of point defects or/ and lattice distortion in polycrystalline OTP materials, as indicated by the much broadened X-ray diffraction peaks than those OTP single crystals which could not be only contributed by the grain size reduction. The defects in OTP films mainly result from the following reasons:

First, the formation of OTP films by low temperature solution or thermal-evaporation processes is quick and thus far from thermodynamic equilibrium, which inevitably generate lots of defects in OTP films during the crystallization of grains.

Second, the stoichiometric ratio in fabricated OTP film is not ideal because it is largely determined by the processing method and the choosing of precursors [37]. For example, in the one-step fabrication method, a precursor molar ratio of 0.6 −0.7:1 for PbI_2 to MAI is needed for the formation of continuous planar $MAPbI_3$ film [38]. Higher PbI_2 to MAI ratio (e.g., over 0.8:1) will lead to the formation of microfibers; In the two-step fabrication method, both excessing PbI_2 or MAI are possible, as witnessed by the *n*- or *p*-type self-doping in OTP films predicted by Yin et al. [30] and independently observed by Qi et al. [39]. Yu et al. studied the influence of stoichiometric ratio on the ion migration and observed an increased ion migration in the sample with excessing PbI_2, which suggested that MA vacancies provide favorable pathway for ion migration [40].

Third, OTP films are easy to decompose due to the "softness" of the chemical bonding, i.e. the defects have low formation energy. Theoretical calculation indicates that Pb^{2-} vacancies (e.g., E_A = 0.29 eV in I-rich/Pb-poor condition) or MA^+ interstitials (e.g., E_A = 0.20 eV in I-poor/Pb-rich condition) have low formation energy in $MAPbI_3$ films, although this prediction has not been verified experimentally yet [30]. Kim et al. calculated that the formation energy of PbI_2 vacancies in $MAPbI_3$ film are only 27−73 meV, which suggests that there should be abundant PbI_2 vacancies formed during the fabrication process [41]. Moreover, Buin et al. calculation suggests that the energy for the $MAPbI_3$ decomposed into pure PbI_2 and MAI phase is as small as ∼0.1 eV [42]. Meanwhile, Walsh et al.'s calculation suggested a low formation energy of ∼0.1 eV for the Schottky defects in $MAPbI_3$ film [43]. The "softness" of OTP materials also explains why the E_A for ion migration in $MAPbI_3$ (0.36 eV) with large atoms is much smaller than those of other perovskite oxides with smaller atoms, such as $LaMnO_3$ (0.73 eV), $LiNbO_3$ (0.75 eV), and $LaFeO_3$ (0.77 eV). The easy decompose nature of $MAPbI_3$ can lead to huge amount of mobile ions, which might be harmful to the stability of OTP solar cells.

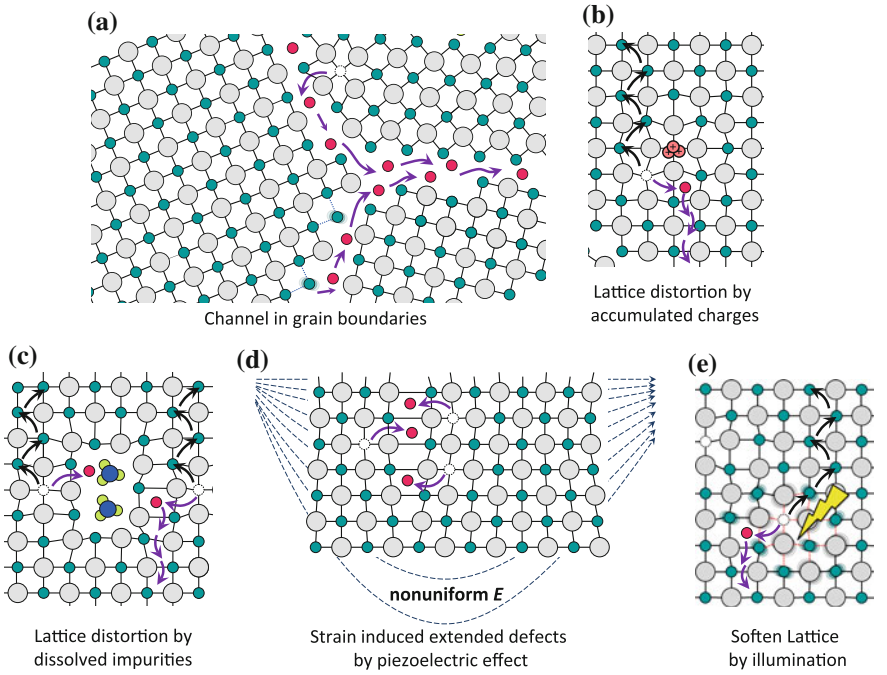

Fig. 5 Schematics of the ion migration channels enabled by **a** wrong bonds and open space at grain boundaries, **b**–**d** local lattice distortions caused by accumulated charges **b**, dissolved impurities, **c** and piezoelectric effect induced nonuniform strain (**d**), and **e** weakened bonding caused by light illumination. This figure reproduced from Ref. [7] with permission from American Chemical Society

In addition to the point defects inside bulk crystal, the surface or grain boundaries of the crystal grains are other extremely important sources of mobile ions (Fig. 5a). This has been shown by Xiao et al. because the device with large grain boundaries were more difficult to be switched than the device with small grains. [4] Grain boundaries are two-dimensional defects that widely exist in OTP polycrystalline films. Due to the defect segregation, dangling bonds, lattice dislocation, or composition change at the grain boundaries, the density of vacancies at the grain boundaries is much higher than that in the bulk crystal. In addition, due to the relative open space, grain misorientation, loose bounding, wrong bonds, or tensile strain, the formation energies of point defects can be much lower than that in bulk crystal. Besides, since OTP materials are readily decomposable at high temperature (e.g., >150 °C) while most OTP films go through a thermal annealing for grain growth, there is a large chance to form non-stoichiometric perovskite at grain boundaries by losing the organic cations [44, 45]. In Yuan et al.'s study in polycrystalline $MAPbI_3$ film along lateral direction, it was found that some ions (defined as "fast ions") start to move at a relatively smaller electrical field around 0.1 V/μm while some ions (defined as "slow ions") only start to move when the electrical field

is over 0.3 V/μm. The origins and difference of "fast ions" and "slow ions" have not been fully understood yet, which might be caused by the ion migration occurs in the bulk crystal and at the grain boundaries, respectively [13].

Moreover, defect formation energy might reduce due to local lattice distortion, which also increase mobile ions generation. Local lattice distortion may occur under some conditions, including the cases with mesoporous scaffold confinement [46], accumulated charges (Fig. 5b) [47], absorbed molecules (Fig. 5c) [48, 49] or etc. In Choi et al.'s study, it was found that, due to the mesoporous scaffold confinement effect, most of $MAPbI_3$ (70 %) in the mesoporous TiO_2 has poor lattice order, which lead to a local perovskite coherence length of only 1.4 nm [46]. The perovskite films with higher degree of lattice disorder tends to generate more mobile ions, which might explain the more significant *I-V* hysteresis in solar cells with mesoporous structure in addition to trapping effect; Besides, it is well known that OTP film can absorb many kinds of chemical molecules to form solid solution, such as moisture [50] and polar organic molecules such as Dimethyl sulfoxide (DMSO) [20, 21], Dimethylformamide (DMF) [51], MA [52], and etc. These molecules dissolved in OTP film can disturb perovskite lattice significantly, some of which even cause a color change of the OTP film due to the interrupted electron cloud overlap. The opening up of the crystal structure is believed to facilitate defect formation and thus ion migration; Leijtens et al. studied the ion migration effect in $MAPbI_3$ film that exposure to different environmental conditions such as moisture and DMF. They observed a much more severe decomposition of the $MAPbI_3$ film accompany with ion migration in moisture or DMF condition [53]. The effect of charge accumulation in the OTP-based solar cells to the hysteresis has been studied by Wu et al., in which a possible lattice distortion caused by accumulated charges has been suggested and used to explain the measured photocurrent hysteresis [47]. Recently Dong et al. shows the piezoelectric effect in OTP single crystal, which can result in lattice strain/distortion in OTP films caused by electrical field. This kind of lattice distortion can also facilitate ion migration (Fig. 5d) [54].

The role of the light illumination on the generation of mobile ions is another open question, as suggested by multiple experimental results that incident light can trigger ion migration significantly. Hole et al. showed that there is a severe phase separation in $MAPbI_{3-x}Br_x$ polycrystalline film when it was illuminated under one sun condition for tens of seconds, which is resulted from the halide ions migration and redistributions [11]. The activation energy for the halide ion migration was measured to be $\sim$0.27 eV which is close to that of the halide ion migration in some other halide perovskite materials, such as $CsPbCl_3$, $CsPbBr_3$, or etc. [1]. This halide segregation is revisable when the film was stored in dark for few minutes, indicating the $MAPbBr_xI_{3-x}$ film have different stable states in dark and under illumination, respectively. The easy ion migration nature enables the transformation between these metastable states. More studies are needed to find out whether this is spinodal decomposition. Bag et al. studied the ion migration in $MAPbI_3$ and $FAPbI_3$ films with electrochemical impedance spectroscopy (EIS) in both dark and illuminated condition [5]. From their EIS result, only significant ion migration (featured as linear Warburg component at the low frequency part, see Fig. 1d) was observed

when the films tested under illumination. The importance of light illumination to the ion migration has been confirmed by excluding the IR-induced heating effect. On the other hand, Juarez-Perez et al. reported that the dielectric constant of $MAPbI_{3-x}Cl_x$ increased by 1000 times (in a frequency range of 0.05−1 Hz, similar to the time scale for ion migration) when it was illuminated at one sun condition [10]. This giant dielectric constant change was primarily explained by the photoinduced charge carriers which may induce lattice distortion. Later it was shown that the ion migration might be a possible origin of the giant dielectric constant since there is $1/f$ dependent of static dielectric constant [10]. Gottesman et al. suggested that the perovskite lattice become even softer under illumination [55]. Their calculation indicated a reduced binding between the MA^+ ions and the inorganic frames (Fig. 5e), which might be a contributing factor for the photon enhanced ion migration. Besides, more insightful understanding regarding to the role of light illumination is desired.

Generally speaking, it is known that OTP materials, e.g., $MAPbI_3$, is electrically benign, which means the point defects or grain boundaries do not form deep traps within their forbidden band [30]. This merit makes OTP materials superior to many other photovoltaic materials such as CdTe [56], $CuInSe_2$ [57], and $CuZnSnSe_4$ [58]. It is believed that the large atomic size and loose crystal structures is one of the major reasons responsible for good defect tolerance in OTP materials. For example, the weak interaction between the I-I wrong bonds at the grain boundary leads to only a small splitting between their antibonding ppσ* orbital and ppσ orbital. Both orbitals hence stay inside the valence band and do not form deep traps [59]. However, from the ion migration point of view, the loose crystal structure of OTP materials is a major reason for the easy ion migration.

4 Impact of the Ion Migration on Photovoltaic Efficiency and Stability

It has been demonstrated that pronounced ions can migrate in $MAPbI_3$ film at a very small electrical filed of $\sim$0.3 V/μm (Fig. 6a), which is ten times smaller than the build-in electrical field in OTP solar cells ($\sim$3 V/μm) [13]. Besides, accumulated ions are readily to diffusion back in a time scale of tens of seconds at room temperature (Fig. 6b). Due to the high migration rate of the mobile ions, the impact of ion migration on the operation/performance of OTP solar cells is ubiquitous.

The charged excess ions in perovskite films can attract carriers with opposite charge from electrodes to maintain an electrically neutral condition, which in effect cause local chemical doping in OTP films. Although the doping efficiency of the excess ions has not been identified quantitatively yet, a fermi level change of 0.35 eV caused by the ion accumulation in pristine $MAPbI_3$ film has been measured by Kelvin probe force microscopy (KPFM, Fig. 6c) [13]. The local chemical doping effect could significantly influence the charge transport and injection by

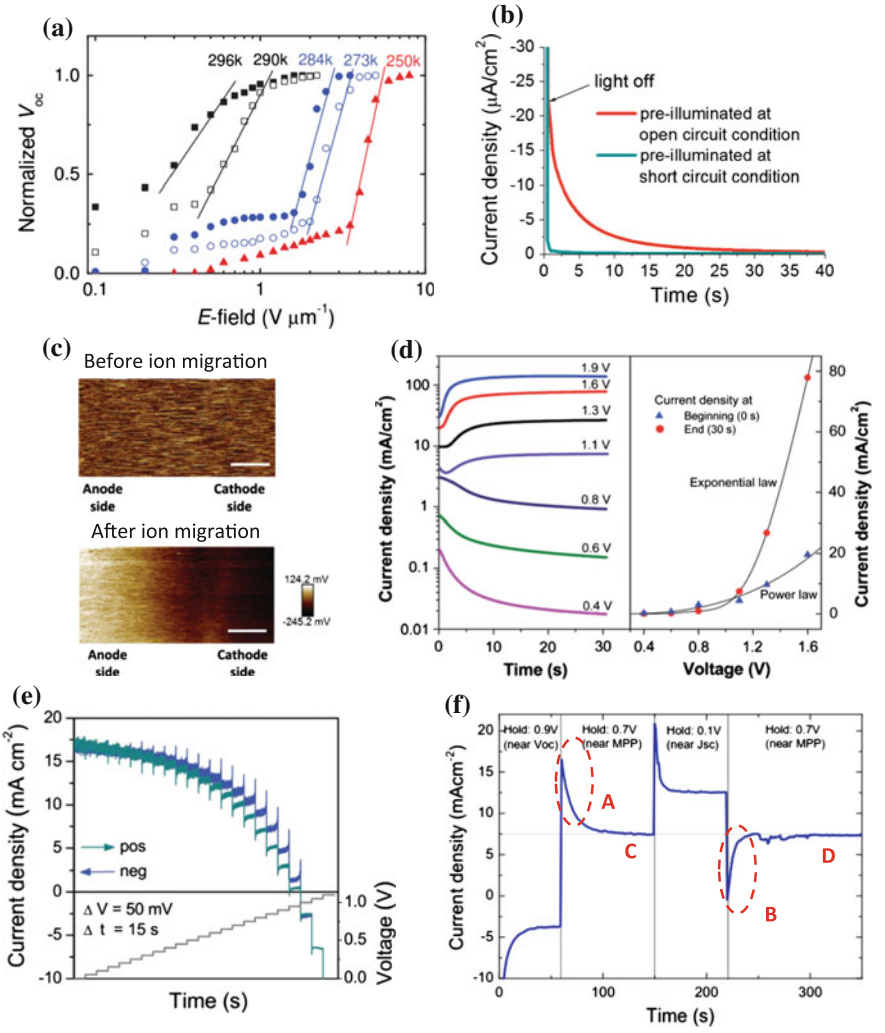

Fig. 6 **a** Dependence of the V_{OC} on the poling electrical field and poling temperature, reflecting the migrating capabilities of ions in $MAPbI_3$ film; **b** Current density at 0 V bias caused by the back diffusion of accumulated ions; **b** reproduced from Ref. [12] with permission from John Wiley and Sons. **c** Surface potential change of $MAPbI_3$ film from uniform distribution (before ion migration) to gradual distribution (after ion migration) measured by KPFM, which demonstrates the ion accumulation caused doping effect. **a**, **c** reproduced from Ref. [13] with permission from John Wiley and Sons. **d** Evolution of the dark current under different constant bias (*left*) induced by slow ion redistribution, which makes the *I-V* curve changed from power law to exponential law. **d** reproduced from Ref. [55] with permission from the Royal Society of Chemistry. **e** Time-dependent current output under step-wise voltage bias, illustrating the current spikes due to capacitive effect. reproduced from Ref. [2] with permission from the Royal Society of Chemistry. **f** Obtained current density from a planar perovskite cell over time, where the cell was held at different voltage conditions and then become stabilized [3]

modulating the build-in electrical field and interfacial energy barriers. Zhao et al. studied the dark current of $MAPbI_3$ solar cells at different biases and found that the ion migration can change the *I-V* curve from power law to exponential law (Fig. 6d), suggesting the device transits from hole-only device to a diode [60]. Shi et al. studied the slow charge response to the applied electrical bias (and light pulse) and suggested a compensation of the build-in electrical field by ion accumulation [24]. Since the ion migration can reduce the interfacial energy barrier and eliminate the contact resistance, it was suggested that the best possible performance of OTP solar cells can be temporarily attained by pre-biasing the device before measurement [61].

Under light illumination, as mentioned above, a widely observed phenomenon related to ion migration in OTP solar cells is the anomalous photocurrent hysteresis effect [2, 3, 7, 62–65]. The *I-V* curves hysteresis in perovskite materials adds difficulty in accurate measurement of the PCE, and brings many concerns to the stability of the OTP solar cells. Xiao et al. reported the giant switchable photovoltaic effect in OTP solar cells at early 2015, which confirmed the ion conducting nature of the OTP materials [4]. The device structure in Xiao's study was ITO/ PEDOT:PSS/ Perovskite/ Au. After electrical poling by a weak electrical field of <1 V/μm, such kind of device can output a switchable short circuit current (J_{SC}) between 18.6 mA/cm^2 and −20.1 mA/cm^2, and a switchable open-circuit voltage (V_{OC}) between 0.42 V and −0.73 V. The switchable J_{SC} is as large as that in optimized OTP solar cells with nonsymmetrical electrodes ($\sim$20 mA/cm^2), demonstrating the ion redistribution has overwhelming tuning effect on the photocurrent. This effect is strong enough to explain the observed *I-V* hysteresis with performance variations generally less than 50 % [2, 3, 61, 66]. When there is no charge blocking layer such as PCBM in their vertical structure OTP solar cells, the V_{OC} can switched between a positive or negative value. If PCBM layer with electron collecting and hole blocking property was used, the V_{OC} after negative bias poling is neglectable (close to zero), and the V_{OC} after positive bias poling increased from $\sim$0.5 V to a range of $\sim$1.0 V [13]. The impact of ion migration on the V_{OC} is significant in both cases.

The *I-V* hysteresis can be influenced by ion migration through some different, but accompanying, mechanisms: first it is well known that there are current spikes immediately after each step-like applied bias in a time scale of $\sim$1 s (Fig. 6e), [2, 55] which was previously explained as a capacitive charging effect since the existence of giant dielectric constants under illumination [67]. Later, Almora et al. explained that the commonly observed capacitive effect is caused by a local rearrangement of ions around the electrode interface [68]. This explanation is consistent with the concerns that the giant dielectric constant might also originated from ion migration [10, 23] in addition to the photo induced structural changes [9, 24, 69]. It has been widely observed that the J_{SC}, $V_{OC,}$ and PCE value of OTP solar cells obtained right after the applied bias (defined as "transient-state," see regions "A" and "B" in Fig. 6f.) is different with the stabilized value (defined as "steady-state," see regions "C" and "D" in Fig. 5f). The "transient-state" varied a lot because it is sensitively influenced by the operation "history" of the device.

Moreover, if the perovskite solar cells with hysteresis work continuously under illumination, the "steady-state" performance can gradually drift to a "steady-state" regardless of it operation condition and pretreatment history [3]. The corresponding time scales, varied from few seconds to hundred seconds, [67, 70] is consistent with the time scale for ion migration but much slower than the trapping/detrapping effect. This process is related to the redistribution of ions in the whole perovskite film due to the applied bias change, which reconstructs the build-in electrical field inside the OTP solar cells. Similar effects have been observed in many other oxide materials-based devices, such as TiO_2 memristors [71] or $SrTiO_3$ memories [72]. In those cases, the "transient-states" are caused by oxide vacancies migration. As a matter of fact, the ion induced doping effect and the resulted tunable *p-i-n* junctions can find more applications in other type of optoelectronic devices. For example, Xiao et al. demonstrated memristors with OTP materials as the active layer, the resistance status of which can be read out both by electrical pulse and optical pulse [4]. Lateral OTP solar cells arrays with all the formed *p-i-n* junctions connected in series has been reported, which can output a very large V_{OC} of 70 V and potentially eliminate the demands of transparent electrodes [13]. In another case, switchable light-emitting electrochemical cells based on OTP materials has been demonstrated by Zhang et al. [35] wherein the device can be turned on by small bias ($\sim$1.5 V) with both forward or backward directions.

Besides the chemical doping effect and the redistribution of build-in electrical field, the easy migration nature of the mobile ions in mixed halide OTP films can reduce the device performance by forming charge traps. As mentioned above, the ion migration induced by illumination cause severe halide segregation in $MAPbBr_xI_{3-x}$ (Fig. 7a, b) [11]. Figure 7a shows the XRD peak of homogeneous $MAPbBr_xI_{3-x}$ film splitted into two peaks after illumination, which is due to the formation of I-enriched and Br-enriched perovskite domains with different lattice constants. Those domains have different electronic structures, where the I-enriched domains have smaller bandgap and act as charge traps, leading to a PL peak shift to lower energy (Fig. 7b). This light-induced charge traps explains the observed poor V_{OC} and PCE in the $MAPbBr_xI_{3-x}$ solar cells. The ion migration is more obvious in mixed halide perovskite film. This is because: (1) there is strain in the lattice due to the halide anions has different ion radius, while the smaller one is easier to move; (2) the alloy $A_{1-x}B_x$ might be intrinsically less stable due to the miscibility problem between the two components, which cause phase separation problem and generate mobile ions [59, 73].

Another phenomenon caused by ion migration is the light-induced self-poling effect (LISP) found by Deng et al. [12]. As introduced above, MA^+ or/and I^- ions in $MAPbI_3$ films can migrate significantly under an electrical field that is much smaller than build-in electrical field, hence those ions migration should also response to the additional electrical field induced by illumination (i.e., a electrical field generated by photovoltage that comparable to the built-in electric field). In Deng's study, it was found that the device performance improvement by electrical poling can be also realized by simple light illumination (Fig. 7c, d). The pristine solar cell showed a poor performance before illumination (i.e., an initial V_{OC} of 0.6 V and

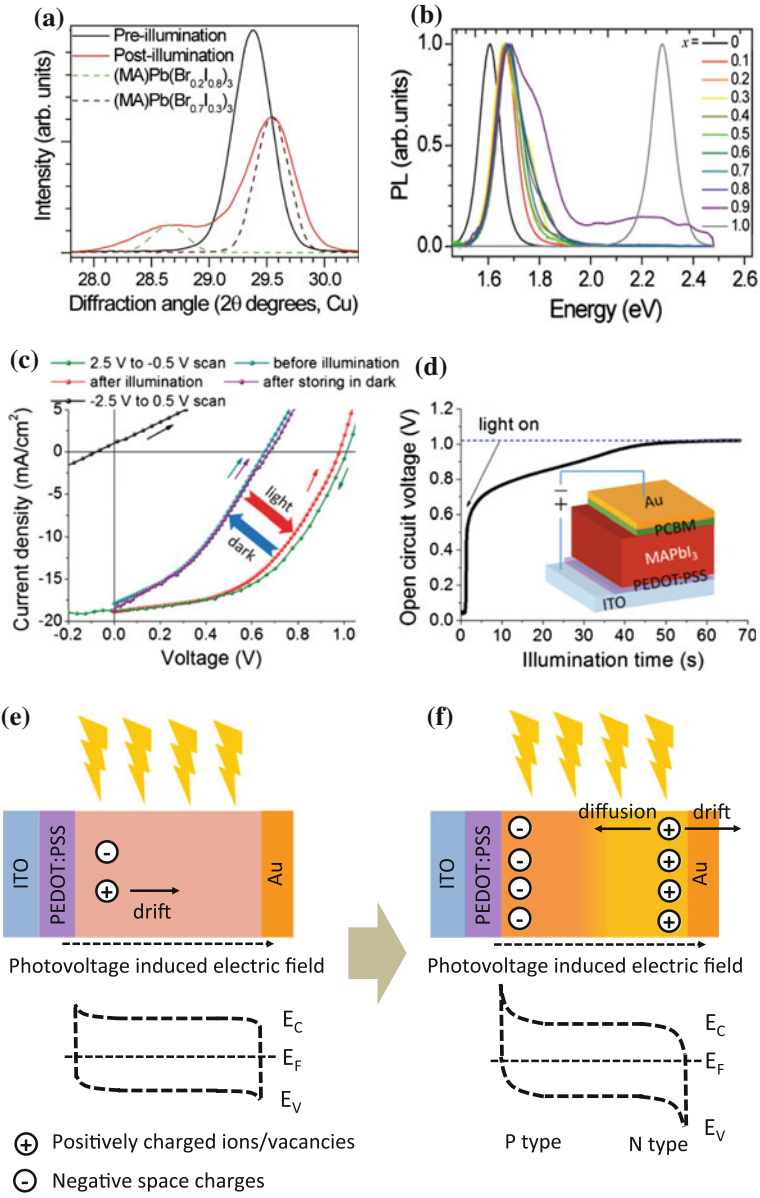

Fig. 7 **a** XRD peak obtained from $MAPbBr_{0.6}I_{2.4}$ film before and after light illumination at one sun condition. **b** New photoluminescence spectrum of $MAPbBr_{0.6}I_{2.4}$ film generated by light illumination due to photoinduced phase separation; **a**, **b** reproduced from Ref. [12] with permission from the Royal Society of Chemistry. **c**, **d** *I-V* curves and steady photocurrents curves of $MAPbI_3$ perovskite solar cells with a structure of ITO/PEDOT:PSS/$MAPbI_3$/Au. **e**–**f** Schematics of ion migration direction and energy diagram change in illuminated solar cells. **c**–**f** reproduced from Ref. [12] with permission from John Wiley and Sons

PCE of 4.3 %). After illuminated at one sun condition for tens of seconds, the device show significantly improved performance (i.e., a higher V_{OC} of 1.02 V and PCE of 8.1 %). This was ascribed to the formation of a favorable *p-i-n* structure due to the ion migration (Fig. 7e, f). This observation is very promising since light-induced ion migration helps to increase the device output. This LISP effect is general but sometimes underestimated or ignored because: (1) usually the devices have been unintentionally illuminated by strong light at open-circuit status before *I-V* measurement; (2) the LISP finishes quickly when the OTP film have suitable condition for fast ion migration. Although LISP tends to increase device performance in a time scale of few hours, so far, whether the ion migration is beneficial to the long-term stability of the OTP solar cells is still unclear.

Beyond the photoactive layer, the mobile ions are also proposed to impact on the charge extraction layer. Bastiani et al. proposed that the mobile MA^+ ions can specifically interact with the organic acceptor layer such as PCBM and cause n-type electrical doping, which facilitates charge extraction and reduce the fermi level of the PCBM layer to form a higher V_{OC} [34].

5 Suppressing Ion Migration for Stable OTP Solar Cells

Up to now, although it is not clear whether ion migration tends to enhance or reduce the long-term stability of OTP solar cells, tremendous efforts have been devoted to eliminate the photocurrent hysteresis caused by ion migration. As discussed in Sect. 3, the imperfections in grains and grain boundaries provide plenty of sites for ion migration. In order to suppress the ion migration in OTPs, it is necessary to figure out whether grain boundaries are the dominating channels for ions migration in polycrystalline OTP films.

Some recent experimental results suggest that grain boundaries are most likely the dominating migration channels although the migration through bulk crystal cannot be completely excluded. A frequently observed fact is that the OTP solar cells with large grain size and less grain boundary area usually have less *I-V* hysteresis [63]. Besides, as compared to OTP solar cells with mesoporous structures, the device with "inverted" planar structure covered with a fullerene electron transport layer usually show significantly smaller *I-V* hysteresis [38]. For explanation, Shao et al. suggested that fullerene deposited on perovskite film could diffuse into the perovskite grain boundaries and hence passivate the charge traps at grain boundaries as well as grain surface (Fig. 8a, b) [62]. Later, Xu et al.'s calculation results showed that the presence of I-Pb antistite defects (Pb sites occupied by I atoms, Fig. 8c) at the grain boundaries could form deep traps and cause *I-V* hysteresis. They also show that there is a strong charge transfer from the I-Pb antistite defects to fullerene (Fig. 8d), which eliminates the deep traps by shifting the gap states from the middle of the forbidden band to the edge of conduction band

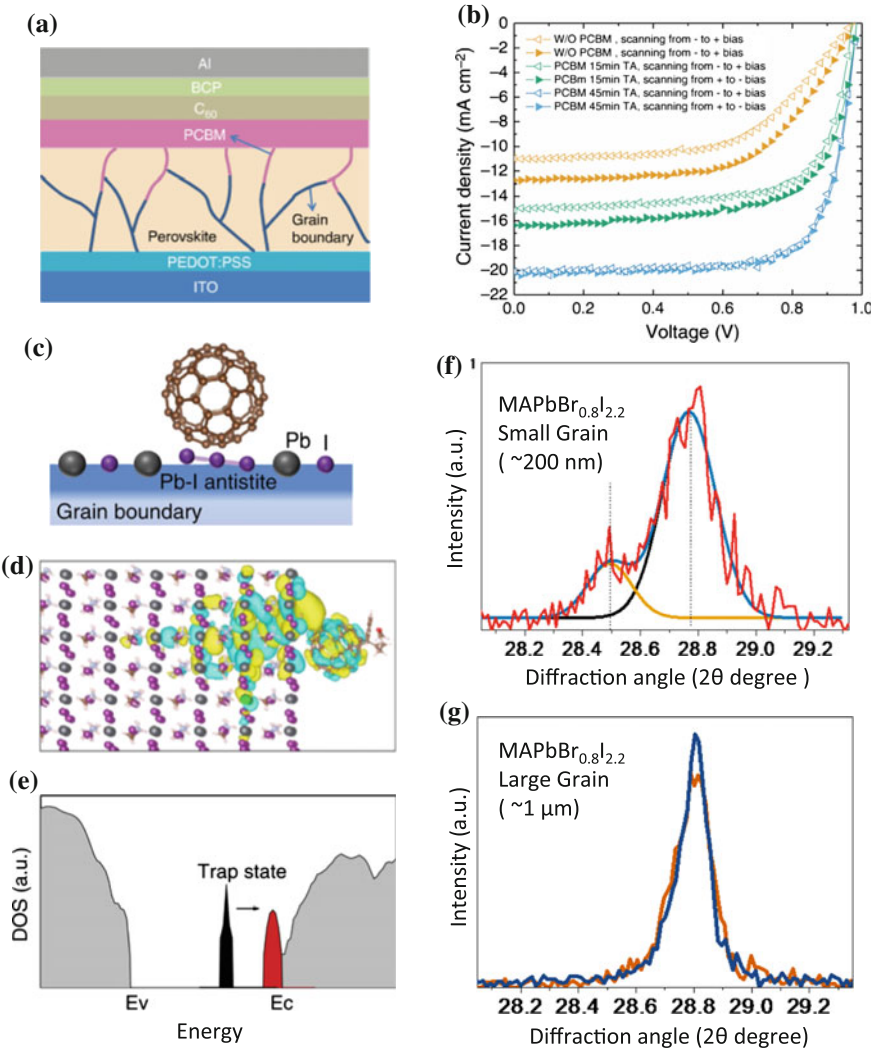

Fig. 8 **a** Schematic of the passivation of $MAPbI_3$ grain surface, and grain boundaries by covering it with PCBM. **b** Vanished *I-V* hysteresis due to PCBM passivation; **c** Schematic of the Pb-I antistite defect and its passivation by PCBM; **a**, **b** reproduced from Ref. [62] with permission from Nature Publishing Group. **d** The wavefunction overlap show the charge transport between PCBM and defective surface **e** Comparison between the calculated density of states of $MAPbI_3$ films with PCBM passivated Pb-I antistite (*red*) and unpassivated Pb-I antistite (*black*); **c**–**e** reproduced from Ref. [76] with permission from Nature Publishing Group. **f** Splitted (200) XRD peak of the $MAPbBr_{0.8}I_{2.2}$ film with small grain size due to light illumination; **g** Unchanged (200) XRD peak of the $MAPbBr_{0.8}I_{2.2}$ film with large grain size before and after light illumination; **f**, **g** reproduced from Ref. [64] with permission from John Wiley and Sons

(Fig. 8e). It was speculated that the fullerene-defect interaction at grain boundaries helps to reduce the ion migration due to the improved binding effect and blocked grain boundaries.

The importance of reduced grain boundary area in the photo-stability of mixed halide perovskite ($MAPbI_{3-x}Br_x$, $x < 1$) has been further proved by Hu et al. [64] By employing the non-wetting hole transport layer of poly(triarylamine) (PTAA) developed by Bi et al. [74]. Hu et al. increased the grain size of $MAPbI_{3-x}Br_x$ film from $\sim$200 nm to >1 μm. The photoinduced phase separation problem in $MAPbI_{3-x}Br_x$ film was then eliminated when the grain size was increased, as verified by XRD and optical characterizations (Fig. 8f, g, no XRD peak splitting observed in $MAPbI_{3-x}Br_x$ film with large grain size) [64]. Meanwhile, the PCE and operation stability of the $MAPbI_{3-x}Br_x$ solar cells was much increased due to the absence of low-bandgap impurity phase and the decreased grain boundary traps.

It has been reported that the ion migration and the corresponding *I-V* hysteresis were suppressed at lower temperature and almost disappeared at temperature less than 160 K. [4, 36, 40] This fact suggests that, for designing new perovskite materials without *I-V* hysteresis at room temperature, we will need to double the activation energy of ion migration. Actually, the OTP materials are known as a kind of loose crystal. Increasing the valence state of the ions is an approach to increase the Columbic interaction between the ions and the crystal frame, which is a general way to increase the activation energy and hence reduce ion migrations. Right now, all the anions at the X site of OTP family are in the −1 valence state, which limited the cations in A site and B site to be in +1 or +2 valence state. This limitation has led to some instability issues in lead-free OTP materials such as $MASnI_3$ since Sn^{2+} ions are less stable than Sn^{4+}. Hence, developing hybrid perovskite materials with higher-valence state anions and cations might be a possible strategy for better intrinsic stability. Besides, co-doping cations with lower- and higher-valence states might be another useful strategy. An existing example is in the lanthanum gallate ($LaGaO_3$) based materials system, co-doping Nb and Mg has been reported to block the oxygen vacancies migration due to the increased Columbic attractions between the dopant and mobile anions [75]. However, the modification of the perovskite crystal might also ruin its fantastic optoelectronic properties. Deeper insights on why hybrid perovskite materials could work so well for photovoltaic application are hence desired for the designs of new OTP materials.

6 Conclusions

In conclusion, this chapter discussed the ion migration phenomenon and its impacts on OTP materials and solar cells. There have been significant advances in past two years. The increasing progress overwhelmingly proved that ion migration takes place in OTP polycrystalline films in many different forms. More deep insights about ion migration in perovskite solar cells are desired for the understanding of device working mechanism, the suppressing of *I-V* hysteresis, and the increasing of

device stabilities. So far, as suggested in our review paper [7], this study is still in its infancy, there are a group of open questions to be answered, such as (1) How many kinds of ions migrate in OTP films at room temperature? (2) How much ions migrate in optimized OTP solar cells with ignorable photocurrent hysteresis? (3) What is the major migration channel in polycrystalline OTP films? (4) How does the ion migration influence the long-term stability of the OTP solar cells? (5) How to modify the composition of the OTP materials to eliminate ion migration without lossing its excellent optoelectronic properties? It is encouraging to see that the performance of OTP solar cells is becoming competitive with silicon solar cells. Because of this, addressing the ion migration effect in OTP materials is rising as one of the most pressing problems for the commercialization of OTP solar cells.

References

1. Mizusaki, J., Arai, K., Fueki, K.: Ionic conduction of the perovskite-type halides. Solid State Ion. **11**, 203–211 (1983)
2. Unger, E., Hoke, E., Bailie, C., Nguyen, W., Bowring, A., Heumüller, T., Christoforo, M., McGehee, M.: Hysteresis and transient behavior in current–voltage measurements of hybrid-perovskite absorber solar cells. Energy Environ. Sci. **7**, 3690–3698 (2014)
3. Snaith, H.J., Abate, A., Ball, J.M., Eperon, G.E., Leijtens, T., Noel, N.K., Stranks, S.D., Wang, J.T.-W., Wojciechowski, K., Zhang, W.: Anomalous hysteresis in perovskite solar cells. J. Phys. Chem. Lett. **5**, 1511–1515 (2014)
4. Xiao, Z., Yuan, Y., Shao, Y., Wang, Q., Dong, Q., Bi, C., Sharma, P., Gruverman, A., Huang, J.: Giant switchable photovoltaic effect in organometal trihalide perovskite devices. Nat. Mater. **14**, 193–198 (2015)
5. Bag, M., Renna, L.A., Adhikari, R.Y., Karak, S., Liu, F., Lahti, P.M., Russell, T.P., Tuominen, M.T., Venkataraman, D.: Kinetics of in ion transport perovskite active layers and its implications for active layer stability. J. Am. Chem. Soc. **137**, 13130–13137 (2015)
6. Tress, W., Marinova, N., Moehl, T., Zakeeruddin, S., Nazeeruddin, M.K., Grätzel, M.: Understanding the rate-dependent J-V hysteresis, slow time component, and aging in CH 3 NH 3 PbI 3 perovskite solar cells: the role of a compensated electric field. Energy Environ. Sci. **8**, 995–1004 (2015)
7. Yuan, Y.; Huang, J.: Ion migration in organometal trihalide perovskite and its impact on photovoltaic efficiency and stability. Acc. Chem. Res. **2016**. doi:10.1021/acs.accounts.5b00420
8. Chin, X.Y., Cortecchia, D., Yin, J., Bruno, A., Soci, C.: Lead iodide perovskite light-emitting field-effect transistor. Nat. Commun. **6**, 7383 (2015)
9. Juarez-Perez, E.J., Sanchez, R.S., Badia, L., Garcia-Belmonte, G., Kang, Y.S., Mora-Sero, I., Bisquert, J.: Photoinduced giant dielectric constant in lead halide perovskite solar cells. J. Phys. Chem. Lett. **5**, 2390–2394 (2014)
10. Lin, Q., Armin, A., Nagiri, R.C.R., Burn, P.L., Meredith, P.: Electro-optics of perovskite solar cells. Nat. Photonics **9**, 106–112 (2014)
11. Hoke, E.T., Slotcavage, D.J., Dohner, E.R., Bowring, A.R., Karunadasa, H.I., McGehee, M. D.: Reversible photo-induced trap formation in mixed-halide hybrid perovskites for photovoltaics. Chem. Sci. **6**, 613–617 (2015)
12. Deng, Y., Xiao, Z., Huang, J.: Light induced self-poling effect in organometal trihalide perovskite solar cells for increased device efficiency and stability. Adv. Energy Mater. **5**, 1500721 (2015)

13. Yuan, Y., Chae, J., Shao, Y., Wang, Q., Xiao, Z., Centrone, A., Huang, J.: Photovoltaic switching mechanism in lateral structure hybrid perovskite solar cells. Adv. Energy Mater. **5**, 1500615 (2015)
14. Hull, S.: Superionics: crystal structures and conduction processes. Rep. Prog. Phys. **67**, 1233 (2004)
15. Ilschner, B.: Determination of the electronic conductivity in silver halides by means of polarization measurements. J. Chem. Phys. **28**, 1109–1112 (1958)
16. Yashima, M.: Diffusion pathway of mobile ions and crystal structure of ionic and mixed conductors-a brief review. J. Ceram. Soc. Jpn. **117**, 1055–1059 (2009)
17. Cherry, M., Islam, M.S., Catlow, C.: Oxygen ion migration in perovskite-type oxides. J. Solid State Chem. **118**, 125–132 (1995)
18. Yashima, M., Nomura, K., Kageyama, H., Miyazaki, Y., Chitose, N., Adachi, K.: Conduction path and disorder in the fast oxide-ion conductor (La 0.8 Sr 0.2)(Ga 0.8 Mg 0.15 Co 0.05) O 2.8. Chem. Phys. Lett. **380**, 391–396 (2003)
19. Yashima, M.; Tsuji, T.: Structural investigation of the cubic perovskite-type doped lanthanum cobaltite La0. 6Sr0. 4CoO3 − δ at 1531 K: possible diffusion path of oxygen ions in an electrode material. J. Appl. Crystal. **40**, 1166–1168 (2007)
20. Yashima, M., Kobayashi, S., Yasui, T.: Positional disorder and diffusion path of oxide ions in the yttria-doped ceria Ce 0.93 Y 0.07 O 1.96. Faraday Discuss. **134**, 369–376 (2007)
21. Yashima, M., Tsuji, T.: Crystal Structure, Disorder, and Diffusion Path of Oxygen Ion CONDUCTORS Y1-x Ta x O1. 5 + x (x = 0.215 and 0.30). Chem. Mater. **19**, 3539–3544 (2007)
22. Eames, C., Frost, J.M., Barnes, P.R., O'regan, B.C., Walsh, A., Islam, M.S.: Ionic transport in hybrid lead iodide perovskite solar cells. *Nat. Commun.* **2015**, 6, 7497
23. Almora, O., Zarazua, I., Mas-Marza, E., Mora-Sero, I., Bisquert, J., Garcia-Belmonte, G.: Capacitive dark currents, hysteresis, and electrode polarization in lead halide perovskite solar cells. J. Phys. Chem. Lett. **6**, 1645–1652 (2015)
24. Shi, J., Xu, X., Zhang, H., Luo, Y., Li, D., Meng, Q.: Intrinsic slow charge response in the perovskite solar cells: Electron and ion transport. Appl. Phys. Lett. **107**, 163901 (2015)
25. Azpiroz, J.M., Mosconi, E., Bisquert, J., De Angelis, F.: Defects migration in methylammonium lead iodide and their role in perovskite solar cells operation. Energy Environ. Sci. **8**, 2118–2127 (2015)
26. Haruyama, J., Sodeyama, K., Han, L., Tateyama, Y.: First-principles study of ion diffusion in perovskite solar cell sensitizers. J. Am. Chem. Soc. **137**, 10048–10051 (2015)
27. Egger, D.A., Kronik, L., Rappe, A.M.: Theory of hydrogen migration in organic–inorganic halide perovskites. Angew. Chem. Int. Ed. **54**, 12437–12441 (2015)
28. Guillemoles, J.-F., Rau, U., Kronik, L., Schock, H.-W., Cahen, D.: Cu (In, Ga) Se2 solar cells: device stability based on chemical flexibility. Adv. Mater. **11**, 957–961 (1999)
29. Bourgoin, J., Corbett, J.: A new mechanism for interstistitial migration. Phys. Lett. A **38**, 135–137 (1972)
30. Yin, W.-J., Shi, T., Yan, Y.: Unusual defect physics in CH3NH3PbI3 perovskite solar cell absorber. Appl. Phys. Lett. **104**, 063903 (2014)
31. Leijtens, T., Hoke, E.T. Grancini, G.. Slotcavage, D.J., Eperon, G.E.; Ball, J.M., De Bastiani, M., Bowring, A.R.; Martino, N., Wojciechowski, K.: Mapping electric field-induced switchable poling and structural degradation in hybrid lead halide perovskite thin films. Adv. Energy Mater. **5** (2015)
32. Yang, T.Y., Gregori, G., Pellet, N., Grätzel, M., Maier, J.: The significance of ion conduction in a hybrid organic-inorganic lead-iodide-based perovskite photosensitizer. Angew. Chem. Int. Ed. **54**, 7905–7910 (2015)
33. Yuan, Y., Wang, Q., Shao, Y., Lu, H., Li, T., Gruverman, A., Huang, J.: Electric field driven reversible conversion between methylammonium lead triiodide perovskites and lead iodide at elevated temperature. Adv. Energy Mater. **6**, 1501803 (2015)

34. De Bastiani, M., Dell'Erba, G., Gandini, M., D'Innocenzo, V., Neutzner, S., Kandada, A.R.S., Grancini, G., Binda, M., Prato, M., Ball, J.M.: Ion migration and the role of preconditioning cycles in the stabilization of the j-v characteristics of inverted hybrid perovskite solar cells. Adv. Energy Mater. **6**, 1501453 (2016)
35. Zhang, H., Lin, H., Liang, C., Liu, H., Liang, J., Zhao, Y., Zhang, W., Sun, M., Xiao, W., Li, H.: Organic-Inorganic perovskite light-emitting electrochemical cells with a large capacitance. Adv. Funct. Mater. **25**, 7226–7232 (2015)
36. Li, C., Tscheuschner, S., Paulus, F., Hopkinson, P.E., Kießling, J., Köhler, A., Vaynzof, Y., Huettner, S.: Iodine migration and its effect on hysteresis in perovskite solar cells. Adv. Mater. (2016). doi:10.1002/adma.201503832
37. Chen, Q., De Marco, N., Yang, Y.M., Song, T.-B., Chen, C.-C., Zhao, H., Hong, Z., Zhou, H., Yang, Y.: Under the spotlight: The organic–inorganic hybrid halide perovskite for optoelectronic applications. Nano Today **10**, 355–396 (2015)
38. Wang, Q., Shao, Y., Dong, Q., Xiao, Z., Yuan, Y., Huang, J.: Large fill-factor bilayer iodine perovskite solar cells fabricated by a low-temperature solution-process. Energy Environ. Sci. **7**, 2359–2365 (2014)
39. Wang, Q., Shao, Y., Xie, H., Lyu, L., Liu, X., Gao, Y., Huang, J.: Qualifying composition dependent p and n self-doping in CH3NH3PbI3. Appl. Phys. Lett. **105**, 163508 (2014)
40. Yu, H., Lu, H., Xie, F., Zhou, S., Zhao, N.: Native Defect-Induced Hysteresis Behavior in Organolead Iodide Perovskite Solar Cells. Adv. Funct. Mater. (2016). doi:10.1002/adfm.201504997
41. Kim, J., Lee, S.-H., Lee, J.H., Hong, K.-H.: The role of intrinsic defects in methylammonium lead iodide perovskite. J. Phys. Chem. Lett. **5**, 1312–1317 (2014)
42. Buin, A., Pietsch, P., Xu, J., Voznyy, O., Ip, A.H., Comin, R., Sargent, E.H.: Materials processing routes to trap-free halide perovskites. Nano Lett. **14**, 6281–6286 (2014)
43. Walsh, A., Scanlon, D.O., Chen, S., Gong, X., Wei, S.H.: Self-regulation mechanism for charged point defects in hybrid halide perovskites. Angew. Chem. Int. Ed. **127**, 1811–1814 (2015)
44. Dong, R., Fang, Y., Chae, J., Dai, J., Xiao, Z., Dong, Q., Yuan, Y., Centrone, A., Zeng, X.C., Huang, J.: High-gain and low-driving-voltage photodetectors based on organolead triiodide perovskites. Adv. Mater. **27**, 1912–1918 (2015)
45. Chen, Q., Zhou, H., Song, T.-B., Luo, S., Hong, Z., Duan, H.-S., Dou, L., Liu, Y., Yang, Y.: Controllable self-induced passivation of hybrid lead iodide perovskites toward high performance solar cells. Nano Lett. **14**, 4158–4163 (2014)
46. Choi, J.J., Yang, X., Norman, Z.M., Billinge, S.J., Owen, J.S.: Structure of methylammonium lead iodide within mesoporous titanium dioxide: active material in high-performance perovskite solar cells. Nano Lett. **14**, 127–133 (2013)
47. Wu, B., Fu, K., Yantara, N., Xing, G., Sun, S., Sum, T.C., Mathews, N.: Charge accumulation and hysteresis in perovskite-based solar cells: an electro-optical analysis. Adv. Energy Mater. **5**, 1500829 (2015)
48. Jeon, N.J., Noh, J.H., Kim, Y.C., Yang, W.S., Ryu, S., Seok, S.I.: Solvent engineering for high-performance inorganic–organic hybrid perovskite solar cells. Nat. Mater. **13**, 897–903 (2014)
49. Lian, J., Wang, Q., Yuan, Y., Shao, Y., Huang, J.: Organic solvent vapor sensitive methylammonium lead trihalide film formation for efficient hybrid perovskite solar cells. J. Mater. Chem. A **3**, 9146–9151 (2015)
50. You, J., Yang, Y.M., Hong, Z., Song, T.-B., Meng, L., Liu, Y., Jiang, C., Zhou, H., Chang, W.-H., Li, G.: Moisture assisted perovskite film growth for high performance solar cells. Appl. Phys. Lett. **105**, 183902 (2014)
51. Xiao, Z., Dong, Q., Bi, C., Shao, Y., Yuan, Y., Huang, J.: Solvent annealing of perovskite-induced crystal growth for photovoltaic-device efficiency enhancement. Adv. Mater. **26**, 6503–6509 (2014)

52. Zhou, Z., Wang, Z., Zhou, Y., Pang, S., Wang, D., Xu, H., Liu, Z., Padture, N.P., Cui, G.: Methylamine-gas-induced defect-healing behavior of CH3NH3PbI3 thin films for perovskite solar cells. Angew. Chem. Int. Ed. **54**, 9705–9709 (2015)
53. Leijtens, T., Hoke, E.T., Grancini, G., Slotcavage, D.J., Eperon, G.E., Ball, J.M., De Bastiani, M., Bowring, A.R., Martino, N., Wojciechowski, K.: Mapping electric field-induced switchable poling and structural degradation in hybrid lead halide perovskite thin films. Adv. Energy Mater. **5**, 1500962 (2015)
54. Dong, Q., Song, J., Fang, Y., Shao, Y., Ducharme, S., Huang, J.: Lateral-structure single-crystal hybrid perovskite solar cells through piezoelectric poling (2015). doi:10.1002/adma.201505244
55. Gottesman, R., Haltzi, E., Gouda, L., Tirosh, S., Bouhadana, Y., Zaban, A., Mosconi, E., De Angelis, F.: Extremely slow photoconductivity response of CH3NH3PbI3 perovskites suggesting structural changes under working conditions. J. Phys. Chem. Lett. **5**, 2662–2669 (2014)
56. Feng, C., Yin, W.-J., Nie, J., Zu, X., Huda, M.N., Wei, S.-H., Al-Jassim, M.M., Yan, Y.: Possible effects of oxygen in Te-rich Σ3 (112) grain boundaries in CdTe. Solid State Commun. **152**, 1744–1747 (2012)
57. Yin, W.-J., Wu, Y., Noufi, R., Al-Jassim, M., Yan, Y.: Defect segregation at grain boundary and its impact on photovoltaic performance of CuInSe2. Appl. Phys. Lett. **102**, 193905 (2013)
58. Yin, W.J., Wu, Y., Wei, S.H., Noufi, R., Al-Jassim, M.M., Yan, Y.: Engineering grain boundaries in cu2znsnse4 for better cell performance: a first-principle study. Adv. Energy Mater. **4**, 1300712 (2014)
59. Yin, W.-J., Yang, J.-H., Kang, J., Yan, Y., Wei, S.-H.: Halide perovskite materials for solar cells: a theoretical review. J. Mater. Chem. A **3**, 8926–8942 (2015)
60. Zhao, Y., Liang, C., Zhang, H., Li, D., Tian, D., Li, G., Jing, X., Zhang, W., Xiao, W., Liu, Q.: Anomalously large interface charge in polarity-switchable photovoltaic devices: an indication of mobile ions in organic–inorganic halide perovskites. Energy Environ. Sci. **8**, 1256–1260 (2015)
61. Zhang, Y., Liu, M., Eperon, G.E., Leijtens, T.C., McMeekin, D., Saliba, M., Zhang, W., De Bastiani, M., Petrozza, A., Herz, L.M.: Charge selective contacts, mobile ions and anomalous hysteresis in organic–inorganic perovskite solar cells. Mater. Horiz. **2**, 315–322 (2015)
62. Shao, Y., Xiao, Z., Bi, C., Yuan, Y., Huang, J.: Origin and elimination of photocurrent hysteresis by fullerene passivation in CH3NH3PbI3 planar heterojunction solar cells. Nat. Commun. **5**, 5784 (2014)
63. Kim, H.-S., Park, N.-G.: Parameters affecting I-V hysteresis of CH3NH3PbI3 perovskite solar cells: effects of perovskite crystal size and mesoporous TiO2 layer. J. Phys. Chem. Lett. **5**, 2927–2934 (2014)
64. Hu, M., Bi, C., Yuan, Y., Bai, Y., Huang, J.: Stabilized wide bandgap mapbbrxi3-x perovskite by enhanced grain size and improved crystallinity. Adv. Sci. (2015). doi:10.1002/advs.201500301
65. Yang, B., Dyck, O., Poplawsky, J., Keum, J., Puretzky, A., Das, S., Ivanov, I., Rouleau, C., Duscher, G., Geohegan, D.: Perovskite solar cells with near 100 % internal quantum efficiency based on large single crystalline grains and vertical bulk heterojunctions. J. Am. Chem. Soc. **137**, 9210–9213 (2015)
66. van Reenen, S., Kemerink, M., Snaith, H.J.: Modeling anomalous hysteresis in perovskite solar cells. J. Phys. Chem. Lett. **6**, 3808–3814 (2015)
67. Chen, B., Yang, M., Zheng, X., Wu, C., Li, W., Yan, Y., Bisquert, J., Garcia-Belmonte, G., Zhu, K., Priya, S.: Impact of capacitive effect and ion migration on the hysteretic behavior of perovskite solar cells. J. Phys. Chem. Lett. **6**, 4693–4700 (2015)
68. Almora, O., Guerrero, A., Garcia-Belmonte, G.: Ionic charging by local imbalance at interfaces in hybrid lead halide perovskites. Appl. Phys. Lett. **108**, 043903 (2016)
69. Coll, M., Gomez, A., Mas-Marza, E., Almora, O., Garcia-Belmonte, G., Campoy-Quiles, M., Bisquert, J.: Polarization switching and light-enhanced piezoelectricity in lead halide perovskites. J. Phys. Chem. Lett. **6**, 1408–1413 (2015)

70. Mei, A., Li, X., Liu, L., Ku, Z., Liu, T., Rong, Y., Xu, M., Hu, M., Chen, J., Yang, Y.: A hole-conductor–free, fully printable mesoscopic perovskite solar cell with high stability. Science **345**, 295–298 (2014)
71. Strukov, D.B., Snider, G.S., Stewart, D.R., Williams, R.S.: The missing memristor found. Nature **453**, 80–83 (2008)
72. Wu, S., Xu, L., Xing, X., Chen, S., Yuan, Y., Liu, Y., Yu, Y., Li, X., Li, S.: Reverse-bias-induced bipolar resistance switching in Pt/TiO2/SrTi0. 99Nb0. 01O3/Pt devices. Appl. Phys. Lett. **93**, 43502 (2008)
73. Noh, J.H., Im, S.H., Heo, J.H., Mandal, T.N., Seok, S.I.: Chemical management for colorful, efficient, and stable inorganic–organic hybrid nanostructured solar cells. Nano Lett. **13**, 1764–1769 (2013)
74. Bi, C., Wang, Q., Shao, Y., Yuan, Y., Xiao, Z., Huang, J.: Non-wetting surface-driven high-aspect-ratio crystalline grain growth for efficient hybrid perovskite solar cells. Nat. Commun. **6**, 7747 (2015)
75. Kharton, V., Viskup, A., Yaremchenko, A., Baker, R., Gharbage, B., Mather, G., Figueiredo, F., Naumovich, E., Marques, F.: Ionic conductivity of La (Sr) Ga (Mg, M) O 3 − δ (M = Ti, Cr, Fe Co, Ni): effects of transition metal dopants. Solid State Ion. **132**, 119–130 (2000)
76. Xu, J., Buin, A., Ip, A.H., Li, W., Voznyy, O., Comin, R., Yuan, M., Jeon, S., Ning, Z., McDowell, J.J.: Perovskite-fullerene hybrid materials suppress hysteresis in planar diodes. Nat. Commun. **6**, 7081 (2015)

Impedance Characteristics of Hybrid Organometal Halide Perovskite Solar Cells

Juan Bisquert, Germà Garcia-Belmonte and Antonio Guerrero

Organometal Halide Perovskite Photovoltaics: Fundamentals and Device Arquitectures.
—Editors Nam-Gyu Park, Michael Grätzel and Tsutomu Miyasaka. Springer.

Abstract This chapter describes the application of impedance spectroscopy and an array of related experimental techniques used to understand the operation principles of lead halide perovskite solar cells and their related materials. The main topic of the chapter is the identification of capacitances and their origin, which is related to ion accumulation, electron accumulation, or a combination of both. In addition to impedance spectroscopy, we examine a number of charging or time transient techniques that are performed by a voltage step or continuous cycling, including capacitance–voltage characterization and Kelvin probe force microscopy. The interpretation is carried out using several experimental modifications such as application of different contacts, sample thickness, and temperature. The relationship of hysteresis to capacitance is also addressed, as well as the degradation at contacts by ionic accumulation and reaction.

1 Introduction

The research on hybrid organic–inorganic perovskite solar cells is growing rapidly with multiple facets nowadays. Efficiencies for these cells have been rising at a phenomenal speed with a certified value over 21 %. A rich variety of fabrication methods have been reported with the aim toward production of low-cost large-scale devices, especially focusing on robust deposition methods and stability of the solar cell. Indeed, an increasing number of composition/configuration types are being investigated and there is a need to clarify optimal preparation methods, i.e., pre-

J. Bisquert (✉) · G. Garcia-Belmonte · A. Guerrero
Institute of Advanced Materials (INAM), Universitat Jaume I, 12006 Castelló, Spain
e-mail: bisquert@uji.es

G. Garcia-Belmonte
e-mail: garciag@uji.es

A. Guerrero
e-mail: aguerrer@uji.es

N.-G. Park et al. (eds.), *Organic-Inorganic Halide Perovskite Photovoltaics*,
DOI 10.1007/978-3-319-35114-8_7

cursors used and preparation routes. These objectives require sound characterization methods that relate the structure of the device to its functioning. At present, it is clear that the hybrid organic–inorganic perovskite materials display a range of fascinating properties that support the extraordinary photovoltaic performance. However, the principles of photovoltaic and photophysical operation are not clear yet in the perovskite photovoltaic devices. A number of key issues hindering further developments need to be investigated thoroughly and solved. For a sound understanding of the solar cell device, it is necessary to clarify the dynamic processes that occur in the low frequency to intermediate frequency domain and their relationship to materials and structure combinations in the device. This chapter will address the challenging characterization of perovskite solar cell devices using impedance spectroscopy and a variety of related techniques that we describe in the following.

The presence of significant time transient behavior has been recognized early on in perovskite solar cells and there are varied and complex phenomena that need a suitable classification [64]. There exists a fundamental correspondence between small perturbation decay in time transient techniques and small perturbation ac methods as impedance spectroscopy, therefore in order to establish a coherent picture of perovskite solar cell internal dynamics it is important to combine an array of experimental methods as indicated in Fig. 1.

When a physical element R_1C_1 as shown in Fig. 1 is perturbed with a step voltage, the electric current decays with exponential shape defined by the characteristic time

$$\tau = R_1 C_1 \tag{1}$$

as indicated in (a). If the perturbation is ac voltage, the relation ac voltage to current is a complex impedance, Z. For the parallel circuit in Fig. 1, the impedance spectrum traces a semicircle in the complex plane as shown in Fig. 1b. In addition a continuous change of voltage outlined in c, shows important information as capacitive components and the steady-state current density-voltage (J–V) curve.

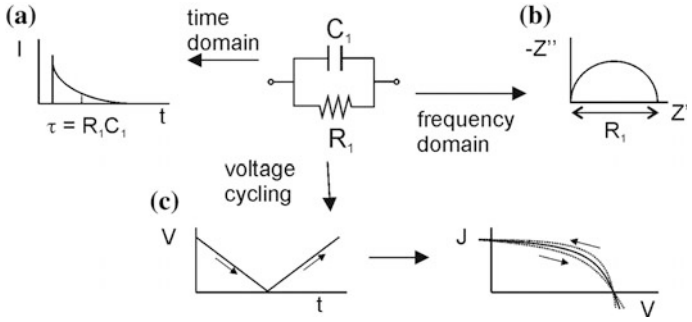

Fig. 1 Parallel RC equivalent circuit, and the experimental signatures in time and frequency domain. **a** Current density decay after a step voltage. **b** Impedance spectroscopy. **c** Voltage cycling leading to current density-voltage curve

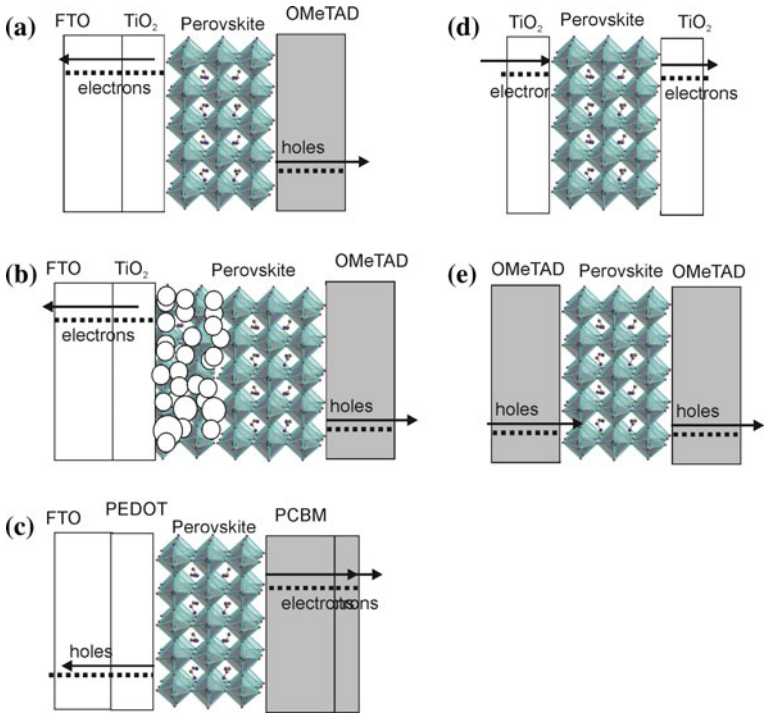

Fig. 2 Different types of samples configurations consisting of perovskite layer with caying contacts. The Fermi levels of electrons and holes at the contacts are sown in dashed line. **a**–**c** diode configuration (solar cell) with **a** mesoporous and **b** planar metal oxide layer at the transparent side. **c** "inverted" structure with a hole conductor at the transparent side. **d**, **e** Symmetric devices with electron selective contacts (**d**) and hole selective contacts (**e**)

In this chapter, we describe the application of these techniques in order to obtain a detailed picture of the operation of perovskite solar cells, based on $CH_3NH_3PbI_3$ (or $MAPI_3$) and their multiple compositional variants. The structure of the cell is formed by perovskite-absorber and selective contacts for extraction of electrons and holes as shown in Fig. 2a. Additional energetic features as band bending will be discussed later on. Particularly important in the study of perovskite solar cells has been the ability to use a variety of contact types, which often modify drastically the performance and properties of perovskite solar cells. As shown in Fig. 2 one may distinguish several typical configurations depending on the contacts: (a) planar or (b) mesoporous metal oxide layer at the transparent side, or use a hole conductor at the transparent side, (c) ("inverted" structure). The use of symmetric devices (d, e) has produced very large rewards in terms of understanding as discussed in Sect. 7.

2 Capacitive Charging and Hysteresis

In the analysis of solar cells, impedance and time transient small perturbation measurement have been widely used for the determination of devices' characteristics and lifetimes [10, 22]. However, the central type of measurement in solar cells is the J–V curve at steady state. From this curve the main parameters that characterize solar to electricity conversion characteristics at steady-state operation are extracted: photocurrent, photovoltage, fill factor, and power conversion efficiency. This measurement requires a nearly continuous voltage scan, which is carried out at certain voltage steps, with simultaneous measurement of current, as indicated in Fig. 2c. The scan can begin at the value of open-circuit voltage, V_{oc}, toward the point of $V = 0$, that is from forward to reverse bias, or the other way around. If the step size ΔV requires a time interval Δt, then the scan rate is

$$s = \frac{\Delta V}{\Delta t} \tag{2}$$

This procedure is the same as in the standard technique of cyclic voltammetry in electrochemistry. It is important to recall the behavior of a capacitor in this type of measurement [23]. For a single constant capacitor C the charging current is obtained by time derivative of the charge in the capacitor,

$$J_C = \frac{\mathrm{d}Q}{\mathrm{d}t} = C\frac{\mathrm{d}V}{\mathrm{d}t} \tag{3}$$

and the result is

$$J_C = Cs \tag{4}$$

As observed in Fig. 3, by cycling the voltage between two points, capacitive charging produces a current that is proportional to scan rate s, and furthermore the current is inverted when the scan direction changes sign. Therefore, the signature of capacitive current is a symmetric current with respect to the average value. For a

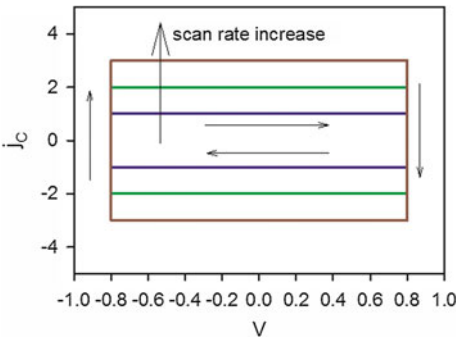

Fig. 3 Capacitive current resulting from cycling the voltage applied to the capacitor at increasing scan rates

single capacitor the average value is 0 as indicated in Fig. 3. But in general the capacitive current is added to other dc currents existing in the system. For a solar cell, the steady-state dc current is well characterized (neglecting internal resistances) by a photocurrent and diode curve of the form

$$J = J_{ph} - J_0\left(e^{qV/mk_BT} - 1\right) \tag{5}$$

Here J_{ph} is the photocurrent density, J_0 is the dark current density, q is elementary charge, k_BT is the thermal energy, and m is the diode quality factor. In consequence, the total current under voltage scan in a solar cell will be given by the addition of the characteristic (5), with capacitive current added or subtracted according to forward or reverse scan, respectively, as suggested by [64]. The result is shown in Fig. 4d, where it is observed that the separation from steady-state curve (the central curve, made at very slow scan rate) increases with voltage speed, as indicated in Fig. 3. This is the mark of capacitive hysteresis [15].

In order to describe in more detail the capacitive charging of the solar cell one needs to observe the transient current for each voltage step as in Fig. 5. In this figure, the response of devices with two different hole selective contacts, spiro-OMeTAD and CuI, are compared [65]. Obviously for the second case the transients are much shorter than for spiro-OMeTAD, which is related to a smaller

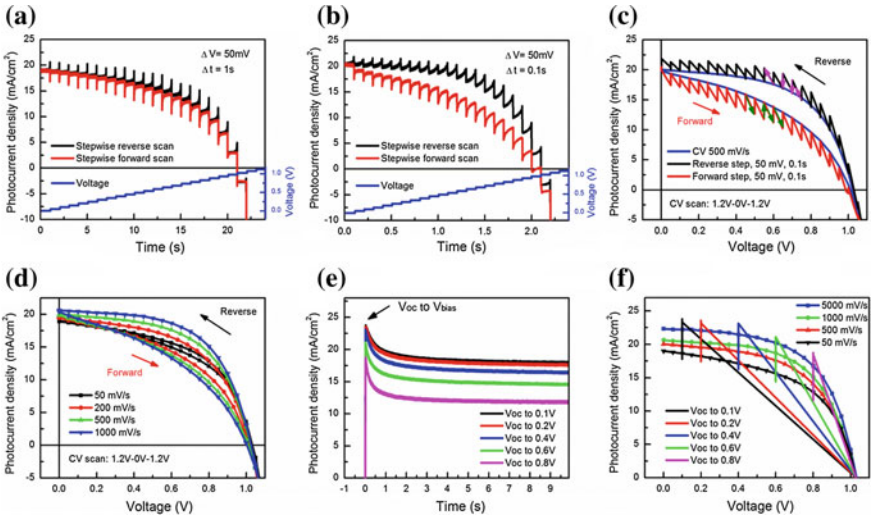

Fig. 4 Time transients of a perovskite solar cell formed by mesoporous (mp) TiO_2 electron contact, with 500 nm $CH_3NH_3PbI_3$ film as the light absorber layer and 150 nm Spiro-OMeTAD as the hole selective layer. Time-dependent photocurrent response under reverse and forward stepwise scans with **a** 1 s step time and **b** 0.1 s step time. **c** *J–V* response for the CV scan with 500 mV/s and corresponding stepwise scan. **d** *J–V* response for PSCs with different CV scan rates. **e** Dynamic photocurrent transient when switching the applied voltage from V_{oc} to different bias. **f** *J–V* response for the different reverse scans and dynamic photocurrent transient in (**e**). Reprinted from [15]

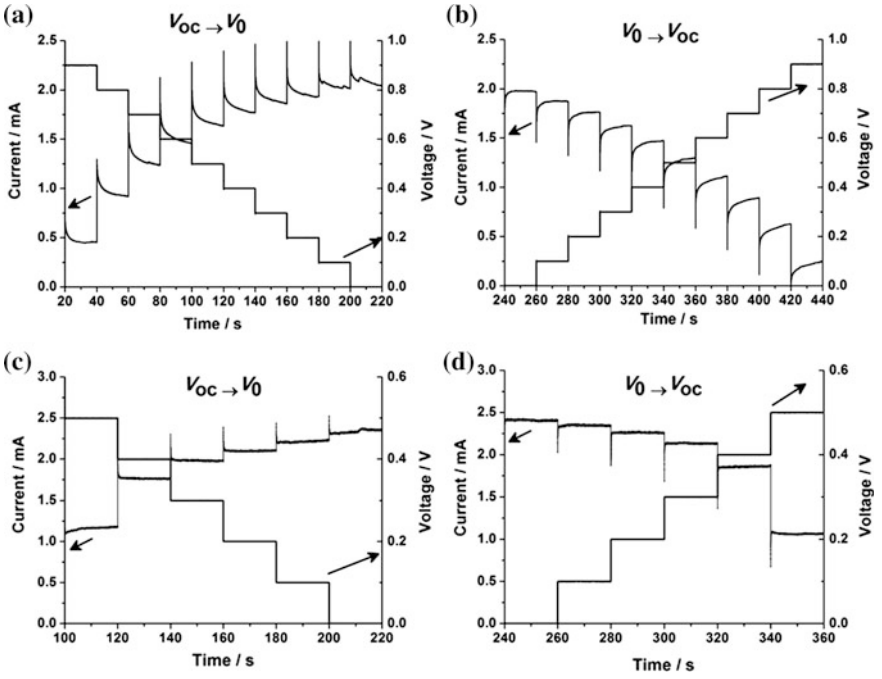

Fig. 5 Time transients using forward and reverse stepwise voltage sweeps for a perovskite solar cell formed by 50 nm planar TiO_2 electron contact, with 300–400 nm $CH_3NH_3PbI_3$ film as the light absorber layer, and two different hole selective contacts, **a**, **b** spiro-OMeTAD and **c**, **d** CuI. Reprinted from [65]

capacitance influencing the decay time as indicated in Fig. 1a. The low-frequency capacitance measured in these cells is shown in Fig. 6b. Similarly, the measurements in Fig. 4a, b illustrate the effect of capacitive current upon *J–V* curve. When the scan rate is slow (large Δt) as in Fig. 4a, the current has sufficient time to reach steady-state value corresponding to Eq. (5) [39, 70]. However, under fast scan rates Δt leaves the current on a transient value before the next voltage step comes in, so that the overall current stays above the stationary value, as shown in Fig. 4b. As expected the opposite sign of capacitive current occurs in the reverse scan, causing the opening of current with respect to steady-state value. This behavior depends on the scan rate indicated in Eq. (2) and not on separate values of Δt and ΔV, provided both are relatively small. Thus two different procedures are applied in Fig. 4c and they provide the same amount of capacitive hysteresis.

In addition to the capacitive hysteresis, another type of hysteresis has been widely reported, that depends not only on scan rate, but on previous pretreatments. Examples are shown in Fig. 7, that reveal that light soaking at forward bias improves the *J–V* characteristic, while light soaking at reverse bias has the opposite effect [70]. These results indicate the dramatic changes that occur in the perovskite solar cell devices when light and voltage have been applied [15, 27, 64].

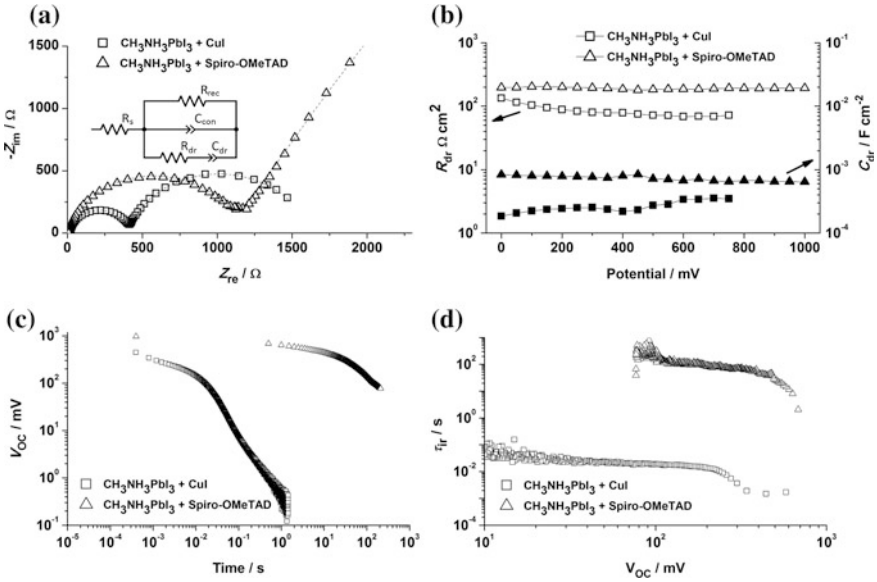

Fig. 6 **a** Complex plane impedance plots obtained for a CuI-based solar cell device (*circles*) and a spiro-OMeTAD-based device (*squares*). Fits are shown in the *dashed lines* and the equivalence circuit used for fitting the impedance response is provided in the inset. **b** Variation in resistance and capacitance as a function of potential for both devices. Impedance measurements were performed under constant illumination. **c** OCVD measurements for CuI-based and spiro-OMeTAD-based devices; and **d** their corresponding instantaneous relaxation time constants, τ_{ir}, as a function of the V_{oc}. Reprinted from [65]

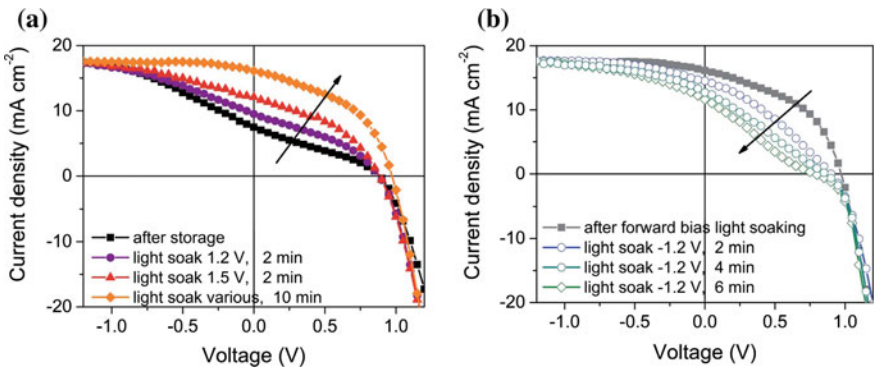

Fig. 7 **a** Light soaking at forward bias positively affects the current–voltage and hence the performance of thin film perovskite-absorber solar cells. The solar cells are formed by mesoporous (mp) TiO_2 electron contact, with 350 nm $CH_3NH_3PbI_3$ film as the light absorber layer and 150 nm Spiro-OMeTAD as the hole selective layer. **b** The reverse effect is observed after light soaking under reverse bias conditions with the IV-curves developing an S-shape. Reprinted from [70]

Importantly, it has been widely reported that the lead halide perovskite is a good ionic conductor, in which interstitials and vacants can move under internal forces [3]. Ionic movement of I^- and MA^+ have been suggested to take place under applied bias and/or illumination conditions [20, 75]. The drift of ions and/or vacancy turns the lead halide perovskite into a mixed ionic-electronic conductor, which creates a number of complexities of interpretation of electrical measurements as outlined in Fig. 8. When a bias voltage is applied to the asymmetric device, it is induced the displacement of different carriers, ionic, and electronic. However, whilst either type of electronic carrier can be transported through the solar cells, at contacts ionic carriers are blocked, so that in dc regime the ionic current is suppressed. This means that the electrochemical potential of ions must be constant, which implies a concentration gradient in opposite sense to the electrical field drift as explained by [32]. Figure 9 shows the study of galvanostatic charging of a thick symmetric sample at a constant current of 2 nA. Initially the current is maintained by both electronic and ionic current, but as an ionic gradient is established the ionic current is suppressed

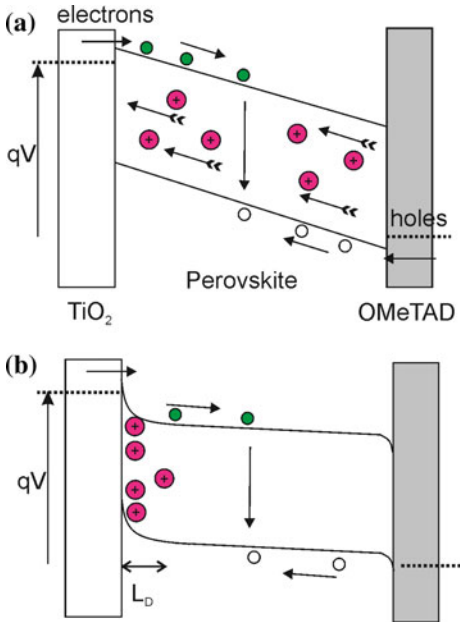

Fig. 8 Schematic diagrams indicating the different components of electric current in asymmetric perovskite device in the dark. **a** Starting from homogenous situation, forward applied bias voltage V introduces a drift field that causes the displacement of positively charged I^- vacants. The electronic current is produced by injection of electrons and holes at the respective contacts and recombination inside the perovskite layer. Note that ionic and electronic currents are marked by different types of *arrows*. **b** After a certain time the ionic drift causes accumulation of ions at the cathode that produces space charge and a diffusion current against the drift field. Eventually an equilibrium distribution of ions mainly at the cathode surface is obtained that will be controlled by the ionic Debye length L_D as indicated. Meanwhile the electronic recombination current persists as long as the voltage is applied

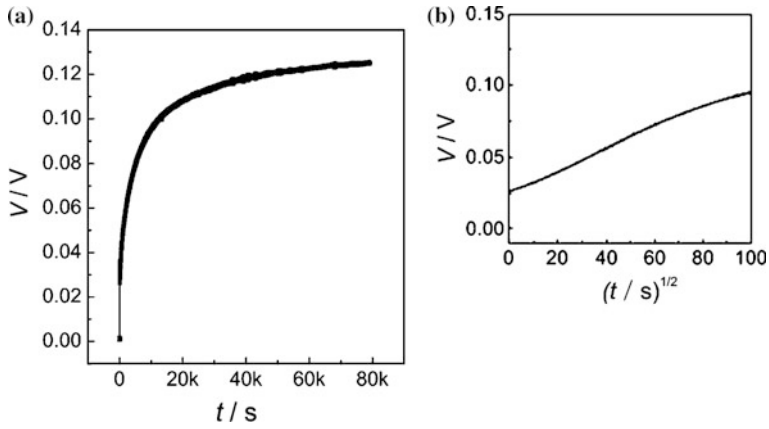

Fig. 9 **a** DC polarization curve for a symmetric Graphite/$MAPbI_3$/Graphite cell (thickness 0.6 mm) measured at 30 °C in Air flow by applying a current of 2 nA. **b** Voltage versus square root of time up to 10^4 s. Reprinted from [75]

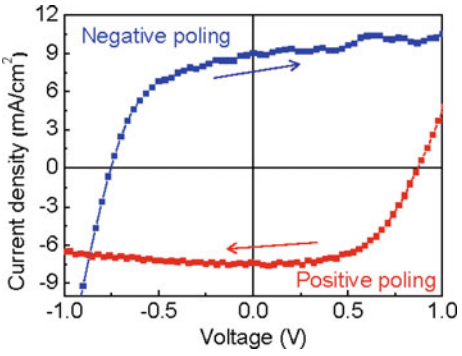

Fig. 10 Performance variation of ITO/PEDOT:PSS/Perovskite (300 nm)/Au vertical structure devices. The devices were poled at 6 V/μm for 20 s. The photocurrents were measured under 1 sun illumination at a sweep rate of 0.14 V/s. Reprinted from [74]

and more voltage is necessary to maintain the value of the current, that is purely electronic [75]. Strong evidence for the effects of ionic migration over contact barriers has been provided by Xiao et al. [74], see Fig. 10, who showed that short-time polarization of the perovskite layer can determine the contact type as hole or electron selective layer, independently of the type of metal contact. This type of inversion of *J*–*V* characteristics with respect to the type of contacts is widely reported in ferroelectric materials, and it is usually associated to the migration of defects or polarization changes that modify the injection barriers at contacts [43]. Reactivity between these moving ions and external contacts can dramatically impact the solar cell operation and stability as further discussed in Sect. 7.

Another widely reported observation is the large dependence of hysteresis on the type of contacts has been observed as shown in examples in Fig. 11. Such changes are strongly correlated with the low-frequency capacitance as indicated in Fig. 12 [37, 38].

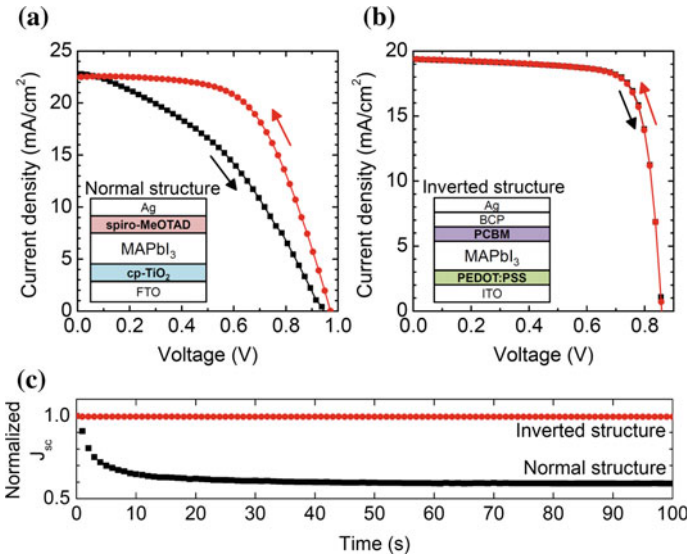

Fig. 11 *J–V* hysteresis and time-dependent photocurrent. **a** Scan direction-dependent *J–V* curves of the planar-TiO_2/$MAPbI_3$/spiro-MeOTAD (normal) structure and (**b**), the PEDOT:PSS/$MAPbI_3$/PCBM (inverted) structure. During *J–V* scan the current was acquired for 100 ms after applying a given voltage. **c** Normalized time-dependent J_{sc} of the normal and the inverted structures. Open-circuit condition under one sun illumination was maintained before measuring J_{sc}. Reprinted from [37, 38]

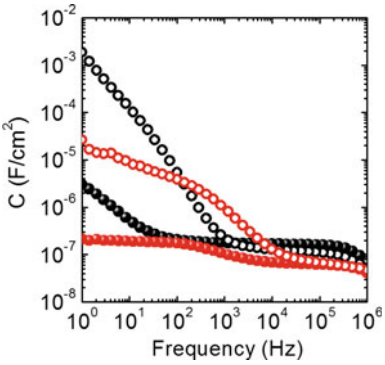

Fig. 12 Frequency-dependent capacitance C-*f* curves of the planar-TiO_2/$MAPbI_3$/spiro-MeOTAD (normal, *black*) structure, thickness 440 nm and the PEDOT:PSS/$MAPbI_3$/PCBM (inverted, *red*) structure, thickness 380 nm, in dark (*filled symbols*) and under one sun illumination at short-circuit condition (bias voltage = 0 V, *empty symbols*). Reprinted from [37, 38]

3 Ferroelectric Properties

Ferroelectric materials are characterized by a permanent electrical polarization. A typical phase transition to a nonferroelectric symmetric crystal phase occurs at the Curie temperature, where the macroscopic polarization ordering cannot be maintained. The transition is accompanied by a large variation of the dielectric constant. The polarization field can switch direction by an applied external field. In ferroelectric layers with metallic contacts the charges in the electrode compensate the bound polarization charge, which removes the internal polarization field. In practice ferroelectric materials can maintain internal electrical fields due to imperfect screening of polarization charge which creates an internal depolarization field.

As many perovskites are ferroelectric, in early studies of organic–inorganic photovoltaic perovskites the ferroelectric property was an appealing explanation of some exotic observations, for example very large dielectric constant, which are typical of oxide perovskites. In lead halide perovskite, three main mechanisms of polarization are expected: the orientational polarization of MA^+ cation (which has significant dipole moment), the ionic polarization induced by the shift of the positive charge center of MA^+ relative to the negative charge center of the PbI_3^- cage, and the ionic polarization induced by the off-center displacement of Pb within the PbI_6 octahedra. In order to determine the interest of such important property for the photovoltaic function, [18] utilized piezoelectric force microscopy (PFM), which is a variant of AFM that is widely used to image polarization structure and local switching in ferroelectric materials. The study of $MAPbI_3$ perovskite films showed piezo-phase hysteresis loops as seen in Fig. 13a. In principle this observation is evidence for ferroelectric polarization, but in contrast to a standard material as $BiFeO_3$, the polarization in the lead halide perovskite thin film vanishes in a matter of seconds. It is also observed that the coercivity is greatly enhanced under illumination, which would indicate the presence of a light-enhanced dipole [73].

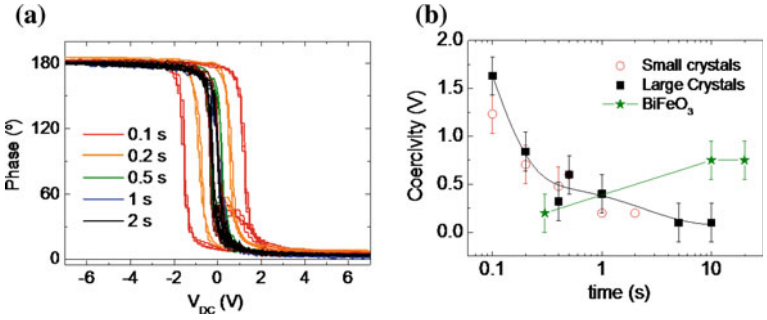

Fig. 13 **a** Piezo-phase hysteresis loops of $MAPbI_3$ thin films with small crystals performed at different acquisition times. **b** Coercivity dependence with time of $MAPbI_3$ films with small (*red open circles*) and large crystals (*black squares*) and 25 nm $BiFeO_3$ thin films (*green stars*). Reproduced from [18]

Another important effect that produces evidence for ferroelectric property is the observation of hysteresis in the cycling of polarization P with respect to voltage (or field). Since measurement of polarization is based on the integrated charge from the current, an internal leakage current completely masks the displacement current due to reordering of ferroelectric domain. This effect plagues the observation of ferroelectric hysteresis and is expected to be large for a high conductivity sample. Indeed [24] measured polarization dependence on applied field has failed to find ferroelectric loops but instead attributed the results to leakage currents. In the samples of [18] only capacitive response was observed, but not hysteresis in the P–V plot.

Being MA^+ the main polarization mechanism, the permanent polarization of $MAPI_3$ is due to alignment of MA cation molecules. The weak ferroelectricity of $MAPbI_3$ described above is in agreement with several theoretical and experimental works which indicate that the molecule is fully activated and free to rotate at room temperature [24, 45, 52, 54, 58, 61]. The observed polarization trends have been explained by computations of polarization ordering in tetragonal and orthorhombic phases [24, 25]. The ferroelectric ordering is effective only when the barrier for rotation of MA becomes significant, below 160 K, when the transition from tetragonal to orthorhombic occurs. This is why at room temperature the poling provides no significant image inversion [37, 38, 42]. Therefore, ferroelectric property does not seem to play a central role in electric and photoelectric behavior of the most widely used organic–inorganic perovskites. However, it is not yet known if the strong polar character of the perovskites is a central attribute to the excellent photovoltaic performance of these materials, e.g., via formation of polarons [79].

4 Nature of Capacitances in Perovskite Solar Cells: The Dark Capacitances

Interpretation of capacitance in perovskite solar cells is complicated by the wide variety of possible phenomena that can potentially cause capacitance response. The classification of these effects has been summarized in [11]. In brief, main aspects of the capacitance include: Dielectric capacitance, chemical capacitance, depletion layer at contact barrier (or possibly accumulation or inversion capacitances), and electrode polarization, consisting on ionic accumulation at the interface.

The main characteristics of measured capacitance in perovskite solar cells, have been described previously [2, 34] and are shown in Figs. 12 and 14. The capacitance in dark at room temperature is characterized by a high-frequency plateau that rises toward very large values as the frequency is reduced. The plateau is more or less visible depending on the onset of the low-frequency capacitance, see Fig. 12. Under illumination there is a very large increase of the low-frequency capacitance as indicated in Figs. 12 and 14, and these effects will be discussed in a separate section of this chapter.

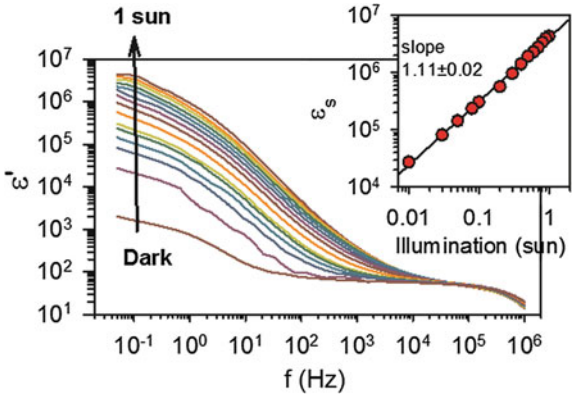

Fig. 14 Plot of the real permittivity as a function of frequency for different incident light intensity (Φ_0) from dark to 1 sun, for TiO_2/meso-Al_2O_3/$CH_3NH_3PbI_{3-x}Cl_x$/Spiro-OMeTAD/Au perovskite solar cell. Measurements have been carried out at room temperature and 0 V applied bias. Inset, linear regression of the dielectric constant at $f = 50$ MHz versus illumination intensity, observing a close to linear dependence between ε_s and intensity of illumination. Reprinted from [34]

The universal shape of capacitance dependence on frequency is composed of a series of plateaus. In between the plateau we obtain capacitance increments associated to different relaxation processes that determine the kinetics of each capacitance. At low frequencies all capacitive processes contribute but they are progressively canceled when moving to high frequencies [11]. Therefore, the general shape of capacitance plot has the form of Fig. 15a and the separate steps need to be physically characterized. However, the presence of frequency dispersion complicates this task. In this case a constant phase element (CPE) $Z = Q(i\omega)^{-n}$, where Q is a prefactor and $0 \leq n < 1$ is a constant exponent, replaces the capacitor. The capacitive impedance of this type provides a steady increment of $C(f)$ that masks the plateaus [11]. Thus the light curves in Fig. 14 have a steady decrease that is held up to very high frequencies, which forms a featureless spectrum that is hard to analyze. Major progress in understanding the dark capacitance has been obtained by measuring samples with modified thickness and temperature. Cooling the sample has revealed the nature of capacitive steps, as shown in Fig. 15b, c. It has thus been possible to separate: (i) the bulk polarization associated to dielectric relaxation of the sample, from (ii) the low-frequency capacitance. This large low-frequency capacitance has been largely ascribed to contact phenomena, in congruence with the hysteresis behavior described in the previous section.

The accumulation of ions at the contact interface produces a capacitance due to surface space charge, that responds in the low-frequency range of the measurement in ordinary ionic conductors [7, 48, 69]. This capacitance occurs in a short distance to the contact and it is independent of the active film thickness d, as indicated in

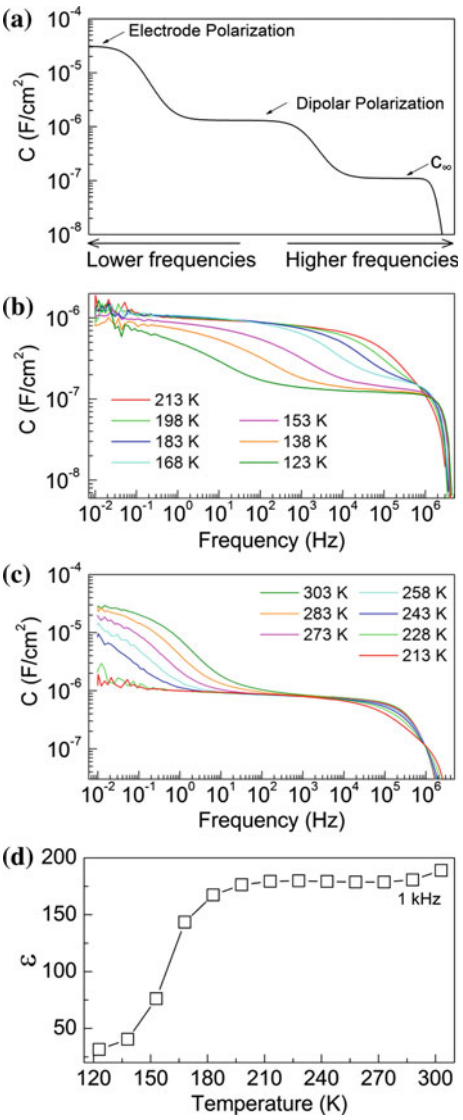

Fig. 15 Capacitance versus frequency at different temperatures (*dark*) of a perovskite solar cell formed by planar TiO_2 electron contact, with 400 nm $CH_3NH_3PbI_3$ film as the light absorber layer and 150 nm Spiro-OMeTAD as the hole selective layer. Reprinted from [2]

Fig. 8b. Electrode polarization gives rise to capacitances of order 10 μF cm^{-2}, and can be modeled following the classical Gouy–Chapman double-layer model [1, 36].

$$Q_{\text{diff}} = \frac{2\varepsilon\varepsilon_0 k_B T}{qL_D} \sinh\left(\frac{q\Delta\varphi}{2k_B T}\right) \tag{6}$$

Q_{diff} corresponds to the charge per unit area, $\Delta\varphi$ is the potential drop between the metallic contact and the absorber bulk, and the ion Debye length is given by

$$L_D = \sqrt{\frac{\varepsilon\varepsilon_0 k_B T}{q^2 N}} \tag{7}$$

Here N accounts for the density of ionic charges. By derivation with respect to the potential, Debye capacitance C_D is obtained at $\Delta\varphi = 0$:

$$C_D = \frac{\varepsilon\varepsilon_0}{L_D} \tag{8}$$

In equilibrium (zero bias) and room temperature, excess ion carriers accumulate within an extension (space charge region) equivalent to the Debye length.

In addition to the low-frequency features, as observed in Fig. 14 for measurement under dark at zero bias, capacitance spectra of $MAPbI_{3-x}Cl_x$–based planar devices show two steps appearing at low temperatures (120–180 K), and high temperatures (180–320 K), respectively, that are interpreted in terms of bulk perovskite polarization processes. The dielectric polarization has two main origins that compose the true dielectric constant ε of the perovskite material. First we have the dipolar relaxation mechanisms, which have been already indicated above in terms of ionic process: MA^+ cation rotation, the shift of MA^+ center relative to PbI_3^- cage, and the off-center displacement of Pb. In addition, when all atoms are frozen at higher frequencies (>1 GHz), electronic polarization phenomena exist that cause a small fraction of the low-frequency dielectric constant.

A number of papers reported previously the dielectric properties of lead halide perovskites. Work by [61] measured effective dielectric constant for $MAPbI_3$ at 300 K to be 33 at a frequency of 90 GHz. Other reports [59] provided a value of ca. 58 at a frequency of 1 kHz. In contrast, the dielectric constant, *in the absence of molecular reorientation*, is predicted to be 24.1 from electronic structure calculations (PBEsol QS*GW*) [12] in good agreement with the value of 23.3 determined from a fit of permittivity measurements over 100–300 K to the Kirkwood–Fröhlich equation.

The *high-frequency plateau* observed in Fig. 15b ($C = 100$ nF cm^{-2}) can be related to the perovskite permittivity of the orthorhombic phase dominating at low temperature in combination with the dielectric contribution of contacts layers as *spiro*-OMeTAD and TiO_2. Figure 15 also allows us to extract conclusions regarding the temperature variation of dielectric constant. Lead halide perovskite $MAPbX_3$ (X = Cl or Br) crystals undergo a phase transformation at $\sim$160 K between orthorhombic (γ-phase with $\varepsilon \approx 24$) and tetragonal (β-phase with $\varepsilon \approx 55$ at 300 K) structures [51]. Figure 15d shows that the phase transformation provokes a large increase of the dielectric constant that is observed when measuring the capacitance spectra of complete perovskite-based solar cells, in agreement with the literature based on symmetric samples. The low-temperature increment in Fig. 15c yields a permittivity value for the β-phase of $\varepsilon = 32.5$ at 300 K, in good agreement with other reports [13, 26]. It should be noted that a considerable extent of disparity is found among reported permittivity values ($\varepsilon \approx$ 24–55). Due to the fact that

perovskite films are polycrystalline and that TiO_2 layer is in some cases mesoporous, one can expect roughness factors as high as 3–5, as pointed out by [60]. Alternatively, when a voltage is applied towards positive bias (forward) the capacitance increases and this increase has been correlated with the modulation of a depletion capacitance as it will be described Sect. 5.

These observations are summarized in Fig. 15a that identifies the general structure of dark capacitance features in lead halide perovskite layers.

5 Capacitance–Voltage, Doping, Defects and Energy Level Diagram

Different mechanisms of collection efficiency in photovoltaic devices are determined by the carrier conductivities, diffusion length, and the electrical field distribution within the semiconductor material that combines diffusion transport with drift transport [41]. Charge transport of minority carriers throughout quasi-neutral zones occurs by diffusion in the bulk of the semiconductor. On the other hand, drift governs the carrier motion within the band bending regions close to the external contacts. The energetic offset between work functions of absorber and each contact material generates a built-in voltage V_{bi} in equilibrium conditions (Fig. 16a). Importantly, several profiles may be formed depending on the type of dopant, doping density and applied voltage.

Two techniques are especially useful to probe the electrical profile close to the contacts: Kelvin Probe Force Microscopy (KPFM) and Capacitance–Voltage (C–V). KPFM allows the direct observation and mapping of the electrical field distribution

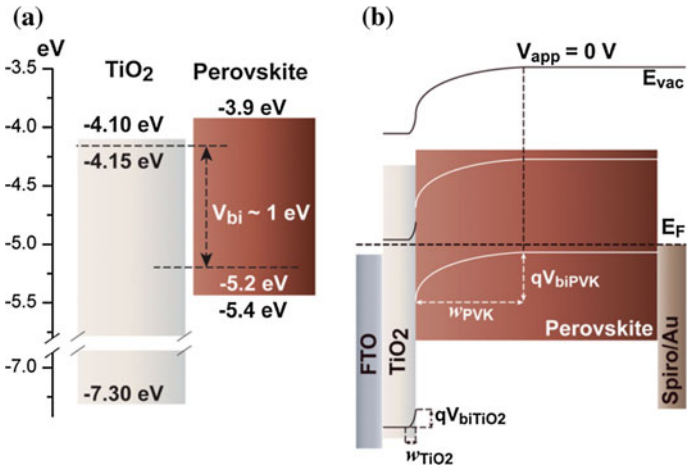

Fig. 16 **a** Illustrative energy diagram of TiO_2 and PVK. A built-in voltage approximately equal to 1 eV is expected. **b** Band diagram in equilibrium showing the formation of a *p-n* (perovskite-TiO_2) type heterojunction. Reproduced with permission from [29]

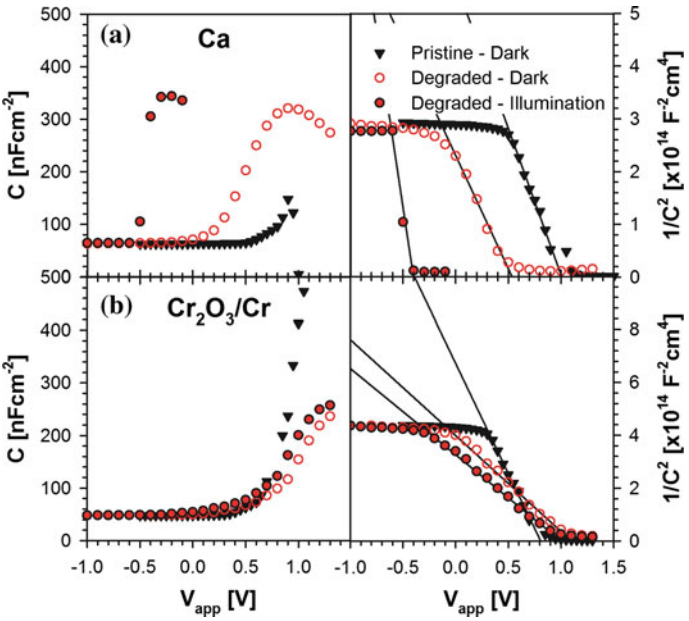

Fig. 17 Capacitance–Voltage and Mott–Schottky plots measured during degradation studies for devices in the configuration ITO/PEDOT:PSS/Perovskite/PCBM/Metal, **a** Ca and **b** Cr_2O_3/Cr. Reproduced with permission from Ref. [31]

in a device. Alternatively, *C–V* is an indirect technique where by measuring the capacitance of the semiconductor one can infer the doping density of defects and voltage at which bands are flat [30]. The operation principle of a *C–V* measurement is similar to that of impedance spectroscopy but the analysis is restricted to a single frequency during the ac perturbation. Capacitance–voltage measurement is a useful nondestructive technique to discriminate between effects taking place at the bulk of active layer and those occurring at the interfaces with the external contacts [28, 29]. Figure 17 shows the *C–V* analysis applied to a degradation experiment of perovskite solar cells.

By coupling of both techniques, perovskite devices have been shown to contain *p*-type defects and a *p-n* heterojunction is formed with the TiO_2 external contact (Fig. 16). In Refs. [29, 33] it was also observed this type of heterojunction at the electron selective contact and a large depletion layer which indicates that drift of minority carriers is necessary despite the long diffusion length generally reported in perovskite layers.

It has been noted in Sect. 4 that the capacitance in the high-frequency region is related to the perovskite permittivity. Indeed, full depletion occurs at negative (reverse) applied voltage and at short-circuit conditions for good performing devices ($\sim$16 % PCE) as the pristine devices shown by [31] in Fig. 17. However, as the voltage is applied toward positive bias (forward) an increase in the

capacitance is observed. This increase in capacitance is correlated to the width of the depletion zone of a Schottky barrier at the cathode, as supported by Kelvin Probe measurements [29]. The depletion zone decreases at positive bias voltage and as a consequence the capacitance increases, and by plotting $C^{-2}(V)$ a straight line is observed. The density of fully ionized defect states (p-doping level) N is derived from the slope by means of the Mott–Schottky relation

$$C^{-2} = \frac{2(V_{fb} - V)}{A^2 q \varepsilon \varepsilon_0 N} \tag{1}$$

where V_{fb} is the voltage at which bands are flat and A the device active surface.

Doping alters the electrical field distribution by the presence of charged impurities or defects of structural or chemical origin introduced during device processing. In addition, defects may pose a detrimental effect on the solar cell performance as it has been shown by investigating the diode behavior of perovskite solar cells that trap-assisted recombination via electron traps is present as a non-radiative loss mechanism [72]. According to fundamental theory, photovoltaic devices where only direct free-carrier recombination occurs show diode ideality factors close to 1 [16]. Alternatively, if trap-assisted recombination is present the diode ideality factor increases to values close to 2 and this has indeed been observed for perovskite solar cells with applied voltages in the range of 0.7–1.0 V [72].

Importantly, it needs to be clarified that neutral vacancy pair defect (Schottky defects), such as PbI_2 and CH_3NH_3I vacancy, do not account for a trap-state, which would reduce carrier lifetime [71]. Alternatively, elemental defects (Frenkel defects) like Pb, I, and CH_3NH_3 vacancies act as dopants, which explains the unintentional doping of methylammonium lead halides [40]. It has also been proved that the n-/p-type can be efficiently manipulated by controlling growth processes. For example, [71] have reported that an excess of MAI produces p-type character defects by having Pb^{2+} vacancies. Alternatively, an excess of PbI_2 induces generation of n-type defects by having I^- vacancy. Interestingly, thermal annealing can convert the p-type perovskite to n-type by removing MAI. In addition, the deposition method also influences the amount of defects as this will determine the crystallinity and the defects confined to the grain boundary.

A clear correlation of the charge carrier mobility with perovskite domain size has been observed using time-resolved microwave conductivity measurements (Fig. 18) [57]. Defects measured in complete photovoltaic devices represent extremely shallow traps with depth in the order of 10 meV that allow the achievement of extremely high charge carried mobilities with minimum values of up to 20 $cm^2\ V^{-1}\ s^{-1}$ attributed to holes for devices prepared using a 2-step process on mesoporous TiO_2. Under best preparation conditions, intrinsic mobilities of each PVK sample of 60–75 $cm^2\ V^{-1}\ s^{-1}$ were obtained. Exceptionally low trap-state densities on the order of 10^9–$10^{10}\ cm^{-3}$ are obtained for single crystal materials which show long carrier diffusion lengths exceeding 10 μm and high mobility 115 $cm^2\ V^{-1}\ s^{-1}$ [66].

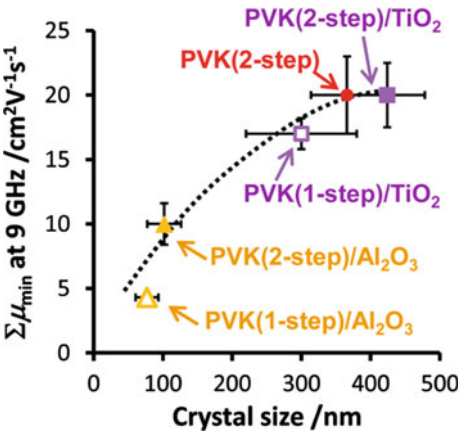

Fig. 18 Plot of $\Sigma\mu_{min}$ measured by time-resolved microwave conductivity at 9 GHz versus averaged crystal size. Reproduced with permission from [57]

To obtain a more complete analysis of the energetic profile and especially close to the contacts one needs to take into account ionic conductivity effects previously discussed in Fig. 8. Therefore, extraction of photogenerated carriers at the contacts may be limited in many cases by the energy level profile but it can also be limited by the chemical reactivity of the external contact with the perovskite material. For example, during cycling of the device under dark conditions reversible generation of Ti–I–Pb bonds have been reported to take place at the interface between the perovskite materials and TiO_2 [14] and this will be discussed in detail in Sect. 7. Depending on the external contact this type of reactivity could generate insulating species that pose a source for series resistance to the device.

Using KPFM microscopy [8] studied the contact potential difference profile of devices containing mesoporous TiO_2 layer under different illumination conditions. It was observed that the electrical field distribution across the devices depends markedly on the illumination conditions, see Fig. 19. The authors showed that under dark conditions the potential drop in the mesoporous TiO_2/perovskite layer was homogenous. Alternatively, in the capping perovskite layer the electrical field was rather confined to the TiO_2. On illumination, a drastic change was observed in the capping layer being the potential drop homogeneous in the middle and the electrical field confined close to both of the external contacts TiO_2 and Spiro-OMeTAD. The authors claimed that on illumination, holes accumulate in front of the hole-transport layer as a consequence of unbalanced charge transport in the device. However, at the time it was not known about the ionic transport to the external contacts so ion accumulation at the contacts could well be responsible for such a behavior. Importantly, after light illumination some permanent changes (within the timescale of the measurement) were observed which were responsible for a modification in the obtained energy level profile. This observation is more consistent with ion movements rather that hole accumulation which tend to decay quite fast.

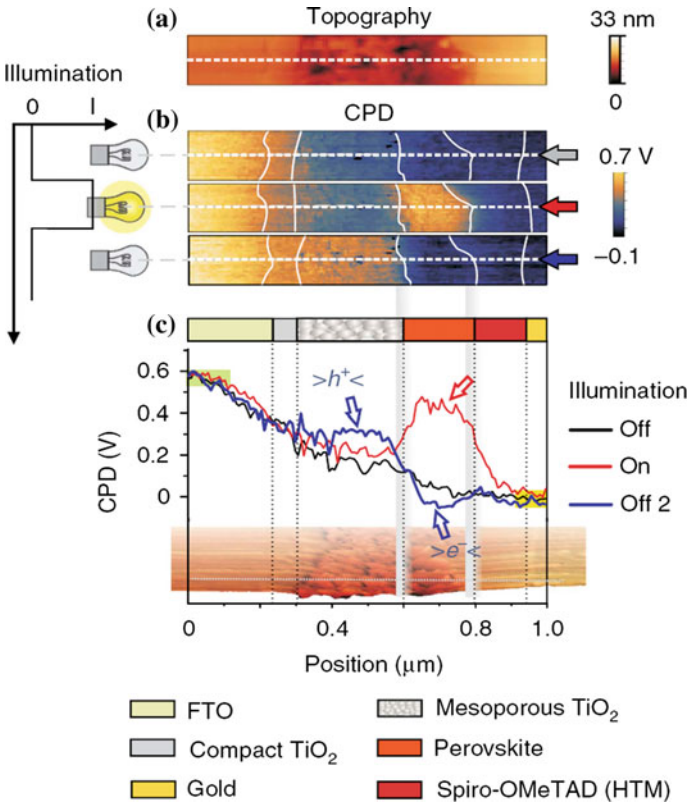

Fig. 19 Comparison of representative KPFM results of a device containing mesoporous TiO_2 measured under dark and light conditions under short-circuit conditions. As can be observed CPD line profiles are different before illumination, during illumination and immediately after illumination. Reprinted from [8]

6 Transient Photovoltage and Photocurrent

Time transient experiments that probe the decay of electrical or optical properties are widely used to obtain the properties of charge generation, recombination and the fundamental mechanisms of voltage and current generation in hybrid organic–inorganic solar cells as dye-sensitized solar cells and organic solar cells [17]. These transient decays consist of the measurement of the response to a step change. Depending on the perturbation several methods are distinguished. Open-circuit voltage decay (OCVD) [77] is a large perturbation method in which illumination is removed and the decay of photovoltage is monitored. Transient Photovoltage Decays (TPD) consists of the decay of a small perturbation step of illumination, again monitoring a photovoltage, while in Transient Absorption Spectroscopy (TAS), the optical absorption properties are probed.

6.1 Open-Circuit Voltage Decay

The method of OCVD has been widely used to determine electron lifetime in dye-sensitized solar cells, which is obtained directly by a reciprocal derivative of the voltage [77]. However, the interpretation of decays in hybrid halide perovskite appears to require a very different framework concerning the physical origin of the decay [9]. Time transient decays in perovskite solar cells span a very complex phenomenology and the model required to extract decay times are often uncertain, ranging from multiple exponentials to stretched exponential [47, 63]. A slow response associated to recovery of the dark polarization in perovskite solar cells [5, 64] should be connected to the observations made by capacitance spectroscopy and voltage sweep methods, that indicate a dominance of complex ionic-electronic relaxation phenomena at the external interfaces of the device. In addition there are faster components, which can be related to the observations by small perturbation TPD [44, 63, 67].

Since the slow decay of OCVD cannot be attributed directly to recombination, and in addition other fast decay components are observed in the transient of photovoltage, we have defined [9] an *instantaneous relaxation time* τ_{ir} that describes a general relaxation phenomenon by the following expression:

$$\frac{\mathrm{d}V}{\mathrm{d}t} = -\frac{1}{\tau_{ir}} V \tag{9}$$

The characteristic time τ_{ir} is a constant only if the voltage decay obeys an ideal relaxation exponential law. Otherwise τ_{ir} is a function of the voltage that can be generally determined as

$$\tau_{ir}(V) = \left(-\frac{1}{V} \frac{\mathrm{d}V}{\mathrm{d}t} \right)^{-1} \tag{10}$$

The time $\tau_{ir}(V)$ describes the instantaneous advance of the relaxation, being different from the [77] definition that applies for a recombination lifetime.

The representation of $\tau_{ir}(V)$ lets us discriminate the different types of relaxation dynamics. In Fig. 6c decays of devices with different hole extraction contacts are shown with nearly constant decay time. Interestingly, the relaxation time is much shorter for the sample that has the smaller capacitance (Fig. 6d), as previously discussed. In contrast to this, samples with mesoporous electrodes show more complex long time decay characteristics as indicated in Fig. 20. Figure 21 shows that a modification of the oxide contact modifies the instantaneous relaxation time of the voltage decay.

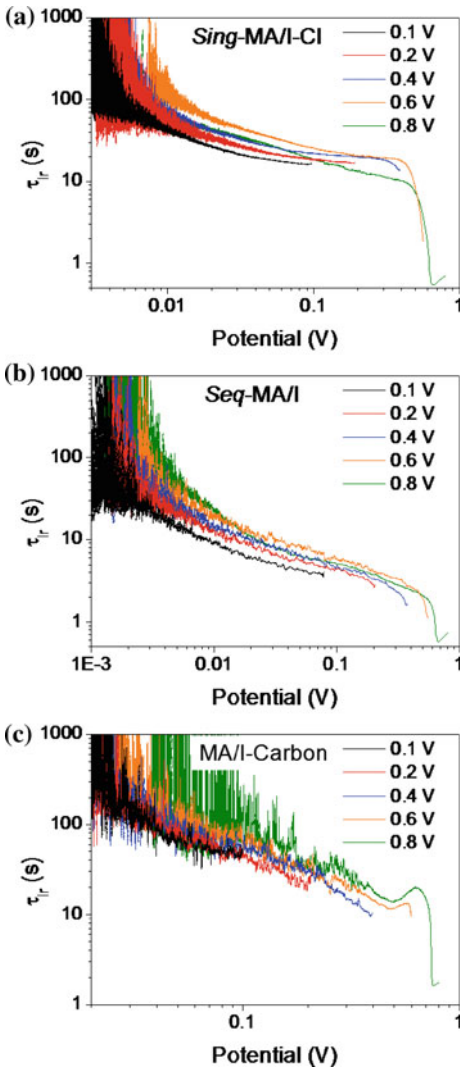

Fig. 20 Instantaneous relaxation time as function of voltage for three different $CH_3NH_3PbI_{3-x}Cl_x$ perovskite solar cells. The starting value of voltage is indicated for each cell. **a** *Sing*-MA/I-Cl is formed by single-step deposition, using $PbCl_2$ precursor, of $CH_3NH_3PbI_{3-x}Cl_x$ onto a compact TiO_2/meso-TiO_2 electrode and using Spiro-MeOTAD as hole contact. **b** *Seq*-MA/I were prepared by exploiting the sequential methodology, which consists on depositing by spin-coating a layer of PbI_2 onto a compact TiO_2/meso-TiO_2 electrode, followed by the addition of a CH_3NH_3I solution to form the $CH_3NH_3PbI_3$ and using Spiro-MeOTAD as hole contact. These two methods, configuration and materials are probably the most extended in the current literature of PSCs. **c** MA/I-Carbon. The third configuration of devices consists on the deposition of $CH_3NH_3PbI_3$ by drop casting onto a meso-TiO_2/meso-ZrO_2/Carbon electrode, thus consisting on a hole conductor-free device. Reprinted from [9]

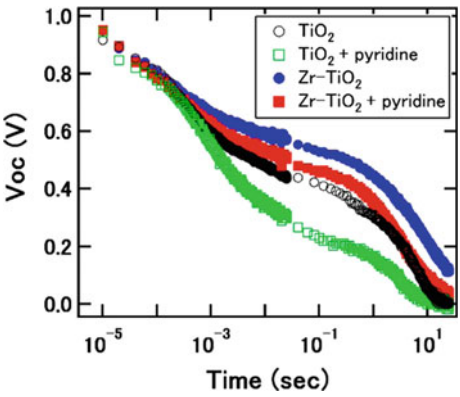

Fig. 21 Open-circuit voltage transients for the four different perovskite device types FTO/Zr−TiO_2 (or TiO_2)/$CH_3NH_3PbI_3$(Cl)/*spiro*-OMeTAD/Au. The oxide contact has different compositions as indicated in the figure legends. Reprinted from [55]

6.2 *Transient Current and Charging*

As discussed in previous sections, accumulation of ionic species in the vicinity of the contact brings about electrode polarization and concomitant capacitive responses. The long-time decays observed in Fig. 20 indicate a complex slow relaxation but so far it has not been identified in terms of a physical process. An alternative way of analyzing ionic charging is by measuring *charge* transients instead of current transients as in Fig. 1a. The advantage of this method from the experimental point of view is that charge yields a growing response as a function of time, while current decreases below usual detection limits. An example of the charge response to a voltage step is depicted in Fig. 22. Thick $CH_3NH_3PbI_3$ samples sandwiched between inert Au electrodes exhibit double exponential charging shapes with typical response time of order 10 s for the slowest component (Fig. 22b) [1]. An analysis of these transients provides important information on the ultraslow relaxation of perovskite solar cells.

Charging profiles reveal the structure of the ionic double-layer made up of Helmholtz layer at $MAPbI_3$/contact interface and electrode-induced local charge imbalance within the ion diffuse layer, as outlined in Fig. 8b. Ionic accumulation within the diffuse layer is well described by Eq. (6).

Based on this interpretation associated to the Gouy-Chapman layer it is proposed that ionic charging, with a typical response time of 10 s, is a local effect confined in the vicinity of the electrode (with extent $L_D \ll L$). This observation entails steady-state ionic space charge of ~ 10 nm-width at the contacts from Eq. (7) using $N \approx 10^{17}$ cm^{-3}, in contrast to other approaches that suggest non-negligible net mobile ionic concentration entering the perovskite bulk. For example the

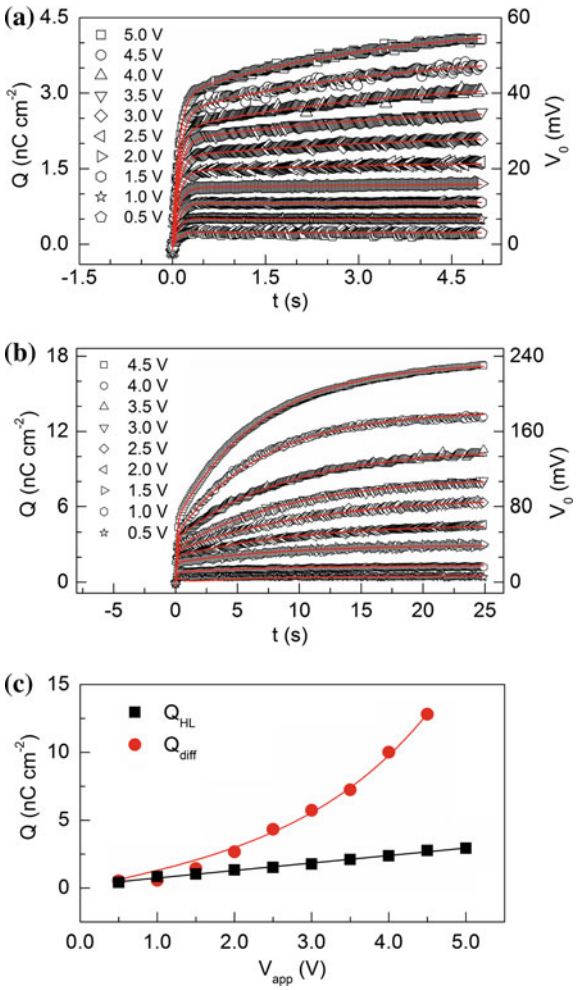

Fig. 22 Example of Q (and V_0) signals of an 800 μm-thick $MAPbI_3$ pellet sandwiched between Au contacts for short (**a**) and long (**b**) measuring times. **c** Values of Q_{HL} (Helmholtz layer) showing a linear trend (*solid line*) in accordance to a plane capacitor behavior. Ionic charge Q_{diff} (diffuse layer) values following fitting of Eq. 8 (*solid line*). Reprinted from [1]

chronoamperometric transient signal obtained upon illumination (Fig. 23) using much shorter perovskite layer thickness (500 nm), has been interpreted in relation of ionic rearrangement in the entire absorber size [4, 20]. Both models predict ion accumulation of different extent that produces partial screening of the electrical field within the perovskite film. Also much longer voltage transients measured with thicker (0.6 mm) samples have been interpreted as resulting from ion movement (Fig. 9) [75].

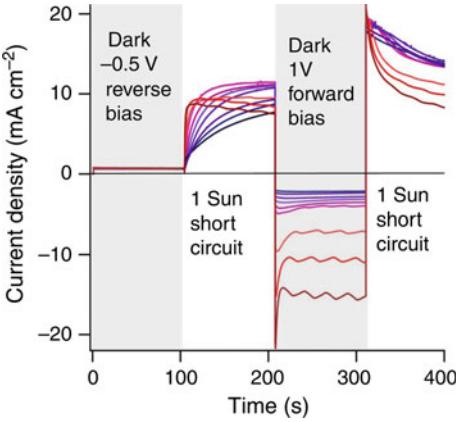

Fig. 23 Chronophotoamperometry measurements of a perovskite-based cell. The measurement sequence in a d-TiO_2/$CH_3NH_3PbI_3$/*spiro*-OMeTAD/Au cell is indicated; measured temperatures (to the nearest 0.5 °C) of the devices were −9.5 (*dark blue*), −5.5, 0.5, 5, 10.5, 15, 19.5, 24.5, 30, 40, and 50 °C (*dark red*). Reprinted from [20]

6.3 Small Perturbation Illumination Methods: Transient Photovoltage and Charge Extraction

Photoinduced time-resolved techniques such as charge extraction (CE) and TPV have been widely employed in the field of dye-sensitized solar cells and organic solar cells to determine capacitances and lifetimes. The results have been found in excellent correlation with those of impedance spectroscopy, which provides a coherent and robust picture of dynamic carrier phenomena in these systems [21]. The key issue when employing CE instead of IS is that the CE decay must be much faster than the TPV decay under 1 sun illumination conditions. The solar cell charge density can be also measured using differential charging, a method that combines the use of TPV and Transient Photocurrent (TPC), with identical results to either IS or CE in devices measured previously as organic or sensitized solar cells.

However, substantial differences between the results of these methods have been found in measurements of lead halide perovskite solar cells, either using mesoporous TiO_2 or not as scaffold, with respect to the former classes of devices. In contrast to the previous systems in the perovskite solar cells, the CE decay results much longer than the TPV decay [50], Fig. 24. In addition the measured charge density when using differential charging is different to the results obtained by CE as shown in Fig. 25.

The main difference between both techniques, CE and differential charging, is the acquisition time. The differential charging method allows one to obtain the cell capacitance through the expression

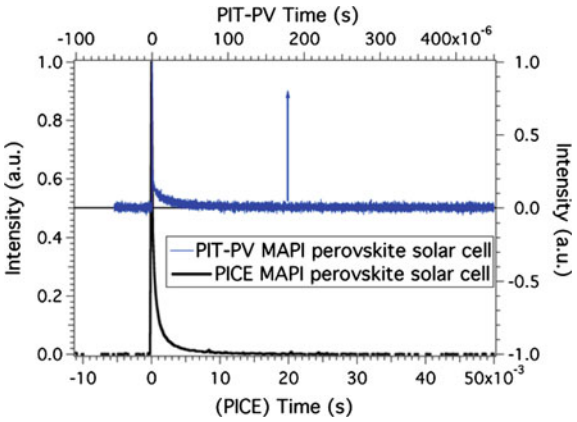

Fig. 24 *Top*, charge extraction decay at 1 sun for a 12.7 % efficient lead perovskite solar cell. *Bottom*, TPV decay at the same light intensity (1 sun) for the same solar cell. Reprinted from [50]

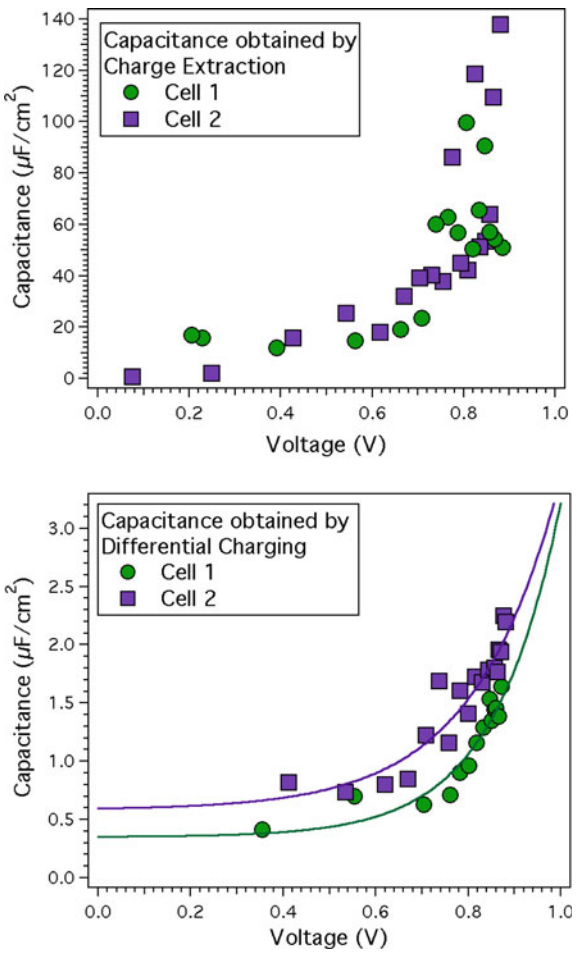

Fig. 25 *Top*, solar cell charge density at different light bias measured using charge extraction. *Bottom*, solar cell charge density measured at different light bias using differential charging. Data courtesy of Emilio Palomares (ICIQ)

$$C(V_{oc}) = \frac{\mathrm{d}Q}{\mathrm{d}t}\left(\frac{\mathrm{d}V}{\mathrm{d}t}\right)^{-1} \tag{11}$$

The $\mathrm{d}V/\mathrm{d}t$ is obtained directly from the TPV transients at different light bias and the $\mathrm{d}Q/\mathrm{d}t$ is measured using TPC. The TPC decay under different light intensities reaches a plateau that can be taken as the maximum charge generation flux. The TPC is the voltage response of a solar cell but measured at short circuit using the same laser pulse as that used for the TPV. The TPC decay is converted into a current transient using a small resistor (typically 40–50 Ω) and applying Ohm's law. Yet, this assumption is only valid if (a) there are not critical charge losses at short-circuit (basically meaning that the device J_{sc} is linear when increasing the light intensity); (b) the $\mathrm{d}Q$ does not change substantially under different light illumination conditions and (c) the TPV decay is slower than the TPC (meaning that charge collection is much faster than charge recombination). Despite the uncertainties associated to the interpretation of this technique (which is common to other transient methods as mentioned before), according to the initial suggestion of [56] the measured charge using differential charging is associated to a given carrier lifetime which can be used to reproduce, within the experimental error, the solar cell photocurrent at a given light bias.

7 Reactivity and Degradation at Electrodes

The property of ionic charging by ionic vacancy or interstitial migration and subsequent accumulation at the outer boundaries of the perovskite layer, has already been commented extensively. Ionic charging may provide complex experimental characterizations, particularly if contacts cannot be considered as blocking electrodes, i.e., when Faradaic currents (non-blocking or reacting electrodes) or high applied voltages may yield large extent space charge regions entering the layer bulk [6]. In these cases the interface polarization is dominated by the complex interaction between electronic and ionic species at both sides of the contact [35, 49] instead of simple Debye capacitances of Eq. (8). Reactivity at the interfaces between the perovskite film and the electron- or hole-transporting contact materials is then an issue of primary concern.

Recent experiments performed on complete solar cells of planar structure FTO/TiO_2/$MAPbI_3$/*spiro*-OMeTAD/Au (Fig. 26a), and symmetrical FTO/TiO_2/$MAPbI_3$/TiO_2/FTO and Au/*spiro*-OMeTAD/$MAPbI_3$/*spiro*-OMeTAD/Au devices (Fig. 26d, e) have enabled progress in the role of interfaces on the capacitive hysteresis and solar cell degradation [14]. Two separate types of reactivity sources (reversible and irreversible) have been identified:

(i) The formation of weak Ti−I−Pb bonds at the TiO_2/$MAPbI_3$ interface that facilitate interfacial accommodation of moving iodine ions. This interaction produces highly reversible capacitive currents (Fig. 26b), without altering steady-state photovoltaic features. As observed in the central voltage window of Fig. 26b, capacitive currents exhibit the expected square-like response previously described in Fig. 3.

(ii) Chemical reaction between *spiro*-$OMeTAD^+$ and moving I^- which progressively reduces the hole-transporting material conductivity and deteriorates solar cell performance. This reaction results in an irreversible redox peak only observable after positive poling at slow scan rates (Fig. 26c).

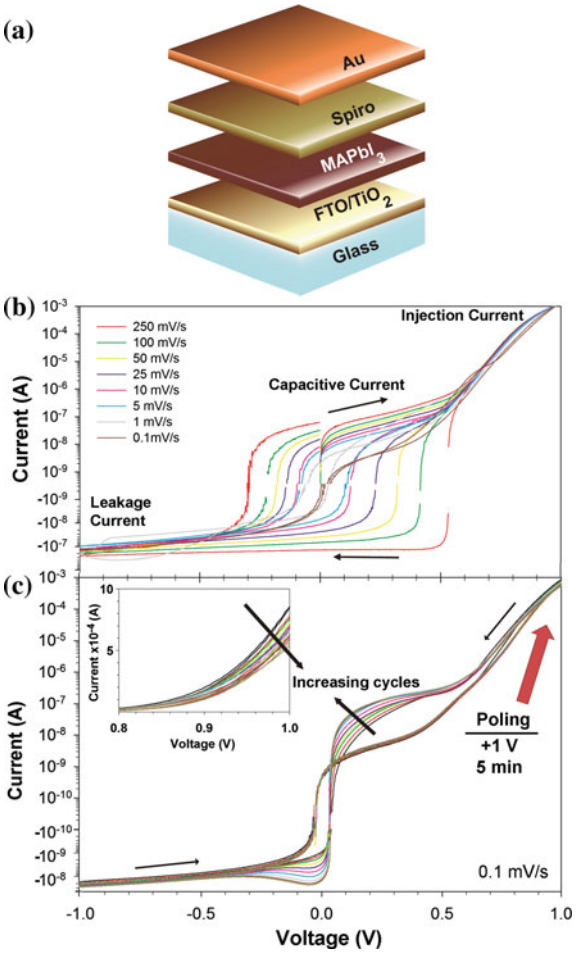

Fig. 26 **a** Structure of the planar solar cells (200 nm $MAPbI_3$ layer). **b** Dark currents measured at different scan rates both for positive and negative sweep. Three different mechanisms are identified: at $V > 0.5$ V operation currents caused by carrier injection, $V < -0.5$ V leakage currents, and central voltage interval shows the presence of scan rate dependent, capacitive currents. **c** Cycled experiments including positive poling during 5 min. Positive scan (no poling) reproduce steady-state behavior. Negative scans induce incremental redox peaks after successive cycles. In the inset: injection current at forward bias decreases with cycling. Reprinted from [14]

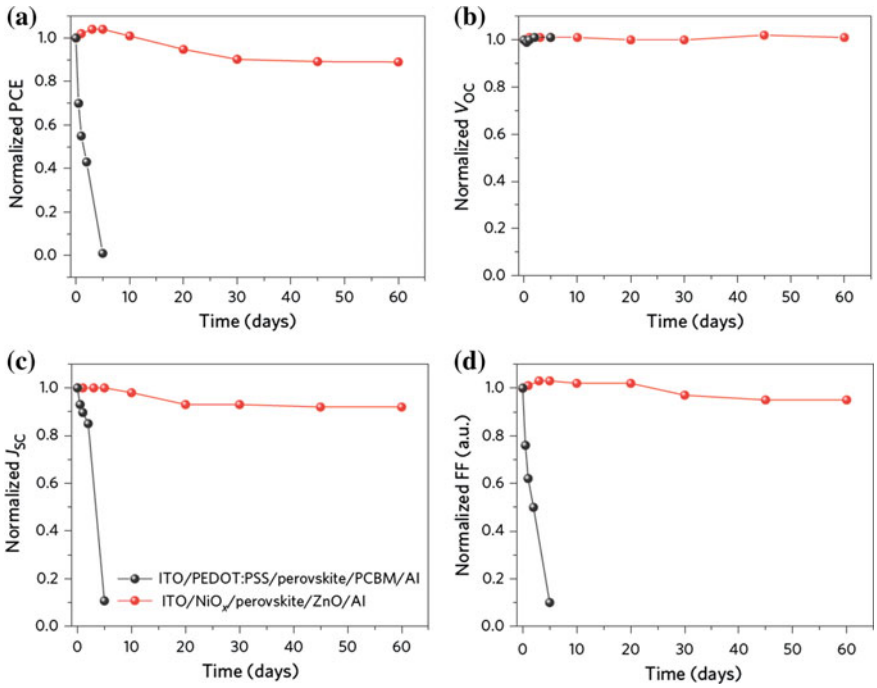

Fig. 27 Stability of the devices in an ambient environment without encapsulation. Device performances of ITO/PEDOT:PSS/perovskite/PCBM/Al (*black*) and ITO/NiO_x/perovskite/ZnO/Al (*red*) structures as a function of storage time in an ambient environment (30–50 % humidity, T = 25 °C). Reprinted from [76]

These results highlight the key role that interlayers used as selective contacts play on perovskite solar cell stability, in addition to the intrinsic reactivity of the perovskite materials [19]. As an example of the dramatic effect of the contact layers it is shown in Fig. 27 the performance of inverted type architectures (Fig. 2c) using oxide and organic compounds. It is evident that oxide layers (NiO_x and ZnO) improve the solar cell stability by protecting it against intrinsic, oxygen, and water reactivity [76].

Degradation of a series of devices in the configuration ITO/PEDOT:PSS/Perovskite/PCBM/Metal has recently been studied using a range of different top metals [31]. Degradation readily occurred after illumination in the gloveblox during 2 h obtaining S-shape J–V curves for devices prepared with either Ca, Al, Ag, or Au. Different techniques were used to understand the degradation processes and all pointed to interfacial degradation which was introducing a source of series resistance that was promoting interfacial recombination processes. In particular, devices showing an S-shape measured in the dark after degradation did not change significantly the doping density indicating that the bulk properties of the devices had not significantly changed. More intriguing was the fact that the V_{fb} shifted

toward negative values for degraded sample indicating that the interface equilibration with the perovskite semiconductor was being modified, see Fig. 18. Measurements under light conditions further shifted V_{fb} toward negative values pointing to generation of light-induced dipoles at perovskite/contact interface. Alternatively, a top metal-based on Cr_2O_3/Cr enhanced the stability against corrosion and no S-shape was observed. Results from *C–V* did not show significant shifts in V_{fb} for fresh and degraded devices either in the dark of light and the most relevant result was a moderate increase in the doping density of the perovskite layer for degraded device.

Trap-induced degradation of perovskite solar cells has recently been reported where a large density of hole traps is formed by continuous solar illumination strongly limiting the device stability [62]. In the experiment devices in the configuration ITO/PEDOT:PSS/Perovskite/$PC_{70}BM$/LiF/Al are prepared. Processing of the perovskite layer takes place either in air or nitrogen and initial efficiencies are very similar. Whilst efficiencies of devices prepared in nitrogen environment only decay about 10 % during the first 500 h devices fabricated in air reduce the efficiency up to 90 % in the same period of time. To investigate the degradation origin the carrier traps were analyzed using the thermally stimulated current (TSC) measurement. In this technique, carrier traps in a cooled device at 77 K are filled with carriers injected from the electrodes under a small forward bias. By gradually increasing the temperature at a constant rate under a small reverse bias the trapped carriers are then released and collected. Figure 28 displays the TSC curves of device fabricated in air before and after degradation by 500 h of illumination. Whilst fresh device does not show any peak in the TSC curve two peaks are clearly observed at temperature of 161 and 213 K for the degraded device originated from the release of carriers from the trap sites. Hole-trap depths of 0.32 and 0.42 eV are calculated from the low and high-temperature TSC, respectively. Generation of these trap states acts as a recombination center reducing the device efficiency. The authors concluded that water molecules included in the $CH_3NH_3PbI_3$ layer were

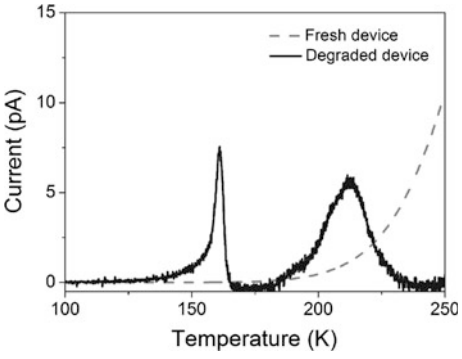

Fig. 28 TSC curves of devices in the configuration ITO/PEDOT:PSS/Perovskite/$PC_{70}BM$/LiF/Al fabricated in air before and after degradation by 500 h of illumination. Reprinted from [62]

responsible for both TSC signals. However, the precise mechanism in which these traps are generated is still unclear and could indeed be a case of reactivity at the contacts.

8 The Light Capacitances

As commented before in Figs. 12 and 14, under illumination the low-frequency capacitances in perovskite solar cells undergo a very large increase, that is observed to depend linearly on illumination [34]. Since measurements of a number of cells have been independently reported [46, 75, 78], the photoinduced capacitance is established as a normal property of lead halide perovskite solar cells. The measurements indicate that this property occurs irrespective of type of contacts (symmetric, asymmetric, nanoporous…), however, the specific features are dramatically changed by contacts as is evident in Fig. 11, which shows a connection between low-frequency capacitance and amount of hysteresis [37, 38].

Different explanations have been presented in the literature to rationalize the photoinduced giant capacitance at low frequency: (a) A change of electrode polarization capacitance. This will be associated to an increasing concentration of mobile ions, caused by the excess electronic carriers. (b) A change of the bulk polarizability. In this model there occurs an enhancement of the elementary dipole in the perovskite octahedral cage caused by light generated carriers [73]. (c) A change of the chemical capacitance, homogeneously in the bulk perovskite layer [75].

As commented above, recent measurements using a variety of methods such as voltage cycling and capacitance spectroscopy point out that the low-frequency capacitance in the dark is associated to ionic pile up at the interface [2]. However, a large rise of the total measured capacitance is prevented by any series capacitor. In the case of ionic space charge, capacitance is limited by the Helmholtz capacitance situated in series, so that one does not expect values substantially higher than μF cm^2. The low-frequency capacitance increase observed in Fig. 29 greatly exceeds the mentioned Helmholtz capacitance limit, so that it is unlikely that this large capacitance can be interpreted in terms of the diffuse ionic double layer.

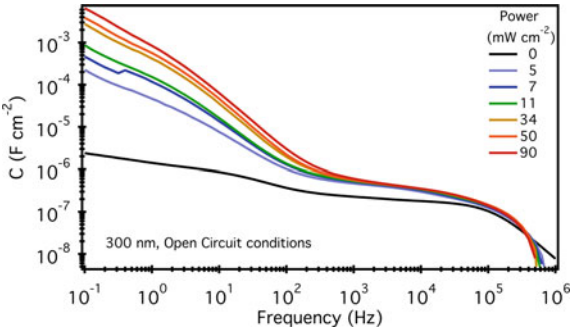

Fig. 29 Capacitance spectra measured in open-circuit conditions for different illumination intensities of 300 nm-thick solar cells of structure FTO/TiO_2/$FAPbI_{3-x}Cl_x$/*spiro*-OMeTAD/Au, where FA is $CH(NH_2)_2$ between 100 and 1 MHz. Dark response at zero bias is also shown. Reprinted from [78]

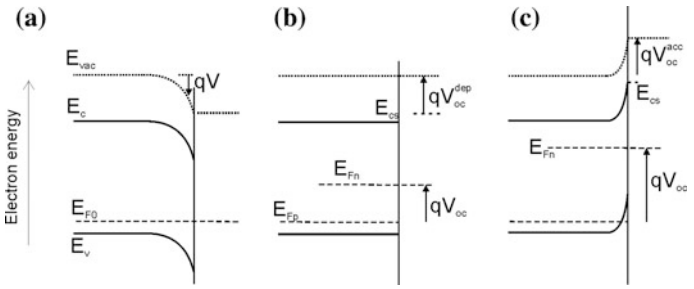

Fig. 30 Energy diagram for electron selective contact to the semiconductor absorber layer at open circuit conditions. **a** Depletion layer at equilibrium. Generation of minority carriers produces flatband condition (**b**) and further accumulation (**c**) of majority carrier. The total open circuit voltage is the increase of minority carrier Fermi level that corresponds to total change of surface vacuum level as $V_{oc} = V_{oc}^{dep} + V_{oc}^{acc}$. Reprinted from [78]

Therefore, it is reasonable to assume a parallel pathway in which *electronic* photogenerated carriers form a large interfacial capacitance. Li et al. [46] assumed that the enhancement of capacitance originates from native defects and their accompanied defect dipoles which need to be activated by photogenerated charge carriers.

Another type of electronic interfacial effect has been suggested by Zarazua et al. [78] that is supported by some experimental evidence. At semiconductor surfaces, very large electronic interfacial capacitance is possible in the domains of accumulation and inversion, as there is no limit to the packing of electrons in a short distance at the vicinity of the contact.

Taking for example the *p*-type semiconductor surface, the conduction band bends upward at the surface and penetrates the Fermi level, as shown in Fig. 30. The charge per unit surface is $Q = qp_b L_D F_s$ [53], where p_b is the bulk carrier density corresponding to dopant density, $F_s \approx \sqrt{2} e^{qV/2k_BT}$, where qV corresponds to local separation of vacuum level (VL) from bulk value. The Debye length is given in Eq. (7). For the capacitance we find the standard expression

$$C_s = \frac{\mathrm{d}Q}{\mathrm{d}V} = \frac{q p_b^{1/2}}{\sqrt{2}} \left(\frac{\varepsilon_r \varepsilon_0}{k_B T} \right)^{1/2} e^{qV/2k_BT} \tag{12}$$

Accumulation capacitance is in fact very common in transistor and metal–insulator–semiconductor devices [68], although the measured capacitance is limited by the series connection of the oxide dielectric capacitance. In a perovskite solar cell, the accumulation region will be connected by two conducting regions (perovskite and oxide semiconductor), so that in principle it can take very large values [78]. It was reported that low-frequency capacitance values increase proportionally with the light intensity, and are also proportional to the perovskite layer thickness. The observation of these two proportionalities (light intensity and film thickness) constitutes a direct proof that the surface capacitance charging is made up of

photogenerated carriers coming from the absorber bulk. In addition the capacitance dependence on voltage shows the characteristic slope of $1/2k_BT$ for solar cells with different absorber perovskite thickness, in agreement with the accumulation capacitance expression (12).

9 Conclusion

The analysis of perovskite solar cells using impedance spectroscopy, time transient decays, and voltage cycling, shows that the phenomenology is extremely varied and complex but nonetheless it is possible to identify some trends of the equivalent circuit elements of the solar cell devices. There is a large impact of ionic accumulation at the interface in the low-frequency response, and furthermore the ionic transport produces temporary and even permanent modifications of the interface of the perovskite with charge extraction layers, that cause phenomena as hysteresis and degradation. Capacitances at high frequency indicate bulk relaxation phenomena but under applied bias they can be related to a depletion capacitance. A widely reported observation of very low-frequency capacitance with illumination has been attributed to electronic accumulation capacitance at the perovskite/contact interface. It is stressed then that hysteresis effects are originated by local charging at the contacts, either ionic as observed in dark responses (Fig. 15), or electronic through the formation of light-induced accumulation zones (Fig. 29). These mechanisms are both largely confined within a short extent near the contacts ($\sim$10 nm) introducing a local modification of the electrical field. These observations pave the way for a fuller understanding of dynamic characteristics of perovskite solar cell that will require insight about the meaning of resistances.

References

1. Almora, O., Guerrero, A., Garcia-Belmonte, G.: Ionic charging by local imbalance at interfaces in hybrid lead halide perovskites. Appl. Phys. Lett. **108**, 043903 (2016)
2. Almora, O., Zarazua, I., Mas-Marza, E., Mora-Sero, I., Bisquert, J., Garcia-Belmonte, G.: Capacitive dark currents, hysteresis, and electrode polarization in lead halide perovskite solar cells. J. Phys. Chem. Lett. **6**, 1645–1652 (2015)
3. Azpiroz, J.M., Mosconi, E., Bisquert, J., De Angelis, F.: Defect migration in methylammonium lead iodide and its role in perovskite solar cell operation. Energy Environ. Sci. **8**, 2118–2127 (2015)
4. Bag, M., Renna, L.A., Adhikari, R.Y., Karak, S., Liu, F., Lahti, P.M., Russell, T.P., Tuominen, M.T., Venkataraman, D.: Kinetics of ion transport in perovskite active layers and its implications for active layer stability. J. Am. Chem. Soc. **137**, 13130–13137 (2015)
5. Baumann, A., Tvingstedt, K., Heiber, M.C., Vath, S., Momblona, C., Bolink, H.J., Dyakonov, V.: Persistent photovoltage in methylammonium lead iodide perovskite solar cells. APL Mater. **2**, 081501 (2014)

6. Bazant, M.Z., Thornton, K., Ajdari, A.: Diffuse-charge dynamics in electrochemical systems. Phys. Rev. E **70**, 021506 (2004)
7. Beaumont, J.H., Jacobs, P.W.M.: Polarization in potassium chloride crystals. J. Phys. Chem. Solids **28**, 657 (1967)
8. Bergmann, V.W., Weber, S.A.L., Javier Ramos, F., Nazeeruddin, M.K., Gratzel, M., Li, D., Domanski, A.L., Lieberwirth, I., Ahmad, S., Berger, R.: Real-space observation of unbalanced charge distribution inside a perovskite-sensitized solar cell. Nat. Commun. **5** (2014)
9. Bertoluzzi, L., Sanchez, R.S., Liu, L., Lee, J.-W., Mas-Marza, E., Han, H., Park, N.-G., Mora-Sero, I., Bisquert, J.: Cooperative kinetics of depolarization in $CH_3NH_3PbI_3$ perovskite solar cells. Energy Environ. Sci. **8**, 910–915 (2015)
10. Bisquert, J., Fabregat-Santiago, F.: Dye-sensitized solar cells. Kalyanasundaram, K. (ed.). CRC Press, Boca Raton (2010)
11. Bisquert, J., Garcia-Belmonte, G., Mora-Sero, I.: Characterization of capacitance, transport and recombination parameters in hybrid perovskite and organic solar cells. In: Como, E.d., Angelis, F.D., Snaith, H., Walker, A. (eds.) Unconventional Thin Film Photovoltaics: Organic and Perovskite Solar Cells, RSC Energy and Environment Series (2016)
12. Brivio, F., Butler, K.T., Walsh, A., van Schilfgaarde, M.: Relativistic quasiparticle self-consistent electronic structure of hybrid halide perovskite photovoltaic absorbers. Phys. Rev. B **89**, 155204 (2014)
13. Brivio, F., Walker, A.B., Walsh, A.: Structural and electronic properties of hybrid perovskites for high-efficiency thin-film photovoltaics from first-principles. APL Mater. **1**, 042113 (2013)
14. Carrillo, J., Guerrero, A., Rahimnejad, S., Almora, O., Zarazua, I., Mas-Marza, E., Bisquert, J., Garcia-Belmonte, G.: Ionic reactivity at contacts and aging of methylammonium lead triiodide perovskite solar cell. Adv. Energy Mater. **6**, 1502246 (2016)
15. Chen, B., Yang, M., Zheng, X., Wu, C., Li, W., Yan, Y., Bisquert, J., Garcia-Belmonte, G., Zhu, K., Priya, S.: Impact of capacitive effect and ion migration on the hysteretic behavior of perovskite solar cells. J. Phys. Chem. Lett. **6**, 4693–4700 (2015)
16. Chih-Tang, S., Noyce, R.N., Shockley, W.: Carrier generation and recombination in P-N junctions and P-N junction characteristics. Proc. IRE **45**, 1228–1243 (1957)
17. Clifford, J.N., Martinez-Ferrero, E., Palomares, E.: Dye mediated charge recombination dynamics in nanocrystalline TiO_2 dye sensitized solar cells. J. Mater. Chem. **22**, 12415–12422 (2012)
18. Coll, M., Gomez, A., Mas-Marza, E., Almora, O., Garcia-Belmonte, G., Campoy-Quiles, M., Bisquert, J.: Polarization switching and light-enhanced piezoelectricity in lead halide perovskites. J. Phys. Chem. Lett. **6**, 1408–1413 (2015)
19. Conings, B., Drijkoningen, J., Gauquelin, N., Babayigit, A., D'Haen, J., D'Olieslaeger, L., Ethirajan, A., Verbeeck, J., Manca, J., Mosconi, E., De Angelis, F., Boyen, H.-G.: Intrinsic thermal instability of methylammonium lead trihalide perovskite. Adv. Energy Mater. **5**, 1500477 (2015)
20. Eames, C., Frost, J.M., Barnes, P.R.F., O/'Regan, B.C., Walsh, A., Islam, M.S.: Ionic transport in hybrid lead iodide perovskite solar cells. Nat. Commun. **6** (2015)
21. Etxebarria, I., Guerrero, A., Albero, J., Garcia-Belmonte, G., Palomares, E., Pacios, R.: Inverted vs standard PTB7:PC70BM organic photovoltaic devices. The benefit of highly selective and extracting contacts in device performance. Org. Electron. **15**, 2756–2762 (2014)
22. Fabregat-Santiago, F., Garcia-Belmonte, G., Mora-Seró, I., Bisquert, J.: Characterization of nanostructured hybrid and organic solar cells by impedance spectroscopy. Phys. Chem. Chem. Phys. **13**, 9083–9118 (2011)
23. Fabregat-Santiago, F., Mora-Seró, I., Garcia-Belmonte, G., Bisquert, J.: Cyclic voltammetry studies of nanoporous semiconductor electrodes. Models and application to nanocrystalline TiO_2 in aqueous electrolyte. J. Phys. Chem. B **107**, 758–769 (2003)
24. Fan, Z., Xiao, J., Sun, K., Chen, L., Hu, Y., Ouyang, J., Ong, K.P., Zeng, K., Wang, J.: Ferroelectricity of $CH_3NH_3PbI_3$ perovskite. J. Phys. Chem. Lett. **6**, 1155–1161 (2015)
25. Filippetti, A., Delugas, P., Saba, M.I., Mattoni, A.: Entropy-suppressed ferroelectricity in hybrid lead-iodide perovskites. J. Phys. Chem. Lett. **6**, 4909–4915 (2015)

26. Frost, J.M., Butler, K.T., Walsh, A.: Molecular ferroelectric contributions to anomalous hysteresis in hybrid perovskite solar cells. APL Mater. **2** (2014)
27. Gottesman, R., Zaban, A.: Perovskites for photovoltaics in the spotlight: photoinduced physical changes and their implications. Acc. Chem. Res. (2016)
28. Guerrero, A., Dörling, B., Ripolles-Sanchis, T., Aghamohammadi, M., Barrena, E., Campoy-Quiles, M., Garcia-Belmonte, G.: Interplay between fullerene surface coverage and contact selectivity of cathode interfaces in organic solar cells. ACS Nano **7**, 4637–4646 (2013)
29. Guerrero, A., Juarez-Perez, E.J., Bisquert, J., Mora-Sero, I., Garcia-Belmonte, G.: Electrical field profile and doping in planar lead halide perovskite solar cells. Appl. Phys. Lett. **105**, 133902 (2014)
30. Guerrero, A., Marchesi, L.F., Boix, P.P., Ruiz-Raga, S., Ripolles-Sanchis, T., Garcia-Belmonte, G., Bisquert, J.: How the charge-neutrality level of interface states controls energy level alignment in cathode contacts of organic bulk-heterojunction solar cells. ACS Nano **6**, 3453–3460 (2012)
31. Guerrero, A., You, J., Aranda, C., Kang, Y.S., Garcia-Belmonte, G., Zhou, H., Bisquert, J., Yang, Y.: Interfacial degradation of planar lead halide perovskite solar cells. ACS Nano **10**, 218–224 (2016)
32. Hebb, M.H.: Electrical conductivity of silver sulfide. J. Chem. Phys. **20**, 185 (1952)
33. Jiang, C.-S., Yang, M., Zhou, Y., To, B., Nanayakkara, S.U., Luther, J.M., Zhou, W., Berry, J. J., van de Lagemaat, J., Padture, N.P., Zhu, K., Al-Jassim, M.M.: Carrier separation and transport in perovskite solar cells studied by nanometre-scale profiling of electrical potential. Nat. Commun. **6** (2015)
34. Juarez-Perez, E.J., Sanchez, R.S., Badia, L., Garcia-Belmonte, G., Gonzalez-Pedro, V., Kang, Y.S., Mora-Sero, I., Bisquert, J.: Photoinduced giant dielectric constant in lead halide perovskite solar cells. J. Phys. Chem. Lett. **5**, 2390–2394 (2014)
35. Kato, Y., Ono, L.K., Lee, M.V., Wang, S., Raga, S.R., Qi, Y.: Silver iodide formation in methyl ammonium lead iodide perovskite solar cells with silver top electrodes. Adv. Mater. Interfaces **2**, 1500195 (2015)
36. Kim, C., Tomozawa, M.: Electrode polarization of glasses. J. Am. Chem. Soc. **59**, 127–130 (1976)
37. Kim, H.-S., Jang, I.-H., Ahn, N., Choi, M., Guerrero, A., Bisquert, J., Park, N.-G.: Control of I-V hysteresis in $CH_3NH_3PbI_3$ perovskite solar cell. J. Phys. Chem. Lett. **6**, 4633–4639 (2015)
38. Kim, H.-S., Kim, S.K., Kim, B.J., Shin, K.-S., Gupta, M.K., Jung, H.S., Kim, S.-W., Park, N.-G.: Ferroelectric polarization in $CH_3NH_3PbI_3$ perovskite. J. Phys. Chem. Lett. **6**, 1729–1735 (2015)
39. Kim, H.-S., Park, N.-G.: Parameters affecting I-V hysteresis of $CH_3NH_3PbI_3$ perovskite solar cells: effects of perovskite crystal size and mesoporous TiO_2 layer. J. Phys. Chem. Lett. **5**, 2927–2934 (2014)
40. Kim, J., Lee, S.-H., Lee, J.H., Hong, K.-H.: The Role of intrinsic defects in methylammonium lead iodide perovskite. J. Phys. Chem. Lett. **5**, 1312–1317 (2014)
41. Kirchartz, T., Bisquert, J., Mora-Sero, I., Garcia-Belmonte, G.: Classification of solar cells according to mechanisms of charge separation and charge collection. Phys. Chem. Chem. Phys. **17**, 4007–4014 (2015)
42. Kutes, Y., Ye, L., Zhou, Y., Pang, S., Huey, B.D., Padture, N.P.: Direct observation of ferroelectric domains in solution-processed $CH_3NH_3PbI_3$ perovskite thin films. J. Phys. Chem. Lett. **5**, 3335–3339 (2014)
43. Lee, D., Baek, S.H., Kim, T.H., Yoon, J.G., Folkman, C.M., Eom, C.B., Noh, T.W.: Polarity control of carrier injection at ferroelectric/metal interfaces for electrically switchable diode and photovoltaic effects. Phys. Rev. B **84**, 125305 (2011)
44. Lee, J.-W., Lee, T.-Y., Yoo, P.J., Gratzel, M., Mhaisalkar, S., Park, N.-G.: Rutile TiO_2-based perovskite solar cells. J. Mater. Chem. A **2**, 9251–9259 (2014)
45. Leguy, A.M.A., Frost, J.M., McMahon, A.P., Sakai, V.G., Kockelmann, W., Law, C., Li, X., Foglia, F., Walsh, A., O/'Regan, B.C., Nelson, J., Cabral, J.T., Barnes, P.R.F.: The dynamics

of methylammonium ions in hybrid organic-inorganic perovskite solar cells. Nat. Commun. **6** (2015)
46. Li, L., Wang, F., Wu, X., Yu, H., Zhou, S., Zhao, N.: Carrier-activated polarization in organometal halide perovskites. J. Phys. Chem. C (2016)
47. Listorti, A., Juarez-Perez, E.J., Frontera, C., Roiati, V., Garcia-Andrade, L., Colella, S., Rizzo, A., Ortiz, P., Mora-Sero, I.: Effect of mesostructured layer upon crystalline properties and device performance on perovskite solar cells. J. Phys. Chem. Lett. **6**, 1628–1637 (2015)
48. Lunkenheimer, P., Bobnar, V., Pronin, A.V., Ritus, A.I., Volkov, A.A., Loidl, A.: Origin of apparent colossal dielectric constants. Phys. Rev. B **66**, 052105 (2002)
49. Mariappan, C.R., Heins, T.P., Roling, B.: Electrode polarization in glassy electrolytes: large interfacial capacitance values and indication for pseudocapacitive charge storage. Solid State Ionics **181**, 859–863 (2010)
50. Marin-Beloqui, J.M., Lanzetta, L., Palomares, E.: Decreasing charge losses in perovskite solar cells through mp-TiO_2/MAPI interface engineering. Chem. Mater. **28**, 207–213 (2016)
51. Masaki, M., Hattori, M., Hotta, A., Suzuki, I.: Dielectric studies on $CH_3NH_3PbX_3$ (X = Cl or Br) single crystals. J. Phys. Soc. Jpn. **66**, 1508–1511 (1997)
52. Mattoni, A., Filippetti, A., Saba, M.I., Delugas, P.: Methylammonium rotational dynamics in lead halide perovskite by classical molecular dynamics: the role of temperature. J. Phys. Chem. C **119**, 17421–17428 (2015)
53. Mönch, W.: Semiconductor Surfaces and Interfaces. Springer, Berlin (1993)
54. Mosconi, E., Quarti, C., Ivanovska, T., Ruani, G., De Angelis, F.: Structural and electronic properties of organo-halide lead perovskites: a combined IR-spectroscopy and ab initio molecular dynamics investigation. Phys. Chem. Chem. Phys. **16**, 16137–16144 (2014)
55. Nagaoka, H., Ma, F., deQuilettes, D.W., Vorpahl, S.M., Glaz, M.S., Colbert, A.E., Ziffer, M. E., Ginger, D.S.: Zr incorporation into TiO_2 electrodes reduces hysteresis and improves performance in hybrid perovskite solar cells while increasing carrier lifetimes. J. Phys. Chem. Lett. **6**, 669–675 (2015)
56. O'Regan, B.C., Barnes, P.R.F., Li, X., Law, C., Palomares, E., Marin-Beloqui, J.M.: Optoelectronic studies of methylammonium lead iodide perovskite solar cells with mesoporous TiO2: separation of electronic and chemical charge storage, understanding two recombination lifetimes, and the evolution of band offsets during J-V hysteresis. J. Am. Chem. Soc. **137**, 5087–5099 (2015)
57. Oga, H., Saeki, A., Ogomi, Y., Hayase, S., Seki, S.: Improved understanding of the electronic and energetic landscapes of perovskite solar cells: high local charge carrier mobility, reduced recombination, and extremely shallow traps. J. Am. Chem. Soc. **136**, 13818–13825 (2014)
58. Onoda-Yamamuro, N., Matsuo, T., Suga, H.: Calorimetric and IR spectroscopic studies of phase transitions in methylammonium trihalogenoplumbates (II)†. J. Phys. Chem. Solids **51**, 1383–1395 (1990)
59. Onoda-Yamamuro, N., Matsuo, T., Suga, H.: Dielectric study of $CH_3NH_3PBX_3$ (X = CL, BR, I). J. Phys. Chem. Solids **53**, 935–939 (1992)
60. Pockett, A., Eperon, G.E., Peltola, T., Snaith, H.J., Walker, A.B., Peter, L.M., Cameron, P.J.: Characterization of planar lead halide perovskite solar cells by impedance spectroscopy, open circuit photovoltage decay and intensity-modulated photovoltage/photocurrent spectroscopy. J. Phys. Chem. C **119**, 3456–3465 (2015)
61. Poglitsch, A., Weber, D.: Dynamic disorder in methylammoniumtrihalogenoplumbates (II) observed by millimeter wave spectroscopy. J. Chem. Phys. **87**, 6373–6378 (1987)
62. Qin, C., Matsushima, T., Fujihara, T., Potscavage, W.J., Adachi, C.: Degradation mechanisms of solution-processed planar perovskite solar cells: thermally stimulated current measurement for analysis of carrier traps. Adv. Mater. **28**, 466–471 (2016)
63. Roiati, V., Colella, S., Lerario, G., De Marco, L., Rizzo, A., Listorti, A., Gigli, G.: Investigating charge dynamics in halide perovskite-sensitized mesostructured solar cells. Energy Environ. Sci. **7**, 1889–1894 (2014)

64. Sanchez, R.S., Gonzalez-Pedro, V., Lee, J.-W., Park, N.-G., Kang, Y.S., Mora-Sero, I., Bisquert, J.: Slow dynamic processes in lead halide perovskite solar cells. Characteristic times and hysteresis. J. Phys. Chem. Lett. **5**, 2357–2363 (2014)
65. Sepalage, G.A., Meyer, S., Pascoe, A., Scully, A.D., Huang, F., Bach, U., Cheng, Y.-B., Spiccia, L.: Copper(I) iodide as hole-conductor in planar perovskite solar cells: probing the origin of J-V hysteresis. Adv. Funct. Mater. **25**, 5650–5661 (2015)
66. Shi, D., Adinolfi, V., Comin, R., Yuan, M., Alarousu, E., Buin, A., Chen, Y., Hoogland, S., Rothenberger, A., Katsiev, K., Losovyj, Y., Zhang, X., Dowben, P.A., Mohammed, O.F., Sargent, E.H., Bakr, O.M.: Low trap-state density and long carrier diffusion in organolead trihalide perovskite single crystals. Science **347**, 519–522 (2015)
67. Stranks, S.D., Burlakov, V.M., Leijtens, T., Ball, J.M., Goriely, A., Snaith, H.J.: Recombination kinetics in organic-inorganic perovskites: excitons, free charge, and subgap states. Phys. Rev. Appl. **2**, 034007 (2014)
68. Sze, S.M.: Physics of Semiconductor Devizes, 2nd edn. Wiley, New York (1981)
69. Tomozawa, M., Shin, D.-W.: Charge carrier concentration and mobility of ions in a silica glass. J. Non-Cryst. Solids **241**, 140–148 (1998)
70. Unger, E.L., Hoke, E.T., Bailie, C.D., Nguyen, W.H., Bowring, A.R., Heumuller, T., Christoforo, M.G., McGehee, M.D.: Hysteresis and transient behavior in current-voltage measurements of hybrid-perovskite absorber solar cells. Energy Environ. Sci. **7**, 3690–3698 (2014)
71. Wang, Q., Shao, Y., Xie, H., Lyu, L., Liu, X., Gao, Y., Huang, J.: Qualifying composition dependent p and n self-doping in $CH_3NH_3PbI_3$. Appl. Phys. Lett. **105**, 163508 (2014)
72. Wetzelaer, G.-J.A.H., Scheepers, M., Sempere, A.M., Momblona, C., Ávila, J., Bolink, H.J.: Trap-assisted non-radiative recombination in organic-inorganic perovskite solar cells. Adv. Mater. **27**, 1837–1841 (2015)
73. Wu, X., Yu, H., Li, L., Wang, F., Xu, H., Zhao, N.: Composition-dependent light-induced dipole moment change in organometal halide perovskites. J. Phys. Chem. Lett. **119**, 1253–1259 (2014)
74. Xiao, Z., Yuan, Y., Shao, Y., Wang, Q., Dong, Q., Bi, C., Sharma, P., Gruverman, A., Huang, J.: Giant switchable photovoltaic effect in organometal trihalide perovskite devices. Nat. Mater. **14**, 193–198 (2015)
75. Yang, T.-Y., Gregori, G., Pellet, N., Grätzel, M., Maier, J.: The significance of ion conduction in a hybrid organic–inorganic lead-iodide-based perovskite photosensitizer. Angew. Chem. Int. Ed. **54**, 7905–7910 (2015)
76. You, J., Meng, L., Song, T.-B., Guo, T.-F., Yang, Y.M., Chang, W.-H., Hong, Z., Chen, H., Zhou, H., Chen, Q., Liu, Y., De Marco, N., Yang, Y.: Improved air stability of perovskite solar cells via solution-processed metal oxide transport layers. Nat. Nanotechnol. **11**, 75–81 (2016)
77. Zaban, A., Greenshtein, M., Bisquert, J.: Determination of the electron lifetime in nanocrystalline dye solar cells by open-circuit voltage decay measurements. ChemPhysChem **4**, 859–864 (2003)
78. Zarazua, I., Bisquert, J., Garcia-Belmonte, G.: Light-induced space-charge accumulation zone as photovoltaic mechanism in perovskite solar cells. J. Phys. Chem. Lett. **7** (2016)
79. Zhu, X.Y., Podzorov, V.: Charge carriers in hybrid organic-inorganic lead halide perovskites might be protected as large polarons. J. Phys. Chem. Lett. **6**, 4758–4761 (2015)

Charge Transport in Organometal Halide Perovskites

Francesco Maddalena, Pablo P. Boix, Chin Xin Yu, Nripan Mathews, Cesare Soci and Subodh Mhaisalkar

1 Introduction

One of the most important features in any semiconductor device is the charge transport of the active materials. The charge transport mode and the effective charge mobility strongly determine whether a material is suitable for a particular application. A clear example is the relative low mobility of organic semiconductors, compared to their crystalline inorganic counterparts, which makes organic semiconductors unsuitable for high-end electronic applications. Moreover, a deep understanding of the charge transport properties of a particular set of materials is essential for the development of new device architectures and the improvement of the available technological applications.

Recently, the use of organometal halide perovskites, in particular $CH_3NH_3PbI_3$, has generated very promising results in the fabrication of efficient low-cost solar cells. Figure 1 shows how the efficiency of perovskite solar cells has rapidly increased in the last 5 years, surpassing most of its "low cost" competitors and reaching efficiencies exceeding 21 % [1], with their excellent charge transport characteristics underpinning their success. Being solution processable, hybrid perovskites offer advantages similar to organic semiconductors in terms of device fabrication and up-scalability. Moreover, hybrid perovskites have shown great

F. Maddalena · P.P. Boix · N. Mathews · S. Mhaisalkar (✉)
Energy Research Institute @ NTU (ERI@N), Research Technoplaza,
Nanyang Technological University, Nanyang Drive, Singapore 637553, Singapore
e-mail: Subodh@ntu.edu.sg

F. Maddalena · C. Xin Yu · C. Soci
Division of Physics and Applied Physics, Nanyang Technological University,
Singapore 637371, Singapore

N. Mathews · S. Mhaisalkar
School of Materials Science and Engineering, Nanyang Technological University,
Nanyang Avenue, Singapore 639798, Singapore

N.-G. Park et al. (eds.), *Organic-Inorganic Halide Perovskite Photovoltaics*,
DOI 10.1007/978-3-319-35114-8_8

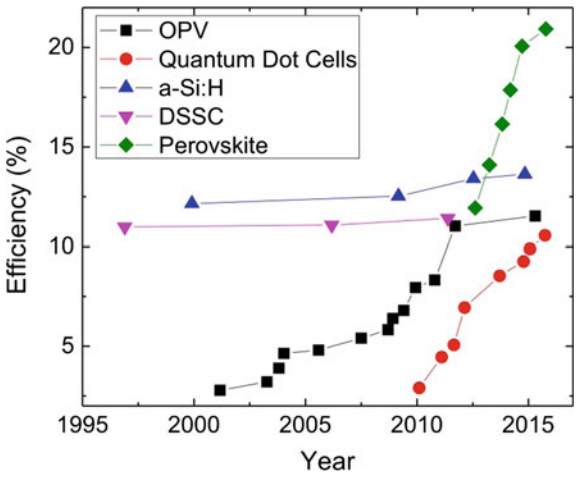

Fig. 1 Evolution of the efficiency of solution-processed perovskite solar cells compared to organic photovolatic (OPV), quantum dot, dye-sensitized (DSSC), and amorphous hydrogenated silicon (a-Si:H) solar cells. Adapted and printed with permission from the National Center for Photovoltaics at NREL solar cell efficiency chart. Reprinted with permission of the National Renewable Energy Laboratory, from http://www.nrel.gov/ncpv/images/efficiency_chart.jpg. Accessed February 12th, 2016

versatility in terms of tunability and efficiency of optoelectronic properties by chemical routes, making them ideal candidates for applications in electroluminescent devices, lasing [2], light-detectors, and thermoelectric energy conversion. Solution-processed perovskite LEDs have already shown very high electroluminescence efficiency and even light-emitting FETs have been reported [3].

In this chapter, we review the theoretical models and experimental observations regarding charge transport in hybrid perovskites available to date, in particular for methylammonium lead iodide and methylammonium lead mixed-halide perovskites, which are currently the most widely studied materials of this class. We will first look at the results from theoretical ab initio calculations of organometallic perovskites, showing potential for very high mobility and efficient charge transport. Then, we shall look at the experimental determination of the diffusion length of charge carriers in organometallic perovskites. Very long diffusion lengths, exceeding the micrometer scale have been experimentally deduced in solution-processed perovskite films and single crystals, making them extremely appealing for various semiconductors applications. Field-effect charge carrier mobilities will then be discussed, which are found to be much lower than the theoretical estimates and the experimental values determined by Hall-effect measurements. Effects of ionic motion and possible ferroelectric effects seem to be responsible for the low performance in FETs and for the large hysteresis and low stability of most organometallic perovskite devices. To conclude, we will give some perspectives on the transport characteristics of emerging two-dimensional (2D) perovskites as well as lead-free compounds, which are attractive alternatives from a commercial and environmental point of view.

2 Theoretical Studies on Charge Transport in Hybrid Perovskites

Following the promising initial results in hybrid perovskite photovoltaics, theoretical studies have been conducted to investigate charge transport characteristics of this class of materials. Ab initio calculations have been performed on models of $CH_3NH_3MI_3$ perovskites (M = Sn, Pb), based on Density Functional Theory (DFT) and many body perturbation theory (MBPT), while approximate models were used to estimate the charge carrier density in the material. The predicted band structure and density of stated (DoS) resulting from the ab initio calculations are shown in Fig. 2.

The investigation of three configurations of $CH_3NH_3PbI_3$, with the dipole of the methylammonium cation along three different orientations ((100), (110), and (111) crystal directions), can help to mimic the disorder in polycrystalline perovskite films. Although the change in the organic cation orientation has noticeable effects on the computed lattice constants, the final calculated energy difference was found to be relatively small between the calculated configurations, within 40 meV. This fact helps explaining the discrepancies between experimental studies [6, 7], where samples may contain different orientations of the organic cations, leading to some variability in the results, as experimentally synthesized perovskites are expected to have lattice constants with values averaged over the all possible configurations. The predicted band structures of the $CH_3NH_3MI_3$ perovskites reveal a quasi-direct bandgap at the R symmetry point of the Brioullin zone, for both the lead and the tin variants. Calculated values of the gaps are 1.36 eV and 1.51 eV for Pb and Sn respectively [16], relatively close to the experimentally determined values of 1.57 eV and 1.20 eV respectively for Pb and Sn [8, 9]

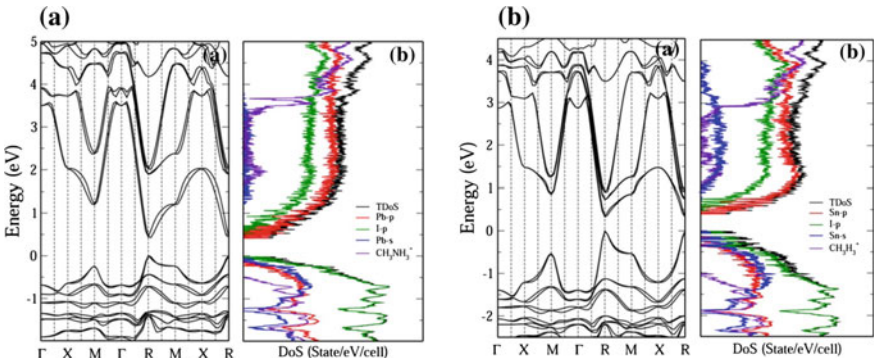

Fig. 2 Band structure (*left panel*) calculated from density functional theory and density of states (DoS) (*right panel*) of methylammonium lead iodide (**a**) and methylammonium tin iodide (**b**). The band structure shown assumes the dipole of $CH_3NH_3^+$ along the (100) direction. The total DoS (TDoS, *black*) is shown along with the partial electronic density of states (DoS) contributions from the metal (Pb or Sn) p-orbitals (*red*), I-p-orbtials (*green*), the metal (Pb or Sn) s-orbitals (*blue*), and the organic cation (*purple*). Adapted and printed with permission from [5]

Theoretical calculations predict very high theoretical mobilities: μ_e = 3100–1500 $cm^2/V\ s$ and μ_h = 500–800 $cm^2/V\ s$ for the lead-based perovskite and μ_e = 2700–1300 $cm^2/V\ s$ and μ_h = 3100–1400 $cm^2/V\ s$ for the tin-based perovskites at charge carrier concentrations of $\sim 10^{16}\ cm^{-3}$. These values, very high compared to other hybrid or organic semiconductors, are of the same order of magnitude of crystalline inorganic semiconductors such as silicon or gallium arsenide.

Calculations have shown that the large carrier mobilities mainly originate from a combination of two factors. First, the small effective masses m^* of electrons and holes (Table 1), with the DoS effective mass being, on average, 0.2333 m_0 and 0.2583 m_0 (m_0 being the rest mass of the electron) for the lead-based perovskite, and 0.3040 m_0 and 0.1906 m_0 for the tin-based perovskite. Such low effective masses were confirmed experimentally through magneto-absorption measurements [10]. The second factor is the relatively weak carrier–phonon interaction, in the range of 6.5–10 eV for both analyzed perovskite materials. The weak electron–phonon coupling is also consistent with the large diffusion lengths determined experimentally for the charge carriers [11–14].

Similar results and conclusions have been reached also by Giorgi et al. [13], which also showed comparably low values for the effective mass of charge carriers (>0.3 m_0) for the methylammonium lead iodide perovskite.

The effective mass and temperature-dependent mobility for two different crystalline phases of $MAPbI_3$, orthorhombic (below T = 160 K), and tetragonal (above T = 160 K) show slightly better conductivity for electrons than holes, as shown in Fig. 3. Low effective masses are predicted, close to the values reported above, with slightly larger values for the orthorhombic phase and overall larger hole effective masses, consistent with lower predicted hole mobilities (tetragonal: m_e^* = 0.197 m_0, m_h^* = 0.340 m_0, orthorhombic: m_e^* = 0.239 m_0, m_h^* = 0.357 m_0). Within the investigated temperature range (78–300 K), electron mobilities exceed hole mobilities by approximately a factor of two, and an increase by nearly one order of magnitude, for both electron and hole mobilities, is predicted below the phase transition temperature (μ_e = 2,577–11,249 $cm^2\ V^{-1}\ s^{-1}$ and μ_h = 1,060–4,630 $cm^2\ V^{-1}\ s^{-1}$ for the orthorhombic phase and μ_e = 466–2,046 $cm^2\ V^{-1}\ s^{-1}$ and μ_h = 140–614 $cm^2\ V^{-1}\ s^{-1}$ for the tetragonal phase).

Experimental determination of the mobility in perovskites by different methods has reflected these high theoretical values. Combining resistivity and Hall-effect

Table 1 Average values of the longitudinal ($m_\parallel^*$), transverse ($m_\perp^*$), conductivity (m_C^*), band (m_b^*) and density of states (m^*), effective mass for electrons (e^-) and holes (h^+) in $MAPbI_3$ and $MASnI_3$

	$MAPbI_3\ e^-$	$MAPbI_3\ h^+$	$MASnI_3\ e^-$	$MASnI_3\ h^+$
$m_\parallel^*$	0.2095	0.3060	0.3332	0.1540
$m_\perp^*$	0.0881	0.0840	0.1027	0.0750
m_I^*	0.1081	0.1107	0.1334	0.0904
m_b^*	0.1166	0.1291	0.1520	0.9530
m^*	0.2333	0.2583	0.3040	0.1906

Adapted and printed with permission from [5]

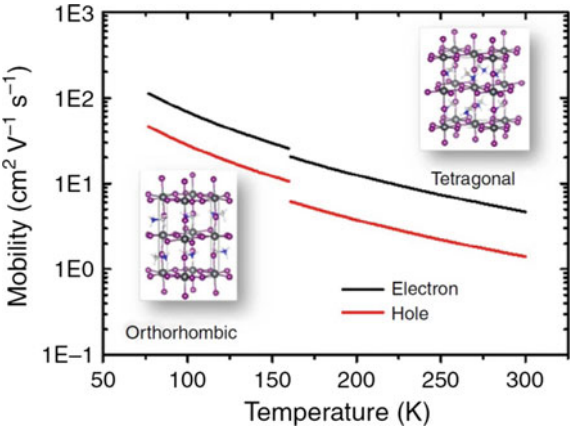

Fig. 3 Calculated temperature dependence hole (*red curves*) and electron (*black curves*) mobility in tetragonal (T = 300–160 K) and orthorhombic (T = 160–77 K) phases of $CH_3NH_3PbI_3$. The crystal unit cells of the two phases are shown as insets. Adapted and printed with permission from [4]

measurements, electron mobilities of $\sim$2320 cm^2/V s in $CH_3NH_3SnI_3$ have been measured [9]. However, for $CH_3NH_3PbI_3$, the experimental mobilities determined by Hall-effect measurements were only of the order of 66 cm^2/V s, significantly lower than the theoretical calculations, although an order of magnitude higher than other solution-processed materials [9, 15].

The influence of the cations and the (halide) anions on the bandgap energy of solution-processed perovskites has been investigated through density functional theory as well [16]. An overview is shown in Fig. 4. The calculations indicate that the bandgap of a perovskite with Orthorhombic structure is distinctively larger than

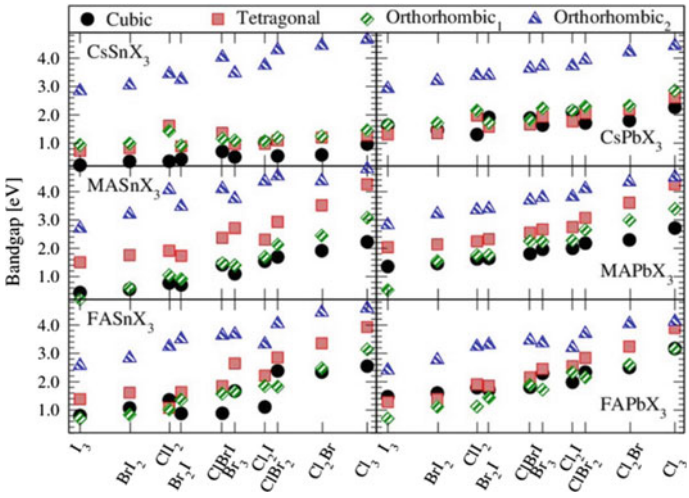

Fig. 4 Theoretically calculated bandgaps as a function of the electronegativity of the anions for different crystalline structures of lead- and tin-based perovskites with different cations are shown: Cesium (Cs), methylammonium (MA) and formamidinium (FA). Adapted and printed with permission from [16]

other crystal structures (cubic, tetragonal). In general, with some exceptions, increasing the tilt of the structure, from cubic to orthorhombic, also leads to an increase of the bandgap. The increase in electronegativity in the anion, ranging from the least electronegative triiodide variant to the most electronegative trichloride, corresponds with a quasilinear increase in the bandgap energy. This trend has been partially confirmed experimentally [8, 9, 17]. The influence of the cations strongly affects the bandgap as well. Increasing the volume of the cation, going from the smallest (Cesium) to the largest (formamidinium) has the effect of increasing the volume of the perovskite unit cell and lattice constants, corresponding to an increase of the bandgap of the material. These results show the tunability and versatility of solution-processable perovskites, especially suitable for optoelectronic applications. The general trends predicted by theoretical calculations, and reflected in current experimental observations, are the basis for the development of novel hybrid perovskites.

3 Charge Carrier Diffusion Length in Hybrid Perovskites

Long electron and hole diffusion lengths, preferably greater than 100 nm, are critical for the development of highly efficient solar cells and junction devices. Large diffusion lengths are responsible for the relatively high efficiencies of solar cells based on classical inorganic semiconductors, like silicon, since they favor electron-hole separation and reduce recombination losses. Polycrystalline organolead trihalide perovskites, such as $CH_3NH_3PbI_3$, have shown very long diffusion lengths, to which was partly attributed the high efficiency of solution-processed solar cells.

Several studies [11–14] have shown that the diffusion lengths for electron and holes in polycrystalline, solution-processed $CH_3NH_3PbI_3$ exceed 100 nm. Such diffusion lengths are at least an order of magnitude larger than those of most organic solution-processed materials (such as P3HT-PCBM bulk heterojunctions), in which diffusion lengths are typically lower than 10 nm [18–20], and are responsible for the high recombination rates.

In good agreement, transient absorption and photoluminescence-quenching measurements determining the electron-hole diffusion lengths in halide perovskites showed balanced diffusion lengths of over 100 nm for both electrons and holes in the triiodide perovskite and, notably, diffusion length of over 1 μm were also reported in the mixed halide variant [11]. Measurements in solar cells showed that the increased diffusion length correlates with an increase in efficiency of photovoltaic devices: from 4.2 to 12.2 % in planar heterojunction solar cells fabricated with the triiodide and the mixed halide perovskite, respectively. Currently, the mechanism that causes the increase of electron-hole diffusion length upon addition of small quantities of chloride ions during the fabrication of $CH_3NH_3PbI_3$, inhibiting nonradiative exciton recombination, is not fully understood. However, it seems to be directly related to film crystallization rather than to material doping [21, 22].

Large charge carrier diffusion lengths for $CH_3NH_3PbI_3$ were also obtained by femtosecond transient optical spectroscopy measurements of bilayers consisting in perovskites with either selective-electron or selective-hole extraction materials (Fig. 5) [12].

Studies on single crystal methylammonium lead iodide have shown diffusion lengths that greatly exceed solution-processed films. Diffusion lengths of over 175 μm under one-sun illumination and diffusion lengths exceeding 3 mm under weak illumination (0.003 % sun) have been observed in solution-grown $CH_3NH_3PbI_3$ single crystals [14]. The enhanced diffusion lengths in single crystals is understood as a combination of greater carrier mobility, longer lifetime, and much smaller trap densities in the single crystals than in polycrystalline thin films. These result from the absence of structural and grain boundary defects that are present in polycrystalline films, indicating possible strategies to improve the electrical properties of perovskite-based devices.

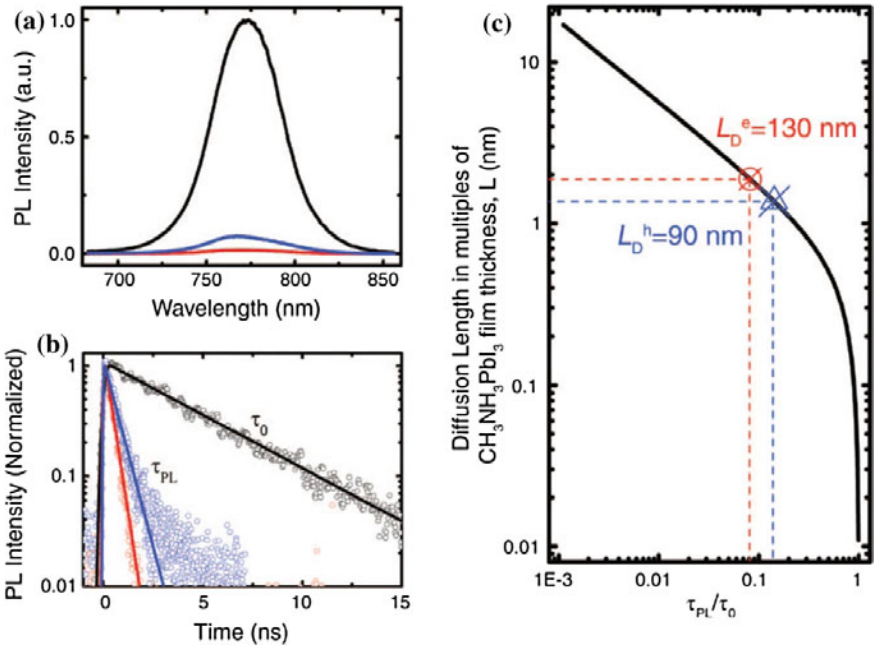

Fig. 5 **a** Time-integrated PL spectra and **b** Time-resolved PL decay transients for quartz/$CH_3NH_3PbI_3$ (*black*), quartz/$CH_3NH_3PbI_3$ (65 nm)/PCBM (*red*), quartz/$CH_3NH_3PbI_3$ (65 nm)/Spiro-OMeTAD (*blue*) films in vacuum after excitation at 600 nm. The *solid lines* in (**b**) are the single-exponential fits of the PL decay transients. **c** A plot of exciton diffusion length versus PL lifetime quenching ratios. Diffusion length is scaled in multiples of $CH_3NH_3PbI_3$ layer thickness (L = 65 nm). Adapted and printed with permission from [12]

4 Charge Carrier Mobility in FET and LED Devices

Although theoretical mobilities in hybrid perovskites are comparable to those of crystalline inorganic semiconductors, and Hall-effect measurements yield very high values, the effective carrier mobility in field-effect transistors (FETs) and diodes is much lower than expected. Peak values for the field-effect mobility in perovskite transistors showed values of the order of 0.5 cm^2/V s for both solution-processed three-dimensional (3D) [4] and 2D-layered perovskites [23]. Several different compositions of organometallic halide perovskites have been investigated in FET configurations, varying the organic cation, the metal cation, or the halide anion. The measured mobilities at saturation fall between 0.01 and 0.1 cm^2/V s, while linear mobilities are usually an order of magnitude lower [24]. Mobilities above 1 cm^2/V s were achieved in melt-processed tin-based organometallic perovskites, where the perovskite films were heated ~5 °C above the melting point and then allowed to recrystallize [25]. Phototransistors showed also mobilities above 0.1 cm^2/V s when the FETs where exposed to white light (10 mW cm^{-2}) [26].

Thus, despite their potential, the best effective mobilities of perovskite FETs are in the same range of state-of-the-art, solution-processed polymer semiconductor FETs (e.g.: N2200, 0.1–1 cm^2/V s for electrons [27]; PBTTT > 0.1 cm^2/V s for holes, [28]). Moreover, since the charge carrier concentration in LED is usually several orders of magnitude lower than in FETs, the low effective charge carrier mobility of solution-processed perovskites presents even more severe problems for the realization of efficient charge injection, charge transport and electroluminescence in light-emitting diodes.

Current studies on solution-processed perovskite FETs have also shown a lack of proper transistor behavior at temperatures above ~200 K [4]. Room temperature transfer characteristics of methylammonium halide FETs show a lack of gating behavior, resulting in transfer curves that are independent of the gate voltage, as depicted in the transfer characteristics in Fig. 6a. Lowering the temperature below ~200 K restores the gating effect in the FETs and increases the current by almost three orders of magnitude (Fig. 6b, c). However, even at low temperatures, the transfer and output characteristics exhibit a strong hysteretic behavior (Fig. 6b, c), similar to the one observed in solar cells [29]. The origin of the hysteresis is uncertain, and it is possibly caused by ionic drift, ferroelectric behavior, and/or presence of traps (see Sect. 5). Experimental measurements on the effective charge carrier mobility in hybrid perovskite FETs have shown a strong dependence on temperature, reflecting some of the theoretical predictions discussed in the previous section [4]. At room temperature, $CH_3NH_3PbI_3$ FETs exhibit very low mobilities, in the range of $\sim 10^{-6}$ cm^2/V s, below even most amorphous organic semiconductors. On the other hand, decreasing the temperature below ~200 K, results in a sharp increase of mobility of over five orders of magnitude as shown in Fig. 7. Previously mentioned theoretical calculations by Chin et al., have shown that above 160 K the perovskite has a morphological change (from a tetragonal to orthorhombic structure) which might be a partial cause of the increase in the

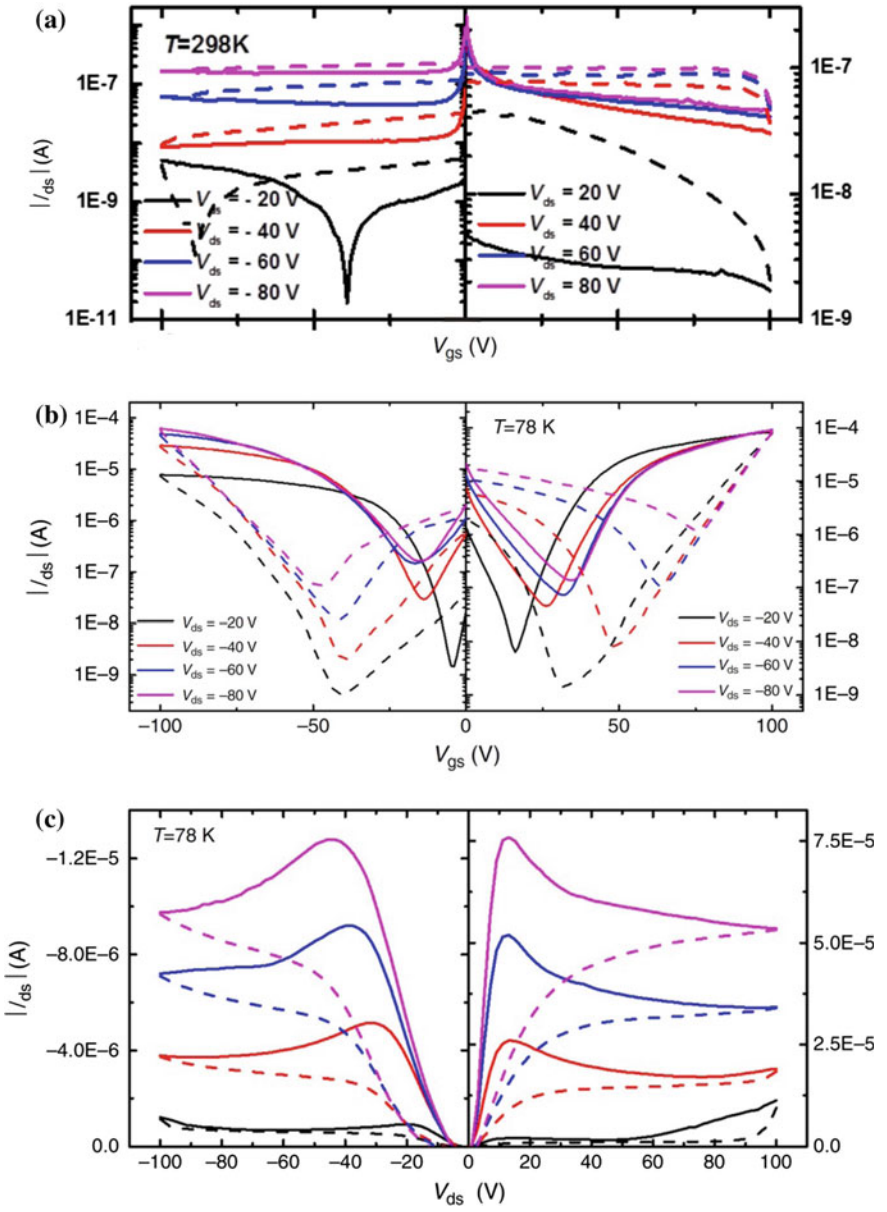

Fig. 6 **a** Transfer characteristics of $CH_3NH_3PbI_3$ FET obtained at 298 K. Transfer (**b**) and output (**c**) characteristics obtained at 78 K. Both the n-type (*right panel*) and p-type (*left panel*) regime. Adapted and printed with permission from [4]

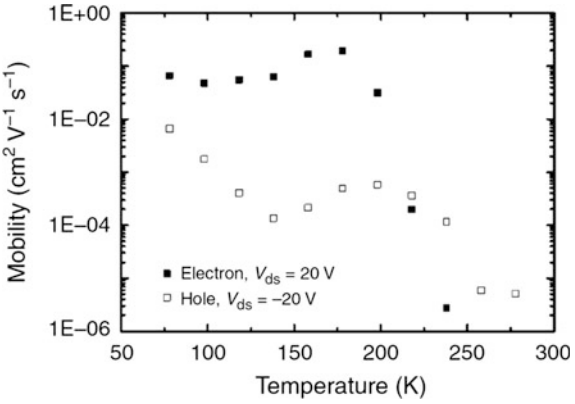

Fig. 7 Temperature dependence of field-effect electron and hole mobilities, extracted from the forward sweeping of transfer characteristics. Adapted and printed with permission from [4]

mobility. However, this phase transition alone is not sufficient to explain the drop in mobility above 180 K, the strong discrepancy between calculated and measured values and the lack of gating at room temperature. The same factors that impair proper gating at temperatures above ~200 K (ionic drift, polarization and/or traps) are probably responsible also for the sudden drop in mobility, however, further investigation is required to fully understand charge transport in perovskites.

It was shown that $CH_3NH_3PbI_3$ FETs operating at room temperature, with an ON/OFF ratio of 10^2 and balanced hole and electron mobilities of 1 cm^2/V s, are possible using top-gate structures with Cytop as the gate insulator, as opposed to prior bottom gate devices with silicon oxide as insulator (Fig. 8) [30]. This suggests that traps at the perovskite-insulator interface might be the major factor limiting charge transport in the devices. Moreover the presence of Cytop, a fluorinated polymer, might protect the highly hygroscopic perovskite from moisture, which might also improve performance of the device. Still, the reported stability of the devices was low and subject to fast degradation.

Previously Kagan et al. and Mitzi et al. [23, 24], also reported perovskite FETs working at room temperatures based on tin-based organometallic perovskites, with ON/OFF ratios higher than 10^4. However, tin-based perovskites are known for their relatively low environmental stability. Moreover, the devices reported by Kagan et al. and Mitzi and coworkers seem to work predominately in p-type conduction mode, rather than the ambipolar behavior achieved with $CH_3NH_3PbI_3$. This may be due to the degradation of the Sn-perovskite resulting in high p-type charge carrier density, as discussed in the corresponding section of this chapter.

In spite of the recent advancements in the fabrication of organometallic perovskite FETs, the origin of the very low mobility of these devices compared to the theoretical expectations still needs further clarifications. Several phenomena, such as ionic drift, polarization, and the presence of traps significantly affect charge transport in these materials, which will be discussed next.

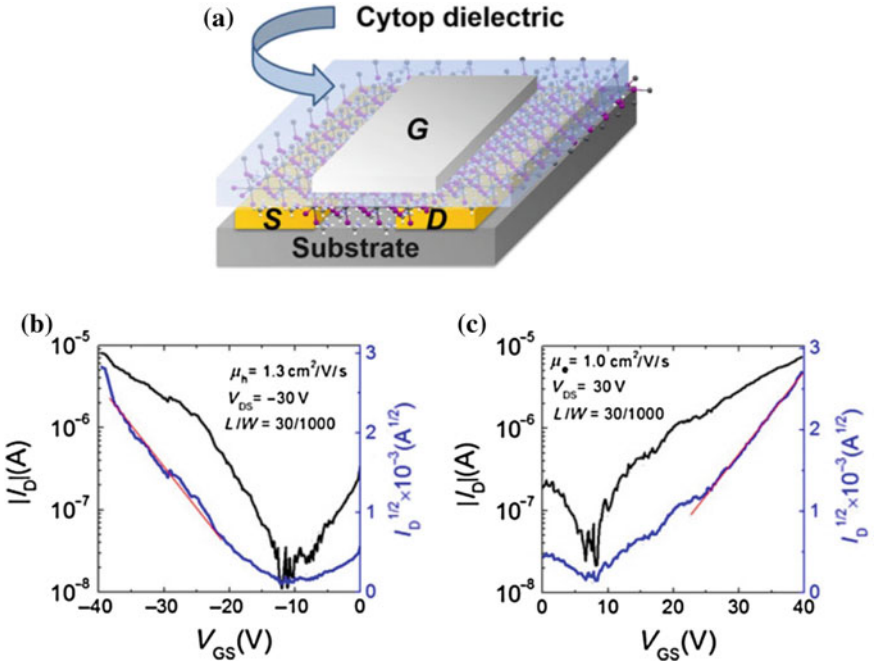

Fig. 8 **a** Schematic structure of the top-gated $CH_3NH_3PbI_{3-x}$ Cl_x FETs having Au source and drain contacts, Cytop gate-dielectric and Al gate electrode. Transfer I–V characteristics for the p-type transport (**b**) and n-type transport (**c**) in $CH_3NH_3PbI_{3-x}$ Cl_x FETs with Cytop gate-dielectric at room temperature. The drain current is plotted versus the gate voltage in *black*, and the square root of the drain current value is plotted in *blue*. The slope used in mobility estimation is shown in *red*. Adapted and printed with permission from [30]

5 The Role of Ion Drift, Polarization, and Traps

One of the most interesting features of organometallic perovskite transport is the anomalous hysteresis observed in IV-curves [31], the cause of which has been tentatively attributed to three effects: ion drift, polarization/ferroelectricity, and the presence of traps. Unraveling these phenomena has strong implications in the understanding of the charge carrier character and the exact transport mechanism in this class of materials. Currently, there is an ongoing debate in the scientific community regarding the importance of these effects, and whether they come to play in the electrical characteristics of hybrid perovskites.

Ion drift can play a dominant role on charge transport properties of $CH_3NH_3PbI_3$ [29]. The reported giant field-switchable photovoltaic effect was best explained by the formation of p–i–n structures induced by ion drift in the perovskite layer. The motion of the ions toward the opposite charged electrodes causes p- and n-type doped regions in the perovskite layer and respective energy band bending, as

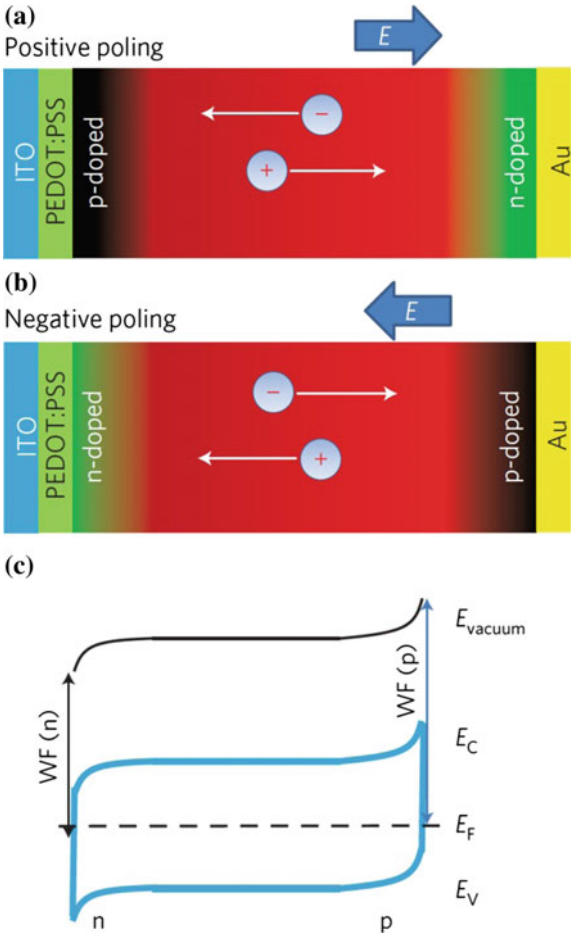

Fig. 9 Schematics of ion drift in perovskite during positive (**a**) and negative poling (**b**), respectively, showing that accumulated ions in the perovskite near the electrodes induced p- and n-doping. **c** Energy diagram of the p–i–n structure after poling (*WF,* workfunction). Adapted and printed with permission from [29]

schematically depicted in Fig. 9. Such self-doping causes a change in the overall resistance and internal electric field of the perovskite layer. Theoretical calculations predicted that negatively charged Pb^{2+} and MA^{+} vacancy could result in p-type doping, whereas positively charged I^{-} vacancy results in n-type doping in $CH_3NH_3PbI_3$ [32, 33]. This behavior was also observed experimentally in composition-dependent studies of $CH_3NH_3PbI_3$, showing evidence of the self-doping of the material [34]. Furthermore, computational modeling of $CH_3NH_3PbI_3$ solar cells shows that the source of the hysteresis is consistent with vacancy assisted migration of iodide ions [35], and the activation energies needed for the ionic drift were found to be in good agreement with experimental kinetic measurements.

On the other hand, ab initio molecular dynamics Monte Carlo simulations [36], indicate that the internal electrical fields associated with microscopic polarization of domains within in $CH_3NH_3PbI_3$ contribute to hysteretic anomalies in hybrid

perovskite devices. The ions present in the perovskite could have high rotational mobility to slowly form ordered polarized domains in response of the applied electric field. The final result is a structured local potential field which is the source of the hysteresis. This polarization hypothesis seems to be corroborated by the different responses of hybrid perovskite devices at different IV-scan rates (Fig. 10) [31], where slower scans, which allow more time for the domain polarization, lead to a higher hysteretic effect.

Investigations of the crystal structure by Stoumpos et al. [9] also noted the possibility for ferroelectric behavior in methylammonium lead iodide and methylammonium tin iodide perovskites. They showed that at room temperature, different possible configurations of the crystal structure of $CH_3NH_3PbI_3$ and $CH_3NH_3SnI_3$ observed by X-ray crystallography are non-centrosymmetric. The space-groups observed are classified in the "ferroelectric distortion" category, where certain symmetries are abolished, including the center of symmetry. This results in the

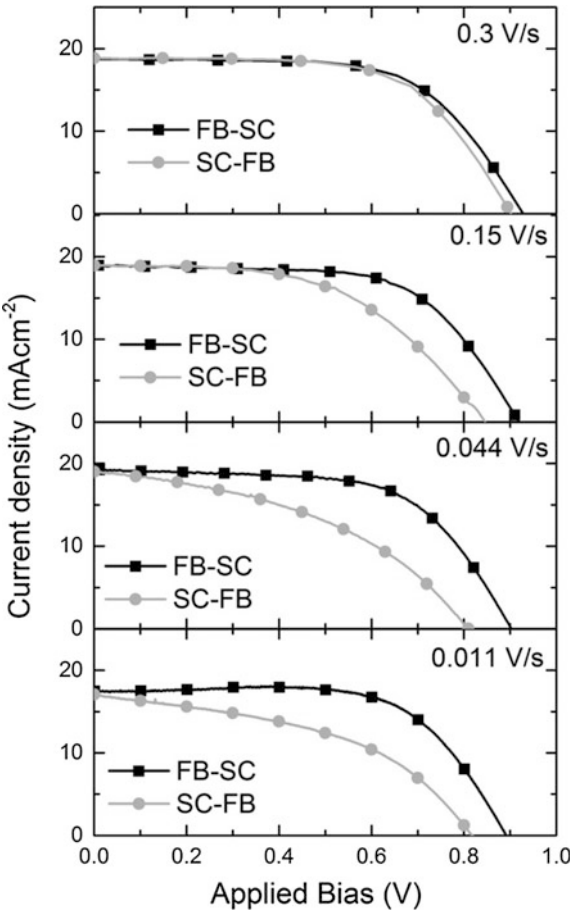

Fig. 10 Influence of scanning conditions on planar heterojunction perovskite solar cell current–voltage characteristics. From forward bias to short circuit (FB-SC, *black*) and from short circuit to forward bias (SC-FB, *gray*) current density–voltage curves for a single solution-processed planar heterojunction perovskite solar cell measured under simulated AM1.5 100 mW cm^{-2} sun light at a range of scan rates from 0.3 to 0.011 V/s. The scans start and finish under forward bias and have 60 s of stabilization time at forward bias (1.4 V) under illumination prior to scanning. Adapted and printed with permission from [31]

displacement of the organic cation from the center of the octahedron in the unit cell. The same experiments note, however, that in addition to ferroelectric distortions also tilting distortions should be taken into consideration.

It has been proposed that the transient processes that occur in IV-characteristics of solar cells are consistent with a polarization response of the $CH_3NH_3PbI_3$ perovskite to the applied electric field [37]. A strong influence of bias preconditioning on IV-measurements seems clear, which could indicate that the internal polarization in the perovskite plays an essential role in the observed current and hysteresis of the device. However, they also notice that the dependence of the hysteretic behavior on bias and light illumination also suggests that photoinduced ion migration might also play an important role in the perovskite transport, especially in regard of slower processes in the device during bias preconditioning.

Finally, it has been demonstrated that by passivating the charge trap states at the interface of the $CH_3NH_3PbI_3$ perovskite by deposition of fullerene layers, the photocurrent hysteresis in perovskite solar cells could be eliminated [38]. Following this approach, the main source of hysteresis in perovskite solar cells would be the trap states at the grain boundaries of the perovskite nanocrystals and the interfaces between the perovskite and the other layers. A schematic depiction of the effect of traps and passivation on charge recombination is shown in Fig. 11. The formation of these traps is explained by the low thermal stability of these materials, which leads to decomposition of the material at higher temperatures (e.g. during annealing), with the introduction of n-doping I-vacancies and compensated by the p-doping in the nondegraded perovskite films. This hysteretic effect is very similar

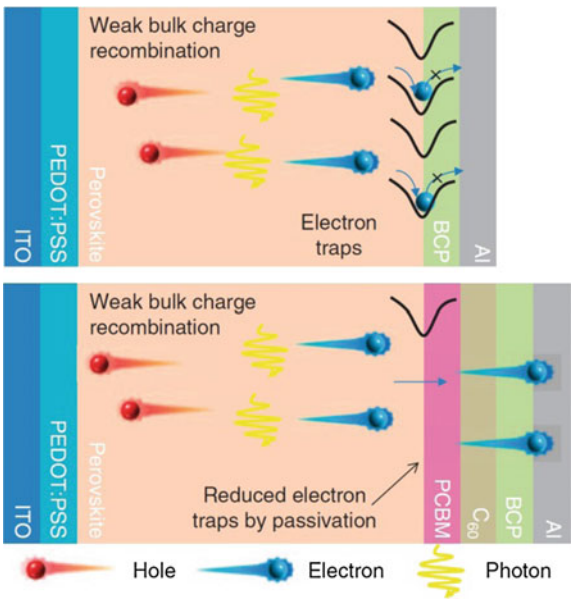

Fig. 11 Schematic depiction of the surface recombination reduction by passivatiing the trap states at the hybrid perovskite interface. Adapted and printed with permission from [38]

to the hysteresis that arises in organic semiconductors with a significant amount of traps [39].

Although different theoretical and experimental results seem to indicate different causes for the hysteresis, there seem to be also correlation between these phenomena. Ionic displacement can be both the source of polarization within a material and also the origin of traps. Polarization can easily induce energetic disorder and broadening of the DoS, hence inducing traps [40]. The debate for the origin, and solution, for the hysteretic behavior in organometallic perovskites is still open, however, the literature here reviewed suggests that more than one single phenomena is at play simultaneously.

6 Polaronic Charge Carriers

The remarkable charge transport features of organometallic halide perovskites discussed above, such as large diffusion length and low recombination rate of the charge carriers, high mobility and low carrier scattering rate [12, 41, 42] seem to suggest that charge carriers originate from scattering with defects, longitudinal optical phonons, and other carriers. Recently, Zhu et al. [43] have proposed that the origin of these remarkable features could be attributed to the polaronic nature of the charge carriers in the hybrid perovskites. The authors hypothesize that a model including the large (delocalized) polarons as charge carriers might explain many of the different peculiar features of metalorganic perovskites. However, the most striking feature is the discrepancy between the very large predicted mobility and the relatively low mobility found in FETs. Although theoretically the effective masses of holes and electrons have been shown to be very small by magneto-absorption measurements [10], there are no reliable measurements of effective carrier mass from transport measurements. However, Zhu et al., note that due to the extremely short lifetimes of the excitons reported in Miyata et al., such absorption measurements only provide information on the nascent electron-hole pairs, before nuclear polarization starts effectively acting on the charge carriers. Hence, the effective masses in the effective transport in diodes, solar cells, and FETs, might be larger than the theoretical expectations, and the currently measured values, and consistent with a large electron–phonon coupling expected in a polaron.

Moreover, the inverse temperature dependence of carrier mobility ($\partial\mu/\partial T < 0$) which has been observed by both spectroscopic [44] and charge transport measurements [4] is consistent with coherent band-like transport of large polarons, where the polaron size and mean-free path is much larger than the lattice constant of the crystal.

Zhu et al. also estimate that the effective mass of electron and holes at room temperature in hybrid perovskites is 100–1000 times larger than the theoretically given values and between 10 m_0 and 300 m_0. Such large values would partially explain the low mobilities in FETs and especially the strong drop in mobility seen above 180 K by [4].

In the case of 2D hybrid perovskites, Cortecchia et al. [59] have shown that the strong charge-phonon coupling resulting from charge confinement in the layered structure causes charge self-localization in specific sites of the inorganic lattice. The resulting strongly localized polarons were found to be responsible for the broad-band light emission observed in various 2D perovskites such as (EDBE) PbX_4 (X = Cl, Br) across the entire visible spectral range, and are thus expected to play a dominant role in the charge transport properties of these materials.

It is important to note that polarons are often the most accurate way to describe electrons and holes within conducting materials, since free charge carriers are usually accompanied by a (local) lattice distortion, coupling phonons, and free electrons or holes [45]. However, the role of polarons in charge transport is dominant only when the electron-phonon coupling becomes sufficiently strong, i.e., in highly polar or ionic conductive solids, [45, 46] such as many II–VI semiconductors and, indeed, (hybrid) perovskites. The cause of the dominant electron/hole-phonon coupling is the stronger Coulomb interaction between a free charge carrier and the lattice ions, compared to less polar materials, such as group IV semiconductors and metals. The stronger coupling leads to a stronger polarization of the lattice, which finally results in an increased effective mass of the charge carrier [47]. Depending on their size, polarons can be classified as either as "small" or "large" [48]. Small polarons are usually involved in hopping transport, such as in organic semiconductors, and have very short diffusion lengths, while large polarons exhibit band-like transport and have very long diffusion lengths, such as the diffusion lengths observed in hybrid perovskites. This is very consistent with the model provided by Zhu et al. and with the relatively low charge carrier mobilities measured in FETs. In conclusion, along with ionic drift, ferroelectric polarization and traps, dominant polaronic charge transport might be one of the main causes of the discrepancy between the theorized high mobilities and the much lower mobilities observed in FETs.

7 Transport in Emerging Perovskite Materials

In spite of the many new advances, organometallic halide perovskites remain a relatively new field in material science, and the main focus of past investigations, with some exceptions, has been mainly aimed at bulk lead-based perovskites. However, recently two particular classes of hybrid perovskites are becoming the target of research. The first class is 2D hybrid perovskites. These materials, unlike graphene or other conventional 2D systems, can be grown from solution, with the possibility to form both 2D-layered structures, such as $(C_6H_5C_2H_4NH_3)2SnI_4$ [23] or even monoatomically thin sheets [49]. Low-dimensional systems offer new interesting challenges and open the possibility to new physical features, also regarding charge transport, thus 2D perovskites are currently gaining attention in the field. The second class of materials is lead-free organometal halide perovskites, which target one of the main concerns in current hybrid perovskite technology: the

presence of lead in the devices. Concerns due to the toxicity of lead may limit widespread implementation of lead-based solar cells and light-emitting devices. Although proper encapsulation and disposal of lead-based devices might minimize any possible risks, this will also increase the costs involved in the production of solar panels or LEDs. These challenges have resulted in increased emphasis on the research of lead-free perovskite materials.

The concept of lower dimensionality (<3D) perovskites lies in the distance between the material layers. The separation of some of these layers in the 3D structure can be achieved, for instance, by the substitution of the cation in the "A" position by a larger sized counterpart (see Fig. 12). The reduction of the stacked layers between the larger cation layers decreases the dimensionality of the material, reaching a typical 2D perovskite when there is a single inorganic layer between the large (organic) cationic layer. Theoretical investigations of 2D organometallic perovskites [50] predict a band structure with very low dispersion in the direction of reciprocal space corresponding to the stacking axis of the layers. Theoretical calculations also show that while the Wannier excitons in 3D hybrid perovskites is strongly screened by collective molecular rotations and vibrations of the inorganic

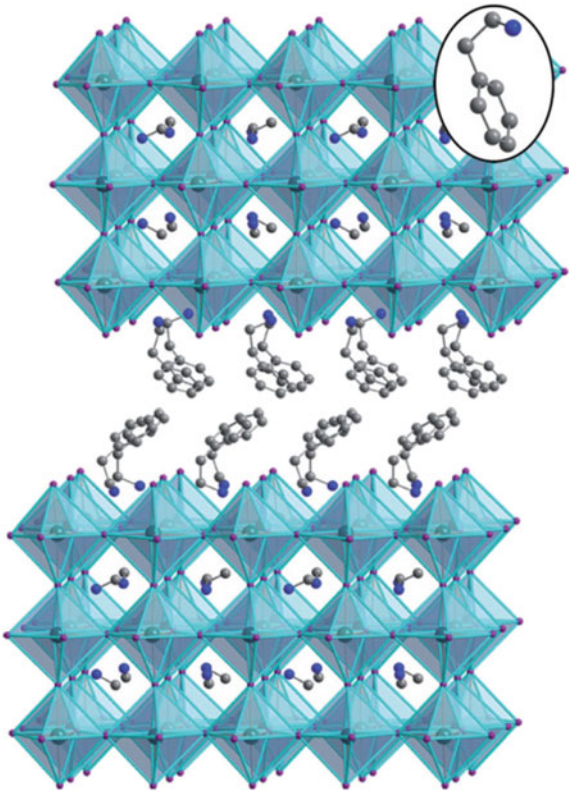

Fig. 12 Schematic representation of a 2D-layered hybrid perovskite. The perovskite had a layered structure, with a few monolayers of perovskite 2D-crystals stacked upon each other and separated by a spacer constituted by an organic molecule bilayer. Adapted and printed with permission from [51]

lattice, this screening does not occur in 2D perovskites [61]. Moreover, a larger bandgap and stronger exciton binding energy is predicted as well.

Experimentally [51], solution-processed 2D-layered perovskites have been achieved. It has been shown that decreasing the dimensionality of the inorganic components, from a 3D- to a 2D-layered structure induces an increase in the bandgap of the perovskite and an increase in the exciton binding energy, which confirms the theoretical predictions.

Despite the increase in exciton binding energy, which can reach up to several 100 meV, the delocalization of the exciton wave function still covers several unit cells in the layer plane, hence it does not have to fully sacrifice the large diffusion lengths that have been observed in 3D perovskites [52].

Recently [49], atomically thin $(C_4H_9NH_3)_2PbBr_4$ 2D perovskites crystals have also been fabricated by solution-phase growth. These 2D structures, only a few monolayers thick, exhibit efficient photoluminescence (Fig. 13), and enable tuning the emission spectrum by changing either the thickness or the chemical composition of the perovskite itself. An exfoliation process can be used for the fabrication of similar 2D perovskites as well [53].

An interesting advantage of the increased bandgap predicted and observed in 2D hybrid perovskites is the possibility for white-light emission. Dohner et al. [54] reported white-light emitting *N*-methylethane-1,2-diammonium lead halide (with a bromine and chloride mixture) 2D perovskites. The observed photoluminescence intensity increases linearly with UV-excitation power density with no signs of saturation, indicating that white-light emission does not depend on the presence of traps within the material, but it is rather a bulk property of the 2D-layered structure of the perovskite.

As previously discussed, Kagan et al., showed tin-based 2D-layered hybrid perovskites in FETs, showing good gating characteristics and mobility even at room temperature. In parallel, 2D-layered perovskite solar cells also showed higher V_{OC} and higher stability to moisture and environmental stability, which is very important for commercialization.

In conclusion, 2D hybrid perovskite structures offer new possibilities for different applications: both in more stable photovoltaic devices, FETs, and electroluminescence applications.

Currently, a few alternatives to lead as the metal cation in hybrid perovskites have already been offered. Several investigations [55–57] have shown promising results in solar cells with tin-based methylammonium halide perovskites, reaching efficiencies up to 5.73 %, in addition to the mentioned tin-based perovskites in FETs. However, tin-based perovskites are very unstable mainly due to p-type doping via Sn^{2+} oxidation, especially when exposed to environmental conditions, leading to very short lifetime of the devices. This has strong implications in the charge transport properties of these materials, going from an almost intrinsic semiconductor model (the case of $CH_3NH_3PbI_3$), to a heavily p-doped one (Sn-based perovskites).

Copper-based organometallic perovskites were investigated from a crystallographic point of view more than 20 years ago [58], mainly in the field of magnetic

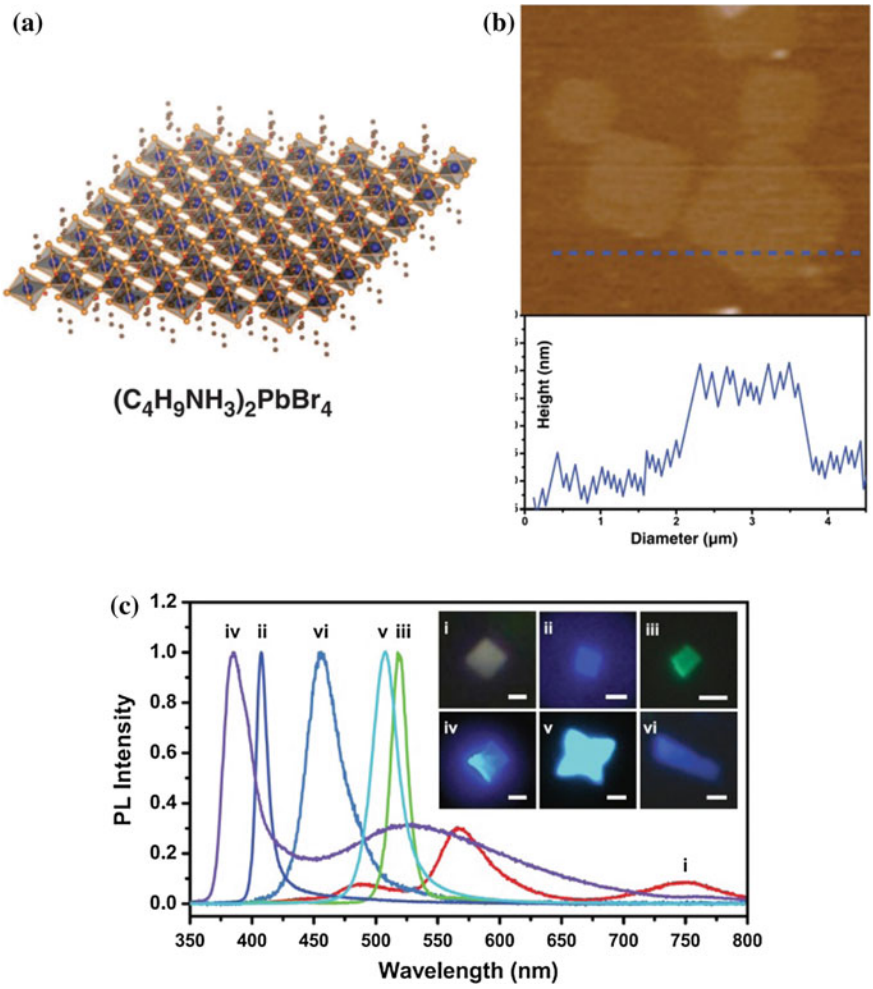

Fig. 13 **a** Structural illustration of a single layer $(C_4H_9NH_3)_2PbBr_4$. **b** AFM image and height profile of several single layers. The thickness is around 1.6 nm (±0.2 nm). **c** Photoluminescence of different 2D hybrid perovskites. $(C_4H_9NH_3)_2PbCl_4$ (*i*), $(C_4H_9NH_3)_2PbBr_4$ (*ii*), $(C_4H_9NH_3)_2PbI_4$ (*iii*), $(C_4H_9NH_3)_2PbCl_2Br_2$ (*iv*), $(C_4H_9NH_3)_2PbbBr_2I_2$ (*v*), and $(C_4H_9NH_3)_2(CH_3NH_3)Pb_2Br_7$ (*vi*) 2D sheets demonstrate that the solution-phase direct growth method is generalizable. The corresponding optical PL images are shown in the inset. Scale bars, 2 mm for (*i*)–(*v*) and 10 mm for (*vi*). Adapted and printed with permission from [49]

materials. Most studies conducted so far have dealt with the synthesis of stable copper-based perovskites, however, no copper-based perovskite device had been reported in the literature until recently, when the first application of copper-based hybrid perovskites $(CH_3NH_3)_2CuCl_xBr_{4-x}$ as light harvester in solar cells was showed [59]. The strong charge transport anisotropy in these layered copper perovskites,

combined with the low absorption coefficient and high hole effective mass, strongly limit the device efficiency. The incorporation of optoelectronically active organic cations in the perovskite scaffold should be used to improve the performance.

Germanium-based lead-free perovskites with promising characteristics for photovoltaic applications [60] have also recently been reported.

In conclusion, despite the progress made toward lead-free efficient hybrid perovskite devices, only the tin-based alternatives have shown some promising results.

Several problems related to the charge transport are hindering the full expansion of 2D and lead-free perovskites. The anisotropy of the charge transport in the low dimensionality perovskites and the strong p-doping in the tin-based ones are clear examples of this. Thus, the full understanding and control of the electrical properties will be a key aspect in the search for 2D and lead-free alternatives. Much theoretical and experimental work still needs to be done to obtain materials with performance comparable to lead-based perovskites.

8 Summary and Conclusions

The field of organometal halide perovskites has shown great progress in the past 5 years, both regarding technological applications and fundamental studies of this relatively new class of materials. This chapter has focused on the charge carrier transport and behavior of this kind of materials. Theoretical investigations have shown results that indicate the characteristic of hybrid perovskites are in many aspects similar to those of crystalline semiconductors, such as low effective mass of the charge carriers, long diffusion lengths, and mobilities in the order of thousands $cm^2\ V^{-1}\ s^{-1}$. Several of these results have also been experimentally confirmed, such as high Hall-effect mobilities and diffusion lengths of charge carriers in the order of hundred micrometers. However, the effective mobilities in devices such as field-effect transistors are much lower than the theoretically predicted values and the values measured by techniques such as Hall-effect, being in the order of $1\ cm^2\ V^{-1}\ s^{-1}$ or less. The discrepancy in the theoretical and effective mobility and the presence of a strong hysteretic behavior in hybrid perovskite devices had given rise to several theories to explain the presence of these anomalies. The possibility of ionic drift, ferroelectric polarization, and trap-states has been thoroughly investigated in the past few years. Although no consensus has been reached yet, it is probable that more than one or even all of these phenomena play a role in charge transport in hybrid perovskites. Recent data has also indicated the possibility that the nature of the charge carrier in hybrid perovskites is polaronic in nature, with higher effective masses than theoretically predicted, which might also explain the lower than expected mobility. Finally, we have also looked at transport in emerging perovskite materials: 2D (layered) perovskites and lead-free perovskites for environmentally-friendly applications. The astounding progress with $CH_3NH_3PbI_3$ solar cells has created a new urgency for the study of organometallic halide perovskites. However, many questions are yet to be fully unanswered and new

developments and applications would undoubtedly stem from the improved understanding of the charge transport phenomena in these multidimensional perovskites.

References

1. Shen, Q., et al.: J. Mater. Chem. A **3**, 9308–9316 (2015)
2. Xing, G., et al.: Nat. Mater. **13**, 476–480 (2014)
3. Tan, Z.-K., et al.: Nat. Nanotechnol. **9**, 687–692 (2014)
4. Chin, X.Y., et al.: Nat. Comm. **6**, 7383 (2015)
5. He, Y., Galli, G.: Chem. Mater. **26**, 5394–5400 (2014)
6. Brivio, F., et al.: APL Mater. **1**, 042111 (2013)
7. Brivio, F., et al.: Phys. Rev. B **89**, 155204 (2014)
8. Eperon, et al.: Energy Environ. Sci. **7**, 982 (2014)
9. Stoumpos, et al.: Inorg. Chem. **52**, 9019–9038 (2013)
10. Miyata, et al.: Nat. Phys. **11**, 582–587 (2015)
11. Stranks, et al.: Science **342**, 341–344 (2013)
12. Xing, et al.: Science **342**, 344–347 (2013)
13. Giorgi, et al.: J. Phys. Chem. Lett. **4**, 4213–4216 (2013)
14. Dong, et al.: Science **347**, 967–970 (2015)
15. Chung, et al.: J. Am. Chem. Soc. **134**, 8579 (2012)
16. Castelli, et al.: APL Mater. **2**, 081514 (2014)
17. Papavassiliou and Koutselas: Synth. Met. **71**, 1713 (1995)
18. Beaujuge, et al.: J. Am. Chem. Soc. **133**, 20009–20029 (2011)
19. Facchetti, Chem: Mater. **23**, 733–758 (2011)
20. Selinsky, et al.: Chem. Soc. Rev. **42**, 2963–2985 (2013)
21. Dharani, et al.: Nanoscale **6**, 13854–13860 (2014)
22. Yantara, et al.: Chem. Mater. **27**, 2309–2314 (2015)
23. Kagan, et al.: Science **286**, 945 (1999)
24. Mitzi, et al.: Chem. Mater. **13**, 3728–3740 (2001)
25. Mitzi, et al.: Adv. Mater. **14**, 1772–1776 (2002)
26. Li, et al.: Nat. Comm. **6**, 8238 (2015)
27. Luzo, et al.: Sci. Rep. **3**, 3425 (2013)
28. McCulloch, et al.: Nat. Mater. **5**, 328–333 (2006)
29. Xiao, et al.: Nat. Mater. **14**, 193–198 (2015)
30. Mei, et al.: MRS Commun. **5**, 297–301 (2015)
31. Snaith, et al.: J. Phys. Chem. Lett. **5**, 1511–1515 (2014)
32. Yin, et al.: Appl. Phys. Lett. **104**, 063903 (2014)
33. Kim, et al.: J. Phys. Chem. Lett. **5**, 1312–1317 (2014)
34. Wang, et al.: Appl. Phys. Lett. **105**, 163508 (2014)
35. Eames, et al.: Nat. Comm. **6**, 7497 (2015)
36. Frost, et al.: APL Mater. **2**, 081506 (2014)
37. Unger, et al.: Energy Environ. Sci. **7**, 3690–3698 (2014)
38. Shao, et al.: Nat. Comm. **5**, 5784 (2014)
39. Lindner, et al.: J. Appl. Phys. **98**, 114505 (2005)
40. Richards, et al.: J. Chem. Phys. **128**, 234905 (2008)
41. Trinnh, et al.: J. Mater. Chem. A **3**, 9285–9290 (2015)
42. Price, et al.: Nat. Comm. **6**, 8420 (2015)
43. Zhu and Podzorov: J. Phys. Chem. Lett. **6**, 4758–4761 (2015)
44. Milot, et al.: Adv. Funct. Mater. **25**, 6218–6227 (2015)

45. Devreese, Encycl: Appl. Phys. **14**, 383–409 (1996)
46. Grundmann, M.: The Physics of Semiconductors; An Introduction Including Nanophysics and Applications. Springer (2010)
47. Emin, D.: Polarons. Cambridge University Press, Cambridge (2013)
48. Appel: Solid State Phys. **21**, 193–391 (1968)
49. Dou, et al.: Science **349**, 1518–1521 (2015)
50. Pedesseau, et al.: Opt. Quant. Electron. **46**, 1225–1232 (2014)
51. Smith, et al.: Angew. Chem. Int. Ed. **53**, 11232–11235 (2014)
52. Lanty, et al.: J. Phys. Chem. Lett. **5**, 3958–3963 (2014)
53. Niu, et al.: Appl. Phys. Lett. **104**, 171111 (2014)
54. Dohner, et al.: J. Am. Chem. Soc. **136**(38), 13154–13157 (2014)
55. Hao, et al.: Nat. Photonics **8**, 489–494 (2014)
56. Kumar, et al.: Adv. Mater. **26**, 7122 (2014)
57. Noel, et al.: Energy Environ. Sci. **7**, 3061–3068 (2014)
58. Willett, et al.: J. Am. Chem. Soc. **110**, 8639–8650 (1988)
59. Cortecchia, et al.: Inorg. Chem. (accepted manuscript) (2016)
60. Krishnamoorthy, et al.: J. Mater. Chem. A (accepted manuscript) (2016)
61. Even, et al.: J. Phys. Chem. C 119, 10161–10177 (2015)

$APbI_3$ (A = CH_3NH_3 and $HC(NH_2)_2$) Perovskite Solar Cells: From Sensitization to Planar Heterojunction

Jin-Wook Lee, Hui-Seon Kim and Nam-Gyu Park

Abstract Since the first report on long-term stable solid-state perovskite solar cell with a power conversion efficiency (PCE) of 9.7 % based on methylammonium lead iodide in 2012, a certified PCE of 21 % was demonstrated in 2015. Methylammonium lead halide perovskite materials were first attempted as sensitizers in a liquid electrolyte based on dye-sensitized solar cell structure in 2009, showing PCE as low as ~4 %, which was almost doubled in performance by intensifying loading concentration of perovskite in the thinner TiO_2 film in 2011. Lead halide perovskites employing organic ammonium cations such as methylammonium and formamidinium are undoubtedly promising photovoltaic materials. In this chapter, emergency and structural evolutions of perovskite solar cell are described. Basic fundamentals of perovskite materials are described in terms of absorption coefficient, refractive index, dielectric constant, and carrier mobility. Since the perovskite film quality is directly related to its photovoltaic performance, effective methods for high PCE solar cells are described based on two-step spin-coating and adduct approach. Lower band gap perovskite with formamidinium is one of the promising materials because of higher photocurrent without losing photovoltage than methylammonium case. High-quality formamidinium lead iodide films can be prepared by two-step or adduct methods, which is related to photovoltaic performance. Stability issues such as photo-, moisture, and thermal-stabilities are mentioned and methodologies to solve the underlying instability problems are proposed.

1 Introduction

Organometal halide perovskite was applied to dye-sensitized solar cells (DSSCs) as a light absorbing material in 2009 [1]. Miyasaka et al. prepared $CH_3NH_3PbI_3$ ($MAPbI_3$) and $CH_3NH_3PbBr_3$ ($MAPbBr_3$) perovskite-based DSSCs which

J.-W. Lee · H.-S. Kim · N.-G. Park (✉)
Department of Energy Science and School of Chemical Engineering,
Sungkyunkwan University, Suwon 440-746, Republic of Korea
e-mail: naprk@skku.edu

N.-G. Park et al. (eds.), *Organic-Inorganic Halide Perovskite Photovoltaics*,
DOI 10.1007/978-3-319-35114-8_9

demonstrated power conversion efficiencies (PCEs) of 3.8 % and 3.1 %, respectively [1]. However, this work cannot attract attention due to their low PCEs along with instability in liquid electrolyte where organometal halide perovskite easily decomposes. In 2011, a PCE of $MAPbI_3$ had been significantly enhanced to 6.5 % by optimizing perovskite precursor solution and electrolyte composition [2]. Despite a considerable increase in PCE based on its extremely high absorption coefficient (1.5×10^4 cm^{-1} at 550 nm) compared to the conventional dye (1.5×10^3 cm^{-1} for the Ruthenium based organic dye called N719 at 540 nm), the instability of $MAPbI_3$ was still regarded as an apparent drawback inhibiting reproducibility and reliability of $MAPbI_3$-sensitized solar cells [2].

In 2012, a major problem in perovskite-sensitized solar cell employing liquid electrolyte was simply solved by replacing liquid electrolyte with 2, 2′, 7, 7′-tetrakis (*N*,*N*-p-dimethoxy-phenylamino)–9, 9′–spirobifluorene (spiro-MeOTAD) as a hole transporting material (HTM) [3, 4]. Park et al. proposed an architecture which resembles solid-state DSSC, where the $MAPbI_3$ nanocrystals were deposited on the mesoporous TiO_2 (mp-TiO_2) instead of dye [3]. It is notable that the $MAPbI_3$-sensitized solid-state solar cell demonstrated 9.7 % of PCE based on merely 0.6 μm-thick mp-TiO_2 film. Similar PCE can be obtained from N719 sensitized solar cell when mp-TiO_2 film approaches 10 μm. Comparable efficiency obtained with sub-micron thick layer is due to the ten times higher absorption coefficient of $MAPbI_3$ [3]. According to the transient absorption spectroscopy (TAS), charge separation was clearly shown for the perovskite/spiro-MeOTAD junction, but it was not obvious for the mp-TiO_2/perovskite junction [3]. The TAS result for the mp-Al_2O_3/perovskite junction, where Al_2O_3 is not electron accepting layer, was similar for the mp-TiO_2 case, which underlines that the oxide layers for the perovskite deposition can be used as scaffold. Organometal mixed halide of $MAPbI_{3-x}Cl_x$ deposited on mesoporous Al_2O_3 film that was formed on a compact TiO_2 (cp-TiO_2) layer was reported to demonstrate a PCE of 10.9 % upon contacting spiro-MeOTAD, which implies that perovskite material can transport electrons by itself in the absence of adjacent electron transporting material [4]. Both configurations and their underlying optoelectronic properties become a basis for the current evolved perovskite solar cells whose certified recording PCE recently reached 21.0 % [5]. $MAPbI_3$ was simply regarded as a sensitizer at the beginning of development; however, better understanding of optoelectronic fundamentals of $MAPbI_3$ has encouraged us to improve photovoltaic performance of perovskite solar cell by optimizing the device configuration in order to fully utilize its beneficial optoelectronic properties. Figure 1 shows the development of device configuration in sequence from sensitization to planar heterojunction, which is described previously.

Several attempts have been made to replace the Pb cation in $MAPbI_3$ with Sn cation ($CH_3NH_3SnI_3$) to solve the underlying toxicity [6–10]. However, strong oxidizing property of Sn^{2+} to be a Sn^{4+} seriously degrades the stability of the organotin halide perovskite under ambient air [6–8]. On contrary, substitution of iodide with bromide to form $MAPbBr_3$ was reported to enhance the stability against the moisture [9]. The conduction band minimum of the perovskite materials is

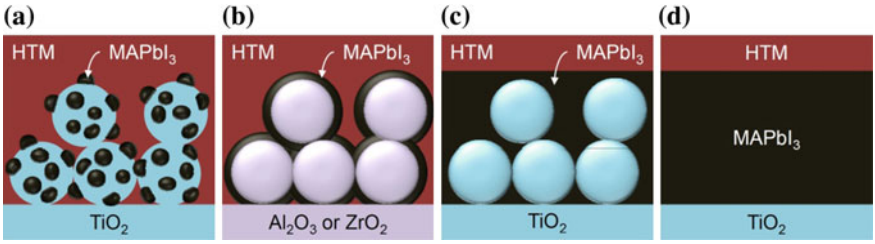

Fig. 1 Evolution of device configuration in perovskite solar cells. **a** sensitization concept, **b** extremely thin layer of perovskite deposited on mesoporous scaffold layer, **c** perovskite infiltration into mesoporous film and **d** planar heterojunction structure

mainly originated from metal cation, while valence band maximum is mainly originated from halide anion [11]. As a result, substitution of metal cation or halide anion results in significant change of optical band gap. For example, the band gap was measured to be 1.3 eV for $CH_3NH_3SnI_3$ and 2.3 eV for $MAPbBr_3$ [6, 9]. Compared to the metal cation and halide anion, organic cation has been attracted less attention because it may not directly affect the band structure. However, studies on the organic cation suggest importance of its role in optoelectronic properties of bulk perovskite and stability as well [12–14].

From the definition of tolerance factor, one can anticipate the structural dependence of perovskite material on organic cation. The stability and crystal structure of ABX_3 (A = organic cation, B = metal cation and X = halide anion) perovskite can be estimated based on tolerance factor (t) [15]. The tolerance factor was simply invented by considering relationship between ionic radius to form ideal cubic perovskite [15]. From the perovskite structure, as shown in Fig. 2, the relationship between ionic radii can be derived by assuming that A and B cations are contact with X anion.

To form ideal cubic perovskite, lattice constants a, b, and c should be same. Therefore, length of yellow lines in Figs. 2a–c should be same, so the relationship between yellow line in (b) and blue line in (c) can be derived as follow (Eq. 1).

$$\frac{r_X + r_A}{\sqrt{2}} = (r_X + r_B) \tag{1}$$

where r_A and r_B are the effective ionic radii for the cations in the cubo-octahedral A and octahedral B sites, respectively, while r_X is the ionic radius of X anion. Goldschmidt's tolerance factor (t) is simply ratio of the left side and right side as expressed in Eq. 2 [15].

$$t = \frac{(r_A + r_X)}{\sqrt{2}(r_B + r_X)} \tag{2}$$

Ionic radii of ions in reported three-dimensional perovskites are summarized in Table 1. Ionic radii of inorganic ions are taken from Shannon's crystal ionic radii,

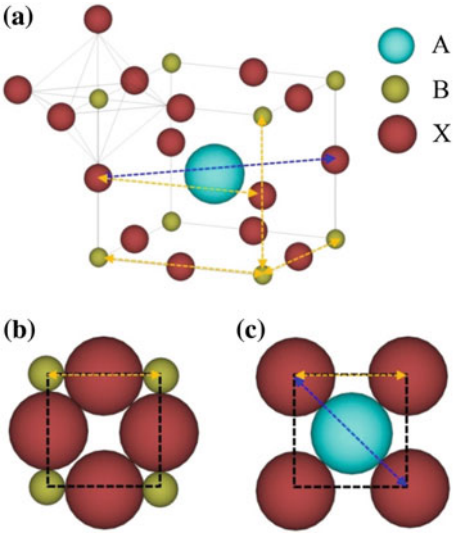

Fig. 2 **a** Ball-stick model for ABX_3 perovskite structure. Cross-sectional view of (001) plane including **b** B and X ions and **c** A and X ions

Table 1 Ionic radii of ions in A, B and X site of ABX_3 perovskite light absorber used for perovskite solar cells

A site	Ionic radii (nm)	B site	Ionic radii	X site	Ionic radii (nm)
Cs^+	0.181	Pb^{2+}	0.119 nm	Cl^-	0.181
$CH_3NH_3^+$ (MA^+)	0.270	Sn^{2+}	0.069 nm	Br^-	0.196
$HC(NH_2)_2^+$ (FA^+)	0.279			I^-	0.220

Ionic radii of inorganic ions are taken from Shannon's crystal ionic radii, while organic cations are taken from the result calculated by discrete Fourier transform (DFT) [14, 16]

while that of organic cations are taken from the result calculated by discrete Fourier transform (DFT) [14, 16]. When t is 0.9–1.0, ideal cubic perovskite is expected, while distorted structures are likely to form orthorhombic, rhombohedral, tetragonal, or hexagonal when t is larger or smaller [14]. For $APbI_3$ perovskite, A cation radius ranges from 2.12 Å for t = 0.9 and 2.60 Å for t = 1.0. For $MAPbI_3$ the most studied perovskite light absorber to date, the ionic radius of $CH_3NH_3^+$ (MA^+) is calculated to be 2.70 Å, as a result it forms tetragonal geometry [17]. Also, the distortion of crystal structure depending on A cation may lead to modification of Pb-I bond length and/or bond angle, which can result in change of optoelectronic properties such as band structure and bandgap [12, 18]. Recently, an extended tolerance factor approach was proposed for organic–inorganic halide perovskites, where more than 600 candidates are expected including alkaline earth metal and lanthanide-based materials [19].

In addition to structural dependence on ionic radius of organic cation, interaction between organic A cation and surrounding PbI_6 octahedra was found to be crucial in thermal and physico-chemical stability [14, 20]. The MA^+ was reported to show temperature dependent dynamic motion (or orientation), which results in

temperature dependent structural change of $MAPbI_3$ [21, 22]. The structural dependence of perovskite light absorber ultimately has an ill effect on thermal stability [23]. Also, degradation of the organometal halide perovskite under light and humidity is related to undesired escape of organic cation from Pb-I framework or reaction of organic cation with external reactant such as oxygen or humidity [24–27].

Because of the presenting issues regarding $MAPbI_3$ perovskite such as temperature-induced phase transition [17, 23], photo-stability [20] and bandgap tuning, an alternative perovskite light absorbers with different organic cation has been suggested [28–30]. Among them, perovskite comprising formamidinium cation ($(HC(NH_2)_2PbI_3$, $FAPbI_3$) is considered as a promising candidate to replace the $MAPbI_3$. In the latter part, methodology for preparation of highly efficient $FAPbI_3$ perovskite solar cell and related issues regarding stability are described.

2 Optical Properties and Band Structure of $CH_3NH_3PbI_3$

Optical property of halide perovskite is primarily important in photovoltaics. Absorption coefficient along with refractive index and dielectric constant will be important criteria to judge the efficient photovoltaic materials. Absorption coefficient of $MAPbI_3$ was first estimated to be 1.5×10^4 cm^{-1} at 550 nm from the transmittance of perovskite film, [2] which was consistent with 5.7×10^4 cm^{-1} at 600 nm [31]. Absorption coefficients of $MAPbI_3$ and $MAPbI_3$:Cl were evaluated by several groups using absorbance data combining with the effect of reflection, spectroscopic ellipsometry (SE) taking into account of polarized reflection and photothermal deflection spectroscopy (PDS), which was summarized in Fig. 3 [32]. At 2.0 eV (= 620 nm), absorption coefficient ranges from 2.5 μm^{-1}(= 2.5×10^4 cm^{-1}) to 8.9 μm^{-1}(= 8.9×10^4 cm^{-1}). Absorption profiles are almost same at

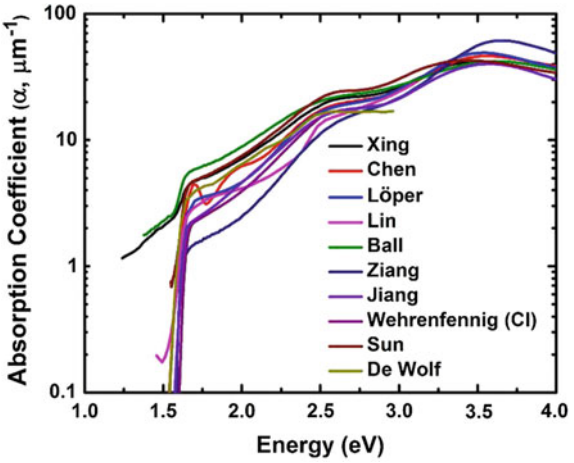

Fig. 3 Room temperature absorption coefficient data for $MAPbI_3$ and $MAPbI_{3-X}Cl_X$. Reprinted with permission from Ref. [32]

absorption edge at 1.6 eV. However, high absorption coefficients measured by ellipsometry are shown even below the band edge in spite of reasonable values at high energies, which indicates that ellipsometry may be inaccurate for low absorption coefficient.

Refractive index and dielectric constants were reported recently by several groups, where the real (n) and imaginary (k) parts of the refractive index are related to those of dielectric constants with the real part ($\varepsilon_1 = n^2 - k^2$) and imaginary part ($\varepsilon_2 = 2nk$). Figure 4 displays the real and imaginary parts of refractive index and dielectric constant [32]. The measured values show quite a bit large deviation, which may be due to different $MAPbI_3$ layer thickness, morphology, chemical composition, material anisotropy, etc., possibly induced by solution-processed deposition procedures. In Fig. 4a, the real part of refractive index ranges between 2.3 and 2.6 for most of the samples except for the sample with larger value of more than 3. A simple approach to estimate refractive index was proposed based on correlation between refractive index and chemical bonding nature in Eq. 3, [33]

$$n^2 - 1 = E_d E_0 / \left(E_0^2 - E^2\right) \tag{3}$$

where E is the photonenergy, $E_d$is the single oscillator energy, and E_0 is the dispersion energy. E_d is equal to $\beta N_c Z_a N_{e,}$ where N_c is the coordination number of the

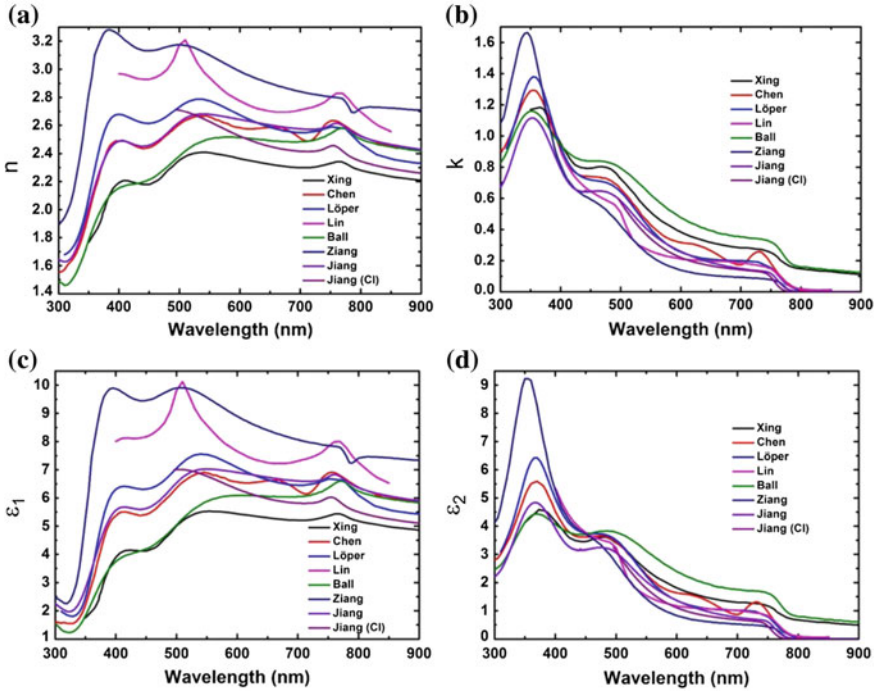

Fig. 4 **a** Real (n) and **b** imaginary (k) part of refractive index and **c** real (ε_1) and **d** imaginary (ε_2) part of dielectric constant of room temperature $MAPbI_3$. Reprinted with permission from Ref. [32]

cation, Z_a the chemical valency of the anion, and N_e the effective number of valence electrons per anion, and β an empirical constant. β is found to be 0.26 ± 0.04 eV for ionic compounds. E_0 is related to direct bandgap energy (E_t), where $E_0 = 1.5 \times E_t$. Thus, the long-wavelength refractive index n(0) is equal to $n(0)^2 - 1 = \beta N_c Z_a N_e / E_0^2$ [33]. For $MAPbI_3$, a value of n = 2.5 can be calculated ($N_c = 6$, $Z_a = 1$, $N_e = 8$, $E_t = 1.6$ eV), which is well consistent with the experimentally obtained data. For $MAPbBr_3$ slightly lower n of 2.1 is calculated due to larger bandgap than iodide case.

$MAPbI_3$ is a direct bandgap material like GaAs, InP, and InGaAs, where the bottom of the conduction band (conduction band minimum, CBM) is aligned with the top of the valence band (valence band maximum, VBM) at the same effective momentum ($k = 0$). The direct bandgap material shows a strong interaction with light, which enable $MAPbI_3$ to become a great attraction for optical devices such as photovoltaic and light emitting diode. When the alignment of bandedges in the valence band and the conduction band occurs at $k = 0$, the band structures can be simply obtained using Eq. 4, [34]

$$E(k) = \frac{\hbar^2 k^2}{2m^*}. \tag{4}$$

where $\hbar (= h/2\pi)$, k, and m^* represent Planck's constant, effective momentum, and effective mass, respectively. On the contrary, indirect bandgap materials (ex. Si) have a relatively weak interaction with electrons due to the energy for transverse light as represented in Eq. 5, [34]

$$E(k) = \frac{\hbar^2 k_x^2}{2m_l^*} + \frac{\hbar^2 \left(k_y^2 + k_z^2\right)}{2m_t^*} \tag{5}$$

where m_l^* and m_t^* represent longitudinal and transverse effective mass, respectively. It is well known that the effective mass is determined by the band structure according to the above equations. Figure 5 shows the band structure and the first Brillouin zones (BZ) for the 3 dimensional cubic ABX_3 ($A = Cs^+, CH_3NH_3^+$, $B = Pb^{2+}, Sn^{2+}$, and X = I, Br, Cl) [35]. For $MAPbI_3$, the valence bands are associated with 5p orbitals of the iodine atom and the conduction bands are associated with Pb 6p orbitals. Compared to the well-known photovoltaic material of GaAs [36], direct bandgap of $MAPbI_3$ is located at the high symmetry point R instead of Γ. At R, a series of other transitions are optically allowed, the lowest in energy corresponding to two secondary transitions $F_{3/2g} \rightarrow E_{1/2u}$ and $E_{1/2g} \rightarrow F_{3/2u}$. The transition between the doubly degenerated $E_{1/2g}$ VB and $E_{1/2u}$ CB states at M is also optically allowed. In E-k diagram, second derivatives $(1/\hbar^2)dE^2/d^2k = 2C_1/\hbar^2 = 1/m_e^*$ for electron and $-2C_2/\hbar^2 = 1/m_h^*$ for hole indicate that the constants C_1 and C_2 in the approximated parabolic curves of CBM for electron and VBM for hole are inversely proportional to effective mass, respectively [37]. As shown in Fig. 5, effective mass of electron and hole is expected to be similar because of similar E-k parabolic

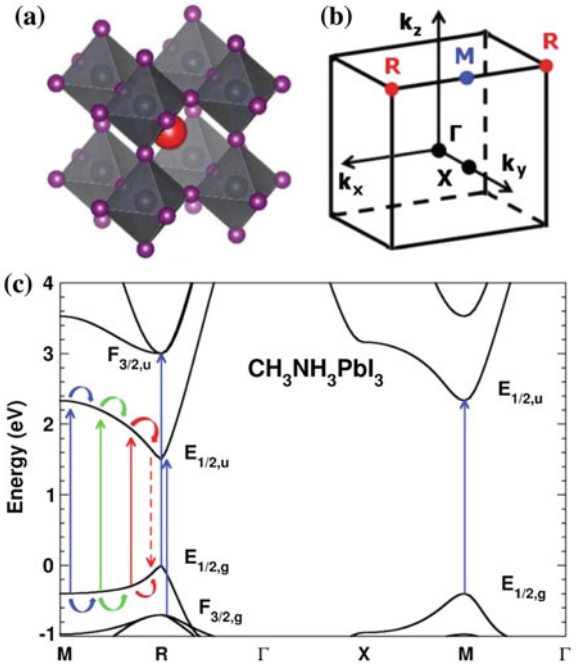

Fig. 5 **a** Real-space 3D view of the cubic crystal structure of AMX_3(A = Cs, $CH_3NH_3^+$, M = Pb, Sn, and X = I, Br, Cl) with the Pm3m space group. $CH_3NH_3^+$ cation (*red ball*) is located at the center of the cube. **b** Reciprocal-space 3D view showing the first BZ of the Pm3m space group. Points of high symmetry in the cubic BZ: Γdenotes the origin of the BZ; X is the center of a *square* face at the BZ boundary; Mis a center of a cube edge; and Rs are vertices of the cube. **c** Electronic band structure for the high-temperature cubic Pm3m phase of $CH_3NH_3PbI_3$ with spin-orbit coupling (SOC) at the local density approximation (LDA) level of theory. An upward energy shift of 1.4 eV has been applied to match the experimental bandgap value at R. Irreducible representations obtained from a Pm3m double group analysis are given at R and M points for the electronic states close to the band gap. *Vertical arrows* show various possible optical transitions close to the band gap energy. Optical transitions along the line between the M and R points generate carriers that easily relax toward the R point. Reprinted with permission from [36]

feature. In $MAPbI_3$, the effective mass of electron and hole was estimated to be 0.23 and 0.29, respectively [38]. The comparable effective mass between electron and hole implies ambipolar characteristics of $MAPbI_3$, which is in well accordance with experimentally measured diffusion coefficients of electron (0.036 cm^2/s) and hole (0.022 cm^2/s) [31]. Recently, carrier-effective masses along with optoelectronic parameters such as exciton binding energy and dielectric constants (Table 2) were estimated for $APbI_3$ perovskites (A = MA and FA) based on a simple two band **k · p** perturbation theory [39].

Table 2 Bandgap (E_g), exciton binding energy (R*), reduced effective mass (μ), effective dielectric constant (ε_{eff}) for $MAPbI_3$ and $FAPbI_3$

High-temperature tetragonal phase					
Compound	E_g (meV)	R^* (meV)	μ (m_e)	ε_{eff}	Temperature (K)
$FAPbI_3$	1521	10	0.095	11.4	140–160
$MAPbI_{3-X}Cl_X$	1600	10	0.105	11.9	190–200
$MAPbI_3$	1608	12	0.104	10.9	155–190
$FAPbBr_3$	2294	24	0.13	8.6	160–170

Reprinted with permission from [39]

3 Sensitized Perovskite Dots in Liquid Electrolyte

3.1 Effect of Precursor Concentration on Photocurrent

As a part of seeking inorganic sensitizers in the form of quantum dot in DSSC to overcome low absorption coefficient of organic sensitizers, $MAPbI_3$ and $MAPbBr_3$ were attempted as inorganic quantum dots. $MAPbI_3$ nanocrystals adsorbed on anatase TiO_2 surface, obtained by spin-coating of gamma-butyrolactone solution of MAI and PbI_2 at rapid spinning rate, was found to deliver photocurrent in the presence of iodide redox electrolyte which, however, did not attract attention due to very low PCE of 3.1–3.8 % because absorbed amount of $MAPbI_3$ was insufficient and quickly dissolved in polar liquid electrolyte [1]. Enough dose of $MAPbI_3$ nanocrystals was successfully introduced to the TiO_2 surface by optimizing concentration of coating solution, which demonstrated doubled PCE of 6.5 % [2]. Photocurrent density (J_{sc}) increases with increasing the concentration of precursor solution as can be seen in Fig. 6, where PCEs increase from 0.32 to 1.38, 2.96, and 4.13 % as the concentration increases from 10.05 to 20.13, 30.18 and 40.26 wt %, respectively, mainly due to increase in J_{sc}, associated with increased absorbance.

3.2 Bandgap Tuning by Ethylammonium Cation

It is well known that the ionic radii of elements determine perovskite crystal structure which can be simply estimated by Goldschmidt tolerance factor (*t*), as discussed previously. Three-dimensional (3-D) perovskite structure is stable with high symmetry (cubic) if *t* is close to 1. In the case of larger *t* than 1 ($t > 1$), BX_6 octahedral cage becomes unstabilized, which leads to two-dimensional (2-D) layer structures with less symmetric tetragonal and orthorhombic phases [40]. The ionic radii of $CH_3CH_2NH_3^+$ (EA^+), $CH_3NH_3^+$ (MA^+), Pb_2^+, and I^- are 0.23, 0.18, 0.119, and 0.220 nm, respectively [40]. Therefore, substitution of EA^+ for MA^+ in organolead iodide perovskite increases *t* from 0.83 to 0.93 under the same octahedral

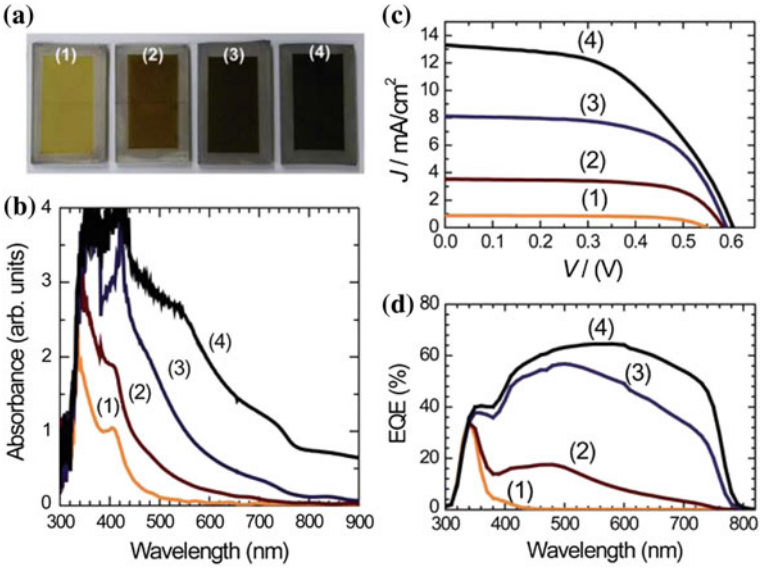

Fig. 6 **a** $MAPbI_3$-sensitized 5.5 μm-thick mesoporous TiO_2 films depending on the concentration of precursor solution of (*1*) 10.05, (*2*) 20.13, (*3*) 30.18 and (*4*) 40.26 wt %. **b** UV-vis absorption spectra of $MAPbI_3$-sensitized 1.4 μm-thick mesoporous TiO_2 film. **c** photocurrent-voltage curves and **d** external quantum efficiency (EQE) spectra of $MAPbI_3$-sensitized 5.5 μm-thick mesoporous TiO_2 films. Reprinted with permission from [2]

factor (μ), $\mu = R_B/R_X$, which is another factor to assume the stabilization of perovskite phase ranging from 0.442 to 0.895 [41]. $CH_3CH_2NH_3PbI_3$($EAPbI_3$) perovskite is determined to be orthorhombic phase with a = 8.7419 Å, b = 8.14745 Å and c = 30.3096 Å. From the atomic structure point of view, the bandgap energy is mainly determined by B and X ions rather than A cation in ABX_3 structure where the VBM is formed by the antibonding coupling between the lone-pair ns^2 orbitals of Pb and the halogen p orbitals and the CBM is determined by mainly unoccupied p orbital of Pb [42]. However, A cation can indirectly affects bandgap by varying the lattice constants of ABX_3. The large size of EA^+ induces large lattice constants which consequently weakens the hybridization of s orbital of Pb and p orbital of I due to the longer distance between atoms. The VBM is shifted down because of the weak hybridization leading to large bandgap. In Fig. 7, the optical bandgap of $EAPbI_3$ was obtained using Kubella–Munk equation showing 2.2 eV. The valence band maximum of $EAPbI_3$ is also shown as 5.6 eV, shifted-down energy level compared to 5.43 eV for $MAPbI_3$, [43] which is in well accordance with the estimation according to the cation size.

The $EAPbI_3$ was also applied to the solar cell with liquid electrolyte [43]. $EAPbI_3$-sensitized solar cell employing 5.4 μm-thick mesoporous TiO_2 film demonstrated photocurrent density (J_{SC}) of 5.2 mA/cm^2, open-circuit voltage (V_{OC})

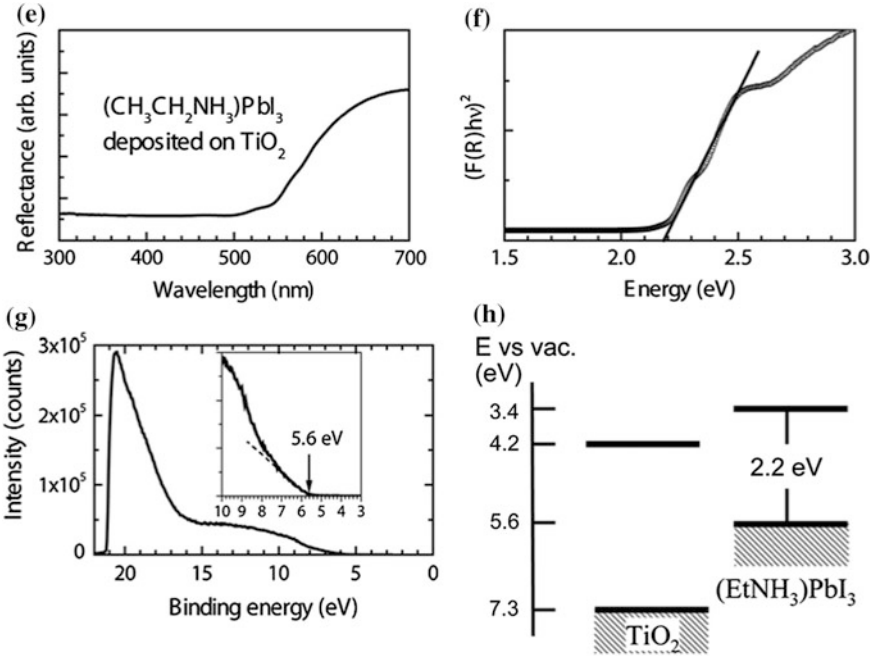

Fig. 7 Diffuse reflectance spectra and the transformed Kubella-Munkfunction, UPS spectrum and schematic energy profile for $CH_3CH_2NH_3PbI_3$ ($EAPbI_3$). Reprinted with permission from [43]

of 0.660 V and fill factor (FF) of 0.704 leading to PCE of 2.4 %. The lowered PCE of $EAPbI_3$ compared to that of $MAPbI_3$ is mainly ascribed to the decreased photocurrent due to its larger bandgap as discussed previously.

4 The First Version of Solid-State $CH_3NH_3PbI_3$ Perovskite Solar Cell

The organolead halide perovskite is easily decomposed by polar solvent for conventional liquid electrolyte, which hinders perovskite from being further developed and studied in depth. In this regard the liquid electrolyte was replaced with a hole transport material (HTM). The very first study on the solid-state perovskite solar cell by Park et al. [3], the $MAPbI_3$ perovskite was employed as a sensitizer as shown in Fig. 8. The 2, 2′, 7, 7′-tetrakis(N, N-p-dimethoxy-phenylamino)–9, 9′–spirobifluorene(spiro-MeOTAD) as HTM was deposited on top of the $MAPbI_3$-sensitized TiO_2 substrate by spin-coating method, which was followed by the evaporation of Au as a top electrode. The HTM was infiltrated in pores of the mesoporous TiO_2 film. The first device showed J_{SC} of 17.6 mA/cm^2, V_{OC} of 0.888 V and FF of 0.62 leading to PCE of 9.7 % under AM 1.5G one

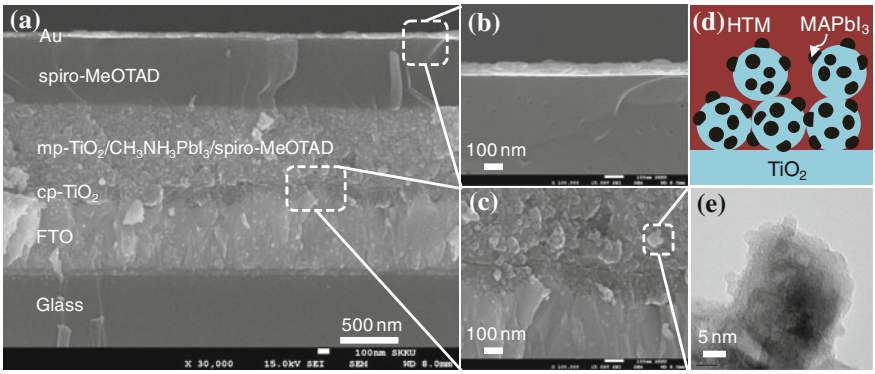

Fig. 8 Cross-sectional scanning electron microscopy (SEM) images and schematic diagram of $MAPbI_3$-sensitized solar cell. Transmission electron microscopy (TEM) image of $MAPbI_3$-sensitized mesoporous TiO_2 film. Reprinted with permission from [3]

sunillumination. The employment of HTM with perovskite not only demonstrated surprising high PCE but also significantly improved device stability maintained for 500 h (ex situ measurement) without encapsulation.

Some unique features were found in $MAPbI_3$-sensitized solar cells. In conventional DSSCs or quantum dot-sensitized solar cells, no change in capacitance was observed in 10^2–10^3 Hz regardless of existence and absence of sensitizers. In $MAPbI_3$-sensitized solar cells, however, increase in capacitance at 10^2–10^3 Hz was evident in the case of the presence of $MAPbI_3$ as can be seen in Fig. 9 [44].

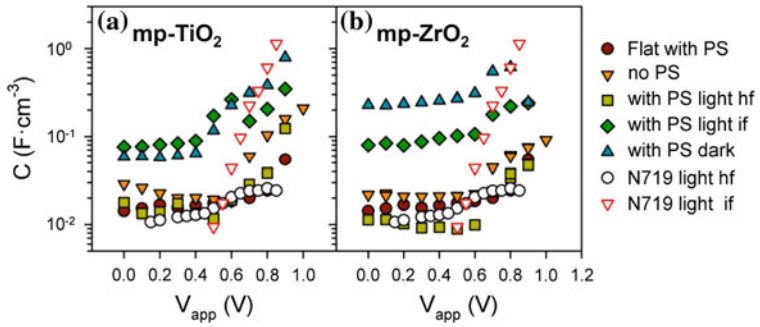

Fig. 9 Capacitance analysis of mesoporous TiO_2 **a** and mesoporous ZrO_2 **b** compared to the solid-state DSSC employing N719 dye. 'Flat with PS' indicates the $MAPbI_3$-sensitized compact TiO_2/spiro-MeOTAD structure. 'no PS' indicates the compact TiO_2/350 nm-thick mesoporous TiO_2/spiro-MeOTAD structure. 'with PS' indicates the compact TiO_2/$MAPbI_3$-sensitized 550 nm-thick mesoporous TiO_2/spiro-MeOTAD structure. 'N719' indicates the compact TiO_2/N719-sensitized 2.2 μm-thick mesoporous TiO_2/spiro-MeOTAD structure. hf and if represent high frequency range (10^5–10^6 Hz) and intermediate frequency range (10^2–10^3 Hz), respectively. Reprinted with permission from [44]

The electron carrier density varied in the semiconductor, closely related to the change of the electron Fermi level, induces capacitance change at 10^2–10^3 Hz. The capacitance affected by the electron density in material is defined as chemical capacitance (C_μ) as shown in Eq. 6, [45]

$$C_\mu = q^2 \frac{\partial n}{\partial E_{F_n}} \tag{6}$$

where q, n, and E_{Fn} are elementary charge, electron carrier density, and Fermi level, respectively. Therefore, the change in C_μ indicates that the $MAPbI_3$ is expected to affect Fermi level and thus sufficiently determine V_{OC}.

Furthermore, it was noticed that the femtosecond transient absorption spectroscopy (TAS) implies an unusual charge separation of $MAPbI_3$. Figure 10 showed TAS spectra with respect to the selective contact [3]. Generally, the electron injection from $MAPbI_3$ to TiO_2 is expected since conduction band edge of TiO_2 is favorably aligned below that of $MAPbI_3$. The photo-generated electron injection into Al_2O_3, meanwhile, is prevented due to the higher conduction band edge of Al_2O_3 than that of $MAPbI_3$. The photo-bleaching band observed in Al_2O_3/$MAPbI_3$ at 483 nm was not obviously relived when the Al_2O_3 was replaced with TiO_2, which indicates that photo-generated electrons tend to stay in $MAPbI_3$ itself rather than subsequent injection into TiO_2 at open-circuit condition. When

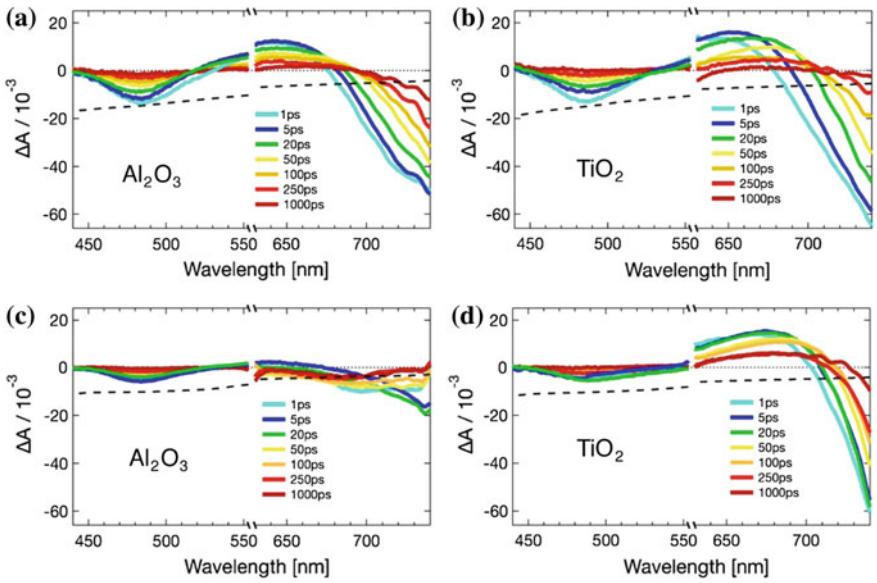

Fig. 10 Femtosecond transient absorbance spectra of Al_2O_3/$MAPbI_3$ (**a**) and TiO_2/$MAPbI_3$ (**b**), spiro-MeOTAD/Al_2O_3/$MAPbI_3$ (**c**), and spiro-MeOTAD/TiO_2/$MAPbI_3$ (**d**). Reprinted with permission from [3]

spiro-MeOTAD was attached, however, the photo bleaching band is evidently reduced due to the reductive quenching of the excited state of $MAPbI_3$.

The result suggests that the device employing Al_2O_3 as a scaffold may act similarly to that employing TiO_2, which is closely related to the second report on solid-state perovskite solar cell, almost coincidentally reported by Snaith et al, where an extremely thin layer of organolead mixed halide, $MAPbI_{3-x}Cl_x$, deposited on mesoporous Al_2O_3 demonstrated PCE as high as 10.2 % [4]. The important insight of charge transporting through organolead halide perovskite encouraged us to regard perovskite solar cells as a thoroughly independent system leading to paradigm shift from DSSC toward the perovskite solar cell with proposing various configuration.

5 Controlled Method for Preparing Perovskite Films

In previous section, the organolead halide perovskite was found to enable photo-generated charges to be accumulated in perovskite itself leading to the change in Fermi level and C_μ. Consequently, the device configuration may be modified from sensitization to heterojunction such as a perovskite/p-type HTM junction or a perovskite/n-type ETM (electron transporting material) junction or a ETM/perovskite/HTM junction. In this case, perovskite in the form of thin film is required instead of nano dot morphology. Here, we introduce an effective methods to prepare $MAPbI_3$ films which are two-step spin-coating method and Lewis acid–base adduct one.

Two-step method, where a deposition of PbI_2 is followed by spin-coating of CH_3NH_3I (MAI) solution to produce $MAPbI_3$, allowed perovskite to be successfully infiltrated in mesoporous TiO_2 remaining $MAPbI_3$ cuboids on the top of TiO_2 film (Fig. 11) [46]. $MAPbI_3$ crystal growth is significantly dependent on the concentration of MAI solution, where low concentration such as 0.038 M leads to sparsely distributed seed crystals at the beginning of nucleation (Fig. 11a), on the other hand, relatively high concentration of 0.063 M results in densely packed seed crystals inhibiting further growth of nuclei (Fig. 11b). Crystal growth mechanism was studied based on thermodynamic Gibbs free energy change [47]. The cuboid size (Y) is found to be correlated with concentration of MAI and temperature, which can be expressed by Eq. 7,

$$\ln Y = \frac{32\overline{\sigma_{sl}^3}}{3kT\left(\frac{kT}{V_m}(\ln X - \ln C_0(T))\right)^2} + C \tag{7}$$

where X is the MAI concentration, C_0 is the equilibrium concentration of MAI, $\overline{\sigma_{sl}}$ is the average surface tension (equal to the change of Gibbs free energy by surface tension), and V_m is the volume of a solute particle. The observed MAI concentration-dependent cuboid size is fitted well with Eq. 7.

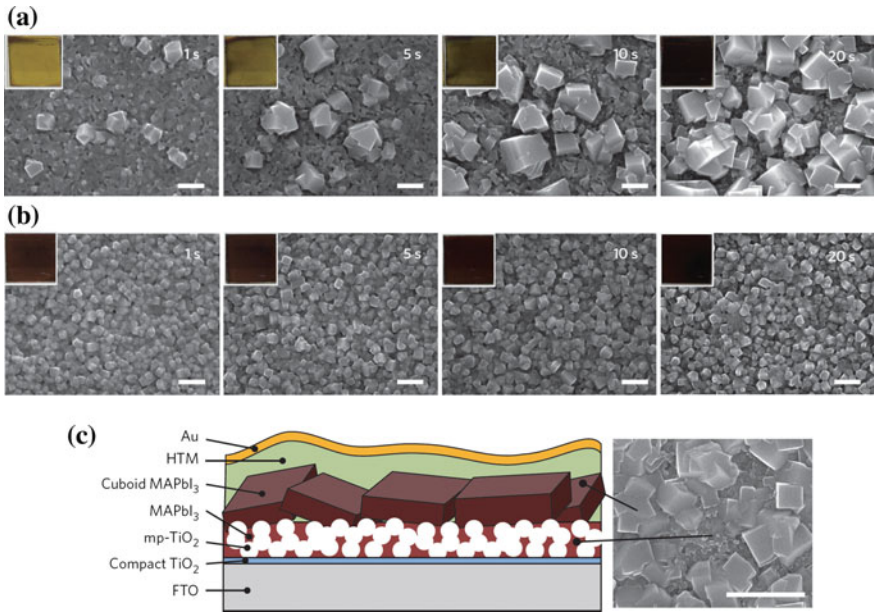

Fig. 11 $MAPbI_3$ crystal growth with respect to the concentration of MAI solution for 0.038 M (**a**) and 0.063 M (**b**). Schematic diagram of device structure based on two-step method and surface SEM image of perovskite deposited on mesoporous TiO_2 film (**c**). Reprinted with permission from [46]

Optimal photovoltaic performance was observed with ca. 700 nm-sized $MAPbI_3$ perovskite cuboids obtained from 0.038 M of MAI solution. The large crystals showed higher charge extraction and light harvesting due to the enhanced internal scattering effect, which led to highest J_{SC} of 21.64 mA/cm^2 compared to the smaller cuboids. However, 700 nm-sized perovskite did not show highest V_{OC} due to slow rate of charge extraction, while medium size of about 200 nm exhibited highest V_{OC} owing to fast mobility. Consequently, a PCE of 17.01 % was achieved using two-step spin-coating method by varying the MAI concentration. Since J_{SC} increases with increasing the cuboid size, one can expect that higher J_{SC} may be possible from lager size. However, much lower J_{SC} of about 17 mA/cm^2 along with V_{OC} as low as 0.92 V was observed from the cuboid size more than one micrometer, prepared using 0.032 M MAI, which is related to non-radiative recombination as confirmed by micro-PL mapping [48].

As one of effective methods, adduct approach was proposed to prepare high quality of $MAPbI_3$ perovskite film [49]. The interaction between N, N-dimethyl sulfoxide (DMSO) as a Lewis base and PbI_2 as a Lewis acid made transparent adduct film which converted to $MAPbI_3$ by removing DMSO. The transparent film shown in Fig. 12a is directly indicative of the formation of adduct, which turns to dark brown during heating process (Fig. 12b). In Fig. 12c, d a stretching vibration of S = O is observed at 1045 cm^{-1} for DMSO solvent, which shifts to 1020 cm^{-1}

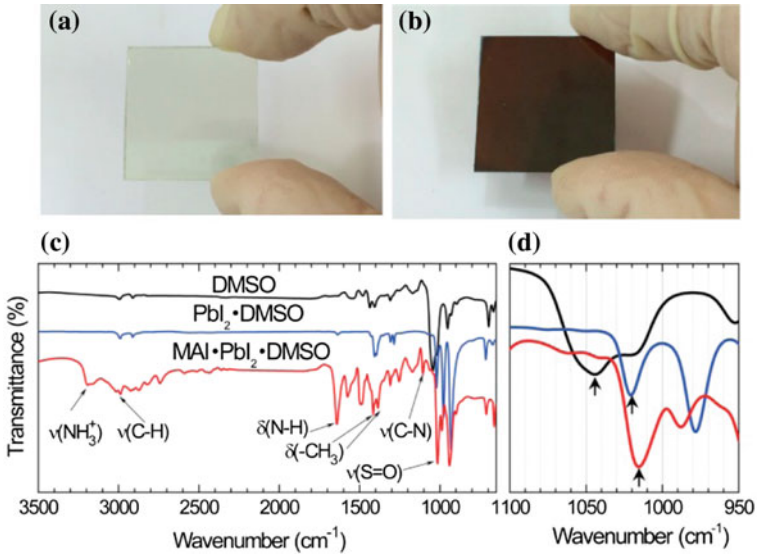

Fig. 12 Adduct-induced $MAPbI_3$ film before **a** and after **b** annealing. Fourier transform infrared spectrometer (FTIR) of DMSO (solution), PbI_2•DMSO (powder), MAI•PbI_2•DMSO (powder) **c** and expanded the fingerprint region for the S = O vibrations. Reprinted with permission from [49]

by interacting DMSO and PbI_2. The vibration shifts further to lower wavenumber of 1015 cm^{-1} when DMSO interacts with both MAI and PbI_2(MAI•PbI_2•DMSO).

The adduct-induced $MAPbI_3$ layer shows planar surface as shown in Fig. 13a where the mesoporous TiO_2 film is completely isolated from spiro-MeOTAD layer by perovskite bulk layer (Fig. 13b). A device employing adduct-induced $MAPbI_3$ demonstrated higher charge carrier mobility of 3.9×10^{-3} cm^2/Vs which is one order of magnitude higher than that of $MAPbI_3$ based on a simple one-step coating procedure containing CH_3NH_3Cl, 3.2×10^{-4} cm^2/Vs [50]. The amount of extracted

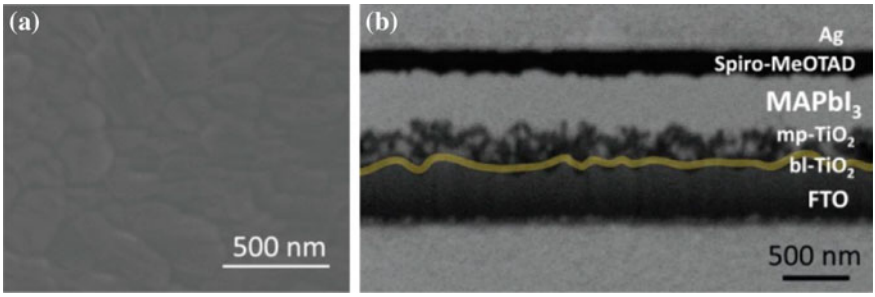

Fig. 13 Surface perovskite layer based on adduct method and cross-sectional FIB-assisted SEM image of device. Reprinted with permission from [49]

charge of the adduct-induced $MAPbI_3$ was obviously increased due to the effectively retarded recombination. Therefore the $MAPbI_3$ induced via adduct significantly improved overall photovoltaic parameters showing J_{SC} of 23.83 mA/cm^2, V_{OC} of 1.086 V, FF of 0.762 and PCE of 19.71 %.

6 Perovskite Solar Cells Based on Formamidinium Lead Iodide

6.1 Adduct Approach for Preparation of $HC(NH_2)_2PbI_3$ Perovskite Film

Formamidinium iodide (FAI) was synthesized and used as a precursor with PbI_2 to form $FAPbI_3$. FAI with high purity is important for fabrication of high-quality $FAPbI_3$ layer. Initially, FAI was synthesized from ethanolic solution of HC(NH)(NH_2) with aqueous HI [51], in which HC(NH)(NH_2) was prepared by reacting HC$(NH_2)_2$Cl with sodium methoxide (MeONa) in methanol. In this process, removal of the precipitate NaCl was not easy. Thus this method may not guarantee FAI purity. Lee et al. replaced the solvent for synthesizing HC(NH)(NH_2) from methanol to ethanol to completely remove the NaCl impurity by considering the solubility of NaCl in ethanol (0.65 g NaCl/1 kg of ethanol) and methanol (14 g NaCl/1 kg of methanol), which was confirmed to yield highly pure $HC(NH_2)_2I$ [30]. Now, the formamidinium acetate, which is cheaper than $HC(NH_2)_2Cl$, is commonly used for synthesis of FAI [29]. $FAPbI_3$ perovskite layer can be prepared by either one-step or two-step method as can be seen in Fig. 14 [28–30].

One-step solution procedure is conducted by spin-coating, the solution containing equimolar FAI and PbI_2 in N, N-dimethyl formamide (DMF) (Fig. 14a) [29, 52]. As seen in Fig. 15a, one-step spin-coating method is normally suffering from the poor coverage of the film because of the difficulty in the control of formation rate constant for perovskite layer [29, 52]. Snaith et al. enhanced the coverage of the $FAPbI_3$ layer by adding hydroiodic acid to increase the solubility of precursors in solution, which results in highly enhanced coverage of $FAPbI_3$ layer on substrate probably due to slower formation rate for $FAPbI_3$ layer (Fig. 15b) [29]. Wang et al. used the $HPbI_3$ as a new precursor for formation of $FAPbI_3$ [52]. As shown in Fig. 15d, utilization of the $HPbI_3$ precursor instead of PbI_2 enable slowdown of crystallization process of $FAPbI_3$ due to exchange reaction of H^+ with FA^+, resulting in highly crystalline and uniform $FAPbI_3$ layer with (110) orientation (Fig. 15c).

Two-step procedure involves reaction of the sequentially deposited PbI_2 with FAI by dipping the PbI_2 layer in 2-propanol solution of FAI [30]. Yellow phase, which is non-perovskite structure, was formed at room temperature, which turned black perovskite phase upon heating at 150 °C. Two-step method showed relatively better coverage of $FAPbI_3$ compared to one-step method. Moreover, grain size can

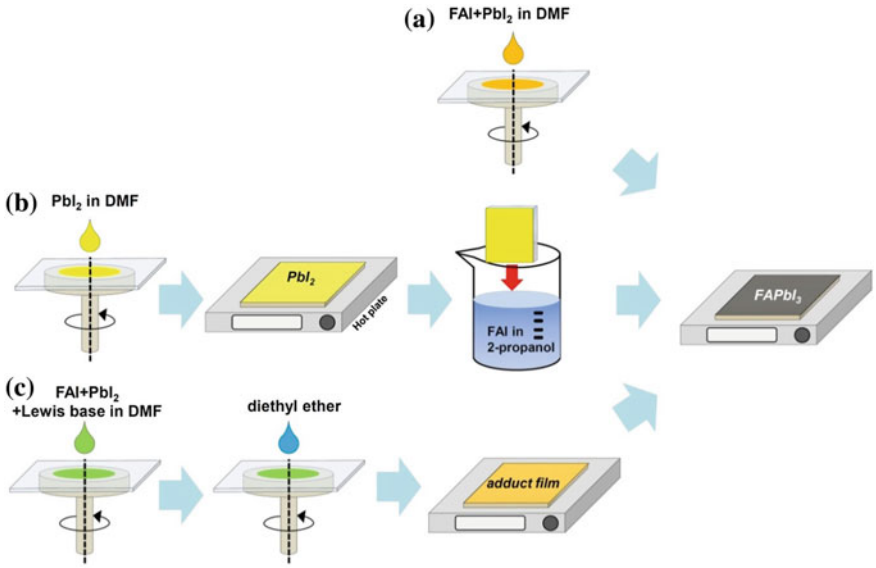

Fig. 14 Deposition procedure for the formation of $FAPbI_3$ film. **a** one-step spin-coating method, **b** two-step sequential method, and **c** adduct approach

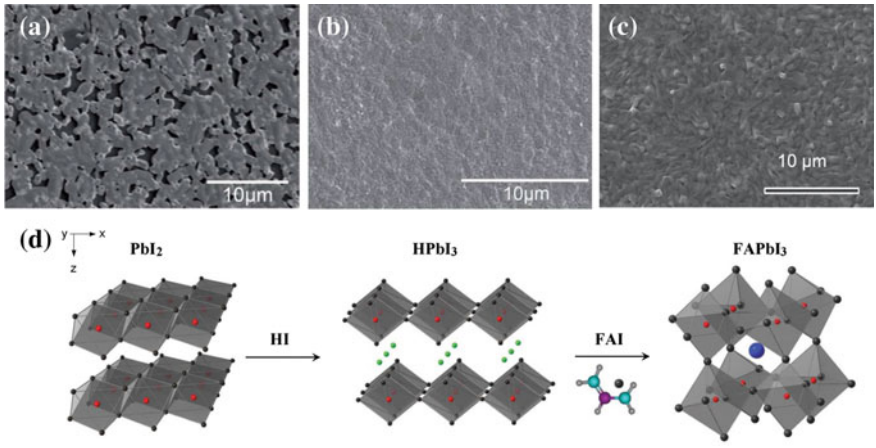

Fig. 15 $FAPbI_3$ perovskite layer formed by one-step spin-coating method. **a** $FAPbI_3$ film formed from equimolar PbI_2 and FAI in DMF. **b** $FAPbI_3$ film formed from the precursor solution containing hydroiodic acid and **c** $HPbI_3$ instead of PbI_2. **d** Schematic illustration of the configurations of PbI_2, $HPbI_3$ and $FAPbI_3$. Reprinted with permission from [29]

be controlled by changing concentration of FAI during the dipping of PbI_2 film in FAI solution [53]. As seen in Fig. 16, grain size of $FAPbI_3$ becomes smaller as the concentration of FAI becomes higher from 40.7 to 58.2 mM, and as a result, the

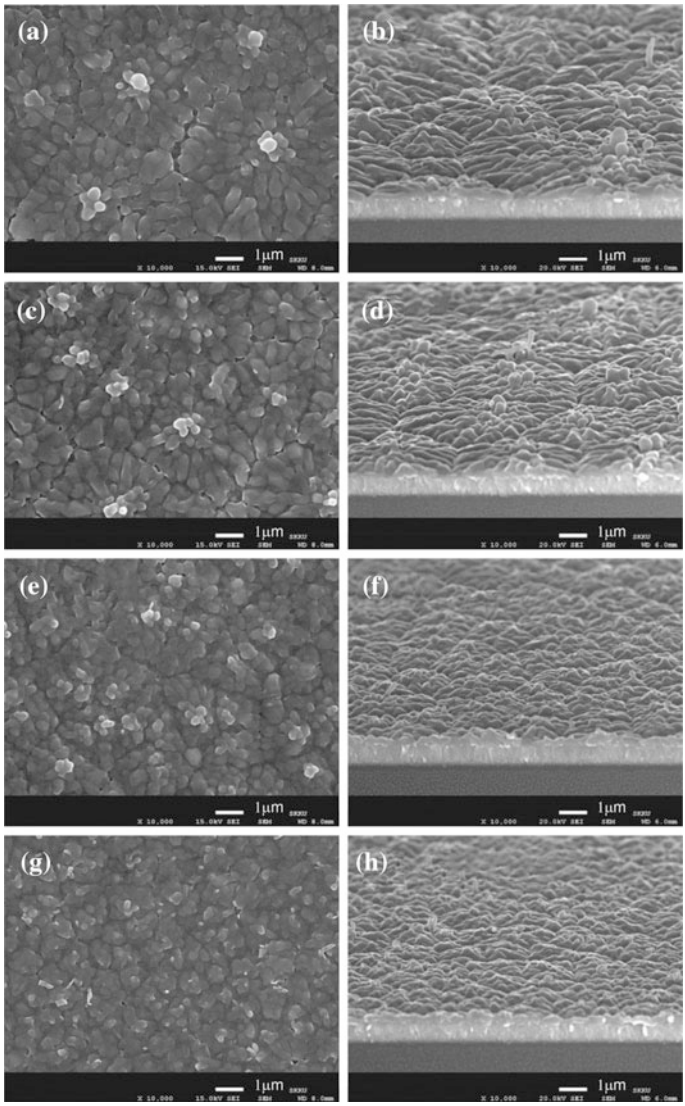

Fig. 16 Plane-view and tilted side-view of SEM images for $FAPbI_3$ using two-step sequential method, in which concentration of FAI was controlled to be **a**, **b** 40.7 mM, **c**, **d** 46.5 mM, **e**, **f** 52.4 mM, and **g**, **h** 58.2 mM of FAI solution, respectively. Scale bars represent 1 μm. Reprinted with permission from [53]

surface roughness increased with the decreased FAI concentration. Controlled size by FAI concentration may be explained similarly using concentration-dependent thermodynamic process as described previously.

The adduct approach was extended for $FAPbI_3$ layer [20]. For the case of $FAPbI_3$ as seen in Fig. 17, utilization of thiourea results in highly uniform $FAPbI_3$

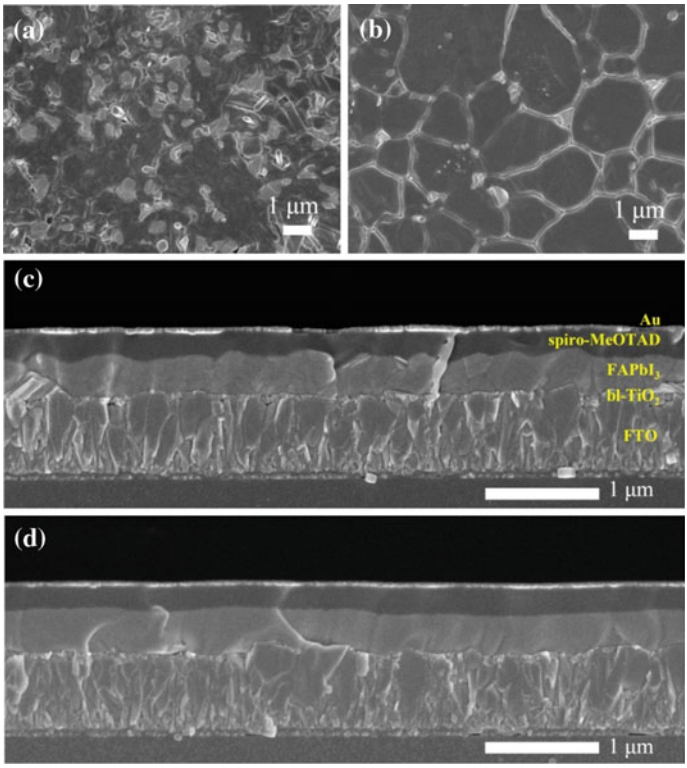

Fig. 17 Surface and cross-sectional SEM images of $FAPbI_3$ perovskite layer and perovskite solar cell formed by adduct approach **a**, **c** without thiourea (only DMSO) and **b**, **d** with thiourea (20 % of DMSO was replaced by thiourea). Reprinted with permission from [54]

layer with much larger domains (from 1 to 4 μm) compared to without thiourea case (from 10 nm to 1 μm) [54], which is likely to correlate with stronger interaction of thiourea in adduct than DMSO, giving kinetically controlled growth. XRD measurement confirmed that the crystallite size of $FAPbI_3$ was significantly enhanced from ca. 50 nm toca. 120 nm when 20 % of DMSO was replaced by thiourea.

6.2 *Photovoltaic Performance of $HC(NH_2)_2PbI_3$-Based Perovskite Solar Cell*

Optical band gap of single crystal $FAPbI_3$ is reported to be 1.41 eV, which is smaller than that of $MAPbI_3$ ($\sim$1.5 eV) [55]. On the other hand, the band gap of the solution-processed $FAPbI_3$ film was measured to range from 1.47 to 1.55 eV depending on the fabrication method [20, 28–30]. Figure 18a compares absorption

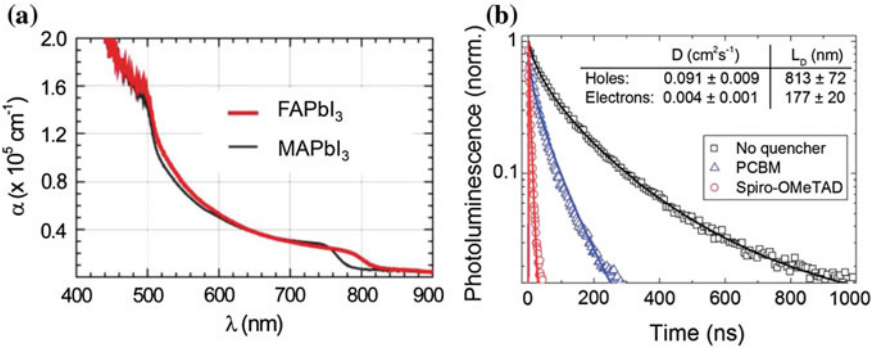

Fig. 18 **a** Absorption coefficient of $FAPbI_3$ and $MAPbI_3$. **b** Normalized time-resolved photoluminescence spectra of bare $FAPbI_3$ (*black*), $FAPbI_3$/PCBM (*blue*) and $FAPbI_3$/spiro-MeOTAD (*red*). The data were fit to stretched exponential decay. The Diffusion coefficients (D) and diffusion lengths (L_D), extracted from the fitting, are shown in the inset. Errors quoted arise predominantly from film thickness variations. Reprinted with permission from [29, 30]

coefficient of $FAPbI_3$ and $MAPbI_3$ [30]. Absorption coefficient of the $FAPbI_3$ film is determined to be 1.53×10^5 cm^{-1} at 500 nm, which is similar or slightly higher than that of the $MAPbI_3$ one. Diffusion coefficient and diffusion length were determined from time-resolved photoluminescence measurement (Fig. 18b) [29], where diffusion coefficient for hole (0.091 ± 0.009 cm^2s^{-1}) is higher than that for electron (0.004 ± 0.001 cm^2s^{-1}), leading to longer diffusion length for holes (813 ± 72 nm) than for electrons (177 ± 20 nm).

According to the DFT calculation, the CBM of $FAPbI_3$ is slightly lower than that of $MAPbI_3$ but the VBM of $FAPbI_3$ is slightly higher than that of $MAPbI_3$ [14]. Koh et al. argued that the CBM of $FAPbI_3$ almost identical with that of TiO_2 might be responsible for lower charge collection of $FAPbI_3$ perovskite solar cell due to weak driving force for electron injection from $FAPbI_3$ to perovskite [28]. However, Lee et al. reported that incorporation of mesoporous TiO_2 layer is beneficial to charge collection in $FAPbI_3$ perovskite solar cell [30]. As mesoporous TiO_2 thickness increases, charge collection is improved as can be seen in Fig. 19a–c, and as a result, J_{SC} is improved from 13 mA/cm^2 for 0 nm (without mp-TiO_2) to 19 mA/cm^2 for 320 nm-thick mp-TiO_2 layer (Fig. 19d). Interestingly, introduction of mp-TiO_2 layer improved the fill factor (FF) due to reduced series resistance and increased shunt resistance, associated with removal of the underlying resistance components in $FAPbI_3$ by TiO_2.

Electron injection from $FAPbI_3$ to TiO_2 was investigated in $FAPbI_3$ perovskite solar cell based on helical TiO_2 (Fig. 20) [56]. Highly crystalline TiO_2 nanohelices were grown by oblique-angle deposition technique using an electron-beam evaporator, which was used in $FAPbI_3$ perovskite solar cell. With same length and diameter, the nanohelix morphology was controlled by changing the pitch (p), turns and radius (r) of the helices (Fig. 20a). The contact area between $FAPbI_3$ perovskite and TiO_2 nanohelices, i.e., the surface area of TiO_2 nanohelices, were changed

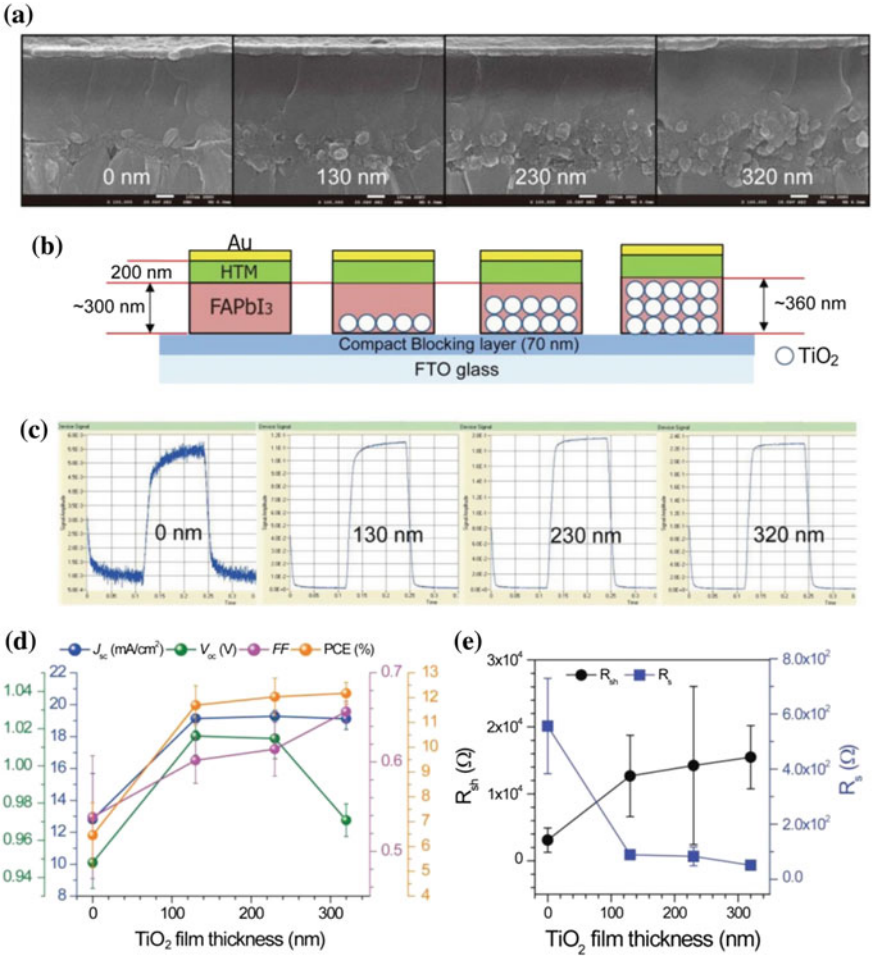

Fig. 19 **a** Cross-sectional SEM images, and, **b** schematic structure of the $FAPbI_3$ layers deposited on 0 (compact blocking TiO_2 layer without mesoporous TiO_2 film), 130-, 230-, and 320 nm-thick mesoporous TiO_2 film. **c** Time-limited photocurrent response as a function of mesoporous TiO_2 film thickness. **d** Dependence of J_{SC}, V_{OC}, FF, and PCE on mesoporous TiO_2 film thickness. **e** Shunt (R_{sh}) and series resistances (R_s) of $FAPbI_3$ perovskite solar cells depending on mesoporous TiO_2 film thickness. More than 9 devices were fabricated for each condition. Reprinted with permission from [30]

(Fig. 20b, c, d), in which increase in contact area between $FAPbI_3$ and TiO_2 leads to higher amount of electron injected, resulting in faster electron diffusion in TiO_2 helix (Fig. 20e–g). This indicates that interfacial electron injection is dominant in heterojunction perovskite solar cell configuration.

Using the mesoscopic structure with two-step deposited $FAPbI_3$ layer, power conversion efficiency of 16.01 % (J_{SC} = 20.97 mA/cm^2, V_{OC} = 1.032, FF = 0.74)

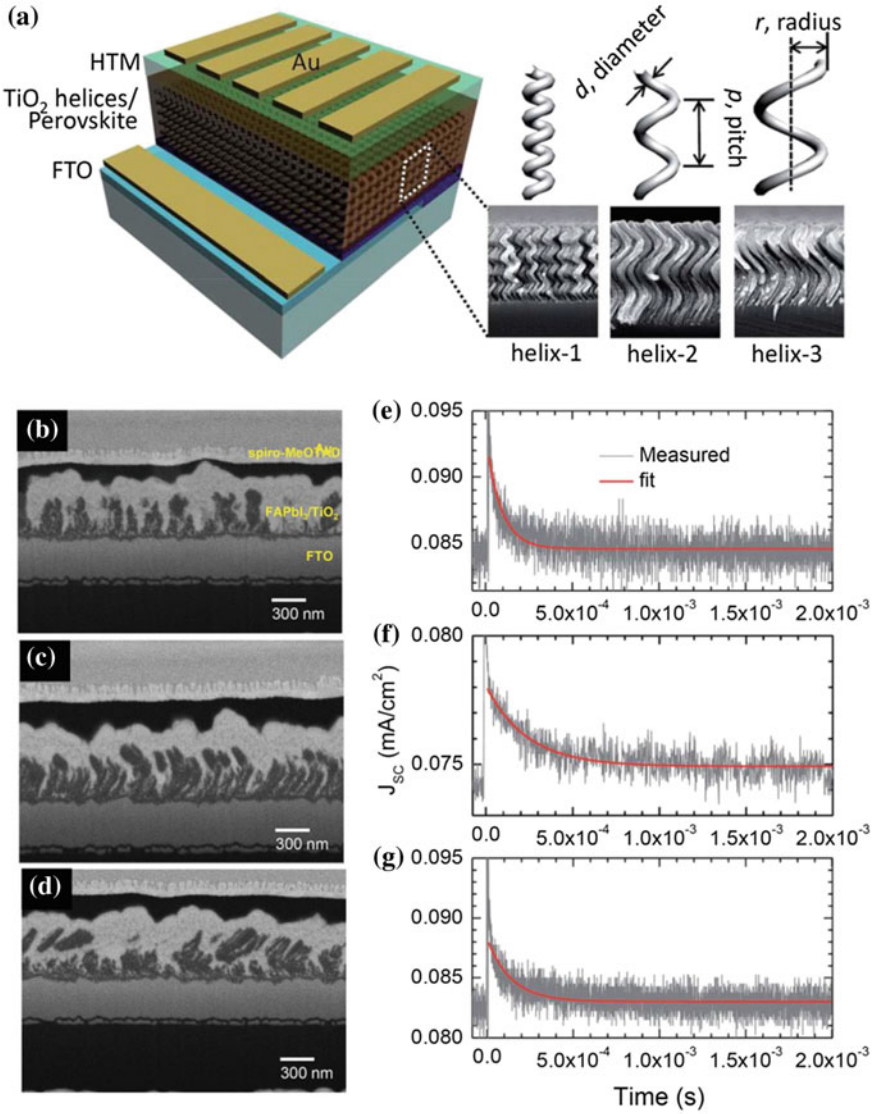

Fig. 20 **a** Schematic description of the perovskite solar cell, consisting of TiO_2 helices and $FAPbI_3$. (**b**–**d**) FIB-assisted SEM images for perovskite solar cells incorporating **b** helix-1, **c** helix-2 and **d** helix-3. Transient photocurrent decay measurement of the $FAPbI_3$ perovskite solar cells based on (**a**) helix-1, (**b**) helix-2, and (**c**) helix-3. A 670 nm monochromatic beam was used as bias light, superimposed on a 532 nm monochromatic laser pulse. Reprinted with permission from [56]

was achieved, in which thin $MAPbI_3$ layer formed on top of the $FAPbI_3$ layer to improve the external quantum efficiency at band edge region [30]. Recently, PCE of 20.1 and 21 % were certified using $(FAPbI_3)_{0.85}(MAPbBr_3)_{0.15}$ [57, 58]. For the case of planar heterojunction system, PCE of 14.2 % was reported using $FAPbI_3$ layer deposited with hydroiodic acid while PCE of 16.5 % was reported with $FA_{0.9}Cs_{0.1}PbI_3$ [20, 29].

6.3 Stability of $HC(NH_2)_2PbI_3$ Perovskite

Since ionic crystal perovskite is sensitive to moisture, stability has been issued for perovskite solar cell. $MAPbI_3$ undergoes serious degradation under light and humidity [24–27]. In presence of humidity and/or light in air, it is decomposed to CH_3NH_2, HI and PbI_2 [24–27]. Although the mechanism of the degradation process is not clearly uncovered, degradation is likely to be related to relatively weak interaction of MA^+ with PbI_6 octahedra via hydrogen bonding [20, 59, 60]. MA^+ cations show dynamic disorder at room temperature within surrounding PbI_6 octahedra, which is indicative of weak interaction between MA^+ and PbI_6 octahedra [21, 22]. It was reported that the interaction become even weaker upon photoexcitation due to charge transfer nature of $MAPbI_3$ band gap which is probably origin of accelerated degradation of $MAPbI_3$ under light [59, 61]. The degradation of $MAPbI_3$ by H_2O might be ascribed to stronger hydrogen bonding between H_2O and PbI_6 octahedra than MA^+ [59].

Interaction of FA cation with surrounding PbI_6 octahedra was reported to be stronger than that of MA cation due to higher probability to form hydrogen bonding [14]. Furthermore, the mechanism for degradation of $MAPbI_3$ under light was reported to be due to generation of hydroiodic acid (HI) resulting from the released proton from MA cation [20, 21]. However, the degree of proton release for FA cation is expected to be less pronounced compared to MA cation because FA cation is more stabilized by resonance characteristics of C-N bonds [20]. As a result, photo-stability will be better for $FAPbI_3$ than for $MAPbI_3$. In Fig. 21, photo-stability of the $FAPb_3$ and $MAPbI_3$ is compared [20], where the perovskite films were illuminated continuously by sulfur lamp (100 mW/cm^2). UV-Vis absorbance at 600 nm is rapidly declined for $MAPbI_3$, whereas $FAPbI_3$ keeps its absorbance for longer time, which indicates that $FAPbI_3$ perovskite solar cell is relatively more stable than $MAPbI_3$ one.

Despite better photo-stability, moisture-stability of $FAPbI_3$ is found to be poor compare to $MAPbI_3$ (Fig. 22) [20]. Black perovskite phase of $FAPbI_3$ (α-phase) was reported to be converted to yellow non-perovskite phase (δ-phase) at room temperature in the presence of liquid interface, which is probably origin of poor moisture-stability of $FAPbI_3$ [51]. Furthermore, FA^+ cation tends to dissociate into ammonia and *sym*-triazine, which further degrades the moisture-stability of $FAPbI_3$ [51]. Partial substitution of MA cation for FA cation may stabilize the black phase

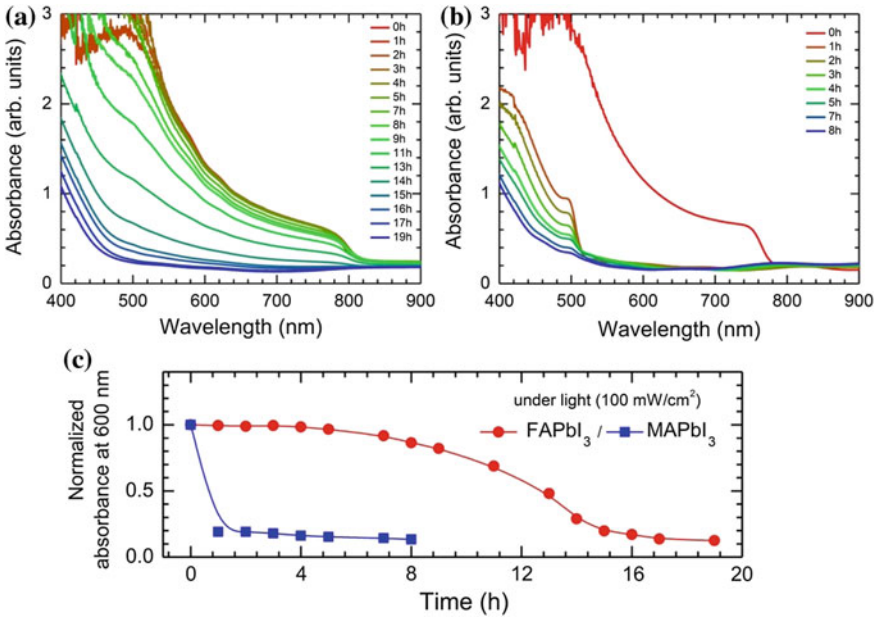

Fig. 21 Evolution of absorption spectra of **a** $FAPbI_3$ and **b** $MAPbI_3$ under continuous one sun illumination (100 mW/cm^2, relative humidity (RH) < 50 %, temperature (T) < 65 °C). **c** The normalized absorbance of $FAPbI_3$ and $MAPbI_3$ films at 600 nm as a function of time. Reprinted with permission from [20]

at room temperature, which, however, deteriorates photo-stability of $FAPbI_3$ due to inclusion of relatively volatile MA cation [20, 62].

Partial substitution of inorganic cesium (Cs) cation in FA site of $FAPbI_3$ was found to be one of effective ways to stabilize trigonal black phase of $FAPbI_3$ [20]. Replacement of 10 % FA by Cs ion ($FA_{0.9}Cs_{0.1}PbI_3$) was found to be optimal composition for single phase. X-ray diffraction (XRD) measurement confirmed the black phase of $FAPbI_3$ with 10 % Cs prepared at room temperature, where lattice constants shrank leading to decrease in unit cell volume from 761.2263 to 749.4836 Å^3, which was due to smaller ionic radius of Cs cation (1.81 Å) than that of FA cation (2.79 Å). Since such a decrease in unit cell volume will reinforce the interaction between organic cation and PbI_6 octahedra, the photo-and moisture-stability of the $FA_{0.9}Cs_{0.1}PbI_3$ is expected to be improved. Figure 23a compares photo- and moisture-stability of $FAPbI_3$ with $FA_{0.9}Cs_{0.1}PbI_3$ [20]. When the $FAPbI_3$ and $FA_{0.9}Cs_{0.1}PbI_3$ are exposed to continuous illumination (100 mA/cm^2), the degree of degradation is severer for $FAPbI_3$ film (85.9 %) than for $FA_{0.9}Cs_{0.1}PbI_3$ film (65.0 %) after 19 h, which is indicative of an improved photo-stability by incorporation of Cs ion. Regarding humidity-stability test at 85 % relative humidity at 25 °C in dark condition, the $FA_{0.9}Cs_{0.1}PbI_3$ film is more stable than the pristine $FAPbI_3$ film (Fig. 23b), which is likely to be due to more stabilized FA ions in the cubo-octahedral cages.

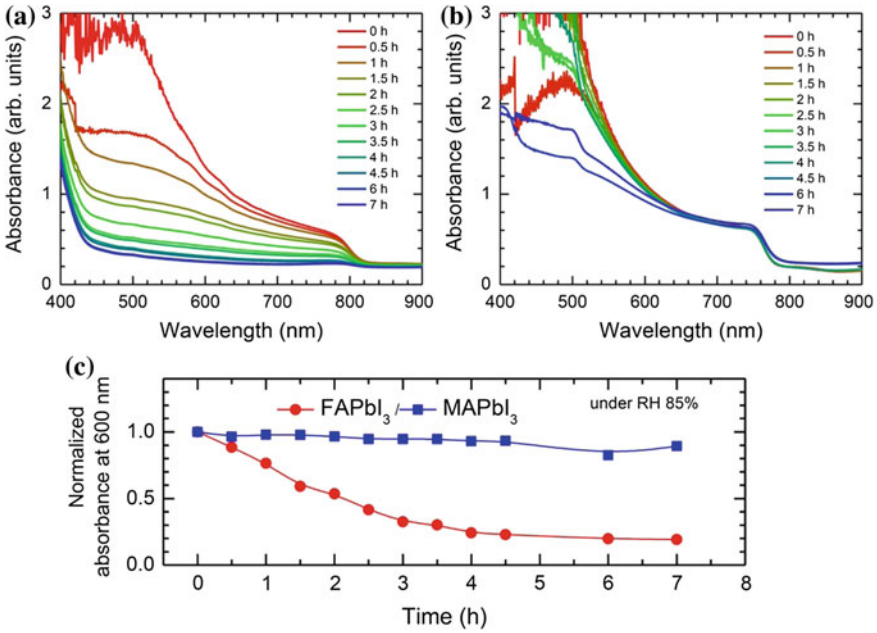

Fig. 22 Evolution of absorption spectra of **a** $FAPbI_3$ and **b** $MAPbI_3$ under relative humidity (RH) of 85 % (dark, $T = 25$ °C). **c** The normalized absorbance of $FAPbI_3$ and $MAPbI_3$ films at 600 nm as a function of time. Reprinted with permission from [20]

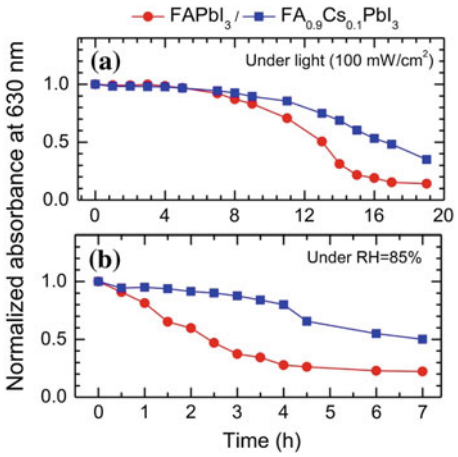

Fig. 23 Normalized absorbance of $FAPbI_3$ and $FA_{0.9}Cs_{0.1}PbI_3$ film stored **a** under sulfur lamp (100 mW/cm^2, relative humidity (RH) < 50 %, temperature (T) < 65 °C), **b** under constant humidity of RH 85 % (dark, $T = 25$ °C) as a function of time. The absorption spectra was measured every hour for photo-stability measurement and every half an hour for measurement of stability against the humidity. Reprinted with permission from [20]

Among the stability issues, thermal stability is one of the key aspects to be addressed in perovskite solar cell. $FAPbI_3$ was found to show better thermal stability than $MAPbI_3$ when the film was stored at 150 °C [29]. $MAPbI_3$ film was changed to yellow PbI_2 film while $FAPbI_3$ film remains black [29]. The better thermal stability of $FAPbI_3$ over $MAPbI_3$ is also related to stronger interaction of FA cation with PbI_6 octahedra than MA cation [14]. Due to the dynamic motion of MA cation, $MAPbI_3$ undergoes structural change from tetragonal to cubic when the temperature becomes higher than 65 °C, which may have ill effect on photovoltaic performance [17, 23]. As demonstrated in Fig. 24, black α-phase of $FAPbI_3$ changes to β-phase at around 200 K (−73.15 °C) and γ-phase below ~130 K (−143.15 °C) [51]. Therefore, $FAPbI_3$ perovskite can escape phase transition at solar cell operating temperature range because no phase transition was detected at the temperature ranging from 25 to 200 °C.

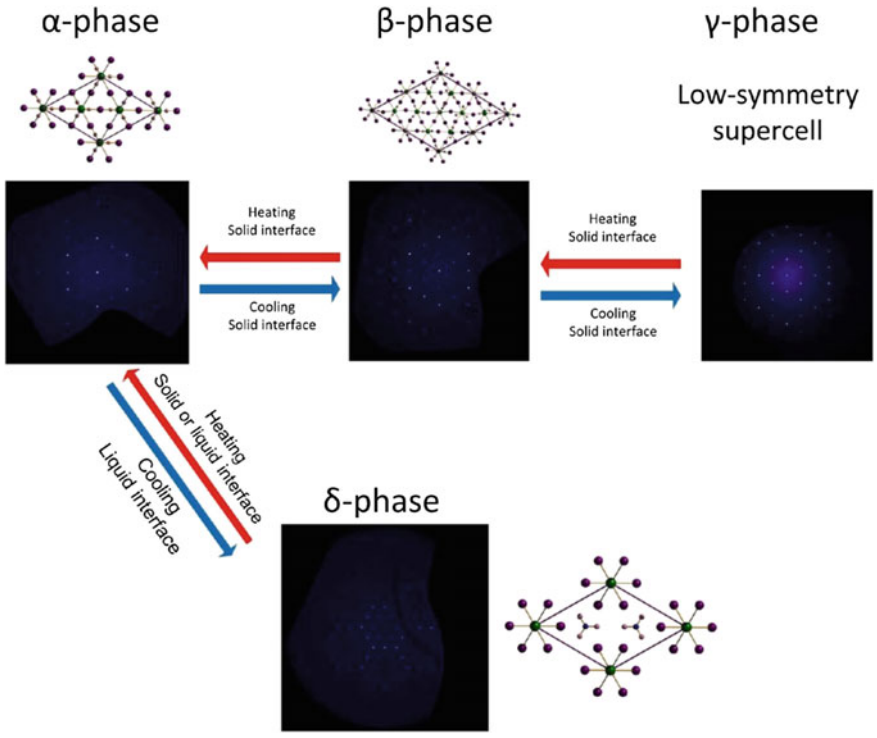

Fig. 24 Graphical scheme of the observed phase transitions of $FAPbI_3$. Starting from the α-phase two possibilities arise: In the presence of a liquid interface (i.e., inside the mother liquor) it converts to the δ-phase upon decreasing the temperature (below 360 K). When dry crystals of the α-phase are cooled, however, a different sequence of phase transitions occur with conversion to the β-(below ~200 K) and γ-(below ~130 K) phases. Precession images are drawn at [006] view. Reprinted with permission from [51]

7 Summary

In this chapter, evolution of organolead halide perovskite solar cell starting from sensitization to planar heterojunction architecture was demonstrated. The underlying beneficial optoelectronic properties of the perovskite light absorber such as high absorption coefficient and ambipolar transport property, which enabled the change of device architecture with rapid enhancement of PCE, were elucidated in aspect of physicochemical bonding nature. The high absorption coefficient and ambipolar transport properties were found due to direct band gap along with comparable and small effective mass of electron and hole in perovskite. At the same time, a variety of technologies for preparation of perovskite films from the conventional two-step technique to a state-of-the-art adduct method were introduced, in which the adduct method was found to be efficient for fabrication of highly uniform and crystalline methylammonium and formamidinium perovskite films. Finally, presenting stability issues for perovskite light absorber were dealt with, where photo- and humidity-stability of the methylammonium- and formamidinium-based perovskites were compared. From the different stability of methylammonium and formamidium perovskites, interaction between organic cation and surrounding PbI_6 octahedra was found to have crucial role in both photo- and humidity-stability.

Acknowledgments This work was supported by the National Research Foundation of Korea (NRF) grants funded by the Ministry of Science, ICT & Future Planning (MSIP) of Korea under contracts No. NRF-2012M3A6A7054861 (Global Frontier R&D Program on Center for Multiscale Energy System), NRF-2015M1A2A2053004 (Climate Change Management Program), and NRF-2012M3A7B4049986 (Nano Material Technology Development Program).

References

1. Kojima, A., Teshima, K., Shirai, Y., Miyasaka, T.: Organometal halide perovskites as visible-light sensitizers for photovoltaic cells. J. Am. Chem. Soc. **131**, 6050–6051 (2009)
2. Im, J.H., Lee, C.R., Lee, J.W., Park, S.W., Park, N.G.: 6.5 % efficient perovskite quantum-dot-sensitized solar cell. Nanoscale **3**, 4088–4093 (2011)
3. Kim, H.S., Lee, C.R., Im, J.H., Lee, K.B., Moehl, T., Marchioro, A., Moon, S.J., Humphry-Baker, R., Yum, J.H., Grätzel, M., Park, N.G.: Lead iodide perovskite sensitized all-solid-state submicron thin film mesoscopic solar cell with efficiency exceeding 9 %. Sci. Rep. **2**, 591 (2012)
4. Lee, M.M., Teuscher, J., Miyasaka, T., Murakami, T.N., Snaith, H.J.: Efficient hybrid solar cells based on meso-superstructured organometal halide perovskites. Science **338**, 643–647 (2012)
5. Best Research-Cell Efficiencies. National Renewable Energy Laboratory, Golden. http://www.nrel.gov/ncpv/images/efficiency_chart.jpg (2016). Accessed 02 Mar 2016
6. Noel, N.K., Stranks, S.D., Abate, A., Wehrenfennig, C., Guarnera, S., Haghighirad, A.A., Sadhanala, A., Eperon, G.E., Pathak, S.K., Johnston, M.B., Petrozza, A., Herz, L.M., Snaith, H.J.: Lead-free organic–inorganic tin halide perovskites for photovoltaic applications. Energy Environ. Sci. **7**, 3061–3068 (2014)

7. Hao, F., Stoumpos, C.C., Cao, D.H., Chang, R.P.H., Kanatzidis, M.G.: Lead-free solid-state organic-inorganic halide perovskite solar cells. Nat. Photonics **8**, 489–494 (2014)
8. Hao, F., Stoumpos, C.C., Chang, R.P.H., Kanatzidis, M.G.: Anomalous band gap behavior in mixed Sn and Pb perovskites enables broadening of absorption spectrum in solar cells. J. Am. Chem. Soc. **136**, 8094–8099 (2014)
9. Noh, J.H., Im, S.H., Heo, J.G., Mandal, T.N., Seok, S.I.: Chemical management for colorful, efficient, and stable inorganic–organic hybrid nanostructured solar cells. Nano Lett. **13**, 1764–1769 (2013)
10. Heo, J.H., Song, D.H., Im, S.H.: Planar CH3NH3PbBr 3 hybrid solar cells with 10.4 % power conversion efficiency, fabricated by controlled crystallization in the spin-coating process. Adv. Mater. **26**, 8179–8183 (2014)
11. Yin, W.J., Yang, J.H., Kang, J., Yan, Y., Wei, S.H.: Halide perovskite materials for solar cells: a theoretical review. J. Mater. Chem. A **3**, 8926–8942 (2015)
12. Geng, W., Zhang, L., Zhang, Y.N., Lau, W.M., Liu, L.M.: First-principles study of lead iodide perovskite tetragonal and orthorhombic phases for photovoltaics. J. Phys. Chem. C **118**, 19565–19571 (2014)
13. Motta, C., El-Mellouhi, F., Kais, S., Tabet, N., Alharbi, F., Sanvito, S.: Revealing the role of organic cations in hybrid halide perovskite $CH_3NH_3PbI_3$. Nat. Commun. **6**, 7026 (2014)
14. Amat, A., Mosconi, E., Ronca, E., Quarti, C., Umari, P., Nazeeruddin, M.K., Grätzel, M., Angelis, F.D.: Cation-induced band-gap tuning in organohalide perovskites: interplay of spin-orbit coupling and octahedra tilting. Nano Lett. **14**, 3608–3616 (2014)
15. Goldschmidt, V.V.M.: Die gesetze der krystallochemie. Naturwissenschaften **21**, 477–485 (1926)
16. Shannon, R.D.: Revised effective ionic radii and systematic studies of interatomic distances in halides and chalcogenides. Acta Cryst. **A32**, 751–767 (1976)
17. Baikie, T., Fang, Y., Kadro, J.M., Schreyer, M., Wei, F., Mhaisalkar, S.G., Grätzel, M., White, T.J.: Synthesis and crystal chemistry of the hybrid perovskite $(CH_3NH_3)PbI_3$ for solid-state sensitised solar cell applications. J. Mater. Chem. A **1**, 5628–5641 (2013)
18. Jung, H.S., Park, N.G.: Perovskite solar cells: from materials to devices. Small **11**, 10–25 (2015)
19. Kieslich, G., Sun, S., Cheetham, A.K.: An extended tolerance factor approach for organic–inorganic perovskites. Chem. Sci. **6**, 3430–3433 (2015)
20. Lee, J.W., Kim, D.H., Kim, H.S., Seo, S.W., Cho, S.M., Park, N.G.: Formamidinium and cesium hybridization for photo-and moisture-stable perovskite solar cell. Adv. Energy Mater. **5**, 1501310 (2015)
21. Poglitsch, A., Weber, D.: Dynamic disorder in methylammoniumtrihalogenoplumbates (II) observed by millimeter-wave spectroscopy. J Chem Phys **87**, 6373–6378 (1987)
22. Leguy, A.M.A., Frost, J.M., McMahon, A.P., Sakai, V.G., Kockelmann, W., Law, C., Li, X., Foglia, F., Walsh, A., O`Regan, B.C., Nelson, J., Cabral, J.T., Barnes, P.R.F.: The dynamics of methylammonium ions in hybrid organic-inorganic perovskite solar cells. Nat. Commun. **6**, 7124 (2015)
23. Cojocaru, L., Uchida, S., Sanehira, Y., Gonzalez-Pedro, V., Bisquert, J., Nakazaki, J., Kubo, T., Segawa, H.: Temperature effects on the photovoltaic performance of planar structure perovskite solar cells. Chem. Lett. (2015). doi:10.1246/cl.150781
24. Niu, G., Li, W., Meng, F., Wang, L., Dong, H., Qiu, Y.: Study on the stability of $CH_3NH_3PbI_3$ films and the effect of post-modification by aluminum oxide in all-solid-state hybrid solar cells. J. Mater. Chem. A **2**, 705–710 (2014)
25. Ito, S., Tanaka, S., Manabe, K., Nishino, H.: Effects of surface blocking layer of Sb_2S_3 on nanocrystalline TiO_2 for $CH_3NH_3PbI_3$ perovskite solar cells. J. Phys. Chem. C **118**, 16995–17000 (2014)
26. Yang, J., Siempelkamp, B.D., Liu, D., Kelly, T.L.: Investigation of $CH_3NH_3PbI_3$ degradation rates and mechanisms in controlled humidity environments using in situ techniques. ACS Nano **9**, 1955–1963 (2015)

27. Misra, R.K., Aharon, S., Li, B., Mogilyansky, D., Visoly-Fisher, I., Etgar, L., Katz, E.A.: Temperature-and component-dependent degradation of perovskite photovoltaic materials under concentrated sunlight. J. Phys. Chem. Lett. **6**, 326–330 (2015)
28. Koh, T.M., Fu, K., Fang, Y., Chen, S., Sum, T.C.: Formamidinium-containing metal-halide: an alternative material for near-IR absorption perovskite solar cells. J. Phys. Chem. C **118**, 16458–16462 (2014)
29. Eperon, G.E., Stranks, S.D., Menelaou, C., Johnston, M.B., Herz, L.M., Snaith, H.J.: Formamidinium lead trihalide: a broadly tunable perovskite for efficient planar heterojunction solar cells. Energy Environ. Sci. **7**, 982–988 (2014)
30. Lee, J.W., Seol, D.J., Cho, A.N., Park, N.G.: High-efficiency perovskite solar cells based on the black polymorph of HC(NH2)2PbI3. Adv. Mater. **26**, 4991–4998 (2014)
31. Xing, G., Mathews, N., Sun, S., Lim, S.S., Lam, Y.M., Grätzel, M., Mhaisalkar, S., Sum, T.C.: Long-range balanced electron-and hole-transport lengths in organic-inorganic $CH_3NH_3PbI_3$. Science **342**, 344–347 (2013)
32. Green, M.A., Jiang, Y., Soufiani, A.M., Ho-Baillie, A.: Optical properties of photovoltaic organic-inorganic lead halide perovskites. J. Phys. Chem. Lett. **6**, 4774–4785 (2015)
33. Wemple, S.H., DiDomenico, M.: Behavior of the electronic dielectric constant in covalent and ionic materials. Phys. Rev. B **3**, 1338–1351 (1971)
34. Singh, J.: Smart Electronic Materials. Cambridge University Press, Cambridge (2005)
35. Even, J., Pedesseau, L., Katan, C., Kepenekian, M., Lauret, J.S., Sapori, D., Deleporte, E.: Solid-state physics perspective on hybrid perovskite semiconductors. J. Phys. Chem. C **119**, 10161–10177 (2015)
36. Even, J., Pedesseau, L., Jancu, J.-M., Katan, C.: J. Phys. Chem. Lett. **4**, 2999–3005 (2013)
37. Neamen, D.A.: Semiconductor Physics and Devices, 4th edn. McGraw-Hill, New York (2012)
38. Giorgi, G., Fujisawa, J.I., Segawa, H., Yamashita, K.: Small photocarrier effective masses featuring ambipolar transport in methylammonium lead iodide perovskite: a density functional analysis. J. Phys. Chem. Lett. **4**, 4213–4216 (2013)
39. Galkowski, K., Mitioglu, A., Miyata, A., Plochocka, P., Portugall, O., Eperon, G.E., Wang, J. T.W., Stergiopoulos, T., Stranks, S.D., Snaith, H.J., Nichola, R.J.: Determination of the exciton binding energy and effective masses for methylammonium and formamidinium lead tri-halide perovskite semiconductors. Energy Environ. Sci. (2016). doi:10.1039/c5ee03435c
40. Green, M.A., Ho-Baillie, A., Snaith, H.J.: The emergence of perovskite solar cells. Nat. Photonics **8**, 506–514 (2014)
41. Li, C., Lu, X., Ding, W., Feng, L., Gao, Y., Guo, Z.: Formability of ABX_3 (X = F, Cl, Br, I) halide perovskites. Acta Crystallogr. B **64**, 702–707 (2008)
42. Yin, W.J., Shi, T., Yan, Y.: Unique properties of halide perovskites as possible origins of the superior solar cell performance. Adv. Mater. **26**, 4653–4658 (2014)
43. Im, J.H., Chung, J., Kim, S.J., Park, N.G.: Synthesis, structure, and photovoltaic property of a nanocrystalline 2H perovskite-type novel sensitizer $(CH_3CH_2NH_3)PbI_3$. Nanoscale Res. Lett. **7**, 353 (2012)
44. Kim, H.S., Mora-Sero, I., Gonzalez-Pedro, V., Fabregat-Santiago, F., Juarez-Perez, E.J., Park, N.G., Bisquert, J.: Mechanism of carrier accumulation in perovskite thin-absorber solar cells. Nat. Commun. **4**, 2242 (2013)
45. Bisquert, J.: Chemical capacitance of nanostructured semiconductors: its origin and significance for nanocomposite solar cells. Phys. Chem. Chem. Phys. **5**, 5360–5364 (2003)
46. Im, J.H., Jang, I.H., Pellet, N., Grätzel, M., Park, N.G.: Growth of $CH_3NH_3PbI_3$ cuboids with controlled size for high-efficiency perovskite solar cells. Nat. Nanotechnol. **9**, 927–932 (2014)
47. Ahn, N., Kang, S.M., Lee, J.W., Choi, M., Park, N.G.: Thermodynamic regulation of $CH_3NH_3PbI_3$ crystal growth and its effect on photovoltaic performance of perovskite solar cells. J. Mater. Chem. A **3**, 19901–19906 (2015)
48. Mastroianni, S., Heinz, F.D., Im, J.H., Veurman, W., Padilla, M., Schubert, M.C., Würfel, U., Grätzel, M., Park, N.G., Hinsch, A.: Analysing the effect of crystal size and structure in highly efficient $CH_3NH_3PbI_3$ perovskite solar cells by spatially resolved photo- and electroluminescence imaging. Nanoscale **7**, 19653–19662 (2015)

49. Ahn, N., Son, D.Y., Jang, I.H., Kang, S.M., Choi, M., Park, N.G.: Highly reproducible perovskite solar cells with average efficiency of 18.3 % and best efficiency of 19.7 % fabricated via Lewis base adduct of lead (II) iodide. J. Am. Chem. Soc. **137**, 8696–8699 (2015)
50. Chen, Y., Peng, J., Su, D., Chen, X., Liang, Z.: Efficient and balanced charge transport revealed in planar perovskite solar cells. ACS Appl. Mater. Interfaces **7**, 4471–4475 (2015)
51. Stoumpos, C.C., Malliakas, C.D., Kanatzidis, M.G.: Semiconducting tin and lead iodide perovskites with organic cations: phase transitions, high mobilities, and near-infrared photoluminescent properties. Inorg. Chem. **52**, 9019–9038 (2013)
52. Wang, F., Yu, H., Xu, H., Zhao, N.: HPbI3: a new precursor compound for highly efficient solution-processed perovskite solar cells. Adv. Funct. Mater. **25**, 1120–1126 (2015)
53. Seol, D.J., Lee, J.W., Park, N.G.: On the role of interfaces in planar-structured HC(NH2)2PbI3 perovskite solar cells. ChemSusChem **8**, 2414–2419 (2015)
54. Lee, J.W., Kim, H.S., Park, N.G.: Lewis acid-base adduct approach for high efficiency perovskite solar cells. Acc. Chem. Res. **49**, 311–319 (2016)
55. Dimesso, L., Quintilla, A., Kim, Y.M., Lemmer, U., Jaegermann, W.: Investigation of formamidinium and guanidinium lead tri-iodide powders as precursors for solar cells. Mater. Sci. Eng. B **204**, 27–33 (2016)
56. Lee, J.W., Lee, S.H., Ko, H.S., Kwon, J.K., Park, J.H., Kang, S.M., Ahn, N., Choi, M., Kim, J. K., Park, N.G.: Opto-electronic properties of TiO_2 nanohelices with embedded $HC(NH_2)_2PbI_3$ perovskite solar cells. J. Mater. Chem. A **3**, 9179–9186 (2015)
57. Yang, W.S., Noh, J.H., Jeon, N.J., Kim, Y.C., Ryu, S., Seo, H., Seok, S.I.: High-performance photovoltaic perovskite layers fabricated through intramolecular exchange. Science **348**, 1234–1237 (2015)
58. Bi, D., Tress, W., Dar, M.I., Gao, P., Luo, J., Renevier, C., Schenk, K., Abate, A., Giordano, F., Baena, J.P.C., Decoppet, J.D., Zakeeruddin, S.M., Nazeeruddin, M.K., Grätzel, M., Hagfeldt, A.: Efficient luminescent solar cells based on tailored mixed-cation perovskites. Sci. Adv. **2**, 1–7 (2016)
59. Christians, J.M., Herrera, P.A.M., Kamat, P.V.: Transformation of the excited state and photovoltaic efficiency of $CH_3NH_3PbI_3$ perovskite upon controlled exposure to humidified air. J. Am. Chem. Soc. **137**, 1530–1538 (2015)
60. Aristidou, N., Sanchez-Molina, I., Chotchuangchutchaval, T., Brown, M., Martinez, L., Rath, T., Haque, S.A.: The role of oxygen in the degradation of methylammonium lead trihalide perovskite photoactive layers. Angew. Chem. Int. Ed. **54**, 8208–8212 (2015)
61. Gottesman, R., Gouda, L., Kalanoor, B.S., Haltzi, E., Tirosh, S., Rosh-Hodesh, E., Tischler, Y., Zaban, A.: Photoinduced reversible structural transformations in free-standing $CH_3NH_3PbI_3$ perovskite films. J. Phys. Chem. Lett. **6**, 2332–2338 (2015)
62. Binek, A., Hanusch, F.C., Docampo, P., Bein, T.: Stabilization of the trigonal high-temperature phase of formamidinium lead iodide. J. Phys. Chem. Lett. **6**, 1249–1253 (2015)

Hysteresis Characteristics and Device Stability

Ajay Kumar Jena and Tsutomu Miyasaka

1 Introduction

The continuous and skyrocketing rise in power conversion efficiency (PCE) of the organometal halide perovskite solar cells [1–3] has attracted enormous attention. The material has become an utmost interest to all working on photovoltaic technologies because of its high absorption coefficient and long range carrier diffusion with minimal recombination, which are the major attributes to large current density and high open circuit voltage, resulting in high PCE. The rapid rise in performance of the cells has been accomplished essentially by minor modifications in the device structure, morphology of the films and fabrication methods, etc. However, there are several fundamental issues besides the efficiency improvement. They are hysteresis in current and voltage curves, wide distribution in performance, performance durability, difficulties in reproducing the results, etc., These issues require deeper scientific understanding and demand serious attention. Among all the above problems, hysteresis has been apparently considered as a major. It has been widely observed that perovsktie solar cells show substantial mismatch between the current density-voltage (J-V) curves measured on forward scan (from short circuit to open circuit) and backward scan (from open circuit to short circuit). Figure 1 shows an example of hysteretic J-V curves of a planar perovskite solar cell fabricated by toluene-dripping method [4] in our lab. Solar cells studied in this chapter commonly employ methylammonium (MA) lead triiodide ($MAPbI_3$) as perovskite and 2, 2′, 7, 7′-tetrakis (N, N-di-p-methoxyphenylamine)-9, 9′-spirobifluorene (spiro-OMeTAD) as hole transport material. The current measured on backward scan, at maximum power, is higher than that collected on forward scan, resulting in higher PCE calculated from backward scan (17.1 %) than for forward scan (13.1 %). J-V hysteresis is also found in dye-sensitized solar cells (DSSCs), organic

A.K. Jena · T. Miyasaka (✉)
Garduate School of Engineering, Toin University of Yokohama,
1614 Kuroganecho, Aoba, Yokohama 225-8503, Japan
e-mail: miyasaka@toin.ac.jp

N.-G. Park et al. (eds.), *Organic-Inorganic Halide Perovskite Photovoltaics*,
DOI 10.1007/978-3-319-35114-8_10

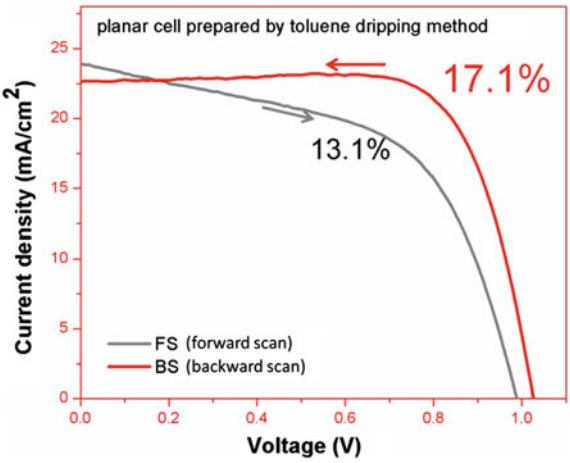

Fig. 1 Hysteretic J-V curves of a planar perovskite solar cell prepared by toluene-dripping method. The scan speed used is 200 mV/s

thin film solar cells (OSCs), and Si solar cells, when the voltage scan is too fast [5]. This hysteresis is explained by the effect of capacitive charge, including space charges and trapped charges. When the scanning speed is faster than the release rate of traps, or faster than the space charge relaxation time, hysteresis is seen. In organic–inorganic perovskite solar cells, hysteresis behavior is much slower but more complex and anomalous. This anomalous property of the perovskite solar cells creates confusion about the actual cell performance [6–8].

Hysteretic J-V curves imply that there is a clear difference in transient carrier collection at a given voltage during the forward and backward scan. It is generally known that backward scan measures higher current than the forward scan, independent of scan sequence. This confirms that carrier collection is always more efficient during the backward scan. In general, carrier collection (or current) in the device depends on carrier generation, separation, and its transport in the bulk of the layers and transfer across different interfaces in the device. As carrier generation and separation are considered fast processes and depend only on illumination (not on the voltage scan) any difference in initial collection must be influenced by transport and/or transfer at the interfaces.

2 Parameters Affecting Hysteresis

As carrier collection depends on the conductivity of perovskite and other layered materials and the connectivity at their interfaces, hysteresis is observed to be affected by many factors that can slightly change the characteristics of the layers in perovskite device. Therefore, the diversity in device structure and the fabrication methods, and even changes in measurement conditions result in wide variation in the trends of hysteresis. As a result, the problem of hysteresis becomes too complex to be understood completely.

2.1 Device Structure and Process Parameters

Perovskite devices of different architecture using the same perovskite but different electron and hole collecting layers show different magnitudes of hysteresis [9]. For instance, the standard planar heterojunction architecture; FTO/TiO_2 compact layer/perovskite/spiro-OMeTAD/Ag, FTO/PCBM/perovskite/spiro-OMeTAD/Ag and FTO/TiO_2-PCBM/perovskite/spiro-OMeTAD/Ag (PCBM is [6, 6]–phenyl-C_{61}-butyric acid methyl ester) often show large hysteresis while the inverted architecture with PCBM as the electron collecting layer (ITO/PEDOT:PSS/$MAPbI_3$/PCBM/Ag and (ITO/NiO/$MAPbI_3$/PCBM/Ag) exhibits zero hysteresis (Figs. 2 and 3) [9].

Although inverted perovskite solar cells have been often observed to show less hysteresis [10–13], the architecture is not the sufficient condition for eliminating hysteresis because the characteristics of the layered structures influence the phenomenon strongly. For instance, use of PCBM may not always result in zero

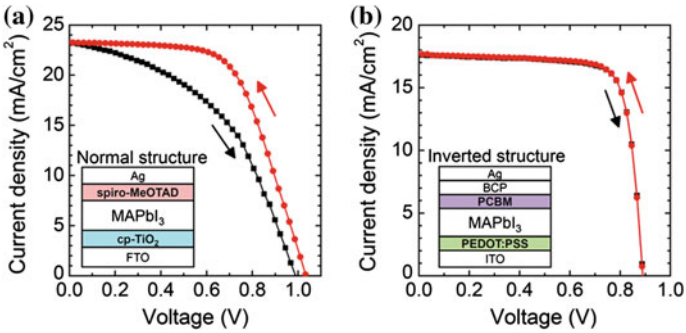

Fig. 2 Forward and backward scan J-V curves of a perovskite ($MAPbI_3$) cells of **a** normal and **b** inverted architecture [9]

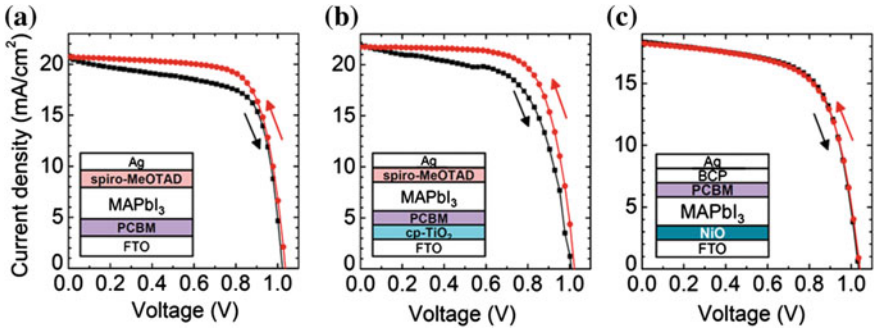

Fig. 3 Forward and backward J-V curves of planar perovskite ($MAPBI_3$) solar cells of normal architecture with **a** PCBM, **b** TiO_2-PCBM as electron collecting layer and **c** inverted architecture with NiO as hole transport layer [9]

hysteresis regardless of its layered structure. Hysteresis in inverted perovskite devices depends on thickness of PCBM. Thin PCBM layers can also behave the same way as TiO_2 compact layer and impart hysteresis in the J-V curves of the inverted planar perovskite cells (Fig. 4) [14]. Even, in some cases, depending on fabrication conditions, the normal trend of hysteresis (i.e., reverse scan showing higher performance than forward scan) becomes opposite; the forward scan shows higher PCE than the backward scan (Fig. 5) [15].

In many cases, TiO_2 meso-structure devices show less hysteresis than the planar heterojunction cells. However, this is not always the case because fabrication methods and properties of the other layers play equally important roles. In the cells using TiO_2 mesoporous layer, hysteresis changes with thickness of capping perovskite layer; thicker capping layer shows greater hysteresis [16]. With all other layers fixed as used in TiO_2 meso-structure cells, Al_2O_3 meso-structure as scaffold in the perovskite cells has been found to show larger hysteresis than TiO_2 [16]. Figure 6 shows an example of changing hysteresis with TiO_2 thickness and wider hysteresis

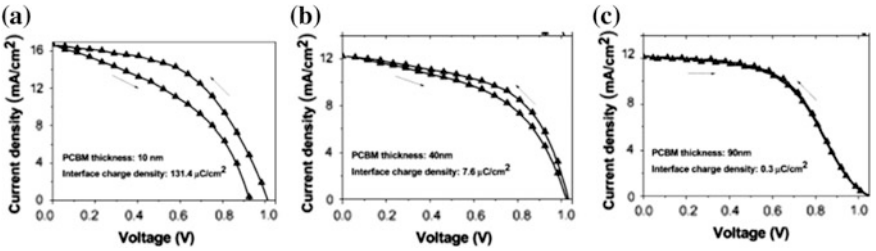

Fig. 4 Influence of PCBM film thickness on J-V hysteresis of inverted perovskite solar cells. Forward and backward J-V curves of inverted perovskite cell (ITO/PEDOT:PSS/$CH_3NH_3PbI_{3-x}Cl_x$/PCBM/Al) with PCBM layer of thickness **a** 10 nm, **b** 40 nm and **c** 90 nm [14]

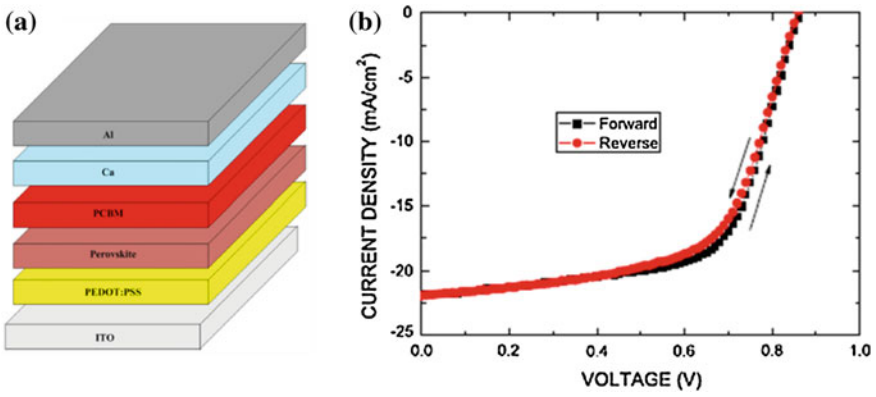

Fig. 5 An opposite trend of hysteresis (forward scan showing higher performance than reverse scan) observed in an inverted perovskite solar cell. **a** Schematic of the device and **b** J-V curves of forward and reverse scan

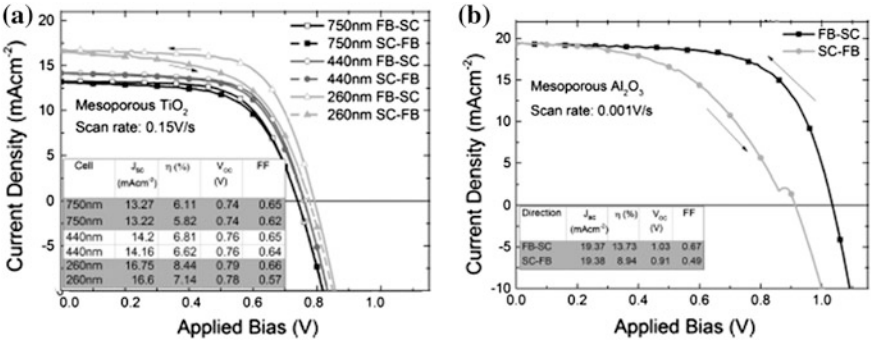

Fig. 6 Hysteresis changing with cell architecture. Forward bias to short circuit (FB-SC) and short circuit to forward bias (SC-FB) J-V curves of perovskite cell with **a** varying TiO_2 mesoporous thickness (perovskite capping layer increasing with decreasing TiO_2 thickness) and **b** Al_2O_3 scaffold [16]

observed for the Al_2O_3 scaffold. In one of our studies, we also found that hysteresis in a planar perovskite device (FTO/TiO_2 compact layer/$CH_3NH_3PbI_{3-x}Cl_x$/Spiro-OMeTAD/Au) increases with thickness of the perovskite film (Fig. 7). The capping layer thickness and morphology (grain size) can be easily controlled by the processing conditions, which eventually alter the hysteresis magnitude. Devices composed of larger and interconnected grains of perovskite with better surface coverage display more tolerance to hysteresis than smaller grains with poor surface coverage [17–19]. An example of dependence of hysteresis on grain size of perovskite ($CH_3NH_3PbI_3$) grown by two-step method using CH_3NH_3I of different concentrations is given in Fig. 8.

Any small and big change in the device structure, which is too sensitive to the processing conditions, can alter the carrier collection at the electrodes and consequently bring changes in the J-V hysteresis of the perovskite solar cells. Although there are evidences of some common characteristics that exhibit suppressed hysteresis, determination of an exclusive condition for eliminating hysteresis for sure becomes difficult. The unfortunate fact of the matter is that the extent of hysteresis can vary drastically even for devices of same architecture fabricated in different laboratories with slight variation in the preparation conditions. This fact would imply that origin of hysteresis is hidden at the interfaces of layered structures rather than the bulk properties of materials.

2.2 Measurement and Prior-Measurement Conditions

Even for the same sample, any change in the measurement conditions can alter the hysteretic behavior of the cell remarkably. Hysteresis depends strongly on the scan speed of the bias voltage. The phenomenon becomes more pronounced with fast scan

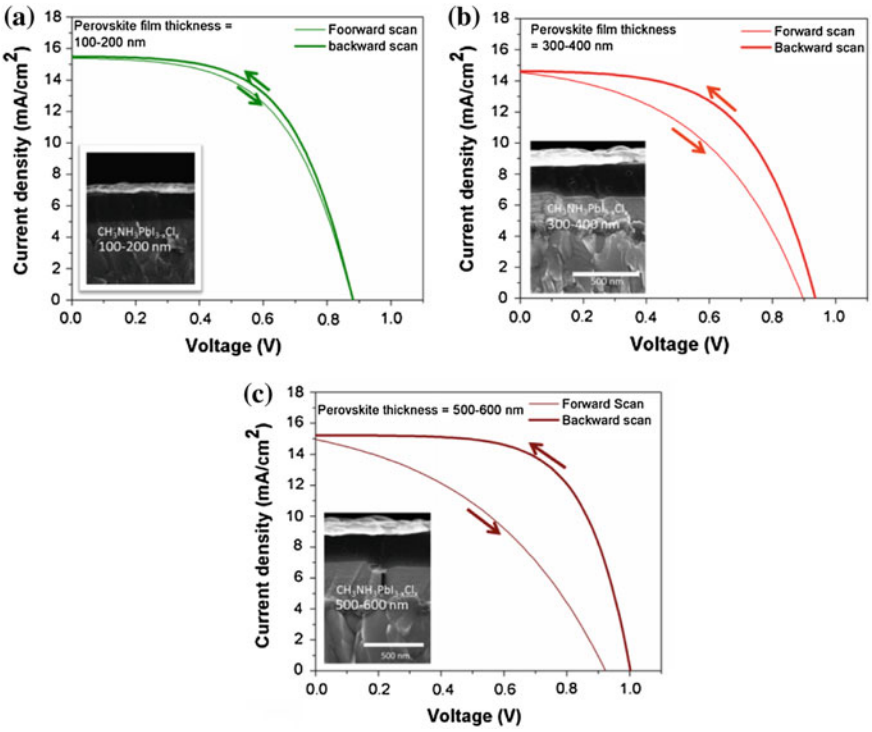

Fig. 7 Hysteresis in planar $CH_3NH_3PbI_{3-x}Cl_x$ perovskite solar cell with increasing perovskite film thickness. Forward scan and backward scan J-V curves of planar perovskite cells with perovskite films of thickness **a** 100–200 nm, **b** 300–400 nm, **c** 500–600 nm. The insets in each figure shows the cross-sectional SEM images of the corresponding devices.

and becomes negligible with very slow and extremely fast scan [16, 20]. An example of such change in hysteresis due to scan rate of the bias voltage is given in Fig. 9.

Dependence of J-V hysteresis on the scan speed implies involvement of a nonsteady-state transient process [21, 22]. Stepwise measurement of photocurrent at different step size (ΔV) and step time (Δt) in both forward and reverse directions shows nonsteady-state photocurrent peaks at each voltage (Fig. 10). This transient photocurrent is always higher than the steady-state current when the scan is from forward bias to short circuit condition (i.e., reverse). On the other hand, for the forward scan, the transient photocurrent value at each voltage is smaller the steady-state values.

The height of nonsteady-state transient photocurrent peak depends on the step size (Fig. 10c) and time (Fig. 10b). For larger step size and smaller step time (i.e., faster scan), the transient current peak height becomes higher, resulting in wider discrepancy in both the J-V curves. Smaller step size and longer step time (slower scan) brings the J-V curves closer, resulting in less hysteresis. Figure 10d shows decreasing trend of hysteresis with decreasing scan rate. The change in forward and reverse J-V curves with different scan rates can be different depending on the cell

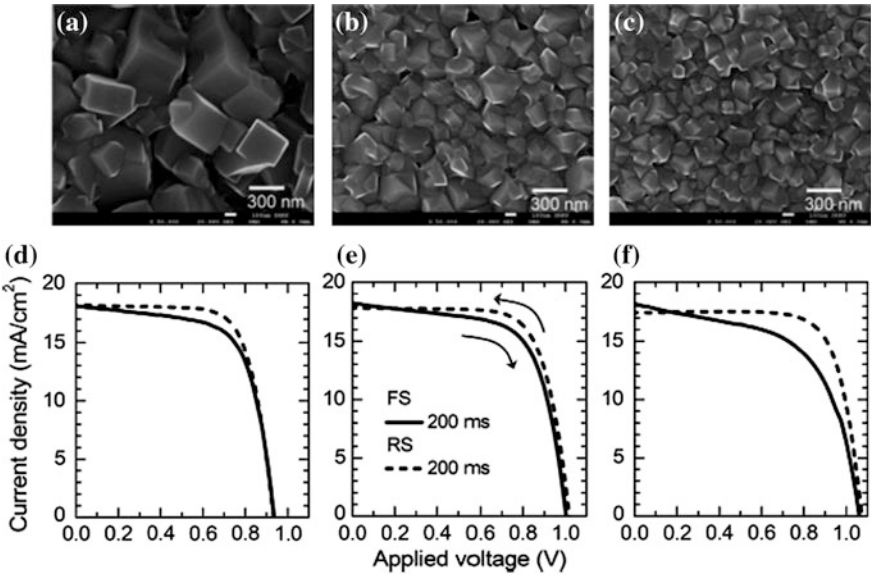

Fig. 8 J-V Hysteresis changing with grain size of perovskite. SEM images of $CH_3NH_3PbI_3$ grown by two-step spin coating method with CH_3NH_3I concentration of **a** 41.94, **b** 52.42, **c** 62.91 mM leading to formation of grains of size 440, 170 and 130 nm. Forward and backward J-V curves of perovskite cells employing the perovskite films with grain size of **d** 440, **e** 170 and **f** 130 nm [17]

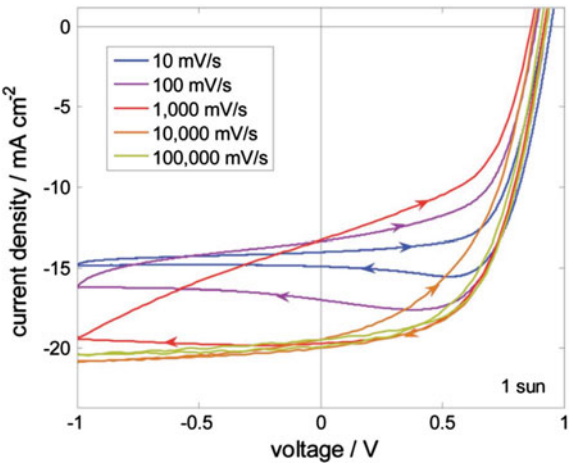

Fig. 9 Current–voltage curves of TiO_2 based $CH_3NH_3PbI_3$ devices measured with different scan rates from 1 to –1 V and back to 1 V. Sweep rates are from 10 to 100,000 mV s^{-1} [20]

structure, its preparation conditions and the preconditioning parameters. In some cases, the reverse scan is more sensitive to scan speed (Fig. 10) while in some other [23] the forward scan shows relatively greater change with the scan speed (Fig. 11). Figure 11 shows change in forward (a) and reverse (b) J-V curves of a perovskite

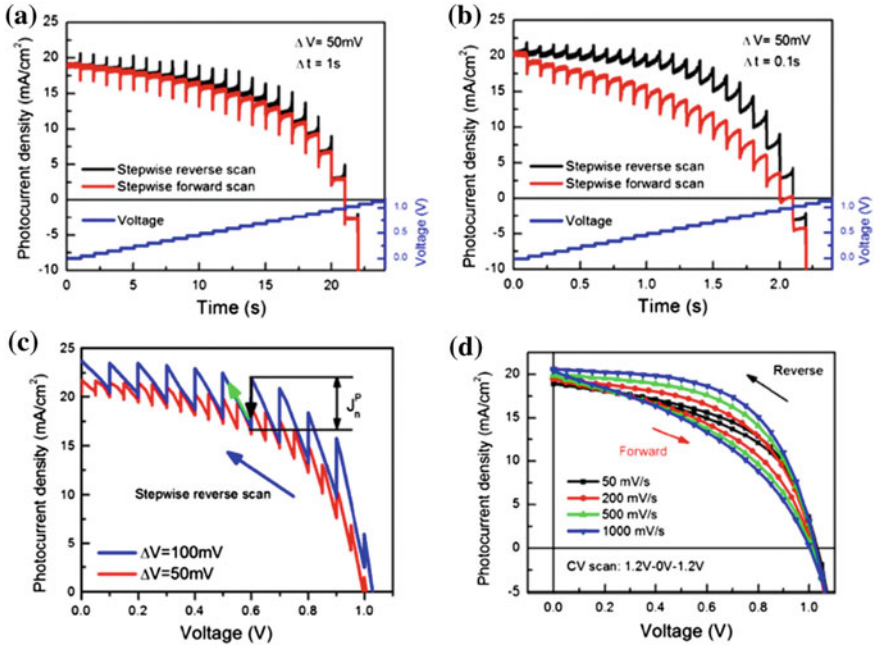

Fig. 10 Time dependent photocurrent response of planar $CH_3NH_3PbI_3$ perovskite solar cells (FTO/TiO_2 compact layer/$CH_3NH_3PbI_3$/spiro-OMeTAD/Au) under reverse and forward stepwise scans with **a** step size of 50 mV and step time of 1 s, **b** step size of 50 mV and step time of 0.1 s. **c** J-V response under stepwise reverse scan from 1.1 to 0 V with step size of 100 and 50 mV; step size equal to 5 s. **d** Forward and reverse J-V curves measured at different scan rates

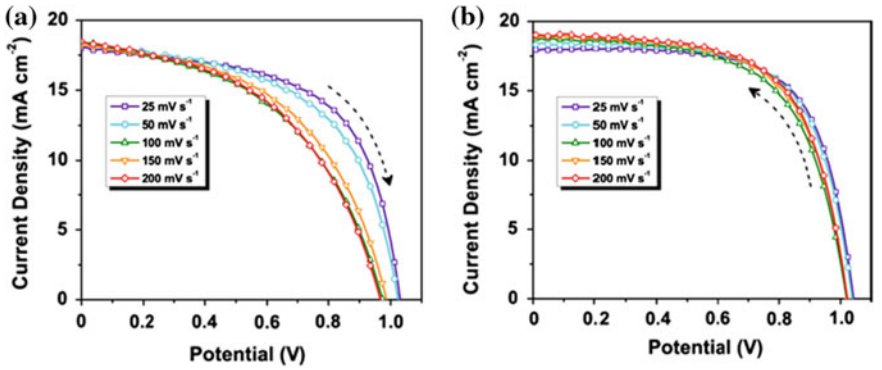

Fig. 11 **a** Forward and **b** reverse J-V curves of TiO_2 mesoscopic perovskite solar cell measured at different sweep rates. In all reverse scan cases, the cell was preconditioned at 1.2 V under illumination for 2 s [23]

cell using TiO_2 mesoporous scaffold (i.e., FTO/TiO_2 compact layer/TiO_2 mesoporous layer/$CH_3NH_3PbI_{3-x}Cl_x$/Au) where all the reverse scans were taken after prebiasing the cell at 1.2 V under illumination for 2 s.

In addition to scan speed and direction, temperature and light intensity can also alter the J-V hysteresis significantly. For a planar perovskite solar cell (FTO/TiO_2 compact layer/perovskite/spiro-OMeTAD/Au), as reported by Ono et al. [24], J-V hysteresis is large at low (250 K) and room temperatures (300 K) whereas the behavior becomes feeble at higher temperature (360 K). The stepwise photocurrent measurement for both forward and reverse directions taken at three different temperatures of sample is depicted in Fig. 12. At 250 and 300 K, the transient photocurrent shows slower decay to steady state and as result, a grater discrepancy is seen in the forward and reverse J-V curves. In consistence to the above results, Grätzel et al. [25] also witnessed hysteresis of iodide based perovskite cells increasing with decrease in temperature (Fig. 13a). The other interesting fact that was noticeable here is that the reverse scan shows minor dependence on the temperature while the forward J-V curve is strongly affected by change in temperature. Even, in case of hysteresis-free perovskite cells of inverted architecture, remarkably large hysteresis comes up when the device is measured at low temperature [26] (Fig. 13b).

Like in other solar cells, photocurrent of perovskite cells increases linearly with light intensity. With increase in photocurrent, the gap between the forward and backward J-V curves increases proportionately. For a planar perovskite cell (FTO/TiO_2 compact layer/$CH_3NH_3PbI_{3-x}Cl_x$/spiro-OMeTAD/Au), as observed in our lab, the difference between the forward and backward performance increases with light intensity (Fig. 12a) . However, when normalized with the photocurrent, the J-V hysteresis looks almost unchanged. For a TiO_2 mesoscopic device (FTO/TiO_2 dense layer/TiO_2 mesoporous layer/spiro-OMeTAD/Au), as reported by Grätzel et al., the

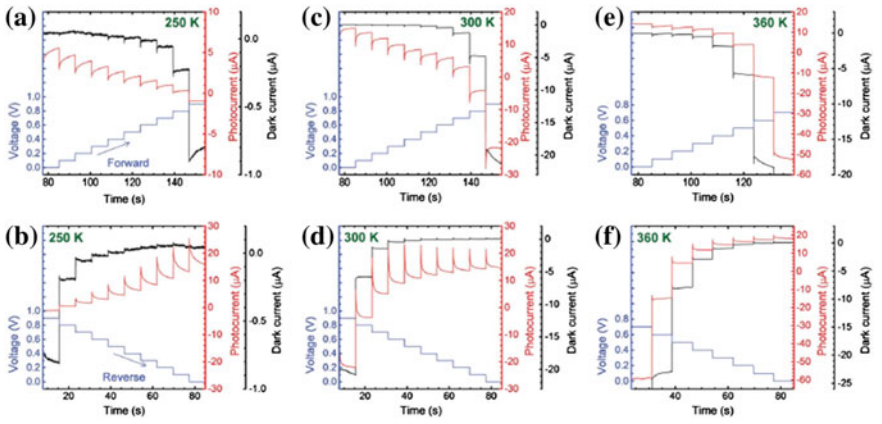

Fig. 12 Effect of temperature on J-V hysteresis of perovskite cell of planar architecture. Stepwise photocurrent and dark current measurement in forward (**a**, **c**, **e**) and reverse (**b**, **d**, **f**) directions at 250, 300 and 360 K

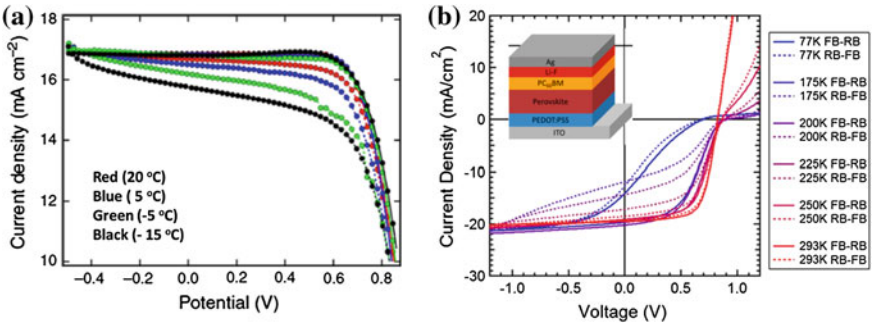

Fig. 13 **a** Forward and reverse J-V curves of an iodide based perovskite solar cell measured at different temperatures (20, 5, –5 and –15 °C). **b** Forward (*dashed line*) and reverse (*solid line*) J-V curves of an inverted perovskite solar cell measured at different temperatures (293, 250, 200, 175 and 77 K)

shape and magnitude of J-V hysteresis remain independent of light intensity (Fig. 12b). Such independence of hysteresis on light intensity rejects direct involvement of the photo-generated carriers in hysteresis (Fig. 14).

Besides the measurement conditions, preconditioning of the perovskite cells prior to J-V measurement also imparts strong effect on hysteresis. Light soaking and prebiasing of the devices with external voltage both in dark [27, 28] and light [23] before the actual performance characterization results in modified J-V curves and hysteresis. As observed in our lab, biasing a planar and an Al_2O_3 meso-structure perovskite cell at different negative voltages in dark for 5 min increases the hysteresis drastically (Fig. 15).

The variation in hysteresis with changing parameters of processing and measurement makes it difficult to affirm the actual conditions that can eliminate

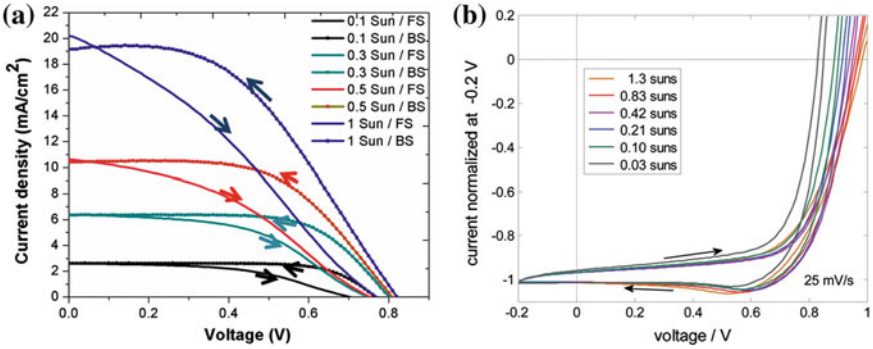

Fig. 14 **a** Hysteretic J-V curves of planar perovskite cell measured under different light intensities (scan speed = 200 mV/s). **b** J-V curves (normalized to current at –0.2 V) of perovskite cells measured under light of different intensities [20]

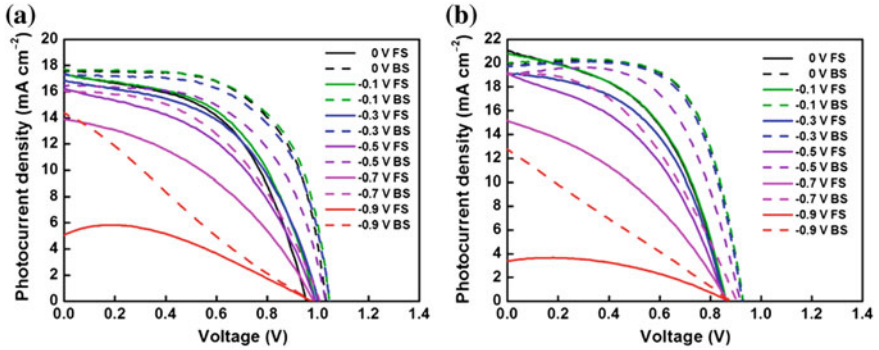

Fig. 15 Forward scan (FS) and backward scan (BS) J-V curves of **a** Al_2O_3 and **b** planar-structure-based perovskite solar cells under 1 sun illumination. All the cells were applied at various bias voltages in the dark for 5 min before the J-V measurements [27]

hysteresis completely. A quantitative analysis and fair comparison of literature becomes impossible as different groups follow different methods for fabrication and measurement. Therefore, a standard protocol of measurement must be adopted soon for better understanding and drawing right conclusions from the studies. In addition, more controlled experiments are required to determine the device structure and processing conditions that can reduce hysteresis. However, reviewing the relevant studies provides insights into carrier transport and collection mechanisms and the possible origins of hysteresis.

3 Mechanism of Origin to Hysteresis

In the recent years, a lot of effort has been made to understand the cause of hysteresis in J-V curves of perovskite solar cells. Different mechanisms of origin to hysteresis have been proposed. Few approaches have also been discovered to reduce/eliminate hysteresis in the devices. It has been proposed that the anomalous hysteresis in J-V characteristics of perovskite solar cells is caused by ferroelectric polarization [16, 21, 27, 29, 30], ion migration [14, 16], carrier dynamics at different interfaces or deeper trap states in the perovskite [16]. Although, at present, there is no single universally accepted mechanism that can explain the phenomenon coherently, the studies done so far have certainly provided deeper insights into the topic. It is unfortunate that the complexity of this problem lies in the facts that the observed hysteresis is strongly or slightly influenced by several different factors such as device structure (planar, mesoporous, and organic-based), perovskite film characteristics, electron collecting layer properties, etc., at the same time. Lack of complete understanding, inadequacy of direct evidences demands further investigation.

3.1 Ferroelectric Property of Perovskite

Ferroelectric property of perovskite metal oxides such as $BaTiO_3$, $PbTiO_3$, etc., has been extensively studied. These materials exhibit hysteretic Polarization-Electric field (P-E) loop due to polarization of domains under external bias potential. In 2013, Stoumpos et al. [31] found that organo Sn and Pb trihalides show structural properties same as metal oxide perovskites and also observed ferroelectric behavior of $CH_3NH_3PbI_3$ (Fig. 16). Piezoresponse force microscopy (PFM) of $CH_3NH_3PbI_3$ at different poling (prebiasing in dark) conditions shows ferroelectric domains (Fig. 17) in $CH_3NH_3PbI_3$ [32–34]. Such poling of the perovskite films alters the cell performance and J-V hysteresis dramatically, which is attributed to polarization of the ferroelectric domains that leads to modification of band structure at the interfaces (Fig. 18).

It was, thus, presumed that hysteresis in $CH_3NH_3PbI_3$ perovskite solar cells might be caused by ferroelectric polarization happening in $CH_3NH_3PbI_3$ [16, 27, 33]. However, the important thing that needs to be understood in relation to ferroelectric polarization is its correlation between change in hysteresis and voltage scan rate. As hysteresis in the J-V curves is actually the outcome of transient current measured at each voltage (Fig. 10), ferroelectric model must explain the transient and steady-state current observed for both the scans. Wei et al. [29] proposed a model to explain this transient effect caused by ferroelectric polarization in a $CH_3NH_3PbI_{3-x}Cl_x$ perovskite device (Glass/FTO/Au/Ti/Perovskite/Al_2O_3/Au). The observed S-shape E-P loop, (Fig. 19a), of the device confirms ferroelectric polarization in $CH_3NH_3PbI_{3-x}Cl_x$. According to the model proposed here (Fig. 19b), polarization (P) that depends directly on internal field (E_{in}) decreases and increases on forward and backward scan, respectively. As P cannot follow the speed of voltage scan, the excess polarization (ΔP) generates a transient state. On forward scan, ΔP falling in parallel to internal field (E_{in}) results in a transient current value lower than the steady-state current. On backward scan, the change in polarization

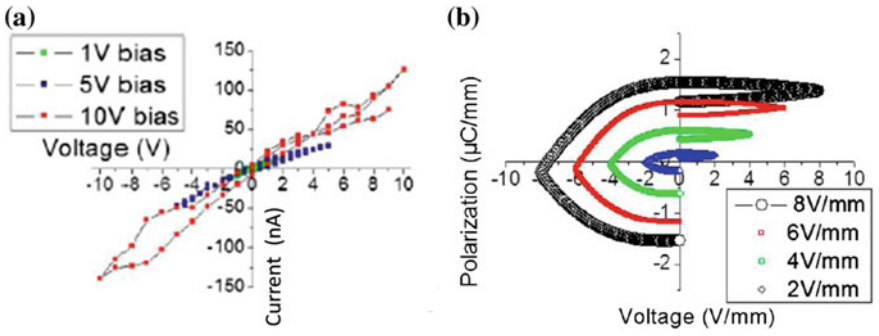

Fig. 16 Hysteresis loops of $CH_3NH_3PbI_3$ prepared by solution process. **a** Voltage and **b** polarization as function of applied bias [31]

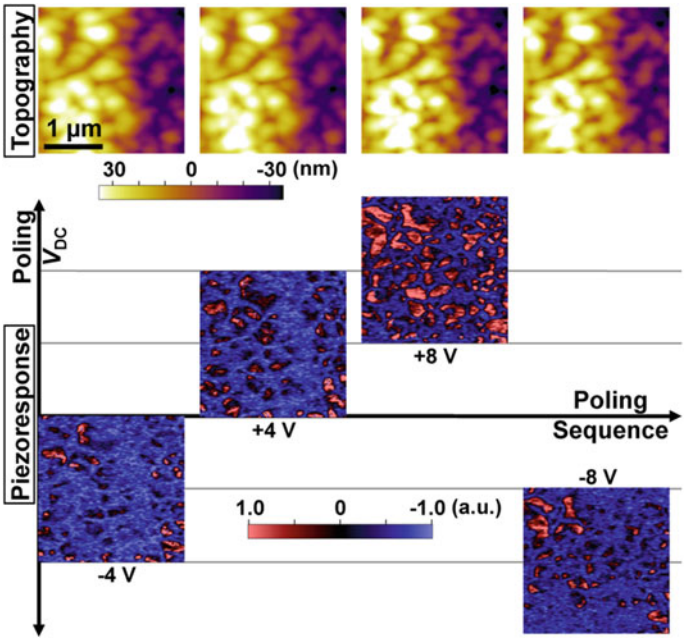

Fig. 17 AFM (atomic force microscopy) topography images (*top row*) of a single 2.5 × 2.5 μm^2 area, with simultaneously acquired PFM images, each scanned after DC poling at the biases indicated (VDC), showing partial, reversible ferroelectric domain switching in as-processed β-$MAPbI_3$ thin film [32]

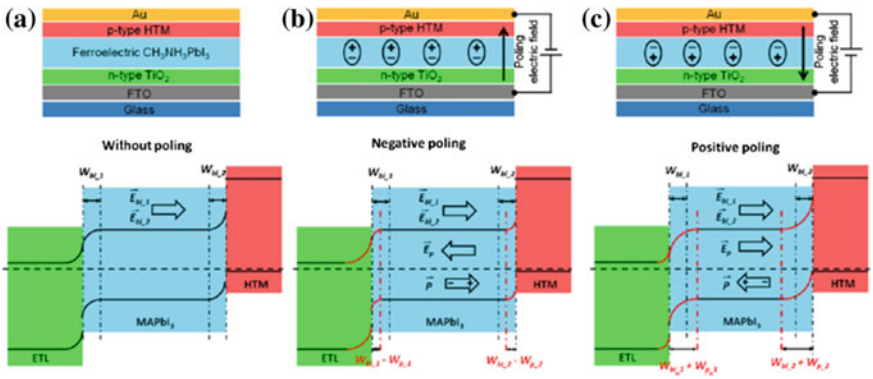

Fig. 18 Schematic and band diagram of perovskite solar cells under different poling conditions: **a** without poling, **b** negative poling, **c** positive poling. E_{bi_1} and E_{bi_2} represent built-in-electric field in perovskite layer close to electron transporting layer and hole transporting material respectively. W_{bi_1} and W_{bi_2} represent width of corresponding depletion regions [34]

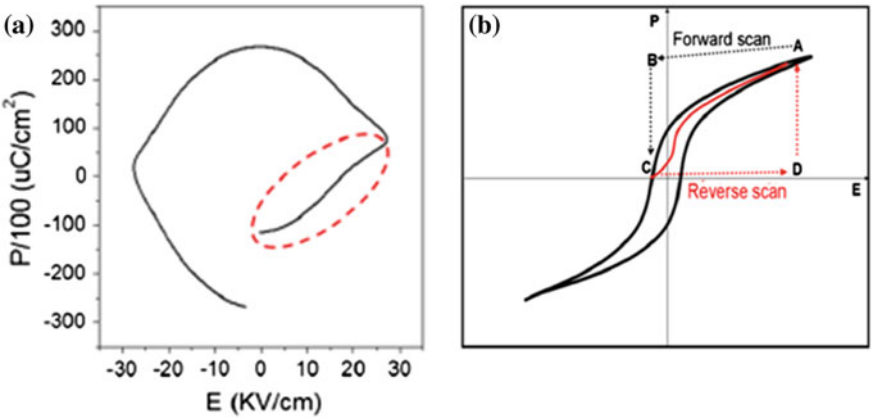

Fig. 19 **a** Schematic diagram of the relationship between polarization P and electric field E in ferroelectric materials; path A−B−C indicates the forward scan under a moderate scan velocity, and path C−D−A indicates the reverse scan. **b** E-P (Electric field-Polarization) measurement plot of the perovskite device (Glass/FTO/Au/Ti/Perovskite/Al_2O_3/Au) [29]

results in transient current higher than the steady-state current. As a result, backward scan always shows higher current and better fill factor.

While some results evidence ferroelectric property of perovskite and support its strong effect on hysteresis some other reports contradict the presumption of hysteresis being caused by ferroelectric polarization [16, 17]. Fan et al. [35] reported that perovskites are not ferroelectric at room temperature although their theoretical calculations predicted the material to be mild ferroelectric. Therefore, exhibition of ferroelectric behavior by the perovskite compound at the operating conditions of the device still remains a debate. Furthermore, the effect in the actual device consisting of thin layers can be different from the bulk ferroelectric property of perovskite in isolation. The explanation of transient effect caused by ferroelectric polarization must be consistent when all the different interfaces are included. Therefore, it is reasonable that the interface properties play equally important role in causing hysteresis.

3.2 Interfacial Carrier Dynamics

Although polarization by prebiasing perovskite was found to enhance hysteresis, in one of our studies [36], we discovered that hysteresis is also exhibited by a cell made of non-ferroelectric PbI_2 (Fig. 20). This result indicated that ferroelectric property cannot be the only reason for hysteresis. Examination of I-V characteristics of different interfaces in simplified structures like FTO/TiO_2 compact layer (CL)/Spiro-OMeTAD/Au and FTO/TiO_2 CL disclosed that the interface between FTO and TiO_2 can be one of the contributors to hysteresis (Fig. 21). Besides, it strongly

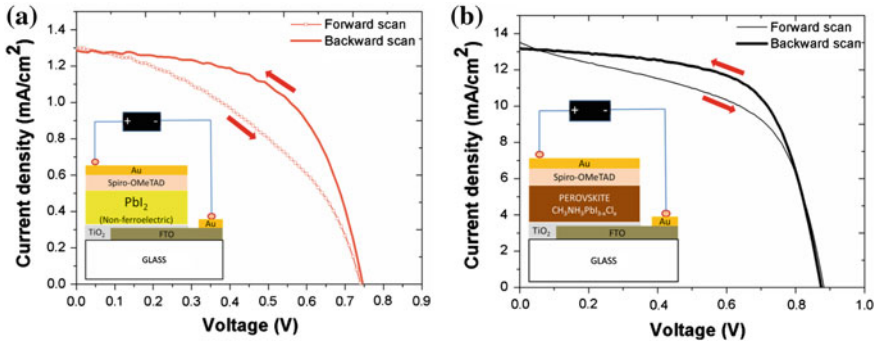

Fig. 20 J-V characteristics of **a** planar heterojunction PbI_2 and **b** $CH_3NH_3PbI_{3-x}Cl_x$ perovskite solar cells. The measurements were taken under 1 sun illumination (100 mW/cm^2) and at a voltage scan speed of 200 mV/s. Insets represent the corresponding device structures [36]

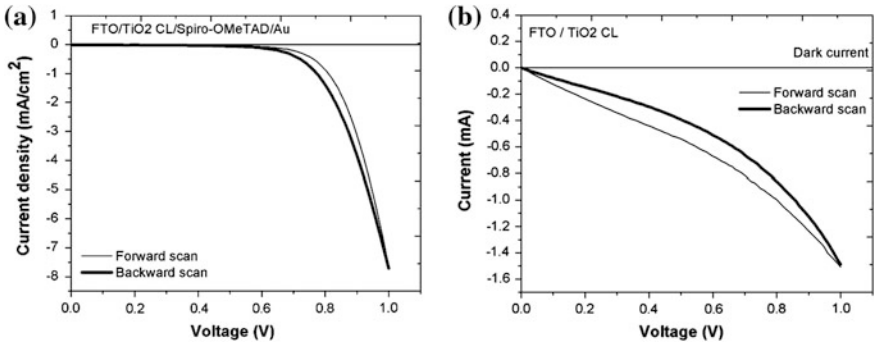

Fig. 21 I-V curves of structures with **a** spiro-OMeTAD sandwiched between TiO_2 CL and Au and **b** only TiO_2 CL on FTO

suggested that the interface between perovskite and TiO_2 can be a major player for hysteretic J-V curves.

In devices made of perovskite, modification of the interface between perovskite and electron collecting layer apparently affects hysteresis. For instance, modification of TiO_2 compact layer (CL) with C60 [37] reduces hysteresis. Incorporation of Zr [38] and Au nanoparticles [39] in the TiO_2 compact layer also reduces hysteresis. In addition, no/negligible hysteresis observed in the perovskite-based cells using organic electron collecting layers [14, 40, 41] instead of TiO_2 compact layer sandwiched between FTO and perovskite also supports the fact that interface properties can be crucial for hysteresis. Unbalanced carrier extraction (hole extraction rate $\neq$ electron extraction rate) caused by imperfect matching of the properties of layers is believed to result in J-V hysteresis. Heo et al. [40] found that perovskite cells of inverted architecture using PCBM as electron collector do not show hysteresis. PCBM being more conductive (0.16 mS/cm) than the widely used

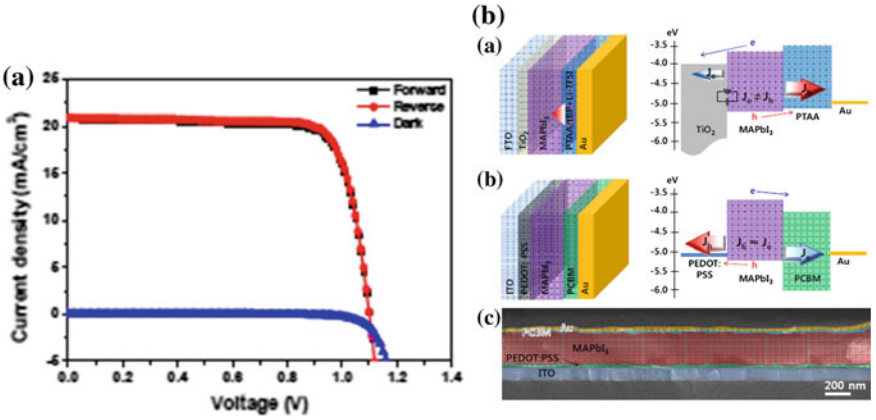

Fig. 22 **a** Forward and reverse scan J-V curves and **b** mechanism of hysteresis based on carrier extraction [40]

TiO_2 (6×10^{-6} mS/cm) collects/separates the electron more efficiently from perovskite ($CH_3NH_3PbI_3$), resulting in balanced carrier extraction (hole extraction rate = electron extraction rate), which in consequence, eliminated hysteresis. Figure 22 shows (a) the non-hysteretic J-V curves of planar peovskite ($CH_3NH_3PbI_3$) and (b) proposed mechanism of hysteresis based on unbalanced carrier extraction in the case of TiO_2 CL.

Real space carrier distribution measurement with the help of Kelvin Probe Force Microscopy also shows unbalanced hole and electron extraction rate in perovskite devices using TiO_2 and spiro-OMeTAD as electron collector and HTM, respectively [42]. It is known that structural defects and/or mismatching at any heterogeneous interface can develop a potential barrier for carrier extraction and thus, results in accumulation of these carries at the interfaces. Therefore, such interfacial defects leads to unbalanced carrier extraction. Carrier extraction depends strongly on physical and electrical contact at the interfaces. Therefore, conductivity of the layers and their morphology, and the interface connectivity play role in causing hysteresis. Gaps at the interfaces can act as capacitors due to carrier accumulation and thereby alter carrier extraction significantly [43]. Although ferroelectrics can be involved in the above-mentioned interfacial phenomena, it is not solely responsible for hysteresis. The carrier dynamics at the interface, which might be influenced either by ferroelectric polarization or ion migration, holds responsible for causing hysteresis.

3.3 Ion Migration

It is well known that metal halide compounds such as AgX, PbX_2, (X=Cl, Br, I) are photosensitive ionic crystals with high-density mobile halide ions, which can

diffuse freely in the three dimensional crystals either in light or under the influence of bias voltage in dark [44]. As organolead halide perovskite compounds are derived from PbX_2, they are also believed to retain high ionic conductivity like the metal halides. The cations and anions (halide) are likely to move freely in the crystals through existing vacancies. In silver halide, mobile cation is the only interstitial Ag^+, which diffuses to the trap site to form latent image (Ag_2) by reaction with photo-excited electrons. However, in the halide perovskites, the possible mobile cations are both lead and organic group cations. Smaller organic cations can diffuse faster than larger organic cations and the halide anions are considered to have significantly high mobility compared to the heavy metal cation (Pb^{2+}). The calculated activation energy for migration of halide vacancies (iodide vacancy) is significantly lower than the organic cation vacancies [45, 46]. Methyammmonium cation (MA^+) and iodide anion (I^-) are freely diffusible in $MAPbI_3$ at room temperature. Even, MA^+I^- is thermally unstable and it can be evaporated from the crystal structure at elevated temperature [47]. Unlike Ag^+ in silver halides, these ions in halide perovskite never undergo reaction with photo-generated carriers and contribute to self-organization electrostatically and geometrically in crystal structure formation. However, migration of the ions in perovskite is considered to cause carrier localization that gives rise to J-V hysteresis. More importantly, the process of ion motion can affect stability of perovskite devices through continuous change in chemical and physical properties of the perovskite under photovoltaic operation.

Ion migration in perovskite has been visualized as color change when the perovskite film is subjected to poling by exposure to DC electric field. Huang et al. observed migration of MA^+ and I^- under electric field of $\sim 1.2\ V\mu m^{-1}$ and accumulation (dark red) and depletion (yellow) of MA at negative and positive electrode, respectively [17]. Such ionic migration under applied voltage to the device has been discussed in relation to generation of hysteresis. Snaith et al., based on photocurrent behavior of preovskite cell influenced by prebiasing, proposed that under forward bias, $MAPbI_3$ becomes polarized due to accumulation of positive and negative space charges near electron and hole collector interfaces [48]. This charge accumulation is assumed to cause n-type and p-type doping at the interfaces (formation of p-i-n structure), which temporarily enhances photocurrent generation. Accumulation of migrated ions at the interfaces can change the polarity [49] (Fig. 23) and the dynamic change in accumulation of these charges with the scanning voltage (changing internal field) is assumed to generate hysteresis in photocurrent of the perovskite devices [48, 49].

Li et al. [50] have recently confirmed iodide migration to positive electrode, leaving iodide vacancies at the negative electrode through DC dependent electroabsorption (EA) spectra, temperature dependent electrical measurement and XPS characterization. According the authors, accumulation of iodide ions at one interface and the corresponding vacancies at the other creates barriers for carrier extraction. Modulation of such interfacial barriers at $CH_3NH_3PbI_{3-x}Cl_x$/Spiro-OMeTAD and $TiO_2/CH_3NH_3PbI_{3-x}Cl_x$, caused by the migration of iodide

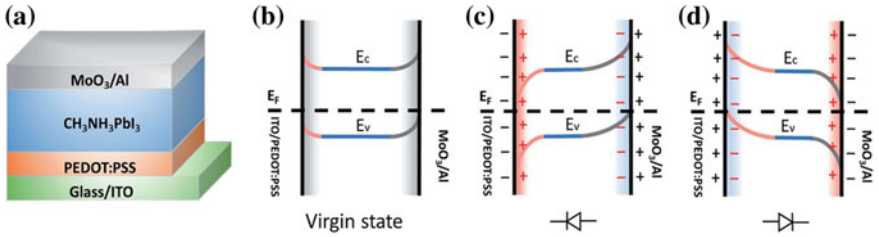

Fig. 23 Device structure (ITO/PEDOT:PSS/$CH_3NH_3PbI_3$/MoO_3-Al) and mechanism of switchable polarity in perovskite photovoltaic devices. **a** Device structure. (**b–d**) Schematic energy band diagrams under equilibrium (dark and short circuits) conditions. **b** Without interface charge the device is a hole-only device. **c** The device is a forward diode due to positive charges near the ITO/PEDOT:PSS electrode. **d** The device is a reversed diode due to positive charges near the MoO_3/Al electrode. Interface charge and screen charge are represented in *red* and *black*, respectively [49]

ions/interstitials driven by an external electrical bias leads to J-V hysteresis in planar (FTO/TiO_2 CL/$CH_3NH_3PbI_{3-x}Cl_x$/Spiro-OMeTAD/Au) perovskite solar cells. Based on temperature dependence of hysteretic change in current density, Grätzel et al. [26] estimated activation energy for diffusion of different ions in $MAPbI_3$ and found that the iodide ions have the highest mobility with lowest activation energy. Hence, it is the halide anions (I^-) not the MA^+ ions which migrate more easily in perovskite, causing polarization and charge accumulation at interfaces under voltage scans and eventually creates hysteresis [26]. Migration of iodide can happen through either the iodide vacancies (V_I') or the interstitial iodides (I_i^*). Vacancy (V_I') assisted iodide migration requires lower activation energy and is favored energetically. It has been also found that MA vacancies help in migration of iodide ions due to reduced steric hindrance of MA in the lattice [51]. As supported by several independent studies, defect mediated slow movement of iodide ions to the interface, bringing changes in the interfacial properties, holds responsible for hysteresis [52]. However, a clear picture of its role in generating the transient current which actually leads to hysteresis is still not seen from the studies. A comprehensive model that can explain the transient photocurrent due to ion migration is needed to conclude that ion migration is the only cause. Moreover, hysteresis-less devices using the same perovskite crystal ($MAPbI_3$) (supposed to exhibit ion migration) but with different electron and hole collectors conflict with the proposals of ion migration being responsible for hysteresis. Although the results need to be carefully compared by taking the extent of hysteresis and scan speed employed into account, this fact implies the involvement of interfacial structures of perovskite cells in enhancing hysteresis. Interfacial ion accumulation not only creates energy barrier through band edge modification but also builds up capacitance at the interfaces [22, 53, 54]. This capacitive effect of the interfaces due to ion accumulation is also considered to cause hysteresis and performance degradation as

well. As ion accumulation can be intensified at junction interfaces (contacts) having non-continuous structure (physical gaps) with voids and defects, it is reasonable to assume that defect-rich interfacial structures enhance the hysteresis originated by ion migration. For example, hysteresis is also observed for formamidium (FA)-based perovskite ($FAPbI_3$) despite its higher tolerance factor decreasing the mobility of large cation (FA^+). Only ion migration being responsible for hysteresis still remains a debate. The models proposed so far cannot explain hysteresis just based on ion migration and include interfacial trap states [51, 52, 55] to successfully explain the anomalous behavior. Therefore, the relation of ion migration with hysteresis is required to be further studied. Apart from hysteresis, the impact of ionic migration on cell performance and its stability under long time operation seeks even more serious attention.

3.4 Trap States

Among all possible causes of hysteresis, trap states are also considered to be major. Even though the recent reports strongly support the hypothesis of ion migration being responsible for hysteresis, most of the proposed models cannot rule out involvement of trap states. While some results partially agree with the assumption that trap sates must be causing hysteresis some other results certainly indicate their participation in the process. Trap states on surface and grain boundaries of perovskite have been proposed to be origin of hysteresis [56]. Fullerene deposition on perovskite is believed to passivate these trap states and thereby eliminate the notorious hysteresis in photocurrent (Fig. 24). In a recent report, Li et al. explained hysteresis based on dynamic charge trapping-detrapping processes [57]. Figure 25 shows the schematics

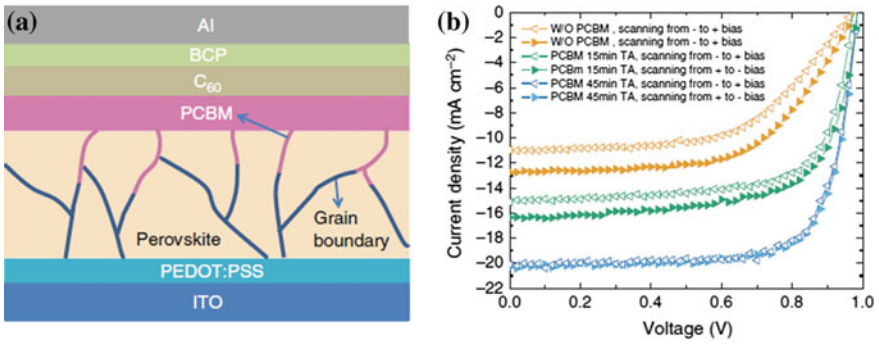

Fig. 24 **a** device structure and **b** forward and backward J-V curves of perovskite cells without and with PCBM (thermally annealed for 15 and 45 min) [56]

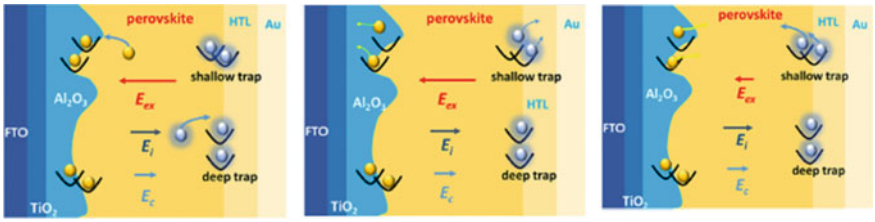

Fig. 25 Schematics showing shallow and deep trap states, and their role in causing hysteresis. Hysteresis on a voltage scan (from 0 to 4 V) is basically caused by releasing of shallow trap states and electric change (E_c) due deeper trap states. E_{ex} and E_{in} represent external field (due to external bias) and inner field (due to separated charge carriers) respectively [57]

illustrating existence of shallow and deep trap states and their role in hysteresis. According to the model proposed by them, hysteresis is caused by two factors; releasing of carriers from shallow traps with changing bias and change in electric field due to deeper trap states. The model applies to both planar and porous structure devices. The proportion of deeper trap states and shallow trap states, which is different in porous and planar cells, decides the magnitude of hysteresis.

While ion migration is being talked much in relation to J-V hysteresis in the present time, lack of more direct evidences and comprehensive models makes it hard to conclude that ion migration is the sole cause of hysteresis. In fact, according to a model proposed by Snaith et al., only ion migration cannot explain hysteresis but ion migration and interfacial trap states together explains hysteresis [55]. The modeled J-V characteristics of perovskite solar cells that comprise only ions, and both ions and trap states are compared in Fig. 26. Therefore, reduction of density of either the mobile ions or the trap states can reduce hysteresis.

However, there are few facts that conflict with the theory of trap states being responsible for hysteresis. One of them is the observed low trap density in perovskite [58, 59]. Relatively small trap density in perovskite is expected to result in slight/no hysteresis if trap states are the only players in hysteresis. In addition, the effective change in trap density with illumination intensity must be reflected as altered hysteresis in the perovskite cells. As trap states are better filled under light of higher intensity, hysteresis is expected to be less in the cases of higher intense illumination. On the contrary, it has been observed that hysteresis increases with light intensity, in proportion to the photocurrent. Therefore, the presumption that trapping–detrapping of existing trap sates in perovskite causes hysteresis is not completely convincing. Further investigation is needed to find more direct and distinct evidences for active participation of trap states in creating hysteresis. Also, mechanism of generation of the trap states and their density in perovskite need to be examined further to support the models based on trap states.

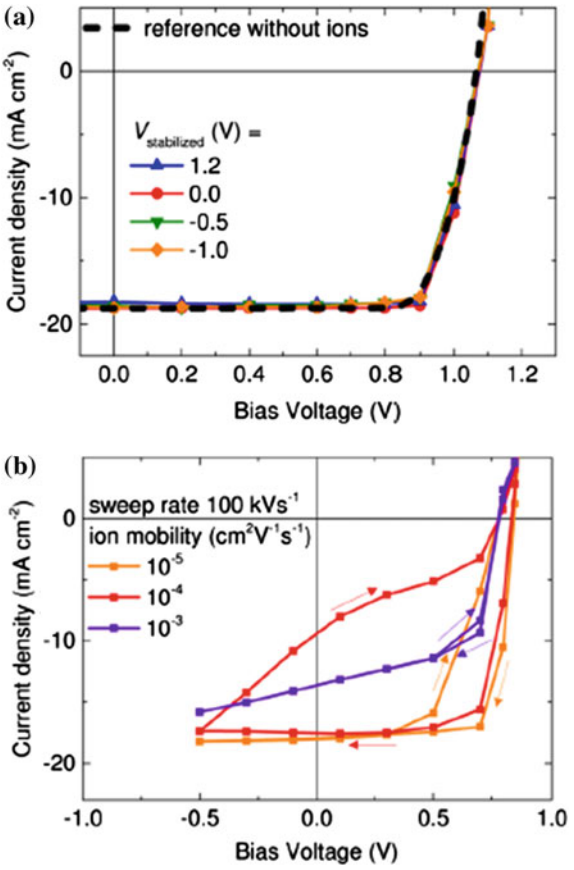

Fig. 26 Modeled J-V characteristics of perovskite solar cells comprising **a** only ions showing no hysteresis and **b** both ions (with different mobility) and trap states showing hysteresis [55]

4 Hysteresis, Stable Power Output and Stability

Although understanding the mechanism of origin to hysteresis is doubtlessly the first step toward finding a solution to this anomalous behavior of perovskite solar cells, determining how hysteresis affects the actual cell performance is more important in the aspect of commercialization. Indeed, it holds more relevance to practical use of the solar cells. The steady-state performance of cells operating at a constant voltage (or across an external load) is what matters for real use of any solar cell. As hysteresis is a transient phenomenon observed only on voltage scan, it may not be considered a big problem as long as the device gives stable and reliable steady-state performance across a constant load over time. The only thing we need to know is the actual performance of devices showing hysteresis while operating at a constant voltage (at maximum power point). If ferroelectric polarization, ion migration, interface carrier dynamic and trap states, which are proposed to be responsible for hysteresis, also affect the steady-state performance of the cells then

stability of the cells must be directly related to hysteresis. In other words, cells showing greater hysteresis are expected to have poorer stability due to larger effect of the above processes.

In majority of cases, stable power output measured at maximum power point (MPP) has been found to be slightly lesser than the performance estimated from backward J-V scan [48, 60, 61] while few reports have shown steady-state (ss) power output matching the backward scan values. In order to verify the above results, in a recent study, we measured steady-state power output of cells showing slight, moderate and large hysteresis, which was essentially controlled by the perovskite film thickness in a planar heterojunction perovskite cell. All the cells were operated with an external load (600 Ω) and the current density was measured for more than 2 min. Figure 27 shows the J-V characteristics and corresponding steady-state current density measured on planar perovskite cells showing hysteresis of different magnitudes. The steady sate current density of cells with large hysteresis was found to be close to the value estimated from the forward scan, significantly lower than the backward scan value. Besides, in some TiO_2 mesoporous perovskite devices showing large hysteresis, which was probably due to thicker capping layer, the steady-state performance measured at different bias voltages (0.5, 0.55, 0.6 and 0.67 V) was found to match closely with the forward scan values (Fig. 28).

While we consistently observed for many samples that the steady-state power output of the cells showing large hysteresis matches closely with the forward scan performance few reports in literature show steady-state performance matching with backward scan values. It seems that matching of steady-state performance with back ward or forward scan performance depends also on the device structure and methods of fabrication. Further studies are required to understand the conditions of

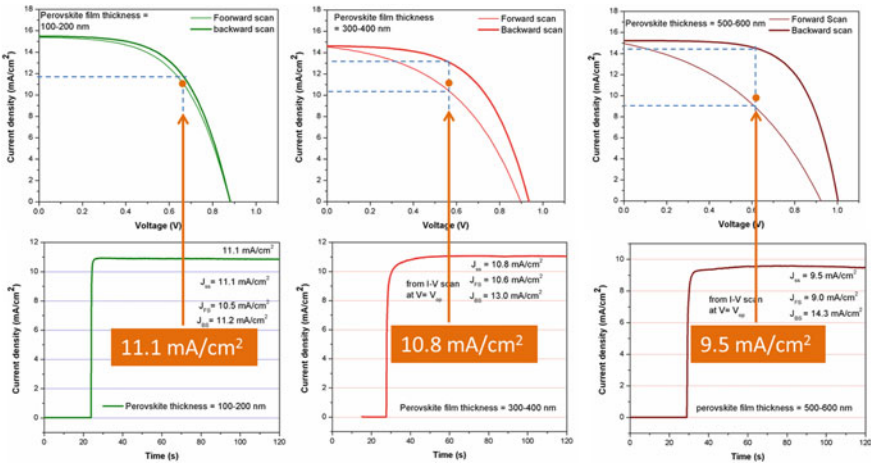

Fig. 27 J-V characteristics (voltage scan speed = 200 mV/s) and steady-state performance (measured with an external load of 600 Ω) of three planar perovskite cells showing hysteresis of different magnitudes

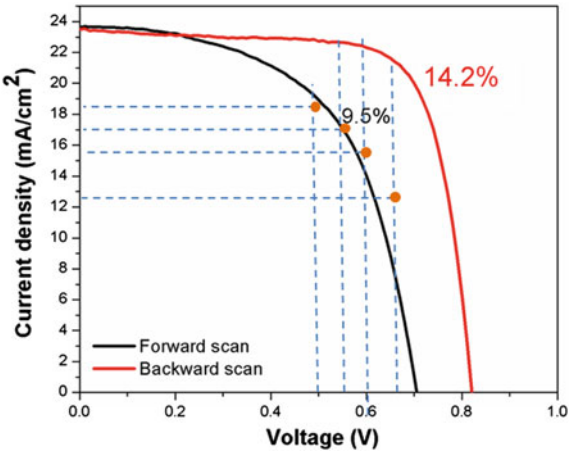

Fig. 28 J-V curves and steady-state current density measured at bias voltages of 0.5, 0.55. 0.6 and 0.67 V bias

preparation and right device structure which can perform steadily at a MPP matching with the backward scan performance.

Although 2 min is long enough for determining the steady-state current values, the duration is too short for evaluating performance stability of the cells. In order to check the performance stability, we measured photocurrent density of the cells (not encapsulated) operated across the load (600 Ω) with cyclic on and off of light (1 sun). The time for each on and off cycle was fixed to 3 min and all the devices were measured for 10 cycles, enduring almost 1 h for the complete measurement. As can be seen in Fig. 29, hysteresis increased and performance stability decreased with thickness of the perovskite film in the planar perovskite solar cells, indicating that hysteresis may be directly related to such performance instability. In order to confirm this relation, we compared the performance of a set of cells with perovskite films of different thicknesses but showing similar hysteresis. Here, the planar perovskite cells

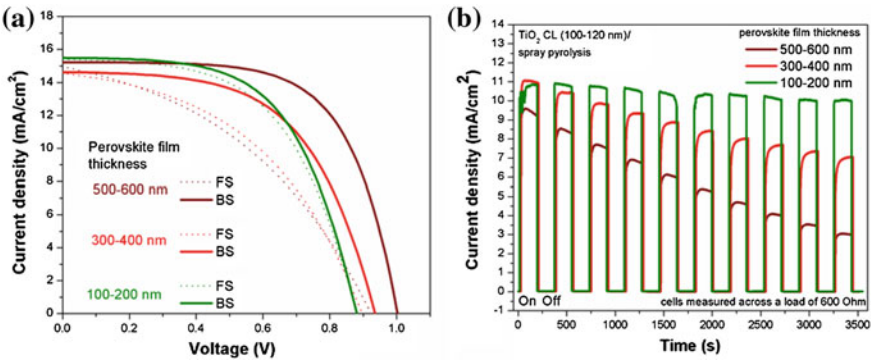

Fig. 29 **a** Forward scan (FS) and backward scan (BS) J-V curves and **b** cyclic photocurrent sand dark current (measured with external load of 600 Ω) of planar perovskite ($CH_3NH_3PbI_{3-x}Cl_x$) solar cells with varying thickness of perovskite film. The TiO_2 compact layer thickness is 100–120 nm

with thicker TiO_2 CL (~200 nm) and perovskite films of different thickness (spin-coated at 1500, 3000 and 6000 rpm) showed substantially lower J_{sc} (believed to be limited by the thicker CL) and similar hysteresis without much dependence on the perovskite thickness. Despite of insignificant difference in hysteresis (Fig. 30a), all these cells demonstrated same decreasing trend of performance with thickness of perovskite (Fig. 30b), as was observed for cells with thinner TiO_2 CL (Fig. 29b) showing hysteresis increasing with perovskite thickness. This confirms that the performance instability is not directly related to hysteresis; both must have different mechanisms. However, hysteresis and performance stability are independently affected by thickness of the perovskite film. It was interesting to find that the performance is not only degraded on cyclic or continuous photocurrent measurement but also degraded when the cells were kept under light at open circuit (no current collected form the devices). This, indeed, evidenced that the cell performance decreases with light soaking, regardless of close or open circuit condition of the device. All the

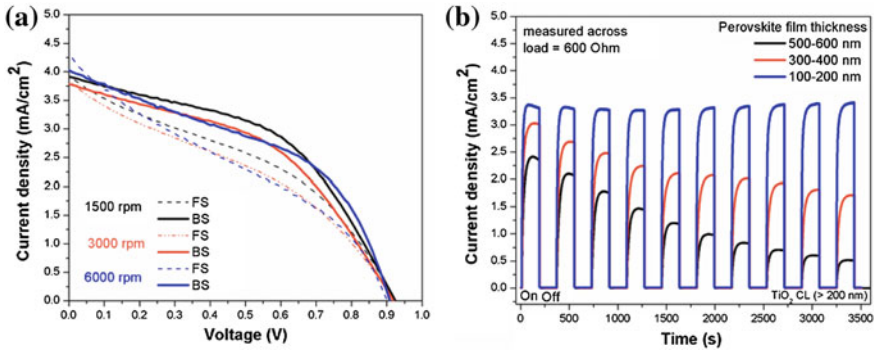

Fig. 30 **a** Forward scan (FS) and backward scan (BS) J-V curves and **b** cyclic photocurrent sand dark current (measured with external load of 600 Ω) of planar perovskite solar cells with varying thickness of perovskite film. The TiO_2 compact layer thickness is >200 nm

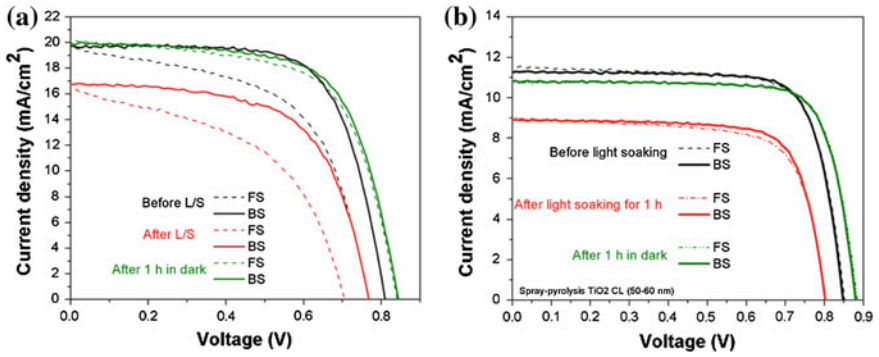

Fig. 31 Effect of light soaking on J-V characteristics of TiO_2 mesoporous perovskite solar cells **a** with and **b** without hysteresis

cells, irrespective of hysteresis, showed same photo-induced reversible performance degradation (Fig. 31). There are reports on different photo-induced effects like giant dielectric constant, photo-induced trap states, reversible structural transformation, etc., observed in perovskite cells. However, no correlation between hysteresis and such photo-induced reversible effect proves that hysteresis is not caused by same process responsible for photo-induced changes.

5 Conclusions

Unlike the materials used in other solar cells, organo lead halide perovskite often exhibits large mismatch between the photocurrent measured on forward and backward voltage scan, resulting in hysteretic J-V curves of perovskite-based solar cells. Such anomalous hysteresis in perovskite cells is influenced by many factors such as, device architecture, characteristics of metal oxide scaffold, thickness and morphology of perovskite films, properties of the electron, and hole conducting layers, and even the conditions of treatment before and during the measurement. It is usually observed that hysteresis increases with scan speed of the bias voltage. Faster the scan, larger is the discrepancy between forward and reverse J-V curves. The observed hysteresis is actually the result of transient photocurrent measured at each bias voltage. This transient current is higher and lower than the steady-state value for the reverse and forward scan, respectively. The decay of this transient current and thus, the J-V hysteresis depends on the device structure. Owing to wide variation in the device structure (bulk layers and interfaces), the physics of hysteresis is not yet thoroughly understood and an exclusive solution for such unusual photovoltaic properties is still missing. Nevertheless, a great amount of effort made to understand the scientific basis of such behavior has generated information about the process and measurement parameters that affect hysteresis slightly or significantly. In many cases, devices with mesoporous TiO_2 layer show little or no hysteresis. On the other hand, the devices with Al_2O_3 scaffold or without any mesoporous scaffold (planar heterojuction cells with metal oxide compact layers) perform with large J-V hysteresis. But, planar perovskite cells of inverted architecture (i.e., TCO/HTM/Perovskite/ECL/Au or Ag or Al) often exhibit negligible or zero hysteresis. However, the TiO_2 mesoscopic structure or the inverted device architecture is not the sufficient condition for eliminating hysteresis because the behavior depends on the characteristics of the layered structures and preparation conditions strongly. Even in the devices of same architecture, hysteresis varies with slight variation in the fabrication methods and conditions in different laboratories, which can change interfacial quality of layered structures. Hence, a quantitative analysis of the phenomenon and fair comparison of the results from different groups is quite difficult. Understanding the mechanism of hysteresis becomes inevitably challenging.

Although there is not a single and unanimously accepted mechanism so far, different studies claiming different origins to hysteresis have provided reasonable insights into the problem. Apparently, more than one phenomenon are involved in

generation of hysteresis and causing performance instability. Besides capacitive effect at the contacts, ferroelectric polarization, ion migration, interfacial carrier dynamics, trapping-detrapping of charge carriers are the possible causes of the transient hysteresis. Unfortunately, none of the above hypotheses explains hysteresis coherently with its wide variation due to changes in device structure and fabrication methods. However, all the proposed mechanisms implicitly refer to altered carrier collection efficiency during the scans. As carrier collection depends both on transport in the bulk and transfer at the interfaces in the device, it is obvious that both the bulk properties (e.g., ferroelectric polarization, high density of mobile ions and trap states, etc.) and the interfacial contacts contribute to hysteresis. Vacancy-assisted ion migration to the interfaces, polarization of ferroelectric domains, slow detrapping of deeper trap states may create root of hysteresis but the physical discontinuity or electrical mismatch of the interfaces will certainly magnify the effect. Therefore, selecting the right interfacial layers with a given composition of perovskite can, in cases, eliminate hysteresis. Also, minimizing the mobile ions and trap states in perovskite will be effective in reducing hysteresis. Recently, mixed cation type perovskite cells of high efficiency (>20 %) have been prepared on metal oxide electron transporting layers. Methylammonium (MA)/ formamidinium (FA) and I/Br mixture perovskite prepared on SnO2 exhibits hysteresis-less performance [62]. Cs/FA/MA and I/Br mixture perovskite on TiO2 also undergoes very small hysteresis [63]. These cells of highly stable performance are assumed to be the results of reduced ionic migration, minimized trap states, and void-less continuous interfacial structures, which are achieved by improvement of materials and interfacial contacts.

Elimination of hysteresis is important but understanding the relation of hysteresis with steady-state power output and performance stability is more important. As the solar cells in real use have to operate at a particular voltage (at MPP) over time, hysteresis observed due to voltage scan may not be a matter of worry as long as the phenomenon does not affect stabilized power output of the device. In other words, it is important to know the actual cell performance and its stability for any cell showing hysteresis. For devices showing hysteresis, the stabilized power output at MPP should be measured as the actual performance. Although, in most cases, the stabilized power output falls closer to the power calculated during the forward scan, it is sensitive to the structure and conditions of preparation. Operation of devices (with or without hysteresis) at a constant voltage (near to the maximum power point) with an external load reveals no direct correlation between hysteresis and performance stability. The photo-induced reversible performance degradation observed in both the devices with and without hysteresis infers that hysteresis or the process that causes hysteresis may not be directly responsible for performance degradation.

References

1. Kojima, A., Teshima, K., Shirai, Y., Miyasaka, T.: Organometal halide perovskites as visible-light sensitizers for photovoltaic cells. J. Am. Chem. Soc. **131**, 6050–6051 (2009)
2. Lee, M.M., Teuscher, J., Miyasaka, T., Murakami, T.N., Snaith, H.J.: Efficient hybrid solar cells based on meso-superstructured organometal halide perovskites. Science **338**, 643–647 (2012)
3. Zhou, H., Chen, Q., Li, G., Luo, S., Song, T.-B., Duan, H.-S., Hong, Z., You, J., Liu, Y., Yang, Y.: Interface engineering of highly efficient perovskite solar cells. Science **345**, 542–546 (2014)
4. Jeon, N.J., Noh, J.H., Kim, Y.C., Yang, W.S., Ryu, S., Seok, S.I.: Solvent engineering for high-performance inorganic–organic hybrid perovskite solar cells. Nat. Mater. **13**, 897–903 (2014)
5. Naoki, K., Yasuo, C., Liyuan, H.: Methods of measuring energy conversion efficiency in dye-sensitized solar cells. Jpn. J. Appl. Phys. **44**, 4176 (2005)
6. Editorial, Solar cell woes. Nat. Photon. **8**, 665–665 (2014)
7. Editorial, Bringing solar cell efficiencies into the light. Nat. Nano. **9**, 657–657 (2014)
8. Editorial, Perovskite fever. Nat. Mater. **13**, 837–837 (2014)
9. Kim, H.-S., Jang, I.-H., Ahn, N., Choi, M., Guerrero, A., Bisquert, J., Park, N.-G.: Control of I-V Hysteresis in CH3NH3PbI3 Perovskite Solar Cell. J. Phys. Chem. Lett. **6**, 4633–4639 (2015)
10. Heo, J.H., Han, H.J., Kim, D., Ahn, T.K., Im, S.H.: Hysteresis-less inverted CH3NH3PbI3 planar perovskite hybrid solar cells with 18.1 % power conversion efficiency. Energy Environ. Sci. **8**, 1602–1608 (2015)
11. Wu, C.-G., Chiang, C.-H., Tseng, Z.-L., Nazeeruddin, M.K., Hagfeldt, A., Gratzel, M.: High efficiency stable inverted perovskite solar cells without current hysteresis. Energy Environ. Sci. **8**, 2725–2733 (2015)
12. Yin, X., Que, M., Xing, Y., Que, W.: High efficiency hysteresis-less inverted planar heterojunction perovskite solar cells with a solution-derived NiOx hole contact layer. J. Mater. Chem. A **3**, 24495–24503 (2015)
13. Tripathi, N., Yanagida, M., Shirai, Y., Masuda, T., Han, L., Miyano, K.: Hysteresis-free and highly stable perovskite solar cells produced via a chlorine-mediated interdiffusion method. J. Mater. Chem. A **3**, 12081–12088 (2015)
14. Zhang, H., Liang, C., Zhao, Y., Sun, M., Liu, H., Liang, J., Li, D., Zhang, F., He, Z.: Dynamic interface charge governing the current-voltage hysteresis in perovskite solar cells. Phys. Chem. Chem. Phys. **17**, 9613–9618 (2015)
15. Chen, L.-C., Chen, J.-C., Chen, C.-C., Wu, C.-G.: Fabrication and properties of high-efficiency perovskite/PCBM organic solar cells. Nanoscale Res. Lett. **10**, 1–5 (2015)
16. Snaith, H.J., Abate, A., Ball, J.M., Eperon, G.E., Leijtens, T., Noel, N.K., Stranks, S.D., Wang, J.T.-W., Wojciechowski, K., Zhang, W.: Anomalous hysteresis in perovskite solar cells. J. Phys. Chem. Lett. **5**, 1511–1515 (2014)
17. Kim, H.-S., Park, N.-G.: Parameters affecting I-V hysteresis of CH3NH3PbI3 perovskite solar cells: effects of perovskite crystal size and mesoporous TiO2 layer. J. Phys. Chem. Lett, **5**, 2927–2934 (2014)
18. Chen, S., Lei, L., Yang, S., Liu, Y., Wang, Z.-S.: Characterization of perovskite obtained from two-step deposition on mesoporous titania. ACS Appl. Mater. Interfaces **7**, 25770–25776 (2015)
19. Binglong, L., Vincent Obiozo, E., Tatsuo, M.: High-performance CH 3 NH 3 PbI 3 perovskite solar cells fabricated under ambient conditions with high relative humidity. Jpn. J. Appl. Phys. **54**, 100305 (2015)
20. Tress, W., Marinova, N., Moehl, T., Zakeeruddin, S.M., Nazeeruddin, M.K., Gratzel, M.: Understanding the rate-dependent J-V hysteresis, slow time component, and aging in

CH3NH3PbI3 perovskite solar cells: the role of a compensated electric field. Energy Environ. Sci. **8**, 995–1004 (2015)
21. Unger, E.L., Hoke, E.T., Bailie, C.D., Nguyen, W.H., Bowring, A.R., Heumuller, T., Christoforo, M.G., McGehee, M.D.: Hysteresis and transient behavior in current-voltage measurements of hybrid-perovskite absorber solar cells. Energy Environ. Sci. **7**, 3690–3698 (2014)
22. Chen, B., Yang, M., Zheng, X., Wu, C., Li, W., Yan, Y., Bisquert, J., Garcia-Belmonte, G., Zhu, K., Priya, S.: Impact of capacitive effect and ion migration on the hysteretic behavior of perovskite solar cells. J. Phys. Chem. Lett. **6**, 4693–4700 (2015)
23. Christians, J.A., Manser, J.S., Kamat, P.V.: Best practices in perovskite solar cell efficiency measurements. Avoiding the error of making bad cells look good. J. Phys. Chem. Lett. **6**, 852–857 (2015)
24. Ono, L.K., Raga, S.R., Wang, S., Kato, Y., Qi, Y.: Temperature-dependent hysteresis effects in perovskite-based solar cells. J. Mater. Chem. A **3**, 9074–9080 (2015)
25. Meloni, S., Moehl, T., Tress, W., Franckevicius, M., Saliba, M., Lee, Y.H., Gao, P., Nazeeruddin, M.K., Zakeeruddin, S.M., Rothlisberger, U., Graetzel, M.: Ionic polarization-induced current-voltage hysteresis in $CH_3NH_3PbX_3$ perovskite solar cells. Nat. Commun. **7** (2016)
26. Bryant, D., Wheeler, S., O'Regan, B.C., Watson, T., Barnes, P.R.F., Worsley, D., Durrant, J.: Observable hysteresis at low temperature in "Hysteresis Free" organic-inorganic lead halide perovskite solar cells. J. Phys. Chem. Lett. **6**, 3190–3194 (2015)
27. Chen, H.-W., Sakai, N., Ikegami, M., Miyasaka, T.: Emergence of hysteresis and transient ferroelectric response in organo-lead halide perovskite solar cells. J. Phys. Chem. Lett. **6**, 164–169 (2014)
28. Lyu, M., Yun, J.-H., Ahmed, R., Elkington, D., Wang, Q., Zhang, M., Wang, H., Dastoor, P., Wang, L.: Bias-dependent effects in planar perovskite solar cells based on CH3NH3PbI3–xClx films. J. Colloid Interface Sci. **453**, 9–14 (2015)
29. Wei, J., Zhao, Y., Li, H., Li, G., Pan, J., Xu, D., Zhao, Q., Yu, D.: Hysteresis analysis based on the ferroelectric effect in hybrid perovskite solar cells. J. Phys. Chem. Lett. **5**, 3937–3945 (2014)
30. Frost, J.M., Butler, K.T., Walsh, A.: Molecular ferroelectric contributions to anomalous hysteresis in hybrid perovskite solar cells. APL Mater. **2** (2014)
31. Stoumpos, C.C., Malliakas, C.D., Kanatzidis, M.G.: Semiconducting tin and lead iodide perovskites with organic cations: phase transitions, high mobilities, and near-infrared photoluminescent properties. Inorg. Chem. **52**, 9019–9038 (2013)
32. Yasemin Kutes, L.Y., Zhou, Yuanyuan, Pang, Shuping, Huey, Bryan D., Padture, Nitin P.: Direct observation of ferroelectric domains in solution-processed CH3NH3PbI3 perovskite thin films. J. Phys. Chem. Lett. **5**, 3335–3339 (2014)
33. Kim, H.-S., Kim, S.K., Kim, B.J., Shin, K.-S., Gupta, M.K., Jung, H.S., Kim, S.-W., Park, N.-G.: Ferroelectric polarization in CH3NH3PbI3 perovskite. J. Phys. Chem. Lett. **6**, 1729–1735 (2015)
34. Chen, B., Zheng, X., Yang, M., Zhou, Y., Kundu, S., Shi, J., Zhu, K., Priya, S.: Interface band structure engineering by ferroelectric polarization in perovskite solar cells. Nano Energy **13**, 582–591 (2015)
35. Fan, Z., Xiao, J., Sun, K., Chen, L., Hu, Y., Ouyang, J., Ong, K.P., Zeng, K., Wang, J.: Ferroelectricity of CH3NH3PbI3 perovskite. J. Phys. Chem. Lett. **6**, 1155–1161 (2015)
36. Jena, A.K., Chen, H.-W., Kogo, A., Sanehira, Y., Ikegami, M., Miyasaka, T.: The interface between FTO and the TiO2 compact layer can be one of the origins to hysteresis in planar heterojunction perovskite solar cells. ACS Appl. Mater. Interfaces **7**, 9817–9823 (2015)
37. Wojciechowski, K., Stranks, S.D., Abate, A., Sadoughi, G., Sadhanala, A., Kopidakis, N., Rumbles, G., Li, C.-Z., Friend, R.H., Jen, A.K.Y., Snaith, H.J.: Heterojunction modification for highly efficient organic-inorganic perovskite solar cells. ACS Nano **8**, 12701–12709 (2014)

38. Nagaoka, H., Ma, F., deQuilettes, D.W., Vorpahl, S.M., Glaz, M.S., Colbert, A.E., Ziffer, M. E., Ginger, D.S.: Zr incorporation into TiO2 electrodes reduces hysteresis and improves performance in hybrid perovskite solar cells while increasing carrier lifetimes. J. Phys. Chem. Lett. **6**, 669–675 (2015)
39. Yuan, Z., Wu, Z., Bai, S., Xia, Z., Xu, W., Song, T., Wu, H., Xu, L., Si, J., Jin, Y., Sun, B.: Hot-electron injection in a sandwiched TiOx–Au–TiOx structure for high-performance planar perovskite solar cells. Adv. Energy Mater. (2015). (n/a-n/a)
40. Im, S.H., Heo, J.-H., Han, H.J., Kim, D., Ahn, T.: 18.1 % hysteresis-less inverted CH3NH3PbI3 planar perovskite hybrid solar cells. Energy Environ. Sci. (2015)
41. Tao, C., Neutzner, S., Colella, L., Marras, S., Srimath Kandada, A.R., Gandini, M., De Bastiani, M., Pace, G., Manna, L., Caironi, M., Bertarelli, C., Petrozza, A.: 17.6 % steady state efficiency in low temperature processed planar perovskite solar cells. Energy Environ. Sci. (2015)
42. Bergmann, V.W., Weber, S.A.L., Javier Ramos, F., Nazeeruddin, M.K., Grätzel, M., Li, D., Domanski, A.L., Lieberwirth, I., Ahmad, S., Berger, R.: Real-space observation of unbalanced charge distribution inside a perovskite-sensitized solar cell. Nat. Commun. **5** (2014)
43. Cojocaru, L., Uchida, S., Jayaweera, P.V.V., Kaneko, S., Nakazaki, J., Kubo, T., Segawa, H.: Origin of the hysteresis in I-V curves for planar structure perovskite solar cells rationalized with a surface boundary-induced capacitance model. Chem. Lett. **44**, 1750–1752 (2015)
44. Tubbs, M.R.: The optical properties and chemical decomposition of halides with layer structures. II. defects, chemical decomposition, and photographic phenomena. Physica Status Solidi (b), **67**, 11–49 (1975)
45. Haruyama, J., Sodeyama, K., Han, L., Tateyama, Y.: First-principles study of ion diffusion in perovskite solar cell sensitizers. J. Am. Chem. Soc. **137**, 10048–10051 (2015)
46. Eames, C., Frost, J.M., Barnes, P.R.F., O/'Regan, B.C., Walsh, A., Islam, M.S.: Ionic transport in hybrid lead iodide perovskite solar cells. Nat. Commun. **6** (2015)
47. Alberti, A., Deretzis, I., Pellegrino, G., Bongiorno, C., Smecca, E., Mannino, G., Giannazzo, F., Condorelli, G.G., Sakai, N., Miyasaka, T., Spinella, C., La Magna, A.: Similar structural dynamics for the degradation of CH3NH3PbI3 in air and in vacuum. ChemPhysChem **16**, 3064–3071 (2015)
48. Zhang, Y., Liu, M., Eperon, G.E., Leijtens, T.C., McMeekin, D., Saliba, M., Zhang, W., de Bastiani, M., Petrozza, A., Herz, L.M., Johnston, M.B., Lin, H., Snaith, H.J.: Charge selective contacts, mobile ions and anomalous hysteresis in organic-inorganic perovskite solar cells. Mater. Horiz. **2**, 315–322 (2015)
49. Zhao, Y., Liang, C., Zhang, H., Li, D., Tian, D., Li, G., Jing, X., Zhang, W., Xiao, W., Liu, Q., Zhang, F., He, Z.: Anomalously large interface charge in polarity-switchable photovoltaic devices: an indication of mobile ions in organic-inorganic halide perovskites. Energy Environ. Sci. **8**, 1256–1260 (2015)
50. Li, C., Tscheuschner, S., Paulus, F., Hopkinson, P.E., Kießling, J., Köhler, A., Vaynzof, Y., Huettner, S.: Iodine migration and its effect on hysteresis in perovskite solar cells. Adv. Mater. (2016). (n/a-n/a)
51. Yu, H., Lu, H., Xie, F., Zhou, S., Zhao, N.: Native defect-induced hysteresis behavior in organolead iodide perovskite solar cells. Adv. Funct. Mater. **26**, 1411–1419 (2016)
52. Richardson, G., O'Kane, S.E.J., Niemann, R.G., Peltola, T.A., Foster, J.M., Cameron, P.J., Walker, A.B.: Can slow-moving ions explain hysteresis in the current-voltage curves of perovskite solar cells?. Energy Environ. Sci. (2016)
53. Almora, O., Zarazua, I., Mas-Marza, E., Mora-Sero, I., Bisquert, J., Garcia-Belmonte, G.: Capacitive dark currents, hysteresis, and electrode polarization in lead halide perovskite solar cells. J. Phys. Chem. Lett. **6**, 1645–1652 (2015)
54. Zhou, Y., Huang, F., Cheng, Y.-B., Gray-Weale, A.: Photovoltaic performance and the energy landscape of CH3NH3PbI3. Phys. Chem. Chem. Phys. **17**, 22604–22615 (2015)
55. van Reenen, S., Kemerink, M., Snaith, H.J.: Modeling anomalous hysteresis in perovskite solar cells. J. Phys. Chem. Lett, **6**, 3808–3814 (2015)

56. Shao, Y., Xiao, Z., Bi, C., Yuan, Y., Huang, J.: Origin and elimination of photocurrent hysteresis by fullerene passivation in CH3NH3PbI3 planar heterojunction solar cells. Nat. Commun. **5** (2014)
57. Li, W., Dong, H., Dong, G., Wang, L.: Hystersis mechanism in perovskite photovoltaic devices and its potential application for multi-bit memory devices. Org. Electron. **26**, 208–212 (2015)
58. Shi, D., Adinolfi, V., Comin, R., Yuan, M., Alarousu, E., Buin, A., Chen, Y., Hoogland, S., Rothenberger, A., Katsiev, K., Losovyj, Y., Zhang, X., Dowben, P.A., Mohammed, O.F., Sargent, E.H., Bakr, O.M.: Low trap-state density and long carrier diffusion in organolead trihalide perovskite single crystals. Science **347**, 519–522 (2015)
59. Oga, H., Saeki, A., Ogomi, Y., Hayase, S., Seki, S.: Improved understanding of the electronic and energetic landscapes of perovskite solar cells: high local charge carrier mobility, reduced recombination, and extremely shallow traps. J. Am. Chem. Soc. **136**, 13818–13825 (2014)
60. Xu, J., Buin, A., Ip, A.H., Li, W., Voznyy, O., Comin, R., Yuan, M., Jeon, S., Ning, Z., McDowell, J.J., Kanjanaboos, P., Sun, J.-P., Lan, X., Quan, L.N., Kim, D.H., Hill, I.G., Maksymovych, P., Sargent, E.H.: Perovskite-fullerene hybrid materials suppress hysteresis in planar diodes. Nat. Commun. **6** (2015)
61. Ryu, S., Seo, J., Shin, S.S., Kim, Y.C., Jeon, N.J., Noh, J.H., Seok, S.I.: Fabrication of metal-oxide-free CH3NH3PbI3 perovskite solar cells processed at low temperature. J. Mater. Chem. A **3**, 3271–3275 (2015)
62. Bi, D., Tress, W., Dar, M.I., Gao, P., Luo, J., Renevier, C., Schenk, K., Abate, A., Giordano, F., Correa Baena, J.–P., Decoppet, J.–D., Zakeeruddin, S.M., Nazeeruddin, M.K., Grätzel, M., Hagfeldt, A.: Efficient luminescent solar cells based on tailored mixed-cation perovskites. Sci. Adv. **2**, e1501170 (2016)
63. Saliba, M., Matsui, T., Seo, J.Y., Domanski, K., Correa-Baena, J.–P., Nazeeruddin, M.K., Zakeeruddin, S.M., Tress, W., Abate, A., Hagfeldt, A., Grätzel, M.: Cesium-containing triple cation perovskite solar cells: improved stability, reproducibility and high efficiency. Energy Environ. Sci. (2016). doi:10.1039/c5ee03874j

Perovskite Solar Cells for the Generation of Fuels from Sunlight

Jingshan Luo, Matthew T. Mayer and Michael Grätzel

1 General Introduction

Fossil fuels are finite energy resources, and their burning causes air pollution and emits large amount of CO_2, leading to global warming. This urges the search for green and sustainable energy sources. Solar energy is plentiful enough to fulfill all of mankind's energy demands as a green and renewable source. In fact, the energy illuminated from the sun in 1 h is sufficient to power the Earth for an entire year [1]. However, its diffuse and intermittent nature requires an efficient harvesting strategy coupled to an effective method for storage before large-scale utilization can be envisaged.

1.1 Energy Demand, Global Warming, and the Need for Storage

The evolution of human lifestyle drives the increasing demand of energy. It was estimated that the world total energy consumption is 16 TW in 2015, and this value will increase to 30 TW by 2050. Presently, most of this energy comes from fossil fuels, which have limited reserve. Though the continuous discovery of new reserves of oil and natural gas make it seems that the world always has 50 years of future consumption stored as reserves in the ground [2], the unbalanced distribution of these reserves and uncertain geopolitical relations complicate the energy supply, and create a fluctuating and vulnerable market. Besides these issues, the effects of fossil fuels consumption on the global environment warrant immediate action. For

J. Luo · M.T. Mayer · M. Grätzel (✉)
Ecole polytechnique fédérale de Lausanne, Institut des sciences et ingénierie chimiques, 1015 Lausanne, Switzerland
e-mail: michael.graetzel@epfl.ch

N.-G. Park et al. (eds.), *Organic-Inorganic Halide Perovskite Photovoltaics*,
DOI 10.1007/978-3-319-35114-8_11

example, due to the burning of coal and rapidly expanding number of cars on the road, major cities in China are facing serious air pollution issues. The situation is so bad that sometime the smog darkens the sky. According to the National Climatic Data Center of the USA, the average global temperature has globally increased 0.75° in the past 4 decades due to the greatly enhanced anthropogenic release of CO_2 in the atmosphere, considered by experts to be close to/beyond the threshold for inducing catastrophic changes. According to predictions, the iceberg in the south and north poles will melt, and the cities near the seashore will be immersed by the water if the temperature continued rising at the current speed. All the participants (186 countries) of the Paris climate change conference in 2015 has reached a common target of keeping the rise in temperature below 2 °C through reducing CO_2 emissions.

All of the above issues urge the search for clean and renewable energy sources. Among all the renewable energy resources, solar is the one that could supply all our demand. In order to efficiently harvest this energy, solar cells with high efficiency and low cost are demanded. As an emerging solar cell technology, perovskite solar cells can be processed by facile low-cost solution process, and exhibit efficiencies recently reaching the level of crystalline silicon [3], which may potentially bring the cost of solar electricity to grid parity. However, solar cells alone are not enough to solve the energy problem, as they do not provide a means for storage. During the night or cloudy days, solar photovoltaics alone cannot supply the energy demand. This is one of the major challenges of using photovoltaics, and it is the same for wind energy. The intermittency of the solar light flux can cause great fluctuation of the electric grid. Thus, it is compulsory to design an effective storage strategy to overcome the solar intermittency. Storage solutions such as lithium ion batteries and supercapacitors remain too expensive for grid-scale energy storage, and possible cheaper alternatives such as redox flow batteries are still under research and development. Actually, nature achieves solar energy storage for billions of years through the process of photosynthesis. The green plants absorb sunlight and split water to produce NADPH a chemically bound form of hydrogen which reduces in turn CO_2 to carbohydrates which serve as fuels and foodstocks for sustain life on earth. Mimicking nature to convert solar energy directly into chemicals fuels presents one of the most promising strategies to harvest solar energy and convert it into fuels such as hydrogen methanol or other high value chemicals through solar-driven water splitting and CO_2 reduction.

1.2 Solar Fuel Generation and Utilization

Splitting water to generate hydrogen and oxygen requires an applied voltage of at least 1.23 V to provide the thermodynamic driving force. Because of the practical overpotentials associated with the reaction kinetics, a substantially larger voltage is generally required, and commercial electrolyzers typically operate at a voltage of 1.8–2.0 V [4]. Hydrogen is widely used as both feedstock for the chemical industry

and clean fuel for transportation. For example, hydrogen is a crucial component of ammonia synthesis, which can be further processed into fertilizer or useful chemicals. Furthermore, as more and more automakers join the fuel cell vehicle market, the demand for hydrogen as fuel will continue to rise. Due to present economic reasons, most of the hydrogen is still produced from fossil fuels through methane reforming, which is not sustainable as it contributes to the green house effect. Though hydrogen is very useful, it is difficult to store. Hydrogen is a gas at ambient pressure and temperature, and its compression and storage requires significant energy. Thus, one step further is to directly make liquid fuel through reducing CO_2, which can close the carbon cycle and stop the rise of anthropogenic CO_2 levels in the atmosphere. One of the most favorable products is methanol, which can be easily stored and used in a similar way as gasoline.

Compared to water splitting, CO_2 reduction is significantly more challenging, and it has caught attention only recently due to its impact on climate change. The possible reduction products of CO_2 are many, such as CO, CH_4, C_2H_4, and methanol. The multi-electron pathways to these products make CO_2 reduction a more complicated process than water splitting, generally requiring larger overpotentials. Product selectivity remains an important research challenge, in particular competition with the hydrogen evolution affects systems operating in water. More detail on the intricacies of photo-driven water splitting and CO_2 reduction will be presented in the sections to follow.

1.3 Fundamental Principles of Solar-to-Fuels (STF) Conversion

The efficiency of solar energy conversion processes is defined as the ratio of power out to power in (P_{out}/P_{in}). The P_{in} term refers to the power of incident irradiation, typically referred to standard solar irradiance spectra such as AM1.5G. By convention, the power of AM1.5 solar radiation is set to 1000 W/m^2. For photovoltaics, the P_{out} term corresponds to electric power, usually taken as the product of current and voltage at the maximum power point. In this case, comparable **solar-to-electricity** power conversion efficiencies (PECs) can be obtained from devices having different bandgaps (e.g. Si, GaInP, perovskite) due to the compensating balance between bandgap and spectral response [5].

The situation differs when defining the **solar-to-fuels** (STF) conversion efficiency, since the P_{out} term is fixed by the energy stored in the chemical product, rather than simply the electrical power. The efficiency for standalone systems operating with light as the only power input is therefore defined as follows:

$$\text{STF efficiency} = [j\,(\text{mA/cm}^2) \times E^{\circ} \times \eta_F]/p_{\text{in}}(\text{mW/cm}^2)$$

Here, j is the operating current density of the device, $E°$ is the thermodynamic potential difference for the fuel-forming reactions, η_F is the Faradic yield of evolved products, and P_{in} is the power of incident illumination [6]. This means the 'voltage' term of the STF efficiency equation is fixed, and only devices generating sufficient Voc for driving the complete reaction can achieve nonzero efficiencies.

Determination of STF efficiency therefore requires the measurement of current density using a light source that matches standard AM1.5 solar light, and measurement of the Faradic efficiency of product evolution. For **solar-to-hydrogen** (STH) conversion from water electrolysis, the reaction products are hydrogen and oxygen, generated from water reduction and oxidation, respectively.

For water electrolysis to generate hydrogen and oxygen, $E°$ is 1.23 V (under standard conditions). When including practical considerations necessary for driving electrolysis at meaningful rates (including but not limited to current density, catalyst-dependent overpotentials, mass transport, product separation, and system design), this voltage demand increases significantly. This exceeds the photo-voltage produced by conventional single-junction photovoltaic cells. Therefore, the driving of fuel-forming reactions like water electrolysis requires new light harvester developing a high photo-voltage and/or tandem configurations.

1.4 Advantages of Perovskite as Light Harvesters for Solar Fuel Generation

Commercial Si, thin film CIGS, and CdTe light harvesters generally produce an open-circuit photo-voltage (Voc) close to 0.7 V under illumination in standard AM1.5 G sunlight, while the voltage generated at the maximum power point (Vmp) is about 100 mV smaller. Hence, in order to drive overall water splitting, three to four cells must be connected in series or a DC–DC power converter must be used to achieve reasonable efficiency [7, 8]. Before the emergence of perovskite solar cells (PSCs), nearly all the high efficiencies for water splitting were achieved with complicated multijunction tandem device or expensive III–V-based light harvesters [9, 10]. For CO_2 reduction, due to slower reaction kinetics, even larger overpotentials are needed, which would require four or five conventional cells connected in series [11].

The unique advantages of perovskite light harvesters for solar fuel generation are their intrinsic high Voc and bandgap tunability [12, 13]. For a 1.5 eV bandgap light harvester based on $FAPbI_3$ and $MAPbBr_3$ mixture, a Voc of 1.19 V is achieved [14], which approaches the theoretical limit of 1.32 V for cells of this bandgap [15]. To date, the highest open-circuit voltage achieved for perovskite cell is 1.61 V, with $CH_3NH_3PbBr_3$ as light harvester and ICBA as acceptor [16]. The high Voc of perovskite PV enables its use for efficient water splitting through various configurations, either by using only one single cell, pairing two together or as a bias source for another light harvester. Furthermore, the tunable bandgap of perovskites

enables judicious tuning of their absorption range and the Voc through composition variation. For example, by mixing $CH_3NH_3PbI_3$ and $CH_3NH_3PbBr_3$ in different ratios, light harvesters with bandgaps between 1.5 and 2.3 eV can be obtained [12, 13, 17]. Last, they can be made semitransparent by using transparent conductive oxides, Ag nanowires, or other transparent materials as contact [18, 19]. These properties are crucial for making dual absorber tandems in stacked configurations.

2 Perovskite Photovoltaic (PV)-Driven Water Splitting

For PV-driven electrolysis in the convention sense, PV modules can be connected via a DC–DC converter to an electrolyzer unit. The DC–DC converter is used to modulate the voltage to best match the power requirements of the electrolyzer, so reaching a high output Voc is less important even though a minimum threshold voltage is required for operating the electronic circuit. However, there is around 10 % loss when using DC–DC power conversion. Another challenge of this approach is that the operating current density of commercial electrolyzer is very high, which requires the use of highly concentrated electrolytes and limits the choice of electrocatalysts apart from rendering the electrolyzers expensive. Here, we take an approach similar to conventional photoelectrochemical water splitting, where the light harvesters and electrocatalysts are integrated with a distributed current density, allowing the use of Earth-abundant materials, and we only discuss solar fuel generation in this manner here.

Driving water electrolysis using PV or photoelectrochemical components can be accomplished using a variety of configurations, ranging from single light harvester to dual absorbers. To clarify, we shall consider devices using two or three identical absorbers as single bandgap absorber systems. As the open-circuit Vocs of conventional perovskite solar cells are generally large, the configurations we discuss below comprise only one or two light harvesters. Herein, we detail the use of one perovskite cell, two cells connected in series, and dual absorber tandems implemented as water splitting devices.

2.1 One Cell-Driven Water Splitting

For PEC water splitting, due to the strict requirement of the band energetics and electrochemical stability, so far only large bandgap oxides have demonstrated overall water splitting by one cell under simulated solar illumination [20]. However, the efficiencies are very low due to limited solar light absorption. Even for the PV electrolysis approach, to date no device has been demonstrated capable of efficient water splitting with only one junction. As the open-circuit voltage of a single perovskite solar cell can be larger than 1.23 V, it is conceivable that, for a system using efficient electrocatalysts to minimize the overpotential, one cell could drive overall

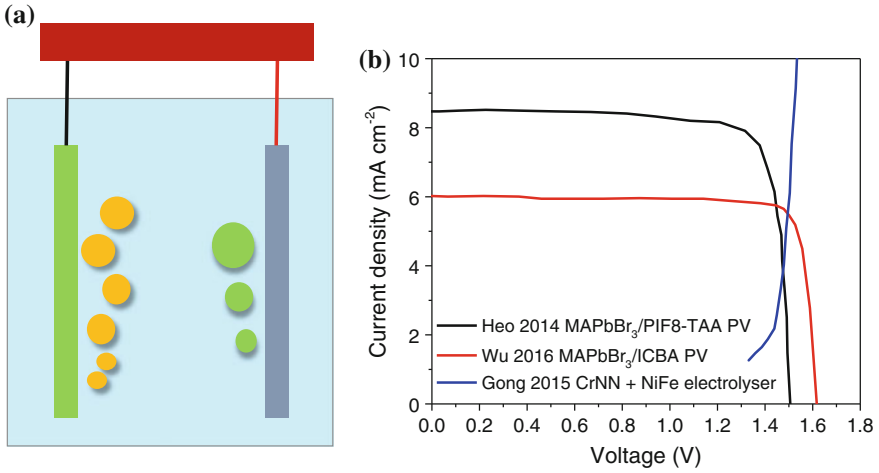

Fig. 1 Hypothetical single-PV photoelectrolysis device. **a** Schematic device featuring one PV cell wired directly to water splitting electrodes. **b** Representative high-voltage photovoltaic performances from recent literature on $MAPbBr_3$ cells (Adapted from Heo et al. [21] and Wu et al. [16]) compared against highly-active Earth-abundant water splitting electrodes (Adapted from Gong et al. [22])

water splitting. For example, Im et al. claimed a $CH_3NH_3PbBr_3$-based perovskite cell with 10.4 % efficiency, 8.4 mA cm^{-2} short circuit current density (Jsc), and 1.51 V open-circuit voltage [21]. More recently, Wu et al. obtained a Voc of 1.61 V, albeit with a Jsc of 6 mA cm^{-2} [16]. Based on efficient Earth-abundant electrocatalysts reported in the literature, which can reach 20 mA cm^{-2} current density at a voltage lower than 1.5 V for overall water splitting [22], it is conceivable to achieve solar to hydrogen conversion efficiency exceeding 10 % with a single perovskite cell (Fig. 1). Nevertheless, the solar to hydrogen conversion efficiency (STHCE) for such single-absorber-driven electrolysis devices remains below 10 % falling short of the targeted goals of the community.

2.2 *Water Splitting Driven by Two in Series Connected Perovskite Cells*

Though one single perovskite solar cell is capable of driving water splitting, the extremely low overpotential requirement limits the choices for suitable Earth-abundant electrocatalysts. In addition, generally the Voc of a solar cell decreases as the illumination intensity decreases. Due to the fluctuation in real sunlight condition, it would be very difficult to match the optimal operating point of the electrocatalyst with a single photovoltaic cell. Thus, using two cells connected in series offers a more favorable configuration.

Besides the light harvester, the choice of appropriate electrocatalysts is also very important. Fortunately, highly efficient Earth-abundant electrocatalysts have been developed for conventional PEC water splitting [23, 24]. Generally, the overpotential is determined for a current density of 10 mA cm^{-2} corresponding to a realistic Jsc value for tandem cells in full sunlight. For example, MoS_2 has been developed as an efficient electrocatalyst for the hydrogen evolution reaction (HER) in acid electrolyte. More recently, new HER electrocatalysts have emerged, such as Ni_2P, CoP, and mixed phosphide and sulphide compounds [25, 26]. For the oxygen evolution reaction (OER) various metal oxides, hydroxide, and mixed compositions have been conceived, with NiFe layered double hydroxide (LDH) standing out with his high activity [27]. Continued advancements of the field of Earth-abundant electrocatalysts will enhance the opportunities for designing fully abundant systems for efficient STF conversion.

By connecting two $CH_3NH_3PbI_3$-based perovskite solar cells in series and coupling them to NiFe LDH electrodes, we demonstrated 12.3 % STH conversion efficiency, as shown in Fig. 2 [28]. This is the first time that efficiency over 10 %

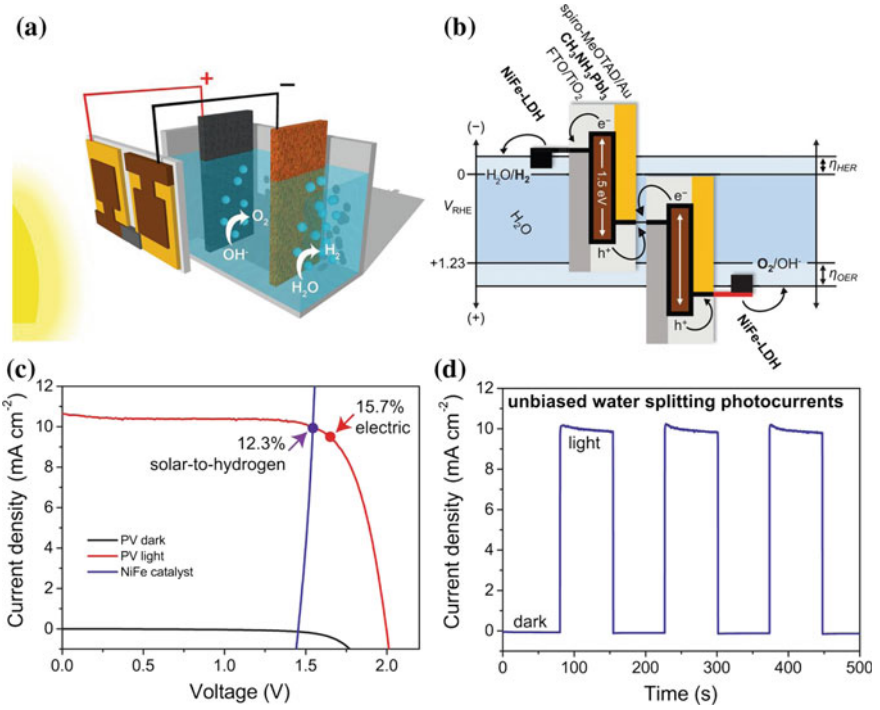

Fig. 2 12.3 % solar-to-hydrogen conversion driven by perovskite photovoltaics. **a** Cell diagram and **b** energy level schematic of two-series connected PV cells wired to bifunctional NiFe-LDH water splitting electrodes. **c** Current density versus voltage behavior for the 2-cell PV and 2-electrode catalyst components of the device. **d** Current density measured on short-circuited device performing unassisted water splitting driven by simulated standard AM1.5 sunlight (Adapted from Ref. [28])

has been achieved with low-cost light harvesters and Earth-abundant electrocatalysts. We discovered in this study that NiFe LDH can also catalyze hydrogen evolution, rendering it a bifunctional electrocatalyst for water splitting. The use of a bifunctional catalyst in an overall water splitting system simplifies the design, providing the possibility of lowering the cost for hydrogen generation.

2.3 *Two Absorber Tandems Under Serial Illumination for Standalone Water Splitting*

While two cells placed side by side achieve STH efficiencies exceeding 12 %, further efficiency gained in this configuration are limited by the fact that the illuminated area is doubled in this configuration and thus the current density halved. For a 1.5 eV bandgap material, the AM1.5G spectrum limits the theoretical efficiency to 17.8 % [28]. Increasing the perovskite bandgap to give larger Vocs would lead to narrower spectral response and therefore smaller photocurrents. Cells with a narrower bandgap can achieve higher currents but the output voltages would eventually fall below the threshold for driving efficient electrolysis. Therefore, alternative strategies are required to push up the efficiency limit.

Two-absorber tandem approaches represent a clear path toward further enhancing the efficiencies achievable by photovoltaic-driven electrolysis systems. This approach benefits from the additive Voc resulting from connecting two cells in electronic series as described above. To enable higher photocurrent densities, two light harvesters of different bandgap are chosen such that their absorption is complementary, thereby allowing the harvesting of a broader range of the solar spectrum. Some possible configurations are drawn in the energy-level schematic in Fig. 3. In each case, the first (top) absorber is of wider bandgap, thereby absorbing

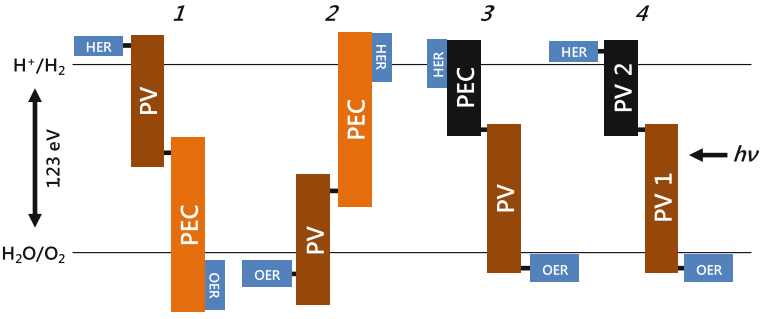

Fig. 3 Energy-level schemes for two-absorber tandem configurations affording water photo electrolysis. The *rectangles* represent the relative bandgaps of light harvesters, with the *top* and *bottom* edges representing conduction and valence bands, respectively. *Brown* perovskite photovoltaic; orange: metal oxide photoelectrode; *black* Si or CIGS light harvester. Water splitting catalysts are labeled as HER or OER for the hydrogen- and oxygen-evolution reactions, respectively. The catalysts are either wired to a PV terminal or directly integrated onto the surface of the PEC electrodes

photons in the high-energy range while allowing lower energy photons to pass through to illuminate the second smaller bandgap absorber.

The two-absorber tandem concept has been widely demonstrated in sunlight-driven water splitting research, mostly on devices employing either one or two photoelectrochemical components. Photoelectrochemical cells (PEC) based on the direct contact between a semiconductor photoelectrode and an aqueous electrolyte has been studied in detail over recent decades [29]. In these devices, often based on metal oxide semiconductors of relatively large bandgap (>2 eV), photogenerated charges are separated by electric fields within the space charge layer that is formed spontaneously upon contacting the semiconductor with the electrolyte. The resulting local fields drive minority carriers to the electrode surface where they enact the corresponding water splitting half reaction. Several useful reviews provide more details on this topic [30–35]. One target of the PEC approach is to pair a photoanode with a photocathode exhibiting complementary spectral response. Despite great effort toward developing such tandems, the best efficiencies have reached only around 1 % [20, 36, 37].

To explore the potential of integrating PEC electrodes into complete tandem devices of enhanced efficiency, the strategy of hybrid tandems employing both PEC and PV components has gained recent interest, benefitting from the Vocs provided by PV cells. In this regard, perovskite cells represent an attractive option, and have been implemented in PEC-PV tandems as both bottom and top absorber, and in conjunction with both photoanodes and photocathodes. Table 1 summarizes the recent reports where perovskite cells are incorporated as either bottom absorber (configuration 1 and 2) or top absorber (configuration 3).

Hematite (Fe_2O_3) represents one of the most widely studied photoelectrode materials since it shows desirable properties such as a suitable bandgap, stability, and natural abundance [38, 39]. Recent progress in advancing the performance of

Table 1 Experimental demonstrations of complete water splitting employing perovskite absorber components

#	Top absorber	Bottom absorber	Ref.
1	**PEC photoanode**	**perovskite PV**	
	Mn:Fe_2O_3 nanowires, Co-Pi catalyst	$MAPbI_3$	[44]
	Si:Fe_2O_3 nano-cauliflower, $FeNiO_x$ catalyst	$MAPbI_3$	[40]
	$BiVO_4$-CoPi	$MAPbI_3$	[45]
	Mo:$BiVO_4$-CoCi	$MAPbI_3$	[47]
2	**PEC photocathode**	**perovskite PV**	
	Cu_2O-AZO-TiO_2-RuO_2	$(FAPbI_3)_{1-x}(MAPbBr_3)_x$	[50]
3	**perovskite PV**	**PEC photoelectrode**	
	$MAPbI_3$ or $MAPbBr_3$	$CuIn_xGa_{1-x}Se_2$ photocathode	[62]
4	**perovskite PV**	**Small bandgap PV**	No reports

MA = methylammonium, CH_3NH_3. FA = formamidinium. AZO = Al-doped ZnO

Fe_2O_3 photoanodes has enabled the demonstration of complete water splitting tandem devices [36]. Morales-Guio et al. examined the key role of top-absorber transparency in a study combining Fe_2O_3 with a perovskite photovoltaic [40]. For the oxygen evolution reaction to occur at low overpotential, an efficient catalysts are necessary. Recent developments have revealed great promise for mixed transition metal oxides based on Ni and Fe, compounds which represent cheap and abundant alternatives to oxides based on oxides of noble metals Ru and Ir [27, 28, 41]. A major challenge for the implementation of these catalysts in photoelectrochemical systems is their substantial optical absorption in the visible [42], a problem which is compounded when high surface area photoelectrodes are employed [43]. The parasitic light attenuation induced by using layers of the mixed oxide catalysts reduces the photocurrent of both the Fe_2O_3 and the perovskite bottom absorber. Hence, the authors sought to develop a synthetic method for depositing thin, transparent films of the catalyst. Using photoelectrochemical deposition from aqueous solutions containing dissolved Fe and Ni salts, a well-controlled formation of thin $FeNiO_x$ films was achieved. As shown in Fig. 4a, the $FeNiO_x$-functionalized Fe_2O_3 photoanode exhibited water photo-oxidation performance comparable to

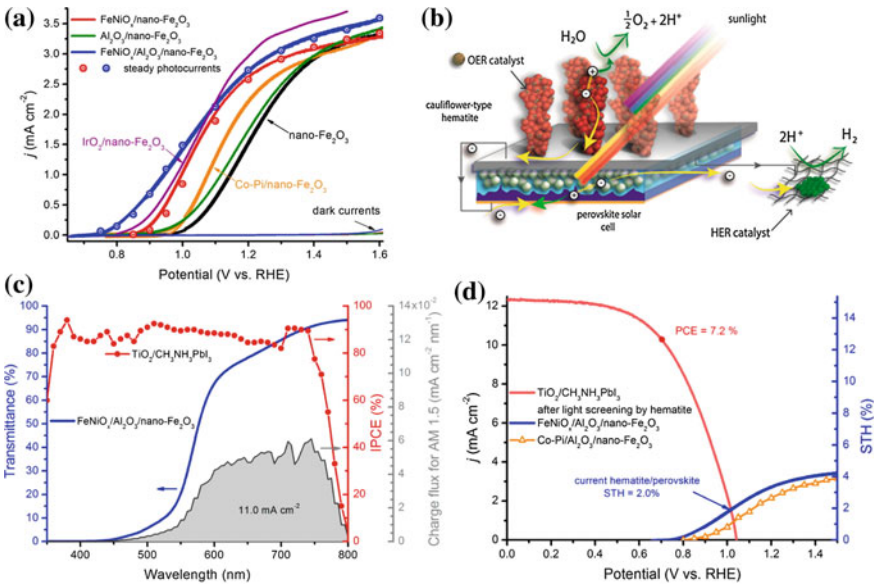

Fig. 4 **a** Photocurrent–potential response of nanostructured Fe_2O_3 photoanodes treated with various oxygen evolution catalysts. **b** Schematic diagram of stacked tandem combining the Fe_2O_3 photoanode with a perovskite solar cell and Ni-Mo cathode. **c** Spectral dependence of the photoanode transmittance (*blue*) and perovskite quantum efficiency (*red*) with the integration of their product over the AM1.5 spectrum representing the predicted photocurrent from the photovoltaic (*gray*). **d** Current–voltage responses of photoanode and photovoltaic components, with the crossing point predicting the operating current density of the tandem (Figure adapted from Ref. [40])

benchmark results employing rare IrO_2 catalyst [43]. This enabled the construction of a PEC-PV tandem associating the photoanode with a $CH_3NH_3PbI_3$-based PV cell and a Ni-Mo cathode (Fig. 4b). The device used only Earth-abundant materials and is capable of standalone water splitting. As shown in Fig. 4c, the good transmittance of the photoanode to wavelengths greater than 550 nm enabled unabated illumination of the perovskite cell. Analysis of the photocurrent-voltage response of each component (Fig. 4d) projected an operating current of about 1.6 mA cm^{-2} corresponding to a STHCE of 1.95 which was confirmed upon assembling the full device. The late photocurrent onset and low photocurrent density of the photoanode represented the primary factors limiting the efficiency. Further research will therefore focus on lowering the onset voltage and increasing the Jsc of the Fe_2O_3 photoanode.

Progress in this direction was made by Gurydayal et al. employed Mn-doped Fe_2O_3 nanowire arrays which, when treated with cobalt-phosphate surface catalyst, could achieve photocurrent densities exceeding 4 mA cm^{-2}, among the best reported to date for this material [44]. For the PV component, a mesoporous $CH_3NH_3PbI_3$-based cell fabricated by a two-step procedure was used. When combining the photoanode and photovoltaic with a platinum cathode for hydrogen evolution, standalone one-sun water splitting photocurrents of nearly 2 mA cm^{-2} were achieved, corresponding to a STH efficiency of nearly 2.4 %.

Besides Fe_2O_3, bismuth vanadate ($BiVO_4$) represents an emerging photoanode material which has shown high quantum efficiencies and large Vocs [30]. Several recent reports achieved standalone water splitting by pairing $BiVO_4$ with a perovskite photovoltaic. Chen et al. demonstrated an all solution-processed tandem combining $BiVO_4$ with a $CH_3NH_3PbI_3$-based cell [45], and Zhang et al. used a TiO_2@$BiVO_4$ photoanode in a similar configuration [46], both achieving standalone photocurrent and measuring the evolution of hydrogen. Kim et al. achieved higher STH efficiencies using a perovskite cell paired with a $BiVO_4$ photoanode doped with Mo and treated with a novel Co-Ci catalyst (Fig. 5) [47]. They reported efficiencies reaching 4.3 % and up to 3.0 % in a wireless "artificial leaf" configuration.

In each of the above cases the hole-collecting contact of the perovskite PV cell was wired to the photoanode conductive substrate, and electrons photogenerated in the photoanode are transported by ohmic contact to the PV to boost their energy by a second photoexcitation (Fig. 3, configuration 1). This two-photon, one-electron process produces electron-hole pairs with sufficient potential difference to drive complete water splitting.

Tandems employing PEC photocathodes and perovskite photovoltaics are also possible (Fig. 3, configuration 2). Whereas n-type light harvesters are used for photoanodes, p-type semiconductors are used for driving the cathodic reaction as photocathodes. Devices based on cuprous oxide (Cu_2O) represent the best-performing metal oxide photocathodes [48, 49], but are typically deposited on opaque Au substrates, inhibiting their implementation as a top absorber in tandem devices. Recently, Dias et al. developed a strategy to make semitransparent Cu_2O photocathodes, finding that lightly treating the conductive glass surface with tiny particles of Au could enable high performance and transparency [50]. As shown in

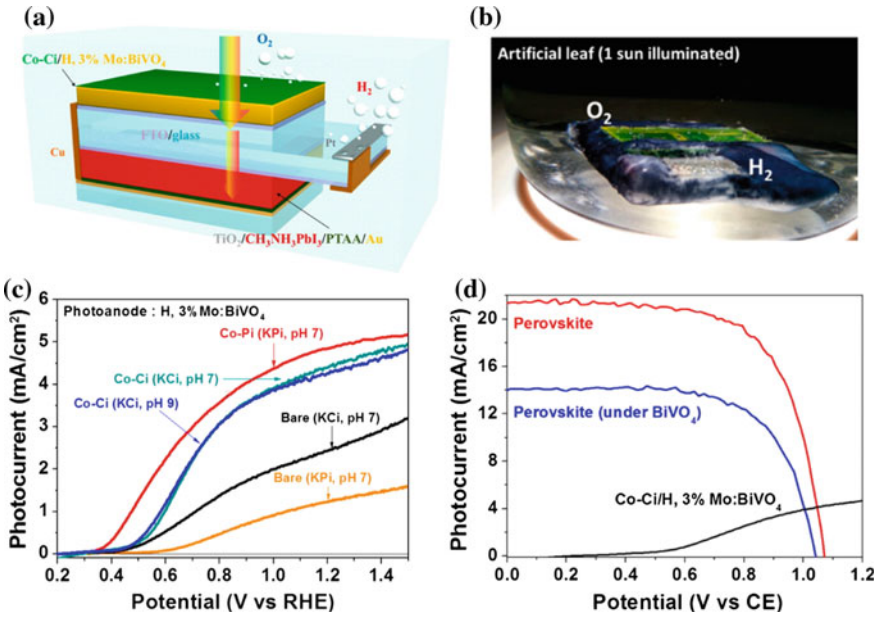

Fig. 5 **a** Schematic illustration and **b** photograph of a wireless water splitting tandem device based on a Mo:$BiVO_4$ photoanode and a perovskite photovoltaic. **c** Photocurrent–potential responses of $BiVO_4$ photoanodes with various catalysts. **d** Current–voltage responses of photovoltaic and photoanode components (Figures adapted from Ref. [47])

Fig. 6, this enabled the construction of a stacked tandem employing the transparent photocathode above a mixed perovskite cell based on $(FAPbI_3)_{1-x}(MAPbBr_3)_x$ (MA: methylammonium; FA: formamidinium), a device with balanced light absorption, and the ability to drive unbiased water splitting at current densities around 2.0 mA cm^{-2}, corresponding to STH efficiencies around 2.5 % with the cautious measurements of both H_2 and O_2 gases.

2.4 Ideal Two Absorber System

Given the requirement of 1.5–1.8 V to drive water splitting with efficient catalysts, theoretical calculation shows that the ideal dual-absorber system can be realized by pairing 1.6–1.8 eV and 1.1 eV bandgap absorbers in a stacked top and bottom configuration [51]. Importantly, the success of this approach requires balanced Voc generation from each component commensurate with their Shockley-Quiesser limits, on the order of 1.0 and 0.6 V for the ideal top and bottom absorbers, respectively. Only then can a tandem device achieve water splitting at high STH efficiencies. In the previous section, perovskite PV cells were used as bottom absorbers, having smaller bandgaps than the wider bandgap metal oxide

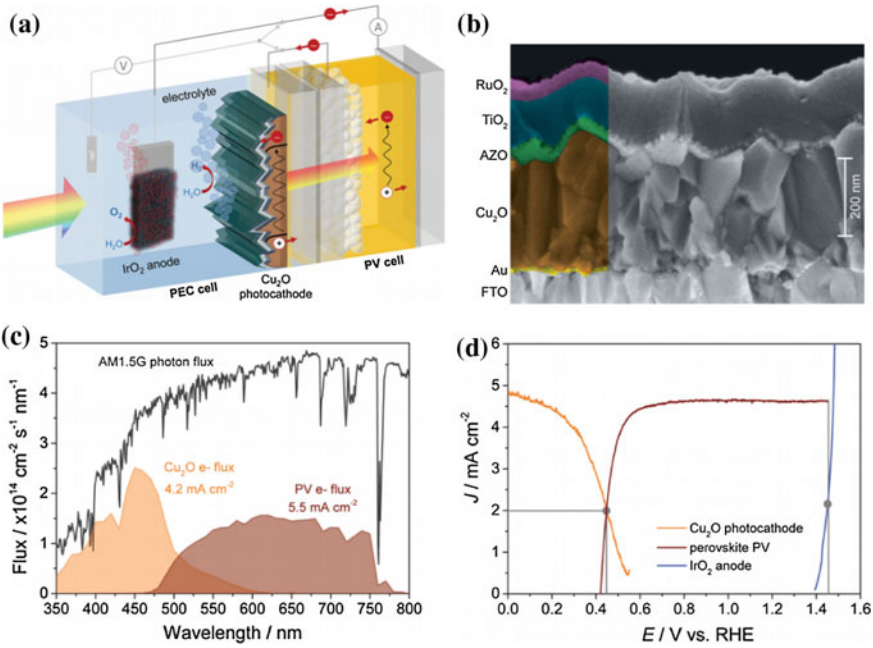

Fig. 6 Cu_2O-perovskite tandem. **a** Schematic of the stacked tandem employing a transparent Cu_2O photocathode, mixed perovskite photovoltaic, and IrO_2 anode. **b** Scanning electron microscopy cross-section image detailing the layers of the photocathode component. **c** Integration of the absorber IPCE responses over the AM1.5G spectrum to determine the expected photocurrent. The Cu_2O photocathode was measured at a potential of +0.3 V versus RHE and the PV was measured at 0 V. **d** J-E plots of photocathode and anode components with the PV curve overlaid, predicting the operating current density of 2 mA cm^{-2} (Adapted from Ref. [50])

photoelectrodes with which they were paired. However, the standard 1.5 eV bandgap for $CH_3NH_3PbI_3$, and the demonstrated tunability of perovskite bandgaps in the range 1.5–2.3 eV [13], suggest that perovskite cells should be more suitable as top absorbers paired above smaller bandgap absorbers. This is presented as configurations 3 and 4 in Fig. 3.

We tried to target this ideal tandem using $CH_3NH_3PbI_3$, $CH_3NH_3PbBr_3$, and their mixtures as top light harvester. In order to use perovskites as top cells the first challenge is to achieve devices with high transparency. Typical PSCs employ Au as the contact for collecting holes, using thick and opaque layers. In addition, before the Au layer, generally a layer of hole transport material (HTM) is needed to achieve high efficiency. The transparency of the hole transport material will affect that of the top cell. Developing semitransparent perovskite solar cells is not only important for solar fuel generation, but also critical for making tandem solar cell with conventional Si or CIGS cells on the bottom to boost their PCE. Actually, the requirements of the two systems are very similar. There are efforts using transparent conductive metal oxides and Ag nanowires to make semitransparent perovskite

solar cells [18, 19]. To this end, we used carbon nanotube (CNT) networks as the contact, which have high conductivity, good transparency, and high chemical stability. To further enhance the transparency, the devices were fabricated without a HTM layer, and to improve the fill factor of the device, gold finger electrodes were deposited on the surface.

For the bottom light harvester, the bandgaps of the conventional Si and CIGS ($CuIn_xGa_{1-x}Se_2$) semiconductors make them nearly ideal for use in tandem devices. As they are commercially available, it is rational to use them as the bottom absorber. Based on the fact that there were still be no efficient two terminal monolithic tandem devices at that time, we choose to immerse CIGS in the electrolyte as the photocathode. It is worth noting that protection layer and catalyst decoration are needed to stabilize CIGS. For Si photocathodes with ALD TiO_2 layer, the device can be stable in 1 M $HClO_4$ for more than two weeks with only less than 5 % degradation [52].

By employing either $CH_3NH_3PbI_3$ (Fig. 7b) or $CH_3NH_3PbBr_3$ (Fig. 7c) perovskite cells as top absorber, a CIGS photocathode as the bottom absorber, and a

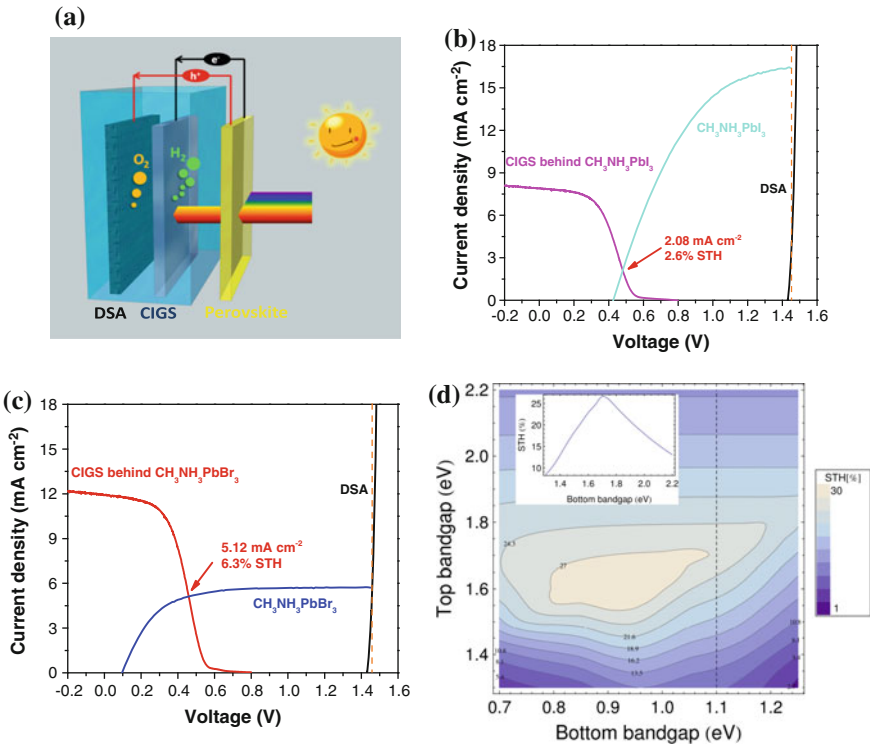

Fig. 7 Perovskite-CIGS tandem. **a** Device schematic. **b** and **c** Current–voltage responses for photocathode, anode, and PV components employing $CH_3NH_3PbI_3$ and $CH_3NH_3PbBr_3$ perovskite cells, respectively. **d** Analysis of predicted STH efficiencies achievable by varying the bandgap of the top and bottom absorbers (Adapted from Ref. [62])

commercially available DSA (dimensionally-stable anode) as an anode for water oxidation, photocurrent densities of 2.1 and 5.1 mA cm^{-2} were achieved, corresponding to STH conversion efficiencies of 2.6 % and 6.3 %, respectively. Attempts of using mixed absorber $CH_3NH_3PbI_xBr_{3-x}$ with 1.7 eV ideal bandgap and high efficiency were unsuccessful. This might be due to the phase separation of the uniformly mixed halide perovskite under strong light illumination, which could induce reversible photoinduced trap formation and reduce the achievable Voc. Thus, although the absorption range of the perovskite light harvesters can be tuned, continued research is required toward delivering fully tunable Voc.

The current device performance is limited by the non-ideality of the perovskite component, with the $CH_3NH_3PbBr_3$ cell producing too little photocurrent due to its narrow absorption range, and the $CH_3NH_3PbI_3$ cell exhibiting too little transmittance and Voc. In order to gain insight into how efficient the present device configuration could perform in the ideal case, we performed a detailed analysis of the two absorber tandem system. The analysis is based on the Shockley–Queisser limit for each absorber, a 0.5 V overpotential for water splitting, perfect transmittance of sub-bandgap photons, and current matching of both absorbers (Fig. 7d). Specifically, for a tandem cell with CIGS (bandgap 1.1 eV) as the bottom absorber, through varying the bandgap of the top absorbers, the idealized STH efficiency could approach 27 %.

3 CO_2 Reduction

Though H_2 is clean and can be used in fuel cells to provide electricity, it is challenging to store and transport hydrogen, as it is in the gas phase under ambient pressure and temperature. For example, in fuel cell vehicles, hydrogen is compressed in a tank with a pressure of around 700 bar, a process which consumes significant energy. Furthermore, the high pressure of the tank needs special protection to ensure safety. Thus, converting solar energy into liquid fuel or other useful commodities is an attractive prospect. CO_2 can serve as the carbon source in this process to make hydrocarbons. In addition, the reduction of CO_2 holds the promise of closing the anthropogenic carbon cycle, avoiding further temperature rise due to the increase of CO_2 levels in the atmosphere.

CO_2 can be reduced either in the gas phase through hydrogenation, or in solution by electrochemical or photoelectrochemical processes [53, 54]. In the current chapter, we focus on the electrochemical reduction of CO_2 through the coupling of perovskite photovoltaics with electrocatalysts. Compared to water splitting, CO_2 reduction has many possible products, including CO, CH_4, C_2H_2, and C_2H_4, and their reaction equations are listed in Table 2.

Table 2 Formal electrochemical potentials for several CO_2 reduction pathways (Adapted from Ref. [53])

Reaction	E^0 versus SHE (V)
$CO_2 + e^- \rightarrow CO_2^{\bullet -}$	–1.85
$CO_{2(g)} + H_2O_{(I)} + 2e^- \rightarrow HCOO^-_{(aq)} + OH^-_{(aq)}$	–0.665
$CO_{2(g)} + H_2O_{(I)} + 2e^- \rightarrow CO_{(g)} + 2OH^-_{(aq)}$	–0.521
$CO_{2(g)} + 3H_2O_{(I)} + 4e^- \rightarrow HCO_{(I)} + 4OH^-_{aq}$	–0.485
$CO_{2(g)} + 5H_2O_{(I)} + 6e^- \rightarrow CH_3OH_{(I)} + 6OH^-_{aq}$	–0.399
$CO_{2(g)} + 6H_2O_{(I)} + 8e^- \rightarrow CH_{4(g)} + {}_8OH^-_{aq}$	–0.246
$2H_2O(I) + 2e^- \rightarrow H_2(g) + 2OH^-(aq)$	–0.414

3.1 Perovskite PV-Driven CO Generation from CO_2

Due to the large Voc of perovskite solar cells, tandem perovskite PVs can drive a complete CO_2 reduction cell. Here, we demonstrate an example of light-driven electrochemical reduction of CO_2 into CO [55]. CO is one of the primary products of CO_2 reduction, and it is the product that stores the largest amount of energy per molecule. CO is a useful product which can be used as a chemical feedstock in the Fischer–Tropsch process to synthesize liquid hydrocarbons.

Au is one of the best catalysts to make CO from electrochemical CO_2 reduction with high Faradic efficiency at low overpotential [56]. Recently, Kanan et al. has shown that oxide derived catalyst displays enhanced performance compared to pristine Au electrodes [57]. We prepared porous Au electrodes by electrochemical anodization according to that previous report. A complete cell for sustainable CO_2 reduction requires a water oxidation half-reaction to supply the electrons. For the oxygen evolution anode we used iridium oxide (IrO_2), chosen for its high activity in neutral water and its stability against dissolution which would risk poisoning the Au cathode. The schematic of the whole system and a generalized energy diagram is depicted in Fig. 8.

Even with Au as catalyst, its Faradic efficiency toward CO_2 reduction still depends on the potential of the electrode (Fig. 8c). In order to maximize the Faradic efficiency of the complete cell, we adjusted the area of the Au electrode to achieve the desired operating potential when driven by the triple-PV cell (Fig. 8e). We achieved 6.5 % solar-to-CO conversion efficiency (Fig. 8f), which is the present record for sunlight-driven CO_2 reduction.

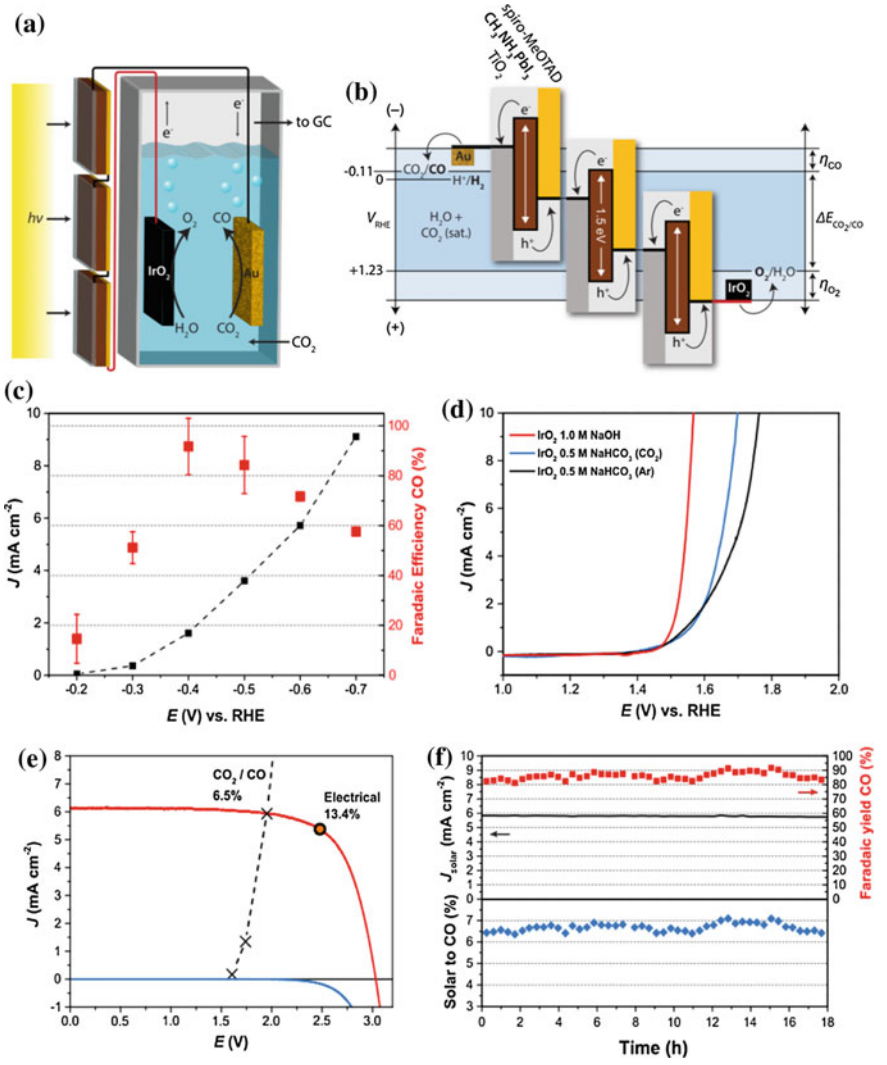

Fig. 8 CO_2 reduction cell driven by perovskite photovoltaics. **a** Schematic and **b** energy level diagrams for three PV cells driving Au and IrO_2 electrodes for CO_2 reduction and water oxidation, respectively. **c** Current density and Faradic efficiency for Au-based CO_2 reduction electrocatalyst at different potentials. **d** Current density versus potential plots for IrO_2 anode in different solutions. **e** J-V curve of triple-perovskite cell with the combined 2-electrode curve for the Au-IrO_2 cell. **f** Current density, Faradic CO yield, and solar-to-CO efficiency during extended operation (Adapted from Ref. [55])

4 Discussion and Perspective

4.1 System Design and Engineering

Conventional photoelectrochemical solar fuel devices rely on the semiconductor and electrolyte interface to separate the charge carriers. As the field evolves, especially given the demand for high efficiency, more and more research groups tend to put photovoltaics into the electrolyte and use them as a buried junction photoelectrode. These devices operate at the same current density as the conventional device with the coating of the catalyst on the surface of the electrode. However, fundamentally, these devices are essentially the same as photovoltaic-driven electrolysis with the PV wired to the catalyst electrodes in the solution, as the source of the Voc is from the solid p-n junction rather than semiconductor and electrolyte interface. There is a long discussion of whether it is rational or better to put PVs in the electrolyte or outside wired to catalyst electrodes in the electrolyte to drive the favorable reactions. We think there is no real advantage of the buried system in the electrolyte to the wired system except that the former looks more elegant. However, this elegance makes the device suffer from the corrosion of the light harvesters in the electrolyte and the blockage of the light absorption by putting protection layer and catalyst on the surface.

In order to meet the terawatt-scale energy demand, the system should meet the criteria for up scaling, and this includes the fabrication process of the device and the abundance of the materials used. From these points of view, perovskite coupled Earth-abundant catalysts system show no barrier in large-scale production. Though wires are necessary to couple the PV to the catalyst electrode, they can be buried into the system to form a monolithic integrated device through smart design. The devices demonstrated in this chapter are all lab scale with size at the centimeter scale. Larger devices more than 10 cm $\times$ 10 cm scales are demanded in the future for demonstration of the operation under real sunlight condition and the evaluation of the efficiency and long-term stability. If they fulfill the economic analysis target, they can be connected together to form large-scale panels in the future.

4.2 Stability Issue and Solution

For the moment, the stability of the solar fuel devices described here are limited by the stability of the perovskite solar cells, which is also the major hurdle for the commercialization of perovskite solar cells. Though it is challenging, progress has been made toward addressing the stability issue. For example, HTM-free carbon cells have shown excellent long-term stability under long-term light soaking [58, 59] and heat stress at 85 °C [58]. Besides using structure engineering, the stability can also be improved by adding certain additives. There are reports showing that the stability of perovskite solar cell is improved after modification with functional

molecules [60]. For the selection of the functional molecules, they should improve the robustness, such as thermal stability, oxygen resistance, and water resistance of the perovskite absorbers. Furthermore, in order not to harm the efficiency, the functional molecules should not induce charge recombination or hinder charge transport. More recently, by using inorganic Cs-based perovskite as additive, the stability of perovskite solar cell was significantly improved [61].

4.3 Perspective

The concept presented here shows that high performances can be realized by simply coupling the perovskite photovoltaics and electrocatalysts together, which shows the promising future toward solar fuel generation. However, we must admit that despite remarkable efficiencies were achieved, there is still a long way to go toward real application.

It is worth noting that none of the above devices used membranes to separate the products. In order to avoid the mixture of the products, which not only add additional cost but also might cause cross reduction or oxidation of the products, or potentially explosive gas mixtures, a membrane is necessary to separate the products. This is especially important for CO_2 reduction, since some of the valued products like methanol or ethanol can be readily oxidized on the anode.

In addition, the devices demonstrated here are all tested under simulated standard AM 1.5G solar illumination condition. In real condition, due to the fluctuation of solar illumination, the efficiency may be significantly lower. As the joining point of the current density versus potential curves of perovskite PV and the catalyst electrodes may not always match the optimized condition, this must be taken into account when designing a real system. Specifically for CO_2 reduction, the solar fluctuation may change the potential at the catalyst electrode, which may change the selectivity of the products.

Finally, an integrated device with a window layer of perovskite tandem photovoltaic cells and an electrochemical cell with catalyst electrodes and membrane in it with smart gas flow design are envisaged to provide electricity supply in the day time and store the excess energy as chemical fuels to keep a continuous energy supply when the sun sets.

References

1. Lewis, N.S., Nocera, D.G.: Proc. Natl. Acad. Sci. U. S. A. **103**, 15729–15735 (2006)
2. Covert, T., Greenstone, M., Knittel, C.R.: J. Econ. Perspect. **30**, 117–138 (2016)
3. NREL. http://www.nrel.gov/ncpv/
4. Zhang, J.Z., Li, J., Li, Y., Zhao, Y.: Hydrogen Generation, Storage and Utilization. Wiley (2014)

5. Green, M.A., Emery, K., Hishikawa, Y., Warta, W., Dunlop, E.D.: Prog. Photovoltaics Res. Appl. **24**, 3–11 (2016)
6. Chen, Z., Jaramillo, T.F., Deutsch, T.G., Kleiman-Shwarsctein, A., Forman, A.J., Gaillard, N., Garland, R., Takanabe, K., Heske, C., Sunkara, M., McFarland, E.W., Domen, K., Miller, E. L., Turner, J.A., Dinh, H.N.: J. Mater. Res. **25**, 3–16 (2011)
7. Gibson, T.L., Kelly, N.A.: Int. J. Hydrogen Energy **35**, 900–911 (2010)
8. Nocera, D.G.: Acc. Chem. Res. **45**, 767–776 (2012)
9. Licht, S., Wang, B., Mukerji, S., Soga, T., Umeno, M., Tributsch, H.: J. Phys. Chem. B **104**, 8920–8924 (2000)
10. Khaselev, O., Bansal, A., Turner, J.A.: Int. J. Hydrogen Energy **26**, 127–132 (2001)
11. Jeon, H.S., Koh, J.H., Park, S.J., Jee, M.S., Ko, D.-H., Hwang, Y.J., Min, B.K.: J. Mater. Chem. A **3**, 5835–5842 (2014)
12. Noh, J.H., Im, S.H., Heo, J.H., Mandal, T.N., Il Seok, S.: Nano Lett. **13**, 1764–1769 (2013)
13. McMeekin, D.P., Sadoughi, G., Rehman, W., Eperon, G.E., Saliba, M., Horantner, M.T., Haghighirad, A., Sakai, N., Korte, L., Rech, B., Johnston, M.B., Herz, L.M., Snaith, H.J.: Science (80-.) **351**, 151–155 (2016)
14. Correa Baena, J.P., Steier, L., Tress, W., Saliba, M., Neutzner, S., Matsui, T., Giordano, F., Jacobsson, T.J., Srimath Kandada, A.R., Zakeeruddin, S.M., Petrozza, A., Abate, A., Nazeeruddin, M.K., Grätzel, M., Hagfeldt, A.: Energy Environ. Sci. **8**, 2928–2934 (2015)
15. Tress, W., Marinova, N., Inganäs, O., Nazeeruddin, M.K., Zakeeruddin, S.M., Graetzel, M.: Adv. Energy Mater. **5**, n/a–n/a (2015)
16. Wu, C.-G., Chiang, C.-H., Chang, S.H.: Nanoscale **8**, 4077–4085 (2016)
17. Eperon, G.E., Stranks, S.D., Menelaou, C., Johnston, M.B., Herz, L.M., Snaith, H.J.: Energy Environ. Sci. **7**, 982 (2014)
18. Bailie, C.D., Christoforo, M.G., Mailoa, J.P., Bowring, A.R., Unger, E.L., Nguyen, W.H., Burschka, J., Pellet, N., Lee, J.Z., Grätzel, M., Noufi, R., Buonassisi, T., Salleo, A., McGehee, M.D.: Energy Environ. Sci. **8**, 956–963 (2015)
19. Werner, J., Dubuis, G., Walter, A., Löper, P., Moon, S.-J., Nicolay, S., Morales-Masis, M., De Wolf, S., Niesen, B., Ballif, C.: Sol. Energy Mater. Sol. Cells **141**, 407–413 (2015)
20. Rongé, J., Bosserez, T., Martel, D., Nervi, C., Boarino, L., Taulelle, F., Decher, G., Bordiga, S., Martens, J.A.: Chem. Soc. Rev. **43** (2014)
21. Heo, J.H., Song, D.H., Im, S.H.: Adv. Mater. **26**, 8179–8183 (2014)
22. Gong, M., Zhou, W., Kenney, M.J., Kapusta, R., Cowley, S., Wu, Y., Lu, B., Lin, M.-C., Wang, D.-Y., Yang, J., Hwang, B.-J., Dai, H.: Angew. Chemie **127**, 12157–12161 (2015)
23. McCrory, C.C.L., Jung, S., Ferrer, I.M., Chatman, S.M., Peters, J.C., Jaramillo, T.F.: J. Am. Chem. Soc. **137**, 4347–4357 (2015)
24. Vesborg, P.C.K., Seger, B., Chorkendorff, I.: J. Phys. Chem. Lett. **6**, 951–957 (2015)
25. Xiao, P., Chen, W., Wang, X.: Adv. Energy Mater. **5**, n/a–n/a (2015)
26. Kibsgaard, J., Tsai, C., Chan, K., Benck, J.D., Nørskov, J.K., Abild-Pedersen, F., Jaramillo, T. F.: Energy Environ. Sci. **8**, 3022–3029 (2015)
27. Gong, M., Dai, H.: Nano Res. **8**, 23–39 (2015)
28. Luo, J., Im, J.-H., Mayer, M.T., Schreier, M., Nazeeruddin, M.K., Park, N.-G., Tilley, S.D., Fan, H.J., Grätzel, M.: Science **345**, 1593–1596 (2014)
29. Walter, M.G., Warren, E.L., McKone, J.R., Boettcher, S.W., Mi, Q., Santori, E.A., Lewis, N. S.: Chem. Rev. **110**, 6446–73 (2010)
30. Sivula, K., van de Krol, R.: Nat. Rev. Mater. **1**, 15010 (2016)
31. Moniz, S.J.A., Shevlin, S.A., Martin, D.J., Guo, Z., Tang, J.: Energy Environ. Sci. **8**, 731 (2015)
32. McKone, J.R., Lewis, N.S., Gray, H.B.: Chem. Mater. **26**, 407–414 (2014)
33. Prévot, M.S., Sivula, K.: J. Phys. Chem. C **117**, 17879–17893 (2013)
34. Joya, K.S., Joya, Y.F., Ocakoglu, K., van de Krol, R.: Angew. Chem. Int. Ed. **52**, 10426–10437 (2013)
35. Zhang, Z., Yates, J.T.: Chem. Rev. (2012)

36. Jang, J.-W., Du, C., Ye, Y., Lin, Y., Yao, X., Thorne, J., Liu, E., McMahon, G., Zhu, J., Javey, A., Guo, J., Wang, D.: Nat. Commun. **6**, 7447 (2015)
37. Bornoz, P., Abdi, F.F., Tilley, S.D., Dam, B., van de Krol, R., Grätzel, M., Sivula, K.: J. Phys. Chem. C **118**, 16959–16966 (2014)
38. Sivula, K., Le Formal, F., Grätzel, M.: ChemSusChem **4**, 432–449 (2011)
39. Bora, D.K., Braun, A., Constable, E.C.: Energy Environ. Sci. **6**, 407 (2013)
40. Morales-Guio, C.G., Mayer, M.T., Yella, A., Tilley, S.D., Grätzel, M., Hu, X.: J. Am. Chem. Soc. **137**, 9927–9936 (2015)
41. Smith, R.D.L., Prévot, M.S., Fagan, R.D., Zhang, Z., Sedach, P.A., Siu, M.K.J., Trudel, S., Berlinguette, C.P.: Science **340**, 60–3 (2013)
42. Trotochaud, L., Mills, T.J., Boettcher, S.W.: J. Phys. Chem. Lett. **4**, 931–935 (2013)
43. Tilley, S.D., Cornuz, M., Sivula, K., Grätzel, M.: Angew. Chemie **122**, 6549–6552 (2010)
44. Gurudayal, D.S., Kumar, M.H., Wong, L.H., Barber, J., Grätzel, M., Mathews, N.: Nano Lett. **15**, 3833–3839 (2015)
45. Chen, Y.-S., Manser, J.S., Kamat, P.V.: J. Am. Chem. Soc. **137**, 974–981 (2015)
46. Zhang, X., Zhang, B., Cao, K., Brillet, J., Chen, J., Wang, M., Shen, Y.: J. Mater. Chem. A **3**, 21630–21636 (2015)
47. Kim, J.H., Jo, Y., Kim, J.H., Jang, J.W., Kang, H.J., Lee, Y.H., Kim, D.S., Jun, Y., Lee, J.S.: ACS Nano **9**, 11820–11829 (2015)
48. Luo, J., Steier, L., Son, M.-K., Schreier, M., Mayer, M.T., Grätzel, M.: Nano Lett. (2016). acs.nanolett.5b04929
49. Tilley, S.D., Schreier, M., Azevedo, J., Stefik, M., Grätzel, M.: Adv. Funct. Mater. **24**, 303–311 (2014)
50. Dias, P., Schreier, M., Tilley, S.D., Luo, J., Azevedo, J., Andrade, L., Bi, D., Hagfeldt, A., Mendes, A., Grätzel, M., Mayer, M.T.: Adv. Energy Mater. **5**, n/a–n/a (2015)
51. Hu, S., Xiang, C., Haussener, S., Berger, A.D., Lewis, N.S.: Energy Environ. Sci. **6**, 2984 (2013)
52. Seger, B., Tilley, S.D., Pedersen, T., Vesborg, P.C.K., Hansen, O., Grätzel, M., Chorkendorff, I.: RSC Adv. **3**, 25902 (2013)
53. White, J.L., Baruch, M.F., Pander III, J.E., Hu, Y., Fortmeyer, I.C., Park, J.E., Zhang, T., Liao, K., Gu, J., Yan, Y., Shaw, T.W., Abelev, E., Bocarsly, A.B.: Chem. Rev. **115**, 12888–12935 (2015)
54. Wang, W.H., Himeda, Y., Muckerman, J.T., Manbeck, G.F., Fujita, E.: Chem. Rev. **115**, 12936–12973 (2015)
55. Schreier, M., Curvat, L., Giordano, F., Steier, L., Abate, A., Zakeeruddin, S.M., Luo, J., Mayer, M.T., Grätzel, M.: Nat. Commun. **6**, 7326 (2015)
56. Hori, Y.: Handbook of Fuel Cells—Fundamentals, Technology and Applications, pp. 1–14. Wiley (2010)
57. Chen, Y., Li, C.W., Kanan, M.W.: J. Am. Chem. Soc. **134**, 19969–19972 (2012)
58. Li, X., Tschumi, M., Han, H., Babkair, S.S., Alzubaydi, R.A., Ansari, A.A., Habib, S.S., Nazeeruddin, Md.K., Zakeeruddin, S.M., Grätzel, M.: Energy Technol. **3**, 551–555 (2015)
59. Mei, A., Li, X., Liu, L., Ku, Z., Liu, T., Rong, Y., Xu, M., Hu, M., Chen, J., Yang, Y., Grätzel, M., Han, H.: Science **345**, 295–298 (2014)
60. Li, X., Ibrahim Dar, M., Yi, C., Luo, J., Tschumi, M., Zakeeruddin, S.M., Nazeeruddin, M.K., Han, H., Grätzel, M.: Nat. Chem. **7**, 703–711 (2015)
61. Yi, C., Luo, J., Meloni, S., Boziki, A., Ashari-Astani, N., Grätzel, C., Zakeeruddin, S.M., Röthlisberger, U., Grätzel, M.: Energy Environ. Sci. **9**, 656–662 (2016)
62. Luo, J., Li, Z., Nishiwaki, S., Schreier, S., Mayer, M.T., Cendula, P., Lee, Y.H., Fu, K., Cao, A., Nazeeruddin, M.K., Romanyuk, Y.E., Buecheler, S., Tilley, S.D., Wong, L.H., Tiwari, A. N., Grätzel, M.: Adv. Energy Mater. **5**, n/a–n/a (2015)

Inverted Planar Structure of Perovskite Solar Cells

Jingbi You, Lei Meng, Ziruo Hong, Gang Li and Yang Yang

Abstract Recently, another emerging structure, referred to as an "inverted" planar device structure (i.e., p-i-n), uses p-type and n-type materials as bottom and top charge transport layers, respectively. This structure derived from organic solar cells, and the charge transport layers used in organic photovoltaics were successfully transferred into perovskite solar cells. The p-i-n structure of perovskite solar cells have shown efficiencies as high as 18 %, lower temperature processing, flexibility, and furthermore, negligible J-V hysteresis effects. In this chapter, we will provide a comprehensive comparison of the mesoporous and planar structures, and also the regular and inverted of planar structures. Later, we will focus the discussion on the development of the inverted planar structure of perovskite solar cells, including film growth, band alignment, stability, and hysteresis. Future development and possible solutions to the remaining challenges facing the commercialization of perovskite solar cells are discussed.

Keywords Perovskite solar cells · Planar structure · Inverted structure

1 Introduction

Inorganic–organic hybrid perovskite solar cells have attracted great attention due to its solution-processing and high performance [1, 2]. It owns ABX_3 crystal structures, where A, B, and X are organic cation, metal cation, and halide anion, respectively (Fig. 1a), and the bandgap can be tuned from the ultraviolet to infrared region through varying these components (Fig. 1b) [2–4]. This family of materials exhibits a myriad of properties ideal for PV such as high dual electron and hole mobility, large absorption coefficients resulting from s-p antibonding coupling, a favorable band gap, a strong defect tolerance and shallow point defects, benign

J. You · L. Meng · Z. Hong · G. Li · Y. Yang (✉)
Department of Material Science and Engineering, University of California, Los Angeles, CA 90095, USA
e-mail: yangy@ucla.edu

N.-G. Park et al. (eds.), *Organic-Inorganic Halide Perovskite Photovoltaics*,
DOI 10.1007/978-3-319-35114-8_12

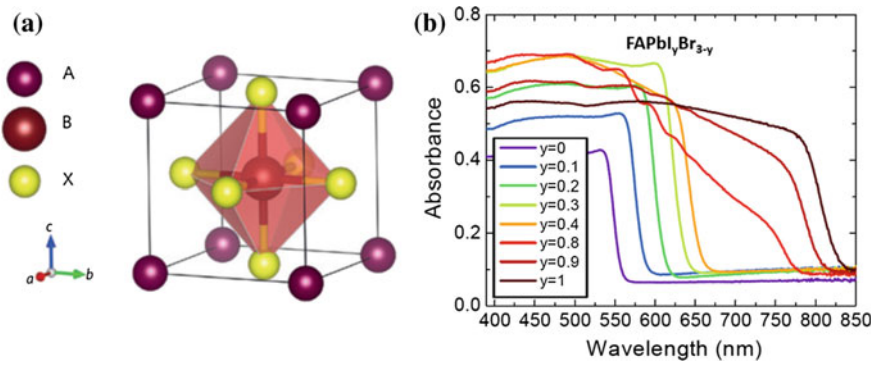

Fig. 1 **a** Crystal structure of the halide perovskite material, A site is typically CH_3NH_3I (MAI), $NH_2CH = NH_2I$ (FAI), Cs; B site is commonly Pb, Sn; X site could be Cl, Br or I **b** Absorption of $FAPbI_yBr_{3-y}$ with different ratios of Br and I. Reprinted with permission from Ref. [4]. Copyright 2014 Royal Society of Chemistry

grain boundary recombination effects, and reduced surface recombination [5]. After 7 years efforts, the power conversion efficiency (PCE) of perovskite solar cells has risen from about 3 % to over 22 % [1, 6–16].

2 Planar Structure

The hybrid perovskite solar cell was initially discovered in a liquid dye sensitized solar cells (DSSCs) [1]. Miyasaka and coworkers were the first to utilize the perovskite ($CH_3NH_3PbI_3$ and $CH_3NH_3PbBr_3$) nanocrystal as absorbers in DSSC structure, achieving an efficiency of 3.8 % in 2009 [1]. Later, in 2011, Park et al. got 6.5 % by optimizing the processing [6]. However, these devices showed fast degradation due to the decomposition of perovskite by liquid electrolyte. In 2012, Park and Gratzel et al. reported a solid state perovskite solar cell using the solid hole transport layer (Spiro-OMeTAD) to improve stability [7]. After that, several milestones in device performance have achieved using DSSCs structure [6–16]. However, these mesoporous devices need a high temperature sintering that could increase the processing time and cost of cell production.

It was found that methylammonium-based perovskites owns long-charge carrier diffusion lengths ($\sim$100 nm for $CH_3NH_3PbI_3$ and $\sim$1000 nm for $CH_3NH_3PbI_{3-x}Cl_x$) [17, 18]. Further studies demonstrated that perovskites exhibit ambipolar behavior, indicating that the perovskite materials themselves can transport both of electrons and holes between the cell terminals [17]. All of these results indicated that a simple planar structure was feasible. The first successful demonstration of the planar structure can be traced back to the perovskite/fullerene structure reported by Guo [19], showing a 3.9 % efficiency. The breakthrough of the planar perovskite structure was obtained using a dual-source vapor deposition, providing dense and

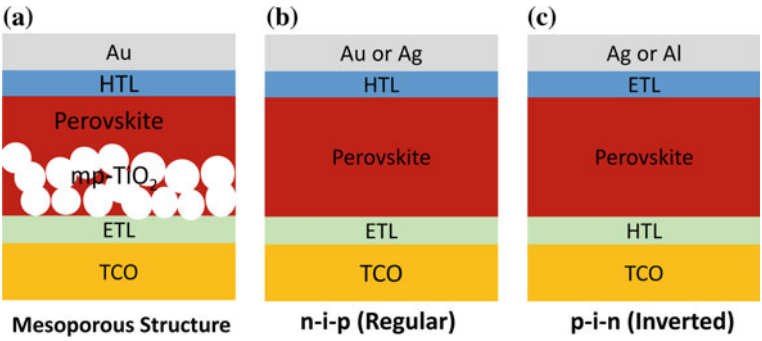

Fig. 2 Three typical device structures of perovskite solar cells **a** mesoporous, **b** regular planar structure and **c** inverted planar structure

high-quality perovskite films that achieved 15.4 % efficiency [20]. Recently, the efficiency of the planar structure was pushed over 19 % through perovskite film morphology control and interface engineering [12]. These results showed that the planar structure could achieve similar device performance as the mesoporous structure. The evolution of the structure of perovskite is shown in Fig. 2.

The planar structure can be divided into regular (n-i-p) and inverted (p-i-n) structure depending on which selective contact is used on the bottom (Fig. 2b, c). The regular n-i-p structure has been extensively studied and was based on dye-sensitized solar cells; while removing the mesoporous layer the p-i-n structure is derived from the organic solar cell, and usually, several charge transport layers used in organic solar cells were successfully transferred into perovskite solar cells [11].

The p-i-n inverted planar of perovskite solar cells showed the advantages of high efficiencies, lower temperature processing and flexibility (Fig. 3), and furthermore, negligible J-V hysteresis effects. In this chapter, we will focus on the inverted

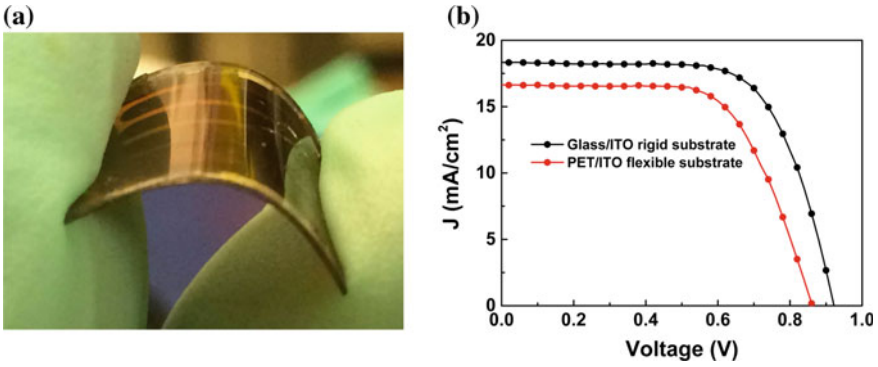

Fig. 3 **a** Image of flexible perovskite solar cell adopting the structure of ITO/PEDOT:PSS/$CH_3NH_3PbI_{3-x}Cl_x$/PCBM/Al, **b** J-V curve of perovskite devices on rigid glass and flexible PET substrates, respectively [22]. Reprinted with permission from Ref. [22]. Copyright 2014 American Chemical Society

planar structure of perovskite solar cells, including their working mechanism, methods for improving efficiency, stability, and hysteresis issues.

3 Inverted Planar Structure

The first inverted planar structure of perovskite solar cells adopted a similar device structure to the organic solar cell (Fig. 4a, b) [19]. The traditional organic transport layers poly(3,4-ethylenedioxythiophene):poly(styrenesulfonic acid) (PEDOT:PSS) and fullerene derivative, was directly implemented as the hole transport layer (HTL) and electron transport layer (ETL) in a perovskite device. Through choosing a proper fullerene derivative and optimizing the processing conditions of the perovskite film, a PCE of 3.9 % was delivered. Later, Sun et al. succeeded in making a thicker and denser perovskite film by introducing two-step sequential deposition into the planar device that increased the device performance to 7.41 % (Fig. 4c) [21]. After 2013, several attempts were made to improve the efficiency, including film formation and interface engineering, which will be discussed in the next sections, the efficiency of inverted planar structure of perovskite solar cells achieve 18 %. The main development of the inverted structure perovskite solar cells are summarized in Table 1.

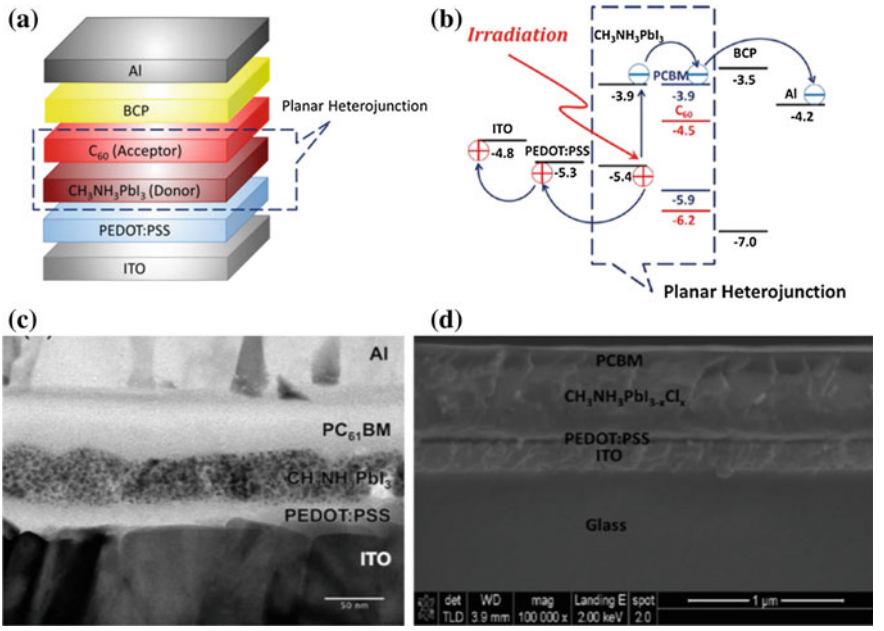

Fig. 4 **a** The device structure of the first inverted planar structure of perovskite solar cell, **b** band alignment. Reprinted with permission from Ref. [19]. Copyright 2013 Wiely-VCH, **c** a thin perovskite film (<100 nm) as the absorber. Reprinted with permission from Ref. [21]. Copyright 2014 Royal Society of Chemistry. **d** Thicker film (about 300 nm) as the absorber [1]. Reprinted with permission from Ref. [22]. Copyright 2014 American Chemical Society

Table 1 Several representative devices performances of inverted planar structured perovskite solar cells

Perovskite processing	HTL	ETL	Voc (V)	Jsc (mA/cm^2)	FF (%)	PCE (%)	Stability	Reference
One-step	PEDOT:PSS	$PC_{61}BM$/BCP	0.60	10.32	63	3.9		[19]
Two-step	PEDOT:PSS	$PC_{61}BM$	0.91	10.8	76	7.4		[21]
One-step (Cl)	PEDOT:PSS	$PC_{61}BM$	0.87	18.5	72	11.5		[22]
One-step (Cl)	PEDOT:PSS	$PC_{61}BM/TiO_x$	0.94	15.8	66	9.8		[23]
Solvent engineering	PEDOT:PSS	$PC_{61}BM$/LiF	0.87	20.7	78.3	14.1		[26]
One-step (Moisture, Cl)	PEDOT:PSS	$PC_{61}BM$/PFN	1.05	20.3	80.2	17.1		[11]
One-step (hot-casting, Cl)	PEDOT:PSS	PCBM	0.94	22.4	83	17.4		[27]
One-step (HI additive)	PEDOT:PSS	$PC_{61}BM$	1.1	20.9	79	18.2		[28]
Co-evaporation	PEDOT:PSS/Poly-TPD	$PC_{61}BM$	1.05	16.12	67	12.04		[24]
Co-evaporation	PEDOT:PSS/PCDTBT	$PC_{61}BM$/LiF	1.05	21.9	72	16.5		[31]
Two-step spin-coating	PTAA:	PCBM/C60/BCP	1.07	22.0	76.8	18.1		[29]
One-step Solvent	PEDOT:PSS	C_{60}	0.92	21.07	80	15.44		[39]
One-step (Cl)	PEDOT:PSS	$PC_{61}BM$/ZnO	0.97	20.5	80.1	15.9	140 h	[42]
One-step (Cl)	PEDOT:PSS	$PC_{61}BM$/ZnO	1.02	22.0	74.2	16.8	60 days	[43]
One-step	NiO_x	$PC_{61}BM$/BCP	0.92	12.43	68	7.8		[33]
One-step	NiO_x:Cu	$PC_{61}BM/C_{60}$-bis surfcant	1.11	19.01	73	15.4	244 h	[35]
Solvent engineering	NiO_x	$PC_{61}BM$/LiF	1.06	20.2	81.3	17.3		[37]
Two-step	NiO_x	ZnO	1.01	21.0	76	16.1	>60 days	[30]
Solvent engineering	NiLiMgO	$PCBM/TiO_2$:Nb	1.07	20.62	74.8	16.2	1000 h (sealed)	[36]

3.1 Film Growth for Improving Efficiency of Inverted Planar Solar Cells

Initial studies adopted a thin perovskite absorbing layer of less than 100 nm, which limited the light harvesting and short circuit current of the devices [19, 21]. After learning that the perovskite materials possess diffusion lengths over 100 nm, thicker absorption layers were possible without sacrificing the charge transport properties. Yang et al. and Snaith et al. first independently used a thicker mixed halide perovskite film (~300 nm) as the absorber (Fig. 4d), showing an efficiency of about 11.5 % and 9.8 %, respectively [22, 23]. Bolink et al. showed 12.04 % efficiency by thermal deposition of 285 nm thick of perovskite and adopting an organic charge transport layer [24]. Later, several processing methods for growth of high quality of perovskite film have been invented. Huang et al. showed a diffusion approach to form high quality $CH_3NH_3PbI_3$ films, which could be considered a modified two-step process, where PbI_2 was first deposited onto PEDOT:PSS and followed by spin-coating of MAI onto the PbI_2 surface and annealing to form the perovskite film (Fig. 5a) [25]. The perovskite film was formed by interdiffusion of CH_3NH_3I into PbI_2, producing efficient devices of 15 % with highly reproducible [25]. Seok et al. transferred the solvent engineering to get pinhole free film and adopted into the inverted structured perovskite solar cells, yielding 14.1 % efficiency [26]. You et al. discovered that annealing the perovskite precursor film under certain humidity condition (<40 % humidity) could improve the film quality (Fig. 5b) and then push the power conversion efficiency to as high as 17.1 % [11]. Nie et al. reported millimeter-sized perovskite gains by coating the hot precursor film onto the hot substrate, for a champion device close to 18 % efficiency [27]. Recently, Im et al. reported a high-quality perovskite film on PEDOT:PSS using HI as an additive to improve the film quality. This produced an 18.1 % efficiency without hysteresis [28].

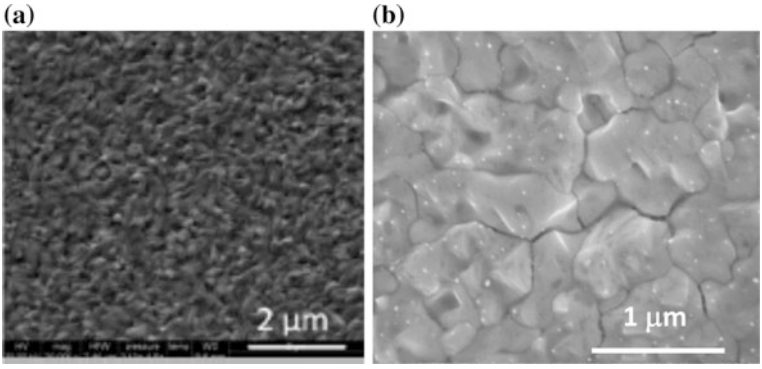

Fig. 5 High quality of perovskite films obtained by various methods **a** Inter-diffusion. Reprinted with permission from Ref. [25]. Copyright 2014 Royal Society of Chemistry. **b** Moisture assisted. Reprinted with permission from Ref. [11]. Copyright 2014 AIP Publishing

Although the inverted planar of perovskite solar cells based on PEDOT:PSS hole transport layer showed promising efficiency, there are still several challenges to overcome for achieving higher efficiencies [3, 11]. The growth of perovskite film on PEDOT:PSS often leads to pinhole generation and incomplete surface coverage resulting in low device performance [3, 11]. Recent results show that perovskite growth is strongly dependent on the bottom substrates [29, 30]. We have showed that NiO_x could yield a better perovskite film than on PEDOT:PSS and give higher Voc [30]. Meredith et al. also observed different crystal quality when perovskite is deposited on different polymer surfaces [31]. Perovskite appears to show better crystallization when a more crystalline bottom substrate is used, indicating that the crystallinity of the substrates could contribute to the film quality of the perovskite layer [31]. Wetting properties between the solvent with the bottom substrate was found to be another issue effecting perovskite film growth. It was found that the crystal size of perovskite film was much larger than that of thickness and demonstrated a higher efficiency using PTAA as the hole transport layers, which was could severe as a non-wetting surface for the solvent used for perovskite, such as DMF [29].

3.2 Interface Engineering Hole Transport Layer

The n-i-p regular structure usually shows an open voltage over 1 V [12–16], while the inverted structure usually shows a slight open circuit voltage drop ($\sim$0.9 V) [19, 21–23, 25, 27, 30]. In addition to the inferior crystal film quality on PEDOT:PSS as mentioned above, the band alignment between perovskite and the traditional hole transport layer PEDOT:PSS could be another issue. The work function of the generally used hole transport layer PEODT:PSS is about 4.9–5.1 eV, which is shallower than that of the valence band of perovskite layer (5.4 eV), leading to an imperfect ohmic contact between perovskite and the p-type transport layer and a consequent Voc loss (Fig. 6). To address this problem, PEDOT:PSS must be modified or replaced by another materials with high work function. The most common polymers such as poly-TPD [24], PCDTBT [31], and PTAA [29], with deep HOMO levels (~ -5.4 eV) have been used to modify the PEDOT:PSS surface, and the devices based on the bilayer hole transport layer (PEDOT:PSS/polymer) showed an enhanced Voc (>1 V) [24, 29, 31]. Unfortunately, these polymers are usually hydrophobic, and thus the perovskite precursor cannot be coated onto these polymer surfaces. Alternatively, evaporation processes of perovskite film must be adopted [24, 31]. Recently, p-type water soluble polyelectrolyte with deep work function (>5.2 eV) showed good device performance when they are using as hole transport layers [32], which could be a good candidate of replacing PEDOT:PSS if it is air stable.

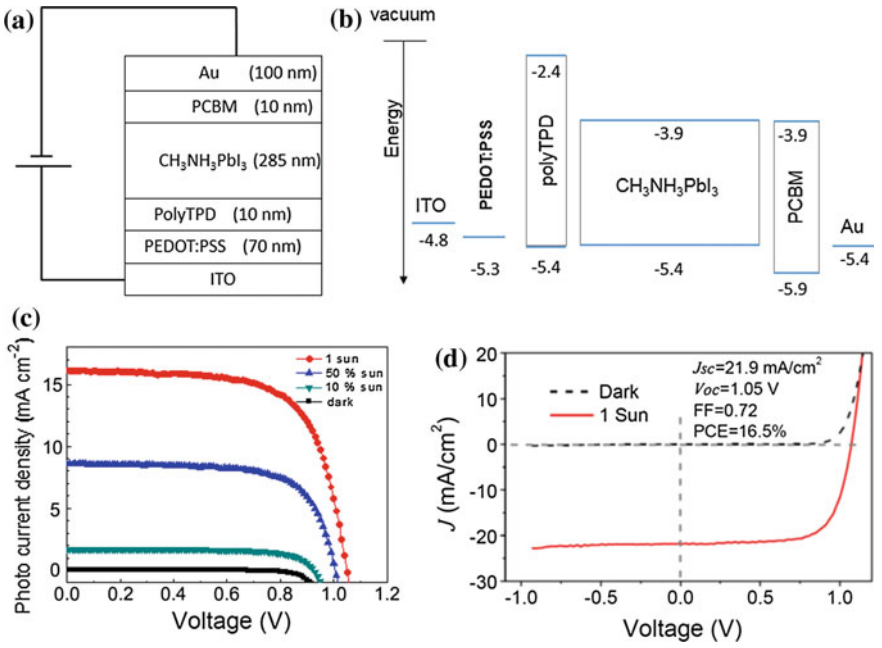

Fig. 6 Device structure and performance of modified PEDOT:PSS-based devices. **a** Device structure, poly-TPD was used as a typical layer. Several other p-type materials could be also used. **b** band alignment, **c** device performance using PEDOT:PSS/poly-TPD bilayer as hole transport layer under different light intensity. Reprinted with permission from Ref. [24]. Copyright 2013 Nature Publishing Group. **d** Device performance using PEDOT:PSS/PCDTBT bilayer as hole transport layer. Reprinted with permission from Ref. [31]. Copyright 2015 Nature Publishing Group

Inorganic metal oxides such as NiO, MoO_3, V_2O_5, and WO_3 own higher work function than PEDOT:PSS, and could be a good candidate of replacing of PEDOT:PSS to get a larger V_{OC}. Guo et al. first reported use of solution processed NiO_x as the hole transport layer, demonstrating an efficiency of about 8 % (Fig. 7a–c) [33]. Han et al. adopted a hybrid interfacial layer of NiO/Al_2O_3 to improve the device efficiency to 13 % with a high fill factor [34]. Jen et al. used Cu-doped NiO_x as a hole transport layer and achieved open circuit voltages as high as 1.1 V with an efficiency of 15.4 % [35]. You and Chen et al. adopted a sol-gel process for high quality NiO_x films, demonstrating an efficiency of 16.1 % and 16.2 %, respectively [30, 36]. Seok et al. reported an inverted structure using a NiO_x film deposited via pulsed laser deposition (PLD), and push the device efficiency as high as high as 17.13 % (Fig. 7d) [37]. In addition to NiO_x, another promising hole transport layer is CuSCN. Significant progress has been made with CuSCN in the n-i-p perovskite solar cell, showing 12.4 % efficiency using a 600–700 nm thick of CuSCN layer [38]. Recently, using electro-deposited CuSCN as a hole transport layer in inverted structure, as high as 16.6 % efficiency have been obtained [39]. Several other metal

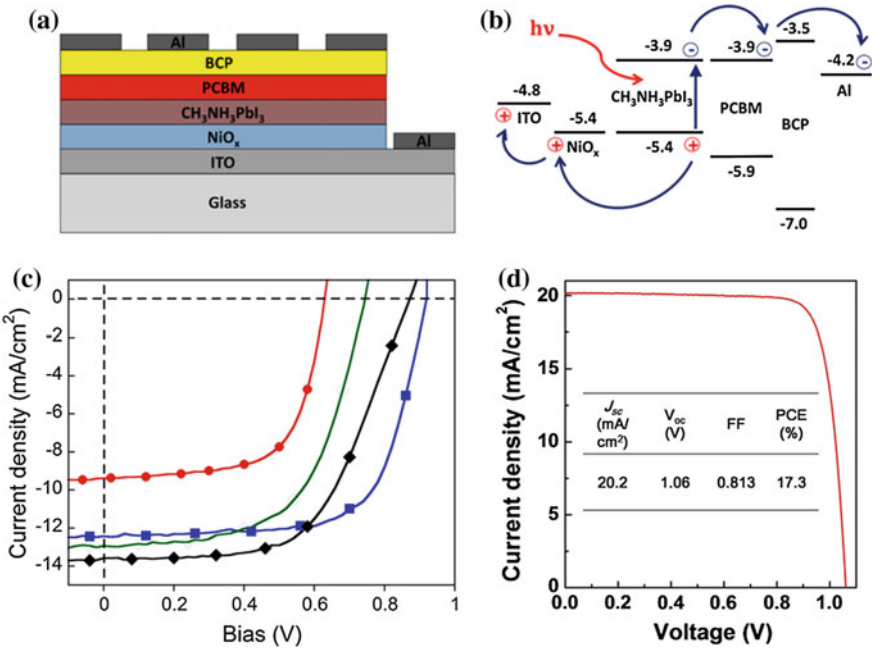

Fig. 7 Device structure and performance using NiO_x as hole transport layer. **a** Device structure, **b** Band alignment, **c** Device performance of the first demonstration using NiO_x as hole transport layers. Reprinted with permission from Ref. [33], Copyright 2014 Wiley-VCH. **d** Present champion device performance using NiO as hole transport layers. Reprinted with permission from Ref. [37], Copyright 2015 Wiley-VCH

oxides such as MoO_3, V_2O_5, WO_3 seem to be suitable for high stability hole transport layers, however, it seems these metal oxide materials are not resistive enough to the acidity of CH_3NH_3I.

3.3 *Interface Engineering of Electron Transport Layer*

For p-i-n perovskite solar cells, fullerenes are usually used as the electron transport layer, where PCBM is the most popular n-type charge transport layer. Recent studies show that C_{60} should be more effective than that of PCBM as an electron transport layer due to the higher mobility and conductivity of C_{60} [40]. Jen et al. showed that the PCE of fullerene-derived perovskite solar cells improves with increasing electron mobility in the fullerene layer, indicating the critical role of bulk transport through fullerene in promoting charge dissociation/transport (Fig. 8a) [40]. As for improving the charge transport properties of the fullerene, Li et al. attempted to dope the PCBM using graphdiyne (GD) to improve the coverage and the conductivity of PCBM, and also improve the device performance from 10.8 to

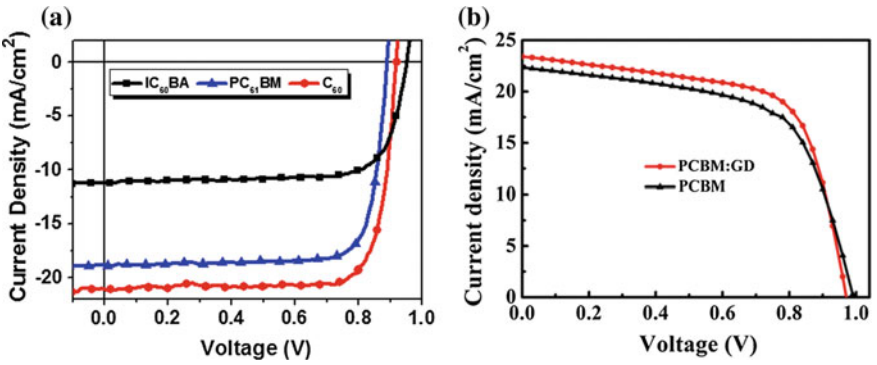

Fig. 8 **a** Inverted planar structure of perovskite solar cells using different fullerenes ($PC_{61}BM$, $IC_{61}BA$ and C_{60}) as electron transport layers. Reprinted with permission from Ref. [40], Copyright 2015 Wiley-VCH. **b** Device performance using PCBM with and without graphdiyne doping. Reprinted with permission from Ref. [41]. Copyright 2015 American Chemical Society

13.9 % (Fig. 8b) [41]. In addition, it was confirmed that the fullerene itself cannot fully form a prefect ohmic contact with a metal such as Al or Ag. Several buffer layers, including BCP [19], PFN [11], LiF [26], and self-assembled C_{60} derivatives [35] can further improve the ohmic contact. Furthermore, metal oxides such as ZnO and TiO_2, combined with fullerene as an electron transport layer, not only improve the ohmic contact but also improve device stability [23, 30, 41, 42].

3.4 Stability of Inverted Structure

The power conversion efficiency of perovskite solar cells has been pushed up to 21 and 18 % for regular and inverted structures, respectively. For practical application, a reliable and stable performance is strongly needed. Present results show that the stability of perovskite is a critical issue, the main problem in stability of perovskite come from the instability of perovskite material itself, which decomposes into PbI_2 and CH_3NH_3I under high humidity, high temperature or continuous light illumination. Another concern is interfacial stability, several organic charge transport layers that have been commonly used in perovskite solar cells can react with oxygen and water in the ambient air while light soaking, thus promoting device degradation. In addition, several electrode materials such as Ag, Al could react with perovskite when they were directly in contact [30].

3.5 *Effect of Electron Transport Layer on Stability*

For inverted structure, electron transport layer is the top most layer exposed to ambient air except for metal electrode. It was found that the fullerene could absorb oxygen or water onto the surface, leading to a dipole moment and a large resistance as a result of degradation (Fig. 9d) [30]. On the other hand, the fullerene layer could not be too thick due to its low conductivity. A thin fullerene layer could not form a continuous film and could not fully cover the perovskite surface, which might lead to physical direct contact between perovskite and electrode. It was found that perovskite and metal such as Al or Ag can react when in a humid environment [30]. Therefore, the devices based on the PCBM ETL showed poor stability (Fig. 9a, b) [30]. To improve the device stability, several metal oxides have been used in the inverted structure [23, 30, 42, 43]. Snaith et al. first reported a PCBM/TiO_x bilayer electron transport layer, improved the coverage of the electron transport layer as the pinholes from the PCBM could be filled [23]. Similarly PCBM/ZnO bilayers were found to be suitable for improving device performance and stability (Fig. 10) [42, 43]. You et al. significantly improved stability through use of ZnO as the top electron charge transport layer. It was found that the device can nearly maintain its

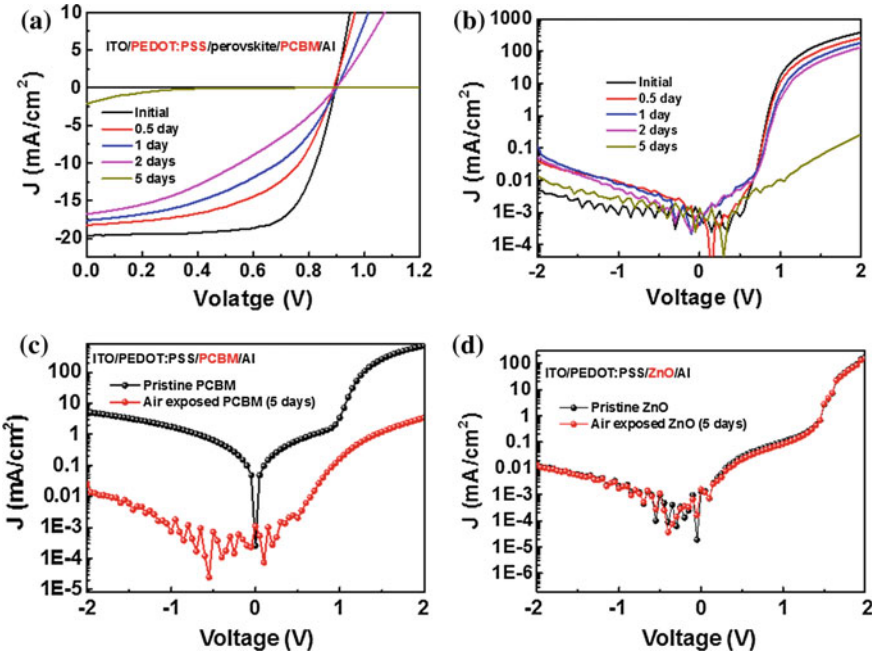

Fig. 9 **a** The degradation of inverted planar structure of perovskite solar cells using ITO/PEDOT:PSS/perovskite/PCBM/Al. **b** Light J-V and dark J-V curve of the devices under storage in ambient air for different time, respectively, **c** and **d** ZnO and PCBM interface stability under ambient air, respectively. Reprinted with permission from Ref. [30]. Copyright 2015 Nature Publishing Group

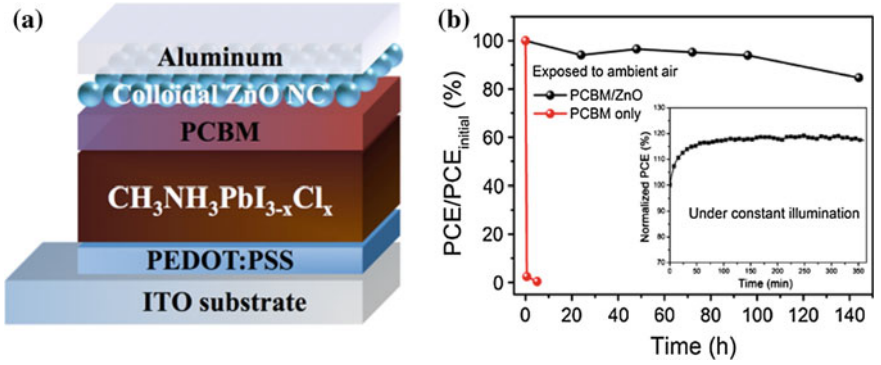

Fig. 10 **a** Device structure of inverted planar structure of perovskite solar cells with bilayer (PCBM/ZnO), **b** Device stability using PCBM/ZnO bilayer structures. Reprinted with permission from Ref. [42]. Copyright 2014 Springer

original efficiency after 60 days of storage in ambient air with room light soaking (Fig. 11) [30]. Recently, Chen et al. also demonstrated that a 15 % efficiency of large scale (1 cm^2) and stable of perovskite solar cells using PCBM/TiO_2:Nb as electron transport layer (Fig. 11) [36]. All of these results confirmed that the metal oxide electron transport layer could improve the device stability.

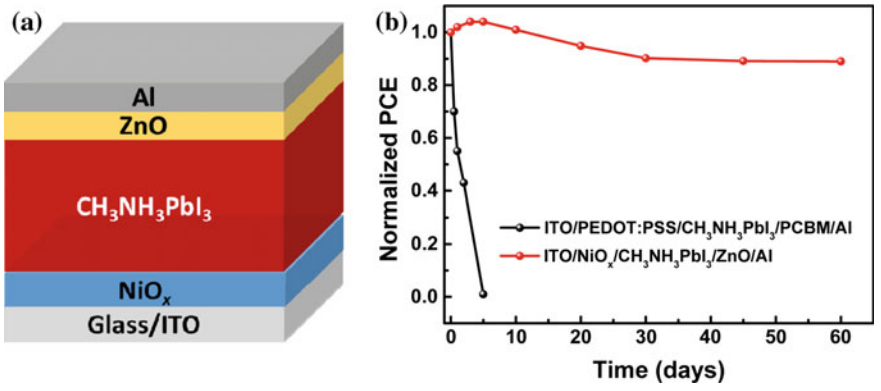

Fig. 11 **a** Inverted planar structure using both of inorganic metal oxide layers as hole and electron transport layers, the structure is: ITO/NiO_x/$CH_3NH_3PbI_3$/ZnO/Al; and **b** comparison of the devices stability using organic and inorganic charge transport layers. The devices can keep its 90 % original efficiency while keeping the unencapsulated devices in ambient air for 60 days. Reprinted with permission from Ref. [30]. Copyright 2016 Nature Publishing Group

3.6 *Effect of Hole Transport Layer on Stability*

PEDOT:PSS has been widely used in organic solar cells as an organic charge transport layer due to its good conductivity. However, PEDOT:PSS is hydrophilic and can easily absorb water from the surrounding environment. In addition, PEDOT:PSS has acidic properties that could potentially react with the bottom transparent metal oxide electrode [44]. Both of which would affect the long-term stability of the perovskite solar cell [30, 35]. According to these concerns, inorganic charge transport layers have been used, such as NiO_x and CuSCN. Jen et al. used $Cu:NiO_x$ as a hole transport layer showing markedly improved air stability as compared to the PEDOT:PSS-based device. The PCE of the $Cu:NiO_x$-based device remains above 90 % of the initial value even after 240 h of storage in air (light soaking has not been mentioned) [35]. You et al. also demonstrated that the air stability of perovskite solar cells can be improved by replacing PEDOT:PSS with NiO_x [30]. Recently, Chen et al. reported that using Li–Mg co-doped NiO_x as the hole transport layer for devices and showed improved stability [36].

3.7 *Perovskite Materials Stability*

Although modification of interface could improve device stability, the intrinsic properties of the perovskite material determin long term stability. The typical perovskite material $CH_3NH_3PbI_3$ shows severe moisture and light instability. The perovskite materials could be easily decomposed into PbI_2 and CH_3NH_3I, followed by decomposition into CH_3NH_2 and HI when exposing the perovskite in a high level of moisture environment. It was also found that perovskite could self-decompose when exposed to light for long periods of time. Exploration of highly stable perovskite materials could be the future direction in perovskite solar cell research. Li et al. reported that the improvement of the stability of perovskite materials via introducing cross-linking group (Fig. 12a, b) [45]. Smith et al. introduced two-dimensional structure of perovskite and showed significant improved stability compare with $CH_3NH_3PbI_3$ (Fig. 12c, d) [46].

3.8 *Hysteresis in Inverted Planar Solar Cells*

I-V Hysteresis is still a controversial and hot topic in perovskite solar cells. This issue was first raised at the beginning of 2014 [12, 13]. It has been found that hysteresis in the regular planar structure is more severe than in the case of the mesoporous [12, 13]. Interestingly, most reports have shown negligible hysteresis in the inverted planar structure with fullerene as electron transport layer, e.g., ITO/HTL/perovskite/PCBM/buffer layer/electrode [11, 22, 30, 47]. The most

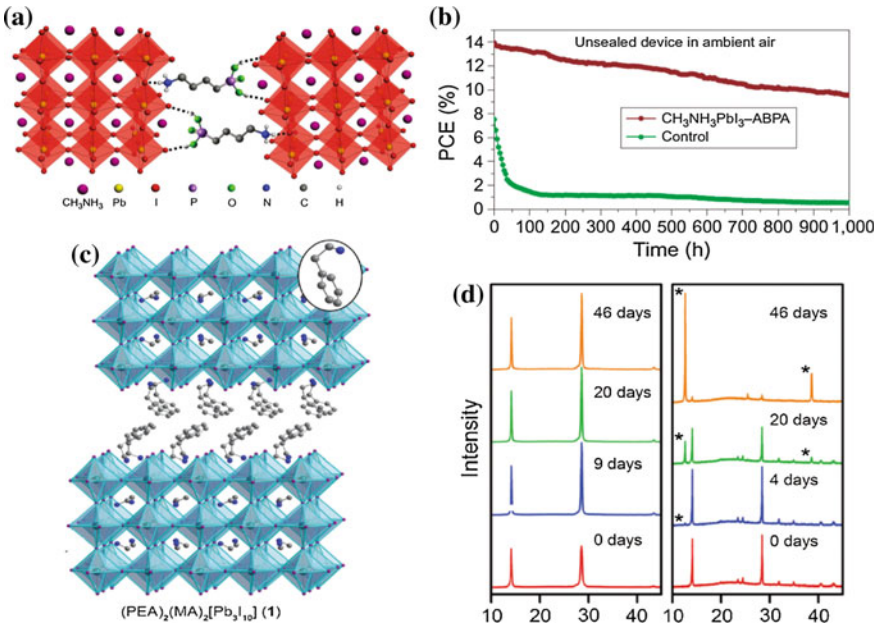

Fig. 12 **a** Schematic illustration of perovskite cross-linked by butylphosphonic acid 4-ammonium chloride (4-ABPACl) hydrogen-bonding interactions, **b** Variation of PCE with time of unsealed heterojunction solar cells based on corresponding perovskite films and stored in ambient air at –55 % humidity in the dark. Reprinted with permission from Ref. [45]. Copyright 2015 Nature Publishing Group. **c** The 2D perovskite $(PEA)_2(MA)_2[Pb_3I_{10}]$ and **d** PXRD patterns of films of $(PEA)_2(MA)_2[Pb_3I_{10}]$, $(MA)[PbI_3]$ formed from PbI_2, which were exposed to 52 % relative humidity. Reprinted with permission from Ref. [46]. Copyright 2014 Wiely-VCH

popular explanation is ion movement stabilization [2, 47–49]. The fullerene penetrate/diffuse into the perovskite layer through the pinholes/grain boundary during processing (spin-coating or annealing [2, 47]). Mobile ions in the perovskite interact with fullerene to form a fullerene halide radical [48], which is thought to stabilize electrostatic properties, reducing the electric field-induced anion migration that may give rise to hysteresis and thus resulting in no hysteresis [49]. Huang et al. also demonstrated that the fullerene penetration into perovskite layer during the annealing and passivate the traps in the perovskite and reduce the hysteresis (Fig. 13). In our opinion, except for ion movement stabilization, neglected charge accumulation and also capacitance could be another reason for hysteresis free. On one hand, while fullerene was diffused into perovskite, the device showed a similar structure as bulk heterojunction (BHJ) or a mesoporous structure (Fig. 13c), there are efficient channels for charge extraction. On the other hand, fast charge transfer between perovskite and fullerene allows efficient charge extraction [30]. While in regular structure, there is limited interface contact between metal oxide and perovskite, and more importantly, the charge transfer between metal oxide and perovskite is not efficient [30], which could lead to serious charge accumulation at the

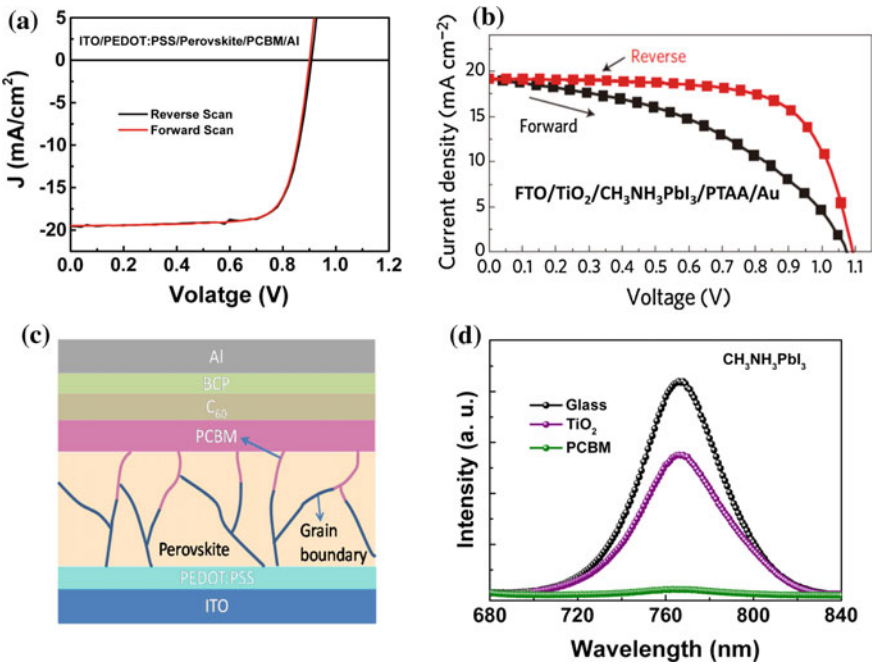

Fig. 13 **a** Hysteresis free from inverted planar structure ITO/PEDOT:PSS/Perovskite/PCBM/Al. Reprinted with permission from Ref. [30]. Copyright 2016 Nature Publishing Group. **b** Obvious hysteresis from regular planar structure FTO/TiO_2/Perovskite/PTAA/Au. Reprinted with permission from Ref. [30]. Copyright 2014 Nature Publishing Group. **c** A proposed mechanism of PCBM diffusion for grain boundaries passivation. Reprinted with permission from Ref. [30]. Copyright 2014 Nature Publishing Group [47]. **d** Photoluminescence (PL) from $CH_3NH_3PbI_3$, $CH_3NH_3PbI_3$/TiO_2 and $CH_3NH_3PbI_3$/PCBM. Reprinted with permission from Ref. [30]. Copyright 2016 Nature Publishing Group

interface between perovskite/metal oxide, and form a large capacitance. Therefore, there is no or neglected hysteresis in inverted structure, while significant hysteresis in regular structure.

4 Conclusions and Future Outlooks

Perovskite solar cells have reached efficiencies over 20 % based on the regular n-i-p mesoporous structures, whereas for the inverted p-i-n structure, the state art of performances are approximately 18 % efficient. To further improve efficiencies of inverted solar cells, it is necessary to modify interfaces, especially the contact between perovskite and the hole charge transport layer. The commonly used PEDOT:PSS surface should be modified or replaced by another material with a higher work function, and also in favor of larger crystal growth. After resolving the band

alignment between hole transport layer and perovskite and also the growth of the perovskite film on the hole transport layer, the efficiency should be much improved and should better compete with the regular structure of perovskite solar cells.

Several processing technologies such as solvent treatment/annealing [26, 47], moisture assisted growth [11], additives [28], hot spin-coating [27] technology have confirmed as an effective way for obtaining high quality of perovskite films. Exploring new methods or combining these existing technologies and further improving the film quality should be our next direction.

The stability of the perovskite is still the main issue for its commercial application. Even though more than 60 days stability under weak room light illumination or above 1000 h light illumination stability with encapsulation have been demonstrated, it is still not enough for practical applications. Further exploration of alternative perovskite material candidates and stabilizing additives may lead to improved perovskite stability in the future. To improve the stability at interfaces, inorganic charge transport layers show better results. At the least, the upmost layer should be robust and relatively impenetrable to moisture and oxygen. At present, metal oxides such as ZnO and TiO_2 colloids have been coated onto the fullerene transport layers for improved device stability. However, these methods could be further improved. In inverted structures, fullerenes can forbid ion movement or enhance the charge transfer to reduce the hysteresis. It seems that metal oxides introduce hysteresis, and a fullerene/metal oxide such as PCBM/ZnO (TiO_x) bilayer system shows promise in terms of reduced hysteresis and improved highly stability.

The planar structure shows a simple device structure and a promising efficiency (close to 20 %). By further improving the perovskite crystallinity and also the interface, it could be anticipated that the efficiency will catch up or be over than that of traditional inorganic thin film solar cells such as CIGS and CdTe. Compared with the inorganic thin films solar cells, which needs high vacuum and temperature processing, planar structure of perovskite solar cells could be fabricated in ambient air or nitrogen-filled glove box at low temperature, this will reduce the fabrication cost. Furthermore, perovskite solar cells are based on solution process, which is compatible with several coating technique, such as blade coating and roll to roll techniques to produce large area and flexible devices. Future study based on perovskite solar cells could be large scale and stability.

Acknowledgement This work was financially supported by a grant from the National Science Foundation (ECCS-1202231), Air Force Office of Scientific Research (FA9550-12-1-0074). Jingbi You acknowledge the financial support from National 1000 Young Talents awards.

References

1. Kojima, A., Teshima, K., Shirai, Y., Miyasaka, T.: J. Am. Chem. Soc. **131**, 6050 (2009)
2. Stranks, S.D., Snaith, H.J.: Nat. Nanotech. **10**, 391 (2015)
3. Bai, S., Jin, Y., Gao, F.: Book chapter 13. Advanced Functional Materials. Wiley (Germany) (2015)

4. Eperon, G.E., Stranks, S.D., Menelaou, C., Johnston, M.B., Herz, L.M., Snaith, H.J.: Energy Environ. Sci. **7**, 982 (2014)
5. Yin, W.J., Yang, J.H., Kang, J., Yan, Y.F., Wei, S.H.: J. Mater. Chem. A **3**, 8926 (2015)
6. Im, J.-H., Lee, C.R., Lee, J.W., Park, S.W., Park, N.G.: Nanoscale **3**, 4088 (2011)
7. Kim, H.S., Lee, C.R., Im, J.H., Lee, K.B., Moehl, T., Marchioro, A., Moon, S., Humphry-Baker, R., Yum, J.H., Moser, J.E., Gratzel, M., Park, N.G.: Sci. Rep. **2**, 591 (2012)
8. Lee, M.M., Teuscher, J., Miyasaka, T., Murakami, T.N., Snaith, H.J.: Science **338**, 643 (2012)
9. Burschka, J., Pellet, N., Moon, S.J., Humphry-Baker, R., Gao, P., Nazeeruddin, M.K., Gratzel, M.: Nature **499**, 316 (2013)
10. Im, J.H., Jang, I.H., Pellet, N., Grätzel, M., Park, N.G.: Nat. Nanotech. **9**, 927 (2014)
11. You, J., Yang, Y., Hong, Z., Song, T.B., Meng, L., Liu, Y., Jiang, C., Zhou, H., Chang, W. H., Li, G., Yang, Y.: Appl. Phys. Lett. **105**, 183–902 (2014)
12. Zhou, H., Chen, Q., Li, G., Luo, S., Song, T.B., Duan, H., Hong, Z., You, J., Liu, Y., Yang, Y.: Science **345**, 542 (2014)
13. Jeon, N.J., Noh, J.H., Kim, Y.C., Yang, W.K., Ryu, S., Seok, S.I.: Nat. Mater. **13**, 897 (2014)
14. Jeon, N.J., Noh, J.H., Yang, W.S., Kim, Y.C., Ryu, S.C., Seo, J., Seok, S.I.: Nature **517**, 474 (2015)
15. Yang, W.S., Noh, J.H., Jeon, N.J., Kim, Y.C., Ryu, S.C., Seo, J., Seok, S.I.: Science **348**, 1234 (2015)
16. http://www.nrel.gov/ncpv/
17. Xing, G.C., Mathews, N., Sun, S.Y., Lim, S.S., Lam, Y.M., Gratzel, M., Mhaisalkar, S., Sum, T.C.: Science **342**, 344 (2013)
18. Stranks, S.D., Eperon, G.E., Grancini, G., Menelaou, C., Alcocer, M.J.P., Leijtens, T., Herz, L.M., Petrozza, A., Snaith, H.J.: Science **342**, 341 (2013)
19. Jeng, J.Y., Chiang, Y.F., Lee, M.H., Peng, S.R., Guo, T.F., Chen, P., Wen, T.C.: Adv. Mater. **25**, 3727 (2013)
20. Liu, M., Johnston, M.B., Snaith, H.J.: Nature **501**, 395 (2013)
21. Sun, S.Y., Salim, T., Mathews, N., Duchamp, M., Boothroyd, C., Xing, G., Sum, T.C., Lam, Y.M.: Energy Environ. Sci. **7**, 399 (2014)
22. You, J., Hong, Z., Yang, Y., Chen, Q., Cai, M., Song, T.B., Chen, C.C., Lu, S., Liu, Y., Zhou, H., Yang, Y.: ACS Nano **8**, 1674 (2014)
23. Docampo, P., Ball, J.M., Darwich, M., Eperon, G.E., Snaith, H.J.: Nat. Comm. **4**, 2761 (2013)
24. Malinkiewicz, O., Yella, A., Lee, Y.H., Espallargas, G.M., Gratzel, M., Nazeeruddin, M.K., Bolink, H.J.: Nat. Photon **8**, 128 (2014)
25. Xiao, Z., Bi, C., Shao, Y., Dong, Q., Wang, Q., Yuan, Y., Wang, C., Gao, Y., Huang, J.: Energy Environ. Sci. **7**, 2619 (2014)
26. Seo, J., Park, S., Kim, Y.C., Jeon, N.J., Noh, J.H., Yoon, S.C., Seok, S.I.: Energy Environ. Sci. **7**, 2642 (2014)
27. Nie, W., Tsai, H., Asadpour, R., Blancon, J., Neukirch, A.J., Gupta, G., Crochet, J.J., Chhowalla, M., Tretiak, S., Alam, M.A., Wang, H.L., Mohite, A.D.: Science **347**, 522 (2015)
28. Heo, J.H., Han, H.J., Dasom, K., Ahn, T.K., Im, S.H.: Energy Environ. Sci. **8**, 1602 (2015)
29. Bi, C., Wang, Q., Shao, Y., Yuan, Y., Xiao, Z., Huang, J.: Nat. Commun. **6**, 7747 (2015)
30. You, J., Meng, L., Song, T.B., Guo, T.F., Yang, Y., Chang, W.H., Hong, Z., Chen, H., Zhou, H., Chen, Q., Liu, Y., Nicholas, D.M., Yang, Y.: Nat. Nanotech. **11**, 75 (2016)
31. Lin, Q., Armin, A., Nagiri, R.C.R., Burn, P.L., Meredith, P.: Nature Photon **9**, 106 (2015)
32. Li, X.D., Liu, X.H., Wang, X.Y., Zhao, L.X., Jiu, T.G., Fang, J.F., Mater, J.: Chem. A **3**, 15024 (2015)
33. Jeng, J.Y., Chen, K.C., Chiang, T.Y., Lin, P.Y., Tsai, T.D., Chang, Y.C., Guo, T.F., Chen, P.T.C., Wen, Y.J., Hsu, T.C.: Adv. Mater. **26**, 4107 (2014)
34. Chen, W., Wu, Y., Liu, J., Qin, C., Yang, X., Islam, A., Chen, Y., Han, L.: Energy Environ. Sci. **8**, 629 (2015)
35. Kim, J.H., Liang, P.W., Williams, S.T., Cho, N., Chueh, C.C., Glaz, M.S., Ginger, D.S., Jen, A.K.-Y.: Adv. Mater. **27**, 695(2015)

36. Chen, W., Wu, Y.Z., Yue, Y.F., Liu, J., Zhang, W.J., Yang, X.D., Chen, H., Bi, E.B., Ashraful, I., Grätzel, M., Han, L.Y.: Science **350**, 944 (2015)
37. Park, J.H., Seo, J., Park, S., Shin, S.S., Kim, Y.C., Jeon, N.J., Shin, H.W., Tae, K.A., Noh, J. H., Yoon, S.C., Hwang, C.S., Seok, S.I.: Adv. Mater. **27**, 4013 (2015)
38. Qin, P., Tanaka, S., Ito, S., Tetreault, N., Manabe, K., Nishino, H., Nazeeruddin, M.K.: M. Graztel Nat. Commun. **5**, 3834 (2014)
39. Ye, S., Sun, W., Li, Y., Yan, W., Peng, H., Bian, Z., Liu, Z., Huang, C.: Nano Lett. **15**, 3723 (2015)
40. Liang, P.W., Chueh, C.C., Williams, S.T., Jen, A.K.-Y.: Adv. Energy Mater. **5**, 1402321 (2015)
41. Kuang, C., Tang, G., Jiu, T., Yang, H., Liu, H., Li, B., Luo, W., Li, X., Zhang, W., Lu, F., Fang, J., Li, Y.: Nano Lett. **15**, 2756 (2015)
42. Bai, S., Wu, Z., Wu, X., Jin, Y., Zhao, N., Chen, Z., Mei, Q., Wang, X., Ye, Z., Song, T., Liu, R., Lee, S.T., Sun, B.: Nano Research. **7**, 1749 (2014)
43. Zhang, L.Q., Zhang, X.W., Yin, Z.G., Jiang, Q., Liu, X., Meng, J.H., Zhao, Y.J., Wang, H.L.: J. Mater. Chem. A **3**, 12133 (2015)
44. de Jong, M.P., van IJzendoorn, L.J., de Voigt, M.J.A.: Appl. Phys. Lett. **77**, 2255–2257 (2000)
45. Li, X., Dar, M.I., Yi, C., Luo, J.S., Tschumi, M., Zakeeruddin, S.M., Nazeeruddin, M.K., Han, H.W., Grätzel, M.: Nat. Chem. **7**, 703 (2015)
46. Smith, I.C., Hoke, E.T., Solis-Ibarra, D., McGehee, M.D., Karunadasa, H.I.: Angew. Chem. Int. Ed. **53**, 11232 (2014)
47. Shao, Y., Xiao, Z., Bi, C., Yuan, Y., Huang, J.S.: Nat. Commun. **5**, 5784 (2014)
48. Xu, J., Buin, A., Ip, A.H., Li, W., Voznyy, O., Comin, R., Yuan, M., Jeon, S., Ning, Z., Mcdowell, J., Kanjanaboos, P., Sun, J., Lan, X., Quan, L., Kim, D.H., Hill, I.G., Maksymovych, P., Sargent, E.H.: Nat. Commun. **6**, 7081 (2015)
49. Bastiani, M.D., Binda, M., Gandini, M., Ball, J., Petrozza, A.: In: Proceedings of MRS Spring Meeting C4.04 (2015)

Flexible Perovskite Solar Cell

Byeong Jo Kim and Hyun Suk Jung

Abstract Recent advent of highly efficient perovskite solar cells whose power conversion efficiency is already over 20 % has triggered exploiting emerging photovoltaic devices for niche photovoltaic market. Since the superior photovoltaic performance is realized with ultrathin perovskite layer, these solar cells are suitable for use as power sources in various flexible electronic devices. Especially, plastic substrate based PSCs can be utilized in niche applications such as portable electronic charger, electronic textiles, and large scale industrial roofing. Compared with other flexible solar cell technologies such as Si, Cu(In,Ga)Se_2, dye-sensitized, and organic photovoltaic solar cells, the PSC is favorable to realize flexible solar cell due to their low temperature and solution process. In this chapter, we discussed the superior physical properties of perovskite materials for use as flexible solar cell materials underlying superior mechanical durability. Recent progress in flexible PSCs with a high photovoltaic performance was also discussed. Moreover, emerging flexible PSCs such as wire-type, ultralight, and stretchable cells were discussed as a potential game changer for niche photovoltaic market.

1 Introduction

Recently, proliferation of wearable electronics has facilitated exploitation of various flexible electronics technologies. Especially, to operate wearable electronic devices, flexible electric power systems such as flexible rechargeable batteries and solar cells has been conceived of as challenging technological issues. In the case of flexible rechargeable batteries, the power-to-weight ratio (or specific power) is of great importance for realizing imperceptible wearable devices with flexibility. Also, flexible and lightweight thin film solar cells have received a great deal of attention for niche applications such as portable electronic charger, electronic textiles, and

B.J. Kim · H.S. Jung (✉)
School of Advanced Materials Science & Engineering, Sungkyunkwan University, Suwon 440-746, Republic of Korea
e-mail: hsjung1@skku.edu

N.-G. Park et al. (eds.), *Organic-Inorganic Halide Perovskite Photovoltaics*,
DOI 10.1007/978-3-319-35114-8_13

large scale industrial roofing due to their convenience of integration and versatile functionality.

To realize flexible thin film solar cells, various types of next-generation photovoltaic technologies such as compound semiconductor, organic, and dye-sensitized solar cells have been employed. However, power conversion efficiency (PCE) of the flexible dye-sensitized, and organic photovoltaic devices are at most about 10 % [1, 2]. To the best of knowledge, only the $Cu(In_{1-x}Ga_x)Se_2$ (CIGS) solar cell using a flexible polyimide substrate was reached to the highest PCE of 20.4 % achieved by Tiwari group [3]. However, the flexible CIGS solar cell was fabricated under an ultra-high vacuum ($\sim 10^{-9}$ Torr) at a high temperature (350 °C). This process is not compatible with a high-throughput and low-cost production owing to the restricted utilization of cheap plastic substrates such as polyethylene terephthalate (PET) and polyethylene naphthalate (PEN). Moreover, the raw materials such as In, Ga, and Se are expensive and not abundant, which restricts the economical viability of CISG solar cells.

The perovskite solar cells (PSCs) employing ultra-thin organometal halide light absorbers with thickness of ~ 1 μm are the most promising candidates as flexible thin film solar cells. The world recorded efficiency of these photovoltaic devices based on a rigid substrate is as high as 21 %, achieved within a few years from the first report of solid state device at 2012 [4]. Most of all, the low temperature and solution-based fabrication process enable to realize the flexible photovoltaic devices based on the plastic substrates. Recently, many groups have attempted to realize plastic substrate-based flexible perovskite solar cells using a low temperature process. The highest efficiency of flexible PSC was reported to be 15.07 % achieved by using $CH_3NH_3PbI_{3-x}Cl_x$ light absorbers [5].

The key challenge to realize flexible PSC is to prepare TiO_2 compact hole blocking layers and/or mesoporous (mp) TiO_2 electron collecting layers at a low temperature (~ 130 °C). Usually, fabrication temperature of TiO_2 layers should be over ~ 500 °C for the excellent hole blocking and electron collecting properties. The process temperature of TiO_2 thin hole blocking layers with $\sim$few tens of nanometer thickness might be lowered by using emerging new technologies such as plasma enhanced atomic layer deposition [6]. However, the mesoporous TiO_2 nanoparticle electron collecting layers with several hundred nanometer thickness are not easily fabricated at a low temperature due to the difficulty in removing residual organic binders and necking TiO_2 nanoparticles. To pass over these critical issues, $CH_3NH_3PbI_{3-x}Cl_x$ light absorbers possessing ~ 1 μm electron diffusion length has been employed [7]. The longer electron diffusion length compared by that of $CH_3NH_3PbI_3$ (~ 140 nm) may lead to removing the mp TiO_2 electron collecting layers, which is suitable to fabricate plastic substrate-based flexible PSCs. Another way is to change the structure of PSC from n-i-p to p-i-n structure that is sometimes called “inverted structure”. In this structure, instead of TiO_2 electron collecting and hole blocking layers, PCBM thin layers that can be prepared at a low temperature are utilized.

In this chapter, the state of art in flexible PSCs is described from viewpoint of solar cell structures (n-i-p and p-i-n). Especially, in n-i-p structure, recent progress

in low temperature preparation technologies of charge collecting and hole blocking layers are covered. The mechanical properties of the flexible perovskite solar cells, also crucial for the real application and commercialization, are discussed. Moreover, emerging flexible PSCs for niche market are introduced.

2 Physical Properties of Perovskite Materials for Flexible Devices

2.1 Advantages of Perovskite Materials for Plastic Solar Cells

For the case of plastic based flexible photovoltaic devices, transparent flexible conductive plastic substrates such as Sn-doped indium oxide/polyethylene naphthalate (ITO/PEN) and Sn-doped indium oxide/polyethylene terephthalate (ITO/PET) have been utilized as substrates. To realize flexible solar cells based on plastic substrates, the fabrication temperature needs to be as low as below 150 °C due to the low glass transition temperature of plastic substrates. Since the highly crystallized organic-inorganic perovskite light absorber films can be fabricated below 150 °C, these PSCs are fairly suitable for realizing plastic based flexible solar cells.

The optical and electrical properties of perovskite materials are beneficial to achieve a high efficiency of flexible solar cell. The extinction coefficient of Perovskite materials is quite high (1.5×10^4 cm^{-1} at 550 nm), which enables to achieve a high photocurrent density with a ultrathin thickness (below 500 nm thickness) [8]. Since ultrathin layer provides higher flexibility than thicker layer, PSC possesses the merit of mechanical tolerance compared to CIGS, DSSC and Si solar cells which contain thick light absorber layer (over 1 μm).

Perovskite materials have ambipolar properties which indicate that Perovskite layer can be replaced as electron transport layer or hole transport layer. These properties are favorable for realizing various types of flexible solar cells [9, 10]. For example, due to the ambipolar characteristics of Perovskite materials, n-i-p or p-i-n structure can be realized.

The excellent mechanical tolerance for Pervskite materials provides PSCs an exceptional flexible durability, which makes the PSCs applicable to the power source of wearable devices. Recent research reported that PSCs are mechanically durable after 1000 cycles bending tests under a bending radius of 10 mm [6]. The details are going to be discussed in “2.2 Mechanical tolerance of flexible perovskite solar cells”.

Flexible solar cells are also capable of being used as building integrated photovoltaic systems (BIPV) such as solar panel window [11]. The bending properties enable the installation of flexible solar panels onto various surface of buildings. In addition to excellent flexibility, the color tunable properties of Perovskite materials

are of great importance for BIPV. The color tunable properties are related to easily changeable bandgap which is simply tuned by changing halide anions (I, Br, Cl and their mixtures) or cations (Pb^{2+}, Sn^{2+} and their combinations). The color of Perovskite materials can vary from dark brown to yellow, corresponding to 1.57 eV and 2.29 in bandgap energy, imparting a "beautiful functionality" to PSCs [12, 13].

2.2 Mechanical Tolerance of Flexible Perovskite Solar Cells

Although flexible PSC shows a high efficiency over 15 %, mechanical flexibility and bending durability of solar cell should be considered. The theoretical prediction of the flexibility of perovskite materials was calculated based on first principles calculations by Feng [14]. The author revealed the elastic properties of perovskite materials, determined by chemical bond of B–X in $CH_3NH_3BX_3$ (B = Sn, Pb; X = Br, I) (Table 1). In addition, he calculated the B/G ratio (B = bulk modulus; G = shear modulus), much higher than 2.0. This ratio implies that perovskite materials retain the mechanical properties under bending, tensile, and compressive force conditions. Also, larger Poisson's ratio of perovskite materials ($\tau > 0.26$) between the rubber's τ (>0.50) and glass's τ (0.18–0.30) is expected that the perovskite materials can possess ductile properties which shows potentials of being used as flexible/stretchable layers on the polymer substrates.

Kim et al. performed bending tests in order to verify the stability of flexible perovskite device against bending radii and cycles (Fig. 1a) [6]. Under the radius of

Table 1 Bulk (B), shear (G) and Young's modulus (E), Poisson's ratio, sound velocity and Debye temperature of $CH_3NH_3BX_3$ (B = Sn, Pb; X = Br, T) materials

Phase	B^{2+}	X^-	B_{VRH} (GPa)	G_{VRH} (GPa)	E (GPa)	τ	B/G	v_l (m/s)	v_t (m/s)	v_m (m/s)	Θ_D (K)
C	Sn	Br	26.2	12.2	37.2	0.26	1.78	3605	2043	2271	272
		I	22.2	12.6	34.5	0.24	1.60	3177	1855	2057	232
	Pb	Br	22.6	10.4	29.1	0.29	1.99	3099	1699	1894	219
		I	16.4	8.7	22.2	0.28	1.89	2612	1455	1620	175
T	Sn	Br	19.5	9.4	26.2	0.28	1.90	3172	1765	1965	230
		I	13.5	6.3	18.2	0.28	1.89	2469	1374	1531	169
	Pb	Br	14.7	5.5	15.1	0.33	2.57	2524	1278	1432	160
		I	12.2	3.7	12.8	0.33	2.52	2135	1087	1218	131
C	Sn	Br	29.2	6.5	24.1	0.36	3.30	3408	1584	1784	213
		I	18.5	4.1	16.7	0.35	2.99	2597	1249	1404	158
	Pb	Br	26.9	9.5	27.9	0.33	2.56	3292	1668	1870	214
		I	18.1	3.6	15.0	0.36	3.30	2494	1159	1305	141

Reprinted with permission from Ref. [14]
VRH Voigt–Reuss–Hill

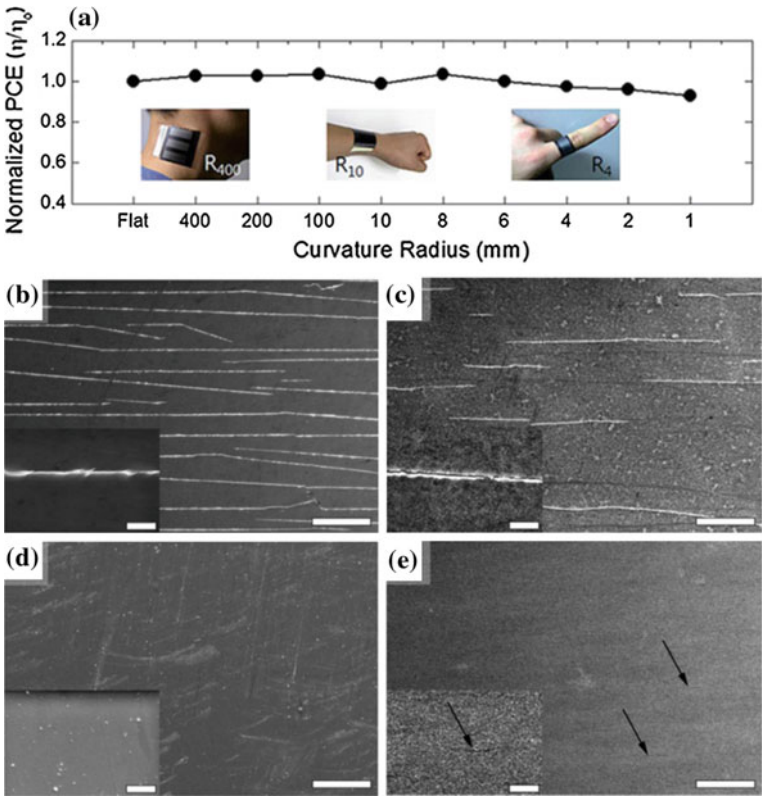

Fig. 1 **a** Normalized PCE measured as bending radius from 400 to 1 mm. The bending radii of 400 mm, 10 mm, and 4 mm is corresponding to human neck, wrist and finger, respectively. The SEM images of the structures, **b** PET/M-In_2O_3, **c** PET/M-In_2O_3/ZnO/$CH_3NH_3PbI_3$, **d** PET/HC-PEDOT, and **e** PET/HC-PEDOT/SC-PEDOT/$CH_3NH_3PbI_3$, after 2000 bending cycles (the scale bars in the low-magnification is 50 μm, in the high-magnification is 5 μm). Reprinted with permission from Refs. [6] (**a**) and [15] (**b–d**)

curvature at 400 to 10 mm, flexible perovskite solar cells, which had structure of PEN/ITO/TiO_x/$CH_3NH_3PbI_{3-x}Cl_x$/Spiro-MeOTAD/Ag, maintained their PCEs during the 1000 bending cycles. For radius of curvature at 4 mm, the PCE significantly decreased by approximately 50 % of initial efficiency after 1000 bending cycles. Since these changes of PCEs were similar with the degradation behaviors of ITO electrodes under application of mechanical force, they performed the in situ resistance-measurement with compressive stain using three different layered structures, i.e., PEN/ITO, PEN/ITO/TiO_x/$CH_3NH_3PbI_{3-x}Cl_x$/Spiro-MeOTAD/Ag and PEN/TiO_x/$CH_3NH_3PbI_{3-x}Cl_x$/Spiro-MeOTAD/Ag. In this experiment, the flexible photovoltaic device with ITO layer exhibited dramatic increase of resistance whereas the resistance of flexible device without ITO did not vary.

This demonstrates that the origin of fatigue was not from the perovskite materials, from the fraction of ITO electrode.

Another study on the bending properties of flexible PSCs without inorganic metal oxide was reported by Kelly et al. (Fig. 1b–e) [15]. The ITO-free flexible PSC using highly conductive PEDOT (HC-PEDOT) as a transparent electrode operated well after 2000 bending cycles whereas the photovoltaic performance of metalized indium oxide (M-In_2O_3)-based PSC was significantly deteriorated. From the results of sheet resistance measurement using perovskite device on both the M-In_2O_3 and HC-PEDOT substrates, they also concluded that the main reason for deterioration of PCE of flexible perovskite solar cell was the formation of cracks from the ITO layer. These results demonstrate that perovskite materials have excellent bending tolerance properties.

3 Recent Progress in Flexible Perovskite Solar Cells

Since the first flexible PSC exhibited an efficiency of 2.64 % in 2013, now the efficiency has increased to more than 15 %. The plastic PEN or PET and metal foils such as Ti and stainless steel have been utilized as substrate materials. Metal foil substrates are durable for heat-treatment process of forming mesoporous and hole blocking metal oxide layers. However, in the case of plastic substrates, the heat-treatment process is restricted due to the glass transition temperature.

Although the cell efficiency for flexible PSC is lower than that for the rigid PSC, the various potential application of flexible PSC has facilitated the research for commercialization. In this section, the 3 types of flexible cells including n-i-p, p-i-n, and metal foil substrates will be discussed (Table 2).

3.1 Flexible Perovskite Solar Cells Based on n-i-p Structure

The n-i-p structure PSCs containing electron transport materials (ETM)/perovskite/hole transport materials (HTM) is hard to be realized as flexible solar cell due to the high temperature necessary to form electron transport layers (also called compact layers) such as TiO_2 and ZnO. Especially, the well crystallized TiO_2 compact layer can be obtained after annealing over 400 °C [37].

The ZnO is a feasible alternative to TiO_2 electron transport layer due to its similar energy level and electrical properties. Also, growth of ZnO nano material based on low temperature has been well known. A ZnO compact layer formed by electrodeposition and ZnO nanorods formed by chemical bath deposition were used as compact layer and electron transport layer, respectively. These were then deposited on PEN/ITO, followed by fabrication of flexible PSCs. This cell was the first generation of flexible PSCs reported by Mathews et al. Even though it showed a low efficiency of 2.62 % (8.90 % on the rigid FTO substrate), it marked the

Table 2 The efficiency chart of various flexible perovskite solar cell as device structures

Device structure	PCE (%)	Refs.
2013		
PET/ITO/c-ZnO/ZnO nanorod/$CH_3NH_3PbI_3$/spiro-MeOTAD/Au	2.62	[16]
PET/ITO/PEDOT:PSS/$CH_3NH_3PbI_{3-x}Cl_x$/[60]PCBM/TiO_x/Al	6.40	[17]
2014		
Stainless steel/c-TiO_2/mp-TiO_2/$CH_3NH_3PbI_3$/Spiro-MeOTAD/CNT sheet	3.30	[18]
PET/AZO/Ag/AZO/PEDOT:PSS/Poly-TPD/$CH_3NH_3PbI_3$/PCBM/AU	7.00	[19]
PET/ITO/PEDOT:PSS/$CH_3NH_3PbI_{3-x}Cl_x$/PCBM/Al	9.20	[20]
PET/ITO/ZnO/$CH_3NH_3PbI_3$/Spiro-MeOTAD/Ag	10.20	[21]
2015		
Ti/c-TiO_2/mp-TiO_2/$CH_3NH_3PbI_3$/Spiro-MeOTAD/ultra-thin Ag	6.15	[22]
Ti/c-TiO_2/mp-TiO_2/$CH_3NH_3PbI_3$/Spiro-MeOTAD/ITO	9.65	[23]
Ti-foil/c-TiO_2/mp-Al_2O_3/$CH_3NH_3PbI_{3-x}Cl_x$/Spiro-MeOTAD/PEDOT:PSS/PET with Ni mesh	10.30	[24]
Ti-wire/TiO_2 nanotube/$CH_3NH_3PbI_{3-x}Cl_x$/Spiro-MeOTAD/CNT sheet	1.12	[25]
Ti-wire/dimple c-TiO_2/mp-TiO_2/$CH_3NH_3PbI_3$/Spiro-MeOTAD/Ag NW	3.85	[26]
CNT fiber/c-TiO_2/mp-TiO_2/$CH_3NH_3PbI_{3-x}Cl_x$/P3HT/SWNT/Ag NW	3.03	[27]
PET/ITO/PEDOT:PSS/$CH_3NH_3PbI_{3-x}Cl_x$/PCBM/ZnO/Ag	4.90	[28]
PET/ITO/c-TiO_2 (ALD)/mp-TiO_2/$CH_3NH_3PbI_3$/Spiro-MeOTAD/Au	7.10	[29]
PET/M-In_2O_3/c-ZnO/$CH_3NH_3PbI_3$/Spiro-MeOTAD/Ag	7.80	[15]
PET/ITO/c-TiO_2 (RF-sputter)/$CH_3NH_3PbI_3$/Spiro-MeOTAD/Au	8.90	[30]
NOA 63/PEDOTLPSS/$CH_3NH_3PbI_{3-x}Cl_x$/PCBM/Gallium-indium eutectic	10.20	[31]
PET foil/PEDOT:PSS//$CH_3NH_3PbI_{3-x}Cl_x$/PCBM/Cr_2O_2/Cr/Au/Polyurethne	12.00	[32]
PEN/ITO/c-TiO_x (ALD)/$CH_3NH_3PbI_3$/Spiro-MeOTAD/Ag	12.20	[6]
PET/ITO/$CH(NH_2)_2PbI_3$/Spiro-MeOTAD/Au	12.70	[33]
PET/ITO/c-TiO_2 (e-beam)/$CH_3NH_3PbI_{3-x}Cl_x$/PTAA/Au	13.50	[34]
PET/ITO/PEDOT:PSS/PEI-HI/$CH_3NH_3PbI_3$/PCBM/LiF/Ag	13.80	[35]
PEN/ITO/Zn_2SnO_4/$CH_3NH_3PbI_3$/PTAA/Au	14.85	[36]
PET/ITO/c-TiO_x (DC sputter)/$CH_3NH_3PbI_{3-x}Cl_x$/Spiro-MeOTAD/Au	15.07	[5]

beginning of the flexible PSCs [16]. Kelly and Liu reported all solution processed flexible PSC which used a ZnO nanoparticle film as an electron transport layer (Fig. 2a, b) [21]. They demonstrated that the effect of thickness of ZnO layer from 0 to 70 nm on the photovoltaic performance. The PSC without ZnO electron transport layer showed a low V_{oc} and FF due to the charge recombination between ITO/perovskite material. At the optimized ZnO thickness of 25 nm, they achieved a PCE of 15.7 % on the rigid substrate and 10.20 % on the PET/ITO substrate.

The atomic layer deposition (ALD) is one of good techniques for preparing compact layer due to the precise control of the film thickness and ability to deposit dense and conformal film. Jung et al. fabricated the 12.2 % flexible PSCs on the

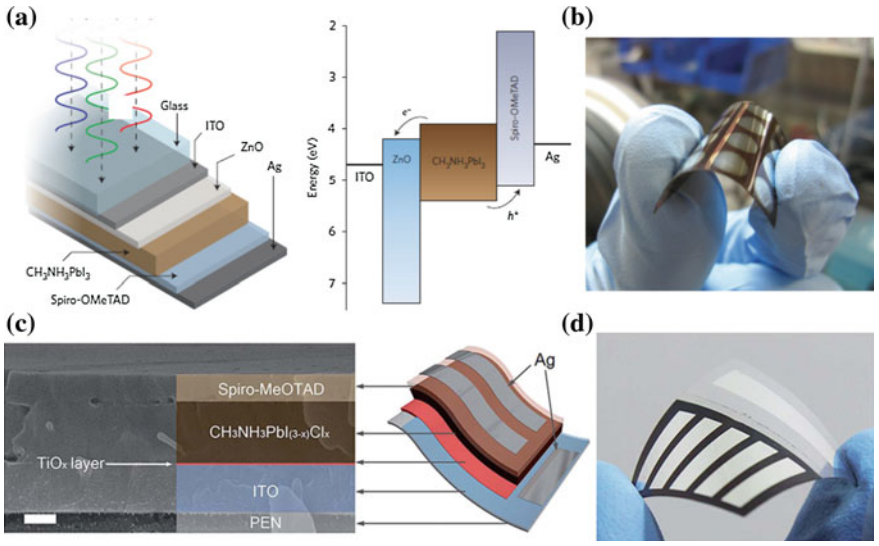

Fig. 2 **a** Device structure, energy level diagram and **b** photograph of low-temperature c-ZnO based flexible perovskite device. **c** Cross-section image, schematics and **d** photograph of low-temperature c-TiO_x based flexible perovskite device. Reprinted with permission from Refs. [21] (**a**, **b**) and [6] (**c**, **d**)

PEN/ITO substrate with amorphous TiO_x compact layer [6]. A 20 nm-thick amorphous TiO_x compact layer deposited by using a plasma enhanced ALD at 80 °C (PEALD) exhibited excellent hole blocking and electron collecting properties (Fig. 2c, d). They observed the PCE maintaining 95 % of the initial value after 1000 bending cycles with a bending radius of 10 mm that is corresponding to bending radius of wrist. This study demonstrates that the flexible PSCs can be used for electrical power source of wearable device. Brown et al. demonstrated large-area (8 cm^2) integrated flexible perovskite photovoltaics module by preparing TiO_2 compact layer by PEALD. The fabricated module was composed of 4 series-connected cell showed PCE of 3.1 % (with 3.39 V of V_{oc}) demonstrating that vacuum deposition method is capable of fabricating large scale flexible perovskite solar modules [29]. Another vacuum technique for compact layer is sputtering system. Li et al. prepared a dense TiO_x compact layer using magnetron sputtering at the room temperature [5]. They demonstrated that TiO_x compact layer possessed a faster electron transport property in comparison with the annealed-TiO_2 compact layer. They showed that the superior electrical properties of TiO_x compact in flexible PSC led to achieving PCE of 15 % (Table 3).

New composition of electron transport layer was explored for fabricating high efficiency flexible PSCs. Seok et al. synthesized well dispersed Zn_2SnO_4(ZSO) nanoparticles at a low temperature (<100 °C) as electron transport layer on flexible PEN/ITO substrate. The PEN/ITO/ZSO film showed higher transmittance

Table 3 The performance parameters of perovskite solar cells with different electron transport layers and substrates

Substrate/ETL	J_{sc} (mA/cm^2)	V_{oc} (V)	FF	PCE (%)
Glass/ITO/am-TiO_2	21.68	1.03	0.72	16.08
PET/ITO/am-TiO_2	20.90	1.03	0.70	15.07
Glass/FTO/an-TiO_2	21.67	1.08	0.69	16.10
Glass/FTO/am-TiO_2	21.87	1.03	0.72	16.22

Reprinted with permission from Ref. [5]
ETL Electron transport layer, *am-TiO_2* amorphous-TiO_2, *an-TiO_2* anatase-TiO_2

compared with bare PEN/ITO substrate over the entire range of visible light due to fairly low refractive index (~1.37) of ZSO film. The PCE of flexible PSC on PEN/ITO/ZSO film was 14.85 % [36].

3.2 Flexible Perovskite Solar Cells Based on p-i-n Structure

The p-i-n structure which is sometimes called "inverted structure" is composed of electron hole transport materials (HTM)/perovskite/transport materials (ETM). Since the electron transport layer does not need to be composed of TiO_2 layer, this structure is relatively easy to incorporate in flexible PSC. The p-i-n structure originates from organic photovoltaics structure. Instead of organic light absorber, the perovskite light absorber is inserted between the hole transport layer (PEDOT:PSS, NiO_x, MoO_x and etc.) and electron transport layer (PCBM, PFN, C60/BCP and etc.). Since conventional process for preparing the electron- and hole transport layers do not require a high temperature annealing process, p-i-n structure has been regarded as a promising flexible PSC structure. The first attempt to prepare p-i-n flexible PSCs was given by Snaith et al. They observed that steady-state photoluminescence of perovskite materials sandwiched into various hole- (NiO, V_2O_5, PEDOT:PSS and Spiro-MeOTAD) and electron transport layer (PCBM, PFN and TiO_2). From selective contacts, p-i-n flexible PSCs composed of PEDOT:PSS/$CH_3NH_3PbI_{3-x}Cl_x$/[60]PCBM/TiO_x/Al on PEN/ITO structure achieved PCE of 6.40 % (Fig. 3) [17]. Yang et al. fabricated a high efficiency p-i-n flexible PSC (9.2 %). They observed PL quenching time at both the interface of PCBM/$CH_3NH_3PbI_{3-x}Cl_x$ and PEDOT:PSS/$CH_3NH_3PbI_{3-x}Cl_x$, and found that charge extraction from PCBM/$CH_3NH_3PbI_{3-x}Cl_x$ is faster than that from PEDOT:PSS/$CH_3NH_3PbI_{3-x}Cl_x$. Also, PL quenching studies of each interface of PCBM/$CH_3NH_3PbI_{3-x}Cl_x$/PEDOT:PSS compared with $CH_3NH_3PbI_{3-x}Cl_x$ demonstrated that high photovoltaics performance was achieved by fast charge separation mechanism at the interface. The flexible perovskite solar cells from this study showed PCE of 9.2 % (Fig. 3b) [20]. Recently, Li et al. discovered the effect of in situ formed $(PEI)_2[PbI_4]$ layered perovskite on the PEDOT:PSS. The newly exploited layers enabled to control the morphology and grain growth of perovskite

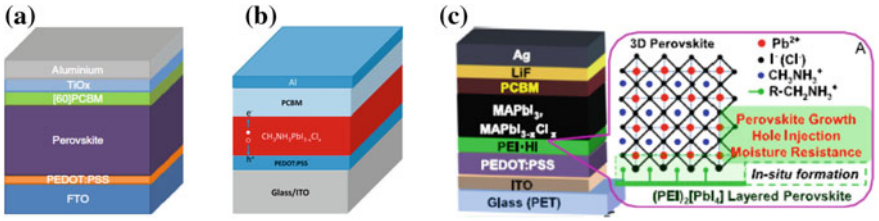

Fig. 3 Schematics and the power conversion efficiencies of the representative p-i-n flexible perovskite solar cells on plastic substrate. In the inverted flexible perovskite, photovoltaic performance was improved by charge separation studies. Reprinted with permission from Refs. [17] (**a**), [20] (**b**) and [35] (**c**)

layer, and reduced the potential energy level difference, thus increasing hole extraction. The improved hole extraction of p-i-n PSCs revealed a balance between the charge separation. This work presented a high PCE of 13.8 % from the p-i-n flexible PSCs (Fig. 3c) [35].

3.3 Metal Substrate-Based Flexible Perovskite Solar Cells

Metal substrates are another potential substrate material for flexible PSC. Due to the superior mechanical and thermal stability, the metal substrate can be an alternative to plastic substrate such as PET/ITO or PEN/ITO. Moreover, the superior electrical conductivity, chemical stability and cost-effectiveness (not using indium in ITO) are beneficial for use as potential substrate materials for flexible PSC. However, the opaque nature of the metal prevents the sunlight passing through substrate to perovskite materials. Therefore, the exploitation of transparent counter electrode possessing a good electrical conductivity with a high optical transmittance is of great importance.

Jun et al. deposited semi-transparent ultra-thin Ag layers as counter electrodes with thickness in the range of 8–20 nm on Ti foil-based flexible PSCs. They observed that the optical transmittance of the Ag layers decreased from 45 to 24 % at the wavelengths of 450–750 nm with the corresponding film thickness (Fig. 4a). The trade-off behavior between optical transmittance and electrical conductivity led to an optimal film thickness of 12 nm, which yielded PCE of 6.15 % [22].

In order to compensate transmittance loss of Ag film electrode and brittle nature of ITO, Jun et al. also explored discontinuous ultra-thin Ag layers inserted into ITO. The Ag nanoparticles (1–2 nm)-embedded ITO exhibited higher transmittance and enhanced mechanical flexibility compared to the bare ITO film or thick Ag film electrode (Fig. 4b). As a result, they achieved the improved PCE of 9.65 % with bending durability [23].

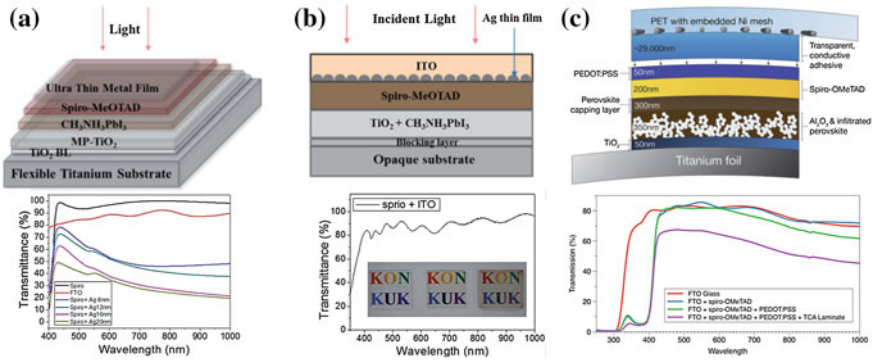

Fig. 4 Transmission spectra for transparent counter electrode of **a** Ultra-thin metal, **b** Ag embedded ITO, **c** Ni mesh embedded PET. Reprinted with permission from Refs. [22] (**a**), [23] (**b**) and [24] (**c**)

A research progress on the metal substrate-based flexible PSC was made by Watson et al. They developed a new cell structure composed of Ti foil/c-TiO_2/mp-Al_2O_3/$CH_3NH3PbI_{3-x}Cl_x$/Spiro-MeOTAD/PEDOT:PSS embedded in a Ni mesh (Fig. 4c). In this study, interlayer of PEDOT:PSS embedded in the Ni mesh increased the current density and FF due to the enhanced electrical conductivity, hence achieving a PCE of 10.3 % with minimal efficiency degradation after repeated bending [24].

4 Emerging Technologies for the Commercialization of Flexible Perovskite Solar Cells

4.1 Fiber-Shaped Perovskite Solar Cells

In addition to bending properties, stretchable and twistable photovoltaic power source will be required for future wearable electronic systems. Fiber-shaped PSCs are one of potential emerging solar cells, which can be applied to wearable electronics (e.g., the self-powering woven e-textiles).

A novel coaxial fiber-shaped PSC was fabricated using stainless steel fiber by Peng et al. (Fig. 5a). A compact layer and mp TiO_2 was prepared by using diluted titanium diisopropoxide bis(acetylacetonate) solution and commercial TiO_2 paste, respectively. Perovskite layer was formed by dip-coating of perovskite precursor solution, followed by annealing at 100 °C for 10 min. Hole transport layer, Spiro-MeOTAD, was coated onto the resultant perovskite layer and then aligned CNT cathode finally wrapped the prepared solar cell. The first fiber-shaped PSC shows a PCE of 3.3 % after optimization, which is higher than PCE of fiber-shaped DSSC or polymer solar cells. Moreover, the PCE remained 95 % of their initial PCE

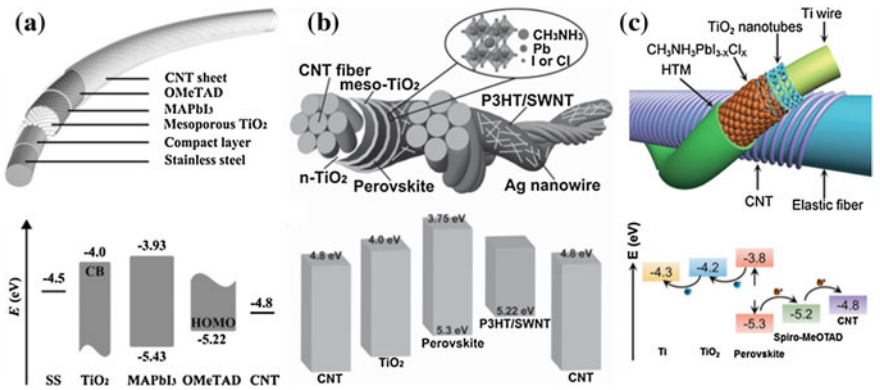

Fig. 5 Various structure of fiber shaped perovskite solar cells on the **a** Stainless steel, **b** CNT fiber, **c** Ti wire with elastic fiber. Reprinted with permission from Refs. [18] (**a**), [27] (**b**) and [25] (**c**)

after 50 bending cycles [18]. Li et al. demonstrated double-twisted PSC by replacing of metal wire electrode with CNT fiber due to their insufficient flexibility, corrosion problem and low active area. Highly flexible CNT fiber was fabricated using spinnable CNT array. Sequentially, compact TiO_2/mp-TiO_2/$CH_3NH_3PbI_{3-x}Cl_x$/P3HT/SWNT/Ag nanowire structure was formed on the CNT fiber (Fig. 5b). Also, they prepared a PMMA sealing layer to protect perovskite layer from external environment. Such CNT fiber based PSCs exhibited a PCE of 3.03 % and long stability (96 h) in the air condition. Also, its mechanical stability was maintained for over 1000 bending cycle without degradation [27]. Peng et al. developed elastic PSC using stretchable CNT-based fiber and spring-like modified Ti wire as two electrodes (Fig. 5c). To optimize stretchable fiber-shaped PSC, 1,8-diiodooctane (DIO) was added to perovskite precursor solution, which made perovskite phase uniform corner-sharing octahedral, and perovskite layer was fabricated by using a electrospray method. The PCE was enhanced to 5.01 % and the efficiency was maintained at 90 % of their initial PCE after 250 stretching times at a strain of 30 % [25]. Those fiber-shaped PSC will be used as electrical power sources for emerging wearable and electronic textiles and advanced next-generation device.

4.2 Ultralight Flexible Perovskite Solar Cells

What will happen if ultralight PSCs are exploited? This innovation will extend the use of solar cell to various applications.

Kaltenbrunner et al. have successfully fabricated ultrathin of 3 μm flexible PSCs including thin flexible plastic substrate, electron-, hole-transport layer, perovskite material, compact layer, electrode and encapsulation layer. DMSO-treated PEDOT:

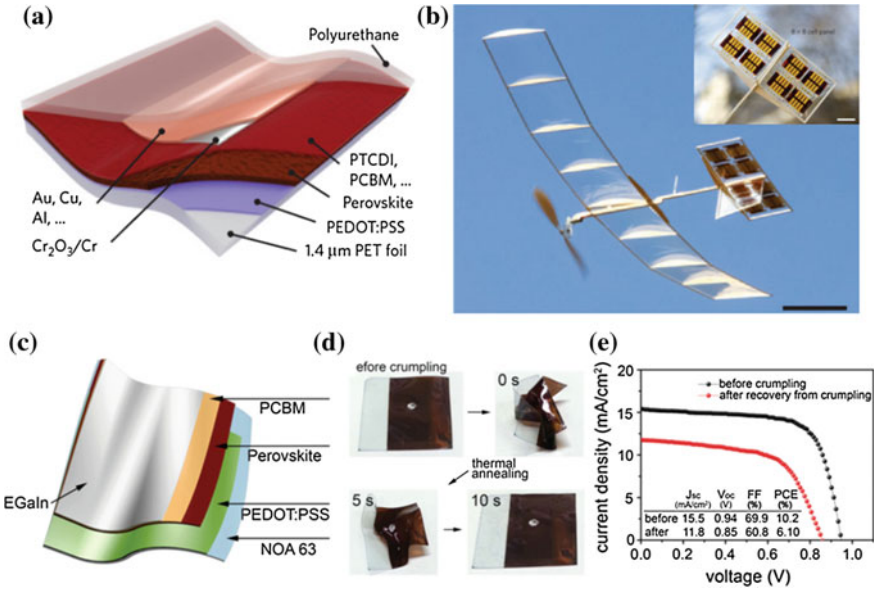

Fig. 6 **a** Schematic of the ultrathin flexible solar cell on the 1.4 μm PET foil, **b** Snapshot of the solar powered aircraft model during outdoor flight (image of the integrated solar panel on the aircraft model in inset). **c** Device schematic of the shape-recoverable perovskite solar cell, **d** the state of device during crumping test, **e** measured *J–V* curve before/after crumping test. Reprinted with permission from Refs. [32] (**a**, **b**) and [31] (**c**–**e**)

PSS as hole transport layer was deposited on the 1.4 μm PET foil, which formed a pinhole-free perovskite layer. An interlayer, a chromium oxide–chromium (Cr_2O_3), provided long stability of PSCs because Cr/Cr_2O_3 was capable of blocking the corrosion reaction such as gold (Au) etching of AuI_2^- or AuI_3, between metallic top contact and iodine of perovskite layer (Fig. 6a). The fabricated cell showed 20 % degradation of PCE after 8 h' operation in the air without any encapsulation. Also, the fabricated photovoltaics exhibited the unchanged performance after applying radial compression up to down 44 % in area. Moreover, aircraft containing a d. c. motor was operated using ~75 mW power output from a connected flexible solar panel (under AM 1.5 irradiance) under outdoor sun condition (Fig. 6b) [32].

The shape recoverable PSC is another emerging technology, and was investigated by Ko et al. A Noland optical adhesion 63 (NOA 63), shape recoverable polymer, was used as substrate materials (Fig. 6c). The fabricated solar cells could recover their shapes after sub-millimeter bending radii. The secret of recoverable solar cell was a Ga–In eutectic alloy stretchable electrode that hindered fracture of perovskite layer (Fig. 6d, e). The best PCE of 10.75 % was maintained without significant degradation of efficiency after bending 1 mm bending radius. Furthermore, the fabricated solar cell maintained the 60 % of initial PCE after 50 crumpling cycles [31].

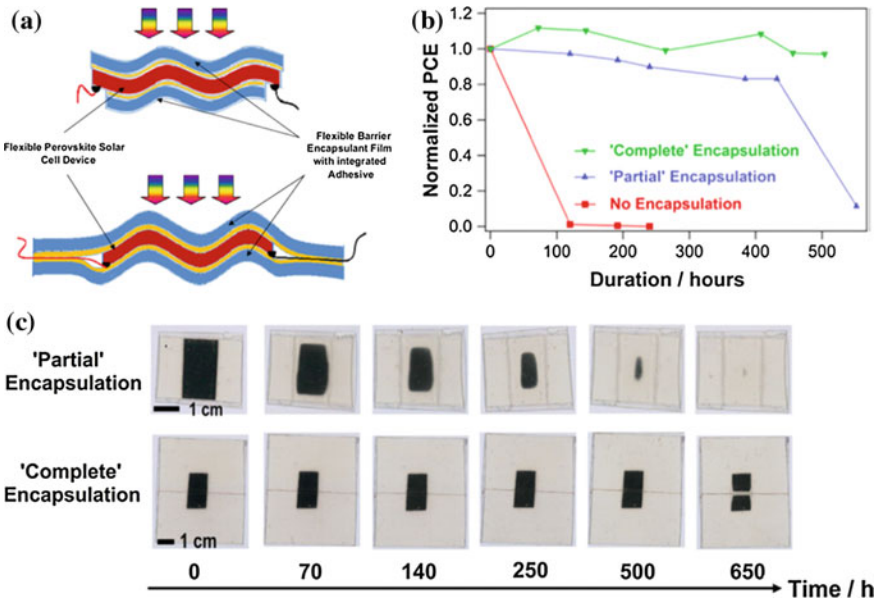

Fig. 7 **a** Schematic of 'partial' (*upper*) and 'complete' (*lower*) encapsulation architectures. **b** Normalized PCE of partially-, completely- and non-encapsulated flexible perovskite solar cell as a function of time in the air condition. **c** the photographs of encapsulated moisture-sensitive Ca film using partially and completely encapsulated flexible PSC under ambient condition. Reprinted with permission from Ref. [38]

The advent of ultralight and stretchable PSCs will definitely encourage the commercialization of PSCs. However, short-term stability of PSC regarding low moisture and oxygen stability is a big burden, which can be circumvented using encapsulation technology. In flexible solar cell, encapsulation is in different situation with rigid substrate solar cell. Recently, Weerasinghe et al. have suggested encapsulation architecture for flexible PSC. In order to protect perovskite layer from moisture and oxygen, they adopted two encapsulation architectures which were called 'partially' and 'completely' (Fig. 7a). Transparent plastic barrier, Viewbarrier® (Mitsubishi plastic, Inc), covered the metal electrode side. As a pre-conditioning step, moisture and oxygen in the cell were removed under vacuum system for 12 h. The encapsulation was completed using 467 MP 3M™ adhesion transfer tape, carried out in a N_2 filled glove box. The effect of encapsulation was verified using a flexible PSC composed of PET/IZO/c-TiO_2/$CH_3NH_3PbI_3$/Spiro-MeOTAD/Au structure in the ambient condition. Complete encapsulation prolonged the life time of cell compared with 'No encapsulation' and 'partial encapsulation' after 500 h (Fig. 7b). Also, to understand degradation behavior, moisture- and oxygen-sensitive Ca films were encapsulated by aforementioned two different methods, and then the degradation behavior was monitored for about 4 weeks. The results of Ca film test showed that the partial encapsulation system was not able to completely block the ingress of moisture and oxygen (Fig. 7c) [38].

5 Summary

In this chapter, we discussed the physical properties of perovskite light absorbing materials for realizing a good flexible solar cell with durable mechanical properties. Also, recent technical progress in plastic substrate-based and metal-foil-based flexible solar cells was introduced. In the case of n-i-p structured flexible cell, low temperature process of electron collecting and hole blocking layer with a good charge transport properties were discussed. The p-i-n structured cell has employed various electron and hole transport materials and many researches have focused on exploiting new transporting materials and optimizing cell efficiency. The various transparent counter electrode materials were discussed for the metal foil-based flexible cells. Moreover, emerging flexible perovskite solar cells such as wire-shaped, ultralight, and stretchable cells were also mentioned to facilitate commercialization of perovskite solar cells.

Since the ultrathin perovskite layer is thinner than copper indium gallium selenide (CIGS) solar cells and is capable of exhibiting a superior photovoltaic performance, the final commercialization product of perovskite solar cell will consist of a plastic based flexible module. To realize commercialization of flexible solar cell, the long term stability issue and high throughput fabrication issue should be solved.

References

1. Yun, H.-G., Bae, B.-S., Kang, M.G.: A simple and highly efficient method for surface treatment of ti substrates for use in dye-sensitized solar cells. Adv. Energy Mater. **1**, 337–342 (2011). doi:10.1002/aenm.201000044
2. Huang, J., Li, C.-Z., Chueh, C.-C., et al.: 10.4 % Power conversion efficiency of ITO-free organic photovoltaics through enhanced light trapping configuration. Adv. Energy. Mater. **5**, n/a–n/a (2015). doi:10.1002/aenm.201500406
3. Chirilă, A., Reinhard, P., Pianezzi, F., et al.: Potassium-induced surface modification of Cu(In, Ga)Se_2 thin films for high-efficiency solar cells. Nat. Mater. **12**, 1107–1111 (2013). doi:10.1038/nmat3789
4. Research Cell Efficiency Records, National Center for Photovoltaics, Denver. http://www.nrel.gov/ncpv/images/efficiency_chart.jpg (2016). Accessed 09 Mar 2016
5. Yang, D., Yang, R., Zhang, J., et al.: High efficiency flexible perovskite solar cells using superior low temperature TiO_2. Energy Environ. Sci. **8**, 3208–3214 (2015). doi:10.1039/C5EE02155C
6. Kim, B.J., Kim, D.H., Lee, Y.-Y., et al.: Highly efficient and bending durable perovskite solar cells: toward a wearable power source. Energy Environ. Sci. **8**, 916–921 (2015). doi:10.1039/C4EE02441A
7. Stranks, S.D., Eperon, G.E., Grancini, G., et al.: Electron-hole diffusion lengths exceeding 1 micrometer in an organometal trihalide perovskite absorber. Science **342**, 341–344 (2013). doi:10.1126/science.1243982
8. Im, J.-H., Lee, C.-R., Lee, J.-W., et al.: 6.5 % efficient perovskite quantum-dot-sensitized solar cell. Nanoscale **3**, 4088–4096 (2011). doi:10.1039/c1nr10867k
9. Ke, W., Wan, J., Tao, H., et al.: Efficient hole-blocking layer-free planar halide perovskite thin-film solar cells. Nat. Commun. **6**, 1–7 (2015). doi:10.1038/ncomms7700

10. Mei, A., Li, X., Liu, L., et al.: A hole-conductor–free, fully printable mesoscopic perovskite solar cell with high stability. Science **345**, 295–298 (2014). doi:10.1126/science.1254763
11. Eperon, G.E., Burlakov, V.M., Goriely, A., Snaith, H.J.: Neutral color semitransparent microstructured perovskite solar cells. ACS Nano **8**, 591–598 (2014). doi:10.1021/nn4052309
12. Suarez, B., Gonzalez-Pedro, V., Ripolles, T.S., et al.: Recombination study of combined halides (Cl, Br, I) perovskite solar cells. J. Phys. Chem. Lett. **5**, 1628–1635 (2014). doi:10.1021/jz5006797
13. Noh, J.H., Im, S.H., Heo, J.H., et al.: Chemical management for colorful, efficient, and stable inorganic-organic hybrid nanostructured solar cells. Nano Lett. **13**, 1764–1769 (2013). doi:10.1021/nl400349b
14. Feng, J.: Mechanical properties of hybrid organic-inorganic CH3NH3BX3 (B = Sn, Pb; X = Br, I) perovskites for solar cell absorbers. APL Mater. **2**, 081801–081809 (2014). doi:10.1063/1.4885256
15. Poorkazem, K., Liu, D., Kelly, T.L.: Fatigue resistance of a flexible, efficient, and metal oxide-free perovskite solar cell. J. Mater. Chem. A: Mater. Energy Sustain. **3**, 9241–9248 (2015). doi:10.1039/C5TA00084J
16. Kumar, M.H., Yantara, N., Dharani, S., et al.: Flexible, low-temperature, solution processed ZnO-based perovskite solid state solar cells. Chem. Commun. **49**, 11089–11093 (2013). doi:10.1039/c3cc46534a
17. Docampo, P., Ball, J.M., Darwich, M., et al.: Efficient organometal trihalide perovskite planar-heterojunction solar cells on flexible polymer substrates. Nat. Commun. **4**, 1–6 (2013). doi:10.1038/ncomms3761
18. Qiu, L., Deng, J., Lu, X., et al.: Integrating perovskite solar cells into a flexible fiber. Angew. Chem. Int. Ed. **53**, 10425–10428 (2014). doi:10.1002/anie.201404973
19. Roldán-Carmona, C., Malinkiewicz, O., Soriano, A., et al.: Flexible high efficiency perovskite solar cells. Energy Environ. Sci. **7**, 994–1004 (2014). doi:10.1039/c3ee43619e
20. You, J., Hong, Z., Yang, Y.M., et al.: Low-temperature solution-processed perovskite solar cells with high efficiency and flexibility. ACS Nano **8**, 1674–1680 (2014). doi:10.1021/nn406020d
21. Liu, D., Kelly, T.L.: Perovskite solar cells with a planar heterojunction structure prepared using room-temperature solution processing techniques. Nat. Photonics **8**, 133–138 (2013). doi:10.1038/nphoton.2013.342
22. Lee, M., Jo, Y., Kim, D.S., Jun, Y.: Flexible organo-metal halide perovskite solar cells on a Ti metal substrate. J. Mater. Chem. A: Mater. Energy Sustain. **3**, 4129–4133 (2015). doi:10.1039/C4TA06011C
23. Lee, M., Jo, Y., Kim, D.S., et al.: Efficient, durable and flexible perovskite photovoltaic devices with Ag-embedded ITO as the top electrode on a metal substrate. J. Mater. Chem. A: Mater. Energy Sustain. **3**, 14592–14597 (2015). doi:10.1039/C5TA03240G
24. Troughton, J., Bryant, D., Wojciechowski, K., et al.: Highly efficient, flexible, indium-free perovskite solar cells employing metallic substrates. J. Mater. Chem. A: Mater. Energy Sustain. **3**, 9141–9145 (2015). doi:10.1039/C5TA01755F
25. Deng, J., Qiu, L., Lu, X., et al.: Elastic perovskite solar cells. J. Mater. Chem. A: Mater. Energy Sustain. **3**, 21070–21076 (2015). doi:10.1039/C5TA06156C
26. Lee, M., Ko, Y., Jun, Y.: Efficient fiber-shaped perovskite photovoltaics using silver nanowires as top electrode. J. Mater. Chem. A: Mater. Energy Sustain. **3**, 19310–19313 (2015). doi:10.1039/C5TA02779A
27. Li, R., Xiang, X., Tong, X., et al.: Wearable double-twisted fibrous perovskite solar cell. Adv. Mater. **27**, 3831–3835 (2015). doi:10.1002/adma.201501333
28. Schmidt, T.M., Larsen-Olsen, T.T., Carlé, J.E., et al.: Upscaling of perovskite solar cells: fully ambient roll processing of flexible perovskite solar cells with printed back electrodes. Adv. Energy Mater. **5**, n/a–n/a (2015). doi:10.1002/aenm.201500569
29. Di Giacomo, F., Zardetto, V., D'Epifanio, A., et al.: Flexible perovskite photovoltaic modules and solar cells based on atomic layer deposited compact layers and UV-irradiated TiO_2

scaffolds on plastic substrates. Adv. Energy Mater. **5**, n/a–n/a (2015). doi:10.1002/aenm.201401808
30. Chen, C., Cheng, Y., Dai, Q., Song, H.: Radio frequency magnetron sputtering deposition of TiO_2 thin films and their perovskite solar cell applications. Sci. Rep. 1–12 (2015). doi:10.1038/srep17684
31. Park, M., Kim, H.J., Jeong, I., et al.: Mechanically recoverable and highly efficient perovskite solar cells: investigation of intrinsic flexibility of organic-inorganic perovskite. Adv. Energy Mater. **5**, n/a–n/a (2015). doi:10.1002/aenm.201501406
32. Kaltenbrunner, M., Adam, G., Głowacki, E.D., et al.: Flexible high power-per-weight perovskite solar cells with chromium oxide–metal contacts for improved stability in air. Nat. Mater. **14**, 1032–1039 (2015). doi:10.1038/nmat4388
33. Xu, X., Chen, Q., Hong, Z., et al.: Working mechanism for flexible perovskite solar cells with simplified architecture. Nano Lett. **15**, 6514–6520 (2015). doi:10.1021/acs.nanolett.5b02126
34. Qiu, W., Paetzold, U.W., Gehlhaar, R., et al.: An electron beam evaporated TiO_2 layer for high efficiency planar perovskite solar cells on flexible polyethylene terephthalate substrates. J. Mater. Chem. A: Mater. Energy Sustain. **3**, 22824–22829 (2015). doi:10.1039/C5TA07515G
35. Yao, K., Wang, X., Xu, Y.-X., Li, F.: A general fabrication procedure for efficient and stable planar perovskite solar cells: morphological and interfacial control by in-situ-generated layered perovskite. Nano Energy **18**, 165–175 (2015). doi:10.1016/j.nanoen.2015.10.010
36. Shin, S.S., Yang, W.S., Noh, J.H., et al.: High-performance flexible perovskite solar cells exploiting Zn_2SnO_4 prepared in solution below 100 °C. Nat. Commun. **6**, 1–8 (2015). doi:10.1038/ncomms8410
37. Jung, H.S., Park, N.-G.: Perovskite solar cells: from materials to devices. Small **11**, 10–25 (2014). doi:10.1002/smll.201402767
38. Weerasinghe, H.C., Dkhissi, Y., Scully, A.D., et al.: Encapsulation for improving the lifetime of flexible perovskite solar cells. Nano Energy **18**, 118–125 (2015). doi:10.1016/j.nanoen.2015.10.006

Inorganic Hole-Transporting Materials for Perovskite Solar Cell

Seigo Ito

1 Introduction

Organo-lead halide perovskites have attracted much attention for solar cell applications due to their high-efficiency—over 20 %—and the low-cost of fabrication without vacuum processing [1–4]. The main research has been performed using organic hole conductors (mostly, 2,2′,7,7′-tetrakis(*N*,*N*′-di-p-methoxyphenylamine)-9,9′-spirobifluorene (spiro-OMeTAD) and poly-[3-hexylthiophene-2,5-diyl] (P3HT)) in an attempt to build efficient hybrid perovskite solar cells. However, the organic hole-transporting materials (HTM) used are normally quite expensive due to complicated synthesis procedures or high purity requirements. Moreover, the instability of these organic compounds has been a major issue with regard to commercial applications. Therefore, instead of organic materials, research of stable and low-cost inorganic materials is very significant for large-scale industrial applications.

In this chapter of book, several inorganic HTM in perovskite solar cells have been reviewed: CuSCN, CuI, Cu_2O, CuO, NiO, MoO_x, and carbon materials (including graphene and carbon nanotube (CNT)). Already, the Chen-Guo group (NCKU, Taiwan) [5] published a good review paper entitled "Inorganic P-type Contact Materials for Perovskite-based Solar Cells" one year before. Hence, this chapter provides new results in this field of inorganic p-type materials for perovskite solar cells with a different viewpoint from the review paper by the Chen-Guo group [5]. Each photovoltaic result which will be introduced in this chapter has been summarized in Table 1.

For reviewing this field, it is necessary to categorize structures by semiconductor deposition order. The semiconductor type attached on TCO should be mentioned

S. Ito (✉)
Department of Materials and Synchrotron Radiation Engineering, Graduate School of Engineering, University of Hyogo, 2167 Shosha, Himeji, Hyogo 671-2280, Japan
e-mail: itou@eng.u-hyogo.ac.jp

N.-G. Park et al. (eds.), *Organic-Inorganic Halide Perovskite Photovoltaics*,
DOI 10.1007/978-3-319-35114-8_14

Table 1 Photovoltaic characteristics of perovskite solar cells using inorganic HTM

Refs.	HTM	Structure	HTM deposition	Cell configuration	V_{oc} (V)	J_{sc} (mA $cm^{-2)}$	FF	Eff. (%)
[8]	carbon	Multi-layered n-i-p	Screen printing	FTO/bl-TiO_2/mp-TiO_2+PVK/mp-ZrO_2+PVK/C	0.878	12.4	0.61	6.64
[9]	carbon	Multi-layered n-i-p	Screen printing	FTO/bl-TiO_2/mp-TiO_2+PVK/mp-ZrO_2+PVK/C	0.858	22.8	0.66	12.84
[10]	carbon	Multi-layered n-i-p	Screen printing	FTO/bl-TiO_2/mp-TiO_2+PVK/mp-ZrO_2+PVK/C	0.894	18.06	0.72	11.63
[11]	carbon	Multi-layered n-i-p	Screen printing	FTO/bl-TiO_2/mp-TiO_2+PVK/mp-ZrO_2+PVK/C	0.900	20.45	0.72	13.14
[12]	carbon	Multi-layered n-i-p	Screen printing	FTO/bl-TiO_2/mp-TiO_2+PVK/mp-ZrO_2+PVK/C	0.867	15.24	0.54	7.08
[17]	CuI	Mesoscopic n-i-p	Doctor blading	FTO/bl-TiO_2/mp-TiO_2/PVK/CuI/Au	0.55	17.8	0.62	6.0
[18]	CuI	Planar n-i-p	Doctor blading	FTO/bl-TiO_2/PVK/CuI/graphite/Cu	0.78	16.7	0.57	7.5
[19]	CuI	Planar p-i-n	Spin coating	FTO/CuI/pvk/PCBM/Al	1.04	21.06	0.62	13.58
[20]	CuSCN	Mesoscopic n-i-p	Doctor blading	FTO/bl-TiO_2/mp-TiO_2/PVK/CuSCN/Au	0.63	14.5	0.53	4.85
[21]	CuSCN	Planar n-i-p	Drop casting	FTO/bl-TiO_2/PVK/CuSCN/Au	0.727	18.53	0.617	6.4
[22]	CuSCN	Mesoscopic n-i-p	Doctor blading	FTO/bl-TiO_2/mp-TiO_2/PVK/CuSCN/Au	1.016	19.7	0.62	12.4
[26]	CuSCN	Planar n-i-p	Doctor blading	FTO/bl-TiO_2/PVK/CuSCN/Au	0.97	18.42	0.40	7.19
[32]	CuSCN	Planar p-i-n	Electrodeposition	FTO/CuSCN/PVK/PCBM/Ag	0.677	8.7	–	3.8
[33]	CuSCN	Planar p-i-n	Electrodeposition	ITO/CuSCN/PVK/$C_6$0/BCP/Ag	1.00	21.9	0.758	16.6
[34]	CuSCN	Planar p-i-n	Spin coating	ITO/CuSCN/PVK/PCBM/LiF-Ag	1.06	15.76	0.632	10.5
[35]	CuSCN	Planar p-i-n	Spin coating	ITO/CuSCN/PVK/PCBM/$C_6$0/Ag (25 % visible transmittance)	1.07	12.2	0.76	10.22
[36]	Cu_2O	Planar p-i-n	Spin coating	ITO/Cu_2O/PVK/PCBM/Ca-Al	1.07	16.52	0.755	13.35
[36]	CuO	Planar p-i-n	Spin coating	ITO/CuO/PVK/PCBM/Ca-Al	1.06	15.82	0.725	12.61
[39]	NiO	Planar p-i-n	Spin coating	ITO/NiO/PVK/PCBM/BCP/Al	0.92	12.43	0.68	7.8
[40]	NiO	Mesoscopic p-i-n	Spin coating	ITO/NiO_x/nc-NiO/PVK/PCBM/BCP/Al	1.040	13.24	0.69	9.51
[41]	NiO	Mesoscopic p-i-n	Screen printing	FTO/bl-NiO/nc-NiO/PVK/PCBM/Al	0.830	4.94	0. 35	1.50
[42]	NiO	Planar p-i-n	Spin coating	ITO/NiO/CH3NH3PbI3/PCBM/Al	1.05	15.4	0.48	7.6
[32]	NiO	Planar p-i-n	Electrodeposition	FTO/NiO/PVK/PCBM/Ag	0.786	14.2	0.65	7.26

(continued)

Table 1 (continued)

Refs.	HTM	Structure	HTM deposition	Cell configuration	V_{oc} (V)	J_{sc} (mA $cm^{-2)}$	FF	Eff. (%)
[43]	NiO	Planar p-i-n	Spin coating	FTO/NiO/PVK/PCBM/Au	0.882	16.27	0.635	9.11
[44]	NiO	Planar p-i-n	Spin coating	ITO/NiOx/PVK/ZnO/Al	1.01	21.0	0.760	16.1
[45]	NiO	Mesoscopic p-i-n	Sputtering	ITO/bl-NiOx/nc-NiO/PVK/PCBM/BCP/Al	0.96	19.8	0.61	11.6
[46]	NiO	Planar p-i-n	Sputtering	FTO/NiO/PVK/PCBM/BCP/Au	1.10	15.17	0.59	9.83
[47]	NiO	Mesoscopic p-i-n	Pulsed laser deposition	ITO/NiO/PVK/PCBM/LiF-Al	1.06	20.2	0.81	17.3
[48]	NiO	Planar p-i-n	Spin coating	ITO/Cu-doped NiO/PVK/PCBM/Ag	1.08	0.66	17.38	12.26
[49]	NiO	Mesoscopic p-i-n	Spray pyrolysis deposition	FTO/NiO/meso-AL2O3+PVK/PCBM/BCP/Ag	1.04	18.0	0.72	13.5
[50]	NiO	Planar p-i-n	Spray pyrolysis deposition	FTO/NiMgLiO/PVK/PCBM/Ti(Nb)Ox/Ag (1.017 cm^2 cell size, certified)	1.090	20.96	0.668	15.00
[51]	NiO	Planar p-i-n	Spin coating	ITO/NiO+PEDOT/PVK/PCBM/Ag	1.04	20.1	0.72	15.1
[52]	NiO	Multi-layered n-i-p	Screen printing	FTO/bl-TiO_2/mp-TiO_2+PVK//mp-NIO+PVK/C	0.890	18.2	0.71	11.4
[53]	NiO	Multi-layered n-i-p	Screen printing	FTO/bl-TiO_2/ mp-TiO_2+PVK/mp-ZrO_2+PVK/mp-NIO+PVK/C	0.917	21.36	0.76	14.9
[54]	NiO	Multi-layered n-i-p	Screen printing	FTO/bl-TiO_2/ mp-TiO_2+PVK/mp-Al_2O_3+PVK/mp-NIO+PVK/C	0.915	21.62	0.76	15.03
[55]	MoO_x	Planar n-i-p	Vacuum thermal evaporation	FTO/TiO_2/PVK/spiro-OMeTAD/MoO_x/Al	0.990	19.55	0.590	11.42
[56]	MoO_3	Planar n-i-p	Vacuum thermal evaporation	ITO/ZnO/PVK/spiro-OMeTAD/MoO_3/Ag	1.04	22.4	0.574	13.4
[57]	MoO_3	Planar p-i-n	Spin coating	ITO/MoO_3/PEDOT:PSS/PVK/C_{60}/Bphen/Ag	1.00	21.49	0.69	14.87
[58]	MoO_x	Planar n-i-p	Mesoporous n-i-p	FTO/TiO_2/PVK/spiro-OMeTAD/MoO_x/Ag	0.938	18.5	0.67	11.6
[58]	MoO_x	Planar n-i-p	Mesoporous n-i-p	FTO/TiO_2/PVK/spiro-OMeTAD/MoO_x/ITO (transparent)	0.821	14.5	0.519	6.2

(continued)

Table 1 (continued)

Refs.	HTM	Structure	HTM deposition	Cell configuration	V_{oc} (V)	J_{sc} (mA $cm^{-2)}$	FF	Eff. (%)
[59]	MoO_3	Planar p-i-n	Vacuum thermal evaporation	ITO/MoO_3/NPB/PVK/C60/BCP/Al	1.12	18.1	0.68	13.7
[61]	Carbon	Mesoporous n-i-p	Doctor blading	FTO/TiO_2/PVK/Carbon	0.80	21.02	0.54	9.08
[62]	Carbon	Planar n-i-p	Doctor blading	FTO/TiO_2/PVK/Carbon	0.77	18.56	0.56	8.07
[63]	Carbon	Planar n-i-p	Inkjet printing	FTO/TiO_2/PVK/Carbon	0.95	17.20	0.71	11.60
[64]	Carbon	Mesoporous n-i-p	Spin coating	FTO/TiO_2/PVK/Carbon	1.01	14.20	0.60	8.61
[65]	Carbon	Mesoporous n-i-p	Rolling transfer	FTO/TiO_2/PVK/Carbon (candle soot)	0.90	17.00	0.72	11.02
[66]	Carbon	Mesoporous n-i-p	Doctor blading	FTO/TiO_2/PVK/Carbon	0.90	16.78	0.55	8.31
[67]	Carbon	Mesoporous n-i-p	Hot press	FTO/TiO_2/PVK/Carbon/Al	1.002	21.30	0.634	13.53
[68]	Carbon	Mesoporous n-i-p	Hot press	FTO/TiO_2/PVK/Carbon/graphite sheet	0.952	18.73	0.572	10.20
[69]	graphene oxide	Planar p-i-n	Spin coating	ITO/graphene oxide/PVK/PCBM/ZnO/Al	0.99	15.59	0.72	11.11
[70]	CNT film	Mesoporous n-i-p	Attaching	FTO/TiO_2/PVK/CNT film	0.88	15.46	0.51	6.87
[71]	reduced graphene oxide	Planar p-i-n	Spin coating	ITO/reduced graphene oxide/PCBM/PCB/Ag	0.98	15.4	0.716	10.8
[72]	multi-layered graphene	Mesoporous n-i-p	Spin coating	FTO/TiO_2/PVK/multi-layered graphene	0.943	16.7	0.73	11.5
[73]	Thiolated nano graphene	Mesoporous n-i-p	Spin coating	FTO/TiO_2/PVK/thiolated nano graphene	0.95	20.56	0.6579	12.81
[74]	Graphene oxide	Mesoporous n-i-p	Spin coating	FTO/TiO_2/PVK/graphene oxide/spiro-OMeTAD/Au (stacked with organic HTM, improving wettability)	1.04	20.2	0.73	15.1
[70]	CNT film	Mesoporous n-i-p	Attaching	FTO/TiO_2/PVK/CNT film+Spiro OMeTAD (for transparent conducting material with organic HTM)	1.00	18.1	0.55	9.90
[75]	Graphene	Planar n-i-p	Chemical vapor deposition and transferred	FTO/TiO_2/PVK/spiro-OMeTAD/PEDOT:PSS/graphene (for transparent conducting layer stacked with organic-HTM, transparent to be bifacial)	0.960	19.17	0.672	12.37

(continued)

Table 1 (continued)

Refs.	HTM	Structure	HTM deposition	Cell configuration	V_{oc} (V)	J_{sc} (mA $cm^{-2)}$	FF	Eff. (%)
[76]	Graphene	Planar n-i-p	Chemical vapor deposition	FTO/TiO2/PVK/spiro-OMeTAD/graphene (for transparent conducting layer stacked with organic HTM, for tandem with Si)	0.90	12.56	0.55	6.2
[77]	Single-walled CNT	Planar p-i-n	Chemical vapor deposition and transferred	Single-walled-CNT/PEDOT:PSS/PVK/PCBM/Al (transparent-conducting substrate stacked with organic HTM)	0.79	14.9	0.54	6.32
[78]	CNT	Mesoporous n-i-p	Chemical vapor deposition and transferred	Ti foil/TiO_2 nanotube/PVK/spiro-OMeTAD+CNT (for transparent-conducting layer with organic HTM)	0.99	14.36	0.68	8.31
[79]	Graphene oxide	Planar p-i-n	Spin coating	ITO/(mixed with organic HTM)	0.88	19.18	0.705	11.90
[80]	SWCNT	Mesoporous n-i-p	Spin coating	FTO/TiO_2/mp-Al_2O_3+PVK/SWCNT+/ spiro-OMeTAD/Ag (mixed with organic HTM)	1.02	21.4	0.71	15.4
[81]	SWCNT	Mesoporous n-i-p	Spin coating	FTO/TiO_2/mp-Al_2O_3+PVK/SWCNT +P3HT-PMMA/Ag (mixed with organic HTM, with waterproof)	1.02	22.71	0.66	15.3
[82]	Bamboo-structured CNT	Mesoporous n-i-p	Spin coating	FTO/TiO_2/PVK/bamboo-structured CNT +P3HT/Au (mixed with organic HTM)	0.86	18.75	0.52	8.3
[83]	MWCNT	Planar n-i-p	Spin coating	FTO/TiO_2/PVK/MWCNT+spiro-OMeTAD/Au (mixed with organic HTM)	–	–	–	15.1
[84]	Iodide-reduced graphene oxide	Mesoporous n-i-p	Spin coating	FTO/TiO_2/PVK/Iodide-reduced graphene oxide +spiro-OMeTAD/Au (mixed with organic HTM)	0.910	16.73	0.61	9.31

The order of the contents in the table is related to that in the main text

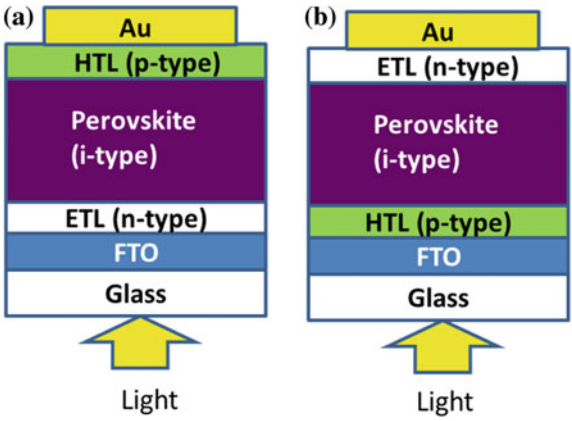

Fig. 1 Types of perovskite solar cells; **a** n-i-p type, and **b** p-i-n type (*HTM* hole-transporting material, *ETL* electron-transporting material)

first. The structure of perovskite solar cells depicted as in Fig. 1a is mentioned as an "n-i-p" structure, which has been the original and conventional one in the field of perovskite solar cells [1–4]. For this n-i-p structure, basically, an n-type inorganic metal-oxide semiconductor (TiO_2) and a p-type organic semiconductor (spiro-OMeTAD and PTAA) have been utilized. On the other hand, the structure of Fig. 1b is mentioned as a "p-i-n" structure, which has been developed in the field of perovskite solar cells using inorganic (metal oxide) p-type and organic n-type materials, called as "inverted structure." The structures of n-i-p or p-i-n are determined by the deposition procedure to the substrate. For example, metal oxides should be deposited before perovskite deposition because of the high temperature annealing and/or of the solvents for oxide-precursor deposition, which can dissolve the perovskite layer.

Another categorizing point is the nanostructure of perovskite solar cells. The conventional and original structure is a "mesoscopic" structure (Fig. 2a), which has utilized a nanocrystal-oxide scaffold layer for perovskite spin-coating deposition. This structure came from solid-state dye-sensitized solar cells (DSCs) [6, 7]. Without nanocrystal metal oxides, the perovskite solar cells can form a "planar" structure (Fig. 2b). As the third type of perovskite solar cells, the "multi-porous-layered" structure is depicted (Fig. 2c) [8–12], which has been referred to as "fully printed perovskite solar cells" (Fig. 3). In order to fabricate the perovskite solar cells, these multiporous layers (for example, stacked layers of <FTO/blocking-TiO_2/porous-TiO_2/porous-ZrO_2/(porous-NiO)/porous-C>) can be prepared by annealing before perovskite deposition. The porous carbon electrode itself can be HTM against perovskite due to the energy level of carbon (−5.0 to –5.1 eV) and perovskite (−4.8 eV) (Fig. 4) [8–12]. The pore in the electrode has the continuous structure from the surface of the carbon electrode to the bottom of the pore at the blocking TiO_2 layer. Since the porous C layer is equipped on the porous layers beforehand already, it can form complete solar cells just after the perovskite-crystal deposition inside of the porous layer (Fig. 3).

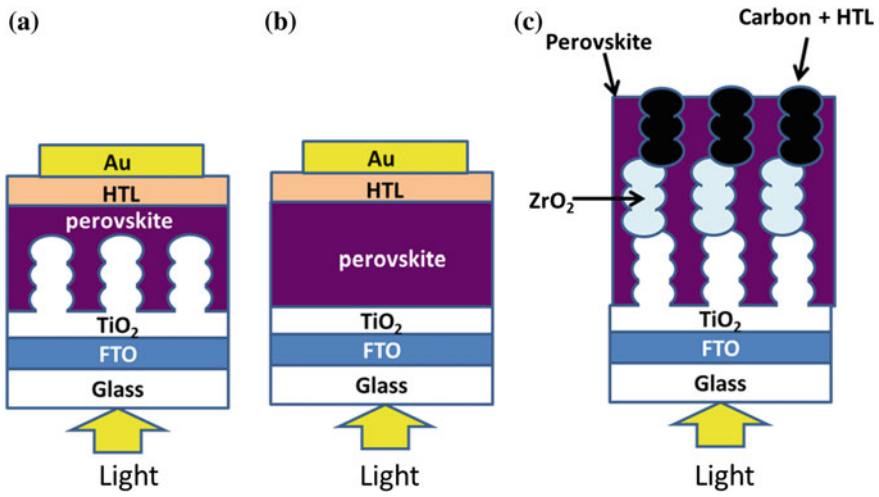

Fig. 2 Structures of perovskite solar cells; **a** mesoporous structure, **b** planar structure, **c** multilayered structure

2 CuI and CuSCN

In the field of DSCs, solid hole-conducting (p-type) materials (CuI and CuSCN [13–15]) have been investigated as a replacement for the electrolyte, and devices of this category are referred to as "solid state DSCs." Such copper-based HTM can be deposited by facile doctor blading [16] (Fig. 5). Since perovskite solar cells have been investigated from the field of DSCs, adapting such inorganic p-type materials to replace spiro-OMeTAD and PTAA to CuI and/or CuSCN is quite a simple and natural idea.

At first, the Kamat group (University of Notre Dame, USA) adopted CuI for use in perovskite solar cells (J_{sc}: 17.8 mA cm^{-2}; V_{oc}: 0.55 V; *FF*: 0.62 V; PCE: 6.0 %) [17], which were the first paper about inorganic hole-conducting materials for mesoscopic n-i-p perovskite solar cells. The conversion efficiency was just 6 % with porous TiO_2 electrodes. Also using CuI, the Bach-Cheng-Spiccia group (Monashi Univ.) [18] subsequently fabricated planar n-i-p structured perovskite solar cells with CuI HTM, resulting in 7.5 % conversion efficiency. Afterward, the Deng-Xie group (Xiamen Univ.) [19] published a paper using CuI for planar p-i-n inverted structured perovskite solar cells with a high conversion efficiency of 13.58 %. The CuI-HTM perovskite solar cells performed with a higher stability than that of spiro-OMeTAD [17, 19].

After the first publication about CuI [17], the Ito group (Univ. of Hyogo) published a paper on CuSCN-HTM perovskite solar cells, which used a mesoscopic n-i-p structure with 4.85 % conversion efficiency [20]. And the Mora-Seró-Tena-Zaera group (Parque Tecnológico de San Sebastián, Universitat Jaume I) published a 6.4 % conversion efficiency result with annealing-temperature

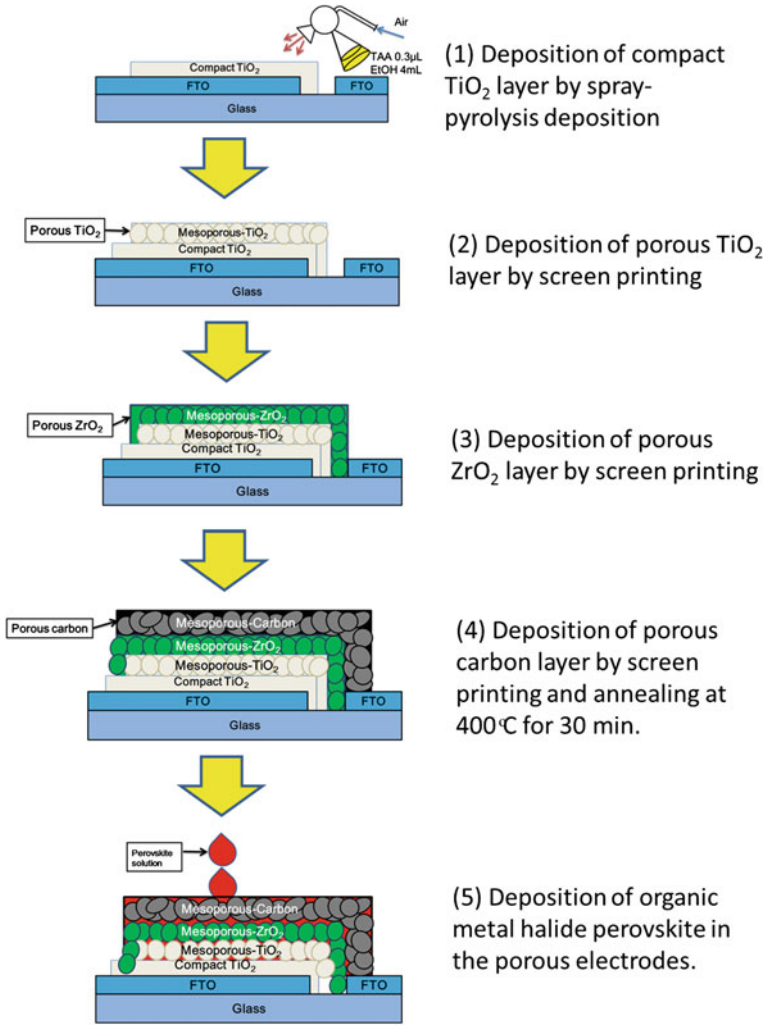

Fig. 3 Fabrication scheme of "fully-printed perovskite solar cells" to be multilayered structure (Fig. 2c) [9]

optimization for planar n-i-p perovskite solar cells [21]. In order to obtain a high-quality perovskite layer, the Ito group tried the special techniques of sequential deposition [3], double-PbI_2 deposition [22] and preheating [22, 23], and published on CuSCN-HTM perovskite solar cells with 12.4 % conversion efficiency [22]. Especially, the preheating can produce a smooth perovskite layer (Fig. 6) and improve the photovoltaic parameters (Fig. 7) effectively [23].

CuSCN was found to be a more stable material than spiro-OMeTAD, because good-efficiency perovskite solar cells with CuSCN HTM can be fabricated on rainy

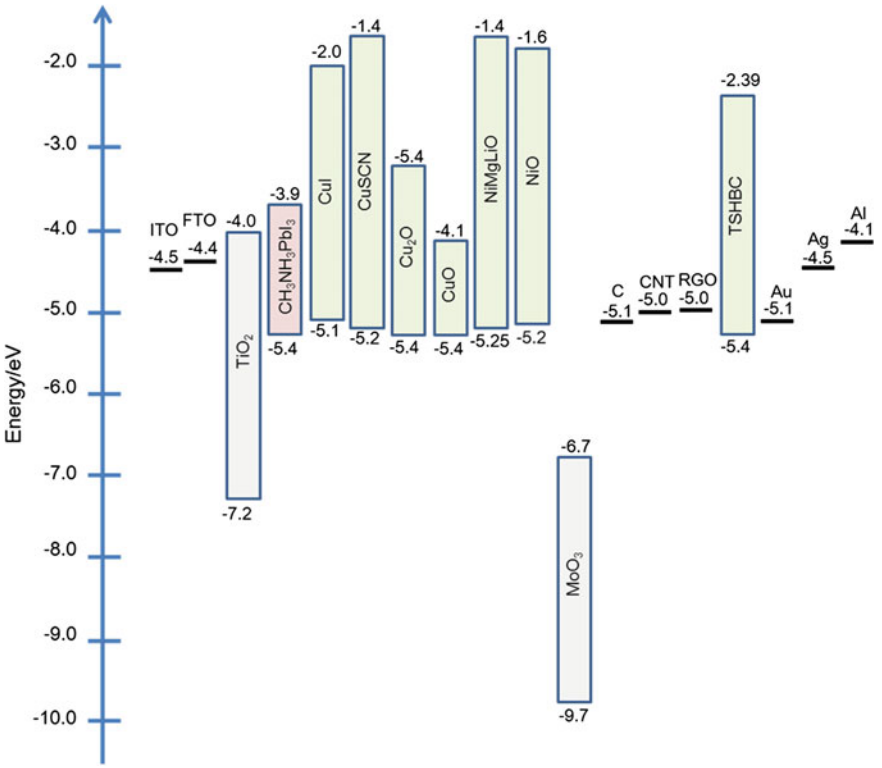

Fig. 4 The corresponding energy levels of In-Sn oxide (ITO), F-doped SnO_2 (FTO), TiO_2, $CH_3NH_3PbI_3$, inorganic hole-transporting materials, spiro-OMeTAD, and cathode electrodes [the data was gathered up from the references in this review]

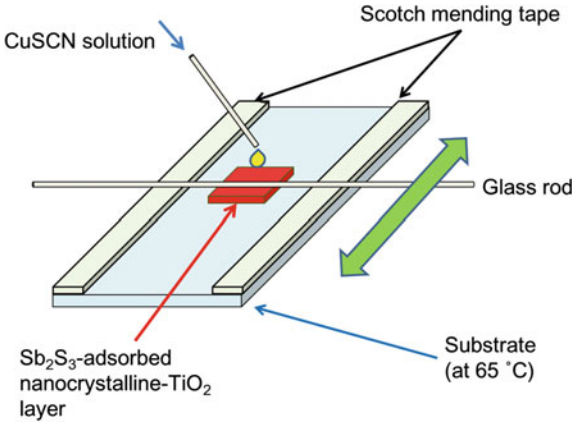

Fig. 5 Scheme of CuSCN deposition method [16]

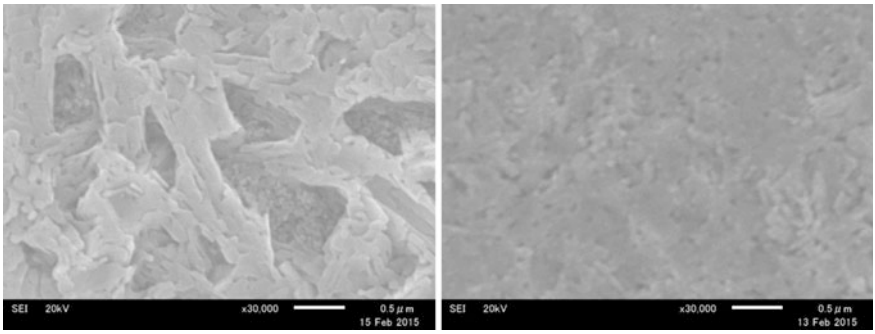

Fig. 6 Surface images of PbI_2 layer without (*left*) and with (*right*) preheating. The size of each scale bar was 0.5 μm

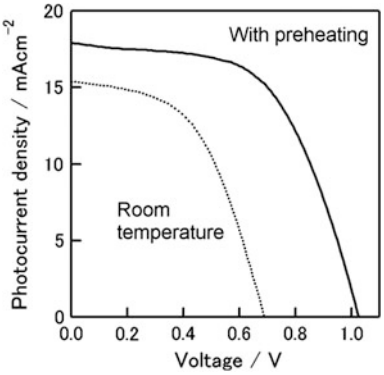

Fig. 7 Photocurrent–voltage curves of the perovskite layer with/without preheating [23]

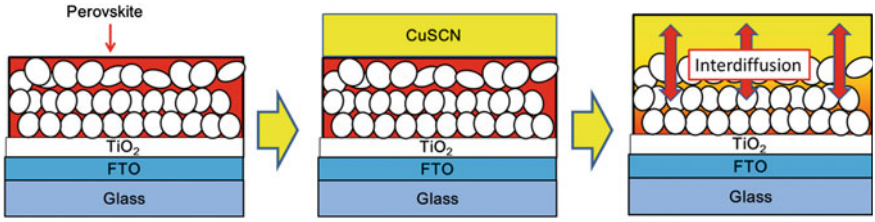

Fig. 8 Image of material diffusion confirmed by elemental analysis by SEM-EPMA [22]

Japanese summer days without glove box (humidity can be over 80 %) [20]. Hence, it is considered that the CuSCN is not as sensitive to the humidity as organic hole-transporting materials. However, the conversion efficiency of CuSCN-HTM perovskite solar cells could not be improved afterward, because of the strong

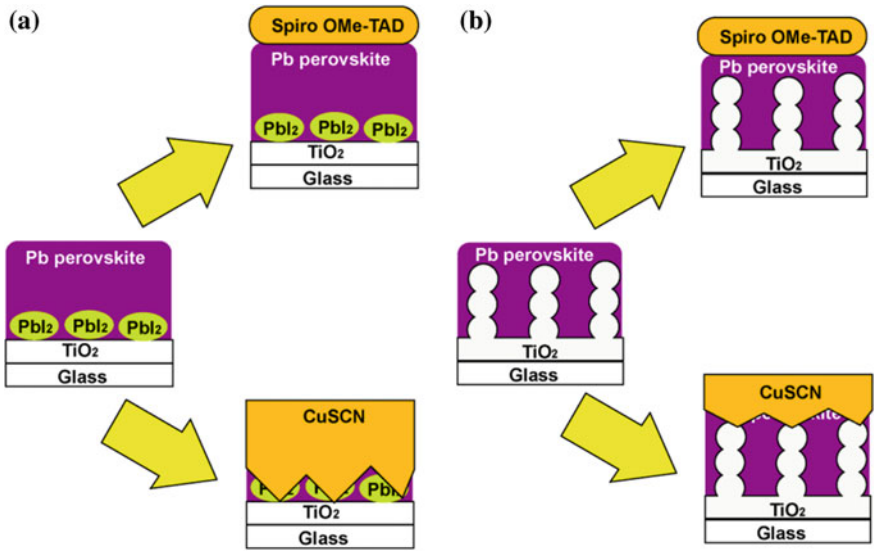

Fig. 9 Schematic images of interdiffusion in perovskite solar cells using CuSCN HTM for planar structure (with strong short circuiting) (**a**) and for mesoporous structure (prevent short circuiting) (**b**)

interdiffusion between perovskite and CuSCN, which can be observed by SEM-EPMA images (Fig. 8) [22]. It can be confirmed that Pb was located in porous TiO_2 before CuSCN coating, but shifted up after CuSCN coating. Hence, $CH_3NH_3PbI_3$ was dissolved to CuSCN. Although CuSCN-HTM solar cells with mesoporous structure can be easily fabricated, the fabrication of planar n-i-p structured CuSCN-HTM solar cells was quite difficult due to short circuiting, which can be aroused by the interdiffusion (Fig. 9) [24]. In DSC, mesoporous-TiO_2 electrodes can prohibit a strong short circuit [25]. Removing pinholes in the planar perovskite layer, the strong short circuit has been prohibited (Fig. 10), but still the *FF* of CuSCN-HTM cells deteriorated without mesoporous TiO_2 layers (Fig. 11) [26].

In order to check the variation of perovskite crystals, each perovskite layer before and after deposition of HTM was measured by XRD [27]. When HTM (including organic HTM) are used in an n-i-p structure for perovskite solar cells, the HTM have to be deposited on the perovskite layer and can change the perovskite crystal. Figure 12 shows a summary of the reaction image between the $CH_3NH_3PbI_3$ perovskite crystal for the deposition of solvents (chlorobenzene and propyl sulfide) and HTM (spiro-OMeTAD and CuSCN). The XRD main peak of perovskite can shift to large angle just by chlorobenzene deposition, which may be due to DMF extraction in perovskite layer by chlorobenzene [28]. In contrast, propyl sulphide (solvent of CuSCN) did not shift the peak position, but decreased the XRD intensity due to the decomposing of the perovskite crystal. The thiocyanate ion (SCN^-) can be

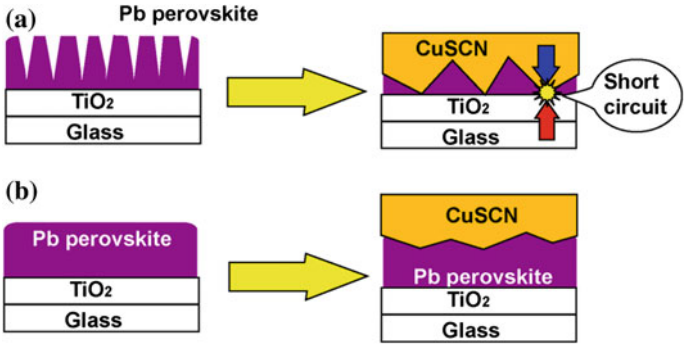

Fig. 10 Schematic images of interdiffusion in perovskite solar cells using CuSCN HTM on rough perovskite layer by MAI-soaking (with strong short circuiting) (**a**) and on smooth perovskite layer by MAI-dripping (prevent short circuiting) (**b**) [26]

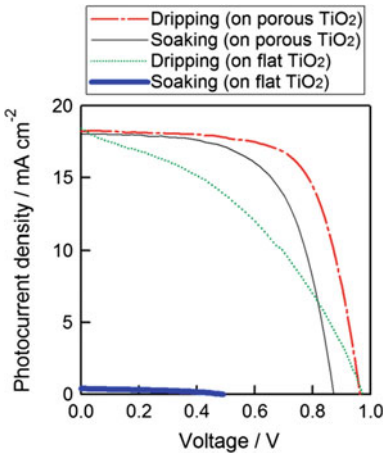

Fig. 11 Photocurrent density–voltage curves of $CH_3NH_3PbI_3$ perovskite solar cells by the MAI-soaking (with pin-holes) and MAI-dripping (without pin-holes) methods on with/without porous TiO_2 layers [26]

exchanged by the iodide ion (I^-) to $CH_3NH_3Pb(SCN)_2I$ perovskite [29], resulting in the prevention of the CuSCN crystal on the $CH_3NH_3PbI_3$ perovskite layer [27]. The Cu^+ ion may enhance the crystallinity of $CH_3NH_3PbI_3$ perovskite [27]. Chloride and bromide ions can enhance the crystallinity and the stability of perovskite solar cells against circumstances, respectively [30, 31], but cannot block the interdiffusion between HTM and $CH_3NH_3PbI_3$ perovskite [27]. Such interdiffusion can deteriorate the conversion efficiency and the stability of perovskite solar cells.

Due to such difficulty of CuSCN deposition on perovskite layers and the effect of interdiffusion, CuSCN-HTM perovskite solar cells with planar p-i-n structure were fabricated [32–35] (as CuI-HTM by the Deng-Xie group [19]). At first, the Sarkar group (Indian Institute of Technology Bombay) has published on such planar p-i-n structure perovskite solar cells using CuI-HTM by electrochemical deposition with 3.8 % conversion efficiency [32]. By optimizing the electrochemical deposition of

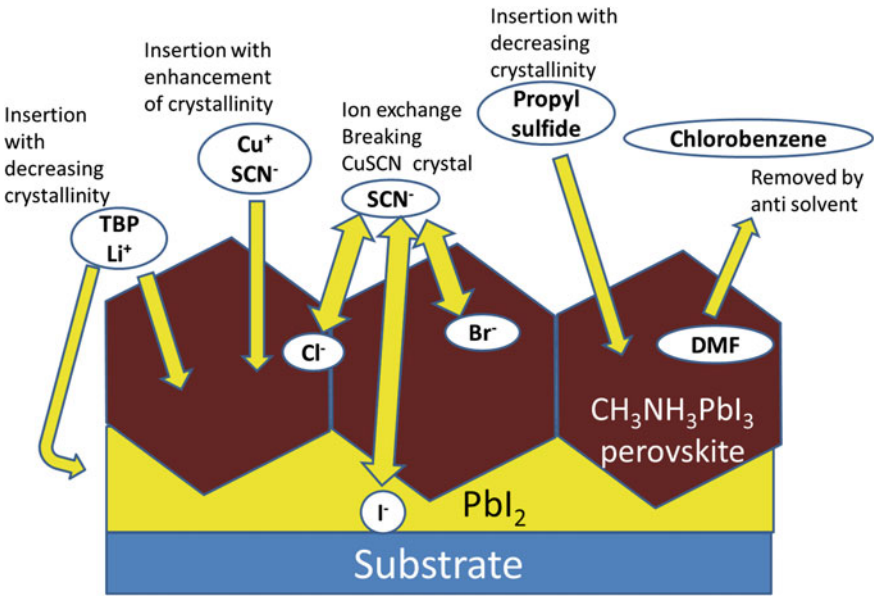

Fig. 12 Summary of the reaction scheme of organo lead halide perovskite layers for $CH_3NH_3PbX_3$ (X: I, Cl or Br) [28]

CuSCN, the Bian group (Peking University) has published a 16.6 % conversion efficiency of planar p-i-n perovskite solar cells with high photo voltage and current with the structure of <ITO/CuSCN/$CH_3NH_3PbI_3$/C_{60}/BCP/Ag> [33]. On the other hand, the Amassion group (KAUST) has fabricated planar p-i-n perovskite solar cells by spin coating of CuSCN-HTM, resulting in 10.5 % conversion efficiency without histolysis [34]. The Jen group (Univ. of Washington) also fabricated perovskite solar cells by spin coating of CuSCN for 25 % visible-light transmittance with 10 % conversion efficiency [35].

3 Cu_2O and CuO

As written in the introduction, the metal-oxide deposition needs a high temperature for the reaction between the precursor and oxygen, the decomposition of organic elements in the precursor to CO_2, and metal-oxide crystallization. Moreover, the solvent of precursor solution can deteriorate the perovskite layer beneath. When using sputtering for the deposition of p-type oxides on perovskite layers, sputtering damage should be considered. Therefore, the Ding group (National Center for Nanoscience and Technology, China) has fabricated planar p-i-n structure of perovskite solar cells using Cu_2O and CuO HTM by spin coating [36]. The Cu_2O and CuO were deposited before perovskite coating. Since the valence bands of Cu_2O

and CuO are located close to each other (Fig. 4), the conversion efficiencies became close to 13.35 % and 12.16 %, respectively.

4 NiO

Before application to perovskite solar cells, NiO has been utilized as HTM for CdS-sensitized solar cells [37, 38]. Now, NiO is the main material in the field of perovskite solar cells using inorganic HTM. The first NiO p-type electrode perovskite solar cells using planar p-i-n structure have been published by the Chen-Guo group (NCKU, Taiwan) with 7.8 % conversion efficiency [39]. The NiO layers were fabricated by spin coating, succeeded by annealing and UV-O_3 treatment. And then, a mesoporous NiO layer was inserted into the planar device, resulting in 9.51 % conversion efficiency [40].

At the same time, the groups of Bochloo (KTH Royal Institute of Technology, Sweden) [41], Tang-Ma (Huazhong University of Science and Technology, Soochow University) [42], and Sarkar (Indian Institute of Technology Bombay) [32] published perovskite solar cells using NiO-HTM with a p-i-n structure, separately. The groups of Bochloo [31] and Tang-Ma [32] fabricated NiO-HTM layers by spin coating. On the other hand, the Sarkar group [22] fabricated them by electrochemical deposition.

Basically, crystallization of NiO is very difficult. For this reason, not many papers have provided the results of XRD data for sol–gel-processed NiO. Still, the Yang group (Hong Kong) reported XRD and XPS data of sol–gel processed NiO for HTM in perovskite solar cells with 9.11 % conversion efficiency using a planar p-i-n structure [43]. They have synthesized the NiO nanoparticle before the spin-coating deposition. The size was confirmed as 10–20 nm by AFM and TEM. The XRD patterns of NiO were observed after annealing at 500 °C for spin-coated NiO on quartz substrate. Such high efficiency was achieved by optimization of NiO thickness at 40 nm (Table 2). Afterward, another Yang group (UCLA) published nanocrystal NiO (d = 50–100 nm) for HTM layers and nanocrystal ZnO (d < 10 nm) for electron-transporting material (ETM) layers, resulting in organic (C=C double bond)-free, high-efficiency (16.1 %), and high-stability perovskite solar cells [44], which improved stability against water and oxygen degradation when compared with devices with organic charge transport layers.

Table 2 Photovoltaic parameters of the perovskite solar cells using NiO HTM [43]

	J_{sc} (mA cm^{-2})	V_{oc} (V)	FF	PCE (%)
NiO NCs-20 nm	13.64	0.704	0.630	6.04
NiO NCs-40 nm	16.27	0.882	0.635	9.11
NiO NCs-70 nm	10.72	0.851	0.612	5.58
NiO thin films	9.82	0.647	0.591	3.75
PEDOT:PSS	8.25	0.613	0.533	2.70

Table 3 Photovoltaic parameters of the PLD-NiO-based perovskite solar cells as a function of oxygen partial pressure and thickness [47]

O_2 pressure	R_{sh} (Ω cm^{-2})	R_s (Ω cm^{-2})	J_{sc} (Ω cm^{-2})	V_{oc} (V)	FF	PCE (%)
10	600	5.5	18.6	0.98	0.65	11.8
200	7800	5.1	17.7	1.07	0.77	14.4
500	4100	5.0	16.1	1.08	0.75	13.0
900	1700	5.0	15.8	1.05	0.74	12.3
Film thickness (nm) at PO_2 = 200 mTorr	R_{sh} (Ω cm^{-2})	R_s (Ω cm^{-2})	J_{sc} (mA cm^{-2})	V_{oc} (V)	FF	PCE (%)
100	3500	3.8	19.2	1.03	0.78	15.3
180	14,500	3.4	17.8	1.08	0.80	15.3
250	14,200	4.5	15.6	1.05	0.80	13.0
340	5200	4.5	14.3	1.03	0.80	11.8

To enhance the quality and homogeneity of NiO thin layers, sputtering and pulsed-laser depositions have been performed, resulting in high-efficiency NiO-HTM-based perovskite solar cells with p-i-n structure [45–47]. Specially, the Seok group has controlled the NiO nanostructure by pulsed-laser deposition (Table 3) and optimized the perovskite solar cells to be 17.3 % conversion efficiency with 20.2 mA cm^{-2} J_{sc}, 1.06 V V_{oc}, and 0.813 *FF* [47].

In order to obtain high-performance and environmentally stable perovskite solar cells, NiO layers have been modified by Cu doping [48], Al_2O_3-nanocrystal coating [49], incorporation of Li and Mg (to be $Li_{0.05}Mg_{0.15}Ni_{0.8}O$) [50], and PEDOT coating [51]. Specially, the Grtäzel-Han group (EPFL and NIMS) published the best results of $Li_{0.05}Mg_{0.15}Ni_{0.8}O$-HTM perovskite solar cells with a large aperture area (1.017 cm^2) showing a high power conversion efficiency (PCE) of 15.0 % with 20.61 mA cm^{-2} of J_{sc}, 0.879 V of V_{oc}, and 0.668 of *FF*, certified by AIST (Japan) [50]. The cell contained organic–inorganic bilayered ETM as <FTO/NiMgLiO/PVK/PCBM/Ti(Nb)Ox/Ag>. The hysteresis in the current–voltage characteristics was eliminated, and the PSCs remained stable at the initial PCE after 1000 h light soaking (>90 %) with sealing. Using a small aperture and a small cell, they obtained 18.39 % (forward bias scan, without hysteresis voltage-scanning condition at 5 mV step width) and 22.35 % (reverse bias scan, with hysteresis voltage-scanning condition at 70 mV step width) PCEs (Table 4).

For industrial applications, such inorganic HTM is very important in the view of cost and stability. At the same time, the processing scheme should be considered, because spin coating is not suitable for large devices. However, the perovskite layers for high-efficiency solar cells have been fabricated by spin coating. To solve this problem, the Han group (HUST, China) published a new type of perovskite solar cell, called a "fully-printed perovskite solar cell" (Fig. 3) [8–12]. In this paper, it was categorized as a "multi-porous-layered" structure, depicted in Fig. 2c. After the emergence of the "multi-porous-layered" structure, the Wang group (HUST,

Table 4 Efficiency parameters of the perovskite solar cell from *J–V* curves obtained at difference scan conditions

Scan direction	Step width/mV	J_{sc} (mA cm$^{-2)}$	V_{oc} (V)	FF	PCE (%)
Reverse (from OC to SC)	70	20.429	1.273	0.859	22.35
	20	20.427	1.167	0.836	19.92
	10	20.401	1.103	0.825	18.56
	5	20.387	1.096	0.823	18.4
Forward (from SC to OC)	70	20.399	1.08	0.823	18.14
	20	20.431	1.084	0.823	18.23
	10	20.411	1.083	0.827	18.29
	5	20.418	1.085	0.83	18.39

China) adopted NiO HTM in perovskite solar cells with a multiporous-layered structure [52–54]. This perovskite solar cell was organic (C=C double bond)-free, high-efficiency (PCE: 15.03 %), and high-stability [54].

5 Molybdenum Oxides (MoOx)

MoO_x is an n-type semiconductor, but the conduction band is located at a lower energy level (−6.7 eV), which is lower than that of valence band of $CH_3NH_3PbI_3$ perovskite (−5.4 eV) [55–59]. But, MoO_x has an ability to extract holes. Although MoO_x was not commonly attached to perovskite surfaces at first directory, the Zhu group (NREL) proposed the merit of MoO_x as effective counter electrodes without using noble/precious metals (e.g., Au or Ag) [55]. Since then, several reports have been published about MoO_x HTM. The groups of Bai-Tian-Fan (Xiamen University) [56] and Su-Wang-Chu (Chinese Academy of Sciences, Changchun) [57] improved the conversion efficiency of perovskite solar cells up to 13.4 % on spiro-OMeTAD and 12.4 % on PEDOT:PSS, respectively, by using MoO_x HTM.

The merit of MoO_x is that it can be deposited by thermal vacuum deposition, without sputtering. Hence, MoO_x can be deposited on organic HTM (e.g., spiro-OMeTAD and PEDOT:PSS) without sputtering damage. Moreover, MoO_x is a transparent material. Therefore, MoOx is suitable to produce transparent back contact to protect organic HTM from sputtering damage at the ITO deposition. The Wolf-Ballif group (EPFL) fabricated MoO_x/ITO-stacked back transparent contact on perovskite solar cells for a tandem device with silicon solar cells [58].

The Kim group (Seoul National University) [59] fabricated MoO_x front-contact p-i-n perovskite solar cells with and without organic HTM. With organic HTM (NPB), the conversion efficiency was 13.7 %. Without organic HTM, however, the conversion efficiency was 6.9 % (Table 5).

Table 5 Photovoltaic characteristics of a perovskite solar cell without the NPB layer for different scan directions

Scan direction	J_{sc} (mA cm^{-2})	V_{oc} (V)	FF	PCE (%)
Forward (SC to OC)	11.1	0.78	0.74	6.4
Reverse (OC to SC)	10.6	0.87	0.75	6.9

The scan step of *J–V* characteristics was 0.02 V with 0.3 s of interval time for each step and the device structure was < ITO (150 nm)/MoO_3 (5 nm)/$CH_3NH_3PbI_3$ (320 nm)/C_{60} (50 nm)/BCP (8 nm)/Al (100 nm) > (supporting information in Ref. [59])

6 Carbon Materials

As a review paper by Batmunkh et al. [60], carbon can act both as electron and hole acceptors. In this chapter, we will concentrate only on its function as a hole acceptor. As already shown in the introduction section of this chapter, carbon can work as a hole extraction layer from perovskite in "multi-porous-layered" perovskite solar cells with a <porous TiO_2/porous ZrO_2 (or Al_2O_3)/porous carbon> structure (Fig. 2c and 3) [8–12], because the energy level of carbon is—5.0–5.1 eV from the vacuum level, which is located in a suitable position to extract holes in perovskite (−5.4 eV) (Fig. 4) [8–12, 61–68].

The groups of Ma (Dalian University of Technology) [61, 62], Yang (The Hong Kong University of Science and Technology) [63–65], and Yang (Dalian University of Technology) [66] coated carbon ink on $CH_3NH_3PbI_3$ perovskite (or PbI_2) for low-temperature processing (e.g., spin coating, doctor blading, ink jet printing, and rolling transfer). An interesting carbon layer made from carbon soot was provided by the Yang group (The Hong Kong University of Science and Technology) [65]. In order to improve the fill factors (FF) of perovskite solar cells, the Meng group (Chinese Academy of Sciences, Beijing) attached Al or graphite foils on perovskite surface using carbon layers by hot press (Fig. 13) [67, 68].

In place of carbon particles, graphene and carbon nanotubes (CNT) have also been utilized as HTM for perovskite solar cells [69–73]. Since the energy levels of single-layered graphene (−4.8 eV), multilayered-graphene (−5.0 eV), and CNT (−5.0 eV) are higher than that of $CH_3NH_3PbI_3$ (−5.4 eV), respectively, graphene and CNT can extract holes from perovskite.

Well-defined thiolated nanographene (perthiolated trisulphur-annulated hexa-peri-hexabenzocoronene, TSHBC) (Fig. 14) can also be a good HTM [73]. Although the valence-band energy level of TSHBC is quite close to that of $CH_3NH_3PbI_3$ perovskite, the high-energy level of the TSHBC conduction band can block the electron flow, resulting in good HTM (Fig. 4).

Since graphene and CNT have good hole-extraction phenomena, they can be attached to organic HTM to enhance the photovoltaics of perovskite solar cells. Graphene can improve the wettability of spiro-OMeTAD on perovskite layer, resulting in the imprudent of the photovoltaic effects [74]. Due to their good ability about hole-extraction, conductivity and transparency, graphene and CNT can work

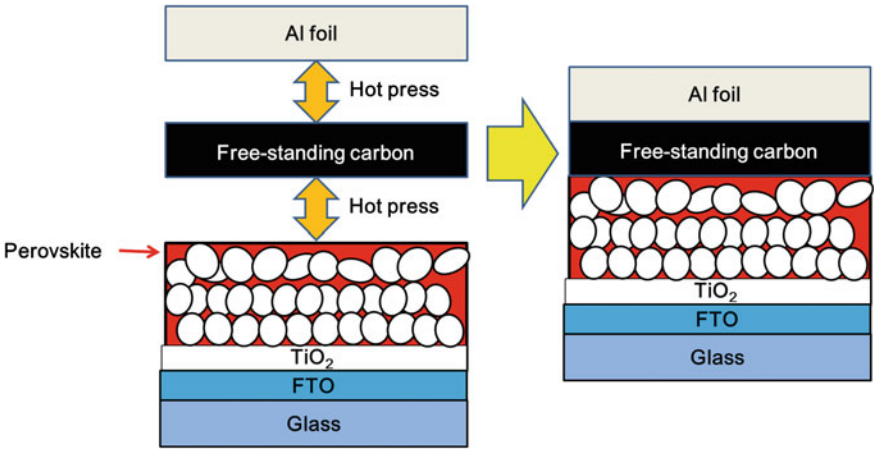

Fig. 13 Fabrication process of Al-conductor-assisted carbon back contact HTM-free perovskite solar cells [67]

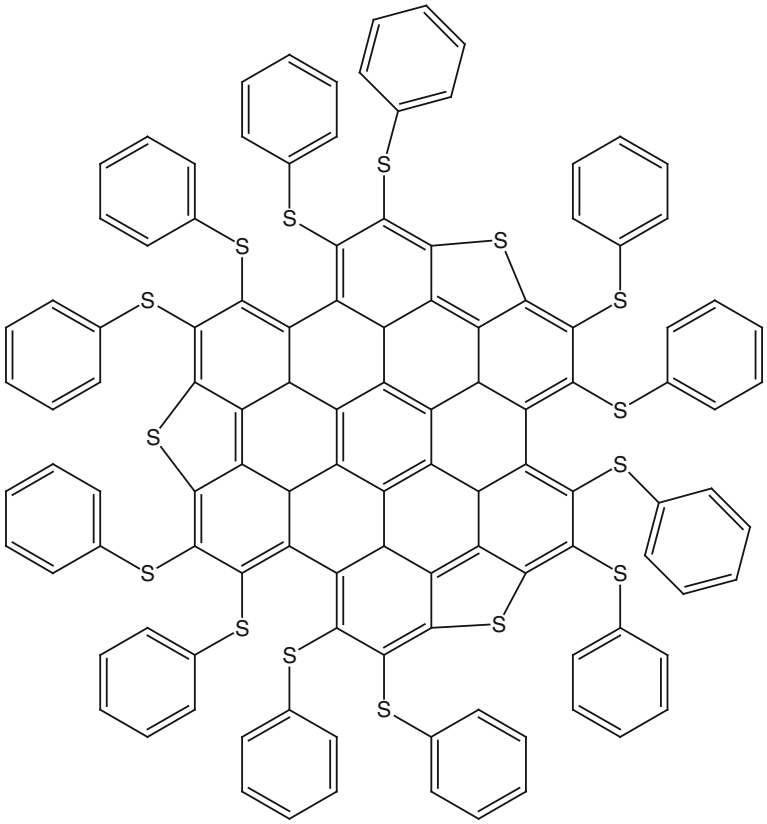

Fig. 14 Structures of TSHBC [73]

Table 6 Efficiency variations of perovskite solar cells based on RGO-1/dopant-free spiro-OMeTAD and Li-TSFI and pyridine doped spiro-OMeTAD

	PCE (%)				
HTM (h)	0	96	192	360	500
RGO	9.31	9.55	9.24	8.41	7.96
Doped Spiro-OMeTAD	12.56	12.01	10.55	6.12	4.53

in place of transparent conducting oxides layers on organic HTM [70, 75–78], resulting in bifacial solar cells, tandem devices, flexible solar cells, and so on.

In order to enhance the photovoltaics of conventional perovskite solar cells, graphene and CNT can be mixed in organic HTM [79–84] due to the hole-extraction ability of graphene and CNT, and the enhancement conductivity of organic HTM. Specially, it was found that iodide-reduced graphene oxide can eliminate dopants from spiro-OMeTAD to form stable perovskite solar cells (Table 6) [84].

7 Conclusion

The progresses of inorganic HTM (CuI, CuSCN, Cu_2O, CuO, NiO, MoO_x, and carbons) in perovskite solar cells have been introduced. The inorganic HTM can be used in place of organic ones. In some case, however, the inorganic HTM can be used with organic ones (stacked and/or mixed). It has been considered that, compared with organic HTM, the inorganic HTM can enhance only the stability of perovskite solar cells, not the conversion efficiency. However, the Grätzel-Han group provided the certified high-PCE of perovskite solar cells using inorganic HTM with an aperture area over 1 cm^{-2}, which has an important meaning in the photovoltaic field, because very small solar cells are not practicable for industrial applications. Therefore, we have understood that inorganic HTM are very important for perovskite solar cells to enhance the PCE and stability. Still, research of perovskite solar cells is quite active. From now on, the inorganic HTM will be important elements in this field.

References

1. Lee, M.M., Teuscher, J., Miyasaka, T., Murakami, T.N., Snaith, H.J.: Science, efficient hybrid solar cells based on meso-superstructured organometal halide perovskites. Science **338**, 643–z647 (2012)
2. Kim, H.-S., Lee, C.-R., Im, J.-H., Lee, K.-B., Moehl, T., Marchioro, A., Moon, S.-J., Humphry-Baker, J.-H., Yum, J.E., Moser, M., Grátzel, N.-G.: Park, lead iodide perovskite sensitized all-solid-state submicron thin film mesoscopic solar cell with efficiency exceeding 9 %. Sci. Rep. **2**, 591 (2012)

3. Burschka, J., Pellet, N., Moon, S.-J., Humphry-Baker, R., Gao, P., Nazeeruddin, M.K., Grátzel, M.: Sequential deposition as a route to high-performance perovskite-sensitized solar cells. Nature **499**, 316–319 (2013)
4. Yang, W.S., Noh, J.H., Jeon, N.J., Kim, Y.C., Ryu, S., Seo, J., Seok, S.I.: High-performance photovoltaic perovskite layers fabricated through intramolecular exchange. Science **348**, 1234–1237 (2015)
5. Li, M.-H., Shen, a P.-S., Wang, K.-C., Guo, T.-F., Chen, P.: Inorganic p-type contact materials for perovskite based solar cells. J. Mater. Chem. A **3**, 9011–9019 (2015)
6. Schmidt-Mende, L., Bach, U., Humphry-Baker, R., Horiuchi, T., Miura, H., Ito, S., Uchida, S., Grätzel, M.: Organic dye for highly efficient solid state dye sensitized solar cells. Adv. Mater. **17**, 813–815 (2005)
7. Burschka, J., Dualeh, A., Kessler, F., Barano, E., Cevey-Ha, N.-L., Yi, C., Nazeeruddin, M.K., Grätzel, M.: Tris(2-(1H-pyrazol-1-yl)pyridine)cobalt(III) as p-Type dopant for organic semiconductors and its application in highly efficient solid-state dye-sensitized solar cells. J. Am. Chem. Soc. **133**, 18042–18045 (2011)
8. Ku, Z., Rong, Y., Xu, M., Liu, T., Han, H.: Full printable processed mesoscopic $CH_3NH_3PbI_3$/TiO_2 heterojunction solar cells with carbon counter electrode. Sci. Rep. **3**, 3132 (2013)
9. Mei, A., Li, X., Liu, L., Ku, Z., Liu, T., Rong, Y., Xu, M., Hu, M., Chen, J., Yang, Y., Grätzel, M., Han, H.: A hole-conductor-free, fully printable mesoscopic perovskite solar cell with high stability. Science **345**, 295–298 (2014)
10. Zhang, L., Liu, T., Liu, L., Hu, M., Yang, Y., Mei, A., Han, H.: The effect of carbon counter electrode on fully printable mesoscopic perovskite solar cell. J. Mater. Chem. A **3**, 9165–9170 (2015)
11. Liu, T., Liu, L., Hu, M., Yang, Y., Zhang, L., Mei, A., Han, H.: Critical parameters in TiO_2/ZrO_2/Carbon-based mesoscopic perovskite solar cell. J. Power Sources **293**, 533–538 (2015)
12. Wang, H., Hu, X., Chen, H.: The effect of carbon black in carbon counter electrode for $CH_3NH_3PbI_3$/TiO_2 heterojunction solar cells. RSC Adv. **5**, 30192–30196 (2015)
13. Yang, L., Zhang, Z., Fang, S., Gao, X., Obata, M.: Influence of the preparation conditions of TiO_2 electrodes on the performance of solid-state dye-sensitized solar cells with CuI as a hole collector. Sol. Energy **81**, 717–722 (2007)
14. Kumara, G.R.R.A., Konno, A., Senadeera, G.K.R., Jayaweera, P.V.V., De Silva, D.B.R.A., Tennakone, K.: Dye-sensitized solar cell with the hole collector p-CuSCN deposited from a solution in n-propyl sulphide. Sol. Energy Mater. Sol. Cells **69**, 195–199 (2001)
15. O'Regan, B., Schwartz, D.T., Zakeeruddin, S.M., Grätzel, M.: Electrodeposited nanocomposite n-p heterojunctions for solid-state dye-sensitized photovoltaics. Adv. Mater. **12**, 1263–1267 (2000)
16. Tsujimoto, K., Nguyen, D.-C., Ito, S., Nishino, H., Matsuyoshi, H., Konno, A., Kumara, G.R.A., Tennakone, K.: TiO_2 surface treatment effects by Mg^{2+}, Ba^{2+}, and Al^{3+} on Sb_2S_3 extremely thin absorber solar cells. J. Phys. Chem. C **116**, 13465–13471 (2012)
17. Christians, J.A., Fung, R.C.M., Kamat, P.V.: An inorganic hole conductor for organo-lead halide perovskite solar cells. Improved hole conductivity with copper iodide. J. Am. Chem. Soc. **136**, 758–764 (2014)
18. Sepalage, G.A., Meyer, S., Pascoe, A., Scully, A.D., Huang, F., Bach, U., Cheng, Y.-B., Spiccia, L.: Copper(I) iodide as hole-conductor in planar perovskite solar cells: probing the origin of J-V hysteresis. Adv. Funct. Mater. **25**, 5650–5661 (2015)
19. Chen, W.-Y., Deng, L.-L., Dai, S.-M., Wang, X., Tian, C.-B., Zhan, X.-X., Xie, S.-Y., Huang, R.-B., Zheng, L.-S.: Low-cost solution-processed copper iodide as an alternative to PEDOT: PSS hole transport layer for efficient and stable inverted planar heterojunction perovskite solar cells. J. Mater. Chem. A **3**, 19353–19359 (2015)
20. Ito, S., Tanaka, S., Vahlman, H., Nishino, H., Manabe, K., Lund, P.: Carbon-double-bond-free printed solar cells from TiO_2/$CH_3NH_3PbI_3$/CuSCN/Au: structural control and photoaging effects. ChemPhysChem **15**, 1194–1200 (2014)

21. Chavhan, S., Miguel, O., Grande, H.-J., Gonzalez-Pedro, V., S´anchez, R.S., Barea, E.M., Mora-Seró, I., Tena-Zaera, R.: Organo-metal halide perovskite-based solar cells with CuSCN as the inorganic hole selective contact. J. Mater. Chem. A **3**, 19353 (2015)
22. Qin, P., Tanaka, S., Ito, S., Tetreault, N., Manabe, K., Nishino, H., Nazeeruddin, M.K., Grätzel, M.: Inorganic hole conductor-based lead halide perovskite solar cells with 12.4 % conversion efficiency. Nat. Commun. **5**, 3834 (2014). doi:10.1038/ncomms4834
23. Ito, S., Tanaka, S., Nishino, H.: Substrate-preheating effects on PbI_2 spin coating for perovskite solar cells via sequential deposition. Chem. Lett. **44**, 849–851 (2015)
24. Murugadoss, G., Mizuta, G., Tanaka, S., Nishino, H., Umeyama, T., Imahori, H., Ito, S.: Double functions of porous TiO_2 electrodes on CH3NH3PbI3 perovskite solar cells: enhancement of perovskite crystal transformation and prohibition of short circuiting. APL Mater. **2,** Article ID 081511 (2014)
25. Ito, S., Zakeeruddin, S.M., Comte, P., Liska, P., Kuang, D., Grätzel, M.: Bifacial dye-sensitized solar cells based on an ionic liquid electrolyte. Nat. Photonics **2**, 693–698 (2008)
26. Ito, S., Tanaka, S., Nishino, H.: Lead-halide perovskite solar cells by CH_3NH_3I dripping on PbI_2−CH_3NH_3I−DMSO precursor layer for planar and porous structures using CuSCN hole-transporting material. J. Phys. Chem. Lett. **6**, 881–886 (2015)
27. Ito, S., Kanaya, S., Nishino, H., Umeyama, T., Imahori, H.: Material exchange property of organo lead halide perovskite with hole-transporting materials. Photonics **2**, 1043–1053 (2015)
28. Xiao, M., Huang, F., Huang, W., Dkhissi, Y., Zhu, Y., Etheridge, J., Gray-Weale, A., Bach, U., Cheng, Y.-B., Spiccia, L.: A fast deposition-crystallization procedure for highly efficient lead iodide perovskite thin-film solar cells. Angew. Chem. Int. Ed. **53**, 9898–9903 (2014)
29. Jiang, Q., Rebollar, D., Gong, J., Piacentino, E.L., Zheng, C., Xu, T.: Pseudohalide-induced moisture tolerance in perovskite $CH_3NH_3Pb(SCN)_2I$ Thin Films. Angew. Chem. Int. Ed. **54**, 7617–7620 (2015)
30. Zhao, Y., Zhu, K.: CH_3NH_3Cl-assisted one-step solution growth of $CH_3NH_3PbI_3$: structure, charge-carrier dynamics, and photovoltaic properties of perovskite solar cells. J. Phys. Chem. C **118**, 9412–9418 (2014)
31. Noh, J.H., Im, S.H., Heo, J.H., Mandal, T.N., Seok, S.I.: Chemical management for colorful, efficient, and stable inorganic-organic hybrid nanostructured solar cells. Nano Lett. **13**, 1764–1769 (2013)
32. Subbiah, A.S., Halder, A., Ghosh, S., Mahuli, N., Hodes, G., Sarkar, S.K.: Inorganic hole conducting layers for perovskite-based solar cells. J. Phys. Chem. Lett. **5**, 1748–1753 (2014)
33. Ye, S., Sun, W., Li, Y., Yan, W., Peng, H., Bian, Z., Liu, Z., Huang, C.: CuSCN-based inverted planar perovskite solar cell with an average PCE of 15.6 %. Nano Lett. **15**, 3723–3728 (2015)
34. Zhao, K., Munir, R., Yan, B., Yang, Y., Kim, T., Amassian, A.: Solution-processed inorganic copper(I) thiocyanate (CuSCN) hole transporting layers for efficient p-i-n perovskite solar cells. J. Mater. Chem. A **3**, 20554–20559 (2015)
35. Jung, J.W., Chueh, C.-C., Jen, A.K.-Y.: High-performance semitransparent perovskite solar cells with 10 % power conversion efficiency and 25 % average visible transmittance based on transparent CuSCN as the hole-transporting material. Adv. Energy Mater. **5**, 1500486 (2015)
36. Zuo, C., Ding, L.: Solution-processed Cu_2O and CuO as hole transport materials for efficient perovskite solar cells. Small **11**, 5528–5532 (2015)
37. Chan, X.-H., Jennings, J.R., Hossain, M.A., Yu, K.K.Z., Wang, Q.: Characteristics of p-NiO thin films prepared by spray pyrolysis and their application in CdS-sensitized photocathodes. J. Electrochem. Soc. **158**, H733–H740 (2011)
38. Safari-Alamuti, F., Jennings, J.R., Hossain, M.A., Yung, L.Y.L., Wang, Q.: Conformal growth of nanocrystalline CdX (X = S, Se) on mesoscopic NiO and their photoelectrochemical properties. Phys. Chem. Chem. Phys. **15**, 4767 (2013)

39. Jeng, J.-Y., Chen, K.-C., Chiang, T.-Y., Lin, P.-Y., Tsai, T.-D., Chang, Y.-C., Guo, T.-F., Chen, P., Wen, T.-C., Hsu, Y.-J.: Nickel oxide electrode interlayer in $CH_3NH_3PbI_3$ perovskite/PCBM planar-heterojunction hybrid solar cells. Adv. Mater. **26**, 4107–4113 (2014)
40. Wang, K.-C., Jeng, J.-Y., Shen, P.-S., Chang, Y.-C., Diau, E.W.-G., Tsai, C.-H., Chao, T.-Y., Hsu, H.-C., Lin, P.-Y., Chen, P., Guo, T.-F., Wen, T.-C.: p-type Mesoscopic nickel oxide/organometallic perovskite heterojunction solar cells. Sci. Rep. **4**, 4756 (2014)
41. Tian, H., Xu, B., Chen, H., Johansson, E.M.J., Boschloo, G.: Solid-state perovskite-sensitized p-Type mesoporous nickel oxide solar cells. ChemSusChem **7**, 2150–2155 (2014)
42. Hu, L., Peng, J., Wang, W., Xia, Z., Yuan, J., Lu, J., Huang, X., Ma, W., Song, H., Chen, W., Cheng, Y.-B., Tang, J.: Sequential deposition of $CH_3NH_3PbI_3$ on planar NiO film for efficient planar perovskite solar cells. ACS Photonics **1**, 547–553 (2014)
43. Zhu, Z., Bai, Y., Zhang, T., Liu, Z., Long, X., Wei, Z., Wang, Z., Zhang, L., Wang, J., Yan, F., Yang, S.: High-performance hole-extraction layer of Sol–Gel-processed NiO nanocrystals for inverted planar perovskite solar cells. Angew. Chem. Int. Ed. **53,** 12571–12575 (2014)
44. You, J., Meng, L., Song, T.-B., Guo, T.-F., Yang, Y., Chang, W.-H., Hong, Z., Chen, H., Zhou, H., Chen, Q., Liu, Y., Marco, N.D., Yang, Y.: Improved air stability of perovskite solar cells via solution-processed metal oxide transport layers. Nat. Nanotechnol. **11**, 75–81 (2016)
45. Wang, K.-C., Shen, P.-S., Li, M.-H., Chen, S., Lin, M.-W., Chen, P., Guo, T.-F.: Low-temperature sputtered nickel oxide compact thin film as effective electron blocking layer for mesoscopic $NiO/CH_3NH_3PbI_3$ perovskite heterojunction solar cells. ACS Appl. Mater. Interfaces **6**, 11851–11858 (2014)
46. Cui, J., Meng, F., Zhang, H., Cao, K., Yuan, H., Cheng, Y., Huang, F., Wang, M.: $CH_3NH_3PbI_3$-based planar solar cells with magnetron-sputtered nickel oxide. ACS Appl. Mater. Interfaces **6**, 22862–22870 (2014)
47. Park, J.H., Seo, J., Park, S., Shin, S.S., Kim, Y.C., Jeon, N.J., Shin, H.-W., Ahn, T.K., Noh, J. H., Yoon, S.C., Hwang, C.S., Seok, S.I.: Efficient $CH_3NH_3PbI_3$ perovskite solar cells employing nanostructured p-Type NiO electrode formed by a pulsed laser deposition. Adv. Mater. **27**, 4013–4019 (2015)
48. Kim, J.H., Liang, P.-W., Williams, S.T., Cho, N., Chueh, C.-C., Glaz, M.S., Ginger, D.S., Jen, A.K.-Y.: High-performance and environmentally stable planar heterojunction perovskite solar cells based on a solution-processed copper-doped nickel oxide hole-transporting layer. Adv. Mater. **27**, 695–701 (2015)
49. Chen, W., Wu, Y., Liu, J., Qin, C., Yang, X., Islam, A., Cheng, Y.-B., Han, L.: Hybrid interfacial layer leads to solid performance improvement of inverted perovskite solar cells. Energy Environ. Sci. **8**, 629–640 (2015)
50. Chen, W., Wu, Y., Yue, Y., Liu, J., Zhang, W., Yang, X., Chen, H., Bi, E., Ashraful, I., Grätzel, M., Han, L.: Efficient and stable large-area perovskite solar cells with inorganic charge extraction layers. Science **350**, 944–948 (2015)
51. Park, I.J., Park, M.A., Kim, D.H., Park, G.D., Kim, B.J., Son, H.J., Ko, M.J., Lee, D.-K., Park, T., Shin, H., Park, N.-G., Jung, H.S., Kim, J.Y.: New hybrid hole extraction layer of perovskite solar cells with a planar p-i-n geometry. J. Phys. Chem. C **119**, 27285–27290 (2015)
52. Liu, Z., Zhang, M., Xu, X., Bu, L., Zhang, W., Li, W., Zhao, Z., Wang, M., Chenga, Y.-B., He, H.: p-Type mesoscopic NiO as an active interfacial layer for carbon counter electrode based perovskite solar cells. Dalton Trans. **44**, 3967–3973 (2015)
53. Xu, X., Liu, Z., Zuo, Z., Zhang, M., Zhao, Z., Shen, Y., Zhou, H., Chen, Q., Yang, Y., Wang, M.: Hole selective NiO contact for efficient perovskite solar cells with carbon electrode. Nano Lett. **15**, 2402–2408 (2015)
54. Cao, K., Zuo, Z., Cui, J., Shen, Y., Moehl, T., Zakeeruddin, S.M., Grätzel, M., Wang, M.: Efficient screen printed perovskite solar cells based on mesoscopic $TiO_2/Al_2O_3/NiO$/carbon architecture. Nano Energy **17**, 171–179 (2015)
55. Zhao, Y., Nardes, A.M., Zhu, K.: Effective hole extraction using MoOx-Al contact in perovskite $CH_3NH_3PbI_3$ solar cells. Appl. Phys. Lett. **104**, 213906 (2014)

56. Liang, L., Huang, Z., Cai, L., Chen, W., Wang, B., Chen, K., Bai, H., Tian, Q., Fan, B.: Magnetron sputtered zinc oxide nanorods as thickness-insensitive cathode interlayer for perovskite planar-heterojunction solar cells. ACS Appl. Mater. Interfaces **6**, 20585–20589 (2014)
57. Hou, F., Su, Z., Jin, F., Yan, X., Wang, L., Zhao, H., Zhu, J., Chu, B., Lia, W.: Efficient and stable planar heterojunction perovskite solar cells with an MoO_3/PEDOT:PSS hole transporting layer. Nanoscale **7**, 9427 (2015)
58. Löper, P., Moon, S.-J., Nicolas, S.M., Niesen, B., Ledinsky, M., Nicolay, S., Bailat, J., Yum, J.-H., Wolf, S.D., Ballif, C.: Organic–inorganic halide perovskite/crystalline silicon four-terminal tandem solar cells. Phys. Chem. Chem. Phys. **17**, 1619–1629 (2015)
59. Kim, B.-S., Kim, T.-M., Choi, M.-S., Shim, H.-S., Kim, J.-J.: Fully vacuum–processed perovskite solar cells with high open circuit voltage using MoO_3/NPB as hole extraction layers. Org. Electron. **17**, 102–106 (2015)
60. Batmunkh, M., Shearer, C.J., Biggs, M.J., Shapter, J.G.: Nanocarbons for mesoscopic perovskite solar cells. J. Mater. Chem. A **3**, 9020–9031 (2015)
61. Zhou, H., Shi, Y., Dong, Q., Zhang, H., Xing, Y., Wang, K., Du, Y., Ma, T.: Hole-conductor-free, metal-electrode-free TiO_2/$CH_3NH_3PbI_3$ heterojunction solar cells based on a low-temperature carbon electrode. J. Phys. Chem. Lett. **5**, 3241–3246 (2014)
62. Zhou, H., Shi, Y., Wang, K., Dong, Q., Bai, X., Xing, Y., Du, Y., Ma, T.: Low-temperature processed and carbon-based ZnO/$CH_3NH_3PbI_3$/C planar heterojunction perovskite solar cells. J. Phys. Chem. C **119**, 4600–4605 (2015)
63. Wei, Z., Chen, H., Yan, K., Yang, S.: Inkjet printing and instant chemical transformation of a $CH_3NH_3PbI_3$/nanocarbon electrode and interface for planar perovskite solar cells. Angew. Chem. Int. Ed. **53**, 13239–23243 (2014)
64. Chen, H., Wei, Z., Yan, K., Yi, Y., Wang, J., Yang, S.: Liquid phase deposition of TiO_2 nanolayer affords $CH_3NH_3PbI_3$/nanocarbon solar cells with high open-circuit voltage. Faraday Discuss. **176**, 271–286 (2014)
65. Wei, Z., Yan, K., Chen, H., Yi, Y., Zhang, T., Long, X., Li, J., Zhang, L., Wang, J., Yang, S.: Cost-efficient clamping solar cells using candle soot for hole extraction from ambipolar perovskites. Energy Environ. Sci. **7**, 3326–3333 (2014)
66. Zhang, F., Yang, X., Wang, H., Cheng, M., Zhao, J., Sun, L.: Structure engineering of hole-conductor free perovskite-based solar cells with low-temperature-processed commercial carbon paste as cathode. ACS Appl. Mater. Interfaces **6**, 16140–16146 (2014)
67. Wei, H., Xiao, J., Yang, Y., Lv, S., Shi, J., Xu, X., Dong, J., Luo, Y., Li, D., Meng, Q.: Free-standing flexible carbon electrode for highly efficient hole-conductor-free perovskite solar cells. Carbon **93**, 861–868 (2015)
68. Yang, Y., Xiao, J., Wei, H., Zhu, L., Li, D., Luo, Y., Wu, H., Meng, Q.: An all-carbon counter electrode for highly efficient hole-conductor-free organo-metal perovskite solar cells. RSC Adv. **4**, 52825–52830 (2014)
69. Wu, Z., Bai, S., Xiang, J., Yuan, Z., Yang, Y., Cui, W., Gao, X., Liu, Z., Jin, Y., Sun, B.: Efficient planar heterojunction perovskite solar cells employing graphene oxide as hole conductor. Nanoscale **6**, 10505–10510 (2014)
70. Li, Z., Kulkarni, S.A., Boix, P.P., Shi, E., Cao, A., Fu, K., Batabyal, S.K., Zhang, J., Xiong, Q., Wong, L.H., Mathews, N., Mhaisalkar, S.G.: Laminated carbon nanotube networks for metal electrode-free efficient perovskite solar cells. ACS Nano **8**, 6797–6804 (2014)
71. Yeo, J.-S., Kang, R., Lee, S., Jeon, Y.-J., Myoung, N., Lee, C.-L., Kim, D.-Y., Yun, J.-M., Seo, Y.-H., Kim, S.-S., Na, S.-I.: Highly efficient and stable planar perovskite solar cells with reduced graphene oxide nanosheets as electrode interlayer. Nano Energy **12**, 96–104 (2015)
72. Yan, K., Wei, Z., Li, J., Chen, H., Yi, Y., Zheng, X., Long, X., Wang, Z., Wang, J., Xu, J., Yang, S.: High-performance graphene-based hole conductor-free perovskite solar cells: Schottky junction enhanced hole extraction and electron blocking. Small **11**, 2269–2274 (2015)

73. Cao, J., Liu, Y.-M., Jing, X., Yin, J., Li, J., Xu, B., Tan, Y.-Z., Zheng, N.: Well-defined thiolated nanographene as hole-transporting material for efficient and stable perovskite solar cells. J. Am. Chem. Soc. **137**, 10914–10917 (2015)
74. Li, W., Dong, H., Guo, X., Li, N., Li, J., Niu, G., Wang, L.: Graphene oxide as dual functional interface modifier for improving wettability and retarding recombination in hybrid perovskite solar cells. J. Mater. Chem. A **2**, 20105–20111 (2014)
75. You, P., Liu, Z., Tai, Q., Liu, S., Yan, F.: Efficient semitransparent perovskite solar cells with graphene electrodes. Adv. Mater. **24**, 3632–3638 (2015)
76. Lang, F., Gluba, M.A., Albrecht, S., Rappich, J., Korte, L., Rech, B., Nickel, N.H.: Perovskite solar cells with large-area CVD-graphene for tandem solar cells. J. Phys. Chem. Lett. **6**, 2745–2750 (2015)
77. Jeon, I., Chiba, T., Delacou, C., Guo, Y., Kaskela, A., Reynaud, O., Kauppinen, E.I., Maruyama, S., Matsuo, Y.: Single-walled carbon nanotube film as electrode in indium-free planar heterojunction perovskite solar cells: investigation of electron-blocking layers and dopants. Nano Lett. **15**, 6665–6671 (2015)
78. Wang, X., Li, Z., Xu, W., Kulkarni, S.A., Batabyal, S.K., Zhang, S., Cao, A., Wong, L.H.: TiO_2 nanotube arrays based flexible perovskite solar cells with transparent carbon nanotube electrode. Nano Energy **11**, 728–735 (2015)
79. Liu, T., Kim, D., Han, H., Yusoff, A.R.b.M., Jang, J.: Fine-tuning optical and electronic properties of graphene oxide for highly efficient perovskite solar cells. Nanoscale **7**, 10708–10718 (2015)
80. Habisreutinger, S.N., Leijtens, T., Eperon, G.E., Stranks, S.D., Nicholas, R.J., Snaith, H.J.: Enhanced hole extraction in perovskite solar cells through carbon nanotubes. J. Phys. Chem. Lett. **5**, 4207–4212 (2014)
81. Habisreutinger, S.N., Leijtens, T., Eperon, G.E., Stranks, S.D., Nicholas, R.J., Snaith, H.J.: Carbon nanotube/polymer composites as a highly stable hole collection layer in perovskite solar cells. Nano Lett. **14**, 5561–5568 (2014)
82. Cai, M., Tiong, V.T., Hreid, T., Bell, J., Wang, H.: An efficient hole transport material composite based on poly(3-hexylthiophene) and bamboo-structured carbon nanotubes for high performance perovskite solar cells. J. Mater. Chem. A **3**, 2784–2793 (2015)
83. Lee, J., Menamparambath, M.M., Hwang, J.-Y., Baik, S.: Hierarchically structured hole transport layers of spiro-OMeTAD and multiwalled carbon nanotubes for perovskite solar cells. ChemSusChem. **8**, 2358–2362 (2015)
84. Luo, Q., Zhang, Y., Liu, C., Li, J., Wang, N., Lin, H.: Iodide-reduced graphene oxide with dopant-free spiro-OMeTAD for ambient stable and high-efficiency perovskite solar cells. J. Mater. Chem. A **3**, 15996–16004 (2015)